frontiers | Research Topics

Community series in translational insights into mechanisms and therapy of organ dysfunction in sepsis and trauma, volume III, 2nd edition

Edited by
Christoph Thiemermann, Bettina Jungwirth, Valentin A. Pavlov, Pietro Ghezzi, Madhav Bhatia, Borna Relja and Sina M. Coldewey

Published in
Frontiers in Immunology

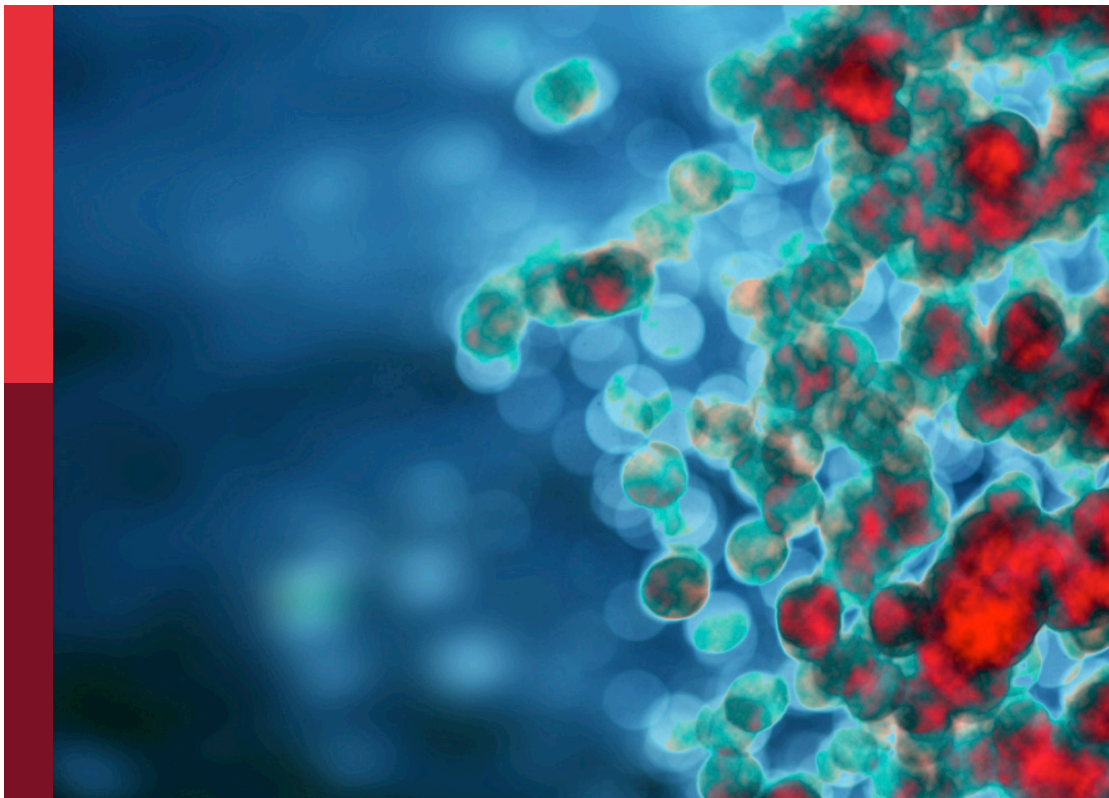

ISSN 1664-8714
ISBN 978-2-8325-5688-7
DOI 10.3389/978-2-8325-5688-7

About Frontiers

Frontiers is more than just an open access publisher of scholarly articles: it is a pioneering approach to the world of academia, radically improving the way scholarly research is managed. The grand vision of Frontiers is a world where all people have an equal opportunity to seek, share and generate knowledge. Frontiers provides immediate and permanent online open access to all its publications, but this alone is not enough to realize our grand goals.

Frontiers journal series

The Frontiers journal series is a multi-tier and interdisciplinary set of open-access, online journals, promising a paradigm shift from the current review, selection and dissemination processes in academic publishing. All Frontiers journals are driven by researchers for researchers; therefore, they constitute a service to the scholarly community. At the same time, the *Frontiers journal series* operates on a revolutionary invention, the tiered publishing system, initially addressing specific communities of scholars, and gradually climbing up to broader public understanding, thus serving the interests of the lay society, too.

Dedication to quality

Each Frontiers article is a landmark of the highest quality, thanks to genuinely collaborative interactions between authors and review editors, who include some of the world's best academicians. Research must be certified by peers before entering a stream of knowledge that may eventually reach the public - and shape society; therefore, Frontiers only applies the most rigorous and unbiased reviews. Frontiers revolutionizes research publishing by freely delivering the most outstanding research, evaluated with no bias from both the academic and social point of view. By applying the most advanced information technologies, Frontiers is catapulting scholarly publishing into a new generation.

What are Frontiers Research Topics?

Frontiers Research Topics are very popular trademarks of the *Frontiers journals series*: they are collections of at least ten articles, all centered on a particular subject. With their unique mix of varied contributions from Original Research to Review Articles, Frontiers Research Topics unify the most influential researchers, the latest key findings and historical advances in a hot research area.

Find out more on how to host your own Frontiers Research Topic or contribute to one as an author by contacting the Frontiers editorial office: frontiersin.org/about/contact

Community series in translational insights into mechanisms and therapy of organ dysfunction in sepsis and trauma, volume III, 2nd edition

Topic editors

Christoph Thiemermann — Queen Mary University of London, United Kingdom
Bettina Jungwirth — Ulm University Medical Center, Germany
Valentin A. Pavlov — Northwell Health, United States
Pietro Ghezzi — University of Urbino Carlo Bo, Italy
Madhav Bhatia — University of Otago, New Zealand
Borna Relja — Universitätsklinikum Ulm, Germany
Sina M. Coldewey — Jena University Hospital, Germany

Citation

Thiemermann, C., Jungwirth, B., Pavlov, V. A., Ghezzi, P., Bhatia, M., Relja, B., Coldewey, S. M., eds. (2024). *Community series in translational insights into mechanisms and therapy of organ dysfunction in sepsis and trauma, volume III, 2nd edition*. Lausanne: Frontiers Media SA. doi: 10.3389/978-2-8325-5688-7

Publisher's note: This is a 2nd edition due to an article retraction.

Table of contents

frontiers | Frontiers in Immunology

TYPE Editorial
PUBLISHED 11 July 2024
DOI 10.3389/fimmu.2024.1447892

OPEN ACCESS

EDITED AND REVIEWED BY
Rudolf Lucas,
Augusta University, United States

*CORRESPONDENCE
Borna Relja
info@bornarelja.com

RECEIVED 12 June 2024
ACCEPTED 04 July 2024
PUBLISHED 11 July 2024

CITATION
Relja B, Ghezzi P, Coldewey SM, Pavlov VA, Bhatia M, Jungwirth B and Thiemermann C (2024) Editorial: Community series in translational insights into mechanisms and therapy of organ dysfunction in sepsis and trauma - volume III. *Front. Immunol.* 15:1447892. doi: 10.3389/fimmu.2024.1447892

Editorial: Community series in translational insights into mechanisms and therapy of organ dysfunction in sepsis and trauma - volume III

Borna Relja[1]*, Pietro Ghezzi[2], Sina M. Coldewey[3], Valentin A. Pavlov[4], Madhav Bhatia[5], Bettina Jungwirth[6] and Christoph Thiemermann[7]

[1]Department of Trauma, Hand, Plastic and Reconstructive Surgery, Translational and Experimental Trauma Research, University Hospital Ulm, Ulm University, Ulm, Germany, [2]University of Urbino Carlo Bo, Urbino, Italy, [3]University Hospital Jena, Jena, Germany, [4]Feinstein Institutes for Medical Research, Manhasset, NY, United States, [5]Department of Pathology and Biomedical Science, University of Otago, Christchurch, New Zealand, [6]Department of Anesthesiology and Intensive Care Medicine, University Hospital Ulm, Ulm University, Ulm, Germany, [7]Queen Mary University of London, London, United Kingdom

KEYWORDS

critical care (7/8), organ failure, therapy, diagnosis, mechanisms, machine learning

Editorial on the Research Topic
Community series in translational insights into mechanisms and therapy of organ dysfunction in sepsis and trauma - volume III

Translational research on trauma, sepsis, and multiple organ damage is continuously evolving, fostering advancements in the development of diagnostics and therapeutics, and improving our understanding of the complex pathophysiological mechanisms underlying these life-threatening conditions. The contributors of this Research Topic explore the different aspects of the pathophysiology of trauma and critical illness. With different approaches, these studies describe novel potential diagnostic markers, innovative therapeutic interventions, and elucidate the complex mechanisms underlying immune responses and organ damage in patients with trauma, sepsis and/or multiple organ failure.

Life-threatening organ dysfunction and failure in trauma and critically ill patients stem from a dysregulated host response to infection and inflammation. Despite advancements in understanding the key signaling pathways involved, translating this knowledge into organ-protective therapies remains challenging. Current treatments primarily rely on infection control, antibiotics, supportive care, and early goal-directed therapy.

Trauma and sepsis-induced organ dysfunction are driven by excessive systemic inflammation, secondary to tissue damage and ischemia-reperfusion injury. The endothelial glycocalyx is a critical early site involved in triggering a pro-inflammatory response. Alterations in its structure lead to the release of degradation products and damage-associated molecular patterns (DAMPs) that, along with pathogen-associated molecular patterns (PAMPs), amplify systemic inflammation and, hence, contribute to organ dysfunction including acute kidney injury, respiratory failure, and cardiomyopathy.

Three major fields of research have been covered by the authors

First, in terms of sepsis diagnosis and treatment, Dennhardt et al. investigate the clinical significance of circulating cell-free DNA (cfDNA) levels in sepsis patients as predictors of both mortality and sepsis-associated acute kidney injury, suggesting elevated cfDNA levels as a potential enhancer of risk assessment in sepsis. Similarly, Qiang et al. explore the therapeutic potential of progesterone in sepsis, presenting promising results in septic mice and patients by inhibiting procathepsin-L-mediated inflammation. Guggemos et al. investigate the impact of specific polymorphisms of the ATP-sensitive P2X7 receptor on sepsis susceptibility and prognosis, revealing their potential role as genetic markers. Wakeley et al. examine the role of Herpes virus entry mediator in neonatal sepsis response, highlighting its importance in vascular and hemodynamic resilience, while Kasper et al. study the effects of hemadsorption therapy on endothelial barrier dysfunction in sepsis *in vitro*, indicating its potential transient clinical improvement.

Second, with a focus on trauma, injury, and organ damage, Horner et al. explore the immune suppressive role of DAMPs in sterile traumatic injury, proposing potential therapeutic strategies to mitigate immune suppression in their review. Wolfschmitt et al. investigate the impact of hyperoxemia on the metabolism of circulating immune cells during intensive care, focusing on granulocytes in models of acute subdural hematoma and hemorrhagic shock. Groven et al. explore the association between circulating miRNA expression in extracellular vesicles (EVs) as biomarkers for specific injuries following multiple trauma and surgical invasiveness. Meng et al. investigate how aging influences liver inflammation and damage after trauma, highlighting dysregulated immune responses, while Zhou et al. examine the exacerbation of lung damage after trauma in aged mice, focusing on the role of NF-κB and inflammasomes. Neu et al. explore the cardiovascular impairment in a murine model of hemolytic-uremic syndrome induced by Shiga toxin, a model which replicates the extrarenal manifestations observed in HUS patients. Fachet et al. propose a feature-based risk assessment system for predicting hyperinflammatory patterns and infectious outcomes in polytrauma patients using predictive machine learning modeling.

The third part of this Research Topic addresses therapeutic interventions and drug repurposing. Verra et al. investigate the effects of baricitinib, a JAK1/JAK2 inhibitor, on sepsis-induced cardiac dysfunction and multiple-organ failure, suggesting its potential for trauma-associated sepsis. Hof et al. study the effects of carbachol on gastric and oral microcirculation during hemorrhagic shock in dogs, highlighting its potential therapeutic use in improving tissue oxygenation. Yamaga et al. discuss potential therapeutic strategies targeting DAMPs to alleviate radiation-induced injury, focusing on the mechanisms of DAMP release and their detrimental effects on the immune system. To advance our understanding of critical illness, Li et al. identify key genes and pathways associated with DNA damage responses, inflammation, and cellular senescence in elderly patients with acute respiratory distress syndrome, offering insights into potential diagnostic biomarkers and therapeutic targets. Murao et al. utilize single-cell RNA sequencing to investigate immune cell responses in sepsis, providing insights into distinct immune cell subsets and their roles in inflammation and tissue repair, thus enhancing our understanding of the pathophysiology of sepsis. Wang et al. conducted the LiBOD study to assess the potential of serum-derived EVs as biomarkers for decision-making in polytrauma cases, suggesting specific EVs as valuable biomarkers for assessing and monitoring the severity of polytrauma and associated organ damage.

These studies collectively contribute to a better understanding of diagnostic markers, therapeutic interventions, immune responses, and the mechanisms underlying organ injury and dysfunction in trauma, sepsis, and related conditions, offering potential avenues for improving care and outcomes of patients with critical illness.

As we review the research presented in this Research Topic, it is clear how scientific research significantly shapes the field of trauma and critical care medicine, addressing the issue of improving patient outcomes, moving towards precision medicine in intensive care.

We conclude this Research Topic with deep gratitude to the researchers, clinicians, and patients whose dedication has made this work possible. We hope the insights from these studies will be interesting and educational to our readers and help developing this area of research on a challenging condition.

Author contributions

BR: Writing – original draft. PG: Writing – review & editing. SC: Writing – review & editing. VP: Writing – review & editing. MB: Writing – review & editing. BJ: Writing – review & editing. CT: Writing – review & editing.

Conflict of interest

The authors declare that the research was conducted in the absence of any commercial or financial relationships that could be construed as a potential conflict of interest.

The author(s) declared that they were an editorial board member of Frontiers, at the time of submission. This had no impact on the peer review process and the final decision.

Publisher's note

frontiers | Frontiers in Immunology

TYPE Review
PUBLISHED 15 August 2023
DOI 10.3389/fimmu.2023.1239683

OPEN ACCESS

EDITED BY
Christoph Thiemermann,
Queen Mary University of London,
United Kingdom

REVIEWED BY
Marcin Filip Osuchowski,
Ludwig Boltzmann Institute for Experimental and Clinical Traumatology, Austria
Tomasz Skirecki,
Medical Centre for Postgraduate Education, Poland

*CORRESPONDENCE
Jon Hazeldine
j.hazeldine@bham.ac.uk

RECEIVED 13 June 2023
ACCEPTED 31 July 2023
PUBLISHED 15 August 2023

CITATION
Horner E, Lord JM and Hazeldine J (2023) The immune suppressive properties of damage associated molecular patterns in the setting of sterile traumatic injury. *Front. Immunol.* 14:1239683. doi: 10.3389/fimmu.2023.1239683

The immune suppressive properties of damage associated molecular patterns in the setting of sterile traumatic injury

Emily Horner[1], Janet M. Lord[1,2] and Jon Hazeldine[1,2]*

[1]Institute of Inflammation and Ageing, University of Birmingham, Birmingham, United Kingdom, [2]National Institute for Health Research Surgical Reconstruction and Microbiology Research Centre, Queen Elizabeth Hospital Birmingham, Birmingham, United Kingdom

Associated with the development of hospital-acquired infections, major traumatic injury results in an immediate and persistent state of systemic immunosuppression, yet the underlying mechanisms are poorly understood. Detected in the circulation in the minutes, days and weeks following injury, damage associated molecular patterns (DAMPs) are a heterogeneous collection of proteins, lipids and DNA renowned for initiating the systemic inflammatory response syndrome. Suggesting additional immunomodulatory roles in the post-trauma immune response, data are emerging implicating DAMPs as potential mediators of post-trauma immune suppression. Discussing the results of *in vitro, in vivo* and *ex vivo* studies, the purpose of this review is to summarise the emerging immune tolerising properties of cytosolic, nuclear and mitochondrial-derived DAMPs. Direct inhibition of neutrophil antimicrobial activities, the induction of endotoxin tolerance in monocytes and macrophages, and the recruitment, activation and expansion of myeloid derived suppressor cells and regulatory T cells are examples of some of the immune suppressive properties assigned to DAMPs so far. Crucially, with studies identifying the molecular mechanisms by which DAMPs promote immune suppression, therapeutic strategies that prevent and/or reverse DAMP-induced immunosuppression have been proposed. Approaches currently under consideration include the use of synthetic polymers, or the delivery of plasma proteins, to scavenge circulating DAMPs, or to treat critically-injured patients with antagonists of DAMP receptors. However, as DAMPs share signalling pathways with pathogen associated molecular patterns, and pro-inflammatory responses are essential for tissue regeneration, these approaches need to be carefully considered in order to ensure that modulating DAMP levels and/or their interaction with immune cells does not negatively impact upon anti-microbial defence and the physiological responses of tissue repair and wound healing.

KEYWORDS

critical care, damage associated molecular patterns, immunosuppression, innate immunity, trauma

1 Introduction

Accounting for an estimated 16% of the global burden of disease (1), and the leading cause of death in individuals aged ≤44 years (2), traumatic injuries are a significant cause of morbidity and mortality. However, due in part to advances in trauma medicine, most notably in the management of coagulopathy where haemorrhage-induced deaths have fallen by more than 12% since the 1980s (3), the likelihood of patients surviving the initial effects of a severe trauma is increasing (4). Consequently, it is the onset of secondary complications such as multiple organ failure (MOF), multiple organ dysfunction syndrome (MODS) and nosocomial infections that are emerging as major determinants of clinical outcomes. Indeed, when compared to those with non-eventful episodes, trauma patients who develop MOF, MODS or hospital-acquired infections (HAIs) experience increased lengths of intensive care unit stay, require prolonged mechanical ventilation, report poorer physical and psychological recovery, and are less likely to return to work (5–10). Of these secondary complications, HAIs are highly prevalent (5, 6, 11–14) and remain a significant clinical challenge, with one recent study estimating that the prevention of pneumonia amongst hospitalised trauma patients would reduce the incidence of end organ dysfunction, mortality and the need for mechanical ventilation by 22.1%, 7.8% and 6.8% respectively (13).

Two opposing and concurrent syndromes underpin the immune and inflammatory response to major trauma. With the intention of localising and eliminating endogenous stressors, and promoting wound repair, a systemic inflammatory response syndrome (SIRS) is triggered within minutes of injury (15). Associated with such physiological changes as tachycardia and tachypnea, the SIRS response is characterised by elevated levels of circulating pro-inflammatory cytokines and immune cell activation. To counteract this state of systemic hyperinflammation, the SIRS response is accompanied by a compensatory anti-inflammatory response syndrome (CARS) (16). Defined in part by raised circulating levels of anti-inflammatory cytokines, lymphocyte apoptosis and decreased cytokine production by endotoxin challenged monocytes, the concomitant CARS response aims to restore immunological homeostasis (17). Over the past decade, it has become increasingly evident that the kinetics of the simultaneous SIRS and CARS responses markedly influence the clinical trajectories of hospitalised trauma patients, with robust, dysregulated and prolonged SIRS/CARS responses associated with delayed physical recovery, organ dysfunction, an increased risk of nosocomial infections and mortality (16, 18, 19). Furthermore, failure to resolve trauma-induced inflammatory responses can lead to the development of persistent inflammation, immunosuppression and catabolism syndrome (PICS). Detected in >40% of patients with chronic critical illness, PICS has been suggested to have replaced MOF as the predominant phenotype of chronic critical illness (20–23). Characterised by lymphopenia, neutrophilia, a persistent acute phase response and ongoing protein catabolism, the development of PICS predisposes to recurrent HAIs, poor wound healing and a greater need for post-discharge rehabilitation in long-term care facilities (20–24).

Hypothesising that factors released into the circulation or present in wound fluids may modulate the local and systemic immune response to sterile injury, several groups have investigated the phenotypic and functional consequences of culturing immune cells isolated from healthy subjects or mice with plasma, serum or wound fluids obtained from their injured counterparts (25–28). Compared to control samples, plasma acquired from trauma patients at day 1 post-injury, wound fluids obtained either 3- or 6-hours post-surgery or from closed drains in injury sites, and serum collected from mice within 30 minutes of injury, were found to promote the expansion of both $CD8^+$ T cells and $CD11c^+$ Natural Killer (NK) cells, and to suppress the anti-microbial responses of neutrophils and monocytes (25–28). These are all features reminiscent of the trauma associated SIRS and CARS responses (15, 29–31). Whilst recognising that a multitude of factors are present in the circulation of trauma patients, the authors suggested a potential role for damage associated molecular patterns (DAMPs) in mediating the effects they observed (25, 26, 28). Detected in the circulation of major trauma patients in the minutes, hours and days following injury (30–33), DAMPs, also known as alarmins, are a heterogeneous collection of cytosolic, nuclear and mitochondrial-derived lipids, proteins and DNA. Passively released from damaged/necrotic tissue, and actively secreted by immune cells (34, 35), DAMPs are detected primarily by pathogen recognition receptors (PRRs), particularly members of the Toll-like receptor (TLR) family (36) (Table 1). To date, much attention has focussed on the immune stimulatory properties of DAMPs (69, 70), with studies showing that *in vitro* exposure to mitochondrial, nuclear and cytosolic-derived DAMPs can trigger ROS generation, degranulation, formation of extracellular traps and the production of pro-inflammatory cytokines by neutrophils, monocytes, macrophages and invariant NKT cells (33, 71–75). Similar pro-inflammatory responses have also been observed in animal studies, where administration of mitochondrial-derived DAMPs (mtDAMPs) has been shown to increase plasma cytokine concentrations and activate neutrophils, systemic responses that result in immune-mediated organ injury (33, 76). Importantly, these observations are aligned with the results of prospective studies of trauma patients, where elevated circulating concentrations of mitochondrial-derived DNA (mtDNA) and the nuclear-derived DAMP high mobility group box-1 (HMGB-1) are associated with the development of SIRS and MODS (76–80).

Interestingly, in addition to their widely accepted role as instigators of the SIRS response, data are emerging that implicates DAMPs as potential mediators of the CARS response, with *in vitro* studies demonstrating that neutrophils and monocytes pre-treated with cytosolic and/or mitochondrial-derived DAMPs exhibit a state of functional tolerance upon secondary stimulation with such inflammatory agonists as bacterial endotoxins and chemokines (30, 35, 41, 61, 65, 81–83) (Table 1). This DAMP-induced immune suppression may also extend to the adaptive arm of the immune system, where it has been suggested that, by promoting interleukin-4 production and T helper 2 immunity, DAMPs may suppress pro-inflammatory T helper 1 responses (81, 84). Alongside DAMPs that are passively released from damaged/necrotic tissue, a novel class of *de novo* synthesised DAMPs with immunosuppressive properties, termed suppressing/inhibiting inducible DAMPs

10.3389/fimmu.2023.1239683

TABLE 1 Summary of the immune suppressive properties of DAMPs.

DAMP	Receptor	Immune suppressive properties	References
Cytosolic			
Heme	TLR4	Decreases TLR2 and TLR4 expression on neutrophils. Inhibits neutrophil ROS production. Suppresses macrophage phagocytic activity.	(27, 37)
HSPs	TLR4, TLR9	Reduces LPS-induced TNF production by monocytes. Inhibits NF-κB signalling. Impairs DC maturation. Enhances immune suppressive activity of Tregs.	(28, 38–40)
S100 proteins	TLR2, TLR4, RAGE	Induces endotoxin tolerance in monocytes. Inhibits p38 MAPK signalling in monocytes. Decreases antigen presentation by DCs. Suppresses neutrophil ROS production. Chemoattractant for MDSCs.	(41–46)
Nuclear			
CIRP	TLR4, TREM-1	Induces endotoxin tolerance in macrophages. Promotes M2 polarisation in macrophages.	(47)
IL-33	ST2	Stimulates IL-5 production and arginase-1 expression in neutrophils. Promotes expansion of ILC2 cells. Induces immune suppressive functions in neutrophils. Drives expansion of IL-10 secreting M2 macrophages. Promotes accumulation of Tregs.	(48–50)
HMGB-1	TLR2, TLR4, TREM-1, RAGE	Suppresses NF-B signalling. Reduces pro-inflammatory cytokine production by macrophages. Decreases macrophage phagocytic activity. Inhibits neutrophil ROS production. Promotes survival, migration and suppressive activity of Tregs. Activates and prolongs survival of MDSCs.	(51–56)
Mitochondrial			
ATP/adenosine	A_{2A}	Inhibits neutrophil phagocytosis, ROS production, degranulation and cytokine production. Suppresses T cell migration and IFN-γ production. Decreases T cell priming by DCs. Inhibits NK cell cytotoxicity. Induces endotoxin tolerance in macrophages.	(57–60)
mtDNA	TLR9	Reduces pro-inflammatory cytokine production by LPS-challenged monocytes. Induces IRAK-M expression in monocytes. Inhibits neutrophil chemotaxis, phagocytosis and bacterial killing. Suppresses activation of CTTN. Promotes IL-10 production by DCs.	(35, 61, 62, 63, 64)
mtFPs	FPR1, FPR2	Decreases neutrophil calcium fluxes. Suppresses neutrophil chemotaxis and ROS production. Downregulates GPCR expression. Inhibits NET formation.	(30, 65–68)

ATP, Adenosine triphosphate; CIRP, Cold-inducible RNA binding protein; CTTN, Cortactin; DAMPs, Damage associated molecular patterns; DC, Dendritic cell; FPR, Formyl peptide receptor; GPCR, G-protein coupled receptor; HMGB-1, High mobility group box-1; HSP, Heat shock protein; IFN, Interferon; IL, Interleukin; ILC2, Group 2 innate lymphoid cells; IRAK-M, Interleukin 1 receptor associated kinase-M; LPS, Lipopolysaccharide; MAPK, Mitogen activated protein kinase; MDSC, Myeloid derived suppressor cell; mtDNA, Mitochondrial-derived DNA; mtFPs, Mitochondrial-derived formyl peptides; NF-κB, Nuclear factor-κβ; RAGE, Receptor for advanced glycation endproducts; ROS, Reactive oxygen species; ST2, Suppression of tumorigenicity; TLR, Toll-like receptor; Treg, Regulatory T cell; TREM-1, Triggering receptor expressed on myeloid cells-1.

(SAMPs), have recently been described. Produced by activated leukocytes, SAMPs, which include prostaglandin E2 and Annexin A1, have been suggested to promote exaggerated anti-inflammatory and hyper-resolution responses that culminate in systemic immunosuppression (82). Thus, exaggerated and/or persistent DAMP driven resolution responses may predispose the hospitalised trauma patient to the development of secondary infections (82). Supporting this idea, a study of 166 adult trauma patients found plasma levels of both mtDNA and cell-free nuclear DNA (used as a generic readout for cell damage and death) were significantly higher at hospital admission in subjects who subsequently developed an infection within 28 days (31). Moreover, the authors reported that plasma concentrations of the cytosolic DAMP, heat shock protein-70 (HSP-70), and nuclear DNA (nDNA) both correlated negatively with the expression of HLA-DR on monocytes (31), a marker of immune competence whose downregulation is associated with a higher risk of nosocomial infections in critically ill patients (85–87).

Proposed as a potential explanation for the failures of randomised clinical trials that have tested the practicalities and benefits of immunomodulatory interventions for the treatment of critically-ill patients, compartmentalisation is a concept that refers to how immune responses differ between anatomical sites within the body (88). Examples of compartmentalisation include the varied phenotypic and morphological features described for neutrophils isolated from the blood and lungs of patients with acute respiratory distress syndrome (ARDS) (89), and the different mediators that drive the phagocytic dysfunction of peripheral blood and alveolar residing neutrophils in critically ill patients (90). To date, almost all studies that have investigated DAMP-induced immunosuppression in an *ex vivo* setting have examined the functional and phenotypic features of circulating leukocytes. Thus, whilst one may assume that DAMPs, whose concentrations at sites of tissue damage exceed those measured in the circulation (91), would also suppress localised immune responses, there is a current paucity of information on whether DAMPs can modulate the behaviours of tissue resident immune cells. That said, with results from a small number of studies demonstrating a role for DAMPs in the impaired *ex vivo* responses of macrophages and T cells (47, 48, 92), and in promoting the expansion of tissue resident myeloid-derived suppressor cells (MDSCs) (93), it does appear that the release of DAMPs from damaged tissue may contribute to the immune dysfunction that develops in different tissue spaces following major trauma.

Bringing together data generated from *in vitro, in vivo* and *ex vivo* studies, the purpose of this review is to summarise our current understanding of DAMP-induced immunosuppression in the setting of sterile injury. The immune suppressive properties of cytosolic, nuclear and mitochondrial-derived DAMPs will be discussed, and where identified, their underlying mechanisms described. Furthermore, with the aim of reducing the susceptibility of critically-ill patients to HAIs, we will highlight the therapeutic strategies that are under consideration as potential approaches for preventing or reversing DAMP-induced immunosuppression.

2 Immunosuppressive properties of DAMPs

2.1 Cytosolic-derived DAMPs

2.1.1 Heme

Heme is an iron containing porphyrin synthesised in the cytosol and mitochondria of erythrocytes. Acting as the prosthetic group for such hemoproteins as haemoglobin, myoglobin and cytochrome P450, heme plays an essential role in a range of biological processes, which include oxygen transport and storage, electron transfer and cellular metabolism (94). However, when released from hemoproteins, unbound heme promotes oxidative stress, inflammation and tissue injury via its ability to catalyse the formation of highly reactive oxygen free radicals, amplify TLR-mediated immune responses and activate the complement cascade (94–98). Thus, in the setting of critical illness, links have been suggested between elevated concentrations of cell-free heme, the SIRS response and organ injury (99). To counteract its cytotoxicity, circulating levels of cell-free heme are regulated primarily by the endogenous heme-binding plasma protein hemopexin (100), with this scavenging system supported by albumin, α-2-macroglobulin and haptoglobin, three heme/haemoglobin binding plasma proteins that assist in the neutralisation, recycling and removal of free heme and iron (94, 95, 99).

Compared to healthy controls, significantly higher concentrations of free heme have been detected in plasma samples obtained from trauma patients at day 1 post-injury (27). Interestingly, insights from a murine model of non-lethal blunt liver trauma suggest a rapid emergence and clearance of circulating heme post-injury, with serial measurements across a 24-hour window (0.5, 1, 4 and 24 hours) detecting a significant trauma-induced increase in plasma heme concentrations only in samples obtained within 30 minutes of injury (27). This apparent discordance in the kinetics of heme release, and its persistence, between humans and mice could potentially reflect species differences in the scavenging of free heme. For instance, in murine models of trauma and burn wound infections, significant increases in plasma levels of hemopexin and haptoglobin have been reported (27, 101, 102), whereas in cohorts of trauma and burns patients, plasma concentrations of hemopexin, haptoglobin and α-2-macroglobulin were found to be comparable to or lower than the levels detected in healthy controls (27, 101–103). In line with these observations, a study of fifty stably resuscitated trauma haemorrhage patients found that within 2-3 hours of resuscitation, plasma hemopexin levels were significantly lower than those of free heme, resulting in a hemopexin:free heme ratio of <1 (37). In addition to the act of trauma itself, medical interventions may influence circulating heme levels, with studies reporting long-term storage of leukoreduced red blood cells resulted in heme release (37, 104, 105). Consequently, when compared to fresh red blood cells, resuscitation with stored red blood cells results in significantly elevated circulating concentrations of free heme (37).

Results of *in vitro* and *in vivo* studies have provided direct evidence of the immune suppressive properties of heme (27, 37). In a murine model of *Staphylococcus aureus* (*S.aureus*) challenge, Lee et al. recovered significantly higher bacterial loads from the bronchoalveolar lavage fluid samples of mice that had been administered heme prior to infection (27), whilst impaired bacterial clearance was reported in hemopexin knockout mice challenged with *S.aureus* following a liver crush injury (27). Moreover, scavenging free heme via systemic administration of hemopexin in mice, either following blunt liver trauma, or prior to resuscitation with stored red blood cells, was shown to improve the clearance rates of *S.aureus* and *Pseudomonas aeruginosa* (27, 37). At the cellular level, data points towards suppression of the innate immune response as being the mechanism by which heme treatment delays the elimination of invading pathogens, with analysis of circulating neutrophils isolated from heme treated mice revealing significantly reduced surface expression of TLR2 and TLR4 (27). Moreover, culturing neutrophils from naïve mice in the presence of serum collected from mice within 30 minutes of a liver crush injury, when circulating heme levels peak, reduced ROS

production in response to *S.aureus* challenge (27). As well as neutrophils, heme treatment has been reported to inhibit the phagocytic activity of macrophages by 90% (37). Interestingly, this inhibitory effect appears to be mediated by a heme-induced release of HMGB-1 by activated macrophages since treating macrophages with an anti-HMGB-1 blocking antibody prior to heme exposure restored their phagocytic activity to a level comparable to that of untreated controls (37).

Due to its well-established cytotoxic, pro-inflammatory and immune amplifying properties, cell-free heme has previously been discussed as a potential therapeutic target for alleviating systemic inflammation and organ injury in critically-ill patients. Heme scavenging via hemopexin therapy and the prevention of heme-induced activation of TLR4 are two examples of strategies considered to date (101, 105). Now, with data implicating heme as a potential mediator of trauma-induced immunosuppression, the idea that modulating the circulating levels of cell-free heme could reduce patient susceptibility to HAIs has been raised (27). However, our understanding of cell-free heme in the setting of traumatic injury, and its relationship with infections, must improve to test the feasibility of such a strategy. As mentioned above, animal-based studies suggest that heme levels peak within 30 minutes of injury, with levels returning to those found in uninjured controls within 4 hours (27). Currently, our knowledge of trauma-induced heme release in humans is limited to a single study whose sample acquisition began post-hospital admission, suggesting that the levels of heme reported to date may not reflect peak concentrations (27). Moreover, no study to our knowledge has examined whether a relationship exists between circulating levels of heme, hemopexin and/or haptoglobin, and the development of infections in hospitalised trauma patients. Finally, given the differences that appear to exist between rodents and humans in how trauma impacts the levels of cell-free heme and/or its scavenger proteins (27, 101–103), using murine models to test potential therapeutic strategies for counteracting heme-induced immunosuppression in human patients may be inappropriate.

2.1.2 Heat shock proteins

A heterogeneous family of proteins, HSPs are molecular chaperones implicated in protein folding, stabilisation and transport (106). Constitutively expressed, and induced by such stressors as heat shock and UV radiation, HSPs are released into the extracellular environment passively, from necrotic tissue, or actively via the non-classic protein release pathway, where they are secreted as free proteins or packaged within extracellular vesicles (107, 108). Linked to the pathology of several chronic inflammatory conditions, HSPs are highly immunogenic, with studies demonstrating their capacity to stimulate cytokine production by monocytes and macrophages (107, 109), promote the maturation of dendritic cells (107) and activate the complement system (110).

Positively associated with injury severity scores (ISS), and indices of illness severity (e.g. sequential organ failure assessment score and simplified acute physiology score 3), significantly higher concentrations of HSP60, HSP70, HSP72 and/or HSP90 alpha have been measured in the circulation of polytrauma and traumatically brain-injured (TBI) patients when compared to healthy controls (31, 111–114). Correlating positively with systemic concentrations of interleukin (IL)-6 and IL-8, elevated levels of HSPs have been detected within minutes of injury and persist for up to ten days (31, 112). Intracellular expression of HSPs are also increased post-trauma, with an injury-induced induction of HSP27, HSP32, HSP60, HSP70 and HSP90 reported in neutrophils and/or monocytes isolated from major burns and trauma patients (115–117). In accordance with their pro-inflammatory nature, prospective studies have measured significantly higher concentrations of HSP60 at hospital admission (118) and HSP70 at 24- and 48-hours post-injury (111) in trauma patients that subsequently develop acute lung injury or MODS respectively. Interestingly, and suggesting a dual inflammatory role for HSPs, Ren et al. detected significantly higher serum concentrations of HSP70 in infected trauma patients 60-90 hours post-injury when compared to their non-infected counterparts (113), whilst a study of 166 adult trauma patients reported plasma HSP70 levels at hospital admission were negatively associated with leukocyte HLA-DR expression (31). Thus, a role for HSPs in mediating the post-injury CARS response has been proposed (28, 119), a theory supported by a body of literature that demonstrates the immune suppressive properties of HSPs.

Using TLR-induced pro-inflammatory cytokine production as a readout of anti-microbial capacity, HSPs have been shown to induce functional tolerance in innate phagocytic cells. Compared to untreated controls, primary human monocytes, or differentiated THP-1 cells, treated with HSP70 exhibit impaired tumour necrosis factor alpha (TNF) production in response to stimulation with lipopolysaccharide (LPS), *S.aureus* peptidoglycan or *Salmonella typhimurium* flagellin (28, 38, 83, 120). Mechanistically, the HSP70-induced impairment in TNF production triggered by LPS stimulation has been attributed to reduced gene transcription, with studies demonstrating HSP70 treatment inhibits activation of the nuclear factor-κβ (NF-κβ) signalling pathway and promotes enrichment of the transcriptional repressors heat shock transcription factor 1 and constitutive HSE-binding factor at the TNF promoter (38, 83). These tolerance-inducing properties of HSP70 contradict data showing that this protein can stimulate monocytes/macrophages to secrete TNF (107, 109). Addressing these contrasting observations, studies have suggested that endotoxin contamination within HSP70 preparations may explain the cytokine-inducing capacity assigned to this DAMP (38, 121). In addition to innate responses, HSPs exert suppressive effects on the adaptive arm of the immune system. Culminating in reduced T cell responses (122), HSP70 treatments have been shown to (1): enhance the immunosuppressive activity of regulatory T cells (39) (2); induce a tolerogenic phenotype in monocyte-derived dendritic cells (DC) (122) (3); impair DC maturation (40) (4); suppress the formation of T helper 1 cells (123). Thus, given the abundance of data demonstrating immune suppressive properties for HSPs, and the suggestion that LPS contamination of preparations may explain their reported pro-inflammatory nature, the idea that HSPs are "DAMPERs" rather than DAMPs appears more likely (124).

2.1.3 S100 proteins

Located within the cytoplasm of leukocytes, microglia and astrocytes, S100 proteins are a family of calcium binding proteins involved in the regulation of cellular proliferation, metabolism and division (125, 126). Detected by the PRRs TLR2 and TLR4, and the receptor for advanced glycation endproducts (RAGE), elevated levels of S100A8, S100A9 and S100B have been detected in the circulation of TBI, polytrauma and burns patients at hospital admission and persist for up to 7 days (41, 127–129). Positively correlated with ISS, percentage total body surface area (TBSA) burn and Glasgow coma scale score (41, 129–131), prospective studies have reported significantly higher levels of S100 proteins as early as day one of injury in patients who subsequently experience poor clinical outcomes such as mortality or long-term disability (41, 127, 130–134). By augmenting the SIRS responses, the anti-apoptotic (135) and pro-inflammatory properties of S100 proteins, which include the activation of neutrophils (136), the amplification of TNF production by monocytes (137) and the promotion of leukocyte transepithelial migration (138), offer potential explanations for how injury-induced elevations in S100 proteins may contribute to poor clinical trajectories.

Studies that have investigated the immune modulatory functions of S100 proteins have shown S100A8, S100A9 and calprotectin, an S100A8/A9 heterodimer, possess immune tolerising properties. In an elegant series of experiments, Austermann et al, who measured acutely and persistently elevated serum concentrations of calprotectin in polytrauma and burns patients, uncovered the molecular mechanisms by which S100A8/A9 inhibits monocyte function (41). Resulting in impaired LPS-induced TNF production, the authors demonstrated that prior exposure of monocytes to calprotectin led to heterochromatin formation at the TNF promoter (41). Underlying this epigenetic modification was a calprotectin-induced recruitment to the TNF promoter of G9a, a methyltransferase that suppresses gene transcription via demethylation of histone H3 on lysine K9 (41). In line with this finding, other studies have shown that pre-treating macrophages or monocytes with S100A8 alone can attenuate pro-inflammatory cytokine production to bacterial challenge, with this induction of tolerance a consequence of reduced activation of the P38 mitogen activated protein kinase (MAPK) signalling pathway following ligation of TLR2/TLR4 (42). In addition to inhibiting monocyte function, S100A8, S100A9 and/or calprotectin have been reported to (1): suppress T cell priming by reducing antigen presentation by DCs (43) (2); inhibit neutrophil chemotaxis (44, 139) (3); suppress LPS and phorbol 12 myristate 13 acetate (PMA)-induced ROS production by neutrophils, with this inhibition attributed to an S100A8 and S100A9 mediated production of adenosine metabolites (140). As well as direct effects on immune cells, raised concentrations of S100 proteins at sites of tissue damage may create a localised immune suppressive environment as both S100A8 homodimers and calprotectin have been shown to act as chemoattractants for MDSCs (45, 46). Through binding to carboxylated N-glycans on such cell surface receptors as RAGE, calprotectin triggers NF-κβ signalling in MDSCs, with MDSC activation resulting in the synthesis and secretion of S100A8/A9 heterodimers (45). Thus, a post-injury vicious cycle of immunosuppression could be established, in which S100 proteins from damaged tissue not only directly suppress the function of infiltrating leukocytes, but recruit MDSCs, whose subsequent activation and production of calprotectin exacerbates existing immune dysfunction and promotes additional immunosuppression.

Interestingly, in the only study to our knowledge to have investigated the relationship between circulating calprotectin and infectious episodes in hospitalised trauma patients, Joly and colleagues found that when compared to their non-infected counterparts, patients who developed a HAI exhibited a smaller increase in plasma calprotectin concentrations during the first five days of hospitalisation (141). If calprotectin exerts suppressive effects on innate and adaptive immune cells, *how can a smaller increase in its circulating levels make patients prone to infection?* Since calprotectin is secreted by activated neutrophils and monocytes (142, 143), the authors speculated that their findings may reflect a sign of systemic immune exhaustion and thus decreased anti-microbial activity, thereby increasing patient susceptibility to HAIs (141).

2.2 Nuclear-derived DAMPs

2.2.1 Cold-inducible RNA binding protein

A regulator of mRNA translation and cell proliferation, CIRP is an RNA chaperone protein, which in the steady state resides in the nucleus (144, 145). In times of stress, triggered by mild hypothermia, hypoxia or oxidation, CIRP is transported into the cytosol, where it is actively secreted, either via the lysosomal pathway or through gasdermin D membrane channels (145–148), or released passively into the extracellular space as a consequence of necroptosis (149).

Signalling through TLR4, triggering receptor expressed on myeloid cells-1 (TREM-1) and NF-κβ (147, 150–153), extracellular CIRP (eCIRP) has been shown to: (1) induce TNF production, ROS generation and extracellular trap formation by macrophages and monocytes (147, 151, 153–155); (2) promote ICAM-1 expression and extracellular trap generation by neutrophils (152, 156, 157); (3) stimulate differentiation of $CD4^+$ T cells to Th1 cells (150); (4) enhance the cytotoxic profile of $CD8^+$ T cells (150). Unsurprisingly therefore, in *in vivo* models of sepsis or haemorrhage, eCIRP amplifies systemic inflammatory responses that culminate in organ dysfunction, injury and increased mortality (147, 148, 150, 151, 153, 158). Interestingly, eCIRP may also exacerbate inflammation by delaying the resolution of inflammatory responses. In a series of *in vitro* co-culture experiments, Chen et al. demonstrated that eCIRP-induced NETs significantly inhibited macrophage efferocytosis, with this suppression a consequence of NET associated neutrophil elastase cleaving the integrins $\alpha_v\beta_3$ and $\alpha_v\beta_5$ from the macrophage surface (157).

eCIRP has been detected in the circulation of critically-ill ICU patients and in the serum of rats subjected to haemorrhagic shock and cecal ligation and puncture (47, 147). As reported for other DAMPs, innate immune cells pre-exposed to CIRP exhibit impaired

functional responses upon secondary stimulation. Compared to vehicle controls, pre-treatment of peritoneal macrophages isolated from healthy mice with CIRP for 24 hours resulted in significantly reduced IL-6 and TNF production upon subsequent LPS challenge (47). This induction of tolerance was confirmed *ex vivo*, with macrophages obtained from mice injected with CIRP exhibiting impaired IL-6 production when stimulated with LPS *in vitro* (47). Mechanistically, this state of endotoxin tolerance was attributed to an eCIRP-mediated activation of STAT3, which was downstream of eCIRP binding to the IL-6 receptor (IL-6R) (47). Indeed, pharmacological inhibition of STAT3 signalling or the use of anti-IL-6R antibodies reversed eCIRP-induced macrophage endotoxin tolerance (47). Pointing towards a role in modulating macrophage polarisation, eCIRP treatment of RAW264.7 cells increased their expression of arginase-1 and CD206 (47). The up-regulation of these markers suggests eCIRP promotes polarisation of macrophages towards an M2 anti-inflammatory phenotype (47). Interestingly, besides inflammatory cytokines, eCIRP treatment of RAW264.7 cells results in secretion of HMGB-1 (147), a DAMP that also possesses endotoxin tolerising properties (51). Thus, a feedback loop of DAMP-induced immunosuppression, initiated by eCIRP and reinforced by HMGB-1, could be established at sites of tissue injury that would result in localised immunosuppression and impaired bacterial clearance.

Given its pro-inflammatory properties and associations with organ dysfunction in models of systemic inflammation, eCIRP has been discussed as a potential therapeutic target for the treatment of sepsis (148, 159). Lending support to this idea, *in vitro* and *in vivo* studies have shown antagonists of CIRP signalling that include C23, which binds to the TLR4-MD2 receptor complex, and M3, which blocks the interaction of eCIRP with TREM-1, can suppress macrophage activation, reduce circulating concentrations of pro-inflammatory cytokines, attenuate organ injury and improve survival rates (151, 153, 158). With a link now emerging between eCIRP, the IL6R and immunosuppression, a call for studies to investigate whether targeting this pathway could negate eCIRP-induced immune tolerance in critically-ill patients has been made, with the suggestion that research should begin by testing small peptide antagonists that target the interaction between eCIRP and IL6R in preclinical models of immune tolerance and secondary infections (47).

2.2.2 Interleukin -33

Constitutively expressed by epithelial, endothelial and stromal cells, and induced in macrophages and DCs in times of inflammation and infection, IL-33 is a member of the IL-1 cytokine superfamily (160, 161). Residing in the nucleus, IL-33 is a dual function protein, acting as a transcriptional repressor and cytokine (160). When released into the extracellular environment, either as a result of cellular damage or active secretion, IL-33 binds to its receptor suppression of tumorigenicity (ST2) (160, 161). Expressed by such cells as mast cells, eosinophils, Th2 cells, group 2 innate lymphoid cells (ILC2) and NK cells, activation of ST2 signalling pathways results in cytokine production, degranulation and T cell polarisation (162, 163).

In a prospective study of 472 blunt trauma patients admitted to ICU, Xu and colleagues detected an early (upon hospital admission) and persistent (up to day 7) post-injury elevation in circulating IL-33 levels (49), a finding that was confirmed in a subsequent independent study of 14 polytrauma patients, in whom plasma IL-33 concentrations were significantly higher 6 to 72 hours post-injury when compared to a mixed control population of monotrauma patients and healthy controls (164). Interestingly, in burns patients, a significant injury-induced decrease in serum IL-33 levels has been reported, with this reduction evident on the day of hospital admission and persisting for up to 28 days (165). Whilst it is debatable whether circulating IL-33 levels are influenced by injury severity (49, 164, 166), differences have been observed in IL-33 concentrations between patients with varied clinical outcomes. For example, in the abovementioned study of 14 polytrauma patients, plasma IL-33 levels at hospital admission were reported to be positively associated with SIRS and Denver MOF scores at day 3 post-injury (164), whereas non-survivors of blunt trauma presented with significantly lower IL-33 concentrations 24-72 hours post-injury when compared to survivors (166). Acting as a decoy receptor and endogenous inhibitor of IL-33, elevated levels of soluble ST2 (sST2) have been detected in the circulation of trauma and burns patients in the days and weeks following injury (49, 165–167), with one prospective study measuring the highest concentrations of sST2 12-24 hours after the peak in IL-33 levels, a delay that was suggested would allow IL-33 to modulate systemic inflammatory responses (49). In respect to clinical outcomes, significantly higher concentrations of sST2 have been detected at several post-injury time points (hospital admission to day 5) in patients who develop pulmonary complications or succumb to their injuries (165, 166)

Suggesting a potential link between raised IL-33 levels and post-trauma immunosuppression, significantly higher concentrations of this DAMP have been measured in plasma samples acquired during the early (4-24 hours) and acute (day 4) post-injury phase from patients that develop HAIs when compared to those who do not (49). Mechanistically, this relationship could potentially be explained by IL-33 activating ILC2 cells and neutrophils to produce the type 2 cytokines IL-4, IL-5 and IL-13, whose plasma levels are significantly elevated in injured patients that experience HAIs (49, 168). Supporting this idea, positive associations have been reported between circulating concentrations of IL-33, IL-4, IL-5 and IL-13 in severely injured individuals (49), whilst in rodent models of trauma haemorrhage, IL-33 signalling is critical for both the post-injury expansion of ILC2 cells and the production of IL-5 by neutrophils (49). Recently, in the context of viral infections, IL-33-mediated production of IL-13 by ILC2 cells was shown to induce arginase-1 expression in neutrophils, the significance of which was demonstrated in neutrophil:T cell co-culture systems, where arginase-1 positive neutrophils significantly inhibited T cell proliferation (50). Relating these observations to traumatic injury, increased arginase-1 expression and activity has been reported in $CD16^{+}$ granulocytes isolated from blunt/penetrative trauma patients for up to two weeks post-injury (169).

By inducing the expansion of IL-10 secreting M2 macrophages, and promoting the accumulation of regulatory T cells (Tregs), IL-33

has been proposed as a potential mediator of long-term immunosuppression in murine models of sepsis (48). Providing clinical relevance, significantly higher concentrations of IL-33 and IL-10, as well as increased frequencies of Tregs, have been detected in the circulation of sepsis survivors sampled 5-10 months post-diagnosis when compared to age and sex-matched controls (48). Thus, *could a similar mechanism underlie the development of PICS in critically-injured subjects?* With the potential to identify therapeutic targets for the treatment of this debilitating condition, future studies that prospectively measure the circulating levels of IL-33, its associated cytokines (e.g. IL-4, IL-5, IL-10 and IL-13) and the frequencies of Tregs in the months following major trauma are warranted. It is of interest that significantly elevated serum concentrations of IL-4, IL-5 and IL-13 have been reported in burns patients for up to three years post-injury (170).

2.2.3 HMGB-1

HMGB-1 is a nuclear residing DNA-binding chaperone protein that regulates gene transcription. Entering the circulation as a consequence of necrosis, pyroptosis or active secretion through a secretory vesicular pathway (171–173), HMGB-1 concentrations are significantly elevated in the minutes, hours and days following major trauma (32, 174, 175). Positively associated with injury severity, base deficit and pro-inflammatory mediators (e.g. MPO, IL-6, IL-8), elevated levels of HMGB-1 have been linked to such poor clinical outcomes as MODS, organ injury and mortality (32, 174, 175). Recognised by several PRRs, which include TLR2, TLR4, TREM-1 and RAGE, HMGB-1 can both activate and inhibit immune cell function, with these opposing traits dependent upon its redox state. The immune suppressive actions of HMGB-1 arise from the terminal oxidation of three cysteine residues located within its DNA binding domains and acidic tail (159)

Like many other DAMPs, exposure to HMGB-1 blunts the pro-inflammatory responses of monocytes. Attributed to impaired activation of NFκB, resulting from reduced phosphorylation and degradation of IκBα, HMGB-1 preconditioning decreases TNF production by differentiated THP-1 cells and bone marrow-derived macrophages challenged with the TLR agonists LPS and lipoteachoic acid (51, 52). For the induction of endotoxin tolerance, HMGB-1 signalling through the RAGE receptor appears to be critical since pre-treatment with HMGB-1 failed to impair TNF production by LPS stimulated macrophages isolated from $RAGE^{-/-}$ mice (51, 52). Contributing to further innate immune dysfunction, HMGB-1 reduces macrophage phagocytic activity (53), promotes the release of immature monocytes from the bone marrow (176) and inhibits neutrophil anti-microbial responses (54). Compared to vehicle controls, neutrophils treated with HMGB-1 exhibit decreased ROS production upon stimulation with PMA, an impairment that is associated with reduced phosphorylation of the NADPH oxidase subunit p40phox (54). In terms of clinical applicability, culturing neutrophils isolated from healthy controls with plasma from critically ill septic shock patients has been shown to significantly decrease their ROS production (54). Suggesting a role for HMGB-1 in mediating this effect, the addition of a neutralising anti HMGB-1 antibody to patient plasma restored neutrophil anti-microbial function (54). Whether similar mechanisms contribute to post-injury immunosuppression is unclear, but in a cohort of 88 blunt trauma patients plasma HMGB-1 levels were significantly higher within 4 hours of injury in those who later developed a HAI (168).

In a study that aimed to investigate the effect of HMGB-1 on T cell-mediated immunity following thermal injury, Huang et al. reported a profound effect of this DAMP on both $CD4^+$ T cells and Tregs in rats (92). Compared to those isolated from sham controls, the authors found that post-burn, T cells from rodents subjected to a 30% TBSA burn exhibited reduced proliferative activity and skewed polarisation towards a Th2 phenotype, whilst Tregs produced greater amounts of IL-10 and expressed higher levels of RAGE (92). Implying a role for HMGB-1 in these responses, administration of an anti-RAGE antibody 6- and 24-hours post-burn injury reversed the burn-induced changes in both T cell function and phenotype (92). Supporting and expanding upon these results, a subsequent *in vitro* study found, in a TLR4 or RAGE dependent manner, that HMGB-1 treatment inhibited IFN-γ production by human $CD4^+$ T cells and promoted the survival, migration and suppressive activity of Tregs (55).

Alongside direct modulation of immune cells, HMGB-1 may promote systemic immunosuppression post-injury by promoting the expansion of MDSCs. MDSCs suppress innate and adaptive immune responses via a number of mechanisms, which include the production of IL-10 and prostaglandin E_2, the sequestration of cysteine, the breakdown of arginine and the generation of ROS (177, 178). Across several studies, HMGB-1 has been shown to promote the differentiation, survival, migration and activation of MDSCs (56). In the context of traumatic injury, elevated frequencies of MDSCs have been detected in the bone marrow, blood and spleen of mice subjected to peripheral tissue trauma, with this elevation prevented by post-injury administration of a blocking anti-HMGB-1 antibody (93). An expansion in spleen resident MDSCs has also been reported in a murine model of neurological trauma, which was accompanied by a significant increase in arginase-1 (ARG-1) expression in $CD11b^+$ monocytes (176). A reduction in MDSC frequency in $RAGE^{-/-}$ mice, and the absence of the trauma-induced increase in ARG-1 expression in monocytes isolated from mice pre-treated with an anti-HMGB-1 antibody, demonstrates a role for this DAMP in mediating systemic immunosuppression (176).

Human monocytes treated with HMGB-1 secrete the peptide hormone resistin (179). Shown *in vitro* to inhibit both neutrophil chemotaxis and ROS generation (180–182), and to suppress TNF production by E.coli or LPS challenged monocytes (183, 184), elevated resistin concentrations have been measured in the circulation of TBI and thermally-injured patients (185–188). Furthermore, and with the potential to create a perpetual cycle of immunosuppression, monocytes treated with physiological concentrations of resistin secrete HMGB-1 and upregulate their expression of TLR4 (189). Thus, systemically, and at sites of tissue damage, HMGB-1 and resistin may combine to create an immune suppressive environment that predisposes the hospitalised trauma patient to secondary infections (Figure 1). Crucially, this cycle may be amenable to therapeutic intervention, with studies showing that *in vitro* hemoadsorption and nucleic acid scavenging microfiber meshes can deplete resistin from serum samples of critically-ill

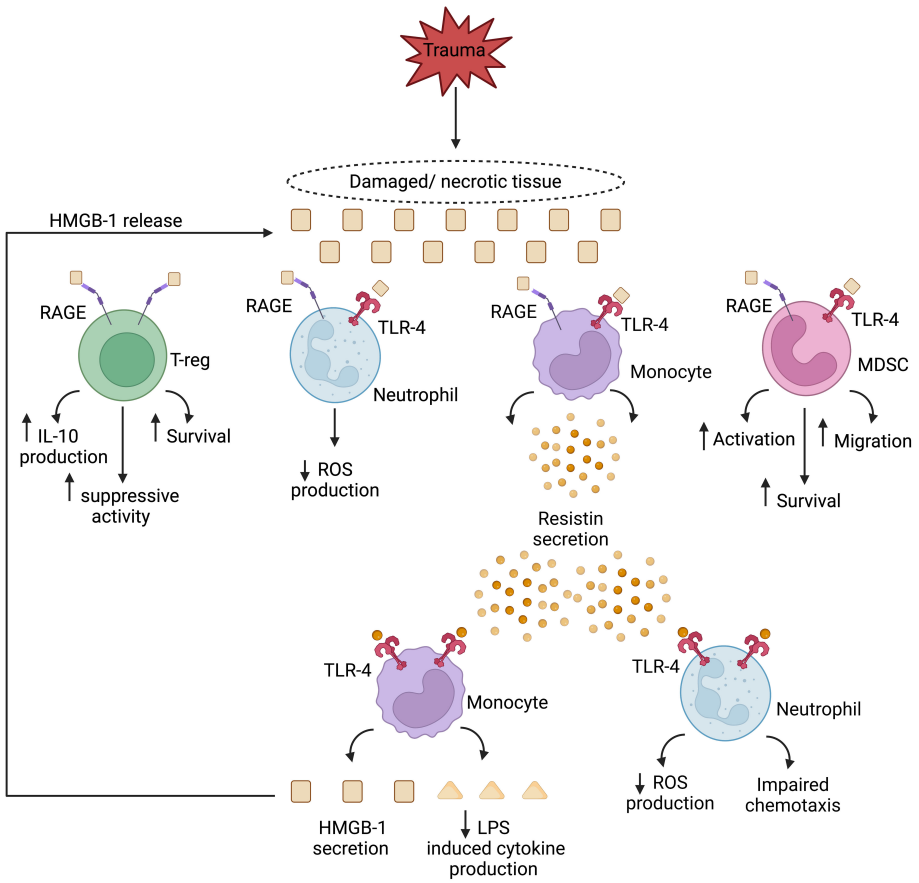

FIGURE 1
Theoretical model of a HMGB-1 and resistin-induced vicious cycle of immunosuppression in the setting of sterile injury. Passively released from damaged/necrotic tissue, the nuclear-derived damage associated molecular pattern high mobility group box-1 (HMGB-1) modulates the functions of innate and adaptive immune cells. Via binding to the pathogen recognition receptors toll like receptor-4 (TLR-4), and receptor for advanced glycation end products (RAGE), HMGB-1 directly inhibits neutrophil anti-microbial functions and enhances the suppressive activities of regulatory T cells and myeloid derived suppressor cells (MDSCs). Monocytes activated by HMGB-1 secrete resistin, an inducer of endotoxin tolerance, and a negative regulator of neutrophil chemotaxis and reactive oxygen species (ROS) production. In a self-perpetuating feedback loop, resistin, through TLR-4 signalling, promotes the secretion of HMGB-1 by monocytes, culminating in a localised immune suppressive environment at the site of tissue injury. IL-10, Interleukin-10; LPS, Lipopolysaccharide. Figure was generated at Biorender.com.

patients (190) and HMGB-1 from supernatants of necrotic cells (191). In the case of resistin, the correction of hyperresistinemia restored neutrophil migration and bacterial killing capacity in serum co-culture assays (190).

2.3 MtDAMPs

2.3.1 ATP

ATP is released non-specifically from necrotic cells, or actively by phagocytes, endothelial cells and apoptotic cells in response to inflammatory challenge, hypoxia or oxidative stress, with its secretion mediated by vesicular exocytosis or through pore-forming channels such as connexins and pannexins (192). Murine models of sepsis have reported elevated plasma concentrations of ATP within two hours of cecal ligation and puncture (193), whilst resuscitation protocols may exacerbate direct trauma-induced increases in circulating ATP levels since *in vitro* exposure to hypertonic saline induces ATP secretion from neutrophils and T cells (194, 195).

Although not reported by all studies (196, 197), the current literature points towards ATP as a DAMP with potent pro-inflammatory properties and an initiator of the SIRS response. For example, signalling through the P2 family of purinergic receptors, ATP (1): promotes inflammasome-mediated secretion of IL-1β by LPS primed macrophages (198) (2); triggers TNF, IL-6 and IL-1α production by macrophages (199); (3) induces T cell activation and IL-2 production (200); (4) augments fMLP-induced superoxide production by neutrophils (194); (5) stimulates neutrophil degranulation, aggregation and adherence to endothelium (201). Moreover, in a murine model of LPS-induced shock, systemic administration of the ATP hydrolase apyrase reduced the cytokine storm, immune cell infiltration into peripheral organs and apoptotic cell death that was observed in vehicle-treated littermates (202). Removal of ATP has therefore been proposed as a potential strategy for dampening the SIRS

response and its associated toxicity in the setting of sterile inflammation (202).

In the extracellular environment, ATP levels are regulated by the ectonucleotidases CD39 and CD73. Expressed by various cell types that include endothelial cells, monocytes, lymphocytes, neutrophils and Tregs, CD39 converts ATP and ADP into AMP, which is subsequently degraded into adenosine by CD73 (203, 204). A potent anti-inflammatory molecule, adenosine inhibits neutrophil phagocytosis, ROS production, degranulation and cytokine production (57), suppresses T cell migration, adhesion and IFN-γ production (58), downregulates antigen presentation and T cell priming by DCs (59), reduces TLR-induced pro-inflammatory cytokine production by macrophages (205) and decreases NK cell cytotoxicity (58). Mechanistically, this suppression is mediated through the A2 receptor family, and in particular the A_{2A} subclass, whose signalling pathways result in the production of cyclic AMP and activation of protein kinase A (57, 59). Interestingly, a recent study reported a trend towards an increased frequency of $CD8^+$ $CD39^+$ T cells in the circulation of trauma patients at days 0/1 post-injury when compared to control patients undergoing elective surgery (206). Immune phenotyping revealed these T cells exhibited signs of immune exhaustion, with increased expression of the markers PD-1 and TIM-3 (206). These changes were accompanied by a trend towards reduced granzyme B content, suggesting potentially reduced cytotoxic capacity (206). Prominent in trauma patients with SIRS, it was speculated that an abundance of immunologically exhausted $CD8^+$ $CD39^+$ $PD\text{-}1^+$ $Tim\text{-}3^+$ T cells may contribute to the state of systemic immune dysfunction that increases the susceptibility of trauma patients to infection (206).

Data are emerging that implies potential interplay between ATP, mtDNA, HSPs and heme metabolism in mediating post-trauma immunosuppression. Suggesting that recognition of mtDNA may enhance T cell mediated conversion of ATP/ADP to its immune suppressive metabolite adenosine, a small cohort study of 11 trauma patients reported a positive association between plasma mtDNA levels and the frequency of $CD8^+CD39^+$ T cells heckler (206). In a series of *in vitro* experiments, Haschemi et al. demonstrated a positive feedback loop between adenosine and HSP32 in suppressing LPS-induced TNF production by macrophages (60). Through activation of the A_{2A} receptor, the authors found adenosine induced expression of heme oxygenase (HSP32) in macrophages (60). Degradation of heme by HSP32 resulted in the production of carbon monoxide, which increased the sensitivity of macrophages to the anti-inflammatory effects of adenosine by increasing surface expression of the A_{2A} receptor (60). Relating these findings to trauma, monocytes isolated from injured patients with severe SIRS have been shown to exhibit increased expression of HSP32 and impaired TNF production following bacterial stimulation (115).

2.3.2 MtDNA

In a seminal study published in 2010, Zhang and colleagues provided mechanistic insights into how sterile traumatic injury results in systemic inflammation and organ dysfunction (33). Passively released from necrotic/damaged tissues, and actively secreted by immune cells (35, 207, 208), they showed that mtDNA, whose levels are acutely and persistently elevated post-trauma (31, 33, 76, 77, 209) is a potent activator of neutrophils, with exposure to this DAMP triggering IL-8 production and activation of MAPKs (33). Subsequent studies have confirmed these observations and demonstrated that mtDNA also induces NET formation and neutrophil degranulation in a TLR9 dependent manner (72, 210, 211). Linking the immunostimulatory properties of mtDNA to systemic inflammation and organ dysfunction, injection of mtDNA into rodents results in hepatic inflammation (210), whilst in models of traumatic injury and shock, plasma mtDNA levels positively associate with lung MPO levels and circulating urea and IL-6 concentrations (76). Providing clinical relevance to these findings, prospective studies of critically-injured subjects have shown plasma mtDNA levels in the early and acute post-injury phase is an independent predictor of SIRS (77, 212). Further, mtDNA load was significantly higher in non-survivors versus survivors as well as patients who develop such secondary complications as ARDS and MODS (76, 78, 213). Interestingly, circulating cell-free mtDNA (cfmtDNA) exists in two forms, a low molecular weight form and a larger form, with the latter comprising 95% of cfmtDNA (214, 215). Comparing these two fractions in plasma samples from 25 major trauma patients, Briggs et al. demonstrated that it was the levels of low molecular weight cfmtDNA that were positively associated with poor clinical outcomes such as ICU length of stay, ventilator use and duration of MOF (216). When interpreting their findings, the authors suggested that the larger forms of cfmtDNA are membrane encapsulated and therefore unable to bind to TLR9 and trigger immune responses (216).

Alongside its pro-inflammatory properties, data are emerging that demonstrates mtDNA is a potent immune suppressor. Treatment of human monocytes with mtDNA inhibits, in a TLR9 dependent manner, their production of IL-1β, IL-6 and TNF upon subsequent stimulation with LPS (61, 62). This mtDNA-induced reduction in cytokine production was attributed to impaired activation of NF-κB signalling and the induction of IRAK-M, a negative regulator of TLR signalling (61). In the setting of sterile neurological trauma, circulating levels of mtDNA are significantly elevated in patients who develop HAIs, with *ex vivo* studies showing that pre-treatment of monocytes isolated from HCs with sera from these patients reduced LPS-induced TNF production, an impairment that was reversed when monocytes were treated with the TLR9 antagonist ODN prior to serum incubation (62). In addition to monocytes, mtDNA induces functional tolerance in neutrophils, with prior exposure to this DAMP inhibiting neutrophil chemotaxis, phagocytosis and bacterial killing (35, 63). A critical step in each of these defence mechanisms is reorganisation of actin filaments, a process that involves activation of such cytoskeletal proteins as the F-actin binding protein cortactin (CTTN). Through activation of G protein coupled receptor kinase 2 (GRK2), mtDNA treatment suppresses CTTN activation by promoting its deacetylation by histone deacetylases (HDACs) (63). Coinciding with elevated plasma mtDNA levels, activated GRK2 and reduced CTTN acetylation have been detected in neutrophils isolated from trauma patients (63). Demonstrating

the potential relevance of these observations to clinical outcomes, GRK2 activity and CTTN acetylation, at days 1-6 post-injury, were increased and decreased respectively in neutrophils of trauma patients who later developed HAIs (63).

With potential implications for the efficiency of adaptive immune responses, mtDNA negatively impacts upon DC function. Actively engulfed from the extracellular environment, elevated cytoplasmic mtDNA levels have been measured in DCs isolated from septic mice and in bone marrow-derived DCs challenged with LPS and mtDNA *in vitro* (64). Through activation of the cGAS-stimulator of interferon genes (STING) pathway, JAK-1/2 and STAT3 signalling, the accumulation of cytoplasmic mtDNA inhibited LPS-induced expression of the co-stimulatory molecules CD40, CD80 and CD86 (64). Accompanied by reduced production of IL-12p70 and enhanced synthesis of IL-10, these phenotypic changes were associated with an impaired ability of DCs to promote the proliferation of $CD4^+$ T cells in co-culture systems (64). Bearing unmethylated CpG islands, mtDNA is a ligand for the surface expressed and endosomal residing PRR TLR9. In murine models of thermal injury, $CD4^+$ T cells cultured with TLR9 activated DCs isolated from burn-injured mice were found to secrete markedly lower levels of Th1 and Th17 cytokines when compared to T cells cultured with DCs from sham controls (217). This shift in T cell polarisation was associated with increased production of IL-10 and reduced secretion of IL-6, IL-12p70 and TNF by TLR9 challenged DCs post-burn (217).

As a DAMP that possesses both immune stimulatory and inhibitory properties, mtDNA and/or its associated signalling pathways have been discussed as possible therapeutic targets for the treatment of post-traumatic SIRS, ARDS and immunosuppression (35, 63, 76, 78, 213). Focussing on the latter, preclinical studies have demonstrated the potential immune enhancing effects of GRK2 and HDAC inhibitors (63). Administered 30 minutes after a liver crush injury and tracheal inoculation of *S.aureus*, a combined therapy of valproate, a HDAC inhibitor, and the GRK2 inhibitor paroxetine restored levels of bacterial clearance to those recorded in uninjured controls and increased survival rates (63). Importantly, for its potential translation into the hospital setting, the treatment regimen was not associated with any evidence of organ injury or failure (63).

2.3.3 Mitochondrial-derived N-formylated peptides

Mitochondria synthesise 13 formylated peptides that share molecular similarities with the formyl peptides derived from bacteria. All but one of these formylated peptides, namely Cox1, have been detected in the circulation of trauma patients, with concentrations of ND6, a subunit of mitochondrial NADH dehydrogenase, significantly elevated within 1-hour of injury and remaining so for up to 72 hours (30, 66).

Detected by surface expressed formyl peptide receptor (FPR) 1 and FPR2 (67), mtFPs are neutrophil chemoattractants, with the proteins that most closely resemble bacterial-derived formylated peptides, namely ND3, ND4, ND5 and ND6 possessing the greatest chemotactic potency (66). Data generated by several studies have demonstrated that neutrophils pre-treated with ND6 exhibit reduced calcium fluxes, chemotactic responses and ROS production upon secondary stimulation with other GPCR agonists such as IL-8, leukotriene B4 (LTB_4) and fMLP (30, 65–68). Contributing to this heterologous receptor desensitisation and suppression in anti-microbial functions is an ND6-mediated downregulation of GPCRs, for which activation of GRK2 is a potential underlying mechanistic explanation (63, 65, 66, 218).

Associated with reduced bacterial clearance, a peripheral fracture injury in animal models has been shown to reduce neutrophil recruitment to the lung following a pulmonary contusion (219). As femoral fracture reamings are a rich source of mtDAMPs (91), it has been proposed that the increased susceptibility of trauma patients to HAIs may arise in part from mtDAMPs impairing host resistance by attracting neutrophils towards distal injury sites and away from regions of pathogenic challenge (219, 220). Supporting this hypothesis, intra-peritoneal injection of mitochondrial debris was shown to markedly attenuate neutrophil migration to the lung following a pulmonary contusion (220). A role for mtFPs in mediating this effect is suggested by the results of another animal study in which administration of the FPR1 receptor antagonist cyclosporin H, alongside mtDAMPs, significantly improved bacterial clearance in the lung following intra-tracheal injection of *S.aureus* (218).

Implicated in the capture, neutralisation and elimination of pathogens, the generation of NETs is significantly reduced post-injury (30, 219). In a series of *in vitro* and *ex vivo* experiments, we attributed this impairment to a mtFP-induced dysfunction in neutrophil metabolism (30). Compared to those isolated from healthy controls, neutrophils obtained from trauma patients, as early as 1-hour post-injury, exhibited reduced glucose uptake and breakdown, two prerequisites for NET formation (30). Replicating these impairments *in vitro*, we showed that treatment of control neutrophils with whole mtDAMP preparations, but not purified mtDNA, inhibited PMA-induced NET production, a defect that was associated with reduced aerobic glycolysis and a mtFP dependent activation of AMP-activated protein kinase, a negative regulator of NET formation (30).

As a DAMP that suppresses a range of neutrophil anti-microbial functions, studies have investigated whether mtFPs may represent a potential therapeutic target to combat post-trauma immunosuppression. Several studies have shown that pre-treatment of neutrophils with FPR1 inhibitors not only prevents mtFP-induced impairments in calcium mobilisation and chemotactic responses (65, 66, 68) but also reduces ND6-mediated downregulation of GPCRs (65, 218). Another strategy under consideration is the intra-tracheal instillation of neutrophils, which aims to overcome the ability of mtFPs generated at regions of tissue injury to direct neutrophils away from sites of pathogenic challenge. In preclinical models of pseudo fracture and bacterial inoculation, intra-tracheal instillation of exogenous bone marrow derived murine neutrophils or neutrophils isolated from human blood samples has been shown to prevent the establishment of and/or treat pneumonia by reversing the mtDAMP-induced impairment in bacterial clearance from the lungs (68, 221, 222). Encouragingly, no adverse effects in respect of organ damage have been detected post-instillation (221, 222). Furthermore, and relevant to its

potential translation to the clinic, preliminary data suggest that cryopreserved neutrophils are just as effective as freshly isolated neutrophils in promoting bacterial clearance from the lung in the presence of mtDAMPs (222).

3 Conclusions

The detection of DAMPs in blood samples obtained from critically-injured patients in the pre-hospital setting offers a mechanistic explanation for the simultaneous induction of the SIRS and CARS response that occurs within minutes of injury (15, 31). Indeed, alongside their renowned pro-inflammatory properties, cytosolic, nuclear and mitochondrial-derived DAMPs are now recognised as potent immune suppressors, impairing the anti-microbial functions of innate and adaptive immune cells either directly or by driving the expansion and differentiation of Tregs and MDSCs. Exacerbating both the local and systemic immune suppressive environments created by the instantaneous release of DAMPs from injured tissues, are secondary insults such as fluid resuscitation, surgical interventions and transfusions with aged blood cell products, which either induce the release of endogenous DAMPs or are themselves a source of exogenous DAMPs. Furthermore, alongside pre-existing DAMPs, a novel class of suppressive inducible DAMPs, termed SAMPs, have recently been described and suggested to activate hyper-resolution responses within minutes of the SIRS response being initiated (82).

Currently, very few prospective studies have investigated whether post-trauma elevations in circulating DAMPs are associated with and/or predictive of the development of HAIs. However, studies in other cohorts of critically-ill patients suggest such a relationship may exist (65, 223). If translatable to trauma patients, then the question arises of whether DAMPs and/or their associated signalling pathways represent feasible therapeutic targets for the prevention and/or treatment of secondary infections post-injury. Scavenging circulating DAMPs via the use of microfiber meshes or polymers, or inhibiting ligand-receptor interactions through delivery of receptor antagonists, are strategies under consideration for treating the secondary complications associated with the post-traumatic SIRS response that may also be suitable for combating the immune suppressive actions of DAMPs (Figure 2) (76, 191). However, the timing of such treatments would need to be carefully considered as it must not be forgotten that the purpose of DAMP release is to alert the body to tissue damage. Thus, a fine balance will exist for achieving an optimal immune response, with excessive or inappropriate removal of DAMPs, or inhibition of

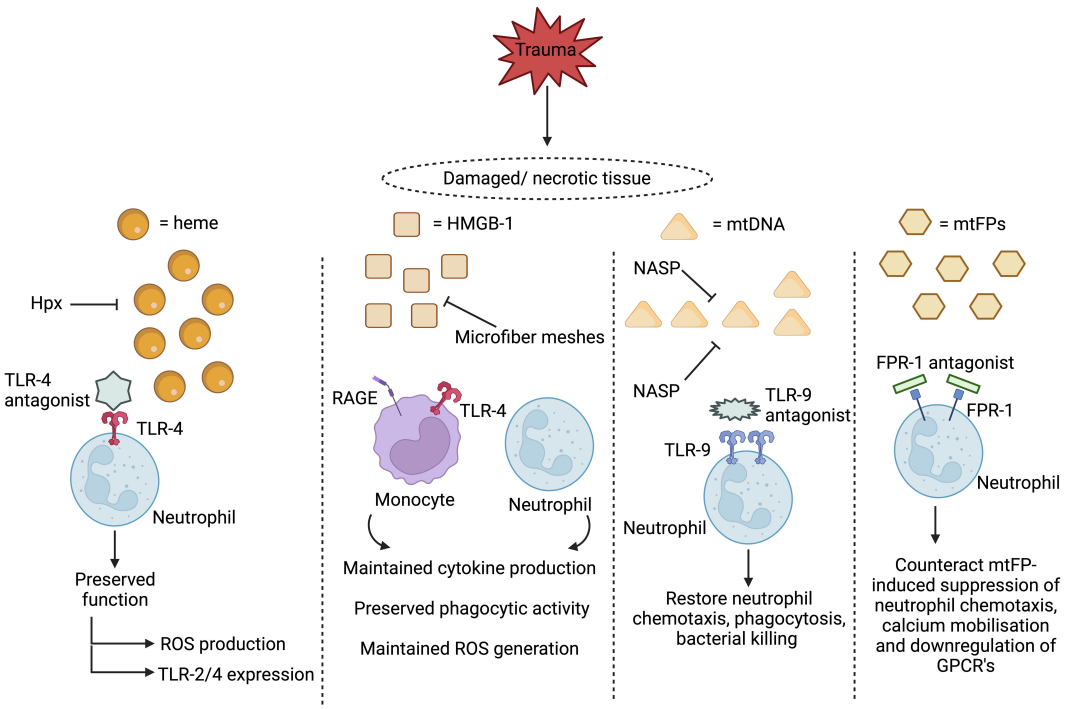

FIGURE 2
Proposed therapeutic strategies for treating damage associated molecular pattern (DAMP)-induced immunosuppression. Two therapeutic approaches under consideration for preventing and/or reversing DAMP-induced immunosuppression are to scavenge circulating DAMPs or to inhibit their activation of immune cells. Restoring circulating levels of hemopexin (Hpx), a heme scavenging protein whose plasma concentrations are reduced post-injury, may help combat heme-induced suppression of neutrophil anti-microbial functions, whilst the use of microfiber meshes or nucleic acid scavenging polymers (NASPs) to reduce the systemic load of circulating mtDNA and HMGB-1 could alleviate the post-trauma impairments reported in monocyte and neutrophil function. Showing promise in *in vitro* studies, blocking DAMP-induced activation of neutrophils through the use of toll-like receptor-9 (TLR-9) or formyl peptide receptor-1 (FPR-1) antagonists prevents the induction of functional tolerance to subsequent secondary stimulation with inflammatory agonists or microbial-derived proteins. HMGB-1, High mobility group box-1, mtDNA, Mitochondrial-derived DNA; mtFPs, Mitochondrial-derived N-formylated peptides; RAGE, Receptor for advanced glycation end products; ROS, Reactive oxygen species; TLR, Toll-like receptor. Figure was were generated at Biorender.com.

immune cell signalling, having the potential to negatively impact upon the DAMP-induced initiation of inflammatory responses that are critical for the regenerative processes of tissue repair and healing.

Author contributions

EH and JH conceived and wrote the manuscript. JL critically appraised and revised the manuscript. All authors contributed to the article and approved the submitted version.

Funding

JH is supported by a Career Development Award from the UKRI-Medical Research Council. JH and JL are members of the National Institute for Health Research Surgical Reconstruction and Microbiology Research Centre.

Conflict of interest

The authors declare that the research was conducted in the absence of any commercial or financial relationships that could be construed as a potential conflict of interest.

Publisher's note

All claims expressed in this article are solely those of the authors and do not necessarily represent those of their affiliated organizations, or those of the publisher, the editors and the reviewers. Any product that may be evaluated in this article, or claim that may be made by its manufacturer, is not guaranteed or endorsed by the publisher.

Author disclaimer

The views expressed here are those of the authors and not necessarily those of the NIHR, NHS or Department of Health and Social Care.

References

1. Krug EG, Sharma GK, Lozano R. The global burden of injuries. *Am J Public Health* (2000) 90:523–6. doi: 10.2105/AJPH.90.4.523

2. The Trauma Audit and Research Network. *Performance comparison: trauma care* . Available at: https://www.tarn.ac.uk/Content.aspx?ca=15 (Accessed 10th June 2023).

3. Pfeifer R, Tarkin IS, Rocos B, Pape HC. Patterns of mortality and causes of death in polytrauma patients–has anything changed? *Injury* (2009) 40:907–11. doi: 10.1016/J.INJURY.2009.05.006

4. Van Breugel JMM, Niemeyer MJS, Houwert RM, Groenwold RHH, Leenen LPH, Van Wessem KJP. Global changes in mortality rates in polytrauma patients admitted to the ICU-a systematic review. *World J Emerg Surg* (2020) 15. doi: 10.1186/S13017-020-00330-3

5. Hessels AJ, Kuo YH, Ahmed N. Epidemiology and impact of healthcare-associated infections in trauma patients: A national data analysis. *Surg Infect (Larchmt)* (2020) 21:871–6. doi: 10.1089/SUR.2019.294

6. Glance LG, Stone PW, Mukamel DB, Dick AW. Increases in mortality, length of stay, and cost associated with hospital-acquired infections in trauma patients. *Arch Surg* (2011) 146:794–801. doi: 10.1001/ARCHSURG.2011.41

7. Kesinger MR, Kumar RG, Wagner AK, Puyana JC, Peitzman AP, Billiar TR, et al. Hospital-acquired pneumonia is an independent predictor of poor global outcome in severe traumatic brain injury up to 5 years after discharge. *J Trauma Acute Care Surg* (2015) 78:396–402. doi: 10.1097/TA.0000000000000526

8. Czaja AS, Rivara FP, Wang J, Koepsell T, Nathens AB, Jurkovich GJ, et al. Late outcomes of trauma patients with infections during index hospitalization. *J Trauma* (2009) 67:805–14. doi: 10.1097/TA.0B013E318185E1FB

9. Manson J, Cole E, De'Ath HD, Vulliamy P, Meier U, Pennington D, et al. Early changes within the lymphocyte population are associated with the development of multiple organ dysfunction syndrome in trauma patients. *Crit Care* (2016) 20. doi: 10.1186/S13054-016-1341-2

10. Cabrera CP, Manson J, Shepherd JM, Torrance HD, Watson D, Longhi MP, et al. Signatures of inflammation and impending multiple organ dysfunction in the hyperacute phase of trauma: A prospective cohort study. *PloS Med* (2017) 14. doi: 10.1371/JOURNAL.PMED.1002352

11. Van Wessem KJP, Hietbrink F, Leenen LPH. Attenuation of MODS-related and ARDS-related mortality makes infectious complications a remaining challenge in the severely injured. *Trauma Surg Acute Care Open* (2020) 5. doi: 10.1136/TSACO-2019-000398

12. Yadollahi M, Kashkooe A, Feyzi M, Bornapour S. Risk factors of mortality in nosocomial infected traumatic patients in a trauma referral center in south of Iran. *Chin J Traumatol* (2018) 21:267–72. doi: 10.1016/J.CJTEE.2018.03.002

13. Lee PT, Krecko LK, Savage S, O'Rourke AP, Jung HS, Ingraham A, et al. Which hospital-acquired conditions matter the most in trauma? An evidence-based approach for prioritizing trauma program improvement. *J Trauma Acute Care Surg* (2022) 93:446–52. doi: 10.1097/TA.0000000000003645

14. Cole E, Davenport R, Willett K, Brohi K. The burden of infection in severely injured trauma patients and the relationship with admission shock severity. *J Trauma Acute Care Surg* (2014) 76:730–5. doi: 10.1097/TA.0B013E31829FDBD7

15. Hazeldine J, Naumann DN, TOman E, Davies D, Bishop JRB, Su Z, et al. Prehospital immune responses and development of multiple organ dysfunction syndrome following traumatic injury: A prospective cohort study. *PloS Med* (2017) 14. doi: 10.1371/JOURNAL.PMED.1002338

16. Xiao W, Mindrinos MN, Seok J, Cuschieri J, Cuenca AG, Gao H, et al. A genomic storm in critically injured humans. *J Exp Med* (2011) 208:2581–90. doi: 10.1084/JEM.20111354

17. Ward NS, Casserly B, Ayala A. The compensatory anti-inflammatory response syndrome (CARS) in critically ill patients. *Clin Chest Med* (2008) 29:617–25. doi: 10.1016/J.CCM.2008.06.010

18. Orr SK, Butler KL, Hayden D, Tompkins RG, Serhan CN, Irimia D. Gene expression of proresolving lipid mediator pathways is associated with clinical outcomes in trauma patients. *Crit Care Med* (2015) 43:2642–50. doi: 10.1097/CCM.0000000000001312

19. Yang YW, Wu CH, Tsai HT, Chen YR, Chang YP, Han YY, et al. Dynamics of immune responses are inconsistent when trauma patients are grouped by injury severity score and clinical outcomes. *Sci Rep* (2023) 13. doi: 10.1038/S41598-023-27969-7

20. Gentile LF, Cuenca AG, Efron PA, Ang D, Bihorac A, McKinley BA, et al. Persistent inflammation and immunosuppression: a common syndrome and new horizon for surgical intensive care. *J Trauma Acute Care Surg* (2012) 72:1491–501. doi: 10.1097/TA.0B013E318256E000

21. Vanzant EL, Lopez CM, Ozrazgat-Baslanti T, Ungaro R, Davis R, Cuenca AG, et al. Persistent inflammation, immunosuppression, and catabolism syndrome after severe blunt trauma. *J Trauma Acute Care Surg* (2014) 76:21–30. doi: 10.1097/TA.0B013E3182AB1AB5

22. Mira JC, Brakenridge SC, Moldawer LL, Moore FA. Persistent inflammation, immunosuppression and catabolism syndrome. *Crit Care Clin* (2017) 33:245–58. doi: 10.1016/J.CCC.2016.12.001

23. Hawkins RB, Raymond SL, Stortz JA, Horiguchi H, Brakenridge SC, Gardner A, et al. Chronic critical illness and the persistent inflammation, immunosuppression, and catabolism syndrome. *Front Immunol* (2018) 9:1511. doi: 10.3389/FIMMU.2018.01511

24. Hesselink L, Hoepelman RJ, Spijkerman R, de Groot MCH, van Wessem KJP, Koenderman L, et al. Persistent inflammation, immunosuppression and catabolism syndrome (PICS) after polytrauma: A rare syndrome with major consequences. *J Clin Med* (2020) 9. doi: 10.3390/JCM9010191

25. Cahill LA, Guo F, Nguyen J, Zhang F, Seshadri A, Keegan J, et al. Circulating factors in trauma plasma activate specific human immune cell subsets. *Injury* (2020) 51:819–29. doi: 10.1016/J.INJURY.2020.03.009

26. Kim HI, Park J, Konecna B, Huang W, Riça I, Gallo D, et al. Plasma and wound fluids from trauma patients suppress neutrophil extracellular respiratory burst. *J Trauma Acute Care Surg* (2022) 92:330–8. doi: 10.1097/TA.0000000000003461

27. Lee GR, Gallo D, de Souza RWA, Tiwari-Heckler S, Csizmadia E, Harbison JD, et al. Trauma-induced heme release increases susceptibility to bacterial infection. *JCI Insight* (2021) 6. doi: 10.1172/JCI.INSIGHT.150813

28. Flohé SB, Bangen JM, Flohé S, Agrawal H, Bergmann K, SChade FU. Origin of immunomodulation after soft tissue trauma: potential involvement of extracellular heat-shock proteins. *Shock* (2007) 27:494–502. doi: 10.1097/SHK.0B013E31802DEC51

29. Hampson P, Dinsdale RJ, Wearn CM, Bamford AL, Bishop JRB, Hazeldine J, et al. Neutrophil dysfunction, immature granulocytes, and cell-free DNA are early biomarkers of sepsis in burn-injured patients: A prospective observational cohort study. *Ann Surg* (2017) 265:1241–9. doi: 10.1097/SLA.0000000000001807

30. Hazeldine J, Dinsdale RJ, Harrison P, Lord JM. Traumatic injury and exposure to mitochondrial-derived damage associated molecular patterns suppresses neutrophil extracellular trap formation. *Front Immunol* (2019) 10:685. doi: 10.3389/FIMMU.2019.00685

31. Timmermans K, Kox M, Vaneker M, van den Berg M, John A, van Laarhoven A, et al. Plasma levels of danger-associated molecular patterns are associated with immune suppression in trauma patients. *Intensive Care Med* (2016) 42:551–61. doi: 10.1007/S00134-015-4205-3

32. Cohen MJ, Brohi K, Calfee CS, Rahn P, Chesebro BB, Christiaans SC, et al. Early release of high mobility group box nuclear protein 1 after severe trauma in humans: role of injury severity and tissue hypoperfusion. *Crit Care* (2009) 13. doi: 10.1186/CC8152

33. Zhang Q, Raoof M, Chen Y, Sumi Y, Sursal T, Junger W, et al. Circulating mitochondrial DAMPs cause inflammatory responses to injury. *Nature* (2010) 464:104–7. doi: 10.1038/NATURE08780

34. Murao A, Aziz M, Wang H, Brenner M, Wang P. Release mechanisms of major DAMPs. *Apoptosis* (2021) 26:152–62. doi: 10.1007/S10495-021-01663-3

35. Konecna B, Park J, Kwon WY, Vlkova B, Zhang Q, Huang W, et al. Monocyte exocytosis of mitochondrial danger-associated molecular patterns in sepsis suppresses neutrophil chemotaxis. *J Trauma Acute Care Surg* (2021) 90:46–53. doi: 10.1097/TA.0000000000002973

36. Gong T, Liu L, Jiang W, Zhou R. DAMP-sensing receptors in sterile inflammation and inflammatory diseases. *Nat Rev Immunol* (2020) 20:95–112. doi: 10.1038/S41577-019-0215-7

37. Wagener BM, Hu PJ, Oh JY, Evans CA, Richter JR, Honavar J, et al. Role of heme in lung bacterial infection after trauma hemorrhage and stored red blood cell transfusion: A preclinical experimental study. *PloS Med* (2018) 15. doi: 10.1371/JOURNAL.PMED.1002522

38. Ferat-Osorio E, Sánchez-Anaya A, Gutiérrez-Mendoza M, Boscó-Gárate I, Wong-Baeza I, Pastelin-Palacios R, et al. Heat shock protein 70 down-regulates the production of toll-like receptor-induced pro-inflammatory cytokines by a heat shock factor-1/constitutive heat shock element-binding factor-dependent mechanism. *J Inflammation (Lond)* (2014) 11. doi: 10.1186/1476-9255-11-19

39. Wachstein J, Tischer S, Figueiredo C, Limbourg A, Falk C, Immenschuh S, et al. HSP70 enhances immunosuppressive function of CD4(+)CD25(+)FoxP3(+) T regulatory cells and cytotoxicity in CD4(+)CD25(-) T cells. *PloS One* (2012) 7. doi: 10.1371/JOURNAL.PONE.0051747

40. Motta A, Schmitz C, Rodrigues L, Ribeiro F, Teixeira C, Detanico T, et al. Mycobacterium tuberculosis heat-shock protein 70 impairs maturation of dendritic cells from bone marrow precursors, induces interleukin-10 production and inhibits T-cell proliferation in vitro. *Immunology* (2007) 121:462–72. doi: 10.1111/J.1365-2567.2007.02564.X

41. Austermann J, Friesenhagen J, Fassl SK, Ortkras T, Burgmann J, Barczyk-Kahlert K, et al. Alarmins MRP8 and MRP14 induce stress tolerance in phagocytes under sterile inflammatory conditions. *Cell Rep* (2014) 9:2112–23. doi: 10.1016/J.CELREP.2014.11.020

42. Coveney AP, Wang W, Kelly J, Liu JH, Blankson S, Di W, et al. Myeloid-related protein 8 induces self-tolerance and cross-tolerance to bacterial infection via TLR4- and TLR2-mediated signal pathways. *Sci Rep* (2015) 5. doi: 10.1038/SREP13694

43. Shimizu K, Libby P, Rocha VZ, Folco EJ, Shubiki R, Grabie N, et al. Loss of myeloid related protein-8/14 exacerbates cardiac allograft rejection. *Circulation* (2011) 124:2920–32. doi: 10.1161/CIRCULATIONAHA.110.009910

44. Sroussi HY, Berline J, Palefsky JM. Oxidation of methionine 63 and 83 regulates the effect of S100A9 on the migration of neutrophils in vitro. *J Leukoc Biol* (2007) 81:818–24. doi: 10.1189/JLB.0706433

45. Sinha P, Okoro C, Foell D, Freeze HH, Ostrand-Rosenberg S, Srikrishna G. Proinflammatory S100 proteins regulate the accumulation of myeloid-derived suppressor cells. *J Immunol* (2008) 181:4666–75. doi: 10.4049/JIMMUNOL.181.7.4666

46. Vrakas CN, O'Sullivan RM, Evans SE, Ingram DMA, Jones CB, Phuong T, et al. The Measure of DAMPs and a role for S100A8 in recruiting suppressor cells in breast cancer lung metastasis. *Immunol Invest* (2015) 44:174–88. doi: 10.3109/08820139.2014.952818

47. Zhou M, Aziz M, Denning NL, Yen HT, Ma G, Wang P. Extracellular CIRP induces macrophage endotoxin tolerance through IL-6R-mediated STAT3 activation. *JCI Insight* (2020) 5. doi: 10.1172/JCI.INSIGHT.133715

48. Nascimento DC, Melo PH, Piñeros AR, Ferreira RG, Colón DF, Donate PB, et al. IL-33 contributes to sepsis-induced long-term immunosuppression by expanding the regulatory T cell population. *Nat Commun* (2017) 8. doi: 10.1038/NCOMMS14919

49. Xu J, Guardado J, Hoffman R, Xu H, Namas R, Vodovotz Y, et al. IL33-mediated ILC2 activation and neutrophil IL5 production in the lung response after severe trauma: A reverse translation study from a human cohort to a mouse trauma model. *PloS Med* (2017) 14. doi: 10.1371/JOURNAL.PMED.1002365

50. Liang Y, Yi P, Yuan DMK, Jie Z, Kwota Z, Soong L, et al. IL-33 induces immunosuppressive neutrophils via a type 2 innate lymphoid cell/IL-13/STAT6 axis and protects the liver against injury in LCMV infection-induced viral hepatitis. *Cell Mol Immunol* (2019) 16:126–37. doi: 10.1038/CMI.2017.147

51. Aneja RK, Tsung A, Sjodin H, Gefter JV, Delude RL, Billiar TR, et al. Preconditioning with high mobility group box 1 (HMGB1) induces lipopolysaccharide (LPS) tolerance. *J Leukoc Biol* (2008) 84:1326–34. doi: 10.1189/JLB.0108030

52. Robert SM, Sjodin H, Fink MP, Aneja RK. Preconditioning with high mobility group box 1 (HMGB1) induces lipoteichoic acid (LTA) tolerance. *J Immunother* (2010) 33:663–71. doi: 10.1097/CJI.0B013E3181DCD111

53. Wang Y, Zhang W, Xu Y, Wu D, Gao Z, Zhou J, et al. Extracellular HMGB1 impairs macrophage-mediated efferocytosis by suppressing the rab43-controlled cell surface transport of CD91. *Front Immunol* (2022) 13:767630. doi: 10.3389/FIMMU.2022.767630

54. Grégoire M, Tadié J-M, Uhel F, Gacouin A, Piau C, Bone N, et al. Frontline Science: HMGB1 induces neutrophil dysfunction in experimental sepsis and in patients who survive septic shock. *J Leukoc Biol* (2017) 101:1281–7. doi: 10.1189/JLB.5HI0316-128RR

55. Wild CA, Bergmann C, Fritz G, Schuler P, Hoffmann TK, Lotfi R, et al. HMGB1 conveys immunosuppressive characteristics on regulatory and conventional T cells. *Int Immunol* (2012) 24:485–94. doi: 10.1093/INTIMM/DXS051

56. Jin S, Yang Z, Hao X, Tang W, Ma W, Zong H. Roles of HMGB1 in regulating myeloid-derived suppressor cells in the tumor microenvironment. *biomark Res* (2020) 8. doi: 10.1186/S40364-020-00201-8

57. Barletta KE, Ley K, Mehrad B. Regulation of neutrophil function by adenosine. *Arterioscler Thromb Vasc Biol* (2012) 32:856–64. doi: 10.1161/ATVBAHA.111.226845

58. Feng LL, Cai YQ, Zhu MC, Xing LJ, Wang X. The yin and yang functions of extracellular ATP and adenosine in tumor immunity. *Cancer Cell Int* (2020) 20. doi: 10.1186/S12935-020-01195-X

59. Silva-Vilches C, Ring S, Mahnke K. ATP and its metabolite adenosine as regulators of dendritic cell activity. *Front Immunol* (2018) 9:2581. doi: 10.3389/FIMMU.2018.02581

60. Haschemi A, Wagner O, Marculescu R, Wegiel B, Robson SC, Gagliani N, et al. Cross-regulation of carbon monoxide and the adenosine A2a receptor in macrophages. *J Immunol* (2007) 178:5921–9. doi: 10.4049/JIMMUNOL.178.9.5921

61. Fernández-Ruiz I, Arnalich F, Cubillos-Zapata C, Hernández-Jiménez E, Moreno-González R, Toledano V, et al. Mitochondrial DAMPs induce endotoxin tolerance in human monocytes: an observation in patients with myocardial infarction. *PloS One* (2014) 9. doi: 10.1371/JOURNAL.PONE.0095073

62. Hernández-Jiménez E, Gutierrez-Fernández M, Cubillos-Zapata C, Otero-Ortega L, Rodríguez-Frutos B, Toledano V, et al. Circulating monocytes exhibit an endotoxin tolerance status after acute ischemic stroke: mitochondrial DNA as a putative explanation for poststroke infections. *J Immunol* (2017) 198:2038–46. doi: 10.4049/JIMMUNOL.1601594

63. Kim HI, Park J, Gallo D, Shankar S, Konecna B, Han Y, et al. Danger signals activate G-protein receptor kinases suppressing neutrophil function and predisposing to infection after tissue trauma. *Ann Surg* (2023). doi: 10.1097/SLA.0000000000005898

64. Tu Q, Li Y, Zhu J, Guo L, Liu C, Liu L, et al. Mitochondrial DNA mediates immunoparalysis of dendritic cells in sepsis via STING signalling. *Cell Prolif* (2022) 55. doi: 10.1111/CPR.13328

65. Kwon WY, Suh GJ, Jung YS, Park SM, Oh S, Kim SH, et al. Circulating mitochondrial N-formyl peptides contribute to secondary nosocomial infection in patients with septic shock. *Proc Natl Acad Sci U.S.A.* (2021) 118. doi: 10.1073/PNAS.2018538118/-/DCSUPPLEMENTAL

66. Kaczmarek E, Hauser CJ, Kwon WY, Rica I, Chen L, Sandler N, et al. A subset of five human mitochondrial formyl peptides mimics bacterial peptides and functionally deactivates human neutrophils. *J Trauma Acute Care Surg* (2018) 85:936–43. doi: 10.1097/TA.0000000000001971

67. Gabl M, Sundqvist M, Holdfeldt A, Lind S, Mårtensson J, Christenson K, et al. Mitocryptides from human mitochondrial DNA-encoded proteins activate neutrophil formyl peptide receptors: receptor preference and signaling properties. *J Immunol* (2018) 200:3269–82. doi: 10.4049/JIMMUNOL.1701719

68. Zhang Q, Kwon WY, Vlková B, Riça I, Kaczmarek E, Park J, et al. Direct airway instillation of neutrophils overcomes chemotactic deficits induced by injury. *Shock* (2021) 56:119–24. doi: 10.1097/SHK.0000000000001691

69. Pugin J. How tissue injury alarms the immune system and causes a systemic inflammatory response syndrome. *Ann Intensive Care* (2012) 2. doi: 10.1186/2110-5820-2-27

70. Comish PB, Carlson D, Kang R, Tang D. Damage-associated molecular patterns and the systemic immune consequences of severe thermal injury. *J Immunol* (2020) 205:1189–97. doi: 10.4049/JIMMUNOL.2000439

71. Schwacha MG, Rani M, Zhang Q, Nunez-Cantu O, Cap AP. Mitochondrial damage-associated molecular patterns activate γδ T-cells. *Innate Immun* (2014) 20:261–8. doi: 10.1177/1753425913488969

72. Itagaki K, Kaczmarek E, Lee YT, Tang IT, Isal B, Adibnia Y, et al. Mitochondrial DNA released by trauma induces neutrophil extracellular traps. *PloS One* (2015) 10. doi: 10.1371/JOURNAL.PONE.0120549

73. Hazeldine J, Hampson P, Opoku FA, Foster M, Lord JM. N-Formyl peptides drive mitochondrial damage associated molecular pattern induced neutrophil activation through ERK1/2 and P38 MAP kinase signalling pathways. *Injury* (2015) 46:975–84. doi: 10.1016/J.INJURY.2015.03.028

74. Yang H, Hreggvidsdottir HS, Palmblad K, Wang H, Ochani M, Li J, et al. A critical cysteine is required for HMGB1 binding to Toll-like receptor 4 and activation of macrophage cytokine release. *Proc Natl Acad Sci U.S.A.* (2010) 107:11942–7. doi: 10.1073/PNAS.1003893107

75. Schwacha MG, Rani M, Nicholson SE, Lewis AM, Holloway TL, Sordo S, et al. Dermal γδ T-cells can be activated by mitochondrial damage-associated molecular patterns. *PloS One* (2016) 11. doi: 10.1371/JOURNAL.PONE.0158993

76. Aswani A, Manson J, Itagaki K, Chiazza F, Collino M, Wupeng WL, et al. Scavenging circulating mitochondrial DNA as a potential therapeutic option for multiple organ dysfunction in trauma hemorrhage. *Front Immunol* (2018) 9:891. doi: 10.3389/FIMMU.2018.00891

77. Gu X, Yao Y, Wu G, Lv T, Luo L, Song Y. The plasma mitochondrial DNA is an independent predictor for post-traumatic systemic inflammatory response syndrome. *PloS One* (2013) 8. doi: 10.1371/JOURNAL.PONE.0072834

78. Simmons JD, Lee YL, Mulekar S, Kuck JL, Brevard SB, Gonzalez RP, et al. Elevated levels of plasma mitochondrial DNA DAMPs are linked to clinical outcome in severely injured human subjects. *Ann Surg* (2013) 258:591–6. doi: 10.1097/SLA.0B013E3182A4EA46

79. McIlroy DJ, Minahan K, Keely S, Lott N, Hansbro P, Smith DW, et al. Reduced deoxyribonuclease enzyme activity in response to high postinjury mitochondrial DNA concentration provides a therapeutic target for Systemic Inflammatory Response Syndrome. *J Trauma Acute Care Surg* (2018) 85:354–8. doi: 10.1097/TA.0000000000001919

80. Wang XW, Karki A, Zhao XJ, Xiang XY, Lu ZQ. High plasma levels of high mobility group box 1 is associated with the risk of sepsis in severe blunt chest trauma patients: a prospective cohort study. *J Cardiothorac Surg* (2014) 9. doi: 10.1186/S13019-014-0133-5

81. Vourc'h M, Roquilly A, Asehnoune K. Trauma-induced damage-associated molecular patterns-mediated remote organ injury and immunosuppression in the acutely ill patient. *Front Immunol* (2018) 9:1330. doi: 10.3389/FIMMU.2018.01330

82. Relja B, Land WG. Damage-associated molecular patterns in trauma. *Eur J Trauma Emerg Surg* (2020) 46:751–75. doi: 10.1007/S00068-019-01235-W

83. Aneja R, Odoms K, Dunsmore K, Shanley TP, Wong HR. Extracellular heat shock protein-70 induces endotoxin tolerance in THP-1 cells. *J Immunol* (2006) 177:7184–92. doi: 10.4049/JIMMUNOL.177.10.7184

84. Westhaver LP, Nersesian S, Nelson A, MacLean LK, Carter EB, Rowter D, et al. Mitochondrial damage-associated molecular patterns trigger arginase-dependent lymphocyte immunoregulation. *Cell Rep* (2022) 39. doi: 10.1016/J.CELREP.2022.110847

85. Bidar F, Bodinier M, Venet F, Lukaszewicz AC, Brengel-Pesce K, Conti F, et al. Concomitant assessment of monocyte HLA-DR expression and ex vivo TNF-α Release as markers of adverse outcome after various injuries-insights from the REALISM study. *J Clin Med* (2021) 11. doi: 10.3390/JCM11010096

86. de Roquetaillade C, Dupuis C, Faivre V, Lukaszewicz AC, Brumpt C, Payen D. Monitoring of circulating monocyte HLA-DR expression in a large cohort of intensive care patients: relation with secondary infections. *Ann Intensive Care* (2022) 12. doi: 10.1186/S13613-022-01010-Y

87. Cheron A, Floccard B, Allaouchiche B, Guignant C, Poitevin F, Malcus C, et al. Lack of recovery in monocyte human leukocyte antigen-DR expression is independently associated with the development of sepsis after major trauma. *Crit Care* (2010) 14. doi: 10.1186/CC9331

88. Conway Morris A, Rynne J, Shankar-Hari M. Compartmentalisation of immune responses in critical illness: does it matter? *Intensive Care Med* (2022) 48:1617–20. doi: 10.1007/S00134-022-06871-2

89. Juss JK, House D, Amour A, Begg M, Herre J, Storisteanu DML, et al. Acute respiratory distress syndrome neutrophils have a distinct phenotype and are resistant to phosphoinositide 3-kinase inhibition. *Am J Respir Crit Care Med* (2016) 194:961–73. doi: 10.1164/RCCM.201509-1818OC

90. Conway Morris A, Kefala K, Wilkinson TS, Dhaliwal K, Farrell L, Walsh T, et al. C5a mediates peripheral blood neutrophil dysfunction in critically ill patients. *Am J Respir Crit Care Med* (2009) 180:19–28. doi: 10.1164/RCCM.200812-1928OC

91. Hauser CJ, Sursal T, Rodriguez EK, Appleton PT, Zhang Q, Itagaki K. Mitochondrial damage associated molecular patterns from femoral reamings activate neutrophils through formyl peptide receptors and P44/42 MAP kinase. *J Orthop Trauma* (2010) 24:534–8. doi: 10.1097/BOT.0B013E3181EC4991

92. Huang LF, Yao YM, Zhang LT, Dong N, Yu Y, Sheng ZY. The effect of high-mobility group box 1 protein on activity of regulatory T cells after thermal injury in rats. *Shock* (2009) 31:322–9. doi: 10.1097/SHK.0B013E3181834070

93. Ruan X, Darwiche SS, Cai C, Scott MJ, Pape HC, Billiar TR. Anti-HMGB1 monoclonal antibody ameliorates immunosuppression after peripheral tissue trauma: attenuated T-lymphocyte response and increased splenic CD11b (+) Gr-1 (+) myeloid-derived suppressor cells require HMGB1. *Mediators Inflammation* (2015) 2015. doi: 10.1155/2015/458626

94. Chiabrando D, Vinchi F, Fiorito V, Mercurio S, Tolosano E. Heme in pathophysiology: a matter of scavenging, metabolism and trafficking across cell membranes. *Front Pharmacol* (2014) 5:61. doi: 10.3389/FPHAR.2014.00061

95. Vissa M, Larkin SK, Vichinsky EP, Kuypers FA, Soupene E. Assessment of total and unbound cell-free heme in plasma of patients with sickle cell disease. *Exp Biol Med (Maywood)* (2023). doi: 10.1177/15353702231157920

96. Lin T, Kwak YH, Sammy F, He P, Thundivalappil S, Sun G, et al. Synergistic inflammation is induced by blood degradation products with microbial Toll-like receptor agonists and is blocked by hemopexin. *J Infect Dis* (2010) 202:624–32. doi: 10.1086/654929

97. Fernandez PL, Dutra FF, Alves L, Figueiredo RT, Mourão-Sa D, Fortes GB, et al. Heme amplifies the innate immune response to microbial molecules through spleen tyrosine kinase (Syk)-dependent reactive oxygen species generation. *J Biol Chem* (2010) 285:32844–51. doi: 10.1074/JBC.M110.146076

98. Roumenina LT, Rayes J, Lacroix-Desmazes S, Dimitrov JD. Heme: modulator of plasma systems in hemolytic diseases. *Trends Mol Med* (2016) 22:200–13. doi: 10.1016/J.MOLMED.2016.01.004

99. Ryter SW. Significance of heme and heme degradation in the pathogenesis of acute lung and inflammatory disorders. *Int J Mol Sci* (2021) 22. doi: 10.3390/IJMS22115509

100. Hvidberg V, Maniecki MB, Jacobsen C, Højrup P, Møller HJ, Moestrup SK. Identification of the receptor scavenging hemopexin-heme complexes. *Blood* (2005) 106:2572–9. doi: 10.1182/BLOOD-2005-03-1185

101. Lin T, Maita D, Thundivalappil SR, Riley FE, Hambsch J, Van Marter LJ, et al. Hemopexin in severe inflammation and infection: mouse models and human diseases. *Crit Care* (2015) 19. doi: 10.1186/S13054-015-0885-X

102. Maile R, Willis ML, Herring LE, Prevatte A, Mahung C, Cairns B, et al. Burn injury induces proinflammatory plasma extracellular vesicles that associate with length of hospital stay in women: CRP and SAA1 as potential prognostic indicators. *Int J Mol Sci* (2021) 22. doi: 10.3390/IJMS221810083

103. Dépret F, Dunyach C, De Tymowski C, Chaussard M, Bataille A, Ferry A, et al. Undetectable haptoglobin is associated with major adverse kidney events in critically ill burn patients. *Crit Care* (2017) 21. doi: 10.1186/S13054-017-1837-4

104. Oh JY, Stapley R, Harper V, Marques MB, Patel RP. Predicting storage-dependent damage to red blood cells using nitrite oxidation kinetics, peroxiredoxin-2 oxidation, and hemoglobin and free heme measurements. *Transfusion (Paris)* (2015) 55:2967–78. doi: 10.1111/TRF.13248

105. Stapley R, Rodriguez C, Oh JY, Honavar J, Brandon A, Wagener BM, et al. Red blood cell washing, nitrite therapy, and antiheme therapies prevent stored red blood cell toxicity after trauma-hemorrhage. *Free Radic Biol Med* (2015) 85:207–18. doi: 10.1016/J.FREERADBIOMED.2015.04.025

106. Hu C, Yang J, Qi Z, Wu H, Wang B, Zou F, et al. Heat shock proteins: Biological functions, pathological roles, and therapeutic opportunities. *MedComm (Beijing)* (2022) 3. doi: 10.1002/MCO2.161

107. Basu S, Binder RJ, Suto R, Anderson KM, Srivastava PK. Necrotic but not apoptotic cell death releases heat shock proteins, which deliver a partial maturation signal to dendritic cells and activate the NF-kappa B pathway. *Int Immunol* (2000) 12:1539–46. doi: 10.1093/INTIMM/12.11.1539

108. De Maio A, Vazquez D. Extracellular heat shock proteins: a new location, a new function. *Shock* (2013) 40:239–46. doi: 10.1097/SHK.0B013E3182A185AB

109. Asea A, Kraeft SK, Kurt-Jones EA, Stevenson MA, Chen LB, Finberg RW, et al. HSP70 stimulates cytokine production through a CD14-dependant pathway, demonstrating its dual role as a chaperone and cytokine. *Nat Med* (2000) 6:435–42. doi: 10.1038/74697

110. Prohaszka Z, Singh M, Nagy K, Kiss E, Lakos G, Duba J Fust G. Heat shock protein 70 is a potent activator of the human complement system. *Cell Stress Chaperones* (2002) 7:17–22. doi: 10.1379/1466-1268

111. Guisasola MC, Ortiz A, Chana F, Alonso B, Vaquero J. Early inflammatory response in polytraumatized patients: Cytokines and heat shock proteins. *A pilot study. Orthop Traumatol Surg Res* (2015) 101:607–11. doi: 10.1016/J.OTSR.2015.03.014

112. Vardas K, Apostolou K, Briassouli E, Goukos D, Psarra K, Botoula E, et al. Early response roles for prolactin cortisol and circulating and cellular levels of heat shock proteins 72 and 90α in severe sepsis and SIRS. *BioMed Res Int* (2014) 2014. doi: 10.1155/2014/803561

113. Ren B, Zou G, Huang Y, Xu G, Xu F, He J, et al. Serum levels of HSP70 and other DAMP proteins can aid in patient diagnosis after traumatic injury. *Cell Stress Chaperones* (2016) 21:677–86. doi: 10.1007/S12192-016-0694-4

114. Pittet JF, Lee H, Morabito D, Howard MB, Welch WJ, Mackersie RC. Serum levels of Hsp 72 measured early after trauma correlate with survival. *J Trauma* (2002) 52:611–7. doi: 10.1097/00005373-200204000-00001

115. Mohri T, Ogura H, Koh T, Fujita K, Sumi Y, Yoshiya K, et al. Enhanced expression of intracellular heme oxygenase-1 in deactivated monocytes from patients with severe systemic inflammatory response syndrome. *J Trauma* (2006) 61:616–23. doi: 10.1097/01.TA.0000238228.67894.D7

116. Ogura H, Hashiguchi N, Tanaka H, Koh T, Noborio M, Nakamori Y, et al. Long-term enhanced expression of heat shock proteins and decelerated apoptosis in polymorphonuclear leukocytes from major burn patients. *J Burn Care Rehabil* (2002) 23:103–9. doi: 10.1097/00004630-200203000-00006

117. Hashiguchi N, Ogura H, Tanaka H, Koh T, Aoki M, Shiozaki T, et al. Enhanced expression of heat shock proteins in leukocytes from trauma patients. *J Trauma* (2001) 50:102–7. doi: 10.1097/00005373-200101000-00018

118. Pespeni M, Mackersie RC, Lee H, Morabito D, Hodnett M, Howard M, et al. Serum levels of Hsp60 correlate with the development of acute lung injury after trauma. *J Surg Res* (2005) 126:41–7. doi: 10.1016/J.JSS.2005.01.012

119. Guisasola MC, Alonso B, Bravo B, Vaquero J, Chana F. An overview of cytokines and heat shock response in polytraumatized patients. *Cell Stress Chaperones* (2018) 23:483–9. doi: 10.1007/S12192-017-0859-9

120. Bangen JM, SChade FU, Flohé SB. Diverse regulatory activity of human heat shock proteins 60 and 70 on endotoxin-induced inflammation. *Biochem Biophys Res Commun* (2007) 359:709–15. doi: 10.1016/J.BBRC.2007.05.167

121. Gao B, Tsan MF. Endotoxin contamination in recombinant human heat shock protein 70 (Hsp70) preparation is responsible for the induction of tumor necrosis factor alpha release by murine macrophages. *J Biol Chem* (2003) 278:174–9. doi: 10.1074/JBC.M208742200

122. Stocki P, Wang XN, Dickinson AM. Inducible heat shock protein 70 reduces T cell responses and stimulatory capacity of monocyte-derived dendritic cells. *J Biol Chem* (2012) 287:12387–94. doi: 10.1074/JBC.M111.307579

123. Tukaj S, Mantej J, Sobala M, Potrykus K, Sitko K. Autologous extracellular Hsp70 exerts a dual role in rheumatoid arthritis. *Cell Stress Chaperones* (2020) 25:1105–10. doi: 10.1007/S12192-020-01114-Z

124. Broere F, van der Zee R, Van Eden W. Heat shock proteins are no DAMPs, rather "DAMPERs. " *Nat Rev Immunol* (2011) 11:565. doi: 10.1038/NRI2873-C1

125. Donato R, Cannon BR, Sorci G, Riuzzi F, Hsu K, Weber DJ, et al. Functions of S100 proteins. *Curr Mol Med* (2013) 13:24–57.

126. Steiner J, Marquardt N, Pauls I, Schiltz K, Rahmoune H, Bahn S, et al. Human CD8(+) T cells and NK cells express and secrete S100B upon stimulation. *Brain Behav Immun* (2011) 25:1233–41. doi: 10.1016/J.BBI.2011.03.015

127. Goyal A, Failla MD, Niyonkuru C, Amin K, Fabio A, Berger RP, et al. S100b as a prognostic biomarker in outcome prediction for patients with severe traumatic brain injury. *J Neurotrauma* (2013) 30:946–57. doi: 10.1089/NEU.2012.2579

128. Andersen RE, Hansson LO, Nilsson O, Dijlai-Merzoug R, Settergren G. High serum S100B levels for trauma patients without head injuries. *Neurosurgery* (2001) 48:1255–60. doi: 10.1097/00006123-200106000-00012

129. Thelin EP, Zibung E, Riddez L, Nordenvall C. Assessing bicycle-related trauma using the biomarker S100B reveals a correlation with total injury severity. *Eur J Trauma Emerg Surg* (2016) 42:617–25. doi: 10.1007/S00068-015-0583-Z

130. Yang Y, Shen L, Xu M, Chen L, Lu W, Wang W. Serum calprotectin as a prognostic predictor in severe traumatic brain injury. *Clin Chim Acta* (2021) 520:101–7. doi: 10.1016/J.CCA.2021.06.009

131. Pfortmueller CA, Drexel C, Krähenmann-Müller S, Leichtle AB, Fiedler GM, Lindner G, et al. S-100 B concentrations are a predictor of decreased survival in patients with major trauma, independently of head injury. *PloS One* (2016) 11. doi: 10.1371/JOURNAL.PONE.0152822

132. Vos PE, Jacobs B, Andriessen TMJC, Lamers KJB, Borm GF, Beems T, et al. GFAP and S100B are biomarkers of traumatic brain injury: an observational cohort study. *Neurology* (2010) 75:1786–93. doi: 10.1212/WNL.0B013E3181FD62D2

133. Raabe A, Grolms C, Sorge O, Zimmermann M, Seifert V. Serum S-100B protein in severe head injury. *Neurosurgery* (1999) 45:477–83. doi: 10.1097/00006123-199909000-00012

134. Golden N, Mahadewa TGB, Aryanti C, Widyadharma IPE. S100B serum level as a mortality predictor for traumatic brain injury: A meta-analysis. *Open Access Maced J Med Sci* (2018) 6:2239–44. doi: 10.3889/OAMJMS.2018.432

135. Kim DH, Gu A, Lee JS, Yang EJ, Kashif A, Hong MH, et al. Suppressive effects of S100A8 and S100A9 on neutrophil apoptosis by cytokine release of human bronchial epithelial cells in asthma. *Int J Med Sci* (2020) 17:498–509. doi: 10.7150/IJMS.37833

136. Sprenkeler EGG, Zandstra J, van Kleef ND, Goetschalckx I, Verstegen B, Aarts CEM, et al. S100A8/A9 is a marker for the release of neutrophil extracellular traps and induces neutrophil activation. *Cells* (2022) 11. doi: 10.3390/CELLS11020236

137. Vogl T, Tenbrock K, Ludwig S, Leukert N, Ehrhardt C, Van Zoelen MAD, et al. Mrp8 and Mrp14 are endogenous activators of Toll-like receptor 4, promoting lethal, endotoxin-induced shock. *Nat Med* (2007) 13:1042–9. doi: 10.1038/NM1638

138. Raquil M-A, Anceriz N, Rouleau P, Tessier PA. Blockade of antimicrobial proteins S100A8 and S100A9 inhibits phagocyte migration to the alveoli in streptococcal pneumonia. *J Immunol* (2008) 180:3366–74. doi: 10.4049/JIMMUNOL.180.5.3366

139. Sroussi HY, Berline J, Dazin P, Green P, Palefsky JM. S100A8 triggers oxidation-sensitive repulsion of neutrophils. *J Dent Res* (2006) 85:829–33. doi: 10.1177/154405910608500910

140. Sroussi HY, Lu Y, Zhang QL, Villines D, Marucha PT. S100A8 and S100A9 inhibit neutrophil oxidative metabolism in-vitro: involvement of adenosine metabolites. *Free Radic Res* (2010) 44:389–96. doi: 10.3109/10715760903431434

141. Joly P, Marshall JC, Tessier PA, Massé C, Page N, Frenette AJ, et al. S100A8/A9 and sRAGE kinetic after polytrauma; an explorative observational study. *Scand J Trauma Resusc Emerg Med* (2017) 25. doi: 10.1186/S13049-017-0455-0

142. Tardif MR, Chapeton-Montes JA, Posvandzic A, Pagé N, Gilbert C, Tessier PA. Secretion of S100A8, S100A9, and S100A12 by neutrophils involves reactive oxygen species and potassium efflux. *J Immunol Res* (2015) 2015. doi: 10.1155/2015/296149

143. Diercks BP, Hauschildt I, Stäb F, Wenck H, Döring O, Peters N. IL-10 promotes secretion of S100A8/A9 from human monocytes trough an inclusion in plasma membranes. *Scand J Immunol* (2013) 77:169–70. doi: 10.1111/SJI.12015

144. Roilo M, Kullmann MK, Hengst L. Cold-inducible RNA-binding protein (CIRP) induces translation of the cell-cycle inhibitor p27Kip1. *Nucleic Acids Res* (2018) 46:3198–210. doi: 10.1093/NAR/GKX1317

145. De Leeuw F, Zhang T, Wauquier C, Huez G, Kruys V, Gueydan C. The cold-inducible RNA-binding protein migrates from the nucleus to cytoplasmic stress granules by a methylation-dependent mechanism and acts as a translational repressor. *Exp Cell Res* (2007) 313:4130–44. doi: 10.1016/J.YEXCR.2007.09.017

146. Tan C, Reilly B, Jha A, Murao A, Lee Y, Brenner M, et al. Active Release of eCIRP via Gasdermin D Channels to Induce Inflammation in Sepsis. *J Immunol* (2022) 208:2184–95. doi: 10.4049/JIMMUNOL.2101004

147. Qiang X, Yang WL, Wu R, Zhou M, Jacob A, Dong W, et al. Cold-inducible RNA-binding protein (CIRP) triggers inflammatory responses in hemorrhagic shock and sepsis. *Nat Med* (2013) 19:1489–95. doi: 10.1038/NM.3368

148. Han J, Zhang Y, Ge P, Dakal TC, Wen H, Tang S, et al. Exosome-derived CIRP: An amplifier of inflammatory diseases. *Front Immunol* (2023) 14:1066721. doi: 10.3389/FIMMU.2023.1066721

149. Reilly B, Tan C, Murao A, Nofi C, Jha A, Aziz M, et al. Necroptosis-mediated eCIRP release in sepsis. *J Inflammation Res* (2022) 15:4047–59. doi: 10.2147/JIR.S370615

150. Bolognese AC, Sharma A, Yang WL, Nicastro J, Coppa GF, Wang P. Cold-inducible RNA-binding protein activates splenic T cells during sepsis in a TLR4-dependent manner. *Cell Mol Immunol* (2018) 15:38–47. doi: 10.1038/CMI.2016.43

151. Zhang F, Brenner M, Yang WL, Wang P. A cold-inducible RNA-binding protein (CIRP)-derived peptide attenuates inflammation and organ injury in septic mice. *Sci Rep* (2018) 8. doi: 10.1038/S41598-017-13139-Z

152. Ode Y, Aziz M, Wang P. CIRP increases ICAM-1+ phenotype of neutrophils exhibiting elevated iNOS and NETs in sepsis. *J Leukoc Biol* (2018) 103:693–707. doi: 10.1002/JLB.3A0817-327RR

153. Denning NL, Aziz M, Murao A, Gurien SD, Ochani M, Prince JM, et al. Extracellular CIRP as an endogenous TREM-1 ligand to fuel inflammation in sepsis. *JCI Insight* (2020) 5. doi: 10.1172/JCI.INSIGHT.134172

154. Lee Y, Reilly B, Tan C, Wang P, Aziz M. Extracellular CIRP induces macrophage extracellular trap formation via gasdermin D activation. *Front Immunol* (2021) 12:780210. doi: 10.3389/FIMMU.2021.780210

155. Li Z, Fan E K, Liu J J, Scott M, Li Y, Li S, et al. Cold-inducible RNA-binding protein through TLR4 signaling induces mitochondrial DNA fragmentation and regulates macrophage cell death after trauma. *Cell Death Dis* (2017) 8. doi: 10.1038/CDDIS.2017.187

156. Ode Y, Aziz M, Jin H, Arif A, Nicastro JG, Wang P. Cold-inducible RNA-binding protein induces neutrophil extracellular traps in the lungs during sepsis. *Sci Rep* (2019) 9. doi: 10.1038/S41598-019-42762-1

157. Chen K, Murao A, Arif A, Takizawa S, Jin H, Jiang J, et al. Inhibition of efferocytosis by extracellular CIRP-induced neutrophil extracellular traps. *J Immunol* (2021) 206:797–806. doi: 10.4049/JIMMUNOL.2000091

158. Zhang F, Yang WL, Brenner M, Wang P. Attenuation of hemorrhage-associated lung injury by adjuvant treatment with C23, an oligopeptide derived from cold-inducible RNA-binding protein. *J Trauma Acute Care Surg* (2017) 83:690–7. doi: 10.1097/TA.0000000000001566

159. Zhou M, Aziz M, Wang P. Damage-associated molecular patterns as double-edged swords in sepsis. *Antioxid Redox Signal* (2021) 35:1308–23. doi: 10.1089/ARS.2021.0008

160. Cayrol C, Girard JP. Interleukin-33 (IL-33): A critical review of its biology and the mechanisms involved in its release as a potent extracellular cytokine. *Cytokine* (2022) 156. doi: 10.1016/J.CYTO.2022.155891

161. Cayrol C, Girard JP. IL-33: an alarmin cytokine with crucial roles in innate immunity, inflammation and allergy. *Curr Opin Immunol* (2014) 31:31–7. doi: 10.1016/J.COI.2014.09.004

162. Hirsiger S, Simmen HP, Werner CML, Wanner GA, Rittirsch D. Danger signals activating the immune response after trauma. *Mediators Inflammation* (2012) 2012. doi: 10.1155/2012/315941

163. Qi L, Zhang Q, Miao Y, Kang W, Tian Z, Xu D, et al. Interleukin-33 activates and recruits natural killer cells to inhibit pulmonary metastatic cancer development. *Int J Cancer* (2020) 146:1421–34. doi: 10.1002/IJC.32779

164. Haupt J, Krysiak N, Unger M, Bogner-Flatz V, Biberthaler P, Hanschen M, et al. The potential of adipokines in identifying multiple trauma patients at risk of developing multiple organ dysfunction syndrome. *Eur J Med Res* (2021) 26. doi: 10.1186/S40001-021-00511-Z

165. Hacker S, Dieplinger B, Werba G, Nickl S, Roth GA, Krenn CG, et al. Increased serum concentrations of soluble ST2 predict mortality after burn injury. *Clin Chem Lab Med* (2018) 56:2079–87. doi: 10.1515/CCLM-2018-0042

166. Billiar IM, Guardado J, Abdul-Malak O, Vodovotz Y, Billiar TR, Namas RA. Elevations in circulating sST2 levels are associated with in-hospital mortality and adverse clinical outcomes after blunt trauma. *J Surg Res* (2019) 244:23–33. doi: 10.1016/J.JSS.2019.05.057

167. Brunner M, Krenn C, Roth G, Moser B, Dworschak M, Jensen-Jarolim E, et al. Increased levels of soluble ST2 protein and IgG1 production in patients with sepsis and trauma. *Intensive Care Med* (2004) 30:1468–73. doi: 10.1007/S00134-004-2184-X

168. Namas RA, Vodovotz Y, Almahmoud K, Abdul-Malak O, Zaaqoq A, Namas R, et al. Temporal patterns of circulating inflammation biomarker networks differentiate susceptibility to nosocomial infection following blunt trauma in humans. *Ann Surg* (2016) 263:191–8. doi: 10.1097/SLA.0000000000001001

169. Bryk JA, Popovic PJ, Zenati MS, Munera V, Pribis JP, Ochoa JB. Nature of myeloid cells expressing arginase 1 in peripheral blood after trauma. *J Trauma* (2010) 68:843–52. doi: 10.1097/TA.0B013E3181B026E4

170. Jeschke MG, Gauglitz GG, Kulp GA, Finnerty CC, Williams FN, Kraft R, et al. Long-term persistance of the pathophysiologic response to severe burn injury. *PloS One* (2011) 6. doi: 10.1371/JOURNAL.PONE.0021245

171. Scaffidi P, Misteli T, Bianchi ME. Release of chromatin protein HMGB1 by necrotic cells triggers inflammation. *Nature* (2002) 418:191–5. doi: 10.1038/NATURE00858

172. Volchuk A, Ye A, Chi L, Steinberg BE, Goldenberg NM. Indirect regulation of HMGB1 release by gasdermin D. *Nat Commun* (2020) 11. doi: 10.1038/S41467-020-18443-3

173. Chen R, Kang R, Tang D. The mechanism of HMGB1 secretion and release. *Exp Mol Med* (2022) 54:91–102. doi: 10.1038/S12276-022-00736-W

174. Yang Z, Simovic MO, Edsall PR, Liu B, Cancio TS, Batchinsky AI, et al. HMGB1 inhibition to ameliorate organ failure and increase survival in trauma. *Biomolecules* (2022) 12. doi: 10.3390/BIOM12010101

175. Fei J, Yu HJ, Zhou J, Huang XK, Liang H, Jiang Y. Study on high mobility group-1 protein in patients with multiple trauma. *Zhongguo Wei Zhong Bing Ji Jiu Yi Xue* (2005) 17:273–5.

176. Liesz A, Dalpke A, Mracsko E, Antoine DJ, Roth S, Zhou W, et al. DAMP signaling is a key pathway inducing immune modulation after brain injury. *J Neurosci* (2015) 35:583–98. doi: 10.1523/JNEUROSCI.2439-14.2015

177. Ostrand-Rosenberg S, Fenselau C. Myeloid-derived suppressor cells: immune-suppressive cells that impair antitumor immunity and are sculpted by their environment. *J Immunol* (2018) 200:422–31. doi: 10.4049/JIMMUNOL.1701019

178. Veglia F, Sanseviero E, Gabrilovich DI. Myeloid-derived suppressor cells in the era of increasing myeloid cell diversity. *Nat Rev Immunol* (2021) 21:485–98. doi: 10.1038/S41577-020-00490-Y

179. Sundén-Cullberg J, Nyström T, Lee ML, Mullins GE, Tokics L, Andersson J, et al. Pronounced elevation of resistin correlates with severity of disease in severe sepsis and septic shock. *Crit Care Med* (2007) 35:1536–42. doi: 10.1097/01.CCM.0000266536.14736.03

180. Cohen G, Ilic D, Raupachova J, Hörl WH. Resistin inhibits essential functions of polymorphonuclear leukocytes. *J Immunol* (2008) 181:3761–8. doi: 10.4049/JIMMUNOL.181.6.3761

181. Singbartl K, Miller L, Ruiz-Velasco V, Kellum JA. Reversal of acute kidney injury-induced neutrophil dysfunction: A critical role for resistin. *Crit Care Med* (2016) 44:e492–501. doi: 10.1097/CCM.0000000000001472

182. Miller L, Singbartl K, Chroneos ZC, Ruiz-Velasco V, Lang CH, Bonavia A. Resistin directly inhibits bacterial killing in neutrophils. *Intensive Care Med Exp* (2019) 7. doi: 10.1186/S40635-019-0257-Y

183. Nieto JC, Perea L, Soriano G, Zamora C, Cantó E, Medina A, et al. Ascitic fluid regulates the local innate immune response of patients with cirrhosis. *J Leukoc Biol* (2018) 104:833–41. doi: 10.1002/JLB.3A0218-072R

184. Jang JC, Li J, Gambini L, Batugedara HM, Sati S, Lazar MA, et al. (2017) 114: E10399–408. doi: 10.1073/PNAS.1716015114

185. Onishi S, Matsuura H, Osuka A, Matsumoto H, Ebihara T, Ogura H. Resistin forms a network with inflammatory cytokines and is associated with prognosis in major burns. *Burns* (2022) 48:1680–9. doi: 10.1016/J.BURNS.2021.10.009

186. Duffy SL, Lagrone L, Herndon DN, Mileski WJ. Resistin and postburn insulin dysfunction. *J Trauma* (2009) 66:250–4. doi: 10.1097/TA.0B013E31815EBAD4

187. Wade CE, Mora AG, Shields BA, Pidcoke HF, Baer LA, Chung KK, et al. Signals from fat after injury: plasma adipokines and ghrelin concentrations in the severely burned. *Cytokine* (2013) 61:78–83. doi: 10.1016/J.CYTO.2012.08.031

188. Dong XQ, Bin YS, FL Z, QW LV, GH Z, Bin HH. Resistin is associated with mortality in patients with traumatic brain injury. *Crit Care* (2010) 14. doi: 10.1186/CC9307

189. Zhang DQ, Deng Y, jie ZL, min L, Qi Y, Wang J, et al. Elevated resistin levels may regulate high mobility group box 1 expression in Guillain-Barré syndrome. *J Neuroimmunol* (2019) 330:59–66. doi: 10.1016/J.JNEUROIM.2019.02.011

190. Bonavia A, Miller L, Kellum JA, Singbartl K. Hemoadsorption corrects hyperresistinemia and restores anti-bacterial neutrophil function. *Intensive Care Med Exp* (2017) 5. doi: 10.1186/S40635-017-0150-5

191. Lee J, Jackman JG, Kwun J, Manook M, Moreno A, Elster EA, et al. Nucleic acid scavenging microfiber mesh inhibits trauma-induced inflammation and thrombosis. *Biomaterials* (2017) 120:94–102. doi: 10.1016/J.BIOMATERIALS.2016.12.024

192. Dosch M, Gerber J, Jebbawi F, Beldi G. Mechanisms of ATP release by inflammatory cells. *Int J Mol Sci* (2018) 19. doi: 10.3390/IJMS19041222

193. Sumi Y, Woehrle T, Chen Y, Bao Y, Li X, Yao Y, et al. Plasma ATP is required for neutrophil activation in a mouse sepsis model. *Shock* (2014) 42:142–7. doi: 10.1097/SHK.0000000000000180

194. Chen Y, Shukla A, Namiki S, Insel PA, Junger WG. A putative osmoreceptor system that controls neutrophil function through the release of ATP, its conversion to adenosine, and activation of A2 adenosine and P2 receptors. *J Leukoc Biol* (2004) 76:245–53. doi: 10.1189/JLB.0204066

195. Woehrle T, Yip L, Manohar M, Sumi Y, Yao Y, Chen Y, et al. Hypertonic stress regulates T cell function via pannexin-1 hemichannels and P2X receptors. *J Leukoc Biol* (2010) 88:1181–9. doi: 10.1189/JLB.0410211

196. Haskó G, Kuhel DG, Salzman AL, Szabó C. ATP suppression of interleukin-12 and tumour necrosis factor-alpha release from macrophages. *Br J Pharmacol* (2000) 129:909–14. doi: 10.1038/SJ.BJP.0703134

197. Li X, Kondo Y, Bao Y, Staudenmaier L, Lee A, Zhang J, et al. Systemic adenosine triphosphate impairs neutrophil chemotaxis and host defense in sepsis. *Crit Care Med* (2017) 45:e97–e104. doi: 10.1097/CCM.0000000000002052

198. Zha QB, Wei HX, Li CG, Liang YD, Xu LH, Bai WJ, et al. ATP-induced inflammasome activation and pyroptosis is regulated by AMP-activated protein kinase in macrophages. *Front Immunol* (2016) 7:597. doi: 10.3389/FIMMU.2016.00597

199. He Y, Taylor N, Fourgeaud L, Bhattacharya A. The role of microglial P2X7: modulation of cell death and cytokine release. *J Neuroinflamm* (2017) 14. doi: 10.1186/S12974-017-0904-8

200. Yip L, Woehrle T, Corriden R, Hirsh M, Chen Y, Inoue Y, et al. Autocrine regulation of T-cell activation by ATP release and P2X7 receptors. *FASEB J* (2009) 23:1685–93. doi: 10.1096/FJ.08-126458

201. Fredholm BB. Purines and neutrophil leukocytes. *Gen Pharmacol* (1997) 28:345–50. doi: 10.1016/S0306-3623(96)00169-3

202. Cauwels A, Rogge E, Vandendriessche B, Shiva S, Brouckaert P. Extracellular ATP drives systemic inflammation, tissue damage and mortality. *Cell Death Dis* (2014) 5. doi: 10.1038/CDDIS.2014.70

203. Pulte ED, Broekman MJ, Olson KE, Drosopoulos JHF, Kizer JR, Islam N, et al. CD39/NTPDase-1 activity and expression in normal leukocytes. *Thromb Res* (2007) 121:309–17. doi: 10.1016/J.THROMRES.2007.04.008

204. Regateiro FS, Cobbold SP, Waldmann H. CD73 and adenosine generation in the creation of regulatory microenvironments. *Clin Exp Immunol* (2013) 171:1–7. doi: 10.1111/J.1365-2249.2012.04623.X

205. Cohen HB, Briggs KT, Marino JP, Ravid K, Robson SC, Mosser DM. TLR stimulation initiates a CD39-based autoregulatory mechanism that limits macrophage inflammatory responses. *Blood* (2013) 122:1935–45. doi: 10.1182/BLOOD-2013-04-496216

206. Tiwari-Heckler S, Lee GR, Harbison J, Ledderose C, Csizmadia E, Melton D, et al. Extracellular mitochondria drive CD8 T cell dysfunction in trauma by upregulating CD39. *Thorax* (2023) 78:151–9. doi: 10.1136/THORAXJNL-2021-218047

207. Thurairajah K, Briggs GD, Balogh ZJ. The source of cell-free mitochondrial DNA in trauma and potential therapeutic strategies. *Eur J Trauma Emerg Surg* (2018) 44:325–34. doi: 10.1007/S00068-018-0954-3

208. Yousefi S, Mihalache C, Kozlowski E, Schmid I, Simon HU. Viable neutrophils release mitochondrial DNA to form neutrophil extracellular traps. *Cell Death Differ* (2009) 16:1438–44. doi: 10.1038/CDD.2009.96

209. Lam NYL, Rainer TH, Chiu RWK, Joynt GM, Lo YMD. Plasma mitochondrial DNA concentrations after trauma. *Clin Chem* (2004) 50:213–6. doi: 10.1373/CLINCHEM.2003.025783

210. Zhang Q, Itagaki K, Hauser CJ. Mitochondrial DNA is released by shock and activates neutrophils via p38 map kinase. *Shock* (2010) 34:55–9. doi: 10.1097/SHK.0B013E3181CD8C08

211. Mallavia B, Liu F, Lefrançais E, Cleary SJ, Kwaan N, Tian JJ, et al. Mitochondrial DNA stimulates TLR9-dependent neutrophil extracellular trap formation in primary graft dysfunction. *Am J Respir Cell Mol Biol* (2020) 62:364–72. doi: 10.1165/RCMB.2019-0140OC

212. Zhang J, Chen X, Liu Z, Wang X, Ren J, Sun T. Association between plasma mitochondrial DNA and sterile systemic inflammatory response syndrome in patients with acute blunt traumatic injury. *Int J Clin Exp Med* (2017) 10:3254–62.

213. Faust HE, Reilly JP, Anderson BJ, Ittner CAG, Forker CM, Zhang P, et al. Plasma mitochondrial DNA levels are associated with ARDS in trauma and sepsis patients. *Chest* (2020) 157:67–76. doi: 10.1016/J.CHEST.2019.09.028

214. Chiu RWK, Chan LYS, Lam NYL, Tsui NBY, Ng EKO, Rainer TH, et al. Quantitative analysis of circulating mitochondrial DNA in plasma. *Clin Chem* (2003) 49:719–26. doi: 10.1373/49.5.719

215. Al Amir Dache Z, Otandault A, Tanos R, Pastor B, Meddeb R, Sanchez C, et al. Blood contains circulating cell-free respiratory competent mitochondria. . *FASEB J* (2020) 34:3616–30. doi: 10.1096/FJ.201901917RR

216. Briggs GD, Gelzinnis S, Meakes S, King KL, Balogh ZJ. Not all cell-free mitochondrial dna is equal in trauma patients. *Shock* (2022) 58:231–5. doi: 10.1097/SHK.0000000000001969

217. Shen H, de Almeida PE, Kang KH, Yao P, Chan CW. Burn injury triggered dysfunction in dendritic cell response to TLR9 activation and resulted in skewed T cell functions. *PloS One* (2012) 7. doi: 10.1371/JOURNAL.PONE.0050238

218. Itagaki K, Kaczmarek E, Kwon WYMPD, Chen L, Vlková B, Zhang Q, et al. Formyl peptide receptor-1 blockade prevents receptor regulation by mitochondrial danger-associated molecular patterns and preserves neutrophil function after trauma. *Crit Care Med* (2020) 48:E123–32. doi: 10.1097/CCM.0000000000004094

219. Li H, Itagaki K, Sandler N, Gallo D, Galenkamp A, Kaczmarek E, et al. Mitochondrial damage-associated molecular patterns from fractures suppress pulmonary immune responses via formyl peptide receptors 1 and 2. *J Trauma Acute Care Surg* (2015) 78:272–81. doi: 10.1097/TA.0000000000000509

220. Zhao C, Itagaki K, Gupta A, Odom S, Sandler N, Hauser CJ. Mitochondrial damage-associated molecular patterns released by abdominal trauma suppress pulmonary immune responses. *J Trauma Acute Care Surg* (2014) 76:1222–7. doi: 10.1097/TA.0000000000000220

221. Itagaki K, Riça I, Zhang J, Gallo D, DePrato M, Otterbein LE, et al. Intratracheal instillation of neutrophils rescues bacterial overgrowth initiated by trauma damage-associated molecular patterns. *J Trauma Acute Care Surg* (2017) 82:853–60. doi: 10.1097/TA.0000000000001413

222. Macáková K, Kaczmarek E, Itagaki K. Can neutrophils prevent nosocomial pneumonia after serious injury? *Int J Mol Sci* (2023) 24. doi: 10.3390/IJMS24087627

223. Nakahira K, Kyung SY, Rogers AJ, Gazourian L, Youn S, Massaro AF, et al. Circulating mitochondrial DNA in patients in the ICU as a marker of mortality: derivation and validation. *PloS Med* (2013) 10:1–12. doi: 10.1371/JOURNAL.PMED.1001577

frontiers | Frontiers in Immunology

TYPE Original Research
PUBLISHED 24 August 2023
DOI 10.3389/fimmu.2023.1239145

OPEN ACCESS

EDITED BY
Sanjeev Choudhary,
Sam Houston State University,
United States

REVIEWED BY
Pedro Elias Marques,
KU Leuven, Belgium
Vladimir M. Pisarev,
Federal Research and Clinical Center of Intensive Care Medicine and Rehabilitation, Russia

*CORRESPONDENCE
Borna Relja
info@bornarelja.com

†These authors have contributed equally to this work

RECEIVED 12 June 2023
ACCEPTED 07 August 2023
PUBLISHED 24 August 2023

CITATION
Meng F, Zhou Y, Wagner A, Bülow JM, Köhler K, Neunaber C, Bundkirchen K and Relja B (2023) Impact of age on liver damage, inflammation, and molecular signaling pathways in response to femoral fracture and hemorrhage.
Front. Immunol. 14:1239145.
doi: 10.3389/fimmu.2023.1239145

Impact of age on liver damage, inflammation, and molecular signaling pathways in response to femoral fracture and hemorrhage

Fanshuai Meng[1,2], Yuzhuo Zhou[1,3], Alessa Wagner[1], Jasmin Maria Bülow[1], Kernt Köhler[4], Claudia Neunaber[3], Katrin Bundkirchen[3†] and Borna Relja[1*†]

[1]Department of Trauma, Hand, Plastic and Reconstructive Surgery, Translational and Experimental Trauma Research, Ulm University Medical Center, Ulm, Germany, [2]Department of Trauma and Reconstructive Surgery, Uniklinik RWTH Aachen, Aachen, Germany, [3]Department of Trauma Surgery, Hannover Medical School, Hannover, Germany, [4]Institute of Veterinary Pathology, Justus Liebig University Giessen, Giessen, Germany

Background: Trauma causes disability and mortality globally, leading to fractures and hemorrhagic shock. This can trigger an irregular inflammatory response that damages remote organs, including liver. Aging increases the susceptibility to dysregulated immune responses following trauma, raising the risk of organ damage, infections, and higher morbidity and mortality in elderly patients. This study investigates how aging affects liver inflammation and damage post-trauma.

Methods: 24 male C57BL/6J mice were randomly divided into four groups. Twelve young (17-26 weeks) and 12 aged (64-72 weeks) mice were included. Mice further underwent either hemorrhagic shock (trauma/hemorrhage, TH), and femoral fracture (osteotomy) with external fixation (Fx) (THFx, n=6) or sham procedures (n=6). After 24 hours, mice were sacrificed. Liver injury and apoptosis were evaluated using hematoxylin-eosin staining and activated caspase-3 immunostaining. CXCL1 and infiltrating polymorphonuclear leukocytes (PMNL) in the liver were assessed by immunostaining, and concentrations of CXCL1, TNF, IL-1β, and IL-10 in the liver tissue were determined by ELISA. Gene expression of *Tnf*, *Cxcl1*, *Il-1β*, and *Cxcl2* in the liver tissue was determined by qRT-PCR. Finally, western blot was used to determine protein expression levels of IκBα, Akt, and their phosphorylated forms.

Results: THFx caused liver damage and increased presence of active caspase-3-positive cells compared to the corresponding sham group. THFx aged group had more severe liver injury than the young group. CXCL1 and PMNL levels were significantly higher in both aged groups, and THFx caused a greater increase in CXCL and PMNL levels in aged compared to the young group. Pro-inflammatory TNF and IL-1β levels were elevated in aged groups, further intensified by THFx. Anti-inflammatory IL-10 levels were lower in aged groups. *Tnf* and *Cxcl1* gene expression was enhanced in the aged sham group. Phosphorylation ratio of IκBα was significantly increased in the aged sham group versus young sham group.

THFx-induced IκBα phosphorylation in the young group was significantly reduced in the aged THFx group. Akt phosphorylation was significantly reduced in the THFx aged group compared to the THFx young group.

Conclusion: The findings indicate that aging may lead to increased vulnerability to liver injury and inflammation following trauma due to dysregulated immune responses.

KEYWORDS

femur fracture, hemorrhagic shock, aging, liver injury, inflammasome, NF-KappaB, Akt

1 Introduction

Traumatic injuries account for 8% of all deaths worldwide and account as one of the leading causes of morbidity and mortality worldwide (1). Fatal initial injuries resulting from trauma can cause early death, while secondary infections and resulting complications can lead to (multiple) organ failure and contribute to post-injury mortality (2). Recovery and outcome after major trauma are therefore influenced by post-injury complications (3). Femoral fractures are frequently accompanied with a massive blood loss, both of which are common in patients with multiple trauma, and result in high mortality rates (4, 5).

Cell death from initial tissue damage, blood loss and subsequent secondary tissue damage cause the release of damage-associated molecular patterns (DAMPs) such as adenosine triphosphate (ATP) (6), which contribute to the inflammatory response, as shown e.g. in ischemia/reperfusion (I/R) liver injury triggered by the activation of inflammasomes in Kupffer cells, which contribute to the local inflammatory response (7). Inflammasomes play a critical role in the maturation of Interleukin-1β (IL-1β) and can cause liver injury in I/R due to the release of pro-inflammatory cytokines and excessive neutrophil infiltration (7, 8). Polymorphonuclear neutrophils are the first inflammatory cells to appear at the site of injury, which can also release local pro-inflammatory mediators, such as IL-1β, tumor necrosis factor (TNF) and diverse DAMPs (9–11), activating the nuclear factor kappa-light-chain-enhancer of activated B-cells (NF-κB) pathway. NF-κB regulates inflammation by increasing the production of inflammatory cytokines, chemokines, and adhesion molecules, as well as regulating cell proliferation, apoptosis, and differentiation (12). Activation of the canonical NF-κB pathway occurs through the phosphorylation of the NF-κB inhibitor alpha (IκBα), which is induced in a controlled manner. The level of phosphorylation of IκBα serves as an indicator of NF-κB pathway activation (13, 14). Previous research has shown that NF-κB is also involved in stimulating the activity of protein kinases B (Akt) (15). Akt, a protein involved in cell survival and growth, also plays an important role in inflammation progression (16, 17). Akt activates the IκB kinase IKK, leading to the degradation of IκB and nuclear translocation of NF-κB, which promotes the expression of cytokines, including IL-1β and TNF-α, and accelerates the inflammatory response (18, 19).

Aging, as defined in biology, refers to the gradual increase in frailty of an organism over time, leading to a decreased ability to handle stress (20). In older individuals, there is a commonly observed condition known as "inflammaging", characterized by a baseline level of inflammation (20–22). Furthermore, aging is associated with a decline in both innate and adaptive immune pathways, resulting in reduced ability to respond to pathogens, a condition known as immunosenescence (21–23). At the cellular level, aging is marked by a chronic, sterile, low-grade inflammation, progressive decline in the function of cells, including their ability to proliferate, differentiate, and carry out physiological functions (21, 22, 24, 25). When injury occurs, the body's systemic inflammatory response to trauma, may be exaggerated in older people due to higher levels of cytokines or reduced production of anti-inflammatory cytokines (26). The presence of noticeable indications of liver degeneration, hepatic inflammation, and fibrosis is closely linked to old age in mice (27). 24 hours after burn injury, indicators of liver damage and levels of C-X-C Motif Chemokine Ligand (CXCL)1 were increased in aged mice when they were treated with lipopolysaccharide compared to young mice, while IL-6 aged knockout mice exhibited reduced liver injury (28). Similarly, aged mice subjected to ischemia, have shown more activated liver-recruited neutrophils, reduced expression of the cytoprotective heat shock protein 70 in the liver, suppressed and delayed NF-κB activation in response to TNF, all together results indicating that multiple cellular and molecular changes contribute to increased liver injury after ischemia in aged mice (29). Interestingly, also age-dependent NOD-like receptor family, pyrin domain containing (NLRP)3 inflammasome activation, and thus inflammation, impaired the capacity to resolve fibrosis during aging (30).

As society continues to age, the number of elderly individuals experiencing severe trauma, particularly fractures accompanied by blood loss, is expected to rise. The aging process affects both the innate and adaptive immune systems, potentially leading to a diminished immunological response to traumatic events compared to younger individuals. Nevertheless, the precise mechanisms that drive age-related changes in inflammation following trauma are not yet fully understood. Against this backdrop, the objective of this study was to explore the impact of aging on inflammatory alterations and the underlying processes

responsible for liver injury in mice subjected to femur fracture and hemorrhagic shock. The study specifically focused on investigating the NF-κB signaling pathway, AKT and inflammasome activation. Our hypothesis suggests that aging may contribute to a heightened inflammatory response and more severe liver damage in the elderly group through trauma-induced inflammasome activation and disrupted NF-κB AKT activation.

2 Materials and methods

2.1 Animal husbandry

This research obtained approval from the local institutional animal care and research advisory committee and received authorization from the local government of Lower Saxony, Germany (approval number: 33.12-42502-04-17/2491). The study utilized young (17-26 weeks) and aged (64-72 weeks) male C57BL/6J mice obtained from Janvier Labs, Le Genest-Saint-Isle, France (31). The mice were housed individually in cages under standardized conditions at the Central Animal Laboratory of Hannover Medical School. The cages, bedding, and drinking bottles were regularly replaced, and standard softwood granules from Altromin GmbH (Lage, Germany) were used as litter material for the experimental animals.

2.2 Group distribution

A total of twenty-four animals were randomly allocated to four groups. The sham groups consisted of six animals in each group (sham young and sham aged). In these groups, the animals underwent femoral artery catheterization at the left leg and were fitted with an external fixator on the right side, but no blood loss or femoral osteotomy was performed. The trauma groups also consisted of six animals in each group (THFx young and THFx aged). In these groups, the animals experienced hemorrhagic shock through blood withdrawal via the left femoral artery catheter and implantation of an external fixator, followed by femoral osteotomy of the right leg. The animals were sacrificed 24 hours after the experimental procedures were conducted.

2.3 Experimental model

All surgical procedures were carried out under deep inhalation anesthesia using isoflurane (Baxter Deutschland GmbH, Unterschleißheim, Germany), following the previously described methods (32, 33). The experiment started once the negative interphalangeal reflex in mice was consistently absent. To maintain the mice`s body temperature, a heating pad was used during surgical procedure, and Bepanthen eye ointment was applied to prevent eye dryness. Subcutaneous injections of 5 mg/kg body weight carprofen and 1 mg/kg body weight butorphanol were administered for intraoperative analgesia. Local anesthesia at the surgical site was achieved with prilocaine hydrochloride. Postoperative analgesia was provided by mixing metamizole at a dose of 200 mg/kg body weight into drinking water, and additional subcutaneous injections of carprofen and butorphanol were administered as required. After surgery, the animals were placed in a warm environment under red light until they regained full consciousness, and then housed separately to prevent aggression that could hinder the healing of the surgical wound. The animals' vital signs and mobility, as well as signs for lameness were regularly monitored and assessed post-surgically.

In both the sham and trauma groups, a catheter was inserted into the left femoral artery and an external fixator (MouseExFix simple L 100%, RISystem, Davos, Switzerland) was implanted in the right femur. Animals in the trauma groups (THFx young; THFx aged) underwent pressure-controlled hemorrhagic shock. For this, blood was withdrawn until the mean arterial blood pressure reached 35 ± 5 mm Hg. The hypovolemic shock state was maintained for a total of 90 minutes. Following that, the animals were re-infused with four times the amount of blood withdrawn (up to a maximum of 2.4 ml) using warm Ringer's solution within 30 minutes, and the catheter was then removed. The fixator was inserted into the right femoral shaft, and the diaphysis was osteotomized centrally between the two middle pins using a 0.44 mm diameter wire saw (Gigly wire saw, RISystem) in the THFx groups. All wounds were sutured using Prolene 6-0 (Ethicon, Cincinnati, USA), and the animals were allowed to move freely immediately after the completion of the surgical procedures.

2.4 Harvesting procedures

After twenty-four hours following the surgery, the animals were euthanized by intraperitoneal injection of 75 mg/kg body weight of ketamine and 1 mg/kg body weight of medetomidine. Once the absence of negative interdigital reflexes was confirmed, the abdominal cavity was opened, and a heparinized sharp 25-gauge syringe was used to puncture the heart and collect blood. Following that, cervical dislocation was performed. The blood was centrifuged at 7000 rpm for 5 minutes at room temperature, and was plasma stored at -80°C until further use. Subsequently, the incision was extended along the chest wall. Twenty ml of PBS was perfused through the heart using a 21-gauge blunt-tipped syringe (BD, Franklin Lakes, USA). The left lateral liver lobe was ligated, swiftly frozen in liquid nitrogen, and stored at - 80°C. Then, for subsequent (immune)histological analyses, mice were perfused with 10 ml of 4% buffered Zn-Formalin (Thermo Fisher Scientific, Waltham, USA) through the heart, and the right liver lobe was removed and fixed overnight for further histological analysis.

2.5 Examination of liver damage

The collected specimens were fixed in 4% buffered Zn-formalin (Thermo Fisher Scientific, Waltham, USA) overnight and subsequently embedded in paraffin. The specimens were then sectioned into 3 µm slices to prepare them for hematoxylin-eosin (HE) and immune histological stainings. The paraffin was removed,

and the liver sections were rehydrated. Subsequently, the sections were stained with hemalum solution (Carl Roth, Karlsruhe, Germany) for 10 minutes at room temperature. After rinsing in water for 10 minutes, the tissue was counterstained with eosin (Carl Roth, Karlsruhe, Germany) for 3 minutes. The sections were then dehydrated using an ascending alcohol series and mounted with a xylene-based mounting medium (Mountex, Medite Medical GmbH, Burgdorf, Germany). The histological assessment of liver damage in the HE-stained sections from different experimental groups was performed by an independent examiner. Briefly, random necrosis, single cell degeneration/necrosis or individualization, zonal necrosis (perivenous), vacuolization of Ito cells, and vacuolization of hepatocytes were scored individually with 0 (not observed), 1 (mild), 2 (moderate) or 3 (marked). Then, the mean out of all individual values was calculated for each sample to provide the liver injury score (LIS). Furthermore, plasma levels of liver damage marker glutamic oxaloacetic transaminase (GOT) or aspartate aminotransferase were determined by Arkray Spotchem EZ SP-4430.

2.6 RNA extraction, reverse transcription and semi-quantitative polymerase chain reaction

RNA extraction was conducted from the liver tissue using the Precellys 24 Homogenizer (Bertin Technologies, Montigny-le-Bretonneux, France) through mechanical disruption. The RNeasy assay buffer (Qiagen, Hilden, Germany) was utilized following the manufacturer's protocol. To eliminate any remaining DNA, the sample underwent treatment with the RNase-free DNase kit (Qiagen, Hilden, Germany). The RNA was qualitatively and quantitatively analyzed using Tecan's NanoQuant Plate on the Spark M10 Microplate Reader (Tecan, Männedorf, Switzerland). For cDNA synthesis, the iScript™ cDNA Synthesis Kit (BioRad, Hercules, USA) was employed according to the manufacturer's instructions. Gene expression levels of *Tnf* (qMnuCED0004141), *Cxcl1* (qMnuCED0047655), *Il-1β* (qMnuCED0045755), and *Cxcl2* (qMmuCED0050757) were quantified using the PrimePCR SYBR Green Assay (BioRad, Hercules, USA) with specific primer sets for mice. The housekeeping gene *Gapdh* (qMnuCED0027467) was quantified as a control. The PCR reaction was performed in a total volume of 25 µl, including the SYBR Green qPCR Master Mix (BioRad), following the manufacturer's instructions. The reaction took place using the C1000 Touch Thermal Cycler with the CFX96 Touch Real-Time PCR Detection System (BioRad, Hercules, USA). Finally, the relative expression level of each target gene was determined using the comparative threshold-cycle (CT) method (2-ΔΔCT method), which involved normalizing the expression of each target gene to that of *Gapdh*.

2.7 Quantification of protein expression levels via ELISA

The liver tissue was homogenized in lysis buffer (FNN0021, Invitrogen™) at 4°C, followed by centrifugation at 20,000 x g for 30 minutes at 4°C. The resulting supernatants were stored at -80°C for future analysis. The protein supernatant extracted from liver tissue was stored at -80°C for later analysis of protein concentration of TNF, IL-1β, IL-10 and CXCL1 using mouse-specific ELISA kits (R&D Systems, Minneapolis, USA) according to manufacturer's guideline. For measuring of CXCL1 plasma samples were diluted in a ratio of 1:2. ELISA quantification was performed using the Infinite M200 microplate reader (Tecan, Männedorf, Switzerland).

2.8 Immunohistological staining of CXCL1, neutrophile elastase and active caspase-3

Paraffin-embedded liver tissue sections (3 µm) were deparaffinized twice for 5 minutes using Roti Histol (Carl Roth, Karlsruhe, Germany), and rehydrated using a gradually decreasing concentration of alcohol at 100%, 90%, and 70%. R-Universal epitope recovery buffer (Aptum, Kassel, Germany) was used to achieve heat-induced epitope retrieval with the 2100-Retriever (Prestige Medical, Blackburn, England) at 121°C for 20 minutes following the manufacturer's manual. Block of endogenous peroxidase was performed using hydrogen peroxide (Peroxidase UltraVision Block, Thermo Fisher Scientific, Waltham, USA) for 20 minutes. Primary antibodies for CXCL1 (abcam, USA, ab269939, rabbit anti-mouse, 1:300), neutrophile elastase (Bioss, USA, bs-6982R, rabbit anti-mouse, 1:200) or active caspase-3 (Cell Signaling Technology, USA, anti-cleaved caspase-3 (Asp175), #9661, rabbit anti-mouse, 1:300) were diluted according to manufacturer's recommendation in Antibody Dilution Buffer (Dako Cytomation) and incubated for one hour at room temperature. Subsequently, the secondary antibody conjugated with horseradish peroxidase (Histofine Simple Stain Mouse MAX PO (R), Nichirei Biosciences Inc, 414311F) was incubated for 30 minutes at room temperature and 3-amino-9-ethylcarbazol (AEC, DCS Innovative Diagnostik-Systeme, Hamburg) was used to detect specific binding. Slides were counterstained with hematoxylin (Carl Roth, Karlsruhe, Germany) and mounted (Medite Medical GmbH, Burgdorf, Germany). Imaging was performed using the Zeiss Axio Observer Z1 microscope (40x objective, Zeiss, Göttingen, Germany). The evaluation was performed using ImageJ software. For CXCL1, mean intensity values were measured, while for neutrophile elastase and active caspase-3, positive-counted cells were measured in 25 high-power fields in the 400x magnification.

2.9 Western blotting

The liver tissue was homogenized in lysis buffer (FNN0021, Invitrogen™) at 4°C, followed by centrifugation at 20,000 x g for 30 minutes at 4°C. The resulting supernatants were stored at -80°C for future analysis. Electrophoresis was conducted on 15 µg of protein lysate, which was separated by a 10% polyacrylamide sodium dodecyl sulfate gel and subsequently transferred to a polyvinylidene difluoride membrane (Thermo Fisher Scientific). The blots were blocked in a blocking buffer (5% nonfat dry milk in 1 mM Tris, 150 mM NaCl, pH 7.4) for one hour at room

temperature. Subsequently, primary antibodies (in 0.5% bovine serum albumin and 0.5% Tween 20) were incubated overnight at 4°C and constant shaking. IκBα Rabbit polyclonal antibody (9242S, 1:1000), Phospho-IκBα Mouse mAb (9246S, 1:1000), Akt Rabbit mAb (4691S, 1:1000), and Phospho-Akt Rabbit mAb (4060S, 1:2000, all Cell Signaling Technology) were used as primary antibodies. Monoclonal beta-Actin antibody (4967S, 1:2000 Cell Signaling Technology) was used as housekeeping gene. Then, a horseradish peroxidase-conjugated secondary antibody (abcam) was subsequently applied for 1 hour at room temperature on the shaker. For detection of Phospho-Akt, Akt and IκBα Goat Anti-Rabbit IgG H&L (HRP) (ab288151, 1:10000, Abcam) and for Phospho-IκBα Goat Anti-Mouse IgG H&L (HRP) (ab97023, 1:10000, Abcam) was used as secondary antibody. Proteins were detected using 1 ml ECL™ Western blot detection reagent. After measuring phosphorylated IκBα and phosphorylated Akt the PDVF membrane was placed in TBS, and washed 2x15 minutes in stripping buffer (0.2 M Glycin, 0.1% SDS, 1% Tween20, pH 2.2), and 3x5 minutes in TBST on a rocker with 50 rpm. The membranes were then blocked again for one hour in blocking buffer and incubated with IκBα and Akt primary antibodies at 4°C. After incubation, the membranes were washed 2x15 minutes with TBST and 1x15 minutes with TBS (20 mM Tris-Base, 0.15 M NaCl, pH 7.6), and incubated with the corresponding secondary antibody for one hour at room temperature on the shaker. After incubation, the membranes were washed 2x15 minutes with TBST and 1x15 minutes with TBS, and then proteins were detected using 1 ml ECL™ Western blot detection reagent. Then stripping was performed and proceeded to incubate β-actin as described above. At last, the integrated density of individual bands was determined using ImageJ software for quantification of protein level normalization to β-actin by densitometry.

2.10 Statistical analysis

The statistical analysis was performed using GraphPad Prism 6 (GraphPad Software, Inc., San Diego, CA). Data were tested for normal distribution using Shapiro-Wilk normality test. As the data was not normally distributed Mann-Whitney U test was performed. The results are presented using box and whiskers and min. to max., and statistically significant differences are indicated as $p<0.05$ (*).

3 Results

3.1 Impact of age on liver damage after THFx

The experimental design is shown in Figure 1A. Hepatic damage resulting from THFx was evaluated by analyzing liver tissue using HE staining (Figure 1B), and a comparison was made among the groups (Figure 1D). The THFx young group exhibited a significant increase in liver damage compared to the sham young group (p<0.05, Figure 1D). Similarly, the THFx aged group displayed a significant increase in liver necrosis compared to the sham aged group (p<0.05, Figure 1D). Moreover, there was a significant elevation in liver damage in the THFx aged group compared to the THFx young group (p<0.05, Figure 1D).

Figure 1C presents the apoptosis induction by THFx in the liver, as demonstrated by immunohistochemical staining of activated caspase-3 (red cells, Figure 1C). The quantification of cells positive for active caspase-3, serving as a direct indicator of apoptosis, is presented in Figure 1E. In the THFx young group, a significant increase in caspase-3 positive stained cells compared to the sham young group was observed (p<0.05, Figure 1E). Additionally, the THFx aged group exhibited a significant increase in caspase-3 positive stained cells compared to the sham aged group (p<0.05, Figure 1E). Plasma GOT levels after THFx compared to the respective sham group were significantly increased (p<0.05, Figure 1F). Moreover, there was a significant increase in GOT levels in the THFx aged group compared to the THFx young group (p<0.05, Figure 1F).

3.2 Impact of age on CXCL1 protein expression, systemic CXCL1 levels and neutrophilic infiltration in the liver after THFx

Figure 2A depicts representative liver sections following immunohistochemical staining of CXCL1, while Figure 2C illustrates the protein expression of CXCL1 for each group. The liver exhibited a significant increase in CXCL1 protein expression after THFx in both young and aged animals compared to the corresponding sham groups (p<0.05, Figure 2C). Moreover, CXCL1 protein expression was significantly higher in the aged groups compared to the respective young groups, particularly in the THFx aged group (p<0.05, Figure 2C).

Given that CXCL1 acts as a chemoattractant for various immune cells, notably neutrophils, we investigated the recruitment of polymorphonuclear leukocytes to the liver after THFx. PMNL infiltration in liver tissue was assessed through immunohistochemical staining (Figure 2B), and the quantification of positively stained cells (red cells) is presented in Figure 2D. There was a significant increase in PMNL infiltration in the THFx young group compared to the sham young group (p<0.05, Figure 2D). Similarly, the THFx aged group exhibited a significant increase in PMNL infiltration compared to the sham aged group (p<0.05, Figure 2D). Additionally, the aged groups displayed a significant increase in PMNL infiltration compared to the respective young group (p<0.05, Figure 2D). Plasma CXCL1 levels after THFx compared to the respective sham group were significantly increased (p<0.05, Figure 2E). Moreover, there was an increase in aged groups compared to young groups (p<0.05, Figure 2E).

3.3 Impact of age on liver inflammatory cytokines after THFx

Protein levels of TNF, IL-1β and IL-10 in homogenized liver tissue were assessed. The results showed that protein concentration

10.3389/fimmu.2023.1239145

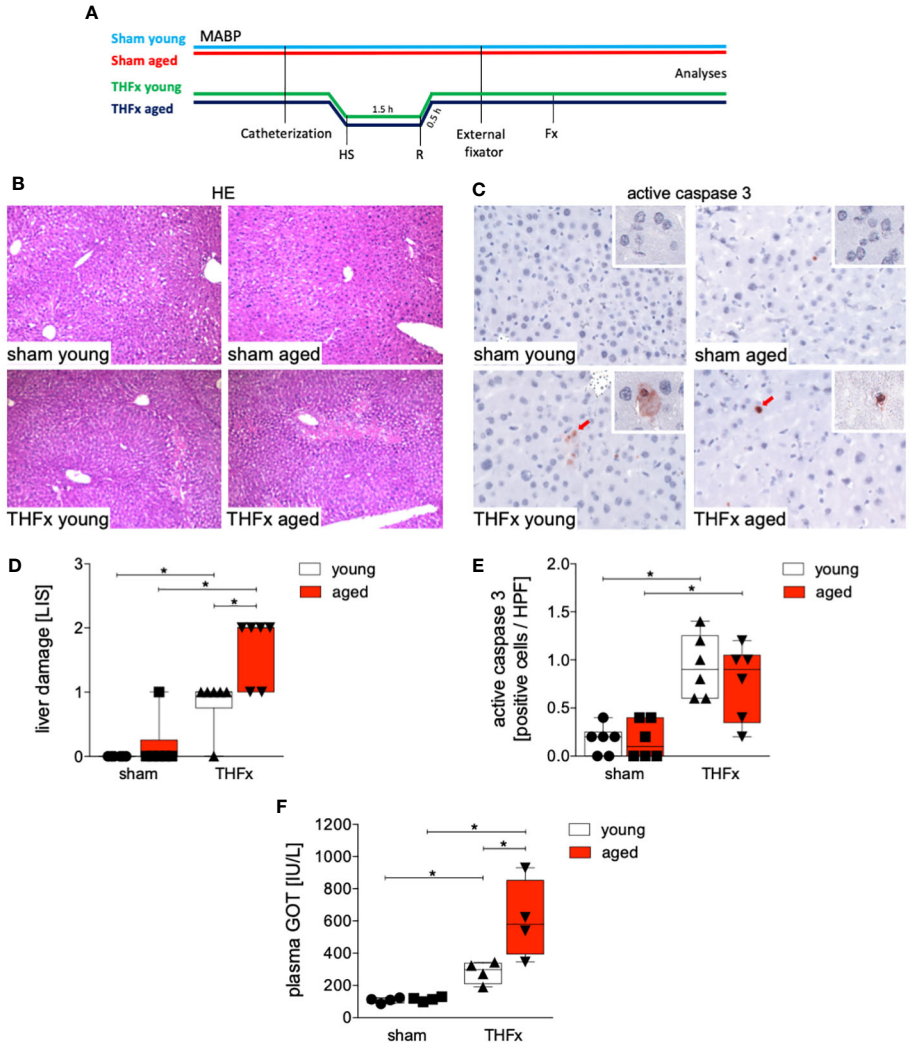

FIGURE 1
Impact of aging on liver damage after hemorrhagic shock (trauma/hemorrhage, TH) and femoral fracture (Fx). **(A)** The experimental design involved young (17-26 weeks) and aged (64-72 weeks) male C57BL/6J mice, as well as sham and trauma groups, with trauma groups undergoing pressure-controlled hemorrhagic shock (HS) followed by resuscitation (R) with Ringer's solution and Fx (via osteotomy) (THFx) (green and blue line), while sham groups received catheterization and an external fixator but no THFx induction (light blue and red line). Liver tissue samples were obtained 24 hours after the experiment. MABP: mean arterial blood pressure. **(B)** Representative liver sections upon hematoxylin/eosin (HE) staining, and **(C)** representative liver sections upon the staining of active caspase-3 of the sham young, sham aged, THFx young and THFx aged groups. Red cells are active caspase-3 positive stained cells. **(D)** Quantification of liver damage. **(E)** Quantification of active caspase-3 positively stained cells per high power field (HPF) **(D, E)**; n=6 in each group. **(F)** Quantification of plasma glutamic oxaloacetic transaminase (GOT); n=4 in each group. * p<0.05 between indicated groups.

of TNF in liver tissue was significantly increased in both aged groups, sham and THFx, compared to the corresponding young group (p<0.05, Figure 3A).

The liver exhibited a significant increase in IL-1β protein level after THFx in both young and aged animals compared to the corresponding sham groups (p<0.05, Figure 3B). Moreover, the aged groups showed a significant rise in IL-1β protein concentration compared to the respective young groups (p<0.05, Figure 3B), particularly, the THFx aged group displayed a significant elevation in IL-1β compared to the THFx young group (p<0.05, Figure 3B).

The concentration of IL-10 in liver tissue was significantly decreased in both aged groups, sham and THFx, compared to the corresponding young group (p<0.05, Figure 3C).

3.4 Impact of age on *Tnf*, *Cxcl1*, *Il-1β*, and *Cxcl2* gene expression after THFx

Figures 4A-D shows the results of *Tnf*, *Il-1β*, *Cxcl1* and *Cxcl2* gene expression. The relative gene expression of *Tnf* in liver tissue was significantly higher in THFx young group compared to the sham young group (p<0.05, Figure 4A). Baseline *Tnf* gene expression in the aged sham group was significantly higher compared to the corresponding young group (p<0.05, Figure 4A).

The relative gene expression of *Cxcl1* was significantly increased in the sham aged group compared to the sham young group (p<0.05, Figure 4B). There were no significant differences in *Il-1β* gene expression among all examined groups (Figure 4C). A

10.3389/fimmu.2023.1239145

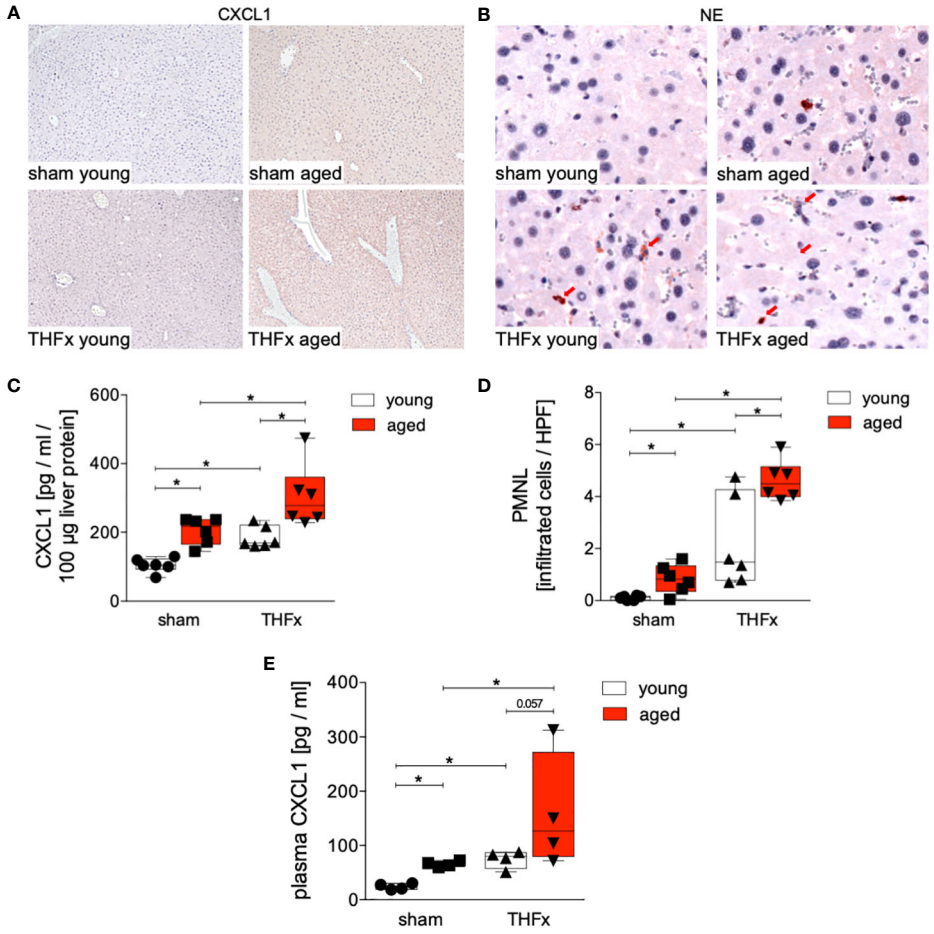

FIGURE 2
Impact of aging on CXCL1 protein expression and neutrophilic infiltration after hemorrhagic shock (trauma/hemorrhage, TH) and femoral fracture (Fx). The experimental design involved young (17-26 weeks) and aged (64-72 weeks) male C57BL/6J mice, as well as sham and trauma groups, with trauma groups undergoing pressure-controlled hemorrhagic shock followed by resuscitation (R) with Ringer's solution and Fx (via osteotomy) (THFx), while sham groups received catheterization and an external fixator but no THFx induction. Liver tissue samples were obtained 24 hours after the experiment. **(A)** Representative liver sections upon the staining of CXCL1 in the sham young, sham aged, THFx young and THFx aged groups. **(B)** Representative immunohistological staining of neutrophil elastase (NE) as a marker of polymorphonuclear leukocytes (PMNL) in liver sections. Red arrows indicate NE-positive stained cells. **(C)** Quantification of CXCL1 protein concentration using mouse-specific ELISA-kits in liver. **(D)** Quantification of NE-positive stained cells per high power field (HPF); n=6 in each group, **(E)** Quantification of plasma CXCL1 levels; n=4 in each group. *: p<0.05 between indicated groups.

significant upregulation of relative gene expression of *Cxcl2 in the* THFx young group compared to all other relevant groups was detected (p<0.05, Figure 4D).

3.5 Impact of age on Akt and IκBα activation after THFx

The impact of aging on Akt and NF-κB pathways was investigated after THFx. Liver tissue homogenates were collected 24 hours after resuscitation, and western blot analysis was performed to measure phosphorylated and non-phosphorylated IκB and Akt. A significant increase in the IκBα phosphorylation ratio in the sham aged group compared to the sham young group was observed (p<0.05, Figures 5A, B). Additionally, the THFx young group exhibited a significant increase in IκB phosphorylation ratio compared to the sham young group (p<0.05, Figure 5B). The THFx aged group displayed a significant decrease in the IκBα phosphorylation ratio compared to the THFx young group as well as to the sham aged group (p<0.05, Figure 5B).

The phosphorylation ratio of Akt was significantly decreased in the THFx aged group compared to all other relevant groups (p<0.05, Figures 5A, C).

4 Discussion

Trauma is a major cause of illness and death worldwide, with initial injuries leading to early mortality and complications contributing to organ failure and post-injury mortality (2, 3). Inflammation plays a crucial role in the recovery and outcome after trauma. Additionally, aging affects the immune system and leads to a chronic, low-grade inflammation known as "inflammaging" (20). Older individuals may have an exaggerated

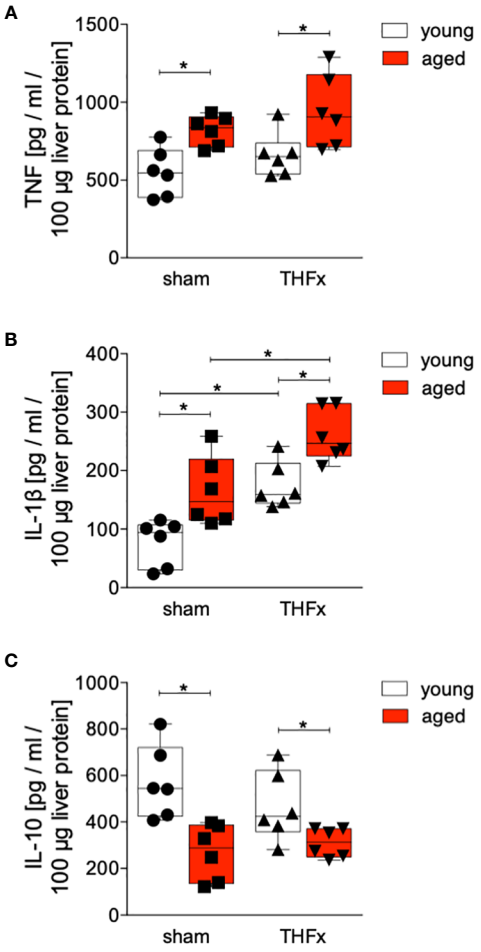

FIGURE 3
The impact of aging on TNF, IL-1β and IL-10 protein expression after hemorrhagic shock (trauma/hemorrhage, TH) and femoral fracture (Fx). The experimental design included young (17-26 weeks) and aged (64-72 weeks) C57BL/6J mice in both sham and trauma groups. The trauma groups underwent a pressure-controlled hemorrhagic shock and Fx (via osteotomy) (THFx), while the sham groups underwent catheterization and received an external fixator, but no THFx was induced. After 24 hours, the mice were euthanized, and sampling was performed. Quantification of **(A)** TNF, **(B)** IL-1β as well as **(C)** IL-10 protein concentration in liver tissue using mouse-specific ELISA-kits is shown. n=6 in each group, *: p<0.05 between indicated groups.

inflammatory response to trauma due to higher cytokine levels or reduced production of anti-inflammatory cytokines (23). In mice, aging is associated with liver degeneration, inflammation, and impaired resolution of fibrosis (27). As the population ages, the number of elderly individuals experiencing severe trauma is expected to rise. Therefore, a deeper understanding of the mechanisms behind age-related changes in inflammation following trauma is important. Our study aimed to investigate the impact of aging on inflammatory alterations and liver injury in mice with femur fracture and hemorrhagic shock. Specifically, it was investigated if the NF-κB as well as Akt signaling pathways, and inflammasome activation are involved in aging-induced heightened inflammatory response and more severe liver damage in mice.

The findings indicate that aging enhances vulnerability to liver injury and inflammation following trauma. In the aged group, more severe liver damage was observed (Figure 1), along with elevated levels of the pro-inflammatory chemokine CXCL1 and PMNL infiltration in the liver (Figures 2A–D). Additionally, the pro-inflammatory cytokines TNF and IL-1β were higher in the aged groups (Figures 3A, B), while the anti-inflammatory cytokine IL-10 was lower (Figure 3C). Gene expression analysis revealed upregulated *Tnf* and *Cxcl1* in the aged sham group (Figures 4A, B). However, no significant differences in gene expression were observed between the young and aged trauma/hemorrhage groups, except for *Cxcl2* (Figure 4C), suggesting a greater impact of aging on protein rather than gene expression levels. Moreover, signaling pathways related to inflammation regulation, such as IκBα phosphorylation and AKT phosphorylation, were impaired in the aged trauma/hemorrhage group (Figures 5). In conclusion, aging amplifies liver inflammation and damage following trauma, as evidenced by the aged group's heightened susceptibility, elevated inflammatory markers, immune cell presence, and disrupted signaling pathways.

The liver plays a crucial role in mediating inflammation by producing acute-phase proteins and modulating immune cell activity (34). It is involved in regulating systemic inflammation and secreting pro-inflammatory cytokines (35). Aging is associated with chronic, low-grade inflammation, which negatively affects

10.3389/fimmu.2023.1239145

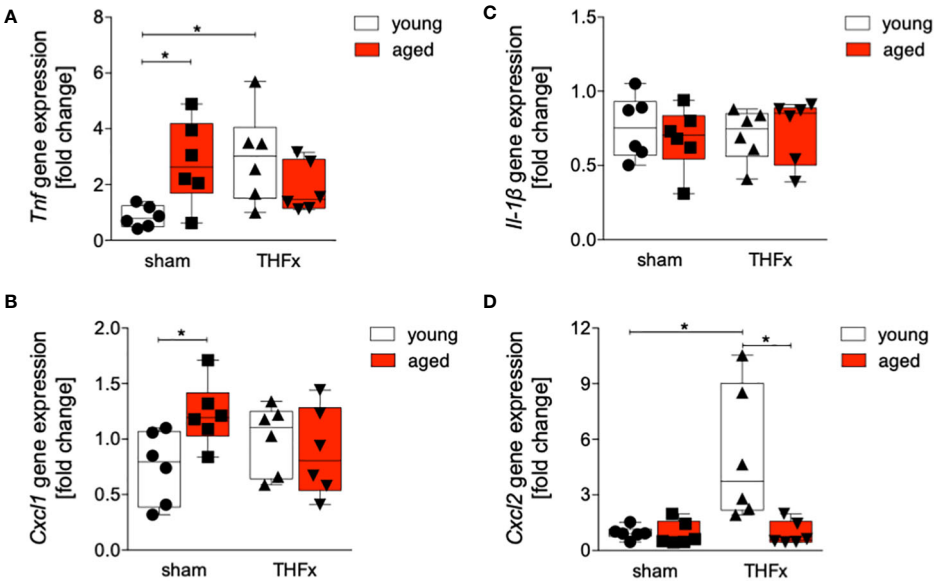

FIGURE 4
Impact of age on Tnf, Cxcl1, Il-1β and Cxcl2 gene expression after hemorrhagic shock (trauma/hemorrhage, TH) and femoral fracture (Fx). The experimental design included young (17-26 weeks) and aged (64-72 weeks) C57BL/6J mice in both sham and trauma groups. The trauma groups underwent a pressure-controlled hemorrhagic shock and Fx (via osteotomy) (THFx), while the sham groups underwent catheterization and received an external fixator, but no THFx was induced. After twenty-four hours, the mice were euthanized, and sampling was performed. The relative gene expression of **(A)** Tnf, **(B)** Cxcl1, **(C)** Il-1β as well as **(D)** Cxcl2 normalized to Gapdh after qRT-PCR was calculated by using the comparative threshold-cycle 2-ΔΔCT method.; n=6 in each group, *: p<0.05 between indicated groups.

physiological function (24). In the context of trauma, the liver's function in regulating inflammation becomes even more significant. Severe trauma triggers an inflammatory response involving various immune components including among others inflammatory cytokines, and PMNL activation, that can lead to liver injury and multiple organ dysfunction as well as increased mortality after trauma (26, 36, 37). In line with these reports, our results demonstrate increased production and release of pro-inflammatory cytokines and chemokines, IL-1β, TNF and CXCL1 in the liver after THFx (Figures 2C, 3A, B). Similarly, in a fracture-based trauma hemorrhagic liver injury model in rats, it was shown that IL-1β, TNF-α, and CXCL2 increased significantly post-trauma, indicating that inflammatory reactions had occurred in the fraction-induced hemorrhage of liver (38). As also evidenced in our study and as reported before, the activity of the immune system as for example displayed by the increased numbers of infiltrating PMNL in the liver post-trauma (Figure 2D), indicates that injury-induced inflammation stimulates immune cells, and that these changes are associated with aggravations of liver injury (38). Recently, it was shown that apoptosis biomarkers including activated and cleaved caspase-3 were increased in a long-term large animal polytrauma model, as also confirmed by our results (Figure 1E), supporting the damage of the liver after trauma (39, 40). Furthermore, our results revealed a significant activation of the inflammasome by increased IL-1β levels in mice with THFx (Figure 3B), which is consistent with findings of Sadatomo et al. showing that liver injury in ischemia/reperfusion arised from pro-inflammatory cytokines and excessive neutrophil infiltration was inflammasome-mediated (7, 8). The observed changes involve the modulation of signaling pathways, particularly those associated with NF-κB activation. Activation of NF-κB triggers the production of pro-inflammatory mediators such as cytokines, chemokines, and enzymes, which in turn, stimulate further NF-κB activation and its upstream signaling machinery, creating a positive feedback loop that intensifies the inflammatory response mediated by NF-κB and tissue injury after trauma (41–44). Enhanced activation of IκBα after THFx suggests that NF-κB activation contributes to the THFx induced increase of the pro-inflammatory effects related to increased cytokine and chemokine production, inflammasome activation and ensuing liver inflammation and injury.

In the field of trauma and inflammation research, most studies have traditionally focused on very young animals, typically between 6 to 12 weeks of age. While these studies have provided valuable insights into the mechanisms of disease, they may not accurately reflect the processes occurring in adult or aged humans. To address this limitation, we conducted a direct comparison between the response to THFx injury in "young/mature adult" mice (17-26 weeks old) and "aged adult" mice (64-72 weeks old). Our aim was to identify the differences between these two age groups and understand how they relate to humans of different age ranges. According to life tables, mice aged 17-26 weeks correspond to approximate human age of approximately above 18 years of age years, while mice aged 64-72 weeks correspond to approximate human age of above 60 years of age (45). Aging or senescent cells and/or tissues secrete a variety of bioactive molecules, including pro-inflammatory cytokines such as IL-1β, chemokines, growth factors, and proteases, collectively referred as senescence-associated secretory phenotype (SASP), that describe a chronic low-grade inflammation, also known as inflammaging (21, 46). This is in line with our findings showing enhanced TNF, IL-1β, and CXCL

10.3389/fimmu.2023.1239145

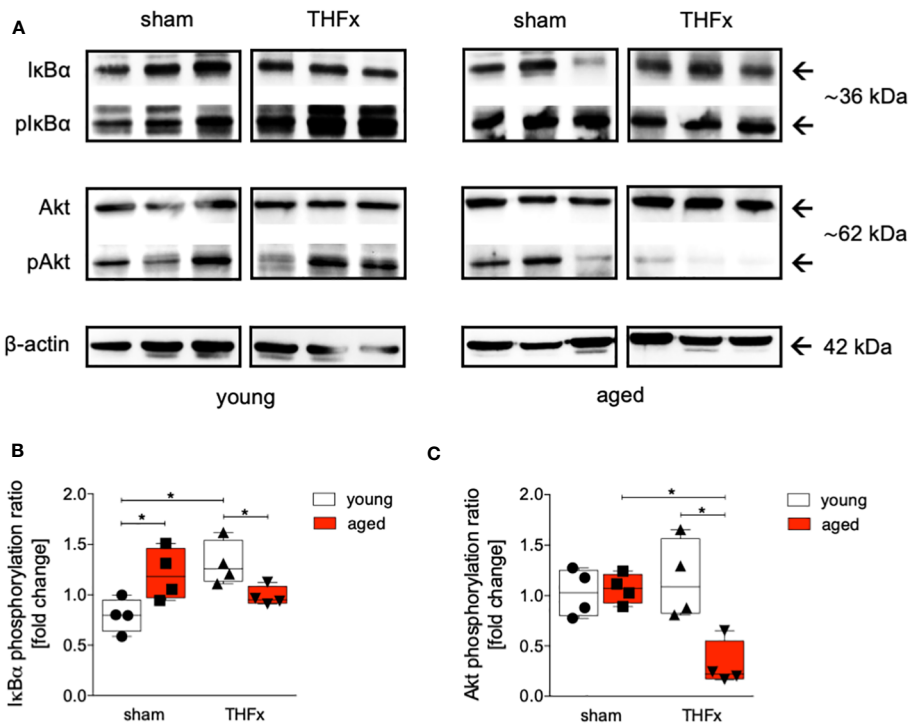

FIGURE 5
The effect of aging on IκBα and Akt following hemorrhagic shock (trauma/hemorrhage, TH) and femoral fracture (Fx) in young (17-26 weeks) and aged (64-72 weeks) male C57BL/6J mice. The experimental design included young (17-26 weeks) and aged (64-72 weeks) C57BL/6J mice in both sham and trauma groups. The trauma groups underwent a pressure-controlled hemorrhagic shock and Fx (via osteotomy) (THFx), while the sham groups underwent catheterization and received an external fixator, but no THFx was induced. After twenty-four hours, the mice were euthanized, and sampling was performed. **(A)** Western blot analysis of phosphorylated and non-phosphorylated IκBα, AKT as well as β-Actin, and quantification of **(B)** the phosphorylation ratio of IκBα, and **(C)** AKT in liver tissue. n=4 in each group, *: p<0.05 between indicated groups.

levels in the liver of aged sham animals (Figures 2C, 3A, B). The retrograde breaching of the endothelium by neutrophils was governed by enhanced production of the chemokine CXCL1 from mast cells that localized at endothelial cell junctions in aged mice (47). Thus, with implication to the dysregulated systemic inflammation associated with aging, the authors conclude that neutrophils stemming from a local inflammatory site contribute to remote organ damage (47). This is in line with our findings showing enhanced neutrophil infiltration into the liver from aged mice (Figure 2D). A large array of inflammatory factors involved in ageing is linked to the NF-κB system, and it was shown that NF-κB activation has been implicated in various age-related diseases and conditions, including chronic inflammation, neurodegenerative disorders, and certain cancers (48). Our findings underlining IκBα activation in aged sham animals also suggest that the dysregulated inflammatory response leading to the release of pro-inflammatory markers and excessive neutrophil activation was associated with NF-κB signaling pathway as potential ageing phenomenon (Figure 5B).

The post-traumatic inflammatory response and the function of NF-κB in aged liver is complex. Clearly, an enhanced vulnerability to inflammation and liver injury following trauma was present. In the aged THFx group, elevated levels of the pro-inflammatory proteins CXCL1, TNF and IL-1β, and reduced levels of the anti-inflammatory cytokine IL-10, compared to the young THFx group were observed (Figures 2C, 3A–C). The local CXCL1 concentrations in the liver were more than doubled compared to systemic CXCL1 levels, indicating, that the hepatic CXCL1 increase is rather induced by a local response than a systemic effect. Along with the elevated hepatic CXCL1 levels, enhanced neutrophil infiltration into the livers of aged animals were observed (Figures 2C, D). This is in line with previous findings from an *in vivo* endotoxin model showing elevated hepatic neutrophil numbers and their activity in aged relative to young animals receiving the same endotoxin stimulus (28). Such presence of hepatic inflammation, and liver degeneration, was closely linked to old age in mice (27), while further data indicate that CXCL1 levels and liver damage were higher in aged mice when they were treated with lipopolysaccharide compared to young mice, while e.g. an IL-6 knockout in aged mice exhibited reduced liver injury (28). Although there were noticeable alterations in proteins within aged animals following THFx, the corresponding changes in gene expression levels were not as pronounced. This implies either a disconnect between the observed changes at the protein level and the corresponding genetic regulation, or that the peak expression period of the pro-inflammatory genes has not been captured upon harvesting the livers of the mice 24 hours after THFx. Hill et al. found that gene expression of IL-1β and TNF peaked within 10-18 hours after cerebral ischemia-reperfusion injury in C57BL/6J mice (49). Similarly, Pestka and Amuzie demonstrated that

deoxynivalenol-induced gene expression of IL-1β and TNF peaked after one hour in mouse livers (50). To obtain more precise mRNA data for inflammatory factors, future studies should consider adding additional time points for liver harvesting. It is worth noting that gene expression is a dynamic process influenced by various factors. The effects of THFx might primarily affect post-transcriptional or translational processes, impacting protein function or stability without causing significant changes in gene expression. Several factors could contribute to this discrepancy. Additionally, it is important to consider the complexity of gene regulation mechanisms, that can be influenced by a wide range of factors, including transcription factors, epigenetic modifications, and non-coding RNAs. It is possible that THFx primarily affects specific post-transcriptional or translational processes, leading to changes in protein levels without significant alterations in gene expression. This is underlined by the findings of Nyugen et al. and Renshaw et al. regarding the association between aging and impaired Pattern Recognition Receptor (PRR) signaling, particularly focusing on Toll-like receptors (TLRs) in innate immune cells (51, 52). Nyugen et al. demonstrated that aging is linked to impaired signaling through PRRs, possibly due to alterations in TLR protein level in innate immune cells when comparing aged to young individuals (51). Similarly, Renshaw et al. reported significant age-related decreases in TLR gene expression in mice, specifically observing a general decrease in the expression of *Tlr1-Tlr9* genes in C57BL/6 aged mice (52). Since the activation of the NF-κB pathway occurs through TLRs on the cell membrane, the reduced expression of TLRs in aged mice may lead to a decrease in NF-κB pathway activation. Also, it was shown before, that NF-κB activation in the liver is greatly reduced in aged mice compared to young mice after hepatic ischemia/reperfusion injury due to the decreased proteasome subunit, non-ATPase 4 expression preventing recruitment of phosphorylated and ubiquitinylated IκBα to the proteasome, resulting in a defect in NF-κB activation (29, 53). This decrease in NF-κB pathway activation is supported by the reduced IκBα phosphorylation ratio in the aged group compared to the young group in the current study utilizing the THFx model (Figure 5B). Also, the crosstalk between the NF-κB and Akt pathway is important in various cellular processes including cell survival, inflammation, and immune response (54, 55). While NF-κB can activate Akt signaling, Akt can also regulate NF-κB activity (54, 55). Since the downregulated AKT phosphorylation was accompanied by reduced IκBα phosphorylation after THFx in aged animals in the current study (Figures 5B, C), the overall link between Akt and NF-κB suggests a complex regulatory network where both molecules can influence each other's activity and downstream effects in THFx. This interplay between Akt and NF-κB potentially orchestrating the cellular responses to THFx and maintaining cellular homeostasis is deregulated in aged animals. However, the increase in IκBα phosphorylation ratio in the sham aged group may also suggest that other inflammatory pathways, mediated by TNF and IL-1β, might be activated. Interestingly, age-dependent inflammasome activation, impairing the capacity to resolve fibrosis during aging as shown before (30), has been observed in our study as well by enhanced IL-1β protein levels in aged livers following THFx (Figure 3B). Thus, the findings suggest that aging may contribute to a heightened inflammatory response and more severe liver damage in the elderly group through trauma-induced inflammasome activation and disrupted NF-κB, Akt activation.

This study acknowledges several limitations that should be considered when interpreting the results. Firstly, the study was conducted using only male mice, and therefore the conclusions drawn from the study can only be applied to male subjects. In future studies, it is important to examine the effect of sex on the inflammatory response and liver damage caused by aging to obtain a more comprehensive understanding of the topic. Another limitation is that the mice used in the study were healthy, which may not fully represent the complexity of patients in a clinical setting who often have concomitant diseases and more intricate systemic conditions. Additionally, the experimental model used in this study involved implanting an external fixator before performing the osteotomy, whereas in clinical practice, fractures occur before fracture fixation. This difference in the sequence of events may have affected the experimental results and should be considered when interpreting the findings. Moreover, the fracture model used in the study employed a wire saw to create a regular fracture, while clinical situations involve various types of fractures and complex scenarios. Furthermore, the study induced controlled hemorrhagic shock in the animal model, whereas uncontrolled bleeding occurs in actual trauma situations. Such controlled settings may not fully reflect the complexity and severity of fractures and trauma-related bleeding, which should be considered when extrapolating the results to clinical practice. The study primarily focused on the local inflammatory response and liver damage, but it did not include indicators of systemic inflammatory response and liver damage, such as inflammatory mediators and liver enzymes in the blood. Including these indicators in future studies would provide a more comprehensive understanding of the overall effects. Lastly, different inflammatory response and liver damage indicators may appear at different time points. To account for this, future studies should consider including multiple time points to capture the dynamic changes and simulate the clinical scenario more accurately, thereby obtaining more comprehensive and accurate results.

Overall, the findings demonstrate that aging exacerbates liver inflammation and damage following trauma, supported by increased susceptibility, elevated inflammatory markers, immune cell presence, inflammasome activation, and disrupted signaling pathways in the aged group.

Data availability statement

The raw data supporting the conclusions of this article will be made available by the authors, without undue reservation.

Ethics statement

The animal study was approved by local government of Lower Saxony, Germany (approval number: 33.12-42502-04-17/2491).

The study was conducted in accordance with the local legislation and institutional requirements.

Author contributions

Conceptualization, CN and BR. Methodology, FM, YZ, KK, and KB. Validation, FM, KB, and BR. Formal analysis, FM and BR. Investigation, FM, YZ, and KB. Resources, CN and BR. Data curation, FM and BR. Writing-original draft preparation, FM, KB, and BR. Writing-review and editing, AW and JB. Visualization, FM and BR. Supervision, KB, CN, and BR. Funding acquisition, CN and BR. All authors contributed to the article and approved the submitted version.

Funding

This research was funded by the German Research Foundation DFG with the grant numbers DFG RE 3304/9-1, and NE 1932/1-3.

Acknowledgments

We thank Baolin Xu for the support during the *in vivo* experimental phase of this project.

Conflict of interest

The authors declare that the research was conducted in the absence of any commercial or financial relationships that could be construed as a potential conflict of interest.

Publisher's note

References

1. World Health Organization. *Preventing injuries and violence: an overview*. (2022).

2. Wafaisade A, Lefering R, Bouillon B, Sakka SG, Thamm OC, Paffrath T, et al. Epidemiology and risk factors of sepsis after multiple trauma: an analysis of 29,829 patients from the Trauma Registry of the German Society for Trauma Surgery. *Crit Care Med* (2011) 39(4):621–8. doi: 10.1097/CCM.0b013e318206d3df

3. Mors K, Braun O, Wagner N, Auner B, Voth M, Störmann P, et al. Influence of gender on systemic IL-6 levels, complication rates and outcome after major trauma. *Immunobiology* (2016) 221(8):904–10. doi: 10.1016/j.imbio.2016.03.005

4. Lane MK, Nahm NJ, Vallier HA. Morbidity and mortality of bilateral femur fractures. *Orthopedics* (2015) 38(7):e588–92. doi: 10.3928/01477447-20150701-56

5. Hildebrand F, Giannoudis P, Kretteck C, Pape HC. Damage control: extremities. *Injury* (2004) 35(7):678–89. doi: 10.1016/j.injury.2004.03.004

6. Relja B, Land WG. Damage-associated molecular patterns in trauma. *Eur J Trauma Emerg Surg* (2020) 46(4):751–75. doi: 10.1007/s00068-019-01235-w

7. Bortolotti P, Faure E, Kipnis E. Inflammasomes in tissue damages and immune disorders after trauma. *Front Immunol* (2018) 9:1900. doi: 10.3389/fimmu.2018.01900

8. Sadatomo A, Inoue Y, Ito H, Karasawa T, Kimura H, Watanabe S, et al. Interaction of neutrophils with macrophages promotes IL-1beta maturation and contributes to hepatic ischemia-reperfusion injury. *J Immunol* (2017) 199(9):3306–15. doi: 10.4049/jimmunol.1700717

9. Fine N, Tasevski N, McCulloch CA, Tenenbaum HC, Glogauer M. The neutrophil: constant defender and first responder. *Front Immunol* (2020) 11:571085. doi: 10.3389/fimmu.2020.571085

10. Lloyd AR, Oppenheim JJ. Poly's lament: the neglected role of the polymorphonuclear neutrophil in the afferent limb of the immune response. *Immunol Today* (1992) 13(5):169–72. doi: 10.1016/0167-5699(92)90121-M

11. Wilgus TA, Roy S, McDaniel JC. Neutrophils and wound repair: positive actions and negative reactions. *Adv Wound Care (New Rochelle)* (2013) 2(7):379–88. doi: 10.1089/wound.2012.0383

12. Liu T, Zhang L, Joo D, Sun SC. NF-kappaB signaling in inflammation. *Signal Transduct Target Ther* (2017) 2:17023–. doi: 10.1038/sigtrans.2017.23

13. Karin M, Delhase M. The I kappa B kinase (IKK) and NF-kappa B: key elements of proinflammatory signalling. *Semin Immunol* (2000) 12(1):85–98. doi: 10.1006/smim.2000.0210

14. Oeckinghaus A, Ghosh S. The NF-kappaB family of transcription factors and its regulation. *Cold Spring Harb Perspect Biol* (2009) 1(4):a000034. doi: 10.1101/cshperspect.a000034

15. Meng F, Liu L, Chin PC, D'Mello SR. Akt is a downstream target of NF-kappa B. *J Biol Chem* (2002) 277(33):29674–80. doi: 10.1074/jbc.M112464200

16. Neary JT, Kang Y, Tran M, Feld J. Traumatic injury activates protein kinase B/Akt in cultured astrocytes: role of extracellular ATP and P2 purinergic receptors. *J Neurotrauma* (2005) 22(4):491–500. doi: 10.1089/neu.2005.22.491

17. Tang B, Tang F, Wang Z, Qi G, Liang X, Li B, et al. Upregulation of Akt/NF-kappaB-regulated inflammation and Akt/Bad-related apoptosis signaling pathway involved in hepatic carcinoma process: suppression by carnosic acid nanoparticle. *Int J Nanomedicine* (2016) 11:6401–20. doi: 10.2147/IJN.S101285

18. Bai D, Ueno L, Vogt PK. Akt-mediated regulation of NFkappaB and the essentialness of NFkappaB for the oncogenicity of PI3K and Akt. *Int J Cancer* (2009) 125(12):2863–70. doi: 10.1002/ijc.24748

19. Li Q, Verma IM. NF-kappaB regulation in the immune system. *Nat Rev Immunol* (2002) 2(10):725–34. doi: 10.1038/nri910

20. Franceschi C, Capri M, Monti D, Giunta S, Olivieri F, Sevini F, et al. Inflammaging and anti-inflammaging: a systemic perspective on aging and longevity emerged from studies in humans. *Mech Ageing Dev* (2007) 128(1):92–105. doi: 10.1016/j.mad.2006.11.016

21. Franceschi C, Bonafè M, Valensin S, Olivieri F, De Luca M, Ottaviani E, et al. Inflamm-aging. An evolutionary perspective on immunosenescence. *Ann N Y Acad Sci* (2000) 908:244–54. doi: 10.1111/j.1749-6632.2000.tb06651.x

22. Fulop T, Larbi A, Dupuis G, Le Page A, Frost EH, Cohen AA, et al. Immunosenescence and inflamm-aging as two sides of the same coin: friends or foes? *Front Immunol* (2017) 8:1960. doi: 10.3389/fimmu.2017.01960

23. Duggal NA, Upton J, Phillips AC, Sapey E, Lord JM. An age-related numerical and functional deficit in CD19(+) CD24(hi) CD38(hi) B cells is associated with an increase in systemic autoimmunity. *Aging Cell* (2013) 12(5):873–81. doi: 10.1111/acel.12114

24. Bloomer SA, Moyer ED. Hepatic macrophage accumulation with aging: cause for concern? *Am J Physiol Gastrointest Liver Physiol* (2021) 320(4):G496–505. doi: 10.1152/ajpgi.00286.2020

25. de Freitas MC, Maruyama SA, Ferreira Tde F, Motta AM. [Perspectives of research in gerontology and geriatrics: review of the literature]. *Rev Lat Am Enfermagem* (2002) 10(2):221–8. doi: 10.1590/S0104-11692002000200015

26. Lord JM, Midwinter MJ, Chen YF, Belli A, Brohi K, Kovacs EJ, et al. The systemic immune response to trauma: an overview of pathophysiology and treatment. *Lancet* (9952) 2014:1455–65:384. doi: 10.1016/S0140-6736(14)60687-5

27. Jin CJ, Baumann A, Brandt A, Engstler AJ, Nier A, Hege M, et al. Aging-related liver degeneration is associated with increased bacterial endotoxin and lipopolysaccharide binding protein levels. *Am J Physiol Gastrointest Liver Physiol* (2020) 318(4):G736–47. doi: 10.1152/ajpgi.00345.2018

28. Gomez CR, Nomellini V, Baila H, Oshima K, Kovacs EJ. Comparison of the effects of aging and IL-6 on the hepatic inflammatory response in two models of systemic injury: scald injury versus i.p. LPS administration. *Shock* (2009) 31(2):178–84. doi: 10.1097/SHK.0b013e318180feb8

29. Okaya T, Blanchard J, Schuster R, Kuboki S, Husted T, Caldwell CC, et al. Age-dependent responses to hepatic ischemia/reperfusion injury. *Shock* (2005) 24(5):421–7. doi: 10.1097/01.shk.0000181282.14050.11

30. Adjei-Mosi J, Sun Q, Smithson SB, Shealy GL, Amerineni KD, Liang Z, et al. Age-dependent loss of hepatic SIRT1 enhances NLRP3 inflammasome signaling and impairs capacity for liver fibrosis resolution. *Aging Cell* (2023) 22(5):e13811. doi: 10.1111/acel.13811

31. Bundkirchen K, Ye W, Nowak AJ, Lienenklaus S, Welke B, Relja B, et al. Fracture healing in elderly mice and the effect of an additional severe blood loss: A radiographic and biomechanical murine study. *Bioengineering (Basel)* (2023) 10(1). doi: 10.3390/bioengineering10010070

32. Bundkirchen K, Macke C, Angrisani N, Schäck LM, Noack S, Fehr M, et al. Hemorrhagic shock alters fracture callus composition and activates the IL6 and RANKL/OPG pathway in mice. *J Trauma Acute Care Surg* (2018) 85(2):359–66. doi: 10.1097/TA.0000000000001952

33. Bundkirchen K, Macke C, Reifenrath J, Schäck LM, Noack S, Relja B, et al. Severe hemorrhagic shock leads to a delayed fracture healing and decreased bone callus strength in a mouse model. *Clin Orthop Relat Res* (2017) 475(11):2783–94. doi: 10.1007/s11999-017-5473-8

34. Sander LE, Sackett SD, Dierssen U, Beraza N, Linke RP, Müller M, et al. Hepatic acute-phase proteins control innate immune responses during infection by promoting myeloid-derived suppressor cell function. *J Exp Med* (2010) 207(7):1453–64. doi: 10.1084/jem.20091474

35. Robinson MW, Harmon C, O'Farrelly C. Liver immunology and its role in inflammation and homeostasis. *Cell Mol Immunol* (2016) 13(3):267–76. doi: 10.1038/cmi.2016.3

36. Huber-Lang M, Lambris JD, Ward PA. Innate immune responses to trauma. *Nat Immunol* (2018) 19(4):327–41. doi: 10.1038/s41590-018-0064-8

37. Relja B, Höhn C, Bormann F, Seyboth K, Henrich D, Marzi I, et al. Acute alcohol intoxication reduces mortality, inflammatory responses and hepatic injury after haemorrhage and resuscitation in *vivo*. *Br J Pharmacol* (2012) 165(4b):1188–99. doi: 10.1111/j.1476-5381.2011.01595.x

38. Lu Q, Lu Y, Zhang Y, Li Z, Xie X. Establishment and evaluation of rat trauma hemorrhagic liver injury model. *Int J Clin Exp Pathol* (2017) 10(7):7340–9.

39. Relja B, Lehnert M, Seyboth K, Bormann F, Höhn C, Czerny C, et al. Simvastatin reduces mortality and hepatic injury after hemorrhage/resuscitation in rats. *Shock* (2010) 34(1):46–54. doi: 10.1097/SHK.0b013e3181cd8d05

40. Shi Y, Greven J, Guo W, Luo P, Xu D, Wang W, et al. Trauma-Hemorrhage Stimulates Immune Defense, Mitochondrial Dysfunction, Autophagy, and Apoptosis in Pig Liver at 72 h. *Shock* (2021) 55(5):630–9. doi: 10.1097/SHK.0000000000001556

41. Patel NM, Oliveira FRMB, Ramos HP, Aimaretti E, Alves GF, Coldewey SM, et al. Inhibition of bruton's tyrosine kinase activity attenuates hemorrhagic shock-induced multiple organ dysfunction in rats. *Ann Surg* (2023) 277(3):e624–33. doi: 10.1097/SLA.0000000000005357

42. Patel NM, Yamada N, Oliveira FRMB, Stiehler L, Zechendorf E, Hinkelmann D, et al. Inhibition of macrophage migration inhibitory factor activity attenuates haemorrhagic shock-induced multiple organ dysfunction in rats. *Front Immunol* (2022) 13:886421. doi: 10.3389/fimmu.2022.886421

43. Senftleben U, Karin M. The IKK/NF-kappa B pathway. *Crit Care Med* (2002) 30 (1 Suppl):S18–26. doi: 10.1097/00003246-200201001-00003

44. Stormann P, Wagner N, Köhler K, Auner B, Simon TP, Pfeifer R, et al. Monotrauma is associated with enhanced remote inflammatory response and organ damage, while polytrauma intensifies both in porcine trauma model. *Eur J Trauma Emerg Surg* (2020) 46(1):31–42. doi: 10.1007/s00068-019-01098-1

45. Dutta S, Sengupta P. Men and mice: Relating their ages. *Life Sci* (2016) 152:244–8. doi: 10.1016/j.lfs.2015.10.025

46. Basisty N, Kale A, Jeon OH, Kuehnemann C, Payne T, Rao C, et al. A proteomic atlas of senescence-associated secretomes for aging biomarker development. *PloS Biol* (2020) 18(1):e3000599. doi: 10.1371/journal.pbio.3000599

47. Barkaway A, Rolas L, Joulia R, Bodkin J, Lenn T, Owen-Woods C, et al. Age-related changes in the local milieu of inflamed tissues cause aberrant neutrophil trafficking and subsequent remote organ damage. *Immunity* (2021) 54(7):1494–1510.e7. doi: 10.1016/j.immuni.2021.04.025

48. Balistreri CR, Candore G, Accardi G, Colonna-Romano G, Lio D. NF-kappaB pathway activators as potential ageing biomarkers: targets for new therapeutic strategies. *Immun Ageing* (2013) 10(1):24. doi: 10.1186/1742-4933-10-24

49. Hill JK, Gunion-Rinker L, Kulhanek D, Lessov N, Kim S, Clark WM, et al. Temporal modulation of cytokine expression following focal cerebral ischemia in mice. *Brain Res* (1999) 820(1-2):45–54. doi: 10.1016/S0006-8993(98)01140-8

50. Pestka JJ, Amuzie CJ. Tissue distribution and proinflammatory cytokine gene expression following acute oral exposure to deoxynivalenol: comparison of weanling and adult mice. *Food Chem Toxicol* (2008) 46(8):2826–31. doi: 10.1016/j.fct.2008.05.016

51. Nyugen J, Agrawal S, Gollapudi S, Gupta S. Impaired functions of peripheral blood monocyte subpopulations in aged humans. *J Clin Immunol* (2010) 30(6):806–13. doi: 10.1007/s10875-010-9448-8

52. Renshaw M, Rockwell J, Engleman C, Gewirtz A, Katz J, Sambhara S. Cutting edge: impaired Toll-like receptor expression and function in aging. *J Immunol* (2002) 169(9):4697–701. doi: 10.4049/jimmunol.169.9.4697

53. Huber N, Sakai N, Eismann T, Shin T, Kuboki S, Blanchard J, et al. Age-related decrease in proteasome expression contributes to defective nuclear factor-kappaB activation during hepatic ischemia/reperfusion. *Hepatology* (2009) 49(5):1718–28. doi: 10.1002/hep.22840

54. Fabregat I, Roncero C, Fernandez M. Survival and apoptosis: a dysregulated balance in liver cancer. *Liver Int* (2007) 27(2):155–62. doi: 10.1111/j.1478-3231.2006.01409.x

55. Mullonkal CJ, Toledo-Pereyra LH. Akt in ischemia and reperfusion. *J Invest Surg* (2007) 20(3):195–203. doi: 10.1080/08941930701366471

frontiers | Frontiers in Immunology

TYPE Original Research
PUBLISHED 22 September 2023
DOI 10.3389/fimmu.2023.1252818

OPEN ACCESS

EDITED BY
Jan Rossaint,
University of Münster, Germany

REVIEWED BY
Nana-Maria Wagner,
University Hospital Münster, Germany
Silke Niemann,
University Hospital Münster, Germany

*CORRESPONDENCE
Sina M. Coldewey
sina.coldewey@med.uni-jena.de

†These authors have contributed equally to this work

RECEIVED 04 July 2023
ACCEPTED 01 September 2023
PUBLISHED 22 September 2023

CITATION
Neu C, Wissuwa B, Thiemermann C and Coldewey SM (2023) Cardiovascular impairment in Shiga-toxin-2-induced experimental hemolytic–uremic syndrome: a pilot study.
Front. Immunol. 14:1252818.
doi: 10.3389/fimmu.2023.1252818

Cardiovascular impairment in Shiga-toxin-2-induced experimental hemolytic–uremic syndrome: a pilot study

Charles Neu[1,2,3†], Bianka Wissuwa[1,2†], Christoph Thiemermann[4] and Sina M. Coldewey[1,2,3*]

[1]Department of Anesthesiology and Intensive Care Medicine, Jena University Hospital, Jena, Germany, [2]Septomics Research Center, Jena University Hospital, Jena, Germany, [3]Center for Sepsis Control and Care, Jena University Hospital, Jena, Germany, [4]William Harvey Research Institute, Barts and the London School of Medicine and Dentistry, Queen Mary University of London, London, United Kingdom

Introduction: Hemolytic–uremic syndrome (HUS) can occur as a systemic complication of infection with Shiga toxin (Stx)-producing Escherichia coli (STEC). Most well-known aspects of the pathophysiology are secondary to microthrombotic kidney disease including hemolytic anemia and thrombocytopenia. However, extrarenal manifestations, such as cardiac impairment, have also been reported. We have investigated whether these cardiac abnormalities can be reproduced in a murine animal model, in which administration of Stx, the main virulence factor of STEC, is used to induce HUS.

Methods: Mice received either one high or multiple low doses of Stx to simulate the (clinically well-known) different disease courses. Cardiac function was evaluated by echocardiography and analyses of biomarkers in the plasma (troponin I and brain natriuretic peptide).

Results: All Stx-challenged mice showed reduced cardiac output and depletion of intravascular volume indicated by a reduced end-diastolic volume and a higher hematocrit. Some mice exhibited myocardial injury (measured as increases in cTNI levels). A subset of mice challenged with either dosage regimen showed hyperkalemia with typical electrocardiographic abnormalities.

Discussion: Myocardial injury, intravascular volume depletion, reduced cardiac output, and arrhythmias as a consequence of hyperkalemia may be prognosis-relevant disease manifestations of HUS, the significance of which should be further investigated in future preclinical and clinical studies.

KEYWORDS

hemolytic-uremic syndrome, Shiga toxin, acute kidney injury, echocardiography, murine model, cardiomyopathy

1 Introduction

Diarrhea-positive hemolytic–uremic syndrome (HUS) is a microthrombotic renal condition often caused by an infection with enterohemorrhagic *Escherichia coli* (EHEC). It is the most frequent cause of acute kidney injury (AKI) in children (1); further symptoms include thrombocytopenia and acute hemolytic anemia. As key virulence factors, EHEC secrete ribosome-inactivating Shiga toxins (Stx, type 1 and 2), which are often responsible for organ failure. Epidemiological data revealed that Stx2 is more frequently associated with the development of hemorrhagic colitis in HUS (2). Aside from renal and hematological symptoms, neurological and cardiac complications are known (3). Several case reports describe an impairment of cardiac function in patients with HUS. Specifically, patients with HUS exhibited a reduced left-ventricular systolic function and an increase in plasma troponin I —the latter of which is a well-known surrogate (bio)marker of myocardial injury (4–6)—as well as the need for cardiopulmonary resuscitation via cardiopulmonary bypass (4). Troponins are sensitive biochemical markers that are released into the bloodstream during myocardial injury. Cardiac troponin I (cTNI), one of three isoforms, is a specific serum marker of cardiac injury. Increases of cTNI can occur prior to and following severe myocardial dysfunction in HUS (5); however, as troponins are excreted via the kidney, their concentrations may also increase during AKI in the absence of myocardial damage [reviewed in (7)]. In some cases, the cause for the observed cardiac events during HUS was suspected to be ischemic in nature (8). Accordingly, case series of autopsied patients with diarrhea-associated HUS showed microthrombi formation in myocardial tissue (9), myocardial infarction (10), or pericardial purpura (11). The pathophysiological mechanisms leading to severe cardiac complications in some patients but not in others have not been fully understood. Furthermore, no specific treatment options exist for this oftentimes fatal extrarenal manifestation of HUS. Likewise, in atypical HUS (aHUS)—caused by mutations in the complement system in the absence of an EHEC infection—cases of cardiac dysfunction have also been reported with similar clinical presentation (12–14). In aHUS, however, immunomodulatory therapy (15) led to a reversal of cardiac impairment (12).

We have previously established and characterized two murine models of HUS based on the intravenous injection of Stx with two distinct courses of disease progression: an acute model of up to 3 days and a subacute model over the course of 1 week (16). In order to investigate the impact of Stx on the development of cardiac dysfunction in experimental HUS, we expanded our previously published models in a proof-of-concept manner, by performing echocardiography and measuring cardiac markers in the plasma of mice in both the acute and subacute model of HUS to better understand the potential and limitations of these models for the assessment of extrarenal cardiac manifestations of HUS in a pilot study. The echocardiography was complemented by hematological analysis and plasma measurements of kidney function as in previous experiments (16).

2 Materials and methods

2.1 Mice (*Mus musculus*)

Male wild-type C57BL/6J mice [aged 10–12 weeks, 20 to 30 g body weight (BW)] were randomly assigned to one of the two models, acute or subacute and treatment groups Stx or sham (acute Stx $n = 11$, all other groups $n = 10$), by a computer-generated list. Mice were kept under standardized laboratory conditions enriched with shredded paper and paper rolls, and received standard rodent chow and water *ad libitum*.

Experiments were performed in accordance with approved guidelines and the German law for animal protection. The animal experiment proposal was approved by the Thuringian State Office for Consumer Protection, Bad Langensalza, Germany (registration number 02-073/16).

2.2 Induction of HUS

HUS was induced by either a single i.v. injection of Stx (300 ng/kg BW in 5 mL/kg NaCl 0.9%; acute model) or two i.v. injections of Stx (25 ng/kg BW in 5 mL/kg BW NaCl 0.9% each; subacute model) on days 0 and 3. Sham mice received 5 mL/kg NaCl 0.9% at the corresponding time points. To account for the exacerbation of the condition of mice during anesthesia for echocardiography, the experimental protocol was shortened by 1 (acute model) and 2 days (subacute model), respectively, but remained otherwise unchanged (16). Stx was obtained from the same stock as previous experiments (16). Investigators were blinded for the treatment allocation of mice during the experiment. All mice received a volume resuscitation of 0.5 mL of Ringer's lactate solution s.c. twice daily in the acute model and 0.8 mL of Ringer's lactate solution s.c. three times a day in the subacute model. Clinical presentation of animals was assessed three times a day throughout the experiment using a scoring system previously described (16). The HUS score categorizes the following degrees of severity: 1 = no signs of illness, 2 = low-grade, 3 = mid-grade, and 4 = high-grade disease. Pre-defined criteria were assessed to determine whether termination of the experiment was necessary employing humane endpoints. Experiments were terminated on day 2 in the acute model and on day 5 in the subacute model of HUS. Blood samples were obtained by cardiac puncture in deep anesthesia during termination of the experiment.

2.3 Echocardiography

Echocardiography was performed with the Vevo 3100 imaging system (FUJIFILM VisualSonics, Inc., Toronto, ON, Canada) using a 32–55 MHz MX550D transducer (FUJIFILM VisualSonics, Inc.). Ultrasound analyses were performed at three time points in both models of HUS. T0 corresponds to the time point before induction of HUS to measure basic values in a healthy condition. T1 and T2 represent day 1 and day 2 in the acute model, and day 3 and day 5 in

the subacute model, respectively. Anesthesia was induced with 3% isoflurane (CP-Pharma, Burgdorf, Germany) and maintained at 1%–1.5%. Ultrasound images were recorded after a stabilization period of approximately 10 min. ECG monitoring was performed during the entire anesthesia using four paw contact electrodes of the Vevo 3100. Body temperature was measured by a rectal thermometer during anesthesia. To assess cardiac function, LV B-mode and M-mode images of parasternal long axis (PSLAX) and short axis (PSAX) as well as B-mode and pulsed-wave (PW) Doppler mode images of the pulmonary artery were recorded. Analyses of ultrasound images were conducted by two independent researchers in a blinded manner using the Vevo LAB 3.2.0 software (FUJIFILM VisualSonics, Inc.). EF and EDV were calculated by manual LV tracing measurement in PSLAX B-mode. Cardiac output (CO) was calculated from the diameter of the pulmonary artery in B-mode and manual velocity time integral (VTI) measurement in PW Doppler mode.

2.4 Hematology and plasma analyses

Whole blood analysis was performed using the scil Vet abc Plus$^+$ hematology analyzer (scil animal care company GmbH, Viernheim, Germany) to quantify red blood cell count, platelet count, hematocrit, hemoglobin, and mean corpuscular volume. Plasma was prepared by centrifugation of heparinized whole blood for 10 min at 3000 g. Creatinine, urea, sodium, and potassium were quantified in plasma samples with the ARCHITECT^{TM} *ci*16200 System (Abbott, Chicago, IL, USA). NGAL was quantified in plasma samples by ELISA (Cat. No. 443707; BioLegend$^{®}$, Inc., San Diego, CA, USA). cTnI levels were determined in plasma samples by ELISA (CTNI-1-HSP; Life Diagnostics, Inc., West Chester, PA, USA). Quantification of brain natriuretic peptide (BNP) was performed by an enzyme immunoassay (RAB0386; Sigma-Aldrich, St. Louis, MO, USA). In some cases, not all measurements were possible due to too little plasma volumes.

2.5 Statistical analysis

Data are displayed as mean ± standard deviation (SD) of n observations representing the number of animals. Data were pooled from two replicate experiments. Statistical analysis was performed using GraphPad Prism 7.05 (GraphPad Software, Inc., San Diego, CA, USA). Data were analyzed by Mann–Whitney U test and two-way repeated measures ANOVA followed by Bonferroni's multiple comparison test as indicated in the respective figure legend (*p < 0.05, **p < 0.01, ***p < 0.001, ****p < 0.0001).

3 Results

3.1 The effect of a single high-dose challenge with Stx on systemic disease and kidney dysfunction and injury

All mice challenged with a single dose of 300 ng/kg Stx (acute model of HUS) developed significant weight loss after 2 days (Figure 1A). When compared with sham-treated mice, plasma concentrations of creatinine, urea, and neutrophil gelatinase-associated lipocalin (NGAL) were increased 2 days after administration of Stx (Figure 1B), indicating acute kidney dysfunction and injury. The disease severity score, i.e., the humane endpoint of this experiment that was implemented as part of the termination criteria (s. HUS score, Supplementary Figure 1A), was significantly increased 48 h after administration of Stx, while sham-treated mice developed no signs of disease. Hematological analysis (Figure 1C) revealed significantly higher levels of hemoglobin and hematocrit in Stx-treated mice than in sham-treated mice. These results were in accordance with our previous work (Dennhardt et al., 2018).

3.2 The effect of repeated administrations of lower doses of Stx on systemic disease and kidney dysfunction and injury

All mice challenged with two doses of 25 ng/kg of Stx (subacute model of HUS) developed significant weight loss after 4 days (Figure 1D), which was more pronounced on the fifth and final day of the experiment. When compared with sham-treated mice, plasma concentrations of creatinine, urea, and NGAL (Figure 1E) were increased 5 days after administration of Stx, indicating acute kidney dysfunction and injury. The disease severity score (s. HUS score, Supplementary Figure 1B) was increased in a subgroup of mice 120 h after administration of Stx, while sham-treated mice showed no signs of disease. The hematological analysis (Figure 1F) revealed higher hemoglobin levels in Stx-treated mice when compared with sham. A subset of mice also developed thrombocytopenia.

3.3 The effect of a single high-dose challenge with Stx on cardiac function

We analyzed left-ventricular function in the acute model of HUS by echocardiography before and after 1 and 2 days after the induction of HUS (Figures 2A–D). When compared with sham-treated mice, ejection fraction (EF) (Figure 2B) and fractional area change (FAC) were increased 2 days after administration of Stx, indicating increased left-ventricular contraction secondary to activation of the sympathetic nervous system (Figure 2D).

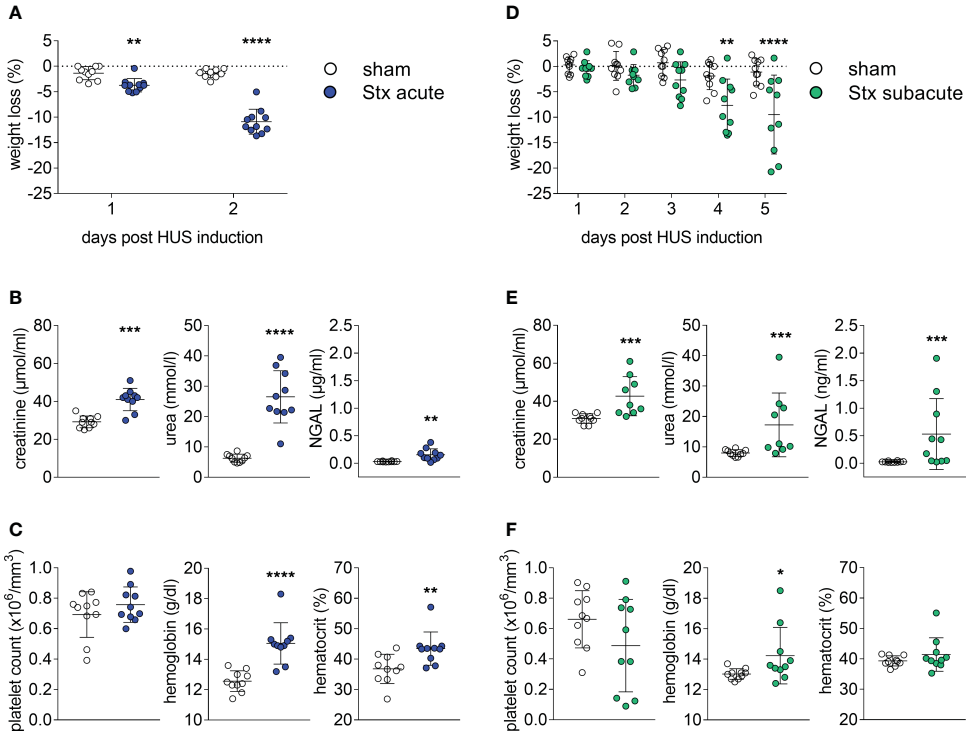

FIGURE 1
Clinical presentation of hemolytic–uremic syndrome (HUS) in mice exposed to different Shiga toxin (Stx) application regimes. **(A–C)** C57BL/6J mice received either a single high dose of 300 ng/kg Stx (Stx acute) or vehicle (sham). Blood was taken at the end of the experiment, 2 days after the induction of HUS **(B, C)**. **(A)** Weight loss percentage of body weight (sham n = 10, Stx acute n = 11). **(B)** Plasma levels of creatinine and urea (sham n = 10, Stx acute n = 9) and neutrophil gelatinase-associated lipocalin (NGAL) (sham n = 10, Stx acute n = 10). **(C)** Platelet count, hemoglobin, and hematocrit (sham n = 10, Stx acute n = 10) **(D–F)**. Mice received either two lower doses of 25 ng/kg Stx (Stx subacute) spaced 72 h apart or vehicle (sham). Blood was taken at end of the experiment, five days after the induction of HUS **(E, F)**. **(D)** Weight loss percentage of body weight (sham n = 10, Stx subacute n = 10). **(E)** Plasma levels of creatinine and urea (sham n = 10, Stx subacute n = 9) and NGAL (sham n = 10, Stx subacute n = 10). Platelet count, hemoglobin, and hematocrit (sham n = 10, Stx subacute n = 10). **(A–F)** Data are presented as scatter dot plot with mean ± SD for n number of observations, *p < 0.05, **p < 0.01, ***p < 0.001 and ****p < 0.0001 vs. the corresponding sham group (**A, D**: two-way repeated measures ANOVA, Bonferroni's multiple comparison test; all other: Mann–Whitney U test).

3.4 The effect of repeated administrations of lower doses of Stx on cardiac function

We analyzed left-ventricular function in the subacute model of HUS, before and after 3 and 5 days after induction of HUS (Figures 2E–H). When compared with sham-treated mice, echocardiographic analysis showed no significant changes in EF (Figure 2F), fractional shortening (FS, Figure 2G), and FAC (Figure 2H) at any time point.

3.5 The effect of a single high-dose challenge with Stx on cardiac function and hemodynamics

We analyzed hemodynamically relevant parameters in the acute model of HUS by echocardiography before and after 1 and 2 days after the induction of HUS (Figures 3A–D). When compared with sham-treated mice, end-diastolic volume (EDV) was reduced 2 days after the induction of HUS (Figure 3A). There were no differences in heart rates (HR) between the groups measured after induction of anesthesia (Figure 3B). Stroke volume (SV) (Figure 3C) and CO (Figure 3D) were reduced 2 days after the induction of HUS, of which CO was also reduced 1 day after the induction of HUS (Figure 3D). There were no differences in heart rates between the groups measured after the induction of anesthesia. Taken together, the hemodynamic changes indicate intravascular volume depletion.

3.6 The effect of repeated administrations of lower doses of Stx on cardiac function and hemodynamics

We analyzed hemodynamically relevant parameters in the subacute model of HUS by echocardiography before and after 3 and 5 days after the induction of HUS (Figures 3E–H). When compared with sham-treated mice, EDV (Figure 3E), HR (Figure 3F), SV (Figure 3H), and CO (Figure 3F) were reduced 5 days after the induction of HUS, of which CO was also reduced 3 days after the induction of HUS. Taken together, the changes indicate intravascular volume depletion exacerbated by bradycardia.

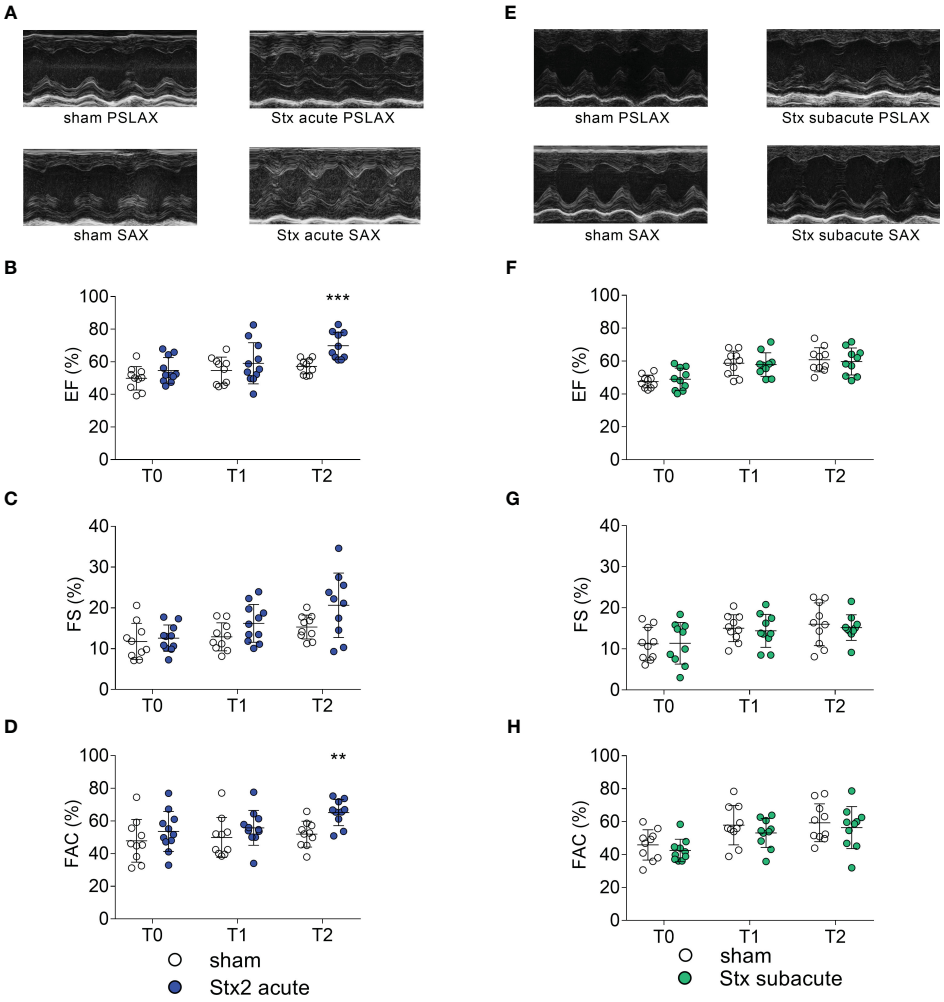

FIGURE 2
Left ventricular cardiac function in mice with hemolytic–uremic syndrome (HUS) exposed to different Shiga toxin (Stx) application regimes. **(A–D)** C57BL/6J mice received either a single high dose of 300 ng/kg of Stx (Stx acute, *n* = 11) or vehicle (sham *n* = 10). Echocardiography was performed before (T0, baseline) and 1 (T1) and 2 (T2) days after induction of HUS. **(A)** Representative parasternal long axis (PSLAX) and short axis (SAX) M-mode echocardiograms (0.5 s each) at T2. Left ventricular (LV) **(B)** ejection fraction (EF), **(C)** fractional shortening (FS), and **(D)** fractional area change **(FAC)** were analyzed to characterize LV cardiac function. **(E–H)** Mice received either two lower doses of 25 ng/kg Stx (Stx subacute *n* = 10) spaced 72 h apart or vehicle (sham *n* = 10). Echocardiography was performed before (T0, baseline) and 1 (T1) and 2 (T2) days approximately 10 min after induction of HUS. **(E)** Representative PSLAX and SAX M-mode echocardiograms (0.5 s each) at T2. LV **(F)** EF, **(G)** FS, and **(H)** FAC were analyzed to characterize LV cardiac function. **(B–D, F–H)** Data are presented as scatter dot plot with mean ± SD, $^{**}p < 0.01$, $^{***}p < 0.001$ vs. the corresponding sham group (Mann–Whitney *U* test).

3.7 The effect of a single high-dose challenge with Stx on plasma biomarkers of cardiac injury

In plasma samples, we determined the concentration of cTnI and BNP as markers of cardiac injury in the acute model of HUS 2 days after the induction of HUS (Figures 4A, B). Three of 10 Stx-treated mice demonstrated increased cTnI levels (Figure 4A). All mice with increased cTnI levels exhibited clinical deterioration (HUS score = 3, Supplementary Figure 1); however, other mice with comparable disease severity regarding clinical presentation and laboratory values did not present with increased cTnI levels. The echocardiographic analysis revealed no apparent differences in this small subgroup compared with the other Stx-challenged mice. There were no differences in BNP levels between Stx- and sham-treated mice (Figure 4B).

3.8 The effect of repeated administrations of lower doses of Stx on plasma biomarkers of cardiac injury

In plasma samples, we determined the concentration of cTnI and BNP as markers of cardiac injury in the subacute model of HUS (Figures 4C, D) 5 days after the induction of HUS. cTnI was only detectable in one of the nine Stx-challenged mice (Figure 4C). This animal exhibited a high level of disease severity (HUS score = 3, Supplementary Figure 1), the highest NGAL level in plasma, and the

10.3389/fimmu.2023.1252818

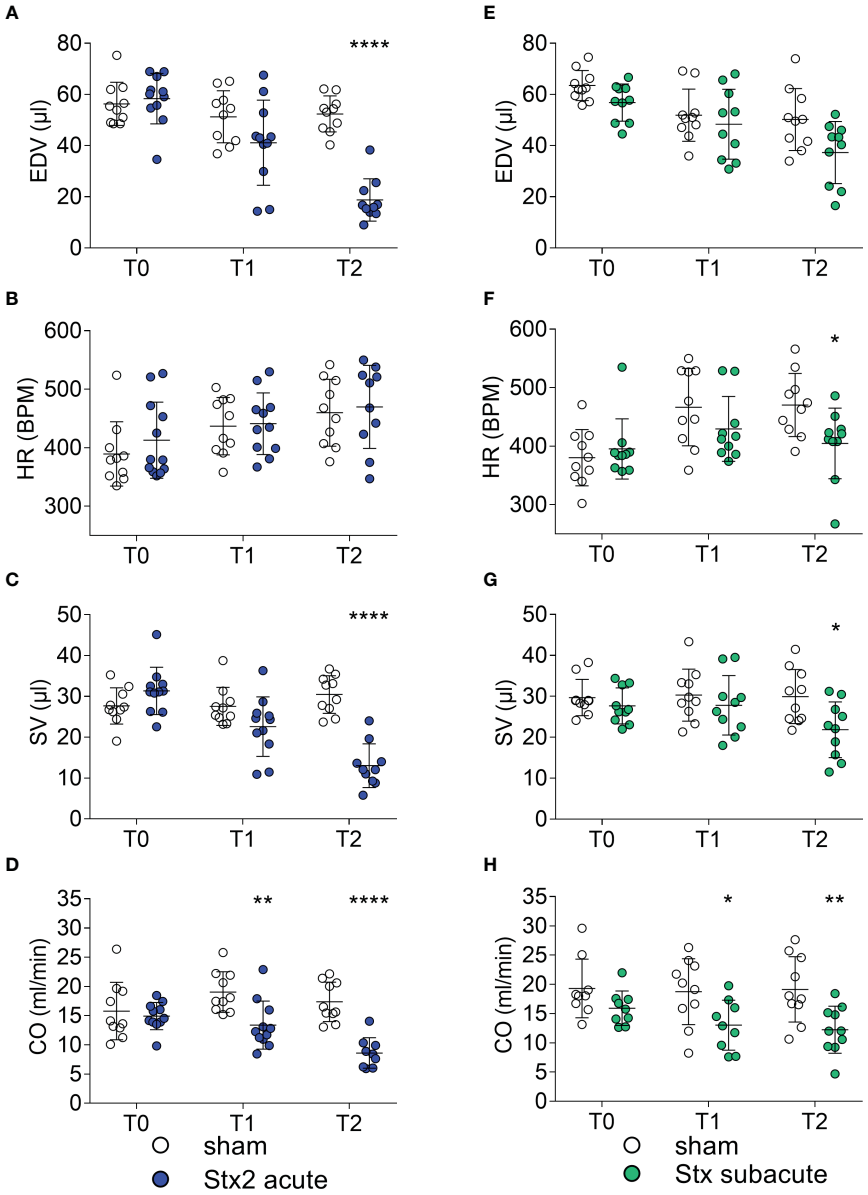

FIGURE 3
Hemodynamic parameters in mice with hemolytic–uremic syndrome (HUS) exposed to different Shiga toxin (Stx) application regimes. **(A–D)** C57BL/6J mice received either a single high dose of 300 ng/kg of Stx (Stx acute, n = 11) or vehicle (sham n = 10). Echocardiography was performed before (T0, baseline) and 1 (T1) and 2 (T2) days after induction of HUS. **(A)** End-diastolic volume (EDV), **(B)** heart rate (HR) in beats per minute (BPM) approximately 10 min after induction of anesthesia, **(C)** stroke volume (SV), and **(D)** cardiac output (CO) were analyzed to characterize hemodynamic changes. **(E–H)** Mice received either two lower doses of 25 ng/kg Stx (Stx subacute n = 10) spaced 72 h apart or vehicle (sham n = 10). Echocardiography was performed before (T0, baseline) and 1 (T1) and 2 (T2) days after induction of HUS. **(E)** EDV and **(F)** HR in BPM approximately 10 min after induction of anesthesia, **(G)** SV, and **(H)** CO were analyzed to characterize hemodynamic changes. **(A–H)** Data are presented as scatter dot plot with mean ± SD, *p < 0.05, **p < 0.01, ****p < 0.0001 vs. the corresponding sham group (Mann–Whitney U test).

lowest CO in this group. There were no differences in BNP levels between Stx- and sham-treated mice in this dose regimen (Figure 4D).

3.9 The effect of a single high-dose challenge with Stx on plasma electrolytes and electrocardiograms

We analyzed the concentrations of electrolytes in plasma samples of mice in the acute model of HUS 2 days after the induction of HUS (Figures 5A, B). When compared with sham-treated mice, plasma sodium concentrations were unchanged (Figure 5A). All but one Stx-treated mouse showed increased potassium levels (hyperkalemia, Figure 5B). The electrocardiograms that were recorded during echocardiography after reaching a steady state of anesthesia showed no morphological abnormalities in sham-treated mice (Supplementary Figure 2). All stx-treated mice with hyperkalemia showed widening of the QRS complexes and increased height of T waves. A subset of hyperkalemic mice showed bradycardia (Supplementary Figure 3).

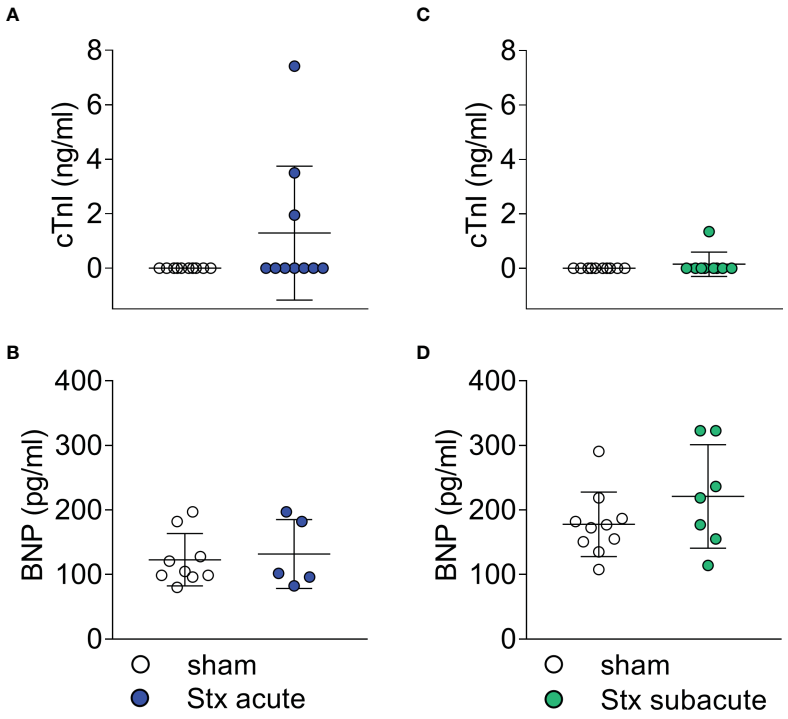

FIGURE 4
Plasma surrogate markers of cardiac injury in mice with hemolytic–uremic syndrome (HUS) exposed to different Shiga toxin (Stx) application regimes. **(A, B)** C57BL/6J mice received either a single high dose of 300 ng/kg Stx (Stx acute) or vehicle (sham). Blood was taken at the end of the experiment, 2 days after the induction of HUS. **(A)** Plasma concentrations of cardiac troponin I (cTnI) (sham n = 10, Stx acute n = 10) and **(B)** brain natriuretic peptide (BNP) (sham n = 9, Stx acute n = 5) were measured as surrogate parameters of cardiac injury. **(C, D)** Mice received either two lower doses of 25 ng/kg Stx spaced 72 h apart (Stx subacute) or vehicle (sham). Blood was taken at the end of the experiment 5 days after the induction of HUS **(C)** Plasma concentrations of cTnI (sham n = 10, Stx acute n = 9) and **(D)** BNP (sham n = 10, Stx subacute n = 7) were measured as surrogate parameters of cardiac injury. **(A–D)** Data are presented as scatter dot plot with mean ± SD, $p < 0.05$ vs. corresponding sham group (Mann–Whitney U test).

3.10 The effect of repeated administrations of lower doses of Stx on plasma electrolytes and electrocardiograms

We analyzed the concentrations of electrolytes in plasma samples of mice in the subacute model of HUS 5 days after the induction of HUS (Figures 5C, D). When compared with sham-treated mice, plasma sodium concentrations showed no significant changes (Figure 5C). Four of nine plasma samples of Stx-treated mice showed hyperkalemia (Figure 5D). The electrocardiograms that were recorded during echocardiography after reaching a steady state of anesthesia showed no morphological abnormalities in sham-treated mice (Supplementary Figure 4). Two Stx-treated mice displayed bradycardia, widening of the QRS complexes, and increased height of T waves (Supplementary Figure 5), of which one had hyperkalemia and one lacked the plasma potassium value due to insufficient blood sample size.

4 Discussion

In this exploratory pilot study, we addressed and described for the first time Stx2-induced cardiovascular impairment in preclinical models of HUS. In two distinct experimental setups, we induced disease by either a single high or repeated lower doses of Stx to model an acute or subacute course of disease in mice and found results comparable with previous experiments in these models (16) regarding clinical and laboratory signs of disease, such as disease severity score, weight loss, and indicators of acute kidney injury. In addition to these previously reported readouts, to assess the effect of Stx on the cardiovascular system, echocardiographic and laboratory assessments of cardiac injury were performed, yielding signs of cardiovascular dysfunction with varying degrees in both Stx-treated groups. Both Stx dosage regimens resulted in an impairment of cardiovascular function as assessed by echocardiography. All of these novel findings are summarized in Figure 6.

4.1 Stx-induced hypovolemia contributes to cardiovascular impairment

Based on an observed hemoconcentration in previous experiments with Stx-induced HUS in mice, we hypothesized that the expected and well-documented hypovolemia may, despite volume substitution, be the cause of the observed cardiovascular dysfunction (which was particularly pronounced in the acute HUS model). We report here for the first time that both murine models of HUS caused by (two different regimens of) administration of Stx

10.3389/fimmu.2023.1252818

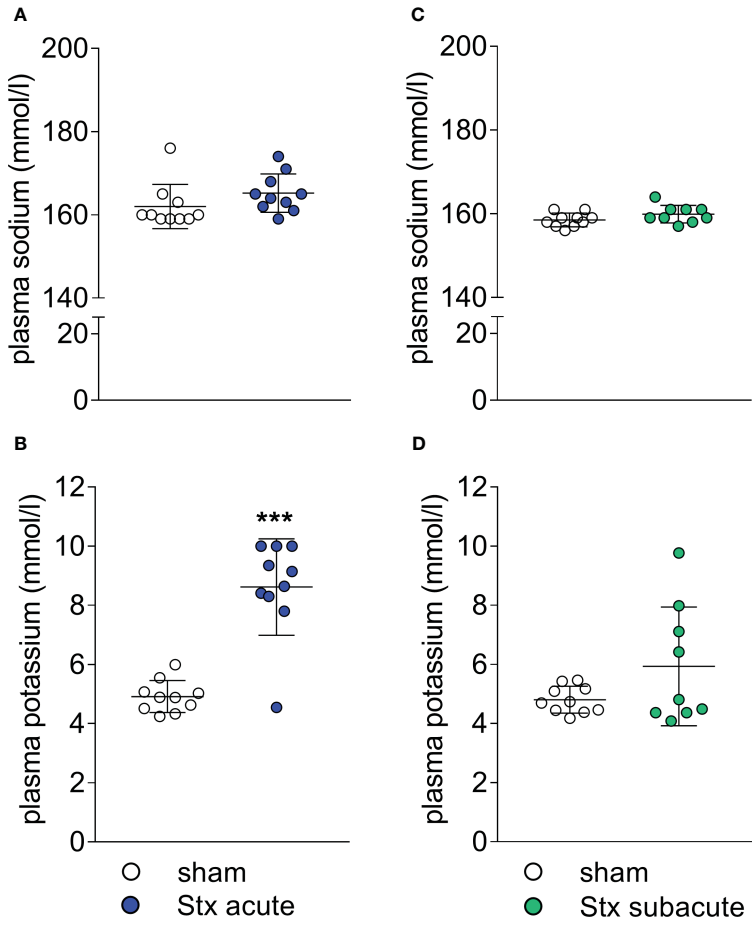

FIGURE 5
Plasma electrolyte concentrations in mice with hemolytic–uremic syndrome (HUS) exposed to different Shiga toxin (Stx) application regimes. **(A, B)** C57BL/6J mice received either a single high dose of 300 ng/kg Stx (Stx acute) or vehicle (sham). Blood was taken at the end of the experiment, 2 days after the induction of HUS. Plasma concentrations of **(A)** sodium and **(B)** potassium (sham n = 10, Stx n = 10). **(C, D)** Mice received either two lower doses of 25 ng/kg Stx spaced 72 h apart (Stx subacute) or vehicle (sham). Blood was taken at the end of the experiment, 5 days after the induction of HUS **(C)**. Plasma concentrations of **(C)** sodium and **(D)** potassium (sham n = 10, Stx n = 9). **(A–D)** Data are presented as scatter dot plot with mean ± SD, ***$p < 0.001$ vs. the corresponding sham group (Mann–Whitney U test).

resulted in a reduction in CO, EDV, and SV. This was associated with reductions in heart rate in hyperkalemic mice, which, in turn, further exacerbated the deleterious effects of Stx on CO. In addition, hemoconcentration was observed in both models. Thus, the loss of intravascular volume (secondary to endothelial injury-dysfunction and plasma leak) results in a reduction in pre-load, which may have importantly contributed to the observed reductions in CO and SV in HUS mice. In the acute model of HUS, we found (in the early stages of the disease) an increase in EF and FAC, which may be reflective of a compensatory response to hypovolemia secondary to activation of the sympathetic nervous system. The increases may appear inconsistent with the observed decrease in CO. As EF is influenced by changes in both (or either) end-diastolic and end-systolic volumes, EF offers no reliable information on the absolute volume ejected from the heart (and, hence, SV or CO). This means that changes in EF are not necessarily mirrored by changes in CO. Interestingly, the increases in EF associated with decreases in CO observed in our murine model of HUS are also frequently observed in patients with sepsis. Notably, the cardiovascular impairment was less pronounced in the subacute model of HUS. Though often masked by hemolytic anemia, hemoconcentration secondary to dehydration is present in human HUS and has been identified as a risk factor for the development of neurological sequelae (17). Capillary leakage, which has been suspected in human HUS (18), may account for or aggravate intravascular hypovolemia. Despite hypovolemia, there was no increase in heart rate in Stx-treated mice compared with controls. This is consistent with findings from other murine models of hypovolemia: Vogel also found no difference in heart rates in hypovolemic compared with euvolemic BALB/c mice (19). In a more recent study, C57BL/6 did not react with an increase in heart rate in response to hemorrhage (20). In this experimental model of hemorrhagic shock, a mean increase in heart rate of 30–40 beats per minute was observed after fluid resuscitation, which is in the range of variance in our mouse model.

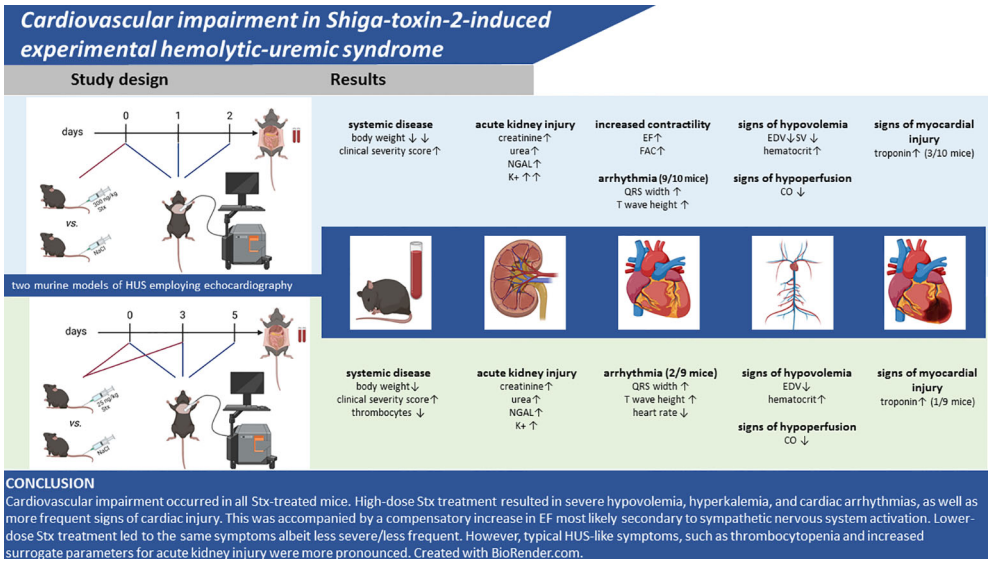

FIGURE 6
Summary of findings. Created with BioRender.com.

4.2 Stx induces cardiac injury in a subset of mice

A third of Stx-challenged mice in the acute model and one mouse in the subacute model showed increases of cTnI. This is likely secondary to cardiac injury (necrosis of cardiomyocytes). The disease severity in these specific mice was high (as judged by the clinical severity score), but other mice in the acute model with no measurable cTnI presented with even more severe disease. Furthermore, these mice showed no reduction in left-ventricular function or differences in the ST segment of the ECG (both if observed could reflect an acute myocardial infarction secondary to the obstruction of a coronary artery; see below) when compared to mice with normal troponin values. Hence, the role of cardiac injury (rise in cTnI levels) in the observed cardiac dysfunction and, indeed, overall outcome in this HUS model remains unclear. Increased troponin levels in pediatric patients with HUS have been described in both case reports and epidemiological studies (3, 6, 21, 22); however, in the absence of larger studies, the incidence of this laboratory finding in human HUS remains unknown. Therefore, the employed models mimic a potentially important part of HUS pathophysiology, previously often neglected. The origin of the increase in cTnI in HUS remains unknown; however, thrombotic microangiopathy of cardiac vessels (see above) has been found in two autopsy studies of children who died from HUS (23). In a case report of cardiovascular impairment in HUS, the temporal dynamics of plasma troponin were recorded around the cardiac event, showing a peak troponin level 24 h after the event and mild elevations 8 h before the event (5). Should the mouse model prove consistent with this finding, the mild increase in cTnI levels seen in some mice could potentially be indicative of a future cardiac event rather than a past one (i.e., acute myocardial infarction). It should be noted that any observed increases in cTnI levels may also be secondary to an impairment in renal function (7). This is particularly important given the presence of acute kidney injury and impaired renal function in both HUS models.

4.3 Arrhythmias secondary to hyperkalemia may be the cause of significant morbidity

In the analysis of plasma, we consistently observed hyperkalemia in a subgroup of Stx-treated mice. Hyperkalemia was found more frequently in mice receiving the higher dose of Stx, which may indicate a dose-dependent mechanism. AKI frequently causes electrolyte imbalances and the presence of hyperkalemia in this murine HUS model reflects findings from studies of human HUS. Hyperkalemia was found in 27.2% of a cohort of 33 children with HUS (24). Zhao et al. found hyperkalemia in 30% of 20 children with diarrhea-positive HUS in their clinical study (25). The frequency of hyperkalemia in humans is, therefore, similar to that seen in our subacute model of HUS. In our mouse model, we also observed electrocardiographic abnormalities in Stx-challenged mice; we found pathological ECGs typical of and exclusively in mice with hyperkalemia, suggesting hyperkalemia as the underlying cause. One case report describes ventricular arrhythmias following myocarditis and hyperkalemia in human HUS (26). In a case–control study of 17 fatal cases of HUS, hyperkalemia was among the causes of death (27). This is also reflected here, as mice with hyperkalemia had a high clinical HUS score.

However, in human HUS, the electrolyte disturbances and associated acid–base imbalance can potentially be treated with drugs or by various renal replacement procedures if diagnosed in a timely manner. If hyperkalemia is not treated, the resulting conduction disturbances may limit animal survival in preclinical models. Future preclinical models could include electrophysiological analyses of Stx-treated cardiomyocytes to investigate an inherent pro-arrhythmogenic effect of Stx.

4.4 Conclusion and outlook

Cardiovascular impairment occurred in all Stx-treated mice. High-dose Stx treatment resulted in severe hypovolemia, hyperkalemia, and cardiac arrhythmias, as well as more frequent signs of cardiac injury. This was accompanied by a compensatory increase in EF most likely secondary to sympathetic nervous system activation. Lower-dose Stx treatment led to the same symptoms albeit less severe/less frequently; however, typical HUS-like symptoms, such as thrombocytopenia and increased surrogate parameters for acute kidney injury, were more pronounced. This exploratory study is limited by its small sample size and lack of mechanistic investigation. The brevity of the model limits the analysis of certain parameters of heart failure such as heart weight/body weight ratio, which may also be skewed by the weight loss of the mice. It poses a first proof of principle, that both models are, in general, suitable models for the investigation of the pathophysiology of cardiovascular events in HUS, as both dose regimens present findings of cardiovascular impairment observed in human HUS. Further experiments should include histopathological analysis, in particular trichrome-stained images of the heart and markers of cardiac inflammation as a first investigation into the mechanisms underlying this impairment. It would be very useful to further gain a more detailed understanding of the hemodynamic alterations associated with both murine models of HUS reported here by characterizing the hemodynamics beyond this pilot study by continuous recording of blood pressure (e.g., an implantable device). This unfortunately was beyond the scope of this study. It is also not clear whether the surgical intervention necessary to implant the device that would allow a remote hemodynamic monitoring (first hit) would affect the subsequent response to Stx (second hit) and, hence, affect disease severity and pathology (even if not related to cardiac dysfunction). Future translational studies should consider the prognostic relevance of cardiovascular impairment, including hyperkalemia-induced arrhythmias, intravascular volume depletion, and decline of CO for the outcome and mortality of this rare but potentially fatal complication.

Data availability statement

The raw data supporting the conclusions of this article will be made available by the authors, without undue reservation.

Ethics statement

The animal study was approved by Thuringian State Office for Consumer Protection, Bad Langensalza, Germany (registration number 02 073/16). The study was conducted in accordance with the local legislation and institutional requirements.

Author contributions

Conceptualization: SC; Methodology: SC; Validation: CN, BW, and SC; Formal analysis: CN and BW; Investigation: CN and BW; Resources: SC; Data curation: CN and BW; Writing—original draft preparation: CN, SC, BW, and CT; Writing—review and editing: CN, CT, and SC; Visualization: BW and CN; Supervision: SC; Project administration: SC; Funding acquisition: SC. All authors contributed to the article and approved the submitted version.

Funding

This work has been supported by the Federal Ministry of Education and Research (BMBF, grant 03Z22JN12 and 03COV07 awarded to SC) and the German Research Foundation (DFG, grant SFB PolyTarget 1278-2021, project no. 316213987, subproject A02, and subproject T01, awarded to SC).

Acknowledgments

We would like to thank Jacqueline Fischer for technical support; Antonia Lange for assistance during animal experiments; Michael Kiehntopf and Cora Richert for the measurement of plasma creatinine, urea, sodium, and potassium at the Institute for Clinical Chemistry and Laboratory Diagnostic of the Jena University Hospital; and Florian Gunzer for kindly providing Shiga toxin.

Conflict of interest

The authors declare that the research was conducted in the absence of any commercial or financial relationships that could be construed as a potential conflict of interest.

Publisher's note

Supplementary material

The Supplementary Material for this article can be found online at: https://www.frontiersin.org/articles/10.3389/fimmu.2023.1252818/full#supplementary-material

References

1. Gerber A, Karch H, Allerberger F, Verweyen HM, Zimmerhackl LB. Clinical course and the role of shiga toxin-producing escherichia coli infection in the hemolytic-uremic syndrome in pediatric patients, 1997-2000, in Germany and Austria: A prospective study. *J Infect Dis* (2002) 186(4):493–500. doi: 10.1086/341940

2. Mayer CL, Leibowitz CS, Kurosawa S, Stearns-Kurosawa DJ. Shiga toxins and the pathophysiology of hemolytic uremic syndrome in humans and animals. *Toxins (Basel)* (2012) 4(11):1261–87. doi: 10.3390/toxins4111261

3. Khalid M, Andreoli S. Extrarenal manifestations of the hemolytic uremic syndrome associated with shiga toxin-producing escherichia coli (Stec hus). *Pediatr Nephrol* (2019) 34(12):2495–507. doi: 10.1007/s00467-018-4105-1

4. Andersen RF, Bjerre JV, Povlsen JV, Veien M, Kamperis K, Rittig S. Hus-induced cardiac and circulatory failure is reversible using cardiopulmonary bypass as rescue. *Pediatr Nephrol* (2017) 32(11):2155–8. doi: 10.1007/s00467-017-3736-y

5. Askiti V, Hendrickson K, Fish AJ, Braunlin E, Sinaiko AR. Troponin I levels in a hemolytic uremic syndrome patient with severe cardiac failure. *Pediatr Nephrol* (2004) 19(3):345–8. doi: 10.1007/s00467-003-1343-6

6. Thayu M, Chandler WL, Jelacic S, Gordon CA, Rosenthal GL, Tarr PI. Cardiac ischemia during hemolytic uremic syndrome. *Pediatr Nephrol* (2003) 18(3):286–9. doi: 10.1007/s00467-002-1039-3

7. Banerjee D, Perrett C, Banerjee A. Troponins, acute coronary syndrome and renal disease: from acute kidney injury through end-stage kidney disease. *Eur Cardiol* (2019) 14(3):187–90. doi: 10.15420/ecr.2019.28.2

8. Palanca Arias D, Lopez Ramon M, Jimenez Montanes L. Biomarkers detect involvement of acute myocardial injury in a paediatric haemolytic-uraemic syndrome patient. *Cardiol Young* (2016) 26(5):983–6. doi: 10.1017/S1047951115002759

9. Upadhyaya K, Barwick K, Fishaut M, Kashgarian M, Siegel NJ. The importance of nonrenal involvement in hemolytic-uremic syndrome. *Pediatrics* (1980) 65(1):115–20. doi: 10.1542/peds.65.1.115

10. Gallo EG, Gianantonio CA. Extrarenal involvement in diarrhoea-associated haemolytic-uraemic syndrome. *Pediatr Nephrol* (1995) 9(1):117–9. doi: 10.1007/BF00858990

11. Richardson SE, Karmali MA, Becker LE, Smith CR. The histopathology of the hemolytic uremic syndrome associated with verocytotoxin-producing escherichia coli infections. *Hum Pathol* (1988) 19(9):1102–8. doi: 10.1016/s0046-8177(88)80093-5

12. Vaughn JL, Moore JM, Cataland SR. Acute systolic heart failure associated with complement-mediated hemolytic uremic syndrome. *Case Rep Hematol* (2015) 2015:327980. doi: 10.1155/2015/327980

13. Kichloo A, Chugh SS, Gupta S, Pandav J, Chander P. Atypical hemolytic uremic syndrome presenting as acute heart failure-a rare presentation: diagnosis supported by skin biopsy. *J Investig Med High Impact Case Rep* (2019) 7:2324709619842905. doi: 10.1177/2324709619842905

14. Dragon-Durey MA, Sethi SK, Bagga A, Blanc C, Blouin J, Ranchin B, et al. Clinical features of anti-factor H autoantibody-associated hemolytic uremic syndrome. *J Am Soc Nephrol* (2010) 21(12):2180–7. doi: 10.1681/ASN.2010030315

15. Loirat C, Fakhouri F, Ariceta G, Besbas N, Bitzan M, Bjerre A, et al. An international consensus approach to the management of atypical hemolytic uremic syndrome in children. *Pediatr Nephrol* (2016) 31(1):15–39. doi: 10.1007/s00467-015-3076-8

16. Dennhardt S, Pirschel W, Wissuwa B, Daniel C, Gunzer F, Lindig S, et al. Modeling hemolytic-uremic syndrome: in-depth characterization of distinct murine models reflecting different features of human disease. *Front Immunol* (2018) 9:1459. doi: 10.3389/fimmu.2018.01459

17. Ardissino G, Dacco V, Testa S, Civitillo CF, Tel F, Possenti I, et al. Hemoconcentration: A major risk factor for neurological involvement in hemolytic uremic syndrome. *Pediatr Nephrol* (2015) 30(2):345–52. doi: 10.1007/s00467-014-2918-0

18. Reising A, Hafer C, Hiss M, Kielstein JT, Menne J, Gueler F, et al. Ultrasound findings in ehec-associated hemolytic-uremic syndrome and their clinical relevance. *Int Urol Nephrol* (2016) 48(4):561–70. doi: 10.1007/s11255-015-1194-7

19. Vogel J. Measurement of cardiac output in small laboratory animals using recordings of blood conductivity. *Am J Physiol* (1997) 273(5):H2520–7. doi: 10.1152/ajpheart.1997.273.5.H2520

20. Matsiukevich D, Piraino G, Lahni P, Hake PW, Wolfe V, O'Connor M, et al. Metformin ameliorates gender-and age-dependent hemodynamic instability and myocardial injury in murine hemorrhagic shock. *Biochim Biophys Acta Mol Basis Dis* (2017) 1863(10 Pt B):2680–91. doi: 10.1016/j.bbadis.2017.05.027

21. Mohammed J, Filler G, Price A, Sharma AP. Cardiac tamponade in diarrhoea-positive haemolytic uraemic syndrome. *Nephrol Dial Transplant* (2009) 24(2):679–81. doi: 10.1093/ndt/gfn649

22. Minary K, Tanne C, Kwon T, Faudeux C, Clave S, Langevin L, et al. Outbreak of hemolytic uremic syndrome with unusually severe clinical presentation caused by shiga toxin-producing escherichia coli O26:H11 in France. *Arch Pediatr* (2022) 29(6):448–52. doi: 10.1016/j.arcped.2022.05.011

23. Argyle JC, Hogg RJ, Pysher TJ, Silva FG, Siegler RL. A clinicopathological study of 24 children with hemolytic uremic syndrome. A report of the southwest pediatric nephrology study group. *Pediatr Nephrol* (1990) 4(1):52–8. doi: 10.1007/bf00858440

24. Ibrahim SH, Bhutta ZA, Khan IA. Haemolytic uraemic syndrome in childhood: an experience of 7 years at the Aga Khan University. *J Pak Med Assoc* (1998) 48(4):100–3.

25. Zhao SA, Ning BT, Mao JH. Clinical characteristics of children with hemolytic uremic syndrome in Hangzhou, China. *World J Pediatr* (2017) 13(2):183–5. doi: 10.1007/s12519-017-0021-x

26. Abu-Arafeh I, Gray E, Youngson G, Auchterlonie I, Russell G. Myocarditis and haemolytic uraemic syndrome. *Arch Dis Child* (1995) 72(1):46–7. doi: 10.1136/adc.72.1.46

27. Oakes RS, Siegler RL, McReynolds MA, Pysher T, Pavia AT. Predictors of fatality in postdiarrheal hemolytic uremic syndrome. *Pediatrics* (2006) 117(5):1656–62. doi: 10.1542/peds.2005-0785

frontiers | Frontiers in Immunology

TYPE Original Research
PUBLISHED 23 October 2023
DOI 10.3389/fimmu.2023.1273612

OPEN ACCESS

EDITED BY
Pietro Ghezzi,
University of Urbino Carlo Bo, Italy

REVIEWED BY
Basilia Zingarelli,
Cincinnati Children's Hospital Medical Center, United States
Kristian-Christos Ngamsri,
University of Tübingen, Germany

*CORRESPONDENCE
Rald Victor Maria Groven
r.groven@maastrichtuniversity.nl

RECEIVED 06 August 2023
ACCEPTED 04 October 2023
PUBLISHED 23 October 2023

CITATION
Groven RVM, Greven J, Mert Ü, Horst K, Zhao Q, Blokhuis TJ, Huber-Lang M, Hildebrand F and van Griensven M (2023) Circulating miRNA expression in extracellular vesicles is associated with specific injuries after multiple trauma and surgical invasiveness.
Front. Immunol. 14:1273612.
doi: 10.3389/fimmu.2023.1273612

Circulating miRNA expression in extracellular vesicles is associated with specific injuries after multiple trauma and surgical invasiveness

Rald Victor Maria Groven[1,2]*, Johannes Greven[3], Ümit Mert[4], Klemens Horst[4], Qun Zhao[3], Taco Johan Blokhuis[2], Markus Huber-Lang[5], Frank Hildebrand[4] and Martijn van Griensven[1]

[1]Department of Cell Biology-Inspired Tissue Engineering, MERLN Institute for Technology-Inspired Regenerative Medicine, Maastricht University, Maastricht, Netherlands, [2]Division of Trauma Surgery, Department of Surgery, Maastricht University Medical Center+, Maastricht, Netherlands, [3]Experimental Orthopaedics and Trauma Surgery, Department of Orthopaedics, Trauma and Reconstructive Surgery, University Hospital Rheinisch-Westfälische Technische Hochschule (RWTH) Aachen, Aachen, Germany, [4]Department of Orthopaedics, Trauma and Reconstructive Surgery, University Hospital Rheinisch-Westfälische Technische Hochschule (RWTH) Aachen, Aachen, Germany, [5]Institute of Clinical and Experimental Trauma Immunology, University Hospital Ulm, Ulm, Germany

Introduction: Two trauma treatment principles are Early Total Care (ETC), and Damage Control Orthopedics (DCO). Cellular mechanisms that underlie the connection between treatment type, its systemic effects, and tissue regeneration are not fully known. Therefore, this study aimed to: 1) profile microRNA (miRNA) expression in plasma derived Extracellular Vesicles (EVs) from a porcine multiple trauma model at different timepoints, comparing two surgical treatments; and 2) determine and validate the miRNA's messengerRNA (mRNA) targets.

Methods: The porcine multiple trauma model consisted of blunt chest trauma, liver laceration, bilateral femur fractures, and controlled haemorrhagic shock. Two treatment groups were defined, ETC (n=8), and DCO (n=8). Animals were monitored under Intensive Care Unit-standards, blood was sampled at 1.5, 2.5, 24, and 72 hours after trauma, and EVs were harvested from plasma. MiRNAs were analysed using quantitative Polymerase Chain Reaction arrays. MRNA targets were identified *in silico* and validated *in vivo* in lung and liver tissue.

Results: The arrays showed distinct treatment specific miRNA expression patterns throughout all timepoints, and miRNAs related to the multiple trauma and its individual injuries. EV-packed miRNA expression in the ETC group was more pro-inflammatory, indicating potentially decreased tissue regenerative capacities in the acute post-traumatic phase. *In silico* target prediction revealed several overlapping mRNA targets among the identified miRNAs, related to inflammation, (pulmonary) fibrosis, and Wnt-signalling. These were, among others, A Disintegrin and Metalloproteinase domain-containing protein 10, Collagen Type 1 Alpha 1 Chain, Catenin Beta Interacting Protein 1, and Signal Transducers and Activators of Transcription 3. Validation of these mRNA targets

in the lung showed significant, treatment specific deregulations which matched the expression of their upstream miRNAs. No significant mRNA deregulations were observed in the liver.

Discussion: This study showed treatment specific, EV-packed miRNA expression patterns after trauma that correlated with mRNA expressions in the lungs, target organs over distance. A systemic response to the increased surgical trauma in the ETC group was identified, with various miRNAs associated with injuries from the trauma model, and involved in (systemic) inflammation, tissue regeneration. EV-transported miRNAs demonstrated a clear role in multiple trauma, warranting further research into tissue-tissue talk and therapeutic applications of EVs after trauma.

KEYWORDS

microRNAs, multiple trauma, extracellular vesicles, early total care, damage control orthopaedics

1 Introduction

Multiple trauma results in a high mortality rate and often invalidating consequences, in part because the sustained injuries can elicit exacerbated immune responses throughout the body, causing conditions such as Systemic Inflammatory Response Syndrome (SIRS) and Compensatory Anti-inflammatory Response Syndrome (CARS) (1). Re-establishing an immunological balance as early as possible after multiple trauma is therefore of vital importance, since this will aid in stabilising the patient and speeding up their recovery. The so called "second hit" inflicted by the surgical trauma potentially aggravates conditions such as SIRS and CARS, warranting for a careful choice between Damage Control Orthopaedics (DCO) and Early Total Care (ETC) in the initial post-traumatic phase (2).

The main difference between DCO and ETC is the invasiveness of the initial fracture treatment. The temporary fixation of long bone fractures in DCO is used to ensure a physiological steady state, prior to converting to more invasive surgical fracture fixation procedures (3). However, primary temporary fixation requires more follow up surgeries which prolongs the inflammatory response and immobilization time. The main aim of ETC is to definitively fixate all long bone fractures within primary fracture surgery, shortening the overall inflammatory response and allowing for more swift recovery (4).

Several studies have identified specific indications for either DCO or ETC, but their exact systemic cellular mechanisms that underlie their differential effects on tissue regeneration after multiple trauma are not yet fully understood (4, 5). Cellular signalling, communication, and functioning are important to adequately respond to traumatic tissue damage, inflammation, and enable for tissues to regenerate. These processes are, in part, facilitated by Extracellular Vesicles (EVs), which are important transporters of cellular mediators. EVs have been increasingly investigated in trauma due to their involvement in the underlying pathophysiology, tissue regeneration, and their ability to enable organ crosstalk (6). The latter is of particular interest in a rather heterogenic condition such as multiple trauma (7). Furthermore, research has shown that multiple trauma enhances the amount of the circulating EVs and influences their composition (8).

Upon stress, cells can release EVs to deliver various compounds, such as lipids, proteins, and microRNAs (miRNAs) at target cells or organs via the systemic circulation (9). MiRNAs are short, non-coding RNA molecules that post-transcriptionally regulate protein expression by blocking messengerRNA (mRNA) translation, or activating the transcription of specific genes by enhancing promoter activity (10). However, the involvement of miRNAs in the field of trauma surgery has predominantly been addressed in the context of local tissue responses, such as bone regeneration (11). Characterization of post-traumatic, systemic miRNA-based cellular communication, e.g. as EV-packed miRNAs, is missing. In particular, the effects of the applied surgical treatment, ETC versus DCO, on the expression of EV-packed miRNAs is still unknown. Transport of EVs to injured organs may facilitate cellular communication over distance in multiple trauma, in part through miRNAs (12).

Taking the above-described characteristics of both EVs and miRNAs into account, we hypothesise that EV-packed miRNAs may be involved in various post-traumatic processes such as immunoregulation and tissue regeneration. A first step in better understanding the role of miRNAs in this complex systemic communication mechanism would therefore be to profile the miRNA fingerprint of circulating EVs after multiple trauma at various timepoints, comparing different surgical treatment strategies.

Therefore, we defined two aims: 1) to profile the expression of miRNAs in plasma-derived EVs from a porcine multiple trauma model at different timepoints after trauma, comparing two different surgical treatment modalities; and 2) to determine and validate the miRNA's mRNA targets.

2 Methods

2.1 Animal care and experimental groups

The data presented in this paper were collected in the context of a larger study in accordance with the 3R principles as set out by the national centre for the replacement, refinement, and reduction of animals in research (13). All sections of this manuscript adhere to the ARRIVE Guidelines for reporting animal research (14). The study was approved by the German governmental office of animal care and use LANUV (Landesamt für Natur, Umwelt und Verbraucherschutz Nordrhein-Westfalen, Recklinghausen, Germany) under the permit number 81.02.04.2020.A215.

All animals were clinically examined by a veterinarian after arriving at the hosting facility. They were subsequently housed for seven days prior to the experiment to acclimatise. For the experiments, a total of 22 male German Landrace pigs (*Sus scrofa*) of 35 ± 5 kg of body weight and 3 months of age were used. The animals were divided in three experimental groups: sham (n=6), ETC (n=8), and DCO (n=8). The sham group received identical instrumentation, anaesthesia, mechanical ventilation, nutrition, and, if required, vasopressive therapy. After multiple trauma induction, either intramedullary nailing (ETC) (T2 System, Stryker GmbH & Co. KG, Duisburg, Germany) or external fixation (DCO) (Radiolucent Fixator, Orthofix, Texas, USA) of both femoral fractures was performed. Parental nutrition (Aminoven, Fresenius Kabi, Germany) was provided under close monitoring of the fluid balance and vasopressive therapy was provided as required.

2.2 Instrumentation and anaesthesia

The model has been previously described in detail (15). Briefly, after 12 hours (h) of fasting with water *ad libitum*, azaperone (Stresnil™, Janssen-Cilag GmbH, Neuss, Germany) and ketamine (Ketanest, Pfizer, New York, USA) were injected intramuscularly as premedication. Intravenous propofol (Fresenius SE & Co. KGaA, Homburg, Germany) was used to induce anaesthesia, after which the animals were orotracheally intubated (7.5 ch; Hi-Lo Lanz™, Tyco Healthcare, Hampshire, England). For the administration of fluids, anaesthesia, and continuous monitoring of central venous pressure, a catheter (Four-Lumen Catheter, 8.5 Fr., Arrow Catheter, Teleflex Medical GmbH, Fellbach, Germany) was placed in the external jugular vein. A three-lumen haemodialysis catheter (12.0 Fr., Arrow Catheter, Teleflex Medical GmbH, Fellbach, Germany) and an arterial line (Vygon GmbH & Co. KG, Aachen, Germany) were placed in the right femoral vein and artery to monitor arterial blood pressure and induce haemorrhagic shock. All animals received a suprapubic catheter (12.0 Fr, Cystofix®, B. Braun AG, Melsungen, Germany). For the duration of the study, general anaesthesia was maintained using intravenous propofol, sufentanyl, and midazolam (Panpharma GmbH, Trittau, Germany). Proper fluid intake was guaranteed by continuous crystalloid infusion (Sterofundin ISO®; 2 ml/kgBW/h) (B. Braun AG, Melsungen, Germany). Mechanical, porcine adapted volume-controlled ventilation was applied (8-12 ml/kgBW); Positive End-Expiratory Pressure (PEEP) 8 mmHg (plateau pressure < 28 mmHg) adjusted by capnometry aiming for a pCO_2 of 35–45 mmHg (Draeger Evita 4, Draeger Safety AG & Co. KGaA, Lübeck, Germany). The following vital parameters were monitored and, in part, depicted in Table 1: body temperature, blood pressure, heart- and breathing-rate, electrocardiogram recordings, electrocardiogram-synchronised pulse oximetry. Furthermore, blood C-reactive protein concentration, leukocyte count, and lactate were determined at pre-determined timepoints (Table 1).

2.3 Trauma induction

Prior to multiple trauma induction, baseline conditions were required to be stable for at least 120 min after instrumentation. The fraction of inspired oxygen (FiO_2) was set at 0.21 throughout instrumentation, as well as during multiple trauma induction and the subsequent shock phase to mimic ambient air. During the 90 min shock phase following multiple trauma induction, body temperature was not controlled to mimic the real life, out of hospital environment and fluid administration was set to 0.1 ml/kgBW/h to keep infusion lines open for later usage. The surgical treatment groups received the standardised multiple trauma (ISS=27) as described below.

A bolt gun machine (Blitz-Kerner, turbocut Jopp GmbH, Bad Neustadt an der Saale, Germany) with cattle-killing cartridges (9 × 17; DynamitNobel AG, Troisdorf, Germany) was used to induce blunt chest trauma by firing the bolt gun machine onto a pair of steel and lead panels (steel 8 mm and lead 10 mm) that were placed on the right dorsal, lower chest. Bilateral femur fractures were induced using a custom-made punch and the bolt gun machine, positioned on the mid-third of the femora.

To mimic liver laceration, a crosswise incision (4.5 x 4.5 cm) half of the tissues' depth was made in the upper left liver lobe. Following 30 s of uncontrolled bleeding, liver packing was performed with five sterile packs of 10 x 10 cm gauze. Haemorrhagic shock was performed by withdrawing maximally 45% of the total blood volume, until a Mean Arterial Pressure (MAP) of 40 ± 5 mmHg was achieved. The combined multiple trauma was left untreated for 90 min to mimic a real life shock phase. If sham animals required vasopressive therapy, this was also only provided after 90 min.

After the shock phase, animals were resuscitated in accordance with existing trauma guidelines (ATLS®, AWMF-S3 guideline on Treatment of Patients with Severe and Multiple Injuries®) by adjusting the FiO_2 to base values for mechanical ventilation, re-infusion of the withdrawn blood (Citrate Phosphate Dextrose Adenine DONOpacks, Lmb Technologie GmbH, Oberding, Germany) as well as fluids administration (Sterofundin ISO®; 2 ml/kgBW/h). A forced-air warming system was used to achieve and/or maintain normothermia for the animals (*sus scrofa*: German landrace) (38.7–39.8 °C). Prior to surgery and every 24 h after multiple trauma induction, 2 g of ceftriaxone (Fresenius SE & Co. KGaA, Homburg, Germany) were administered via intravenous infusion. Animals were turned every four to six hours to support the respiratory mechanics in the mechanically ventilated animals.

10.3389/fimmu.2023.1273612

TABLE 1 Overview of the following clinical parameters: mean arterial pressure (MAP), heart rate, noradrenaline requirement, C-reactive protein (CRP) concentration, leukocyte count, and lactate.

	1.5 hours	2.5 hours	24 hours	72 hours
MAP (mmHg; IQR)				
ETC *DCO*	40; 29 39; 1	65; 8 77; 16	64; 6 64; 10	65; 20 69; 12
Heart rate (BPM; IQR)				
ETC *DCO*	99; 63 74; 20	76; 55 78; 30	55; 52 72; 33	72; 11 65; 31
Noradrenalin (ml/h; IQR)				
ETC *DCO*	0.1; 0.4 0.1; 0.1	0.1; 0 0.1; 0	2.8; 2.9 0.1; 0	1.8; 2.6 0.1; 0
CRP (mg/l; IQR)				
ETC *DCO*	2.0; 2.0 2.0; 3.0	1.0; 3.0 3.0; 3.5	5.0; 4.0 6.5; 5.8	9.5; 4.8 5.0; 3.3
Leukocytes (10^3/μL; IQR)				
ETC *DCO*	18.2; 5.7 18.1; 11.7	19.0; 5.5 17.3; 9.5	18.8; 16.4 13.7; 15.7	8.7; 8.2 11.2; 7.8
Lactate (mmol/l; IQR)				
ETC *DCO*	2.2; 2.2 1.7; 1.0	1.6; 1.4 0.9; 1.0	0.5; 0.4 0.4; 0.3	0.4; 0.1 0.4; 0.2

Values are represented as median accompanied by the interquartile range (IQR).

2.4 Sample collection and EV isolation

Per animal of each experimental group, 1 ml of plasma was collected at the following timepoints: 1.5, 2.5, 24, and 72 h. For the isolation of EVs, samples were subjected to the following standard operating procedure, isolating EVs from 30 to 1000 nm. Plasma samples were sequentially centrifuged at 300 x g for 10 min, 2000 x g for 15 min, and 5000 x g for 15 min at 4°C. Cells, cell debris, and apoptotic bodies were eliminated respectively. The EVs were then pelleted by further centrifugation at 20000 x g for 90 min at 4°C (Avanti J-26XP, Beckman Coulter BV, Woerden, the Netherlands). The acquired precipitate was gathered and suspended in 100 μl Phosphate Buffered Saline (Sigma-Aldrich, St Louis, USA) (52, 53). The collected EVs were then stored at − 80°C.

2.5 RNA isolation and cDNA synthesis

RNA extraction was performed by chloroform phenol extraction, using 1 ml of Trizol reagent (Thermo Fisher Scientific, Waltham, USA) per 100 μl EV containing suspension. Furthermore, GlycoBlue co-precipitant (Thermo Fisher Scientific, Waltham, USA) was used according to the manufacturer's instructions. The amount and purity of the RNA were determined by spectrophotometry using a CLARIOstar Plate Reader and LVis Plate Adapter (Isogen Life Science, De Meern, The Netherlands), after which the RNA was stored at -80˚C. Per animal, RNA was then used for the transcription of miRNA to cDNA using the miRCURY LNA RT kit (Qiagen, Venlo, The Netherlands) according to manufacturer's instructions.

2.6 miRNA qPCR arrays

For this study, miRCURY LNA miRNA Serum/Plasma Focus PCR panels (YAHS-106YD-8, Qiagen, Venlo, The Netherlands) were used. This panel kit consists of 179 primers for unique miRNAs, excluding several PCR and reverse transcription controls, housekeeper genes, and interplate calibrators. The expression of miRNAs was determined in the pooled sample per respective treatment group and for each specific timepoint. Gene expression was normalised according to the global Cq method. Sham samples of the respective timepoints were used as control. MiRNA gene expression levels were determined via qPCR by the cycle number (Cq), using the CFX96 Real-Time PCR system (Bio-Rad GmbH, Munich, Germany). To assess the quality of the qPCR array reactions, melting curve analyses were performed in combination with a chosen cut off Cq value of 35, above which miRNAs were not considered for further analysis due to minute or absent presence. Fold regulation (FR) was calculated using comparative $2^{-\Delta\Delta Ct}$ method, in which a downregulation was represented as the negative inverse of the acquired $2^{-\Delta\Delta Ct}$ value. A deregulation, as represented by a FR of ≥ 2 or ≤ -2, was considered significantly deregulated. For each timepoint, a selection of the 20 most deregulated miRNAs among the two treatment groups was composed, and from that, miRNAs that

were deregulated at minimally two timepoints were selected for bioinformatic analysis and mRNA target validations.

2.7 Bioinformatic analyses of miRNA-mRNA interactions

Possible miRNA-mRNA interactions were estimated using the analytical platform tools4miRs as well as an extensive literature review. Five different mRNA target prediction algorithms were applied: miRanda, miRmap, RNA22, RNAhybrid, and TargetSpy. A main focus was put on genes that were involved in multiple trauma, SIRS, CARS, MODS, sepsis, and bone regeneration. A miRNA-mRNA interaction was included if it resulted as a true hit in minimally three algorithms.

2.8 mRNA target validation

To examine the systemic effects of the deregulated miRNA *in vivo*, a selection of mRNAs of interest was analysed in lung and liver samples by means of qPCR based on the *in silico* target prediction and literature review. The following genes were included for qPCR: A Disintegrin and Metalloproteinase domain-containing protein 10 (ADAM10), Collagen Type 1 Alpha 1 Chain (COL1A1), Catenin Beta Interacting Protein 1 (CTNNBIP1), and Signal Transducers and Activators of Transcription 3 (STAT3). The amplification primers are listed in Supplemental Table 1. Controls included positive and negative PCR controls, as well as reverse transcription controls.

MRNA expression levels were determined via qPCR by the cycle number (Cq), using a CFX96 Real-Time PCR system (Bio-Rad GmbH, Munich, Germany). To assess the quality of the individual qPCR reactions, melting curve analyses were performed in combination with a chosen cut off Cq value of 35, above which mRNAs were not considered expressed. Data were processed using comparative $2^{-\Delta\Delta Ct}$ method, using GAPDH as a housekeeper gene. A FR of ≥ 2 or ≤ -2 was considered significantly deregulated.

2.9 Statistical analyses

Analyses were performed with GraphPad Prism version 9.5.0 (GraphPad Software, San Diego, USA). Shapiro-Wilks test was performed to assess normality. Data are represented as mean or median, accompanied by standard error of the mean or interquartile range as appropriate. Significance was determined using one-way ANOVA with Holm-Šidák's multiple comparison test. A $p \leq 0.05$ was considered statistically significant.

3 Results

Overall, 179 unique miRNAs were examined per timepoint, for each treatment group. In total, 136 miRNAs were deregulated at minimally one timepoint after multiple trauma. Figures 1, 2 display significantly deregulated miRNAs, maximally 10 up and downregulated per timepoint, from the ETC and DCO groups respectively. Table 1 displays the following vital parameters, monitored on the respective timepoints: mean arterial pressure (MAP), heart rate, noradrenaline requirement, and blood C-reactive protein concentration, leukocyte count, and lactate.

In short, compared to the sham control, four and 40 EV-derived miRNAs were respectively down- and upregulated at 1.5 h after multiple trauma in the ETC group. Throughout the acute post-traumatic phase, at 2.5 h after trauma, the number of upregulated miRNAs increased to 51 while six miRNAs were downregulated. At 24 h after multiple trauma, the number of downregulated miRNAs doubled in the ETC group, while the total of upregulated miRNAs decreased from 51 to 12. At 72 h after multiple trauma induction, the overall miRNA expression profile normalised to baseline. Overall, the early circulatory EV-derived miRNA expression signature of the ETC group showed strong deregulations of both anti- and proinflammatory miRNAs, such as miR-29a and miR-192 respectively, as well as miRNAs related to angiogenesis, such as miR-122, and the formation of granulation tissue/fibrosis, such as miR-133a. At 72 h, these expression profiles changed, showing increased expression of miRNAs important for cellular proliferation and differentiation, as well as osteogenesis.

Compared to the sham control, miRNA expression profiles in the DCO group showed significant differences at all timepoints, most prominently at 24 h. For all timepoints, the number of downregulated miRNAs was higher in the DCO group compared to the ETC group. At 1.5 h after multiple trauma, 17 and 13 miRNAs were respectively down- and upregulated. The expression profile changed within the following hour, resulting in 7 down- and 42 upregulated miRNAs at 2.5 h after trauma. This trend reversed itself at 24 h, showing a significant drop in the number of overall upregulated miRNAs to 8, and an increase in the total number of downregulated miRNAs to 27. Lastly, at 72 h after multiple trauma induction, miRNA expression showed strong downregulations, with 35 down- and merely 5 upregulated miRNAs (Supplemental Table 2). Collectively, EV-derived miRNA expression in the acute post-traumatic phase was characterised by an increased expression of anti-inflammatory miRNAs, while also showing both up and downregulations for several miRNAs that are involved in cellular proliferation, migration, and cellular senescence. The later timepoints showed downregulations of miRNAs that were, e.g., anti-apoptotic such as miR-29a, while showing upregulations of miRNAs that enhanced cellular proliferation and differentiation in the ETC group, such as miR-885 and miR-29c.

3.1 Most deregulated miRNAs

MiRNAs that exhibited the greatest difference in fold regulation (FR) between the two surgical treatment groups at minimally two timepoints after trauma were selected from the identified 136 unique miRNAs. In total, this provided 13 miRNAs (Figures 3, 4).

The more invasive character of ETC resulted in an overall upregulation of EV-packed miRNAs. In the acute phase until 2.5 h after multiple trauma, most deregulated miRNA expressions were

10.3389/fimmu.2023.1273612

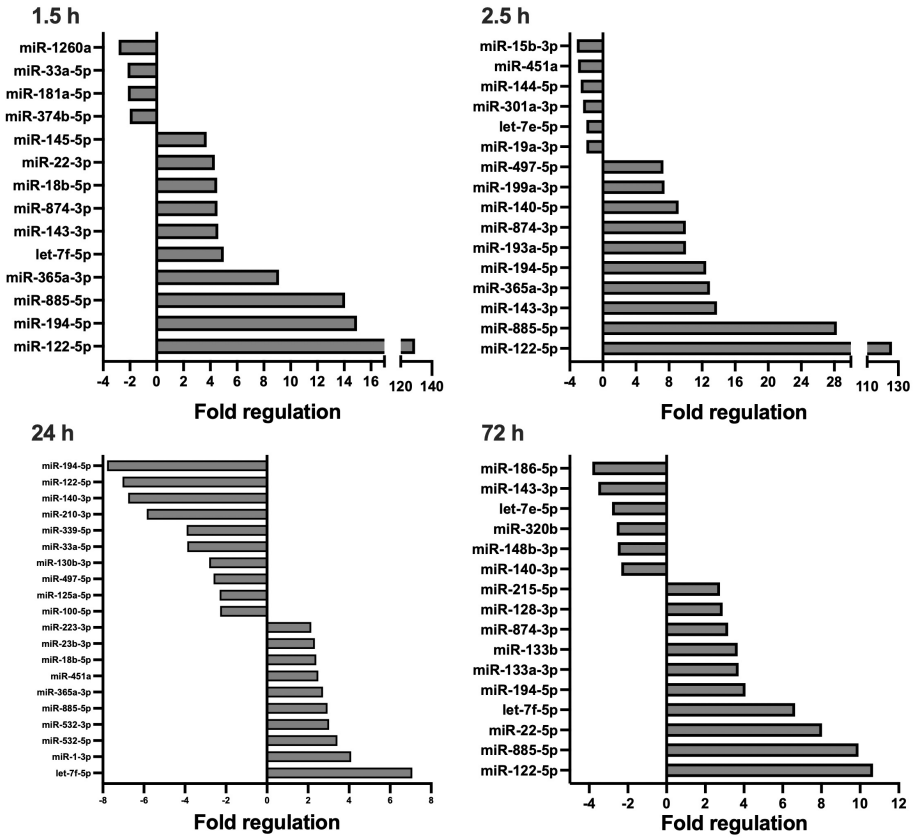

FIGURE 1
Circulating, extracellular vesicle-packed miRNA expression signature of the ETC group at four timepoints after trauma: 1.5, 2.5, 24, and 72 h.. All depicted miRNAs were significantly deregulated at the respective timepoint. A maximum of 10 up- and downregulated miRNAs are shown. Fold regulation (FR) was calculated using comparative $2^{-\Delta\Delta Ct}$ method, in which a downregulation was represented as the negative inverse of the acquired $2^{-\Delta\Delta Ct}$ value.

present in the ETC group, with a steady upregulation over time for several specific miRNAs as compared to control. Contrarily, the DCO group showed less deregulation at 1.5 h than ETC, as compared to baseline. At 2.5 h, various miRNAs revealed significant up- and downregulations. For the ETC group, EV-derived miRNA expression started to normalise at 24 h after multiple trauma, whereas the DCO group demonstrated evident downregulations for all of the selected miRNAs. These highly significant downregulations in the DCO group at 24 h after trauma normalised at 72 h. For the ETC group, strong upregulations were present at 72 h for few miRNAs, but the overall expression profile remained comparable to that of 24 h after trauma.

3.2 Bioinformatic analyses

Tools4miRs identified 214 targets for the 13 selected miRNAs. Targets were involved in various aspects of the immune responses and tissue regeneration, such as response to hypoxia, chemotaxis, inflammation, apoptosis, cellular migration and differentiation, and fibrosis. Interestingly, several miRNAs and their targets were identified that matched (organ) specific injuries from the multiple trauma model. Examples of these are the hepato-specific miR-122, miRNAs 29a and 133 with key functions in pulmonary fibrosis, and the involvement of miRNAs 133 and 192 in systemic inflammation. The *in silico* target prediction and literature review showed that several mRNA targets overlapped between the identified miRNAs.

3.3 qPCR for mRNA targets

Four key mRNA targets of the deregulated miRNAs were analysed by means of qPCR to assess the potential effect of the deregulated miRNAs in target organs. The mRNA targets were selected based on the bioinformatic analyses combined with the overview of the most deregulated, EV-packed miRNAs between the two treatment groups. A total of four miRNA targets, ADAM10, COL1A1, CTNNBIP1, and STAT3, were chosen for validation in lung and liver samples, based on their functions in tissue regenerative processes in these organs, such as in (pulmonary) fibrosis after trauma, regulation of the inflammatory response, Wingless-related integration site signalling pathway (Wnt-signalling), and liver- and alveolar-tissue homeostasis. MiR-122 and 365, both showing significant deregulations over time, were among the upstream targets of ADAM10. Furthermore, miR-133a,

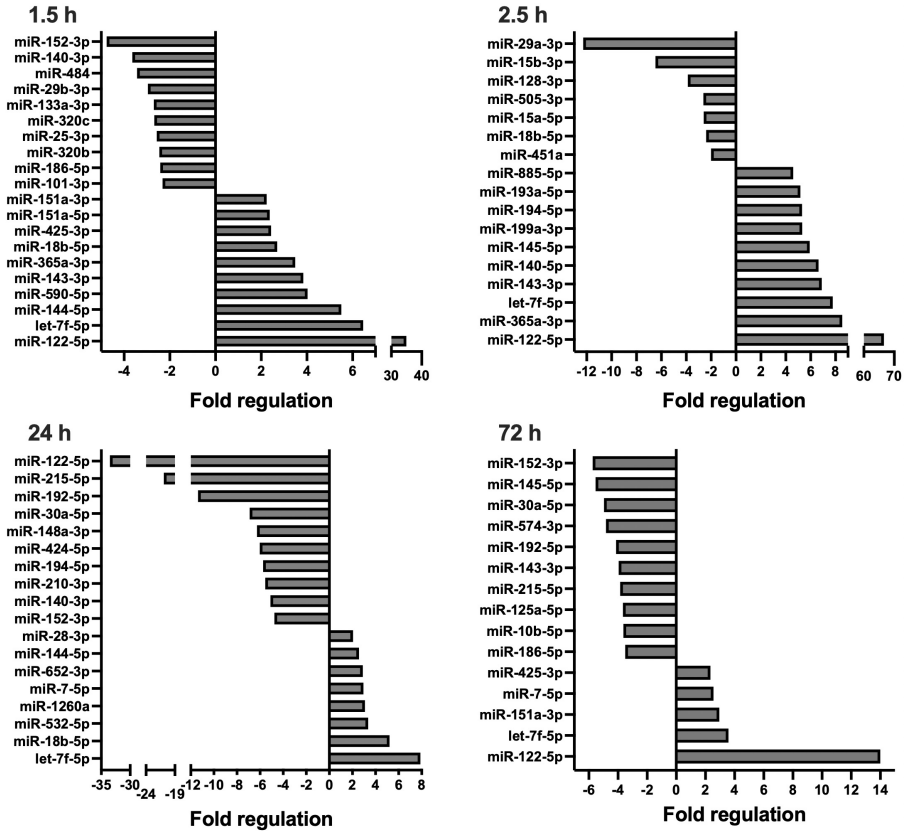

FIGURE 2
Circulating, extracellular vesicle-packed miRNA expression signature of the DCO group at four timepoints after trauma: 1.5, 2.5, 24, and 72 h.. All depicted miRNAs were significantly deregulated at the respective timepoint. A maximum of 10 up- and downregulated miRNAs are shown. Fold regulation (FR) was calculated using comparative $2^{-\Delta\Delta Ct}$ method, in which a downregulation was represented as the negative inverse of the acquired $2^{-\Delta\Delta Ct}$ value.

miR-29a, and -29c targeted COL1A1, while CTNNBIP1 was the mRNA target of miR-215 and -885. Lastly, STAT3 was regulated by miR-22 and -29a. Lung and liver samples were of interest due to the nature of the multiple trauma, combined with the observed tissue specific miRNA expression profiles. In the lung, the four analysed mRNA targets were significantly deregulated between the treatment groups (all $p < 0.0001$). Three of the four mRNA targets, ADAM10, COL1A1, and STAT3, were significantly downregulated in lung tissue from the ETC group. One of the four mRNA targets, CTNNBIP1, was significantly upregulated in lung tissue from the DCO group. These mRNA deregulations were consistent with the deregulation of its upstream miRNAs as well as the *in silico* target prediction (Figure 5). However, no significant deregulations were observed in the liver.

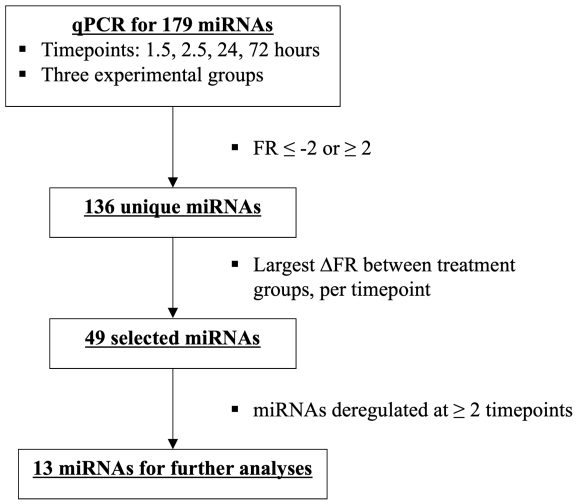

FIGURE 3
Flowchart depicting miRNA selection of the most deregulated miRNAs among the two treatment groups, ETC vs DCO.

4 Discussion

Multiple trauma is often complicated by severe, complex immune responses both locally at the sites of injury, as well as in the systemic circulation, influencing tissue damage clearance and regenerative processes (1). This study examined the systemic post-traumatic response by profiling the expression of EV-packed miRNAs in a porcine multiple trauma animal model. In this clinically relevant model, two different surgical treatment methods were compared, ETC and DCO, to examine the effect of surgical invasiveness on miRNA-based organ crosstalk after multiple trauma, using EVs as carriers.

10.3389/fimmu.2023.1273612

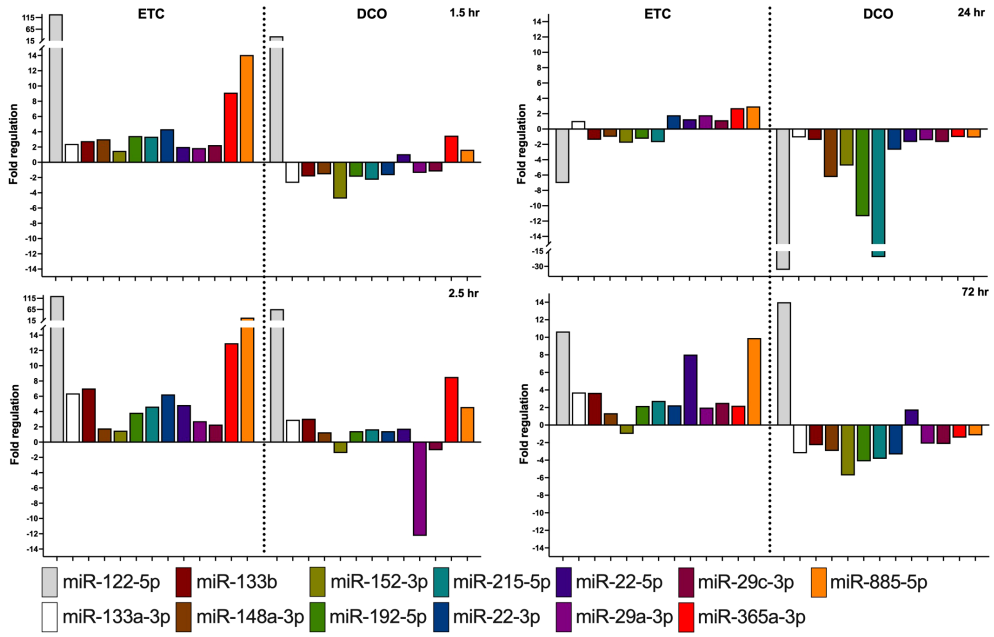

FIGURE 4
Most significantly deregulated miRNAs between the ETC and DCO treatment groups. All depicted miRNAs were significantly up or downregulated at minimally two timepoints after surgical intervention. Fold regulation (FR) was calculated using comparative $2^{-\Delta\Delta Ct}$ method, in which a downregulation was represented as the negative inverse of the acquired $2^{-\Delta\Delta Ct}$ value.

Looking at the miRNA expression data, the individual injuries of the multiple trauma model seem to be represented in the systemic EV-packed miRNA expression. MiR-122 for example, the most abundant liver-specific miRNA, was strongly upregulated in both treatment groups in the acute phase after trauma. This miRNA is a specific systemic biomarker for hepatocyte damage upon acute liver injury, modelled in this current porcine multiple trauma model (16). Consistent with these findings, miR-365 was upregulated in both treatment groups. MiR-365 is an upstream inducer of pro-apoptotic protein synthesis and may be involved in programmed cell death after trauma (17). The kinetics of these two miRNAs were similar between the treatment groups, showing significant upregulations in the acute post-traumatic phase followed by decreased expression at 24 h. The greater upregulation of the hepato-specific miR-122 in the ETC group could indicate that more invasive surgery in the acute phase after multiple trauma aggravates hepatocyte damage, potentially through increased systemic inflammation. This is in line with clinical findings in which the stress response to enhanced surgical trauma increases the risk of liver decompensation in patients with chronic liver disease (18). Unfortunately, translational research on the circulating expression of miR-122 and its potential correlations with liver function in patients suffering from multiple trauma without prior liver disease is lacking.

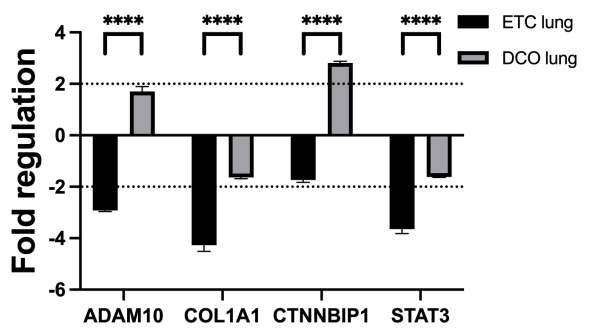

FIGURE 5
miRNA targeted mRNAs are deregulated in lung tissue, depending on the applied surgical treatment strategy: intramedullary nailing (Early-Total-Care) versus external fixation (Damage-Control-Orthopaedics). Black dotted line displays the threshold of a fold regulation of $|\geq 2|$ above or below which a mRNA was considered significantly deregulated. Significant differences in mRNA expression between the same sample types from different treatment groups are marked as follows: ****p-value<0.0001. Error bars depict standard error of the mean.

Both miR-365 and miR-122 have also been connected to pulmonary inflammation (16, 19, 20). MiR-365 elicits anti-inflammatory effects by reducing the expression of inflammatory cytokines after IL-17 provocation in asthmatic inflammation during bronchial asthma (19). MiR-122, accounting for 70-80% of the total miRNA expression in the liver, has proven to elicit acute pulmonary inflammation after liver damage, and aggravate pulmonary infections (20, 21). Moreover, increased circulating miR-122 due to acute liver damage has also been associated with mortality in patients suffering from ARDS (16). The fact that both these miRNAs can affect the lungs are in accordance with the findings from this study in which upregulations of circulating, EV-packed, miR-122 and miR-365 were observed, combined with matching downregulations of its mRNA targets in the lungs. Among others, ADAM10 is targeted by miR-122 and miR-365 and was

significantly downregulated in lung tissue from the ETC group, matching the stronger upregulations of both miRNAs in this treatment group (Figures 4, 5).

MiR-885 has also shown associations with both lung and liver pathologies, in part by targeting the Wnt-signalling. It was overexpressed at all timepoints in the ETC group, most evidently in the acute phase after trauma. Apart from being a tumour suppressor gene, miR-885 expression has also shown positive correlations with increased serum liver enzymes (22, 23). Furthermore, miR-885 can alleviate bronchial epithelial cell injury (24). Again, the invasiveness of the applied surgical technique influences systemic, EV-packed expression of this miRNA. While being upregulated at all timepoints in the ETC group, it has only shown a comparatively moderate upregulation at 2.5 h after trauma in the DCO group.

Another key component of the multiple trauma model was the induced haemorrhagic shock. Haemorrhagic shock drives immune and organ failure and contributes to among other SIRS, subsequent CARS, and potentially sepsis (1, 2, 25, 26). MiRNAs 133a and 192 are considered potential biomarkers for the development and severity of sepsis and SIRS (27–29). Both miRNAs showed significant deregulations in both treatment groups, being upregulated at almost all timepoints in the ETC group, while revealing significant downregulations in the DCO group, particularly at 24 and 72 h after trauma. These treatment specific deregulations match the increased surgical trauma and subsequent systemic inflammation, keeping their functions in mind. Consistent with these findings was the expression of COL1A1, a mRNA target of miR-133a, in lung tissue from both treatment groups. COL1A1 expression was downregulated in the ETC group, matching the marked upregulations of its upstream miR-133a.

In fact, the targeting of COL1A1 by miR-133a is an important factor in its involvement in pulmonary fibrosis. Overexpression of miR-133a has been reported to be anti-fibrotic and is thereby involved in the physiological response upon lung injury (30). Another miRNA that is involved in the pathogenesis of pulmonary fibrosis is miR-29a. In fact, a miR-29a mimic has been developed to target COL1A1 as a treatment option for pulmonary fibrosis (31). Furthermore, miR-29a reduces alveolar epithelial PANoptosis *in vivo* by which it improves acute lung injury (32). MiR-133a and miR-29a exhibited similar expression kinetics within each treatment group, showing most deregulation in the ETC group, consistently upregulated at all timepoints. This overexpression could thus protect against pulmonary fibrosis and inflammatory cell death upon blunt chest trauma (30–32). The expression of COL1A1 in lung tissue from both treatment groups is consistent with its upstream regulator miR-29a (Figures 4, 5).

MiR-29a also has systemic implications in relation to sepsis by targeting STAT3, a key regulator of the inflammatory response in sepsis (33). Like miR-29a, miR-22 also targets STAT3. Both miRNAs resulted similarly deregulated in both treatment groups, with the significant downregulation in pulmonary STAT3 expression matching the upregulations of upstream miRNAs 29a and 22 (Figures 4, 5). Although miR-22 has been identified as an *in vivo* protective factor in LPS-induced acute lung injury, research into the biomolecular functioning of miR-22 in relation to lung injury, and even more so in relation to liver injury, is scarce (34, 35).

Lastly, miR-215 showed minor upregulations in the ETC group at all timepoints, except at 24 h after trauma. Notably, this miRNA showed strong downregulations in the DCO group, most evidently at 24 and 72 h after trauma. One of its targets is CTNNBIP1, a protein that negatively regulates Wnt-signalling by binding to β-catenin, the main activator of the Wnt-signalling pathway (36). The expression of CTNNBIP1 was significantly downregulated in lung tissue from the ETC group as compared to that of the DCO group. This corresponds to the strong downregulation of miR-215 in the DCO group, reducing the post-transcriptional silencing of its target CTNNBIP1. Although miR-215 has been broadly investigated in various fields, suggesting for example a relation between lung cancer and the upregulation of miR-215, research on miR-215 in relation to trauma is lacking (37). The marked systemic downregulations upon less invasive surgery as compared to upregulations upon more invasive surgery do imply that there might be a systemic involvement of miR-215 after multiple trauma.

The nature of multiple trauma implies an abrupt alteration in physiology that changes the tissue's overall state and functioning. Immune and tissue regenerative processes are subsequently activated, often starting with inflammation followed by more deliberate, intricate processes that aim at restoring tissues. EVs have gained interest in the field of trauma research due to their role as transporters of cellular mediators in these processes after multiple trauma (7). Limitations of this study are the 72 h duration of the model, which is too short to observe long term complications. The 72 h duration also makes it unfit to investigate clinical outcome in the long term. However, this study is among the first to investigate the expression and role of circulating, EV-packed miRNAs in a multiple trauma model in which two different surgical treatment strategies were compared. This study also showed that, in this translational multiple trauma model, DCO results in a reduced expression of pro-inflammatory miRNAs in the systemic circulation.

5 Conclusion

Multiple trauma is an extraordinary condition that, unlike other diseases, rarely presents with identical symptoms in different patients. Multiple trauma management can therefore be challenging since several injuries in different tissue types and organs require tailored treatment plans. The systemic circulation plays an important role in multiple trauma, first and foremost since it carries oxygen and nutrients to the tissues at stake, but also due to the role that it plays in communication between tissues. This study revealed distinctive, treatment specific EV-packed miRNA expression patterns that correlated to mRNA expressions in target organs. Furthermore, this study demonstrates that EV-derived miRNA expression is a lively process, revealing dynamic miRNA expression kinetics throughout the acute phase until 72 h after multiple trauma. Various of the identified miRNAs are involved in (systemic) inflammatory and tissue regenerative processes which correlated to the key injuries from the multiple trauma model.

These miRNA expression patterns exhibited a clear systemic response to the increased surgical trauma in the ETC group, suggesting that inflammatory responses from the sustained injuries may be aggravated, and that the subsequent increase in systemic inflammation requires a more elaborate compensatory anti-inflammatory response. This study demonstrated that EV-transported miRNAs have a clear systemic involvement in multiple trauma, opening doors for further research into tissue-tissue talk in multiple trauma as well as therapeutic applications of EVs.

Data availability statement

The original contributions presented in the study are publicly available. This data can be found here: https://doi.org/10.34894/NYKLDA.

Ethics statement

The animal study was approved by the German governmental office of animal care and use LANUV (Landesamt für Natur, Umwelt und Verbraucherschutz Nordrhein-Westfalen, Recklinghausen, Germany) under the permit number 81.02.04.2020.A215. The study was conducted in accordance with the local legislation and institutional requirements.

Author contributions

RG: Data curation, Formal Analysis, Investigation, Writing – original draft, Writing – review & editing. JG: Investigation, Writing – review & editing. ÜM: Investigation, Writing – review & editing. KH: Writing – review & editing. QZ: Investigation, Writing – review & editing. TB: Funding acquisition, Writing – review & editing. MH-L: Conceptualization, Funding acquisition, Writing – review & editing. FH: Conceptualization, Funding acquisition, Writing – review & editing. MG: Conceptualization, Data curation, Formal Analysis, Funding acquisition, Writing – original draft, Writing – review & editing.

Funding

The authors declare financial support was received for the research, authorship, and/or publication of this article. This study was partially financially supported by the University Fund Limburg/SWOL and by the German Research Foundation 429837092.

Conflict of interest

The authors declare that the research was conducted in the absence of any commercial or financial relationships that could be construed as a potential conflict of interest.

Publisher's note

Supplementary material

The Supplementary Material for this article can be found online at: https://www.frontiersin.org/articles/10.3389/fimmu.2023.1273612/full#supplementary-material

References

1. Huber-Lang M, Lambris JD, Ward PA. Innate immune responses to trauma. *Nat Immunol* (2018) 19(4):327–41. doi: 10.1038/s41590-018-0064-8

2. Pape HC, Moore EE, McKinley T, Sauaia A. Pathophysiology in patients with polytrauma. *Injury* (2022) 53(7):2400–12. doi: 10.1016/j.injury.2022.04.009

3. Volpin G, Pfeifer R, Saveski J, Hasani I, Cohen M, Pape H-C. Damage control orthopaedics in polytraumatized patients- current concepts. *J Clin Orthopaedics Trauma* (2021) 12(1):72–82. doi: 10.1016/j.jcot.2020.10.018

4. Blokhuis TJ, Pape HC, Frölke JP. Timing of definitive fixation of major long bone fractures: Can fat embolism syndrome be prevented? *Injury* (2017) 48 Suppl 1:S3–s6. doi: 10.1016/j.injury.2017.04.015

5. Pape HC, Pfeifer R. Safe definitive orthopaedic surgery (SDS): repeated assessment for tapered application of Early Definitive Care and Damage Control?: an inclusive view of recent advances in polytrauma management. *Injury* (2015) 46(1):1–3. doi: 10.1016/j.injury.2014.12.001

6. Seibold T, Schönfelder J, Weeber F, Lechel A, Armacki M, Waldenmaier M, et al. Small extracellular vesicles propagate the inflammatory response after trauma. *Adv Sci (Weinh)* (2021) 8(24):e2102381. doi: 10.1002/advs.202102381

7. Alsaadi N, Srinivasan AJ, Seshadri A, Shiel M, Neal MD, Scott MJ. The emerging therapeutic potential of extracellular vesicles in trauma. *J Leukoc Biol* (2022) 111(1):93–111. doi: 10.1002/JLB.3MIR0621-298R

8. Kuravi SJ, Yates CM, Foster M, Harrison P, Hazeldine J, Hampson P, et al. Changes in the pattern of plasma extracellular vesicles after severe trauma. *PloS One* (2017) 12(8):e0183640. doi: 10.1371/journal.pone.0183640

9. Doyle LM, Wang MZ. Overview of extracellular vesicles, their origin, composition, purpose, and methods for exosome isolation and analysis. *Cells* (2019) 8(7):727–51. doi: 10.3390/cells8070727

10. O'Brien J, Hayder H, Zayed Y, Peng C. Overview of microRNA biogenesis, mechanisms of actions, and circulation. *Front Endocrinol (Lausanne)* (2018) 9:402. doi: 10.3389/fendo.2018.00402

11. Groven RVM, van Koll J, Poeze M, Blokhuis TJ, van Griensven M. miRNAs related to different processes of fracture healing: an integrative overview. *Front Surg* (2021) 8:786564. doi: 10.3389/fsurg.2021.786564

12. Veziroglu EM, Mias GI. Characterizing extracellular vesicles and their diverse RNA contents. *Front Genet* (2020) 11:700. doi: 10.3389/fgene.2020.00700

13. Lupu L, Horst K, Greven J, Mert Ü, Ludviksen JAK, Pettersen K, et al. Simultaneous C5 and CD14 inhibition limits inflammation and organ dysfunction in pig polytrauma. *Front Immunol* (2022) 13:952267. doi: 10.3389/fimmu.2022.952267

14. Percie du Sert N, Hurst V, Ahluwalia A, Alam S, Avey MT, Baker M, et al. The ARRIVE guidelines 2.0: Updated guidelines for reporting animal research. *PloS Biol* (2020) 18(7):e3000410. doi: 10.1371/journal.pbio.3000410

15. Horst K, Simon TP, Pfeifer R, Teuben M, Almahmoud K, Zhi Q, et al. Characterization of blunt chest trauma in a long-term porcine model of severe multiple trauma. *Sci Rep* (2016) 6:39659. doi: 10.1038/srep39659

16. Rahmel T, Rump K, Adamzik M, Peters J, Frey UH. Increased circulating microRNA-122 is associated with mortality and acute liver injury in the acute respiratory distress syndrome. *BMC Anesthesiol* (2018) 18(1):75. doi: 10.1186/s12871-018-0541-5

17. Li M, Yang Y, Kuang Y, Gan X, Zeng W, Liu Y, et al. miR-365 induces hepatocellular carcinoma cell apoptosis through targeting Bcl-2 Retraction. *Exp Ther Med* (2017) 13(5):2279–85. doi: 10.3892/etm.2017.4244

18. Bleszynski MS, Bressan AK, Joos E, Morad Hameed S, Ball CG. Acute care and emergency general surgery in patients with chronic liver disease: how can we optimize perioperative care? A review of the literature. *World J Emergency Surg* (2018) 13(1):32. doi: 10.1186/s13017-018-0194-1

19. Wang W, Li Y, Fan J, Qu X, Shang D, Qin Q, et al. MiR-365-3p is a negative regulator in IL-17-mediated asthmatic inflammation. *Front Immunol* (2022) 13:953714. doi: 10.3389/fimmu.2022.953714

20. Wang Y, Liang H, Jin F, Yan X, Xu G, Hu H, et al. Injured liver-released miRNA-122 elicits acute pulmonary inflammation *via* activating alveolar macrophage TLR7 signaling pathway. *Proc Natl Acad Sci U.S.A.* (2019) 116(13):6162–71. doi: 10.1073/pnas.1814139116

21. Collison AM, Sokulsky LA, Kepreotes E, Pereira de Siqueira A, Morten M, Edwards MR, et al. miR-122 promotes virus-induced lung disease by targeting SOCS1. *JCI Insight* (2021) 6(7):e127933. doi: 10.1172/jci.insight.127933

22. Zhang Z, Yin J, Yang J, Shen W, Zhang C, Mou W, et al. miR-885-5p suppresses hepatocellular carcinoma metastasis and inhibits Wnt/β-catenin signaling pathway. *Oncotarget* (2016) 7(46):75038–51. doi: 10.18632/oncotarget.12602

23. Raitoharju E, Seppälä I, Lyytikäinen L-P, Viikari J, Ala-Korpela M, Soininen P, et al. Blood hsa-miR-122-5p and hsa-miR-885-5p levels associate with fatty liver and related lipoprotein metabolism—The Young Finns Study. *Sci Rep* (2016) 6(1):38262. doi: 10.1038/srep38262

24. Shen Y, Jiang A, Chen R, Gao X, Song G, Lu H. MicroRNA-885-3p alleviates bronchial epithelial cell injury induced by lipopolysaccharide *via* toll-like receptor 4. *Bioengineered* (2022) 13(3):5305–17. doi: 10.1080/21655979.2022.2032939

25. Pantalone D, Bergamini C, Martellucci J, Alemanno G, Bruscino A, Maltinti G, et al. The role of DAMPS in burns and hemorrhagic shock immune response: pathophysiology and clinical issues. Review. *Int J Mol Sci* (2021) 22(13):7020–32. doi: 10.3390/ijms22137020

26. Halbgebauer R, Braun CK, Denk S, Mayer B, Cinelli P, Radermacher P, et al. Hemorrhagic shock drives glycocalyx, barrier and organ dysfunction early after polytrauma. *J Crit Care* (2018) 44:229–37. doi: 10.1016/j.jcrc.2017.11.025

27. Tian X, Li L, Fu G, Wang J, He Q, Zhang C, et al. miR-133a-3p regulates the proliferation and apoptosis of intestinal epithelial cells by modulating the expression of TAGLN2. *Exp Ther Med* (2021) 22(2):824. doi: 10.3892/etm.2021.10256

28. Tacke F, Roderburg C, Benz F, Cardenas DV, Luedde M, Hippe HJ, et al. Levels of circulating miR-133a are elevated in sepsis and predict mortality in critically ill patients. *Crit Care Med* (2014) 42(5):1096–104. doi: 10.1097/CCM.0000000000000131

29. Caserta S, Mengozzi M, Kern F, Newbury SF, Ghezzi P, Llewelyn MJ. Severity of systemic inflammatory response syndrome affects the blood levels of circulating inflammatory-relevant microRNAs. *Front Immunol* (2017) 8:1977. doi: 10.3389/fimmu.2017.01977

30. Wei P, Xie Y, Abel PW, Huang Y, Ma Q, Li L, et al. Transforming growth factor (TGF)-β1-induced miR-133a inhibits myofibroblast differentiation and pulmonary fibrosis. *Cell Death Dis* (2019) 10(9):670. doi: 10.1038/s41419-019-1873-x

31. Chioccioli M, Roy S, Newell R, Pestano L, Dickinson B, Rigby K, et al. A lung targeted miR-29 mimic as a therapy for pulmonary fibrosis. *EBioMedicine* (2022) 85:104304. doi: 10.1016/j.ebiom.2022.104304

32. Cui Y, Wang X, Lin F, Li W, Zhao Y, Zhu F, et al. MiR-29a-3p improves acute lung injury by reducing alveolar epithelial cell PANoptosis. *Aging Dis* (2022) 13(3):899–909. doi: 10.14336/AD.2021.1023

33. Zheng Y, Cheng J, Zhang A, Wang Y, Dai C, Li J. Acetylation of histone 3 promotes miR-29a expression and downregulates STAT3 in sepsis. *Injury* (2022) 53 (2):416–21. doi: 10.1016/j.injury.2021.09.018

34. Zheng Y, Liu J, Chen P, Lin L, Luo Y, Ma X, et al. Exosomal miR-22-3p from human umbilical cord blood-derived mesenchymal stem cells protects against lipopolysaccharid-induced acute lung injury. *Life Sci* (2021) 269:119004. doi: 10.1016/j.lfs.2020.119004

35. Yang X, Su W, Li Y, Zhou Z, Zhou Y, Shan H, et al. MiR-22-3p suppresses cell growth *via* MET/STAT3 signaling in lung cancer. *Am J Transl Res* (2021) 13(3):1221–32.

36. Liu J, Xiao Q, Xiao J, Niu C, Li Y, Zhang X, et al. Wnt/β-catenin signalling: function, biological mechanisms, and therapeutic opportunities. *Signal Transduct Target Ther* (2022) 7(1):3. doi: 10.1038/s41392-021-00762-6

37. Vychytilova-Faltejskova P, Slaby O. MicroRNA-215: From biology to theranostic applications. *Mol Aspects Med* (2019) 70:72–89. doi: 10.1016/j.mam.2019.03.002

frontiers | Frontiers in Immunology

TYPE Original Research
PUBLISHED 15 November 2023
DOI 10.3389/fimmu.2023.1279496

OPEN ACCESS

EDITED BY
Pietro Ghezzi,
University of Urbino Carlo Bo, Italy

REVIEWED BY
Dianne Cooper,
Queen Mary University of London, United Kingdom
Basilia Zingarelli,
Cincinnati Children's Hospital Medical Center, United States

*CORRESPONDENCE
Miroslaw T. Kornek
Miroslaw_Theodor.Kornek@ukbonn.de

†These authors have contributed equally to this work and share last authorship

RECEIVED 18 August 2023
ACCEPTED 23 October 2023
PUBLISHED 15 November 2023

CITATION
Wang B, Wöhler A, Greven J, Salzmann RJS, Keller CM, Tertel T, Zhao Q, Mert Ü, Horst K, Lupu L, Huber-Lang M, van Griensven M, Mollnes TE, Schaaf S, Schwab R, Strassburg CP, Schmidt-Wolf IGH, Giebel B, Hildebrand F, Lukacs-Kornek V, Willms AG and Kornek MT (2023) Liquid Biopsy in Organ Damage: small extracellular vesicle chip-based assessment of polytrauma. *Front. Immunol.* 14:1279496. doi: 10.3389/fimmu.2023.1279496

Liquid Biopsy in Organ Damage: small extracellular vesicle chip-based assessment of polytrauma

Bingduo Wang[1], Aliona Wöhler[2], Johannes Greven[3], Rebekka J. S. Salzmann[1], Cindy M. Keller[1], Tobias Tertel[4], Qun Zhao[3], Ümit Mert[3], Klemens Horst[3], Ludmila Lupu[5], Markus Huber-Lang[5], Martijn van Griensven[6], Tom Erik Mollnes[7,8,9], Sebastian Schaaf[2], Robert Schwab[2], Christian P. Strassburg[1], Ingo G. H. Schmidt-Wolf[10], Bernd Giebel[4], Frank Hildebrand[3], Veronika Lukacs-Kornek[11†], Arnulf G. Willms[11,12†] and Miroslaw T. Kornek[1,2*†]

[1]Department of Internal Medicine I, University Hospital Bonn of the Rheinische Friedrich-Wilhelms-University, Bonn, Germany, [2]Department of General, Visceral and Thoracic Surgery, German Armed Forces Central Hospital, Koblenz, Germany, [3]Department of Orthopaedics, Trauma and Reconstructive Surgery, University Hospital Rheinisch-Westfälische Technische Hochschule (RWTH) Aachen, Aachen, Germany, [4]Institute for Transfusion Medicine, University Hospital Essen, University of Duisburg-Essen, Essen, Germany, [5]Institute of Clinical and Experimental Trauma Immunology, University Hospital Ulm, Ulm, Germany, [6]Department of Cell Biology-Inspired Tissue Engineering, MERLN Institute for Technology-Inspired Regenerative Medicine, Maastricht University, Maastricht, Netherlands, [7]Research Laboratory, Nordland Hospital Bodø, Bodø, Norway, [8]Department of Immunology, Oslo University Hospital, and University of Oslo, Oslo, Norway, [9]Center of Molecular Inflammation Research, Norwegian University of Science and Technology, Trondheim, Norway, [10]Department of Integrated Oncology, Center for Integrated Oncology, University Hospital Bonn of the Rheinische Friedrich-Wilhelms-University, Bonn, Germany, [11]Institute of Molecular Medicine and Experimental Immunology, University Hospital Bonn of the Rheinische Friedrich-Wilhelms-University, Bonn, Germany, [12]Department of General and Visceral Surgery, German Armed Forces Hospital, Hamburg, Germany

Background: Despite major advances in medicine, blood-borne biomarkers are urgently needed to support decision-making, including polytrauma. Here, we assessed serum-derived extracellular vesicles (EVs) as potential markers of decision-making in polytrauma.

Objective: Our Liquid Biopsy in Organ Damage (LiBOD) study aimed to differentiate polytrauma with organ injury from polytrauma without organ injury. We analysed of blood-borne small EVs at the individual level using a combination of immunocapture and high-resolution imaging.

Methods: To this end, we isolated, purified, and characterized small EVs according to the latest Minimal Information for Studies of Extracellular Vesicles (MISEV) guidelines from human blood collected within 24 h post-trauma and validated our results using a porcine polytrauma model.

Results: We found that small EVs derived from monocytes $CD14^+$ and $CD14^+CD61^+$ were significantly elevated in polytrauma with organ damage. To be precise, our findings revealed that $CD9^+CD14^+$ and $CD14^+CD61^+$ small EVs exhibited superior performance compared to $CD9^+CD61^+$ small EVs in accurately indicating polytrauma with organ damage, reaching a sensitivity and

a specificity of 0.81% and 0.97%, respectively. The results in humans were confirmed in an independent porcine model of polytrauma.

Conclusion: These findings suggest that these specific types of small EVs may serve as valuable, non-invasive, and objective biomarkers for assessing and monitoring the severity of polytrauma and associated organ damage.

KEYWORDS

monocytes, trauma, extracellular vesicles, exosomes, liquid biopsy, biomarker, triage

Background

Blood-borne biomarkers are the simplest and most non-invasive source of biomarkers for all types of diseases, including severe COVID-19 and cancer (1, 2). In the last decade, many exciting biomarkers have been explored, discovered, or validated for clinical use as detectable biomarkers in blood. Among these biomarkers, such as circulating cell-free DNA (ccfDNA), circular RNAs (circRNAs), circulating tumour cells (CTCs), and soluble proteins, extracellular vesicles (EVs) have recently received the most attention (2–5). EVs are vesicles that are naturally released from cells. They consist of a lipid bilayer, lack a functional nucleus, and cannot proliferate. In addition, EVs are classified according to their biogenesis and cellular origin (6, 7). The "Minimal Information for Studies of Extracellular Vesicles 2018" (MISEV2018) includes caveats and protocols and defines small EVs as fractions that may consist of EVs derived from late endosomes (8). EVs are released under steady-state conditions and secreted by activated and apoptotic cells (9).

EVs have been shown to be beneficial for cancer screening in pancreatic carcinoma (10), biliary carcinomas in the gallbladder and cholangiocarcinoma (11), other cancer entities such as hepatocellular carcinoma (12), brain tumours (13), and other non-malignant diseases (14). However, the EV methodology is not limited to cancer screening, and few research groups have explored the potential of EVs in polytrauma and trauma care (15, 16), leading to the conclusion that small EVs might also be beneficial. Recently, it was reported that small EVs may be attributed to a higher mortality rate in polytrauma with haemorrhagic shock (17) and altered platelet levels (18).

Polytrauma remains one of the leading causes of death worldwide and the leading cause of disability in patients younger than 35 years (19). However, classifying potentially severely injured patients in prehospital care and objectively classifying and quantifying the complexity and quality of trauma remain problematic Algorithmic and objective data-based strategies are needed when decisions must be made when medical resources are scarce, not only in triage situations (20, 21). Only limited information about visible and recognizable damage can be obtained during the initial assessment of patients at the scene, in the emergency department, or during transport until maximum care is provided. Novel blood-borne assessment methods based on liquid biopsy could be supportive and objectively provide the required information.

The aim of our Liquid Biopsy in Organ Damage (LiBOD) study was to investigate whether small EVs are altered in polytrauma, including internal organ injury, such as rupture of parenchymal organs, in humans and a porcine polytrauma model. The physiological response to trauma is a complex process, as outlined by Lord et al., who summarized the inflammatory cascades triggered by trauma (22). Following traumatic injury, there is an increase in the frequency of the classic inflammatory monocyte subset in humans, characterized as $CD14^{+}CD16^{-}$, post-injury (23). We employed the ExoView® Reader R100 to immobilize small EVs and distinguish between different subpopulations of monocytes and platelets, including megakaryocytes, aiming to assess their clinical performance in both human polytrauma (injury severity score (ISS) ≥ 15) and porcine polytrauma models. Our findings revealed that $CD9^{+}CD14^{+}$ small EVs derived from monocytes exhibited superior performance compared to $CD9^{+}CD61^{+}$ small EVs in accurately indicating polytrauma with organ damage.

Methods

Ethics: human specimens

This study was developed as a non-interventional and retrospective study according to the Clinical Trials Directive (EU) 2001/20/EC and Clinical Trials Regulation (EU) NO 536/2014. The Ethics Committee of the responsible State Chambers of Medicine in Rhineland-Palatinate, Germany (ANr.: 2020-15050) approved the human study part. Informed consent was obtained from all the patients or their legal representatives. The presented data are part of a study that has been registered on the International Clinical Trials Registry Platform through the German Registry for Clinical Trials (DRKS 00026025; https://drks.de/search/en/trial/DRKS00026025).

Human study cohort

Polytrauma patients were included if they had injury severity scores (ISS) ≥ 15 and i) penetrating injuries to the torso-cervical

region, ii) fell from a height of more than 1.5 m, iii) had a traffic accident with frontal impact or intrusion of more than 50–75 cm or change in speed of delta > 30 km/h, and iv) had a two-wheeler collision, such as in a motorcycle, bicycle, e-bike, or e-scooter. Typically, polytrauma patients were excluded when i) there were any doubts about the patient's ability to provide consent or their legal representatives had signs of dementia, ii) patients were younger than 18 years, or iii) they were pregnant. The general characteristics of the patients are summarized in Supplementary Table 1 and Figure 1. Additionally, blood parameters such as erythrocyte, thrombocyte, and leucocyte levels, in addition to medications and drugs given after admission, are summarized in Supplementary Figure 1. Inclusion and exclusion criteria were set according to the Level 3 guidelines on the treatment of patients with severe or multiple injuries (Association of the Scientific Medical Societies, AWMF Register-Nr. 012/019 - Polytrauma Guideline Update Group).

Human cell lines

For details, please see Supplement Material and Methods.

Differentiation and stimulation of THP-1 monocyte cells *in vitro*

Please see Supplement Material and Methods.

Cell surface staining for flow cytometric analysis of THP-1 human cell lines

Please see Supplement Material and Methods.

Isolation and purification of THP-1-derived small EVs by size exclusion chromatography and ultrafiltration from cell culture supernatant

Please see Supplement Material and Methods.

Isolation of THP-1-derived large EVs by centrifugation from cell culture supernatant

Please see Supplement Material and Methods.

Isolation of serum from human blood

Please see Supplement Material and Methods.

Isolation of small EVs from human serum

Human serum (1 mL) was centrifuged at 10,000 × *g* for 10 min to remove lipemia and most of the large EVs. EV-containing supernatant was filled up to 2 mL with filtered phosphate-buffered saline (PBS) (pH 7.4, 0.22 µm). Diluted and precleared serum (2 mL) was loaded onto a qEV2/70 size exclusion chromatography (SEC) column, and a buffer flow volume of 14.1 mL was discarded, after which five fractions (2 mL each) were collected. These five fractions (each 2 mL) were pooled together and concentrated to 1 mL of the large EV-depleted small EV fraction with a 3-kDa molecular weight cut-off (MWCO) filter for the ExoView® Reader-based study.

Isolation and purification of small EVs from pig plasma

Porcine plasma (1 mL) was centrifuged at 2,500 × *g* for 15 min at room temperature (RT). The supernatant was filled to 2 mL with filtered PBS (pH 7.4, 0.22 µm). Diluted and precleared porcine plasma (2 mL) was loaded onto a qEV2/70 SEC column. A buffer flow volume of 14.1 mL was discarded, and five fractions (2 mL each) were collected. These five fractions were pooled and concentrated to 1 mL using a 3-kDa MWCO filter for the ExoView® Reader-based study.

Transmission electron microscopy of EVs

Please see Supplement Material and Methods.

Protein isolation and quantification from small EVs

Please see Supplement Material and Methods.

Western blotting analysis

Please see Supplement Material and Methods.

Nanoparticle tracking analysis of small EVs

Please see Supplement Material and Methods.

Small EV quantification

Isolated and purified human and porcine small EV samples were characterized by a single-particle interferometric reflectance imaging sensor (SP-IRIS) using the ExoView® R100 Reader

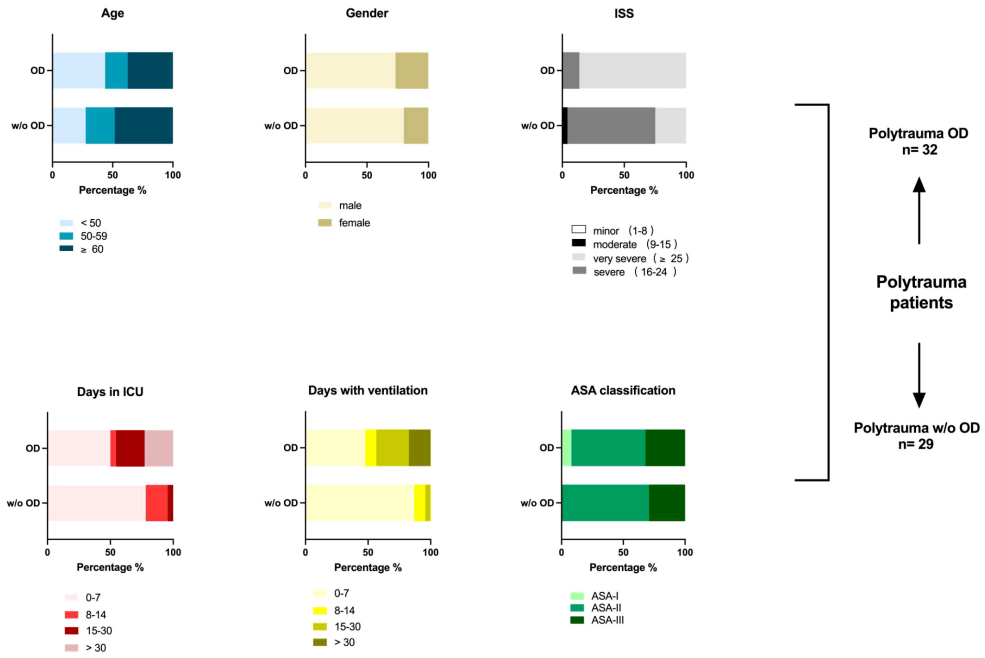

FIGURE 1
Demographics of polytrauma (ISS ≥ 15) patients. Overview of patient's parameters post-trauma, including ISS score, days in ICU, days with invasive ventilation, and ASA classification (if available), in addition to age and gender distribution. A total of 61 polytrauma patients with internal organ damage (polytrauma OD, n = 32) and polytrauma patients without internal organ damage (polytrauma w/o OD, n = 29) were included in this human study in agreement with the given regulations of the responsible State Chambers of Medicine in Rhineland-Palatinate, Germany (ANr.: 2020-15050). Polytrauma OD includes subgroups such as lacerated parenchymal internal organs such as the liver and spleen, kidney rupture, severe lung contusion, vascular dissection of the aorta, and amputation. Amputation was added to the internal organ damage group due to its severity and strain on the amputee regarding blood loss and pathogen infiltration. For further details, see Supplementary Table 1. ISS, injury severity score; ICU, intensive care unit; ASA, American Society of Anesthesiologists.

(Unchained Labs, Boston, MA, USA; previously NanoView® Biosciences, Boston, MA, USA). According to the ExoView® kit assay protocol (v380.6, revised August 2021), the human ExoView® Tetraspanin Chip (Unchained Labs, Boston, MA, USA; previously NanoView® Biosciences, Boston, MA, USA, Product No.: EV-TETRA-C) was pre-scanned to detect debris before loading the samples. The human ExoView® Tetraspanin Chips were precoated with anti-CD81, anti-CD63, and anti-CD9 EV capture antibodies and MIgG capture controls to ensure optimal performance.

Small EV samples were diluted in 1 × incubation solution I and immobilized on a human ExoView® Tetraspanin Chip overnight (18 h) at RT. After incubation, the human ExoView® Tetraspanin Chips were washed three times in 1 × solution A, followed by incubation with anti-human tetraspanin antibodies such as anti-CD9, anti-CD63, and anti-CD81 (Supplementary Table 4) for 1 h. The ExoView® Tetraspanin Chips were then washed in 1 × solution B, dried, and imaged using ExoView® R100. The acquired data were analysed using ExoView Analyzer (Version 3.1.4) (24).

For quantification of porcine-derived small EVs, antibody-uncoated ExoFlex® chips were coated with commercially available anti-pig CD9 antibody (Supplementary Table 4) according to the manufacturer's recommendations. Briefly, CD9 monoclonal antibody (MA1-80307, Invitrogen, Thermo Fisher, Waltham, MA, USA) was conjugated with linker 1 and incubated on ExoFlex® chips. ExoFlex® chips with immobilized $CD9^+$ small EVs were incubated with anti-pig CD14 fluorescein isothiocyanate (FITC) (MA5-28286, Invitrogen) for 1 h, washed in solution B, dried, and imaged using ExoView® R100. The acquired data were analysed using the ExoView Analyzer.

Fluorescent cut-offs were set relative to the MIgG control: anti-human CD14 APC in the CF647 channel, 450; anti-human CD61 PE in the CF555 channel, 300; and anti-pig CD14 FITC in the CF488 channel, 450. All the anti-human and anti-porcine antibodies used are summarized in Supplementary Table 4.

Ethics: porcine study

This study was approved by the responsible State Agency for Nature, Environment, and Consumer Protection of North Rhine-Westphalia (Landesamt für Natur, Umwelt und Verbraucherschutz Nordrhein-Westfalen AZ: 81-02.04.2020. A215). Furthermore, a porcine study was designed considering the German legislation governing animal studies, which followed the Principles of Laboratory Animal Care (25). Additionally, all porcine experiments of this study adhered to the ARRIVE Guidelines for reporting animal research (26).

Animals: porcine study

The porcine model was previously established by the Department of Orthopedics, Trauma, and Reconstructive Surgery

at the University Hospital RWTH Aachen and has been published elsewhere (27–29). The results of this study were part of a larger study design that included an additional group [for additional subgroup information, see Lupu et al. (29)]. In total, 22 male pigs [German Landrace (*Sus scrofa*)] weighing 35 ± 5 kg were used for multiple trauma induction experiments. All pigs underwent an initial clinical examination, were acclimated to a new environment for 7 days prior to operation/trauma induction, and were housed in ventilated rooms with food and water *ad libitum*.

Multiple trauma model: porcine study

a) Instrumentation and anaesthesia

Please see Supplement Material and Methods.

b) Trauma and haemorrhage

Please see Supplement Material and Methods.

c) Group allocation

Please see Supplement Material and Methods.

Plasma isolation from full-blood porcine study

Please see Supplement Material and Methods.

Statistical analysis

All data are presented as medians with a 95% confidence interval (CI). A one-way ANOVA was used to analyse differences among the three experimental groups, followed by a *post-hoc* test. Fisher's least significant difference (LSD) test was applied for multiple comparisons of subgroups when one-way ANOVA was positive, and Bartlett's test for equal variance was successful. The differences between two independent experimental subsets were determined using a two-tailed, unpaired t-test. The area under the receiver operating characteristic curve (AUROC), sensitivity, specificity, and associated cut-off values were calculated. Pearson's correlation coefficient was calculated to measure the linear correlations between the two sets of data. Statistical results were considered significant if the *p*-value was <0.05. The experimental strength was calculated *post-hoc*.

Fluorescence-activated cell sorting (FACS) data were analysed using FlowJo 10 for MAC OSX (Tree Star Inc., Ashland, OR, USA). ExoView data were processed using the ExoView® Analyzer (Version 3.1.4, Unchained Labs). Statistical analysis was performed using GraphPad Prism 9 (GraphPad Software Inc., La Jolla, USA) and the G*Power program (version 3.1.9.2, Düsseldorf, Germany). Figures were created using GraphPad Prism version 9. Some figures were done with the help of BioRender.com.

Results

Antibody validation on cultured THP-1 cells for EV detection

First, we confirmed that non-stimulated THP-1 cells lacked CD14 expression (Figure 2A) (30). Stimulation with phorbol 12-myristate 13-acetate (PMA) or PMA/lipopolysaccharide (LPS) is required to markedly increase CD14 expression. For CD61 and $CD14^+CD61^+$ cells, a similar upregulation was achieved with PMA/LPS. Therefore, THP-1 cells are suitable for the evaluation of anti-CD14 and anti-CD61 antibody testing of THP-1-derived EVs *in vitro*.

THP-1 cell culture-derived small EVs and their tetraspanin expression

Per the ExoView® Tetraspanin Chip, 8.5×10^{11} EVs derived from THP-1 cells after SEC and ultrafiltration (UF) purification were used. The EV yield and purity were evaluated *via* nanoparticle tracking analysis (NTA) measurements, allowing us to load the ExoView® Tetraspanin Chips with the same small EV numbers. Small EVs were captured/immobilized on the chip using CD9, CD63, and CD81. Immobilized small EVs were distributed among CD63, CD81, and CD9 capture antibodies and designated as isotype control MIgG. The whole small EV isolation and analysis procedure including THP-1 cultering is graphically summarised in Figure 2B.

The amount of immobilized small EVs captured by the ExoView® Tetraspanin Chip was set to 100%, and the distribution of small EVs was calculated among designated capture antibody spots: anti-CD63 24,9%, CD81 13%, and CD9 62% (Figure 2C). The captured small EVs were stained for CD14 and CD61. Accordingly, a relatively low number of $CD9^+CD14^+$ small EVs was observed compared with $CD63^+CD14^+$ and $CD81^+CD14^+$ EVs. In the case of CD61, $CD9^+CD61^+$ small EVs were predominant over $CD63^+CD61^+$ and CD81$CD61^+$ small EVs. The associated representative spot pictures can be found in supplementary (Supplementary Figure 2). Importantly, these data unequivocally demonstrated that our chosen antibodies, anti-CD14, and anti-CD61, were able to detect CD14 and CD61 surface antigens located on small EVs derived from human monocytes/macrophages. Figure 2D depicts the median EV diameters as captured by the CD9/CD63/CD81 probes on the ExoView® Tetraspanin Chip.

We used Western blotting to characterize isolated small EVs based on their protein content, in particular, plasma membrane-associated tetraspanin CD63, secreted calreticulin, cytosolic protein TSG101, and housekeeping protein β-actin as a loading control (see Supplementary Figure 3). In addition to negative calreticulin, CD63, and TSG101 were positive in our isolated small EVs. β-Actin served as a loading control. The preparation of large EVs was run as a control, which led to no detectable signals for TSG101 and calreticulin. CD63 is faint in large EVs and typically enriched in small EVs.

10.3389/fimmu.2023.1279496

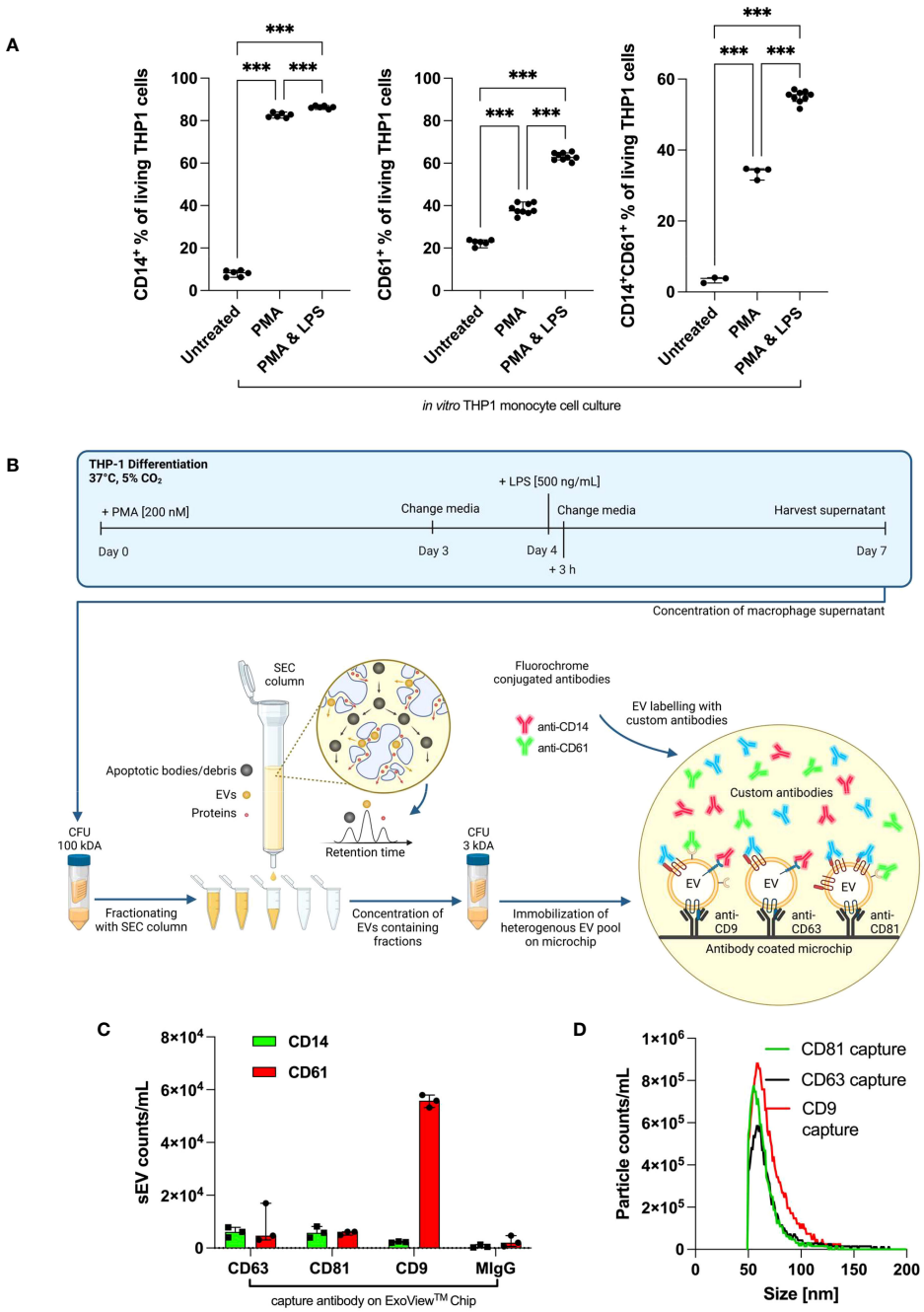

FIGURE 2
Antibody validation on cultured THP-1 cells and THP1-derived small EVs. **(A)** *In vitro*, human THP-1 monocyte cells were treated with PMA alone or PMA/LPS (each n ≥ 3). Values are given as mean with SEM. Column statistical analysis performed by one-way ANOVA test including Fisher's LSD *post-hoc* test for multiple comparisons (*$p < 0.05$; **$p < 0.01$; ***$p < 0.001$; $CD14^+$: F = 9325, df = 2, $CD61^+$: F = 754.7, df = 2; $CD14^+CD61^+$: F = 1337, df = 2). **(B)** Overview of small EV generation, SEC isolation, and the use of the ExoView® Tetraspanin kit. Typically, THP-1 was stimulated with 200 nM of PMA and 500 ng/mL of LPS to complete a cell type-specific phenotypical changing cycle within 1 week. **(C)** EV counts as immobilized by CD9, CD63, and CD81 capture antibodies and subsequently stained with anti-CD14 and anti-CD61 on the ExoView® Tetraspanin microchip. **(D)** EV size distributions for particles as immobilized by CD9, CD63, and CD81 capture antibodies on the ExoView® Tetraspanin microchip. CFU, centrifugal filter unit; EVs, extracellular vesicles; PMA, phorbol 12-myristate 13-acetate; LPS, lipopolysaccharide; LSD, least significant difference; SEC, size exclusion chromatography.

Human serum-derived small EVs are predominantly CD63- and CD9-positive

Figure 3A depicts our standard operating procedure (SOP) for the isolation of small EVs, starting with 1 mL of human serum. Isolated human serum-derived small EVs were characterized by the ExoView® Tetraspanin Chip using anti-CD9, anti-CD63, and anti-CD81 as custom antibodies for exact quantification of small EV subpopulations ($CD9^+$, $CD63^+$, and $CD81^+$ small EVs). The immobilized small EVs were mostly CD9 and CD63 positive, and

10.3389/fimmu.2023.1279496

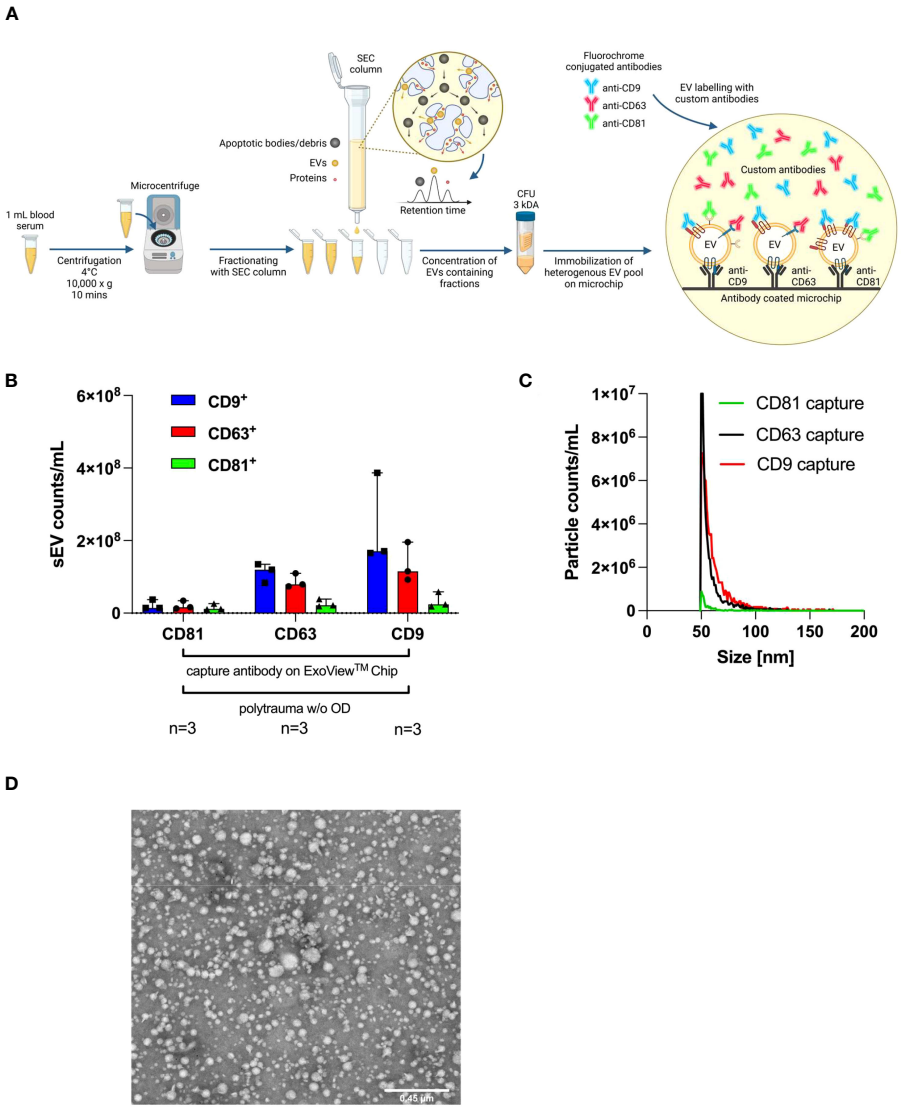

FIGURE 3
Characterisation of small EVs isolated from polytrauma patients' serum samples by surface antigens, size, and TEM. ExoView® Reader 100 is capable of determining the diameter of individual captured small EVs binding to a precoated ExoView® Tetraspanin Chip with anti-CD9, anti-CD63, and anti-CD81 on designated capture spots by manufacture. **(A)** Workflow SOP for isolation from 1 mL of human serum collected from polytrauma patients (ISS ≥ 15), including isolation *via* SEC and UF and a final interferometric detection system with the ExoView® Reader 100-based methodology. Manufacturer-supplied antibodies, anti-CD9 (CF488A), anti-CD63 (CF647), and anti-CD81 (CF555) were used for the detection of indicated tetraspanins on captured small EVs. **(B)** Tetraspanin distribution on $CD9^+$, $CD63^+$, or $CD81^+$ captured small EVs on the ExoView® Tetraspanin Chip (n= 3). The graph depicts the median with a 95% confidence interval (CI). **(C)** Sizes of EVs as immobilized with $CD9^+$, $CD63^+$, or $CD81^+$ on ExoView® Tetraspanin Microchips. **(D)** Representative transmission electron microscopy (TEM) picture of SEC-isolated small EVs demonstrating small EV sizes ranging from 50 nm to 200 nm. CFU, centrifugal filter unit; EVs, extracellular vesicles; SOP, standard operating procedure; ISS, injury severity score; SEC, size exclusion chromatography; UF, ultrafiltration.

a small population was CD81 positive (Figure 3B). ExoView® SP-IRIS measurements demonstrated that the size of each captured small EV ranged from 50 nm to 70 nm in diameter (Figure 3C). Accordingly, transmission electron microscopy (TEM; Figure 3D) was used to detect EVs within a size range measured on the chip. Isolated small EVs showed typical morphology and size for EVs, as previously published (24).

EV subpopulations show unique distribution in polytrauma patients

Anti-CD9, anti-CD63, and anti-CD81 precoated ExoView® Tetraspanin Chips allow quantification of the individual numbers of the three small EV subpopulations as defined by CD9/CD63/CD81 (31). Among all investigated small EV subpopulations and our

additional antibodies targeting CD14 and CD61, the following subpopulations could be distinguished: $CD9^+CD14^+$ small EVs, $CD9^+CD61^+$ small EVs, and double-positive $CD9^+CD14^+CD61^+$ small EVs. All three types of small EV subpopulations exhibited a higher median count [$CD9^+CD14^+$ small EVs (Figure 4A), $CD9^+CD61^+$ small EVs (Figure 4B), and double-positive $CD9^+CD14^+CD61^+$ small EVs (Figure 4C)] and were capable of distinguishing patients with polytrauma organ damage (OD) from patients without polytrauma (polytrauma without OD). Representative ExoView® Tetraspanin capture spots are depicted in Supplementary Figure 4. Accordingly, $CD9^+CD14^+$ small EVs in polytrauma OD (median, 5.372×10^5/mL serum) were significantly increased by 11.2-fold ($p < 0.001$) compared to those in polytrauma without OD (median, 48.0×10^4/mL serum) with a calculated cut-off of 3.6×10^5/mL serum. The associated clinical performance was as follows: AUROC = 0.9461, sensitivity = 81.25%, and specificity = 96.55% (Figure 4A). $CD9^+CD61^+$ small EVs (median, 1.747375×10^8/mL serum, Figure 4B) and $CD9^+CD61^+CD14^+$ small EVs (median, 1.1525×10^5/mL serum, Figure 4C) were 2.6-fold ($p < 0.001$) and 2.9-fold ($p < 0.001$) elevated compared to polytrauma without OD, respectively (polytrauma w/o OD: $CD9^+CD61^+$ small EVs = 6.74935×10^7/mL serum and $CD9^+CD14^+CD61^+$ small EVs = 4.0×10^4/mL serum). Associated cut-offs were set for $CD9^+CD61^+$ small EVs at 1.05860505×10^8/mL serum with an AUROC of 0.8599, sensitivity of 78.13%, and specificity of 86.21%; for $CD9^+CD14^+CD61^+$ small EVs, the cut-off was 8.7×10^4/mL serum, AUROC of 0.8699, sensitivity of 86.36%, and specificity of 86.21%. All data for the individual small EV populations and subpopulations are summarized in Supplementary Table 5.

The composition of small EV subpopulations follows the 7-day recovery period for polytrauma patients

Here, we randomly selected 14 polytrauma OD patients based on serum sample availability to be assessed on day 7 post-trauma. Overall, we observed that the median number of $CD9^+CD14^+$ small EVs dropped sharply on day 7 from a median of 9.4925×10^5/mL serum (day 1) to a median of 1.3005×10^5/mL serum ($p = 0.0002$) (Figure 5A). A similar decrease was observed from 24 h post-trauma to day 7 post-trauma for $CD9^+CD61^+$ small EVs from a median of 2.0203725×10^8/mL serum to a median of 7.985925×10^7/mL serum $CD9^+CD61^+$ small EVs ($p = 0.0004$) (Figure 5C).

Next, we studied whether the measured small EV subpopulations in polytrauma patients would correlate with ISS. Indeed, median $CD9^+CD14^+$ small EVs (Figure 5B) and $CD9^+CD61^+$ small EVs (Figure 5D) values isolated from serum taken within 24 h post-trauma significantly correlated with ISS (both $p < 0.001$) with r_{sp} values of 0.46 and 0.52 (n = 56), respectively.

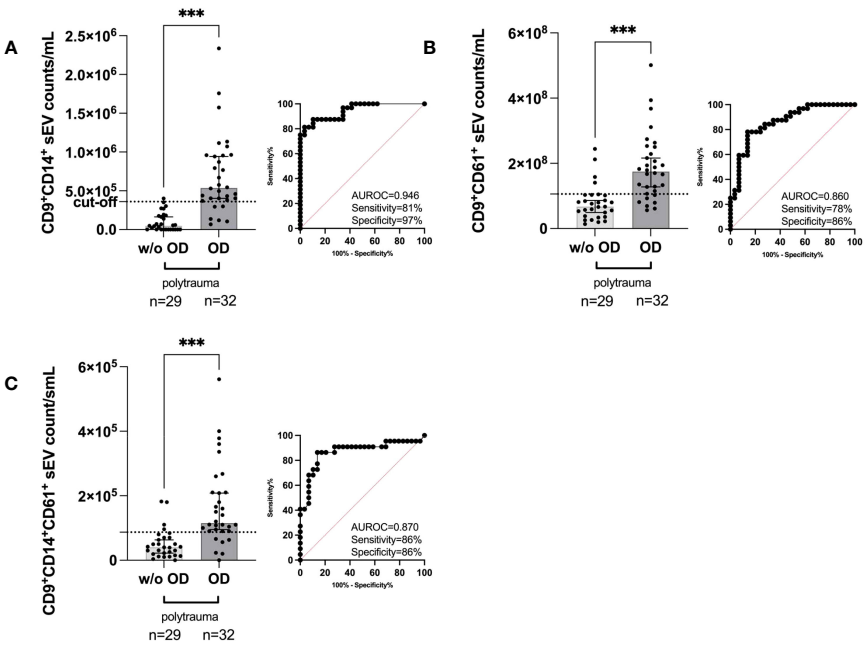

FIGURE 4
Quantification of the indicated human serum-derived small EV subpopulation as defined by the small EV marker CD9 plus custom anti-CD14 and anti-CD61 on ExoView® Tetraspanin Chips. **(A)** $CD9^+CD14^+$ small EV counts in polytrauma (ISS ≥ 15, within 24 h post-trauma) with internal organ damage (polytrauma OD) *vs.* polytrauma without internal organ damage (polytrauma w/o OD). **(B)** $CD9^+CD61^+$ small EV counts in small EVs in polytrauma OD *vs.* polytrauma w/o OD. **(C)** $CD9^+CD14^+CD61^+$ small EV counts in small EVs in polytrauma OD *vs.* polytrauma w/o OD. Statistical significance was assessed by a two-tailed, unpaired t-test (*$p < 0.05$; **$p < 0.01$; ***$p < 0.001$; **(A)** t = 6.248, df = 59; **(B)** t = 5.100, df = 59; **(C)** t = 4.679, df = 59). All these scatter dot plots show lines at the median with a 95% CI. *Post-hoc* calculated power (1 – β err prob) is 1.0. Including corresponding AUROC, sensitivity, specificity, and cut-off values. CFU, centrifugal filter unit; EV, extracellular vesicle; ISS, injury severity score; AUROC, area under the receiver operating characteristic curve.

Of note, the focus on different qualities and severity of trauma in our study raises the question of whether the presence of small EV subpopulations could predict disease outcomes. This could be measured as the duration of invasive ventilation and an intensive care unit (ICU) stay. Supplementary Figures 5A, B depict Spearman's correlations of median $CD9^+CD14^+$ small EVs and median $CD9^+CD61^+$ small EVs as determined 24 h post-trauma with days of invasive ventilation. Median $CD9^+CD14^+$ small EVs correlated significantly with the duration of invasive ventilation (p = 0.003), whereas median $CD9^+CD14^+$ small EVs did not (p = 0.12). However, the r_{sp} values were below 0.5, 0.42 (Supplementary Figure 5A), and 0.23 (Supplementary Figure 5B). Therefore, they were not useful in the clinical setting and were neglected. Another critical patient parameter was the duration of ICU stay. Here, Spearman's r_{sp} values were lower than 0.5: for $CD9^+CD14^+$ small EVs, r_{sp} = 0.47 (p <0.001, Supplementary Figure 5C), and for $CD9^+CD61^+$ small EVs, r_{sp} = 0.32 (p = 0.03, Supplementary Figure 5D).

Alteration in small EV subpopulations distinguishes injured animals in a porcine model of polytrauma

To evaluate whether the porcine polytrauma model would follow small EV distributions as in humans and serve for further evaluation of our study, we investigated 14 pigs before and after surgical induction of polytrauma, as depicted in Figure 6A and described in the Methods section in greater detail. Porcine ethylenediaminetetraacetic acid (EDTA) plasma was utilized as a small EV source before ExoFlex® chip incubation (Figure 6A). Briefly, 16 experimental pigs were traumatized, eight pigs were stabilized with external fixation (Exfix), and eight pigs were stabilized with non-reaming intramedullary nailing (IMN). An additional eight experimental pigs underwent a control-sham operation. Owing to the restricted availability of ExoFlex® chips and anti-porcine antibodies, 14 porcine samples were randomly measured (Figure 6B). Interestingly, an increase in $CD9^+CD14^+$

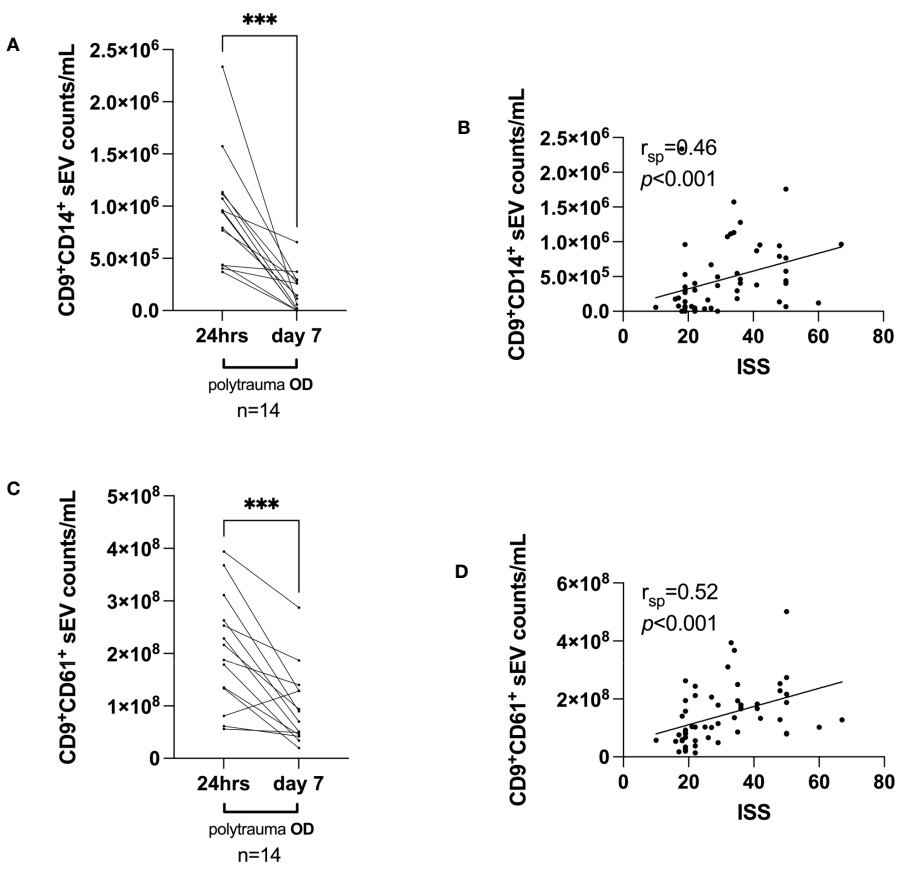

FIGURE 5
Small EV release on the investigated time axis (day 7 post-trauma) and correlations with ISS, days of invasive ventilation, and duration of ICU. **(A)** Median $CD9^+CD14^+$ small EV values and **(C)** median $CD9^+CD61^+$ small EV values within 24 h post-trauma *vs.* day 7 post-trauma in polytrauma OD patients, selected based on the availability of serum samples at day 7. Statistical significance was assessed by a two-tailed, unpaired t-test (*p < 0.05; **p < 0.01; ***p < 0.001; **(A)** t = 5.063, df = 13; **(C)** t = 4.783, df = 13). *Post-hoc* calculated power (1 – β err prob) is 1.0. **(B, D)** Spearman's correlation (r_{sp}) analyses for median $CD9^+CD14^+$ small EVs and $CD9^+CD61^+$ small EV values and associated ISS value (n = 56) as assessed 24 h post-trauma. p and r_{sp} values as indicated. EV, extracellular vesicle; ISS, injury severity score; ICU, intensive care unit.

10.3389/fimmu.2023.1279496

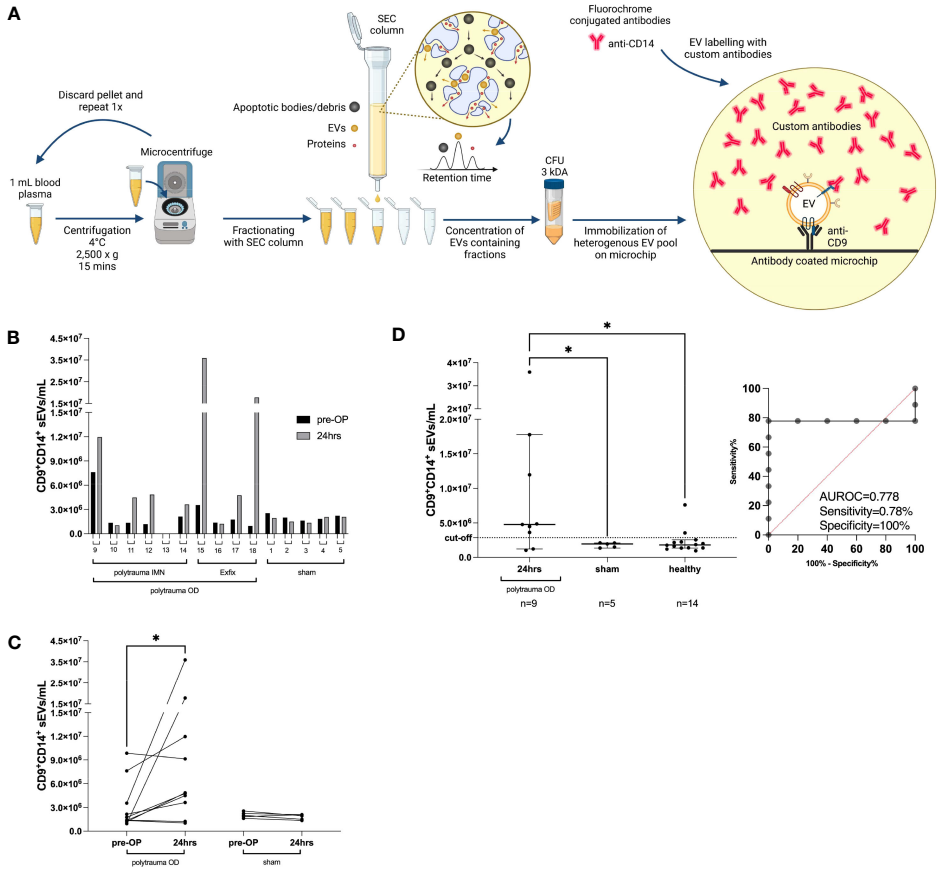

FIGURE 6
Porcine polytrauma model and $CD9^+CD14^+$ small EV performance before and after polytrauma induction. **(A)** Porcine plasma requires platelet removal by two 2,500 × *g* centrifugations prior to SEC-based EV purification, followed by UF of the first five fractions by 3-kDa MWCO centrifugation filters. The ExoFlex® chip was coated with anti-porcine CD9 for the capture of $CD9^+$ EVs. **(B)** Overview of individual $CD9^+CD14^+$ small EV values before and after trauma (24 h) induction for each pig, including the pig's experimental number. Pigs are divided into three groups: polytrauma OD with external fixation (Exfix, n = 4), eight pigs with non-reaming intramedullary nailing (IMN), and the sham group (n = 5). **(C)** Overview of intragroup changes before (healthy) and after trauma induction (24 h) in the polytrauma OD and sham groups. **(D)** Median values of $CD9^+CD14^+$ EVs post-trauma in the polytrauma OD pigs compared to sham at 24 h and healthy pigs (defined as all pigs prior to polytrauma induction, baseline values; statistics assessed as follows: **(D)** one-way ANOVA including Fisher's LSD *post-hoc* test for multiple comparisons, F = 3.959, df = 2; **(C)** two-tailed, unpaired t-test (*$p < 0.05$; **$p < 0.01$; ***$p < 0.001$; t = 1.928, df = 9). Note: CFU, centrifugal filter unit; EV, extracellular vesicle; SEC, size exclusion chromatography; UF, ultrafiltration; MWCO, molecular weight cut-off; OD, organ damage; LSD, least significant difference.

small EVs of 1.6-fold to 18.6-fold was detectable in seven out of nine polytrauma OD pigs compared to the median $CD9^+CD14^+$ small EV values prior to *vs.* post-polytrauma OD (Figure 6C). Small $CD9^+CD14^+$ EVs in the sham group remained stable at low levels.

The overall count of $CD9^+CD14^+$ small EVs in pigs with polytrauma OD was elevated compared to the sham-operated group (polytrauma OD 24 h: median = 4.762353×10^6/mL plasma $CD9^+CD14^+$ small EVs, n = 9, $p = 0.04$; sham group 24 h: median = 1.945706×10^6/mL plasma $CD9^+CD14^+$ small EVs, n = 5, $p = 0.04$) and compared to the healthy group (blood taken prior to operation: median = 1.799789×10^6/mL plasma $CD9^+CD14^+$ small EVs, n = 14) (Figure 6D). One-way ANOVA with Fisher's LSD test *post-hoc* test indicated a significant difference ($p < 0.01$) between the polytrauma OD (24 h) and sham groups (24 h) but no significance was found between the sham group (24 h) and healthy pigs prior to operation (Figure 6D). The calculated cut-off for $CD9^+CD14^+$ small EVs was 2.856334×10^6/mL plasma, associated with an AUROC of 0.7778, a sensitivity of 78%, and a specificity of 100% (Figure 6D). The associated representative spot pictures are shown in Supplementary Figure 5.

Discussion

The aim of our LiBOD pilot study was to investigate whether circulating blood-derived small EVs allow objective differentiation between polytrauma patients with and without internal organ damage. To this end, in our retrospective LiBOD pilot study, we offered insights into an objective assessment of polytrauma quality using a liquid biopsy and subsequent quantification of the indicated small EV subpopulations such as $CD9^+CD14^+$, $CD9^+CD61^+$ small EVs, and $CD9^+CD14^+CD61^+$. These results could be crucial in practice to capture the quality of polytrauma, for example, when triage is required while medical resources, especially human resources such as paramedics, are scarce or insufficient (20, 21).

In addition, overtriage and undertriage could be reduced or prevented. Overtriage may lead to a misperception of urgency and unnecessary consumption of scarce resources (32). Conversely, undertriage may lead to higher patient mortality but is more likely to result in inadequate medical care (33).

The ExoView® Tetraspanin Chips that were used are capable of detecting and quantifying various subpopulations of small EVs derived from monocytes and platelets, including megakaryocytes. The specific antigen combinations used to define these subpopulations are as follows: for monocyte-derived subpopulations, $CD9^+CD14^+$, $CD63^+CD14^+$, $CD81^+CD14^+$, $CD9^+CD14^+CD61^+$, $CD63^+CD14^+CD61^+$, and $CD81^+CD14^+CD61^+$; for platelet-, monocyte-, and megakaryocyte-derived small EVs, $CD9^+CD61^+$, $CD63^+CD61^+$, and $CD81^+CD61^+$. It is important to note that small EVs lacking expression of the three major tetraspanins, CD9, CD63, and CD81, were not immobilized on the ExoView® Tetraspanin Chips (31). Therefore, the method we chose is similar to that of studies using anti-CD9, anti-CD63, and anti-CD81 beads to detect EV subpopulations (34). The advantage of the current measurement technique is its ability to stain the captured EVs on the chip simultaneously distinguish between subpopulations and determine their individual sizes. Thus, this technique allows single-EV resolution for these parameters.

Our analysis of the small EV subpopulations revealed that the $CD9^+CD14^+$ subpopulation of small EVs derived from monocytes appeared to be superior overall in accurately indicating polytrauma with organ damage, delivering sensitivity and specificity of 81% and 97%, respectively (Figure 4A), associated with an AUROC of >0.90 (Figure 4A and Supplementary Table 5). These values are more than acceptable in triage conditions and allow for prospective assessment of internal organ damage in blunt trauma in the absence of open wounds, which would clearly indicate internal organ injury. A typical scenario for undertriage can be fatal if internal injuries are not detected in a timely manner or at the first symptoms of unconsciousness due to internal bleeding/haemorrhagic shock (35).

Going in line with our monocyte small EV data, we detected significantly increased levels of $CD9^+CD61^+$ small EVs in the sera of patients with polytrauma OD (Figures 4B, C). These small EVs likely originated in part from subsets of monocytes and most likely from platelets and their precursors as megakaryocytes. Platelet activation is an early event in injury, and platelets release EVs (16, 36). However, CD61 alone does not pinpoint platelets as the source of $CD9^+CD61^+$ small EVs, which were inferior compared to monocyte-derived small EVs (Supplementary Table 5). Thus, $CD9^+CD61^+$ small EVs could likely be released by a novel subset of monocytes, as recently suggested by Hamers A.A.J. et al. based on their high-dimensional mass cytometric analyses of three human $CD16^+$ non-classical monocyte subsets and four $CD14^+$ classical monocyte subsets (37). The classical subset 1 appeared to have high CD61 and CD9 expression (37), making them also potential EV donors for $CD9^+CD14^+CD61^+$ small EVs (Figure 4C).

We observed a marked and significant decrease in small $CD9^+CD14^+$ and $CD9^+CD61^+$ EVs 7 days post-trauma compared with 24-h values in patients who did not develop any post-trauma complications such as systemic inflammatory response syndrome (SIRS), acute respiratory distress syndrome (ARDS), or sepsis (38). Other studies have reported that $CD14^+$ small EVs are elevated in ARDS (39). This rapid decrease contrasts with reports in which an increase in $CD45^+$ large EVs was measured over time up to day 28 (40). This discrepancy could easily be explained by the fact that the authors measured $CD45^+$ large EVs (40), $CD14^+$ is only a small part of the $CD45^+$ compartment, and large EVs might have different pharmacokinetic behaviours than small EVs *in vivo*. As described by Yáñez-Mó et al., the clearance time of EVs in circulation may depend on their steady-state level and the balance between the generation and clearance of each EV population (41, 42).

Next, we investigated whether correlations could be calculated between the measured small EV populations and the ISS. Our data showed that $CD9^+CD14^+$ small EVs and $CD9^+CD61^+$ small EVs were significantly correlated with ISS [Spearman's r_{sp} = 0.46 (Figure 5B) and r_{sp} = 0.52 (Figure 5D)]. However, several variables need to be considered: ISS assessment is highly subjective and prone to observer error (43). In their study, the authors observed a probability of only 28% that the assessments of 16 trauma patients by 15 trauma and injury experts were consistent and a probability of 51% for assigning individual cases to the same severity group (43). This limits the validity of our correlations between ISS and reported subpopulations of small EVs. For large EVs, a correlation between ISS and $CD61^+$ large EVs in trauma was reported, with an r_{sp} value of 0.635 (n = 22) (15). We calculated a ranked correlation for $CD9^+CD61^+$ small EVs with an r_{sp} value of 0.52 (Figure 5D), showing a similar trend.

As our LiBOD pilot study included only 61 severely injured patients (ISS ≥ 15), we chose a polytrauma animal model for independent validation. Here, we took advantage of an already established porcine trauma model (28, 29, 44) in which pigs received blunt chest trauma, bilateral femur fractures, and standardized liver laceration combined with pressure-controlled haemorrhagic shock (35 ± 5 mmHg) for 90 min, mimicking typical polytrauma (ISS ≥ 15) with internal organ damage (polytrauma OD). Our porcine polytrauma study data mirrored our human patient data, and $CD9^+CD14^+$ small EVs successfully separated injured animals from sham-operated animals and samples collected before trauma (Figure 6D). While we were able to successfully replicate our findings from the human study using a porcine trauma model, it is important to note that we intentionally chose porcine plasma as the source of small EVs instead of serum. The binding of small EVs to the thrombus when using serum as an EV source remains speculative and presents a potential systematic flaw in human samples. To mitigate any potential bias or artefacts associated with serum as an EV source, we opted to utilize plasma as the small EV source in our porcine model, thereby ensuring more reliable and accurate results.

Moreover, by using the porcine polytrauma model to validate our findings, we were able to confirm that the medication and drugs administered to human polytrauma patients, such as fibrinogen and tranexamic acid (among others, which can be found in Supplementary Figure 1), did not have a relevant impact on the release of EVs. We conducted Spearman's correlation analysis to examine the potential relationship between the administered drugs and the release of EVs, as well as their influence on specific subpopulations of small EVs, including $CD9^+CD14^+$. The results of this analysis are summarized in Supplementary Table 6.

Conclusion

Our LiBOD pilot study has to be evaluated in a larger cohort size with an increased diversity of traumas, including brain trauma, likely associated with undertriage (45). Desired sampling would be at the scene of the accident to best determine the trauma level as early as possible or during transport to a trauma centre providing an appropriate level of trauma care. Such early decision-making based on LiBOD could potentially not only avoid undertriage but also reduce cost per patient in cases of overtriage (32). Overall, a small EV assessment as part of LiBOD has the potential to assist subjective triage with an objected value to prevent undertriage and overtriage and to assist in providing the best and fastest medical care for trauma patients.

Data availability statement

The raw data supporting the conclusions of this article will be made available by the authors, without undue reservation.

Ethics statement

The studies involving humans were approved by the State Chambers of Medicine in Rhineland-Palatinate, Germany (ANr.:2020-15050). The studies were conducted in accordance with local legislation and institutional requirements. The participants provided their written informed consent to participate in this study. The animal study was approved by the State Agency for Nature, Environment, and Consumer Protection of North Rhine-Westphalia (Landesamt für Natur, Umwelt und Verbraucherschutz Nordrhein-Westfalen AZ:81-02.04.2020. A215).

Author contributions

BW: Formal analysis, Investigation, Validation, Writing – original draft, Data curation. AW: Data curation, Investigation, Project administration, Resources, Writing – review & editing. JG: Data curation, Methodology, Project administration, Resources, Writing – original draft, Writing – review & editing. RJSS: Formal analysis, Methodology, Visualization, Writing – original draft, Writing – review & editing. CK: Investigation, Visualization, Writing – review & editing. TT: Investigation, Resources, Writing – original draft, Writing – review & editing. QZ: Investigation, Methodology, Resources, Writing – review & editing. ÜM: Investigation, Methodology, Resources, Writing – review & editing.. KH: Investigation, Methodology, Resources, Writing – review & editing. LL: Methodology, Resources, Writing – review & editing. MH-L: Investigation, Methodology, Resources, Writing – review & editing. MG: Investigation, Methodology, Resources, Writing – review & editing. TM: Investigation, Methodology, Resources, Writing – original draft, Writing – review & editing. SS: Data curation, Investigation, Methodology, Resources, Writing – original draft, Writing – review & editing. RS: Funding acquisition, Investigation, Methodology, Resources, Writing – original draft, Writing – review & editing. CS: Resources, Writing – review & editing. IS-W: Resources, Writing – review & editing. BG: Methodology, Resources, Validation, Writing – original draft, Writing – review & editing. FH: Investigation, Methodology, Resources, Writing – review & editing. VL-K: Conceptualization, Funding acquisition, Investigation, Methodology, Project administration, Resources, Supervision, Validation, Writing – original draft, Writing – review & editing. AGW: Conceptualization, Data curation, Funding acquisition, Investigation, Project administration, Resources, Supervision, Writing – original draft, Writing – review & editing. MTK: Conceptualization, Formal analysis, Funding acquisition, Investigation, Methodology, Project administration, Resources, Supervision, Validation, Visualization, Writing – original draft, Writing – review & editing.

Funding

The author(s) declare that financial support was received for the research, authorship, and/or publication of this article. Studies were supported by the German Armed Forces (Bundeswehr, project number 31K1-S-10 2023) to AW, SS, RS, AGW, and MTK and the Deutsche Forschungsgemeinschaft (DFG, German Research Foundation) to MTK (DFG project number 410853455). VL-K is funded by the Deutsche Forschungsgemeinschaft (DFG, German Research Foundation) under Germany's Excellence Strategy (EXC 2151 – 390873048) and DFG Project numbers 411345524 and 432325352.

Conflict of interest

The authors declare that the research was conducted in the absence of any commercial or financial relationships that could be construed as a potential conflict of interest.

The author(s) declared that they were an editorial board member of Frontiers at the time of submission. This had no impact on the peer review process or the final decision.

Publisher's note

Supplementary material

The Supplementary Material for this article can be found online at: https://www.frontiersin.org/articles/10.3389/fimmu.2023.1279496/full#supplementary-material

References

1. Girard TJ, Antunes L, Zhang N, Amrute JM, Subramanian R, Eldem I, et al. Peripheral blood mononuclear cell tissue factor (F3 gene) transcript levels and circulating extracellular vesicles are elevated in severe coronavirus 2019 (COVID-19) disease.*J Thromb Haemost* (2023) 21(3):629–38. doi: 10.1016/j.jtha.2022.11.033

2. Slomka A, Wang B, Mocan T, Horhat A, Willms AG, Schmidt-Wolf IGH, et al. Extracellular Vesicles and Circulating Tumour Cells - complementary liquid biopsies or standalone concepts? *Theranostics* (2022) 12(13):5836–55. doi: 10.7150/thno.73400

3. Ignatiadis MA-O, Sledge GA-O, Jeffrey SA-O. Liquid biopsy enters the clinic - implementation issues and future challenges. *Nat Rev Clin Oncol* (2021) 18(5):297–312. doi: 10.1038/s41571-020-00457-x

4. Kristensen LA-O, Jakobsen T, Hager H, Kjems J. The emerging roles of circRNAs in cancer and oncology. *Nat Rev Clin Oncol* (2022) 19(3):188–206. doi: 10.1038/s41571-021-00585-y

5. Spitzberg JA-O, Ferguson S, Yang KA-OX, Peterson HA-O, Carlson JA-O, Weissleder RA-O. Multiplexed analysis of EV reveals specific biomarker composition with diagnostic impact. *Nat Commun* (2023) 14(1):1239. doi: 10.1038/s41467-023-36932-z

6. Stein JM, Luzio JP. Ectocytosis caused by sublytic autologous complement attack on human neutrophils. The sorting of endogenous plasma-membrane proteins and lipids into shed vesicles. *Biochem J* (1991) 274(Pt 2):381–6. doi: 10.1042/bj2740381

7. Cocucci E, Meldolesi J. Ectosomes and exosomes: shedding the confusion between extracellular vesicles. *Trends Cell Biol* (2015) 25(6):364–72. doi: 10.1016/j.tcb.2015.01.004

8. Thery C, Witwer KW, Aikawa E, Alcaraz MJ, Anderson JD, Andriantsitohaina R, et al. Minimal information for studies of extracellular vesicles 2018 (MISEV2018): a position statement of the International Society for Extracellular Vesicles and update of the MISEV2014 guidelines. *J Extracell Vesicles* (2018) 7(1):1535750. doi: 10.1080/20013078.2018.1535750

9. Kornek M, Popov Y, Libermann TA, Afdhal NH, Schuppan D. Human T cell microparticles circulate in blood of hepatitis patients and induce fibrolytic activation of hepatic stellate cells. *Hepatology* (2011) 53(1):230–42. doi: 10.1002/hep.23999

10. Melo SA, Luecke LB, Kahlert C, Fernandez AF, Gammon ST, Kaye J, et al. Glypican-1 identifies cancer exosomes and detects early pancreatic cancer. *Nature* (2015) 523(7559):177–82. doi: 10.1038/nature14581

11. Urban SK, Sanger H, Krawczyk M, Julich-Haertel H, Willms A, Ligocka J, et al. Synergistic effects of extracellular vesicle phenotyping and AFP in hepatobiliary cancer differentiation. *Liver Int* (2020) 40(12):3103–16. doi: 10.1111/liv.14585

12. Julich-Haertel H, Urban SK, Krawczyk M, Willms A, Jankowski K, Patkowski W, et al. Cancer-associated circulating large extracellular vesicles in cholangiocarcinoma and hepatocellular carcinoma. *J Hepatol* (2017) 67(2):282–92. doi: 10.1016/j.jhep.2017.02.024

13. Lane R, Simon TA-O, Vintu M, Solkin B, Koch B, Stewart NA-O, et al. Cell-derived extracellular vesicles can be used as a biomarker reservoir for glioblastoma tumor subtyping. *Commun Biol* (2019) 2:315. doi: 10.1038/s42003-019-0560-x

14. Kornek M, Lynch M, Mehta SH, Lai M, Exley M, Afdhal NH. Circulating microparticles as disease-specific biomarkers of severity of inflammation in patients with hepatitis C or nonalcoholic steatohepatitis. *GASTROENTEROLOGY* (2012) 143:448–58. doi: 10.1053/j.gastro.2012.04.031

15. Frohlich M, Schafer N, Caspers M, Bohm JK, Sturmer EK, Bouillon B, et al. Temporal phenotyping of circulating microparticles after trauma: a prospective cohort study. *Scand J Trauma Resusc Emerg Med* (2018) 26(1):33. doi: 10.1186/s13049-018-0499-9

16. Dyer MR, Alexander W, Hassoune A, Chen Q, Brzoska T, Alvikas J, et al. Platelet-derived extracellular vesicles released after trauma promote hemostasis and contribute to DVT in mice. *J Thromb Haemost* (2019) 17(10):1733–45. doi: 10.1111/jth.14563

17. Weber B, Sturm R, Henrich D, Marzi I, Leppik L. CD44+ and CD31+ extracellular vesicles (EVs) are significantly reduced in polytraumatized patients with hemorrhagic shock - evaluation of their diagnostic and prognostic potential. *Front Immunol* (2023) 14:1196241. doi: 10.3389/fimmu.2023.1196241

18. Weber B, Henrich D, Schindler CR, Marzi I, Leppik L. Release of exosomes in polytraumatized patients: The injury pattern is reflected by the surface epitopes. *Front Immunol* (2023) 14:1107150. doi: 10.3389/fimmu.2023.1107150

19. Alberdi F, Garcia I, Atutxa L, Zabarte M. Trauma, Neurointensive Care Work Group of the S. Epidemiology of severe trauma. *Med Intensiva* (2014) 38(9):580–8. doi: 10.1016/j.medin.2014.06.012

20. Harris GH, Cobb JP, Evans L. Crisis triage in the era of COVID-19: old tools, new approaches, and unanswered questions. *Crit Care Med* (2023) 51(1):148–50. doi: 10.1097/CCM.0000000000005723

21. Brizio A, Faure V, Baudino F, Wilmet A, Gonzalez JP. Hospital-based autonomous pre-clinical screening of COVID-19: An emergency triage using a vital signs recording system, Paris-Ile de France region. *Health Serv Manage Res* (2023) 36(4):291–2. doi: 10.1177/09514848221100746

22. Lord JM, Midwinter MJ, Chen YF, Belli A, Brohi K, Kovacs EJ, et al. The systemic immune response to trauma: an overview of pathophysiology and treatment. *Lancet* (2014) 384(9952):1455–65. doi: 10.1016/S0140-6736(14)60687-5

23. Janicova A, Becker N, Xu B, Simic M, Noack L, Wagner N, et al. Severe traumatic injury induces phenotypic and functional changes of neutrophils and monocytes. *J Clin Med* (2021) 10(18):4139. doi: 10.3390/jcm10184139

24. Breitwieser K, Koch LF, Tertel T, Proestler E, Burgers LD, Lipps C, et al. Detailed characterization of small extracellular vesicles from different cell types based on tetraspanin composition by exoView R100 platform. *Int J Mol Sci* (2022) 23(15):8544. doi: 10.3390/ijms23158544

25. Garber JC, Barbee RW, Bielitzki JT, Clayton LA, Donovan JC, Kohn DF, et al. *Guide for the Care and Use of Laboratory Animals. 8th ed*. Washington, DC: National Academies Press (2011). doi: 10.17226/12910

26. Kilkenny C, Browne WJ, Cuthill IC, Emerson M, Altman DG. Improving bioscience research reporting: the ARRIVE guidelines for reporting animal research. *Vet Clin Pathol* (2010) 41(1):27–41. doi: 10.1111/j.1939-165X.2012.00418.x

27. Horst K, Greven J, Luken H, Zhi Q, Pfeifer R, Simon TP, et al. Trauma severity and its impact on local inflammation in extremity injury-insights from a combined trauma model in pigs. *Front Immunol* (2019) 10:3028. doi: 10.3389/fimmu.2019.03028

28. Horst K, Simon TP, Pfeifer R, Teuben M, Almahmoud K, Zhi Q, et al. Characterization of blunt chest trauma in a long-term porcine model of severe multiple trauma. *Sci Rep* (2016) 6:39659. doi: 10.1038/srep39659

29. Lupu L, Horst K, Greven J, Mert U, Ludviksen JAK, Pettersen K, et al. Simultaneous C5 and CD14 inhibition limits inflammation and organ dysfunction in pig polytrauma. *Front Immunol* (2022) 13:952267. doi: 10.3389/fimmu.2022.952267

30. Bosshart H, Heinzelmann M. THP-1 cells as a model for human monocytes. *Ann Transl Med* (2016) 4(21):438. doi: 10.21037/atm.2016.08.53

31. Kalluri R, LeBleu VS. The biology, function, and biomedical applications of exosomes. *Science* (2020) 367(6478):eaau6977. doi: 10.1126/science.aau6977

32. Newgard CD, Staudenmayer K, Hsia RY, Mann NC, Bulger EM, Holmes JF, et al. The cost of overtriage: more than one-third of low-risk injured patients were taken to major trauma centers. *Health Aff (Millwood)* (2013) 32(9):1591–9. doi: 10.1377/hlthaff.2012.1142

33. Haas B, Gomez D, Zagorski B, Stukel TA, Rubenfeld GD, Nathens AB. Survival of the fittest: the hidden cost of undertriage of major trauma. *J Am Coll Surg* (2010) 211(6):804–11. doi: 10.1016/j.jamcollsurg.2010.08.014

34. Karimi N, Dalirfardouei R, Dias T, Lotvall J, Lasser C. Tetraspanins distinguish separate extracellular vesicle subpopulations in human serum and plasma - Contributions of platelet extracellular vesicles in plasma samples. *J Extracell Vesicles* (2022) 11(5):e12213. doi: 10.1002/jev2.12213

35. Nakahara S, Matsuoka T, Ueno M, Mizushima Y, Ichikawa M, Yokota J, et al. Predictive factors for undertriage among severe blunt trauma patients: what enables them to slip through an established trauma triage protocol? *J Trauma* (2010) 68(5):1044–51. doi: 10.1097/ta.0b013e3181aca144

36. Lopez E, Srivastava AK, Burchfield J, Wang YW, Cardenas JC, Togarrati PP, et al. Platelet-derived- extracellular vesicles promote hemostasis and prevent the development of hemorrhagic shock. *Sci Rep* (2019) 9(1):17676. doi: 10.1038/s41598-019-53724-y

37. Hamers AAJ, Dinh HQ, Thomas GD, Marcovecchio P, Blatchley A, Nakao CS, et al. Human monocyte heterogeneity as revealed by high-dimensional mass cytometry. *Arterioscler Thromb Vasc Biol* (2019) 39(1):25–36. doi: 10.1161/ATVBAHA.118.311022

38. Schroeder JE, Weiss YG, Mosheiff R. The current state in the evaluation and treatment of ARdS and SIRS. *Injury* (2009) 40(Suppl 4):S82–9. doi: 10.1016/j.injury.2009.10.041

39. Mahida RA-O, Price J, Lugg ST, Li H, Parekh D, Scott A, et al. CD14-positive extracellular vesicles in bronchoalveolar lavage fluid as a new biomarker of acute respiratory distress syndrome. *Am J Physiol Lung Cell Mol Physiol* (2022) 322(4):L617–24. doi: 10.1152/ajplung.00052.2022

40. Kuravi SJ, Yates CM, Foster M, Harrison P, Hazeldine J, Hampson P, et al. Changes in the pattern of plasma extracellular vesicles after severe trauma. *PloS One* (2017) 12(8):e0183640. doi: 10.1371/journal.pone.0183640

41. Yanez-Mo M, Siljander PR, Andreu Z, Zavec AB, Borras FE, Buzas EI, et al. Biological properties of extracellular vesicles and their physiological functions. *J Extracell Vesicles* (2015) 4:27066. doi: 10.3402/jev.v4.27066

42. Ayers L, Nieuwland R, Kohler M, Kraenkel N, Ferry B, Leeson P. Dynamic microvesicle release and clearance within the cardiovascular system: triggers and mechanisms. *Clin Sci (Lond)* (2015) 129(11):915–31. doi: 10.1042/CS20140623

43. Zoltie N, de Dombal FT. The hit and miss of ISS and TRISS. *Yorkshire Trauma Audit Group BMJ* (1993) 307(6909):906–9. doi: 10.1136/bmj.307.6909.906

44. Horst K, Eschbach D, Pfeifer R, Hubenthal S, Sassen M, Steinfeldt T, et al. Local inflammation in fracture hematoma: results from a combined trauma model in pigs. *Mediators Inflammation* (2015) 2015:126060. doi: 10.1155/2015/126060

45. Schellenberg M, Benjamin E, Bardes JM, Inaba K, Demetriades D. Undertriaged trauma patients: Who are we missing? *J Trauma Acute Care Surg* (2019) 87(4):865–9. doi: 10.1097/TA.0000000000002393

frontiers | Frontiers in Immunology

TYPE Original Research
PUBLISHED 12 December 2023
DOI 10.3389/fimmu.2023.1281674

OPEN ACCESS

EDITED BY
Sanjeev Choudhary,
Sam Houston State University,
United States

REVIEWED BY
Lynn Xiaoling Qiang,
Northwell Health, United States
Susana Fernandes,
Universidade de Lisboa, Portugal

*CORRESPONDENCE
Borna Relja
info@bornarelja.com

RECEIVED 22 August 2023
ACCEPTED 23 November 2023
PUBLISHED 12 December 2023

CITATION
Fachet M, Mushunuri RV, Bergmann CB, Marzi I, Hoeschen C and Relja B (2023) Utilizing predictive machine-learning modelling unveils feature-based risk assessment system for hyperinflammatory patterns and infectious outcomes in polytrauma. *Front. Immunol.* 14:1281674. doi: 10.3389/fimmu.2023.1281674

Utilizing predictive machine-learning modelling unveils feature-based risk assessment system for hyperinflammatory patterns and infectious outcomes in polytrauma

Melanie Fachet[1], Raghava Vinaykanth Mushunuri[1], Christian B. Bergmann[2], Ingo Marzi[3], Christoph Hoeschen[1] and Borna Relja[2,3]*

[1]Institute for Medical Technology, Medical Systems Technology, Faculty of Electrical Engineering and Information Technology, Otto von Guericke University Magdeburg, Magdeburg, Germany, [2]Translational and Experimental Trauma Research, Department of Trauma, Hand, Plastic and Reconstructive Surgery, Ulm University Medical Center, University Ulm, Ulm, Germany, [3]Department of Trauma, Hand and Reconstructive Surgery, Medical Faculty, Goethe University Frankfurt, Frankfurt, Germany

Purpose: Earlier research has identified several potentially predictive features including biomarkers associated with trauma, which can be used to assess the risk for harmful outcomes of polytraumatized patients. These features encompass various aspects such as the nature and severity of the injury, accompanying health conditions, immune and inflammatory markers, and blood parameters linked to organ functioning, however their applicability is limited. Numerous indicators relevant to the patients` outcome are routinely gathered in the intensive care unit (ICU) and recorded in electronic medical records, rendering them suitable predictors for risk assessment of polytraumatized patients.

Methods: 317 polytraumatized patients were included, and the influence of 29 clinical and biological features on the complication patterns for systemic inflammatory response syndrome (SIRS), pneumonia and sepsis were analyzed with a machine learning workflow including clustering, classification and explainability using SHapley Additive exPlanations (SHAP) values. The predictive ability of the analyzed features within three days after admission to the hospital were compared based on patient-specific outcomes using receiver-operating characteristics.

Results: A correlation and clustering analysis revealed that distinct patterns of injury and biomarker patterns were observed for the major complication classes. A k-means clustering suggested four different clusters based on the major complications SIRS, pneumonia and sepsis as well as a patient subgroup that developed no complications. For classification of the outcome groups with no complications, pneumonia and sepsis based on boosting ensemble classification, 90% were correctly classified as low-risk group (no complications). For the high-

risk groups associated with development of pneumonia and sepsis, 80% of the patients were correctly identified. The explainability analysis with SHAP values identified the top-ranking features that had the largest impact on the development of adverse outcome patterns. For both investigated risk scenarios (infectious complications and long ICU stay) the most important features are SOFA score, Glasgow Coma Scale, lactate, GGT and hemoglobin blood concentration.

Conclusion: The machine learning-based identification of prognostic feature patterns in patients with traumatic injuries may improve tailoring personalized treatment modalities to mitigate the adverse outcomes in high-risk patient clusters.

KEYWORDS

risk assessment, clinical decision making, classification, explainability, SHAP values, blood, biomarker

1 Introduction

Severe trauma stands as a noteworthy global public health challenge, constituting nearly 8% of all deaths and resulting in over 4.4 million deaths worldwide annually (1). The World Health Organization highlights road traffic accidents, suicides and homicides as primary contributors to injury and violence-related deaths (1). Advances in prehospital transport and resuscitation strategies have significantly influenced the patterns of traumatic deaths over recent decades (2). Trauma-related fatalities display a bimodal distribution, with a majority occurring in the initial days following the injury, often due to severe head injury or uncontrollable bleeding. Survivors of the initial traumatic event frequently confront a critical illness characterized by prolonged stays in intensive care units (ICU) or hospitals (length of stays, LOS), along with an elevated risk of inflammatory complications (3, 4).

In the realm of post-injury scenarios, the pivotal determinant of outcomes lies in the concurrent immuno-inflammatory response (5, 6). When this response is appropriately controlled in terms of both intensity and duration, it plays a crucial role in restoring the host homeostasis. Conversely, an irregular response is associated with the onset of multiple organ dysfunction syndrome (MODS), culminating in prolonged critical illness and a sustained elevated susceptibility to complications and mortality even post-discharge (7). Experiencing multiple traumas triggers substantial blood loss and the accumulation of necrotic or devitalized tissue within an ischemic-hypoxic environment devoid of oxygen and nutrients, both of which contribute to coagulatory and inflammatory alterations. The inflammatory response following polytrauma plays a pivotal role in the body`s molecular defense mechanisms. The initial phase of inflammation after polytrauma involves two coordinated processes: the systemic inflammatory response syndrome (SIRS) representing a pro-inflammatory reaction, and the compensatory anti-inflammatory response syndrome constituting an anti-inflammatory reaction (8). SIRS manifests through changes in heart rate, respiratory rate, temperature regulation, and activation of immune cells. In the typical course of the inflammatory response following trauma, a delicate equilibrium is maintained between the pro- and anti-inflammatory reactions, ensuring biological homeostasis and fostering controlled regeneration processes that support a normal recovery without significant complications. However, an exaggerated inflammatory response following trauma has the potential to simultaneously activate both innate pro- and anti-inflammatory mediators while suppressing adaptive immunity, that can lead to the early onset of multiple organ dysfunction syndrome (MODS) (9). Furthermore, an extended and dysregulated immune-inflammatory state is linked to delayed recovery and complications, particularly the emergence of late-stage MODS. The intricate interplay of these factors can result in severe SIRS, acute respiratory distress syndrome, sepsis, acute kidney injury, and ultimately MODS. Various influencing factors include the type of injured tissue, post-injury surgical management, age, sex, genetics, and critically, underlying comorbidities and physical conditions, encompassing both exogenous and endogenous factors (7, 10). Accurately identifying the risks faced by patients in ICUs after

Abbreviations: AIS, Abbreviated injury scale; AP, Alkaline phosphatase; APACHE, Acute physiology and chronic health evaluation; AUC, Area under the curve; CRP, C-reactive protein; D, d, Day, days; dl, Deciliter; ED, Emergency department; f, Female; g, Gram; GCS, Glasgow coma scale; GGT, Gamma glutamyl transpeptidase; GLDH, Glutamate dehydrogenase; GOT, Glutamic oxaloacetic transaminase; GPT, Glutamic pyruvic transaminase; Hb, Hemoglobin; Ht, Hematocrit; ICU, Intensive care unit; IL, Interleukin; INR, International normalized ratio; ISS, Injury severity score; K, Potassium; l, Liter; LOS, Length of stay; m, Male; mg, Milligram; ml, Milliliter; mmol, Millimoles; MODS, Multiple organ dysfunction syndrome; MV, Mechanical ventilation; n, Sample size; Na, Sodium; nl, Nanoliter; pg, Picogram; PT, Prothrombin time; PTT, Partial thromboplastin time; ROC, Receiver operating characteristics; SIRS, Systemic inflammatory response syndrome; SHAP, SHapley Additive exPlanations; SMOTE, Synthetic Minority Oversampling Technique; SOFA, Sequential organ failure assessment; U, Units; y, Years of age.

traumatic injuries is essential for tailoring existing treatment strategies and mitigating subsequent complications, particularly in high-risk patient sub-groups. Consequently, the identification of patients with a heightened risk of unfavorable outcomes can aid clinicians in ascertaining the optimal care setting and treatment modalities during trauma management (11).

Within clinical medicine, there is an increasing interest towards utilizing model predictions. Machine learning tools have been applied to predict outcomes such as acute kidney injury or sepsis and septic shock in hospitalized patients (12–16). Nevertheless, there exists a scarcity of studies exploring the use of distinct machine learning algorithms for predicting risks related to infectious complications and LOS in polytraumatized patients. To address this gap in knowledge, we conducted a cohort study to thoroughly assess the performance of various machine learning algorithms in identifying features including biomarkers for risk assessment and informing clinical decision-making. The aim of this study is to create a prognostic machine learning approach that combines data from electronic medical records, including patient demographics, injury patterns and severity, and laboratory data of polytraumatized patients. The methodology outlined in this study involves the sequential application of feature selection, correlation analyses, clustering, classification, and explainability techniques to anticipate adverse outcome patterns in a cohort of polytrauma patients. Serial blood measurements taken within the first three days of hospital admission, along with routinely recorded data from electronic medical records, were utilized. The risk classification model, employing an ensemble classification algorithm, demonstrated accurate predictions of the risk of infectious complications and prolonged stays in the ICU or hospital with high precision when tested on an independent patient dataset. Furthermore, critical clinical and inflammatory biomarkers for the early-stage prediction of risk patterns following hospitalization were identified.

2 Materials and methods

2.1 Data collection and sampling

A total of 317 polytraumatized patients were enrolled in the study at the emergency department (ED) of the University Hospital Frankfurt of the Goethe University from 2012 to 2016. The enrollment was done prospectively in accordance with the ethical committee approval and the Declaration of Helsinki as well as following the Strengthening the Reporting of Observational Studies in Epidemiology guidelines (17). All included patients provided the written informed consent forms themselves or informed consent was obtained from the nominated legally authorized representative consented on the behalf of participants as approved by the ethical committee (312/10). Part of the data that were obtained in the ED was published before (18). The study included polytraumatized patients with an injury severity score (ISS) of 16 or higher, aged 18 or above, who were admitted to the ICU and expected to survive beyond the initial 24 h post-injury. Certain exclusion criteria were applied, such as known pre-existing immunological disorders, immunosuppressive and anti-coagulant medication, burns, concomitant acute myocardial infarction, or thromboembolic events. All patients were treated in the ED according to the Advanced Trauma Life Support standards and the guidelines for polytrauma management (19).

Demographic and clinical data were collected from electronic medical records, including age, sex, ISS, abbreviated injury scale (AIS), length of stay (LOS) in the ICU and hospital LOS. Various severity scores were calculated daily during hospitalization, including the Glasgow Coma Scale (GCS), acute physiology and chronic health evaluation (APACHE) II and sequential organ failure assessment (SOFA) score.

Blood samples were collected daily on ten consecutive days post-injury from the patients in pre-chilled ethylenediaminetetraacetic acid tubes (BD vacutainer, Becton Dickinson Diagnostics, Aalst, Belgium) and kept on ice. Blood was centrifuged at 2000×g for 15 min at 4°C and the supernatant was stored at -80°C until IL-6 or IL-10 analyses according to the manufacturer`s instructions (IL-6 and IL-10 Elipair ELISA-Assay Diaclone, Hoelzel Diagnostica, Cologne, Germany). Blood was withdrawn daily as follows: the initial blood draw upon arrival in the ED; within 24h (D1), 48h (D2) and 72h (D3) of admission to the ED as a part of routine care. Data were obtained from ED to day ten post-injury. For the machine-learning approach described in Section 2.2, the mean of the results from D1-D3 were applied for analysis to predict the trauma associated outcome patterns at an early stage after admission to the ED. In some instances, it was not possible to obtain samples due to conflicts with clinical care or removal from the ICU.

2.1.1 Optimization of the study cohort

The polytrauma cohort study was designed to investigate complications such as SIRS, pneumonia, and sepsis in trauma patients. The prospectively collected data were based on previous theory on risk factors for polytrauma such as injury patterns, injury severity scores, blood markers for organ dysfunction as well as immune and inflammatory markers. For the proposed classification model, a subset of all collected data was selected as candidate predictor variables based on the consideration that data should be readily available and routinely collected also in the ICU. We considered 29 variables as candidate predictors and two variables (procalcitonin and antithrombin activity) were excluded due to missing values exceeding 70%.

2.1.2 Outcomes

The primary outcome of the predictive model was the classification of polytrauma patients into different complication patterns: no complications (n=194), SIRS (n=51), pneumonia (n=39) and sepsis (n=33). The criteria for diagnosing SIRS, pneumonia, and sepsis were based on established definitions and guidelines. Briefly, SIRS definition met the following criteria: heart rate >90 beats per minute; respiratory rate >20 breaths per minute or arterial carbon dioxide tension <32 mmHg; body temperature >38°C or <36°C; and white blood cell count >12.000 cells/mm^3 or <4.000 cells/mm^3, or with >10% immature (band) forms. SIRS was diagnosed when two or more of these criteria were fulfilled. The diagnose of pneumonia was defined by clinical, radiologic, and bacteriologic findings including new

pulmonary infiltrates on chest X-ray as well as one of the following criteria: positive blood culture, bronchial alveolar lavage, and/or sputum culture (20). Sepsis was assessed by applying the 2005 criteria outlined by the International Sepsis Forum diagnosing sepsis by fulfilling SIRS criteria and having a proven infection (21). Apart from the inflammatory complication patterns described above, we have defined a second outcome scenario associated with a long stay in the ICU or total-hospital stay. In order to identify and compare biomarker risk patterns corresponding to a long LOS in LCU or hospital, we have defined a threshold of ICU stay for >14 days and/or LOS for >30 days as a separate class for polytrauma patients at higher risk.

2.2 Model development

2.2.1 Feature extraction and correlation analysis

The feature extraction and correlation analysis were performed based on the Spearman's correlation coefficient with respect to their importance on the outcome class, and features with positive correlation and which has significant correlation with class labels were selected for the classification workflow described in Sec. 2.3.

2.2.2 Filtered *k*-means clustering

To identify distinct patient risk patterns, present in the first 3 days after injury, the patients outcome risk class for the 317 patients admitted to the ICU after trauma were subjected to filtered k-means clustering. The euclidian distance was used as a distance function with S=15 as seed number.

2.3 Classification

The classification was carried out using Python and pycharm. Missing data was imputed using k-nearest-neighbor imputation with the number of neighbors n=3. Hyperparameter of different classifiers (random forest, naive bayes and ensemble classifiers) were optimized to minimize the final prediction error.

2.3.1 Synthetic data creation

The original data set contained information on 317 patients, with 194 patients having no complications and 123 patients exhibiting hyperinflammatory or infectious complication patterns, such as SIRS (n=51), pneumonia (n=39) and sepsis (n=33). The class imbalance in the data set for the adverse outcomes (pneumonia and sepsis as infectious complications or risk for long ICU stay or long total hospitalization time) was addressed using Synthetic Minority Oversampling Technique (SMOTE), which generates synthetic training examples by linear interpolation for the minority class (22). These synthetic training examples are generated by randomly selecting one or more of the k-nearest neighbors for each example in the minority class. SMOTE technique is applied for oversampling in which each sampled instance of minority class is generated using 3 nearest neighbors. After the oversampling process, the data is reconstructed, and various classification techniques can be employed for the processed data.

2.3.2 Evaluation of model performance

The model performance evaluation was done by a k-fold cross validation ranging from 2-fold to 20-fold during the model development using a train-test split for the patient data. In this method, 20% of the patients were excluded while training the model and the excluded patients were then used to test the model. The model performance was assessed using area under the receiver operating characteristic (ROC) curve (AUC), F1 score and predication accuracy. The best performing model from the above criteria is then used to interpret the biomarker importance with exploitability methods.

2.3.3 Model interpretation using SHAP values

We have explained our models that are used for classification using SHAP (SHapley Additive exPlanations) values that offer a high level of interpretability for our proposed risk analysis model (23). The SHAP values for each patient feature explain the intensity and direction of impact on predicting the class labels (11). The SHAP tree explainer was used to explain the XGBoost prediction, which uses decision trees for classification, and to visualize the results in beeswarm plots.

2.4 Statistical analysis

Descriptive statistics and non-parametric tests were used to analyze the demographic, clinical, and inflammatory data using Origin (Version 2019b). Descriptive measures included mean, median, standard error of the mean, and interquartile range for continuous variables and percentages for categorical variables. Furthermore, non-parametric tests were used for testing whether group means, or medians are distributed the same across groups by ranking each attribute from our data set. The non-parametric Wilcoxon rank-sum test of the null hypothesis between two independent samples (patient subgroup showing no complications with patient subgroups showing complications) was tested in MATLAB using the function rank-sum. The extension of the Wilcoxon rank-sum test for more than two groups, the Kruskal-Wallis ANOVA test was conducted in Origin (Version 2019b). A significant Kruskal–Wallis test indicates that at least one sample stochastically dominates one other sample.

3 Results

3.1 Demographics and outcome-related features for risk assessment

The aim of this study was to utilize feature selection and correlation analysis to identify the most important features from clinical patients` data for polytrauma outcome classification. For optimization of our study cohort, patients discharged prior to day 10 from the ICU and 21 patients who died before discharge were excluded, which yielded a total of 317 patients used in the current study. We utilized feature extraction, clustering, and classification

to identify attributes correlating with complication patterns (SIRS, pneumonia, and sepsis) observed in the patient cohort (Figure 1). Demographic metrics, injury patterns and other outcome related characteristics for the 317 trauma patients for the analysis are shown in Table 1 and Supplementary Figures S1–S4.

Subsequently, the patient cohort (n=317) was divided into four sub-groups based on commonly occurring complications of trauma patients. Out of 317 patients, 16.1% developed SIRS, 12.3% had pneumonia and 10.5% were septic within 10 days after admission to the ED, whereas the majority of 61.2% patients showed none of the previously mentioned complications. The patient sub-group with sepsis had the longest hospital stay (Table 1). No statistically significant differences among the sub-groups in regard to age or sex were detected. The sub-group with sepsis had significantly higher ISS compared to the no complication and pneumonia sub-groups (Table 1).

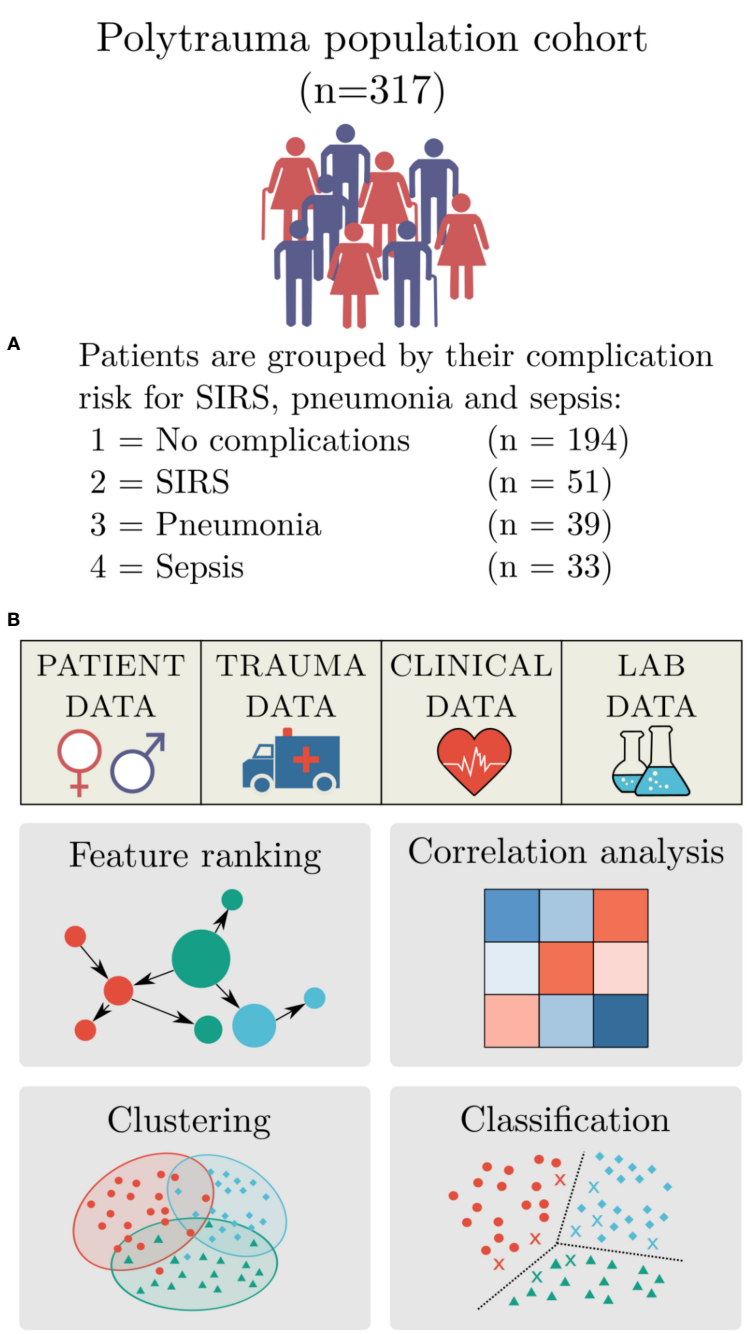

FIGURE 1
Study design. **(A)** Summary of the polytrauma patient cohort, including their outcome pattern: group 1 - no complications (n=194), group 2 – systemic inflammatory response syndrome (SIRS) (n=51), group 3 - pneumonia (n=39), and group 4 - sepsis (n=33). **(B)** Study design for machine-learning-based data analysis for risk assessment included: Identification of feature importance, correlation analysis, clustering and classification.

10.3389/fimmu.2023.1281674

TABLE 1 Overview of the polytrauma patient cohort and associated injury patterns.

	No complications (n=194)	SIRS (n=51)	Pneumonia (n=39)	Sepsis (n=33)	p < 0.05
Demographics					
Age (y)	45.9 ± 1.3	44.7 ± 2.4	53.5 ± 3.0	45.2 ± 3.2	n.s.
Sex (m/f)	149/45	43/8	33/6	24/9	n.s.
ISS	24.8 ± 0.7	27.6 ± 1.3	26.7 ± 1.7	32.7 ± 1.8	a, b
AIS					
Head	2.1 ± 0.1	2.3 ± 0.2	3.4 ± 0.3	1.7 ± 0.3	b, c, d,
Thorax	2.0 ± 1.1	2.3 ± 0.2	1.5 ± 0.3	2.7 ± 0.3	b
Abdomen	0.8 ± 0.1	0.5 ± 0.1	0.7 ± 0.2	1.0 ± 0.3	n.s.
Extremities	1.1 ± 0.1	1.4 ± 0.2	0.8 ± 0.2	1.8 ± 0.2	a, b
Cytokines					
IL-6 ED (pg/ml)	153.5 ± 21.4	180.6 ± 50.8	266.3 ± 78.3	343.5 ± 118.4	n.s.
IL-6 D1 (pg/ml)	189.8 ± 21.3	264.7 ± 69.8	269.3 ± 53.5	329.5 ± 83.8	n.s.
IL-6 D2 (pg/ml)	158.3 ± 34.8	112.0 ± 20.8	175.5 ± 47.4	304.3 ± 86.0	n.s.
IL-6 D3 (pg/ml)	69.7 ± 8.8	56.9 ± 8.3	105.0 ± 19.8	146.7 ± 32.0	a, c
IL-10 ED (pg/ml)	90.4 ± 12.6	108.2 ± 26.1	146.2 ± 38.6	138.2 ± 31.7	n.s.
IL-10 D1 (pg/ml)	15.6 ± 2.5	20.1 ± 5.1	34.8 ± 9.1	51.0 ± 15.1	a, c
IL-10 D2 (pg/ml)	10.0 ± 1.9	9.2 ± 3.0	7.0 ± 1.3	18.6 ± 8.5	n.s.
IL-10 D3 (pg/ml)	6.6 ± 1.8	10.7 ± 3.5	6.1 ± 1.2	33.4 ± 18.6	n.s.
Outcome					
SIRS ED (n, %)	7, 3.6	29, 56.9	10, 25.6	14, 42.4	d, e
SIRS D1 (n, %)	0, 0	20, 39.2	11, 28.2	15, 45.4	e
SIRS D2 (n, %)	0, 0	19, 37.3	7, 17.9	9, 27.3	d, e
SIRS D3 (n, %)	0, 0	17, 33.3	8, 20.5	15, 45.4	b, e
SIRS ED-D10 (n, %)	7, 3.6	51, 100	16, 41.0	33, 100	b, d, e
SIRS total (d)	0.1 ± 0.1	2.8 ± 0.3	2.0 ± 0.5	7.5 ± 1.0	b, d, e
MV (d)	2.9 ± 0.3	6.6 ± 0.6	7.7 ± 0.7	2.9 ± 4.0	e
ICU LOS (d)	6.6 ± 0.5	12.4 ± 1.3	12.6 ± 1.5	7.8 ± 0.7	e
Hospital LOS (d)	16.4 ± 0.8	25.5 ± 2.9	19.6 ± 1.9	36.6 ± 4.2	f, g
In-hospital mortality (n, %)	22, 11.3	4, 7.8	4, 10.3	1, 3.0	n.s.

D, day; d, days; ED, emergency department; f, female; ICU, intensive care unit; ISS, injury severity score; IL, interleukin; LOS, length of stay; y, years; m, male; ml, milliliter; MV, mechanical ventilation; n, sample size; n.s., not significant; pg, picogram; SIRS, systemic inflammatory response syndrome. Significant differences ($p < 0.05$) between the groups are indicated as follows: a: no complications vs. sepsis, b: pneumonia vs. sepsis, c: no complications vs. pneumonia, d: SIRS vs. pneumonia, e: no complications vs. all, f: no complications vs. SIRS, g: sepsis vs. all.

3.2 SIRS patients showed the weakest feature correlation among the investigated complications

The prospectively collected data was subjected to the non-parametric Wilcoxon rank-sum test for two independent samples (patient sub-group showing no complications with patient-subgroups showing complications) and the Kruskal-Wallis ANOVA test for multiple independent samples with a significance level of $p<0.05$. The results in Table 2 show that the least statistical significance is observed for the SIRS group with 8 out of 29 features that reject the null hypothesis, followed by the pneumonia group with 9 out of 29 features (Table 2). The highest degree of significance is observed for the septic group with 19 out of 29 attributes. The Glasgow Coma Scale based on motor responsiveness, verbal performance and eye opening to an appropriate stimulus was designed to assess the depth and duration coma and impaired consciousness after traumatic injuries is showing a high significance in all complication sub-groups compared to the reference

10.3389/fimmu.2023.1281674

TABLE 2 Kruskal-Wallis ANOVA test and Wilcoxon rank sum test for discrimination between patient sub-groups with no complications with patient sub-groups having systemic inflammatory response syndrome (SIRS), pneumonia or sepsis for a significance level of $p < 0.05$.

Attribute	Kruskal-Wallis ANOVA	Wilcoxon rank sum test		
		SIRS	Pneumonia	Sepsis
ISS	70.26	0.017	0.435	$2.05 \cdot 10^{-5}$
AIS Head	7.16	0.837	$2.99 \cdot 10^{-4}$	0.220
AIS Thorax	3.47	0.214	0.141	0.025
AIS Abdomen	5.53	0.478	0.720	0.560
AIS Extremities	3.66	0.148	0.207	0.002
GCS	32.87	$4.71 \cdot 10^{-4}$	$1.54 \cdot 10^{-4}$	$1.81 \cdot 10^{-4}$
APACHE II score	19.60	0.267	0.001	$4.11 \cdot 10^{-4}$
SOFA score	11.27	0.195	0.023	0.022
IL-6	19.90	0.602	0.032	$3.26 \cdot 10^{-4}$
IL-10	11.52	0.662	0.164	0.002
AP	2.01	0.571	0.034	0.109
GLDH	5.25	0.977	0.581	0.030
GGT	3.13	0.647	0.013	0.705
GOT	17.07	0.079	0.924	$5.04 \cdot 10^{-4}$
GPT	12.52	0.412	0.857	0.003
Leukocytes	5.73	0.031	0.589	0.947
CRP	2.59	0.346	0.762	0.248
Lactate	4.72	0.991	0.211	0.061
PT	27.05	0.010	0.305	$4.81 \cdot 10^{-6}$
INR	27.33	0.011	0.267	$5.61 \cdot 10^{-6}$
PTT	31.25	0.016	0.001	$2.24 \cdot 10^{-6}$
Fibrinogen	1.75	0.476	0.784	0.265
Platelets	7.40	0.261	0.071	0.028
Na+	5.16	0.110	0.254	0.138
K+	5.92	0.267	0.868	0.015
Creatinin	7.19	0.541	0.421	0.035
Hematocrit	19.70	0.026	0.121	$6.65 \cdot 10^{-5}$
Bilirubin	2.20	0.377	0.319	0.383
Hb	28.07	0.011	0.024	$1.98 \cdot 10^{-6}$
Features that reject the null hypothesis	13/29	8/29	9/29	19/29

The green table color indicates a rejection of the null hypothesis, whereas the red table coloring indicates that there is not enough evidence to reject the null hypothesis. The $\chi 2$-values from the Kruskal-Wallis ANOVA test and p-values from the Wilcoxon rank sum test for the different subgroups are given as table entries. AIS, abbreviated injury scale; AP, alkaline phosphatase; APACHE, acute physiology and chronic health evaluation; CRP, C-reactive protein; GCS, glasgow coma scale; GLDH, glutamate dehydrogenase; GGT, gamma glutamyl transpeptidase; GOT, glutamic oxaloacetic transaminase; GPT, glutamic pyruvic transaminase; Hb, hemoglobin; IL, interleukin; INR, international normalized ratio; ISS, injury severity score; K, potassium; Na, sodium; PT, prothrombin time; PTT, partial thromboplastin time; SOFA, sequential organ failure assessment.

group having no complications (Table 2). Moreover, the partial thromboplastin time (PTT) that is a measure for the overall clotting speed of the blood by the intrinsic pathway and common pathway of coagulation as well as hemoglobin (Hb), the oxygen-binding metalloprotein of erythrocytes were found to be significant in all risk groups (Table 2). Based on the feature importance ranking and the correlation analysis, the most informative features in classifying a certain complication pattern are shown in Figure 2 and Supplementary Figure

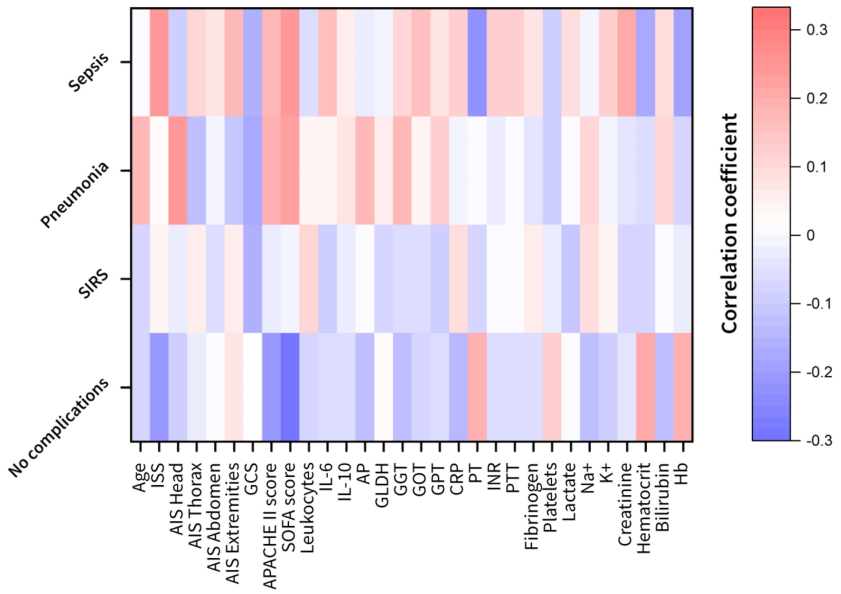

FIGURE 2
Heat maps of the feature correlation of the clinical attributes with respect to the different complication classes (no complication, systemic inflammatory response syndrome (SIRS), pneumonia and sepsis). Correlation strength is color-coded (red to white: positive correlations; white to blue: negative correlations). AIS, abbreviated injury scale; AP, alkaline phosphatase; APACHE, acute physiology and chronic health evaluation; CRP, C-reactive protein; GCS, glasgow coma scale; GLDH, glutamate dehydrogenase; GGT, gamma glutamyl transpeptidase; GOT, glutamic oxaloacetic transaminase; GPT, glutamic pyruvic transaminase; Hb, hemoglobin; IL, interleukin; INR, international normalized ratio; ISS, injury severity score; K, potassium; Na, sodium; PT, prothrombin time; PTT, partial thromboplastin time; SOFA, sequential organ failure assessment.

S5. The highest ranking and therefore most-informative features for infectious complications are the SOFA score (rank 1) and the GCS (rank 3, Supplementary Figure S5). Besides, the overall injury severity represented by the ISS (rank 6) has shown that the traumatic injury pattern is of relevance for the risk assessment with AIS Head (rank 11) among the top 20 ranking features. The Hb level as a measure for assessing acute blood loss after trauma were ranked on position 13, respectively. The transpeptidase and transaminases gamma glutamyl transpeptidase (GGT, rank 5), glutamic oxaloacetic transaminase (GOT, rank 17) and glutamic pyruvic transaminase (GPT, rank 18) were found to be of high relevance for identification of adverse outcome patterns in the investigated patient cohort (Supplementary Figure S5).

3.3 Cluster analysis revealed distinct biomarker patterns for hyperinflammatory and infectious complications

To identify the number of patient risk clusters, present during the 3 days after injury, 317 patients admitted to the ICU after trauma were subjected to filtered k-means clustering. This analysis yielded four major cluster groups that were distinguished by distinct inflammatory profiles for days 0-3 post-injury. These clustering techniques produced the following patient groups: a favorable outcome group with “no complications” (cluster 1), a SIRS group with high inflammatory load (cluster 3) and unfavorable infectious outcome groups suffering from sepsis or pneumonia (cluster 2 and 4) (Table 3 and Supplementary Table S1).

In the following, we discuss the unique parameter differences and additional clinical considerations for each respective patient cluster and their associated outcome risk. The identified cluster revealed a very distinct injury pattern among each other (Figure 3).

Patients that belonged to cluster 1 (n=101) were mainly associated to the sub-group showing no complications. Therefore, the AIS related to different body parts, the disease severity scores APACHE II and SOFA, and the cytokines IL-6 and IL-10 are significantly lower than the average of the overall patient cohort (Table 3). The 99 patients clustered in cluster 2, where the majority of septic patients was observed, showed a low AIS of the head (0.31 points) and a high AIS of the thorax (3.18 points) with significantly elevated level of IL-6 (257.93 pg/ml), GPT (101.23 U/l) and GOT (169.71 U/l) compared to the centroid of the full data set (Table 3). In comparison to the patients in cluster 2 with high thorax and low head injury, 58 patients in cluster 3 had high AIS for head (3.67 points) and thorax (3.17 points) injury and showed mainly a pro-inflammatory complication pattern (SIRS) accompanied with higher cytokine levels (IL-6 concentration of 229.61 pg/ml and IL-10 concentration of 56.52 pg/ml) and disease severity scores (APACHE II of 16.38 points and SOFA of 5.73) above average (Table 3). 59 patients in cluster 4 have significantly higher head injury scores (AIS Head with 4.25 points) whereas the other body regions were mostly without traumatic injuries and showed pneumonia as a main complication class (Table 3). The patients with an isolated traumatic brain injury in cluster 4 had lower cytokine levels (IL-6 concentration of 127.98 pg/ml and IL-10 concentration of 37.37 pg/ml) and lower levels of biomarkers related to the liver function (GLDH, GGT, GOT, GPT) that were comparable with cluster 1 (mainly patients with no complications) (Table 3).

10.3389/fimmu.2023.1281674

TABLE 3 Overview of polytrauma patient cohort and associated injury patterns.

Attribute	Full data (n=317)	Cluster 1 (n=101)	Cluster 2 (n=99)	Cluster 3 (n=58)	Cluster 4 (n=59)	p<0.05
ISS (–)	26.35	20.97	28.05	36	23.27	b
AIS Head (–)	2.27	2.23	0.31	3.67	4.25	e
AIS Thorax (–)	2.01	1.34	3.18	3.17	0.09	n.s.
AIS Abdomen (–)	0.76	0.51	1.52	0.71	0	e
AIS Extremities (–)	1.15	0.96	1.53	1.46	0.52	n.s.
GCS (–)	8.45	14.32	7.68	3.56	4.54	b
APACHE II score (–)	13.12	7.06	15.91	16.38	15.58	n.s.
SOFA score (–)	4.11	1.66	5.56	5.73	4.24	b
IL-6 (pg/ml)	165.81	60.98	257.93	229.61	127.98	a
IL-10 (pg/ml)	43.26	24.78	57.86	56.52	37.37	n.s.
AP (U/l)	47.97	52.98	43.16	44.70	50.68	n.s.
GLDH (U/l)	18.01	8.32	29.83	22.95	9.91	a
GGT (U/l)	38.68	45.46	36.23	27.20	42.47	b
GOT (U/l)	97.11	53.25	169.71	97.08	50.40	f
GPT (U/l)	63.98	40.33	101.23	75.03	31.09	f
Leukocytes (U/nl)	10.24	10.00	9.74	10.47	11.24	f
CRP (mg/dl)	3.21	3.36	2.52	3.52	3.78	f
Lactate (mg/dl)	19.29	16.73	21.68	19.85	19.13	a
PT (%)	84.53	91.42	79.55	79.57	85.96	n.s.
INR (–)	1.16	1.09	1.22	1.21	1.16	a
PTT (s)	31.31	27.49	33.76	34.01	31.13	b
Fibrinogen (mg/dl)	309.87	307.52	330.20	308.32	281.32	f
Platelets (cells/nl)	168.19	185.12	151.84	157.57	176.61	a
Na+ (mmol/l)	143.19	139.55	145.03	142.65	146.87	c
K+ (mmol/l)	4.07	4.01	4.18	4.04	4.06	a
Creatinine (mg/dl)	0.92	0.83	1.02	0.91	0.92	a
Hematocrit (%)	31.02	34.56	28.36	29.25	31.17	a
Bilirubin (mg/dl)	0.66	0.66	0.69	0.62	0.67	d
Hb (g/dl)	10.41	11.69	9.49	9.85	10.29	a

The cluster numbers allocate to the following complication patterns: 1 – no complications, 2 – sepsis, 3 – systemic inflammatory response syndrome (SIRS), and 4 – pneumonia. AIS, abbreviated injury scale; AP, alkaline phosphatase; APACHE, acute physiology and chronic health evaluation; CRP, C-reactive protein; dl, deciliter; g, gram; GCS, glasgow coma scale; GLDH, glutamate dehydrogenase; GGT, gamma glutamyl transpeptidase; GOT, glutamic oxaloacetic transaminase; GPT, glutamic pyruvic transaminase; Hb, hemoglobin; IL, interleukin; INR, international normalized ratio; ISS, injury severity score; K, potassium; l, liter; mg, milligram; ml, milliliter; mmol, millimoles; Na, sodium; nl, nanoliter; n.s., not significant; pg, picogram; PT, prothrombin time; PTT, partial thromboplastin time; SOFA, sequential organ failure assessment; U, units. Significant differences ($p < 0.05$) between the groups are indicated as follows: a: cluster 1 vs. cluster 2, b: cluster 1 vs. cluster 3, c: cluster 1 vs. cluster 4, d: cluster 2 vs. cluster 3, e: cluster 2 vs. cluster 4, f: cluster 3 vs. cluster 4.

3.4 Ensemble classifiers predicted adverse outcomes with high accuracy

Classification analysis was conducted on the patient cohort illustrated in Figure 1 with the demographics and outcomes given in Table 1. The patient subgroup with SIRS was neglected in the classification due to their relatively low impact on adverse outcome patterns (Figure 2) and the weakest correlation observed in the Wilcoxon rank sum test compared to the sub-group that showed no complications (Table 2). The patient sub-group with pneumonia and sepsis are combined in an "infectious complication" group since more than 72% of the patients with sepsis also developed pneumonia during their hospitalization. For the classification of polytrauma patients in risk groups (no complications, infectious complication) several classifiers (naive bayes, random forest and ensemble classifiers) were optimized to achieve a high F1 score and

10.3389/fimmu.2023.1281674

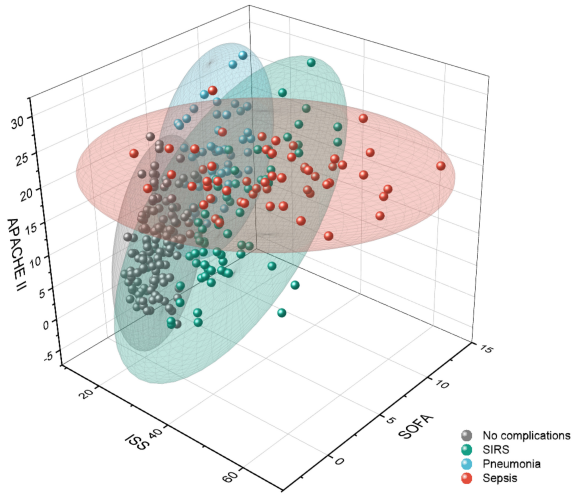

FIGURE 3
Visualization of outcome-related patient clusters with respect to clinical scores: the total injury severity represented by the injury severity score (ISS) and the disease severity scores acute physiology and chronic health evaluation (APACHE) II and sequential organ failure assessment (SOFA). Data points represent the individual patients, and the colored ellipsoids represent the cluster areas. SIRS, systemic inflammatory response syndrome.

best receiver operating characteristics (ROC) (Supplementary Tables S2, S3).

The best classification performance was achieved with the ensemble classifier XGBoost, a boosting algorithm designed to turn week classifiers such as decision trees as base classifiers into an ensemble of strong classifiers. XGBoost performs well even for imbalanced class problems. The biomarker predictor ranking was analyzed by gradient boosting and features governing these results are explained using SHAP values (Figure 4). Based on boosting ensemble classification XGBoost, 18 from 20 patients (90%) in the test set were correctly classified as low-risk group (no complications). For the high-risk groups associated with development of pneumonia and sepsis, 8 from 10 patients in the test set (80%) were correctly identified (Figure 5).

The classification results were explained by SHAP values, which calculate the importance of a feature by comparing the model predictions with and without the selection of certain features. Based on the explainability analysis with SHAP values, the clinical and immunological trauma features that had the largest importance on the model performance were identified. The top clinical feature for both investigated risk scenarios (infectious complications and long ICU stay) were SOFA score, GCS, Lactate, GGT and Hb in a slightly varying order (Figure 4). Furthermore, the immunological features of total leukocyte counts and IL-6 concentration were found to be top ranking in both scenarios, whereas the anti-inflammatory cytokine IL-10 had a higher feature importance in the infectious complication patterns than in the length of stay risk prediction.

Figure 5 is showing the resulting decision tree after ten learning cycles (M = 10) with a learning rate of 0.001. According to the feature ranking, the disease severity scores SOFA score and GCS, the injury-related scores such as ISS and AIS, the anti-inflammatory biomarker IL-10, the liver function parameters (GGT and GOT) as well as bleeding and coagulation-related parameters (Hb) were branches of the decision tree (Figure 5).

In comparison to the infectious classification scenario, the prediction accuracy for the length of stay risk classification (ICU

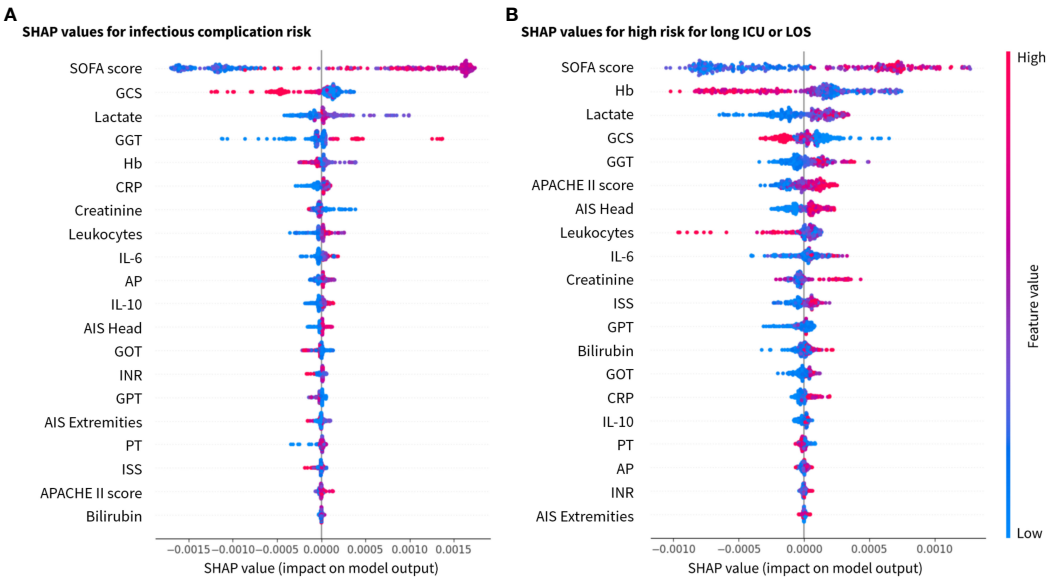

FIGURE 4
SHAP values for the 20 most relevant features in the XGBoost model for the investigated class labels **(A)** for infection risk, and **(B)** risk for long stay (ICU and total hospital stay) ranked by mean absolute values. x-axis: SHAP values and y-axis: features ranked by importance. AIS (–), abbreviated injury scale; AP (U/l), alkaline phosphatase; APACHE, acute physiology and chronic health evaluation; CRP (mg/dl), C-reactive protein; GCS, glasgow coma scale; GGT (U/l), gamma glutamyl transpeptidase; GOT (U/l), glutamic oxaloacetic transaminase; GPT (U/l), glutamic pyruvic transaminase; Hb (g/dl), hemoglobin; IL(pg/ml), interleukin; INR, international normalized ratio; ISS, injury severity score; PT (%), prothrombin time; SOFA, sequential organ failure assessment.

10.3389/fimmu.2023.1281674

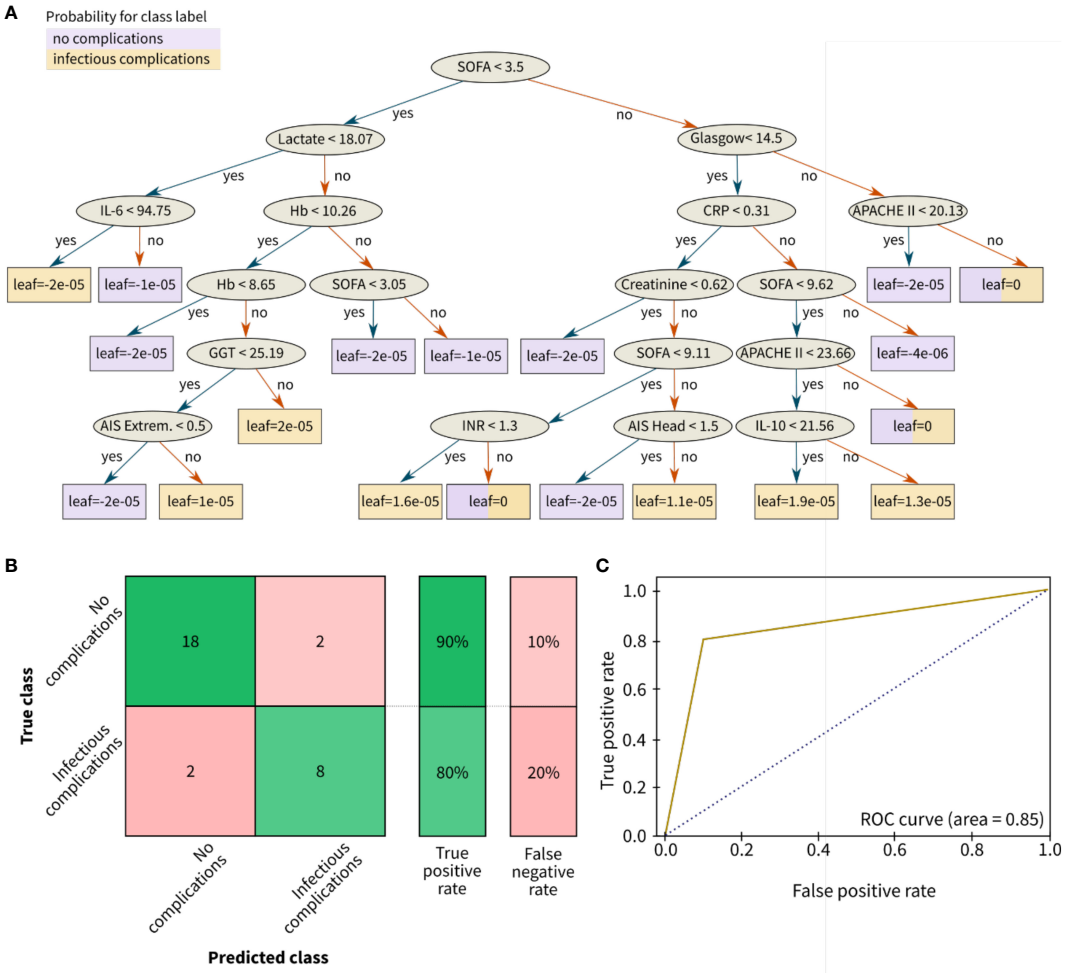

FIGURE 5
Results for the classification of infectious outcomes in polytrauma patients. **(A)** Decision tree, **(B)** Confusion matrix, and **(C)** Receiver operating characteristic (ROC) curve for risk classification with the following outcome groups as classes: group 1 (with no complications) and group 2 with infectious complications (pneumonia and/or sepsis). The leaves of **(A)** correspond to the final nodes of the decision tree where the data does not split any further and points to the predicted risk classes of the respective patient cohort: no complications (purple) and infectious complications (yellow). The prediction accuracy between the true class (columns) and the predicted class (rows) is given in % as true positive or false negative rate. The confusion matrix for the classification problem was achieved by the ensemble learning algorithm XGBoost. AIS, abbreviated injury scale; APACHE, acute physiology and chronic health evaluation; CRP (mg/dl), C-reactive protein; Extrem., extremities; Glasgow, glasgow coma scale; GGT (U/l), gamma glutamyl transpeptidase; Hb (g/dl), hemoglobin; IL (pg/ml), interleukin; INR, international normalized ratio; SOFA, sequential organ failure assessment.

stay for >14 days and/or LOS for >30 days) slightly decreased to 67% for the low-risk group and 87% for the high-risk group (Figure 6).

4 Discussion

The objective of this study was to use various machine learning algorithms and explainability based on SHAP values based on clinical features collected in the early hospitalization phase to identify clinical and inflammatory biomarker in a polytrauma study cohort with various injury patterns. The focus was on adverse outcome patterns such as SIRS and infectious complications like pneumonia and sepsis, analyzing feature patterns within three days post-injury. Through filtered k-means clustering, four distinct clusters with different injury and feature patterns were identified. These clusters exhibited variations in clinical features and inflammatory profiles upon admission and during the initial three days post-injury.

Regarding the risk classification of patient sub-groups, the results showed that ensemble-based methods outperformed naive Bayes or random forest classifiers in terms of accuracy. The best classification performance was achieved with XGBoost, a boosting algorithm designed to turn week classifiers such as decision trees as base classifiers into an ensemble of strong classifiers. XGBoost is an ensemble approach which is efficient in predicting the plausible classes accurately since sometimes only base classifier alone cannot classify the class labels and the predictions can be biased. Gradient boosting helps in overcoming this effect by building sequence of base classifiers such that each successor aims in reducing the error

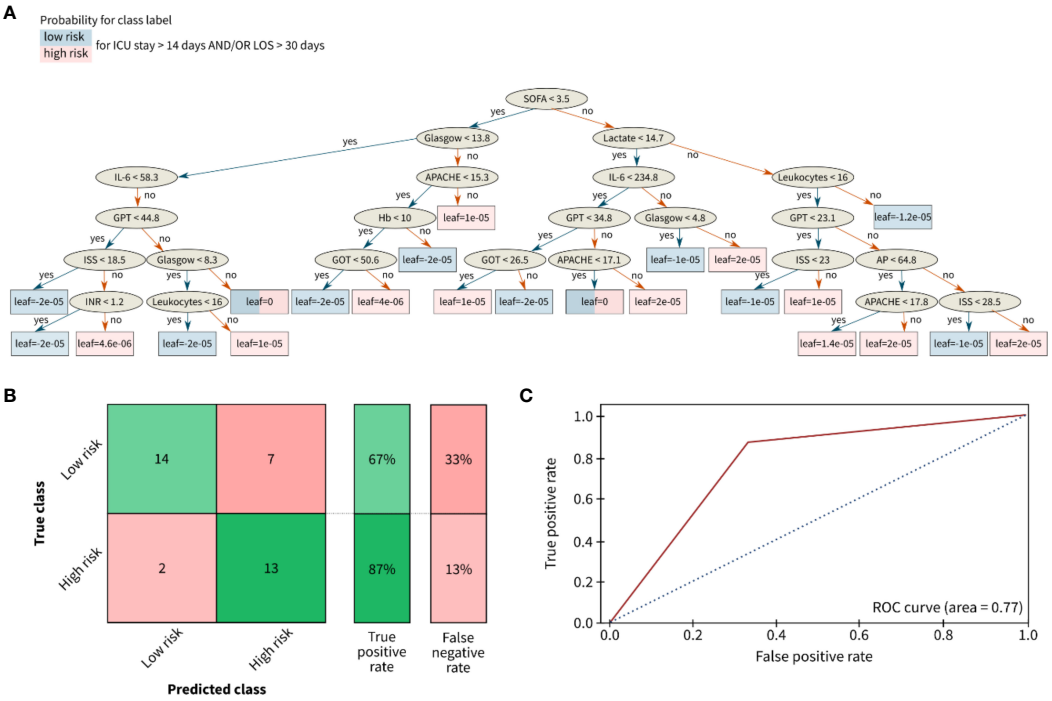

FIGURE 6
Results for the classification of the length of stay of polytrauma patients in the ICU or the total hospital stay. **(A)** Decision tree, **(B)** Confusion matrix, and **(C)** Receiver opertainig characteristic (ROC) curve for risk classification with the following outcome groups as classes: group 1 (with low risk) and group 2 with high risk for a long LOS. The leaves of **(A)** correspond to the final nodes of the decision tree where the data does not split any further and points to the predicted risk classes of the respective patient cohort: low risk (blue) and high risk (red). The prediction accuracy between the true class (columns) and the predicted class (rows) is given in % as true positive or false negative rate. The confusion matrix for the classification problem was achieved by the ensemble learning algorithm XGBoost. AP (U/l), alkaline phosphatase; APACHE, acute physiology and chronic health evaluation; Glasgow, glasgow coma scale; GOT (U/l), glutamic oxaloacetic transaminase; GPT (U/l), glutamic pyruvic transaminase; Hb (g/dl), hemoglobin; IL (pg/ml), interleukin; INR, international normalized ratio; ISS, injury severity score; SOFA, sequential organ failure assessment.

of the predecessor employing a gradient descent approach. Extreme gradient boosting is a type of gradient boosting approach which uses second order optimization function to optimize the errors in the predictions (24). The exact form of the pseudo-loss is under control of the algorithm so that the weak classifier can focus also on the groups which are hardest to distinguish from the correct group. The XGBoost ensemble classifier achieved 90% accuracy in classifying patients without complications and 80% accuracy in identifying patients with infectious complications (pneumonia and sepsis). The higher rate of misclassified cases in the pneumonia and sepsis group may be attributed to complex comorbidities and medication history of these patients. Due to the relatively small sample size of patients with sepsis (n=33) and pneumonia (n=39), future validation studies in larger cohorts and a rigorous study designs are needed to enhance classification accuracy further.

Even though disease severity scores are not the key elements of treatment, they are however, an essential part of improvement in clinical decisions and in identifying patients with unexpected outcomes, such as the investigated subjective score variables APACHE II and SOFA that are collected daily in our study (25).Consistent with the previous results of Tranca et al. (2016), the ensemble classifier predicts that most patients with a SOFA cut-off score below 3.45 points did not develop sepsis (26). Moreover, in line with Tranca et al. (2016) (26), it was confirmed that patients with APACHE II score below 10 points did not develop sepsis and indicate a discrimination between the pneumonia subgroup from patients without complications. Based on the AIS head, a cut-off score of AIS head=1.5 in combination with other predictive features were found to separate low-risk from the high-risk patient sub-group.

Consistent with previous studies, this prospective machine learning study also highlighted the importance of measuring pro- and anti-inflammatory cytokines (e.g. IL-6 and IL-10) for risk classification in trauma patients (27, 28). The immunological features of total leukocyte counts and IL-6 concentration were found to be top ranking in both scenarios (infectious complications and long ICU stay), whereas the anti-inflammatory cytokine IL-10 had a higher feature importance in the infectious complication patterns than in the length of stay risk prediction. Together, elevated IL-6 levels (>95 pg/ml) and decreased IL-10 levels (<21 pg/ml) in combination with other features were predictive of infectious risk classification. This study demonstrated the potential for early risk stratification of severely injured trauma patients into sub-groups at risk for specific clinical trajectories. This approach may aid in tailored research and clinical therapies for polytrauma patients, aligning with the findings of Liu et al. (2020) (7). By utilizing the explainability analysis based on SHAP values, it was elucidated how clinical and immunological biomarkers that were routinely collected during ICU admission impact the decision-making process of black-box machine learning

models. Thus, the present study validated the clinical predictors for infectious complications and the LOS in the hospital.

Some additional features including the importance of GGT as a feature for clustering remain intriguing. Fisher et al. have shown that GGT as a useful and simple biomarker at admission is among the independent indicators and predictors of in-hospital mortality in older hip fracture patients (29). In the realm of clinical models, the role of GGT is intricate, and subject to various factors and contextual nuances. GGT, an enzyme distributed in the liver, biliary tract, and diverse tissues, can undergo elevation in response to a spectrum of medical conditions, encompassing liver damage, alcohol consumption, and cholestatic liver disease (30, 31). Its levels can also be influenced by medications and concurrent health issues. To discern why GGT assumes a noteworthy role in this study, several key considerations come into play. It is essential to note that individuals with a documented history of chronic diseases were deliberately excluded from this study. However, the impact of GGT in this model may hinge on the timing of measurements. The model employs the mean GGT value from the first three days post-admission. Nonetheless, the fluctuating nature of GGT levels over time should be acknowledged, as elevated levels can signify distinct conditions at different stages of illness. Moreover, undisclosed pre-existing medical conditions and concurrent health issues among patients could significantly impact GGT levels and their clinical relevance, potentially confounding the results. Understanding the interrelationships between GGT, GOT, GPT, bilirubin levels, and other markers of liver function is pivotal. These relationships could offer a more comprehensive understanding of liver health and potential causes of their elevation, since notably, these markers rank among the top 20 most relevant features for classification in our model.

Our study contains several limitations. The sepsis sub-group meets the SIRS criteria, with the added specificity of including individuals with bloodstream infections. It's important to note that the sepsis sub-group also encompasses patients with pneumonia who developed sepsis, whereas the pneumonia group does not involve sepsis, and the SIRS group excludes both pneumonia and sepsis cases. It must be acknowledged that a re-classification of patients according to the more recent sepsis-3 definition will be of higher clinical relevance (32). A retrospective re-classification of patients from the present study according to sepsis-3 criteria was performed, however, there are serious limitations in the patient records, which only provided a single daily recording of the worst SOFA score for ten consecutive days post-hospital admission. Thus, the retrospective re-classification according to sepsis-3 criteria referred only to SOFA score changes of ≥2 points within 24 hours. Despite this challenge, all 33 septic patients in the presented sub-group do meet the sepsis-3 criteria based on the records. This data should not be overinterpreted, although Kim et al. have reported that some validity on the assessment of the prognostic accuracy of the initial SOFA score at the time of sepsis recognition which was lower than the 24-h maximal SOFA score in ED patients with septic shock (33). Their insights, while valuable, emphasize the need for continuous monitoring of SOFA scores over an extended period. Our study, on the other hand, contends that assessing the worst SOFA score within 24 hours may capture a critical moment in a patient's condition, offering practicality in historical data analyses. While the retrospective nature of such approaching definitely poses limitations, the assessment of the worst SOFA score within 24 hours during the hospital stay may provide some clinically relevant information. Yet, clearly, prospective studies with continuous SOFA scoring during the progression of sepsis are crucial for a more comprehensive understanding, and we acknowledge the need for further validation through such studies.

In addition, the distinction between the sepsis group, characterized by systemic infection, and the pneumonia group, where bacteriological diagnosis primarily resides in the lungs, underscores the complexity of infections in trauma patients. A pivotal question emerges regarding the utility of antibiotic treatment initiation on a specific day as a surrogate for infection. The lack of valid and reliable records on antibiotic regimens in the assessed patient cohort complicates such assessment. Sepsis, a complex condition, may not always necessitate bacteriological confirmation, as demonstrated in the present study where a bacteriological diagnosis was consistently found. Its definition has evolved to reflect a dysregulated host response to infection, irrespective of the infectious agent's nature—bacteria, viruses, fungi, or even non-infectious triggers. While bacteriological confirmation holds value, sepsis diagnosis relies significantly on clinical presentation and established criteria encompassing signs such as body temperature fluctuations, increased heart rate, and abnormal white blood cell counts (32). The notion of using the initiation of antibiotic treatment on a certain day as a surrogate for infection poses challenges. Prophylactic antibiotic use is crucial in certain trauma scenarios, such as traumatic brain injuries (TBI), penetrating injuries, open fractures, and high-risk orthopedic procedures (34). However, initiating antibiotics early, though important in suspected infections, does not inherently confirm the presence of an infection, and must be critically discussed in terms of their role in the development of post-traumatic infections and microbial selection (34). Empirical antibiotic initiation in critically ill patients is often a necessity, with subsequent treatment decisions guided by culture results and clinical response. Clinical judgment, complemented by other diagnostic modalities such as blood cultures, imaging studies, and biomarkers, should collectively guide the diagnosis and management of sepsis and associated infections in trauma patients. In addition, trauma patients, particularly those with brain injuries, may face an elevated risk of developing ventilator-associated pneumonia (VAP) (35), confirming the data from the present study revealing higher AIS head values in patients with pneumonia compared to other groups. Thus, multiple factors including compromised immune function, prolonged mechanical ventilation, impaired airway protection mechanisms but also the injury patterns demand a careful management including antibiotics regimes to prevent complications such as VAP in trauma patients.

The model development process and findings in the present study could be employed to predict the clinical course and identify high-risk individuals for inflammatory or infectious complications among severely injured trauma patients. The presented ensemble methods identified key features in polytraumatized patients, that allowed to predict patient`s outcomes. Thus, implementing such models may enhance clinical decision-making by enabling personalized treatment strategies based on individual risk profiles in future.

Data availability statement

The raw data supporting the conclusions of this article will be made available by the authors, without undue reservation.

Ethics statement

The studies involving humans were approved by University Hospital Frankfurt of the Goethe University (nr.: 312/10). The studies were conducted in accordance with the local legislation and institutional requirements. Written informed consent for participation in this study was provided by the participants' legal guardians/next of kin.

Author contributions

MF: Conceptualization, Data curation, Formal Analysis, Investigation, Methodology, Software, Writing – original draft. RM: Formal Analysis, Investigation, Methodology, Visualization, Writing – review & editing. CB: Formal Analysis, Validation, Writing – review & editing. IM: Funding acquisition, Resources, Writing – review & editing. CH: Resources, Writing – review & editing. BR: Conceptualization, Data curation, Formal Analysis, Funding acquisition, Investigation, Methodology, Project administration, Resources, Supervision, Validation, Writing – original draft.

Funding

The author(s) declare financial support was received for the research, authorship, and/or publication of this article. This study was conducted in the framework of the NTF consortium FOR5417/1, funded by the DFG (DFG, German Research Foundation) project number 465409392 and DFG RE 3304/12-1.

Conflict of interest

The authors declare that the research was conducted in the absence of any commercial or financial relationships that could be construed as a potential conflict of interest.

The author(s) declared that they were an editorial board member of Frontiers, at the time of submission. This had no impact on the peer review process and the final decision.

Publisher's note

Supplementary material

The Supplementary Material for this article can be found online at: https://www.frontiersin.org/articles/10.3389/fimmu.2023.1281674/full#supplementary-material

SUPPLEMENTARY TABLE 1
Misclustered instances from filtered clustering based on k-means algorithm. Abbreviation: SIRS, systemic inflammatory response syndrome.Supplementary information for classification analysis

SUPPLEMENTARY TABLE 2
Accuracy of different classifiers for infectious complications.

SUPPLEMENTARY TABLE 3
Accuracy of different classifiers for risk of long intensive care unit (ICU) and length of stay (LOS) prediction.

SUPPLEMENTARY FIGURE 1
Box plots of outcome associated parameters related to the complication risk. Lower and upper box boundaries correspond to 25th and 75th percentiles, respectively. The line inside represents the box median. The lower and upper error lines (whiskers) correspond to the 10th and 90th percentiles, respectively. The asterisk next to the 10th and 90th percentiles indicate statistical significance between the complication group and the patient group having no complications. Points above and below the whiskers indicate outliers outside the 10th and 90th percentiles. Abbreviations: APACHE, acute physiology and chronic health evaluation; SIRS, systemic inflammatory response syndrome; SOFA, sequential organ failure assessment.

SUPPLEMENTARY FIGURE 2
Box plots of cytokines and predictive markers related to the complication risk. Lower and upper box boundaries correspond to 25th and 75th percentiles, respectively. The line inside represents the box median. The lower and upper error lines (whiskers) correspond to the 10th and 90th percentiles, respectively. The asterisk next to the 10th and 90th percentiles indicate statistical significance between the complication group and the patient group having no complications. Points above and below the whiskers indicate outliers outside the 10th and 90th percentiles. Abbreviations: IL, interleukin; PCT, procalcitonin; SIRS, systemic inflammatory response syndrome.

SUPPLEMENTARY FIGURE 3
Box plots of serum markers for liver function related to the complication risk. Lower and upper box boundaries correspond to 25th and 75th percentiles, respectively. The line inside represents the box median. The lower and upper error lines (whiskers) correspond to the 10th and 90th percentiles, respectively. The asterisk next to the 10th 29 and 90th percentiles indicate statistical significance between the complication group and the patient group having no complications. Points above and below the whiskers indicate outliers outside the 10th and 90th percentiles. Abbreviations: AP, alkaline phosphatase; CRP, C-reactive protein; GLDH, glutamate dehydrogenase;

GGT, gamma glutamyl transpeptidase; GOT, glutamic oxaloacetic transaminase; GPT, glutamic pyruvic transaminase.

SUPPLEMENTARY FIGURE 4
Box plots of serum markers for coagulation factors related to the complication risk. Lower and upper box boundaries correspond to 25th and 75th percentiles, respectively. The line inside represents the box median. The lower and upper error lines (whiskers) correspond to the 10th and 90th percentiles, respectively. The asterisk next to the 10th and 90th percentiles indicate statistical significance between the complication group and the patient group having no complications. Points above and below the whiskers indicate outliers outside the 10th and 90th percentiles. Abbreviations: INR, international normalized ratio; PTT, partial thromboplastin time. Supplementary information for statistical tests and correlation analysis

SUPPLEMENTARY FIGURE 5
Feature importance ranking based on the F1 score with respect to the two investigated risk scenarios: (A) Risk for infectious complications, and (B) risk for a long stay in the intensive care unit (ICU) or total length of stay (LOS) in hospital. Abbreviations: Abbreviations: AIS, abbreviated injury scale; APACHE, acute physiology and chronic health evaluation; GGT, gamma glutamyl transpeptidase; GOT, glutamic oxaloacetic transaminase; GPT, glutamic pyruvic transaminase; SOFA, sequential organ failure assessment. GGT - Gamma glutamyl transpeptidase, GOT-Glutamic oxaloacetic transaminase, GPT-Glutamic pyruvic transaminase. Supplementary information for clustering analysis

References

1. World Health Organization. *Global status report on road safety 2018* Geneva: World Health Organization (2018). Available at: https://iris.who.int/handle/10665/276462.

2. Spahn DR, Bouillon B, Cerny V, Duranteau J, Filipescu D, Hunt BJ, et al. The European guideline on management of major bleeding and coagulopathy following trauma: fifth edition. *Crit Care Lond Engl* (2019) 23(1):98. doi: 10.1186/s13054-019-2347-3

3. Bardes JM, Inaba K, Schellenberg M, Grabo D, Strumwasser A, Matsushima K, et al. The contemporary timing of trauma deaths. *J Trauma Acute Care Surg* (2018) 84 (6):893–9. doi: 10.1097/TA.0000000000001882

4. Liu T, Li F, Li Y, Li J, Chen L, Yang Z, et al. Epidemiological characteristics and factors influencing hospitalization burden among trauma patients: a retrospective analysis. *Eur J Trauma Emerg Surg Off Publ Eur Trauma Soc* (2023). doi: 10.1007/s00068-023-02353-2

5. Relja B, Horstmann JP. Traumatic injury. In: Cordero MD, Alcocer-Gómez E, editors. *Inflammasomes: clinical and therapeutic implications*. Cham, Switzerland: Springer International Publishing (2018). p. 85–110. doi: 10.1007/978-3-319-89390-7_5

6. Relja B, Land WG. Damage-associated molecular patterns in trauma. *Eur J Trauma Emerg Surg Off Publ Eur Trauma Soc* (2020) 46(4):751–75. doi: 10.1007/s00068-019-01235-w

7. Liu D, Namas RA, Vodovotz Y, Peitzman AB, Simmons RL, Yuan H, et al. Unsupervised clustering analysis based on MODS severity identifies four distinct organ dysfunction patterns in severely injured blunt trauma patients. *Front Med* (2020) 7:46. doi: 10.3389/fmed.2020.00046

8. Relja B, Mörs K, Marzi I. Danger signals in trauma. *Eur J Trauma Emerg Surg Off Publ Eur Trauma Soc* (2018) 44(3):301–16. doi: 10.1007/s00068-018-0962-3

9. Lord JM, Midwinter MJ, Chen YF, Belli A, Brohi K, Kovacs EJ, et al. The systemic immune response to trauma: an overview of pathophysiology and treatment. *Lancet* (2014) 384(9952):1455–65. doi: 10.1016/S0140-6736(14)60687-5

10. Schultebraucks K, Shalev AY, Michopoulos V, Grudzen CR, Shin SM, Stevens JS, et al. A validated predictive algorithm of post-traumatic stress course following emergency department admission after a traumatic stressor. *Nat Med* (2020) 26 (7):1084–8. doi: 10.1038/s41591-020-0951-z

11. Subudhi S, Verma A, Patel AB, Hardin CC, Khandekar MJ, Lee H, et al. Comparing machine learning algorithms for predicting ICU admission and mortality in COVID-19. *NPJ Digit Med* (2021) 4(1):87. doi: 10.1038/s41746-021-00456-x

12. Nagy M, Onder AM, Rosen D, Mullett C, Morca A, Baloglu O. Predicting pediatric cardiac surgery-associated acute kidney injury using machine learning. *Pediatr Nephrol Berl Ger* (2023). doi: 10.1007/s00467-023-06197-1

13. Mirijello A, Fontana A, Greco AP, Tosoni A, D'Agruma A, Labonia M, et al. Identifying predictors associated with risk of death or admission to intensive care unit in internal medicine patients with sepsis: A comparison of statistical models and machine learning algorithms. *Antibiot Basel Switz* (2023) 12(5):925. doi: 10.3390/antibiotics12050925

14. Ramos G, Gjini E, Coelho L, Silveira M. Unsupervised learning approach for predicting sepsis onset in ICU patients. *Annu Int Conf IEEE Eng Med Biol Soc IEEE Eng Med Biol Soc Annu Int Conf* (2021) 2021:1916–9. doi: 10.1109/EMBC46164.2021.9629559

15. Su L, Xu Z, Chang F, Ma Y, Liu S, Jiang H, et al. Early prediction of mortality, severity, and length of stay in the intensive care unit of sepsis patients based on sepsis 3.0 by machine learning models. *Front Med* (2021) 8:664966. doi: 10.3389/fmed.2021.664966

16. Christie SA, Conroy AS, Callcut RA, Hubbard AE, Cohen MJ. Dynamic multi-outcome prediction after injury: Applying adaptive machine learning for precision medicine in trauma. *PloS One* (2019) 14(4):e0213836. doi: 10.1371/journal.pone.0213836

17. von Elm E, Altman DG, Egger M, Pocock SJ, Gøtzsche PC, Vandenbroucke JP. Strengthening the reporting of observational studies in epidemiology (STROBE) statement: guidelines for reporting observational studies. *BMJ* (2007) 335(7624):806–8. doi: 10.1136/bmj.39335.541782.AD

18. Mörs K, Wagner N, Sturm R, Störmann P, Vollrath JT, Marzi I, et al. Enhanced pro-inflammatory response and higher mortality rates in geriatric trauma patients. *Eur J Trauma Emerg Surg Off Publ Eur Trauma Soc* (2021) 47(4):1065–72. doi: 10.1007/s00068-019-01284-1

19. Bouillon B, Probst C, Maegele M, Wafaisade A, Helm P, Mutschler M, et al. Schockraummanagement polytrauma: ATLS® und S3-leitlinie. *Chir* (2013) 84(9):745–52. doi: 10.1007/s00104-013-2476-1

20. Bauer TT, Lorenz J, Bodmann KF, Vogel* F. Aktualisierte Kurzfassung der Leitlinien zur Prävention, Diagnostik und Therapie der nosokomial erworbenen Pneumonie. *Med Klin* (2005) 100(6):355–60. doi: 10.1007/s00063-005-1045-x

21. Calandra T, Cohen J. The international sepsis forum consensus conference on definitions of infection in the intensive care unit. *Crit Care Med* (2005) 33(7):1538–48. doi: 10.1097/01.CCM.0000168253.91200.83

22. Blagus R, Lusa L. SMOTE for high-dimensional class-imbalanced data. *BMC Bioinf* (2013) 14:106. doi: 10.1186/1471-2105-14-106

23. Lundberg SM, Erion G, Chen H, DeGrave A, Prutkin JM, Nair B, et al. From local explanations to global understanding with explainable AI for trees. *Nat Mach Intell* (2020) 2(1):56–67. doi: 10.1038/s42256-019-0138-9

24. Chen T, Guestrin C. *XGBoost: A scalable tree boosting system*. San Francisco California USA: ACM: Proceedings of the 22nd ACM SIGKDD International Conference on Knowledge Discovery and Data Mining (2016) p. 785–94. doi: 10.1145/2939672.2939785

25. Rapsang A, Shyam DC. Scoring systems in the intensive care unit: A compendium. *Indian J Crit Care Med* (2014) 18(4):220–8. doi: 10.4103/0972-5229.130573

26. Trancă S, Petrisor C, Hagău N, Ciuce C. Can APACHE II, SOFA, ISS, and RTS severity scores be used to predict septic complications in multiple trauma patients? *J Crit Care Med* (2016) 2(3):124–30. doi: 10.1515/jccm-2016-0019

27. Jastrow KM, Gonzalez EA, McGuire MF, Suliburk JW, Kozar RA, Iyengar S, et al. Early cytokine production risk stratifies trauma patients for multiple organ failure. *J Am Coll Surg* (2009) 209(3):320–31. doi: 10.1016/j.jamcollsurg.2009.05.002

28. Raymond SL, Hawkins RB, Wang Z, Mira JC, Stortz JA, Han F, et al. Prospective validation of a transcriptomic metric in severe trauma. *Ann Surg* (2020) 271(5):802–10. doi: 10.1097/SLA.0000000000003204

29. Fisher A, Fisher L, Srikusalanukul W, Smith PN. Usefulness of simple biomarkers at admission as independent indicators and predictors of in-hospital mortality in older hip fracture patients. *Injury* (2018) 49(4):829–40. doi: 10.1016/j.injury.2018.03.005

30. Banciu T, Weidenfeld H, Marcoane E, Berinde L. Serum gamma-glutamyltranspeptidase assay in the detection of alcohol consumers and in the early and stadial diagnosis of alcoholic liver disease. *Med Interne* (1983) 21(1):23–9.

31. Liu J, Yu C, Yang Q, Yuan X, Yang F, Li P, et al. The clinical implication of gamma-glutamyl transpeptidase in COVID-19. *Liver Res* (2021) 5(4):209–16. doi: 10.1016/j.livres.2021.09.001

32. Shankar-Hari M, Phillips GS, Levy ML, Seymour CW, Liu VX, Deutschman CS, et al. Developing a new definition and assessing new clinical criteria for septic shock: for the third international consensus definitions for sepsis and septic shock (Sepsis-3). *JAMA* (2016) 315(8):775–87. doi: 10.1001/jama.2016.0289

33. Kim TH, Jeong D, Park JE, Hwang SY, Suh GJ, Choi SH, et al. Prognostic accuracy of initial and 24-h maximum SOFA scores of septic shock patients in the emergency department. *Heliyon* (2023) 9(9):e19480. doi: 10.1016/j.heliyon.2023.e19480

34. Schindler CR, Woschek M, Franz JN, Störmann P, Henrich D, Marzi I. Influence of antibiotic management on microbial selection and infectious complications after trauma. *Front Med* (2021) 8:678382. doi: 10.3389/fmed.2021.678382

35. Caceres E, Olivella JC, Yanez M, Viñan E, Estupiñan L, Boada N, et al. Risk factors and outcomes of lower respiratory tract infections after traumatic brain injury: a retrospective observational study. *Front Med* (2023) 10:1077371. doi: 10.3389/fmed.2023.1077371

frontiers | Frontiers in Immunology

TYPE Original Research
PUBLISHED 09 January 2024
DOI 10.3389/fimmu.2023.1319986

OPEN ACCESS

EDITED BY
Sina M. Coldewey,
Jena University Hospital, Germany

REVIEWED BY
Inge Bauer,
University Hospital of Düsseldorf, Germany
Michael Schwarzer,
University Hospital Jena, Germany

*CORRESPONDENCE
Eva-Maria Wolfschmitt
eva-maria.wolfschmitt@uni-ulm.de

RECEIVED 11 October 2023
ACCEPTED 15 December 2023
PUBLISHED 09 January 2024

CITATION
Wolfschmitt E-M, Vogt JA, Hogg M, Wachter U, Stadler N, Kapapa T, Datzmann T, Messerer DAC, Hoffmann A, Gröger M, Münz F, Mathieu R, Mayer S, Merz T, Asfar P, Calzia E, Radermacher P and Zink F (2024) ^{13}C-Metabolic flux analysis detected a hyperoxemia-induced reduction of tricarboxylic acid cycle metabolism in granulocytes during two models of porcine acute subdural hematoma and hemorrhagic shock.
Front. Immunol. 14:1319986.
doi: 10.3389/fimmu.2023.1319986

^{13}C-Metabolic flux analysis detected a hyperoxemia-induced reduction of tricarboxylic acid cycle metabolism in granulocytes during two models of porcine acute subdural hematoma and hemorrhagic shock

Eva-Maria Wolfschmitt[1]*, Josef Albert Vogt[1], Melanie Hogg[1], Ulrich Wachter[1], Nicole Stadler[1], Thomas Kapapa[2], Thomas Datzmann[3], David Alexander Christian Messerer[1,4], Andrea Hoffmann[1], Michael Gröger[1], Franziska Münz[1,3], René Mathieu[5], Simon Mayer[5], Tamara Merz[1,3], Pierre Asfar[6], Enrico Calzia[1], Peter Radermacher[1] and Fabian Zink[1]

[1]Institute for Anesthesiological Pathophysiology and Process Engineering, University Hospital Ulm, Ulm, Germany, [2]Clinic for Neurosurgery, University Hospital Ulm, Ulm, Germany, [3]Clinic for Anesthesia and Intensive Care, University Hospital Ulm, Ulm, Germany, [4]Institute for Transfusion Medicine, University Hospital Ulm, Ulm, Germany, [5]Clinic for Neurosurgery, Bundeswehrkrankenhaus, Ulm, Germany, [6]Département de Médecine Intensive – Réanimation et Médecine Hyperbare, Centre Hospitalier Universitaire, Angers, France

Introduction: Supplementation with increased inspired oxygen fractions has been suggested to alleviate the harmful effects of tissue hypoxia during hemorrhagic shock (HS) and traumatic brain injury. However, the utility of therapeutic hyperoxia in critical care is disputed to this day as controversial evidence is available regarding its efficacy. Furthermore, in contrast to its hypoxic counterpart, the effect of hyperoxia on the metabolism of circulating immune cells remains ambiguous. Both stimulating and detrimental effects are possible; the former by providing necessary oxygen supply, the latter by generation of excessive amounts of reactive oxygen species (ROS). To uncover the potential impact of increased oxygen fractions on circulating immune cells during intensive care, we have performed a ^{13}C-metabolic flux analysis (MFA) on PBMCs and granulocytes isolated from two long-term, resuscitated models of combined acute subdural hematoma (ASDH) and HS in pigs with and without cardiovascular comorbidity.

Methods: Swine underwent resuscitation after 2 h of ASDH and HS up to a maximum of 48 h after HS. Animals received normoxemia (P_aO_2 = 80 – 120 mmHg) or targeted hyperoxemia (P_aO_2 = 200 – 250 mmHg for 24 h after treatment initiation, thereafter P_aO_2 as in the control group). Blood was drawn at time points T1 = after instrumentation, T2 = 24 h post ASDH and HS, and T3 =

48 h post ASDH and HS. PBMCs and granulocytes were isolated from whole blood to perform electron spin resonance spectroscopy, high resolution respirometry and ^{13}C-MFA. For the latter, we utilized a parallel tracer approach with 1,2-$^{13}C_2$ glucose, U-^{13}C glucose, and U-^{13}C glutamine, which covered essential pathways of glucose and glutamine metabolism and supplied redundant data for robust Bayesian estimation. Gas chromatography-mass spectrometry further provided multiple fragments of metabolites which yielded additional labeling information. We obtained precise estimations of the fluxes, their joint credibility intervals, and their relations, and characterized common metabolic patterns with principal component analysis (PCA).

Results: ^{13}C-MFA indicated a hyperoxia-mediated reduction in tricarboxylic acid (TCA) cycle activity in circulating granulocytes which encompassed fluxes of glutamine uptake, TCA cycle, and oxaloacetate/aspartate supply for biosynthetic processes. We further detected elevated superoxide levels in the swine strain characterized by a hypercholesterolemic phenotype. PCA revealed cell type-specific behavioral patterns of metabolic adaptation in response to ASDH and HS that acted irrespective of swine strains or treatment group.

Conclusion: In a model of resuscitated porcine ASDH and HS, we saw that ventilation with increased inspiratory O_2 concentrations (P_aO_2 = 200 – 250 mmHg for 24 h after treatment initiation) did not impact mitochondrial respiration of PBMCs or granulocytes. However, Bayesian ^{13}C-MFA results indicated a reduction in TCA cycle activity in granulocytes compared to cells exposed to normoxemia in the same time period. This change in metabolism did not seem to affect granulocytes' ability to perform phagocytosis or produce superoxide radicals.

KEYWORDS

Bayesian modeling, glucose metabolism, glutamine utilization, hyperoxia, immunometabolism, mass isotopomer distribution, peripheral blood mononuclear cells, reactive oxygen species

1 Introduction

Hemorrhage and traumatic brain injury (TBI) are the major determinants of outcome after severe physical injury. Hemorrhage results in tissue oxygen debt (1) due to the blood loss-related reduction of circulating blood volume and O_2 transport capacity. In patients with TBI, it is well established that ischemic or hypoxic tissue regions can persist despite adequate systemic resuscitation measures (2). Consequently, increasing the inspired O_2 concentration is often used during the acute management of TBI and hemorrhagic shock (HS) to alleviate harmful effects of hypoxia like hypoxia-induced inflammation (3). Theoretically, hyperoxemia could be especially beneficial for patients with atherosclerosis or coronary artery disease suffering from inherent perfusion impairment (4). In fact, we had demonstrated that therapeutic hyperoxia during the early phase of resuscitation attenuated heart and kidney injury in swine with coronary artery disease (5). Similar positive effects could manifest for TBI patients by counteracting TBI-induced vasodilation and brain edema due to allowing the reduction of intracranial pressure (ICP) while maintaining tissue oxygen supply (6). In this regard, we had recently demonstrated that targeted hyperoxemia improved neurological function in a porcine model of combined acute subdural hematoma (ASDH) and HS (7, 8).

However, therapeutic hyperoxia remains a contentious topic in critical care. Hyperoxemia causes increased reactive oxygen species (ROS) generation (6, 9), especially in the context of ischemia reperfusion injury, e.g. during resuscitation from HS. Both oxygen availability and physical injuries are known factors that can interact with immune cell behavior and metabolism and potentially affect their effector functions (10, 11). Furthermore, hyperoxemia has been associated with increased oxidative stress in a broad variety of cells (12–14) including platelets and leukocytes. It is theorized that this increase in oxidative stress could potentially impact the immune and coagulatory functions of these cell subsets (14, 15).

Immunometabolism explores how changes in the metabolism of immune cells direct and guide their function (16, 17). These metabolic alterations can be elucidated by metabolic flux analysis (MFA), a technique for calculating production, consumption, and transformation rates within a biological system (18, 19). MFA most commonly relies on balancing fluxes within a stoichiometric network and employing nonlinear regressions. We have adapted MFA to a Bayesian approach, which is more computationally intensive than the conservative method, but in turn yields full probability distributions of fluxes, their joint credibility intervals, and their correlations (20). With a parallel tracer approach of 1,2-$^{13}C_2$ glucose, $^{13}C_6$ glucose, and $^{13}C_5$ glutamine we were able to cover major glycolytic and glutamine-fueled pathways like glycolysis, the pentose phosphate pathway (PPP), and the tricarboxylic acid (TCA) cycle.

In the present study, we utilized high resolution respirometry and ^{13}C-MFA to investigate whether shock and targeted hyperoxemia impact the immunometabolism of circulating immune cells, specifically peripheral blood mononuclear cells (PBMCs) and granulocytes, in healthy and atherosclerotic pigs. We further investigated immune cell function by analyzing their capacity to perform phagocytosis and produce ROS with flow cytometry and electron spin resonance (ESR) spectroscopy, respectively. As hyperoxia could either have beneficial or ROS-mediated detrimental effects on immune cells, we placed special focus on the interplay between metabolic pathways and superoxide ($O_2^{\bullet-}$) production. For this reason, we analyzed systematic changes in metabolism and function with a principal component analysis (PCA), which allowed capturing both cell type-specific and time-dependent metabolic plasticity of circulating immune cells during combined porcine ASDH and HS, and resuscitation. With these methods, we explored cell type-specific immunometabolic patterns of adaptation with the potential effects of *i)* exposure to hyperoxia, *ii)* cardiovascular co-morbidity, and *iii)* the response to combined ASDH and HS, and resuscitation *per se*.

2 Methods

2.1 Animals, preparation, and sample origin

Experiments were performed according to the guidelines of the National Institute of Health on the Use of Laboratory Animals and the European Union "Directive 2010/63 EU on the protection of animals used for scientific purposes" after approval from the local Animal Care Committee of Ulm University and the Federal Authorities for Animal Research (Regierungspräsidium Tübingen, Germany, Reg.-Nr. 1316). This study is an exploratory *post hoc* analysis of blood samples obtained during two long-term studies of combined ASDH and HS investigating swine with or without coronary artery disease over a period of three days (7, 8). The experimental procedures were identical for both studies except for the utilization of the two different swine strains (7, 8). Data of studies pertaining to survival, hemodynamics, gas exchange, acid-base state, brain perfusion, oxygenation, and neurologic outcome are reported in the respective publication. Briefly, animals were instrumented and ASDH was induced by injection of 0.1 mL/kg autologous blood into the subdural space. HS was initiated by passive removal of 30% of the animals' calculated blood volume under maintenance of a cerebral perfusion pressure (CPP, difference between mean arterial pressure (MAP) and ICP) ≥ 50 mmHg. For resuscitation, the shed blood was returned 2 h after induction of HS and noradrenaline (NoA) was continuously administered intravenously as required to restore the MAP to pre-shock levels and maintain CPP ≥ 75 mmHg. Animals were randomly assigned to control (normoxemia (NormOx), target arterial partial pressure of oxygen (P_aO_2) = 80 – 120 mmHg) or targeted hyperoxemia (HyperOx, target P_aO_2 = 200 – 250 mmHg for 24 h after treatment initiation, thereafter target P_aO_2 as in the control group). Resuscitation was maintained to a maximum of 48 h after shock before experiment termination. The experimental protocol is visualized in Figure 1.

The first data set originated from a study that investigated Familial hypercholesterolemia-Bretoncelles Meishan (FBM) pigs. It comprised 14 adult pigs of either sex (6 females, 8 castrated males) with a median body weight of 63 kg (interquartile range (IQR) 56;71) and a median age of 38 months (IQR 36;41). This strain is characterized by a homozygous R84C mutation in the low-density lipoprotein receptor, making them susceptible to atherosclerosis and coronary artery disease. Animals were fed a cholesterol-enriched diet for at least 9 months to encourage atherosclerotic progression.

The second analyzed data set included 14 adult pigs of the Bretoncelles-Meishan-Willebrand (BMW) strain with a median body weight of 75 kg (IQR 73;76) and an age of 16 months (IQR 15;18) of both sexes (4 females and 10 castrated males). As pigs are typically hypercoagulatory (21) and this strain presents with reduced activity of the von Willebrand factor, the resulting reduced coagulatory phenotype resembles that of humans (22). In contrast to the coronary artery disease present in the FBM strain, BMW are cardiovascularly healthy (7, 8, 23, 24).

2.2 Cell isolation from whole blood

We isolated PBMCs and granulocytes from whole blood samples to detect changes in immunometabolism in response to combined ASDH and HS and hyperoxemia as previously described (20, 25). Blood was drawn at three different time points over the course of the experiment: T1: after (neuro)surgical instrumentation following a stabilization period; T2: 24 h after ASDH and HS, i.e. at the end of the exposure to targeted hyperoxia; T3: 48 h after ASDH and HS, i.e. at the end of the intensive care period. The precise timeline is depicted in Figure 1. Approximately 125 mL of arterial blood were drawn in lithium heparin monovettes (9 mL, Sarstedt, Nümbrecht, Germany) and 1:1 (v/v) diluted with PBS (without $CaCl_2$, $MgCl_2$) at each time point. For cell separation, the dilution was layered on top of two density gradient solutions (9 mL 1.119 and 8 mL 1.088 g/mL solution, Pancoll, PAN Biotech, Aidenbach, Germany) and centrifuged at 764 g for 20 min at room temperature (RT) with the break deactivated. This procedure yielded a PBMC

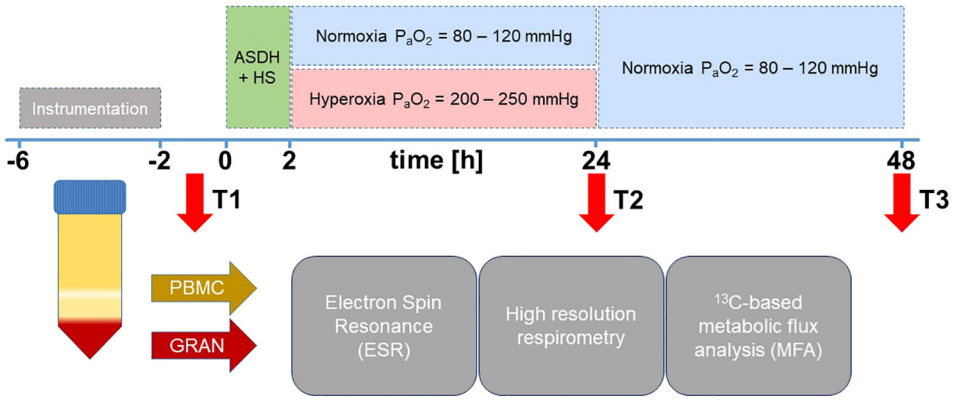

FIGURE 1
Experimental setup. After instrumentation, pigs were subjected to ASDH and HS by injection of 0.1 mL/kg autologous blood into the subdural space and passive removal of 30% of the calculated blood volume. After 2 h of ASDH and shock, swine underwent resuscitation comprising retransfusion of shed blood, fluid resuscitation and i.v. NoA titration to maintain MAP at pre-shock levels and CPP ≥ 75 mmHg. Intensive care was maintained up to a maximum of 48 h. Animals were randomly assigned to control (normoxemia, target P_aO_2 = 80 – 120 mmHg) or targeted hyperoxemia (target P_aO_2 = 200 – 250 mmHg for 24 h after treatment initiation. Thereafter, target P_aO_2 as in the control group). Resuscitation was maintained to a maximum of 48 h after shock before experiment termination. Blood was drawn at time points T1 = after instrumentation, T2 = 24 h post ASDH and HS, and T3 = 48 h post ASDH and HS. PBMCs and granulocytes were isolated from whole blood to perform ESR for superoxide quantification, high resolution respirometry and ^{13}C-MFA.

top layer and a bottom layer containing red blood cells (RBCs) and granulocytes. RBC residuals were removed by osmotic lysis. A single lysis was sufficient for PBMCs, while the granulocyte-RBC layer had to be subjected to osmotic lysis three times before all RBC contamination was removed. Subsequently, cells were washed once with 1× PBS and counted in a Neubauer counting chamber.

2.3 High resolution respirometry

Mitochondrial respiration of isolated cells was derived from the measurement of O_2 consumption with high resolution respirometry. We used the Oroboros-2K (Oroboros Instruments, Innsbruck, Austria) for this purpose, which is a device for simultaneous recording of the O_2 concentration in two parallel chambers (20, 25). Briefly, chambers were calibrated with 2 mL of mitochondrial respiration medium MiR05 (composition available in Supplementary Table 1) adjusted to pH 7.1 with KOH and equilibrated with 21% O_2 at 37°C. For measurement of cell respiration, we filled each chamber with 10× 10^6 PBMCs/granulocytes suspended in MiR05. Within the chambers, cells were continuously stirred at 750 rpm. After sealing, the first derivative of the O_2 concentration was recorded and yielded the oxygen flux (JO_2), which was normalized for the cell number. The subsequent injection of substrates and inhibitors enabled the analysis of specific mitochondrial respiration functions: i) Routine respiration was recorded prior to injecting inhibitors or substrates once a stable JO_2-value was achieved. ii) The LEAK-state represents the respiratory activity required to maintain a stable membrane potential in absence of ATP-turnover and was measured after addition of 2.5 µM oligomycin to block the ATP-synthase. iii) The ETS-state is defined as the maximum respiratory activity in the uncoupled state and corresponds to state 3 of Chance and Williams et al. (26). It was achieved by titration of carbonyl cyanide p-(trifluoromethoxy)-phenylhydrazone (FCCP) in 1 µM steps.

2.4 Quantification of superoxide anion with electron spin resonance spectroscopy

Immediately after arterial blood withdrawal at the same time points as for cell isolation, 25 µL of whole blood were mixed 1:1 (v/v) with CMH spin probe solution containing 400 µM CMH spin probe (1-hydroxy-3-methoxycarbonyl-2,2,5,5-tetramethylpyrrolidine), 25 µM deferoxamine, and 5 µM diethyldithiocarbamate solved in Krebs-HEPES-Buffer (KHB) (Noxygen, Elzach, Germany). As previously described (20, 25), the mixture was transferred to a 50 µL glass capillary, sealed, and placed in an EMXnano ESR spectrometer (Bruker, Billerica, MA, USA). After a 5 min incubation period at 37°C, the measurement was started with device settings detailed in the Supplementary File. $O_2^{\bullet-}$ quantification was performed with eight radical standards of various CP$^\bullet$ (3-Carboxy-2,2,5,5-tetramethyl-1-pyrrolidinyloxy) concentrations solved in KHB. The blank sample (KHB mixed 1:1 with spin probe solution) was subtracted from the result for final values.

For the determination of $O_2^{\bullet-}$ production by immune cells, 25 µL of cell suspension (2.5× 10^6 cells/mL RPMI 1640 medium (glucose 1.8 mg/mL, glutamine 0.6 mg/mL, $NaHCO_3$ 100 µg/mL)) were mixed 1:1 (v/v) with CMH spin probe solution directly prior to the measurement. Samples were measured 8 times over a 30 min interval to calculate $O_2^{\bullet-}$ production rates. All other settings were analogous to whole blood radical determination. The blank sample (RPMI 1640 mixed 1:1 with spin probe solution) was subtracted from the result for final values. We used the Xenon_nano software

(version 1.3; Bruker BioSpin GmbH, Rheinstetten, Germany) and Microsoft Excel for data analysis.

2.5 Phagocytosis assay

Purified granulocytes were resuspended in fluorescence-activated cell sorting (FACS) buffer + 10% pig serum (Bio-Rad Laboratories, Hercules, CA, USA) and kept on ice before staining. Cells were used within 3 h from blood withdrawal and 1 h from purification. Granulocytes were treated according to manufacturer's instructions of the pHrodo™ Bioparticles Phagocytosis Kit for Flow Cytometry (Thermo Fisher Scientific, Waltham, MA, USA). Briefly, 10×10^6 granulocytes, were initially blocked with 100% pig serum and incubated on ice for 10 min. 1×10^6 cells per sample were transferred into 100 µL RPMI-medium and kept on ice for further processing. Negative control on ice (Nci) and Negative control at 37°C (Nc37), each containing cells only, were incubated at 4°C (Nci) or 37°C (Nc37) for 20 min. Positive Control on ice (Pci), Positive control at 37°C (Pc37) and samples were incubated with 20 µL of 1 mg/mL pHrodo® *E.coli* BioParticles® conjugate at 37°C for 10 min and 20 min (Pci and Pc37), respectively. Phagocytosis was stopped by transferring the samples onto ice and washing with washing buffer. The samples were subsequently resuspended in FACS buffer containing 10% pig serum for incubation with porcine-specific antibodies against granulocyte markers (2B2, 6D10; Bio-Rad Laboratories, Hercules, CA, USA). The samples were transferred to FACS buffer without pig serum and kept on ice until further analysis with a Beckman Coulter CytoFLEX Flow Cytometer (Beckman Coulter Life Sciences, Brea, CA, USA).

Granulocytes were gated according to their forward (FSC) and side scatter (SSC) characteristics in conjunction with porcine granulocyte specific antibody staining ($2B2^+$, $6D10^+$). Fluorescence spillover was corrected by compensation using single stained porcine specific antibodies and pHrodo™ signal. Gating approaches included post-density gradient separation, live/dead cell distinction (PI-staining), exclusion of doublet signals (FSC-H vs. FSC-A blot), and pHrodo-positive granulocyte populations ($6D10^+$, $2B2^+$, $pHrodo^+$). A total of 20,000 events were acquired for each sample. The phagocytic activity of each population was foremost measured by the median fluorescent intensity (MFI) of the pHrodo signal (PE-channel) and subsequently normalized (27). Briefly, MFI scores of Pc37 were divided by the MFI of their dedicated sample with thermally inhibited phagocytosis at 4°C (Pci), concluding with normalized MFI (nMFI) as describing dimension. Thus, phagocytic activity was calculated using Equation 1:

$$\boldsymbol{nMFI} = \frac{MFI\ sample\ incubated\ at\ 37\,°C(\boldsymbol{Pc37})}{MFI\ inhibited\ phagocytosis(\boldsymbol{Pci})} \quad (1)$$

As the fluorogenic pHrodo dye increases fluorescence as its surroundings become more acidic, PE signal intensity directly correlated with internalized particles. For statistical validation, positive control at 37°C (Pc37) samples were tested as triplicates, all other samples were measured as singular values. All samples were analyzed with CytExpert 2.4 software (Beckman Coulter Life Sciences, Brea, CA, USA).

2.6 *Ex vivo* ^{13}C tracer experiments

This method has been previously utilized and described in detail in Wolfschmitt et al. (20). For ^{13}C parallel tracer experiments, we incubated three times 5×10^6 cells in 1 mL RPMI supplemented with one of the following tracers each: 1,2-$^{13}C_2$ glucose, $^{13}C_6$ glucose, and $^{13}C_5$ glutamine (Cambridge Isotope Laboratories, Andover, MA, USA). Directly prior to the start of the 3-day experiment, the respective medium was supplemented with the tracers and $NaHCO_3$ and pH was adjusted to 7.4 by addition of 1M HCl or NaOH. Final concentrations are specified in Supplementary Table 2. Cells were incubated at 37°C for 2 h for ^{13}C labeling experiments. For analysis of stimulated granulocyte metabolism, 5×10^6 of freshly isolated cells were washed with RPMI and subsequently resuspended in 200 µL RPMI + 10% pig serum. 50 µL of pHrodo® *E.coli* BioParticles® conjugate were added to the cells and tubes were incubated in a water bath at 37°C for 20 min. Afterwards, cells were washed with 1 mL washing buffer and then resuspended in 1 mL RPMI supplemented with isotopic tracers. All other steps followed those of the parallel tracer approach of granulocytes/PBMCs.

After incubation for 2 h, 850 µL of supernatant were transferred to a crimp neck glass vial after spin down centrifugation at 4°C for analysis of $^{13}CO_2$ production and lactate released into the medium. The vial was frozen upside down at −20°C to prevent gas from escaping until gas chromatography/mass spectrometry (GC/MS) analysis. The leftover supernatant was discarded. Pellets were frozen at −80°C after washing them once with 1× PBS and removal of all liquid.

2.6.1 Quantification of $^{13}CO_2$ release

The cumulative cellular $^{13}CO_2$ production was calculated with enrichment analysis. We injected 25 µL 1M HCl through the septum into the thawed supernatant and shook the sample to release CO_2 from the $NaHCO_3$ buffer system into the gaseous phase. Each sample was measured 10 times with each 5 µL headspace gas injected into the GC/MS system (Agilent 6890 GC/5975B MSD, Agilent Technologies, Waldbronn, Germany). To capture both labeled and unlabeled CO_2, we analyzed the *m/z* of 44 and 45 in the selected ion monitoring (SIM) mode. The isotopic enrichment tracer-to-tracee-ratio (TTR) was calculated for each sample according to Equation 2:

$$TTR = \left(\frac{^{13}CO_2}{^{12}CO_2}\right)_{sample} - \left(\frac{^{13}CO_2}{^{12}CO_2}\right)_{background} \quad (2)$$

This resulted in the calculation of the $^{13}CO_2$ production with Equation 3

$$^{13}CO_2\ production\left[\frac{nmol}{1\times 10^6 cells}\right] = \frac{TTR\times E[\mu M]}{cell\ density\left[\frac{1\times 10^6 cells}{mL}\right]} \quad (3)$$

where E is the concentration of sodium bicarbonate in the RPMI medium. After analysis, the medium was frozen at −20°C until lactate measurement with GC/MS.

2.6.2 Measurement of lactate released into the medium

For lactate quantification, two times 100 µL of supernatant were thawed and one of the 100 µL samples was spiked with 1 µg of internal standard (IS, corresponding to 20 µL of 50 µg/mL $^{13}C_3$ sodium lactate solution). 500 µL acetonitrile were added to each replicate. After centrifugation (13000 rpm, 5 min, RT), samples were decanted into vials suited for derivatization and dried in a Savant2010 SPD 2010 SpeedVac concentrator (Thermo Scientific, Waltham, MA, USA) (45°C, 14 mTorr) for about 50 min. For derivatization of lactate, 100 µL acetonitrile and 25 µL N-(tert-butyldimethylsilyl)-N-methyltrifluoroacetamide (MTBSTFA, abcr, Karlsruhe, Germany) were added and samples were incubated at 80°C for 1 h. Standard samples comprised the following: 0.1 µg/0.2 µg/0.5 µg/0.75 µg/1 µg of sodium lactate with an additional 1 µg of IS each, samples with 1 µg of IS only, samples with blank RPMI, and samples RPMI with 1 µg of IS. Detailed equations for lactate quantification can be found in the *supplements* of Wolfschmitt et al. (20).

2.6.3 Detection of intracellular metabolites

All steps of extraction were performed on ice to avoid enzyme activation. For metabolite extraction from intracellular compartments, pellets were resuspended in 100 µL of ice-cold water, sonicated for 10 min, and mixed with 500 µL of acetonitrile. After centrifugation, the clear supernatant was transferred into a GC/MS vial suitable for derivatization. In analogy to the measurement of supernatant-derived lactate, we derivatized the intracellular metabolites with MTBSTFA. Steps of derivatization are mentioned in *2.6.2*. Standards were prepared as follows: one standard series with 0.1 µg/0.2 µg/0.5 µg/0.75 µg/1 µg of lactate and a mix with the respective amount of aspartate, glutamine, and glutamate.

We performed GC/MS detection of TBDMS metabolites and corresponding suitable ion fragments (Supplementary Table 4) with SIM for an optimal signal to noise ratio. SIM methods, device settings, and oven programs are mentioned in the Supplementary File. Peak area integration was performed with our in-house program (28). Mass isotopomer distributions (MIDs) were converted into carbon mass distributions (CMDs) by deducting isotopic interferences with a correction matrix approach (20, 29). It is important to note that our definition of "labeling" includes natural ^{13}C abundance, which was not corrected for.

2.7 Metabolic flux analysis

We have implemented a model for combined PPP/glycolysis and TCA cycle metabolism in RStan (R interface to stan, package rstan) (30). This model has been utilized in a previous form in Stifel et al. (31) and in a similar scope in our work investigating the effect of sodium thiosulfate on circulating immune cells (20).

Rstan is a sampling-based tool for Bayesian statistics. In our implementation, it draws random values for all parameters (fluxes) and calculates the corresponding theoretical CMDs for metabolites in the network according to our model description. If the theoretical CMDs come close to the actual GC/MS data, the value is considered a true value of the underlying posterior distribution and collected in a Markov chain Monte Carlo (MCMC) chain. The mathematical model of the biological network used for CMD calculations was built with the elementary metabolite unit (EMU) strategy (32). Detailed model explanations can be found in the *supplements* of Wolfschmitt et al. (20). Statistical properties like posterior mean, posterior standard deviations and credibility intervals were derived from the final MCMC chain of each parameter. Our priors were chosen to be relatively uninformative. Details of parameter bounds and prior specifications are listed in Supplementary Tables 5 and 6. Quantification was achieved by inclusion of $^{13}CO_2$ production and lactate secretion into the medium. Briefly, ratios were determined by CMD data only with a first Rstan model and then transformed into absolute values with another stan model by accordingly scaling ratios to fit lactate release and $^{13}CO_2$ production data. The parallel tracer setup of 1,2-$^{13}C_2$ glucose, $^{13}C_6$ glucose, and $^{13}C_5$ glutamine enabled improved flux determination, as all posterior parameters must apply to sets of measurements obtained from each tracer.

2.8 Statistical analysis

This study included samples from 14 FBM and 14 BMW pigs. Animals were randomly assigned to Hyperoxia or Normoxia treatment groups (FBM: NormOx and HyperOx; BMW: NormOx and HyperOx; each n = 7) (7, 8). Data are presented as median with IQR. Due to the nature of this project, a previous sample size determination was impossible due to the lack of preexisting data. Furthermore, original power estimations were calculated with clinical parameters as primary criteria rather than the immunometabolic analysis. Therefore, missing measurement time points for T1 and T3 due to insufficient cell yield and/or premature termination of an experiment greatly impacted our options for statistical evaluations (e.g. the use of repeated measures methods). For this reason, we present individual data points for better transparency and emphasize the exploratory nature of this study. P values should be treated with the latter in mind. Experimental data were considered to be non-parametric due to small sample sizes. We conducted the comparison between groups with Mann-Whitney U tests, while the effect of time within one group was analyzed with the Kruskal-Wallis rank sum test and a *post hoc* Dunn's multiple comparisons test. Statistical and graphical presentation was performed with GraphPad Prism 10, version 10.0.2 (GraphPad Software Inc., La Jolla, CA, USA).

The PCA was performed with varying combinations of the following data sets: FBM PBMCs (n = 34), BMW PBMCs (n = 28), FBM granulocytes (n = 27), BMW granulocytes (n = 31), and BMW *E.coli* bioparticle-stimulated granulocytes (n = 31). All relevant fluxes were included in this analysis, as well as data from $O_2^{\bullet-}$ production and mitochondrial Routine respiration (n = 22 parameters total). Data were standardized to a sample mean of zero and a unit sample

SD of 1. The PCA was performed in R (version 4.3.1 (2023-06-16 ucrt)) and RStudio (version 2023.06.1) with prcomp, varimax, pracma and fviz_eig. To ensure PCA stability, we employed the jackknife method, a cross validation technique that works according to a "leave one out" principle. Briefly, it estimates a parameter for the whole data set and subsequently skips one element before recalculating the parameter as a "partial estimate" (33). This procedure was extended to correct for a directional change in the scores and loadings ("reflection", as proposed by (34)) and was repeated until each element had been dropped once. Mean and SD of all partial estimates were then calculated. If the mean for the PCA parameter was still significant, this parameter was considered for interpretation as a significant contributor.

3 Results

This is an exploratory study of data obtained from two studies investigating the effects of hyperoxia during ASDH and HS in different swine strains. In the following, we will discuss the respective impact of targeted hyperoxia, swine strain, and ASDH and HS on immune cell behavior. We have analyzed each of these factors according to their influence on immunometabolism. For this reason, we took both absolute values and the differences between measurement time points into consideration. The latter indicated the progression of individual animals over time, as it excluded pre-existing particularities presented at baseline.

3.1 Targeted hyperoxia dampened TCA cycle activation in circulating granulocytes

As a first factor we investigated the impact of increasing O_2 availability on the metabolism of circulating immune cells with a focus on changes that persist after *ex vivo* isolation of PBMCs and granulocytes from whole blood. In this context, the metabolic network comprising glycolysis, PPP, and the TCA cycle was of particular interest (Figure 2). The complete metabolic model with all flux balances is provided in the Supplementary Figure 1. Animals had been exposed to targeted hyperoxia or control between time points T1 and T2 for a period of 24 hours. In conclusion, we observed both the absolute values of groups at T2 as well as the time-related development between those two measurement time points (i.e., the difference between values at T1 and T2 for individual animals, ΔT2-T1). As data from both swine strains were pooled for this analysis, we have indicated the respective origin of each data point in the graphs.

Figure 3 shows flux results obtained for granulocytes. The most striking difference between HyperOx and NormOx groups was seen in glutamine-fueled TCA cycle activity, as HyperOx-treated granulocytes displayed a dampened increase in TCA cycle fluxes (F3, F4), glutamine utilization (F8), and aspartate/oxaloacetate "loss" (L_{OAA}) from T1 to T2 (Δ T2-T1) (Figure 3B). In our analysis, "losses" were defined as the flux of metabolite leaving the described metabolic network, e.g., for protein or nucleotide biosynthesis. In addition, also the absolute values for TCA cycle fluxes (F3, F4) were reduced in the HyperOx group at T2, i.e., the end of targeted hyperoxemia treatment (Figure 3C). In summary, the typically occurring increase in TCA cycle activity from the first to the second measurement time point was dampened under targeted hyperoxia (Figure 3A).

The HyperOx-mediated reduction in TCA cycle fluxes was still visible in granulocytes after *ex vivo* stimulation with *E.coli* bioparticles for both absolute (Figure 3D) and ΔT2-T1 values (Figure 3E). Interestingly, stimulated HyperOx granulocytes further displayed reduced ability to increase non-oxidative PPP (dTAL, net flux Q9-Q10) fluxes from T1 to T2 (Figure 3E). However, phagocytic stimulation was only performed for BMW animals, so data analysis suffered from low sample availability. This is also reflected in the rather large data spread.

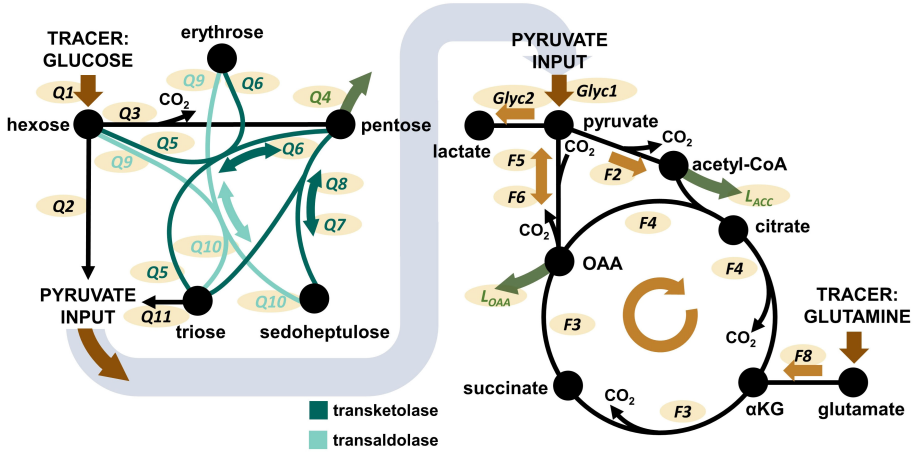

FIGURE 2
Overview over the pathways covered by the Bayesian ^{13}C-MFA model. Left: PPP model. Right: TCA cycle model. Glyc: glycolytic flux. Q: flux within the PPP. F: flux within the TCA cycle. L: flux of metabolite leaving the network, e.g. for biosynthetic processes. Additional considered metabolite inputs (pyruvate, OAA, acetyl-CoA) and losses (pyruvate) are not shown in the graphic, but are presented and visualized in Supplementary Figure 1. The Figure is taken from Wolfschmitt et al. (20), with permission.

10.3389/fimmu.2023.1319986

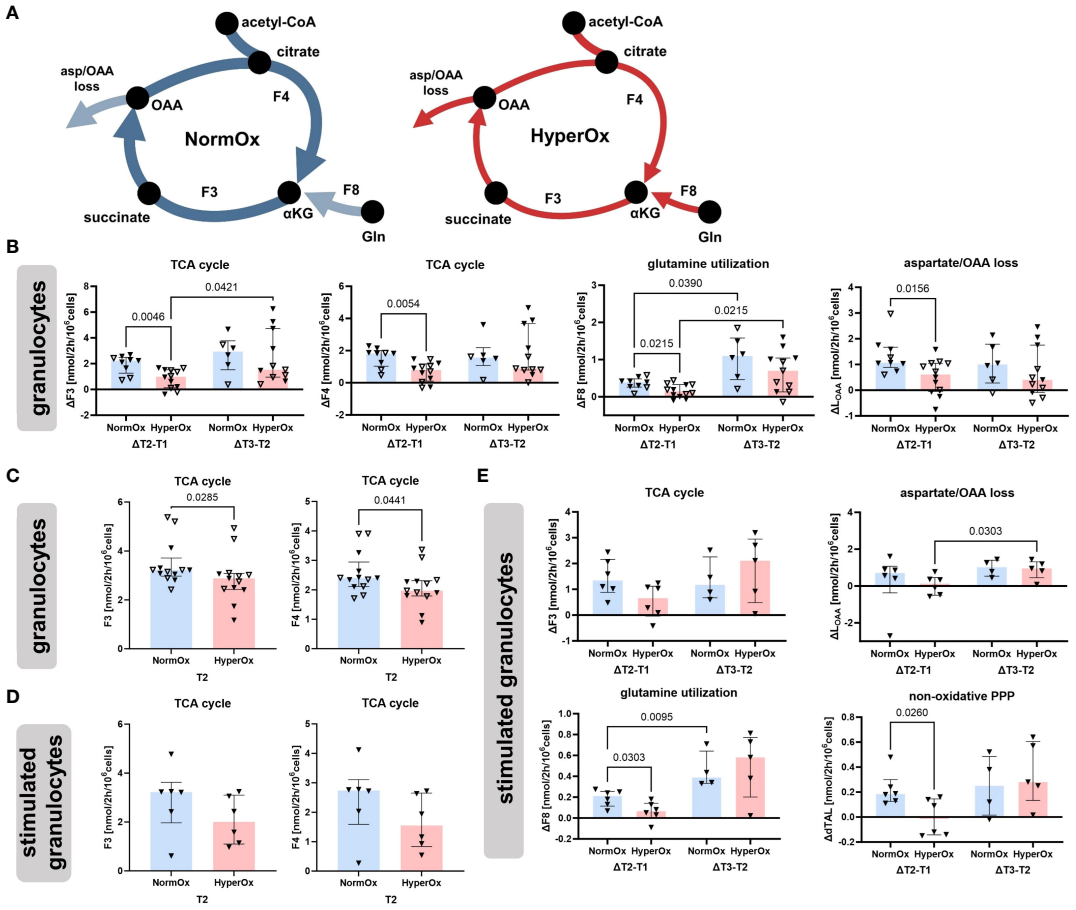

FIGURE 3
Effects of targeted hyperoxia on circulating granulocytes. Triangles with filled symbols indicate data originating from BMW animals, and empty symbols FBM data. Bars indicate the median with IQR (NormOx: blue bars, HyperOx: red bars). **(A)** The increase in TCA cycle activity from the first to the second measurement time point was reduced after cells were exposed to targeted hyperoxia. **(B)** Differences in time-related behavior of fluxes between NormOx and HyperOx groups. On the left side of each graph is the change in flux between T1 and T2, on the right side the change between T2 and T3. ΔT2-T1: NormOx (FBM n = 3, BMW n = 6), HyperOx (FBM n = 6, BMW n = 6), and ΔT3-T2: NormOx (FBM n = 2, BMW n = 4), HyperOx (FBM n = 6, BMW n = 5). **(C)** Absolute flux values of central TCA cycle fluxes at T2. Graphs including all measurement time points are available in Supplementary Figure 2. NormOx (FBM n = 7, BMW n = 6), HyperOx (FBM n = 7, BMW n = 6). **(D)** Absolute values of central TCA cycle fluxes at T2 in isolated granulocytes after *ex vivo* stimulation with *E.coli* bioparticles. Graphs including all measurement time points are available in Supplementary Figure 3. NormOx (BMW n = 6) and HyperOx (BMW n = 6). **(E)** Differences in time-related behavior of fluxes between NormOx and HyperOx groups in isolated granulocytes after stimulation with *E.coli* bioparticles. ΔT2-T1: NormOx (BMW n = 6), HyperOx (BMW n = 6), and ΔT3-T2: NormOx (BMW n = 4), HyperOx (BMW n = 4). F3: flux from α-ketoglutarate to oxaloacetate, F4: oxaloacetate to α-ketoglutarate. F8: glutamate to α-ketoglutarate. L_{OAA}: flux indicating amount of oxaloacetate/aspartate leaving the investigated network. dTAL: net flux in non-oxidative PPP activity (Q9-Q10). P-values are indicated in the graphs. We performed Mann-Whitney U tests for intergroup differences, and Kruskal-Wallis rank sum tests for time-related effects.

Targeted hyperoxia-mediated effects on circulating PBMCs were less pronounced. We found a hyperoxia-induced decrease in oxidative PPP utilization (Q3) from T2 to T3, while NormOx PBMCs increased Q3 in the same time frame. This decrease in ΔQ3 coincided with the same behavior in acetyl-CoA loss (L_{ACC}). Both pathways are involved in lipid synthesis, the former by providing NADPH and the latter by supplying acetyl-CoA. However, this effect only applied to BMW animals (Figure 4). Overall, effects of targeted hyperoxia on PBMCs pertained to the readaptation to normoxia rather than immediate effects at T2 and did not apply to animals with cardiovascular co-morbidity.

Graphs depicting absolute values for all measurement time points, $O_2^{\bullet-}$ production, and respiration are available in the supplements (Supplementary Figures 2–5).

3.2 Strain-specific differences in immunometabolism

As a second factor, we were interested in distinct and characteristic immunometabolic patterns that can be attributed to the different phenotypes of the FBM and BMW swine strains. Figure 5A shows that PBMCs and granulocytes from the hypercholesterolemic FBM animals displayed increased $O_2^{\bullet-}$ production levels compared to BMW animals after T1. With progressing measurement time points, this trend became clearer for both PBMCs (T2: $p = 0.1782$, T3: $p = 0.0012$) and granulocytes (T2: $p = 0.0045$, T3: $p = 0.0005$). Similarly, FBM animals also showed higher whole blood $O_2^{\bullet-}$ concentrations when combining data from both treatment groups (T2: $p = 0.0426$; T3: $p = 0.0464$).

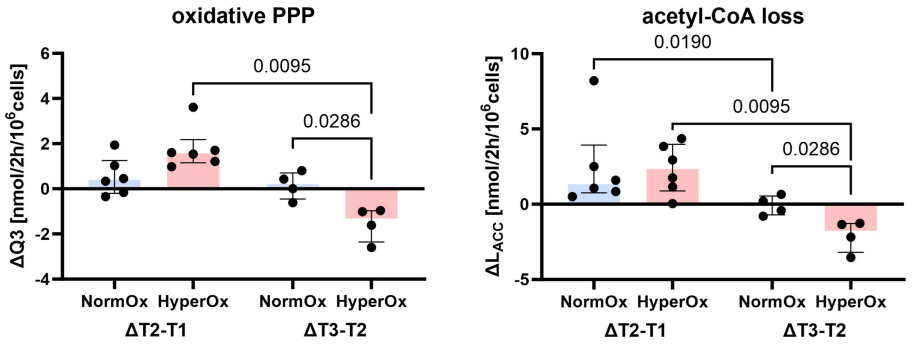

FIGURE 4
Effects of targeted hyperoxia on circulating PBMCs of BMW animals. Bars indicate the median with IQR (NormOx: blue bars, HyperOx: red bars). Fluxes with differences in time-related development between NormOx (ΔT2-T1: n = 6, ΔT3-T2: n = 4) and HyperOx (ΔT2-T1: n = 6, ΔT3-T2: n = 4) groups in isolated PBMCs from BMW animals. Q3: flux representing oxidative PPP activity. L_{ACC}: flux indicating amount of acetyl-CoA leaving the investigated network. P-values are indicated in the graphs. We performed Mann-Whitney U tests for intergroup differences, and Kruskal-Wallis rank sum tests for time-related effects.

As visualized in Figure 5A, BMW data points were much more "consistent", i.e., displayed a noticeably lower spread in $O_2^{\bullet-}$ data than FBM animals. Interestingly, FBM animals also required much more cardiovascular support, which manifested in doubled median NoA infusion rates required to achieve hemodynamic targets during the experiment (FBM 1.76 µg/kg·min (IQR 0.8;2.3), BMW 0.86 µg/kg·min (IQR 0.56;0.98), p = 0.031).

As shown in Figure 5B, stimulated granulocytes from BMW animals had higher phagocytic activity than FBMs at T1 and T2, which had normalized by T3. Furthermore, the percentage of granulocytes engaging in phagocytosis gradually decreased in FBMs, while BMW cells increased the fraction from T2 to T3. Unstimulated granulocytes also differed regarding their oxidative PPP. In FBM granulocytes, the oxidative PPP flux Q3 decreased upon ASDH and HS, while it increased slightly in BMWs (Figure 5C). This relationship reversed from T2 to T3 for both strains, however, with overall marginal differences between groups. We further detected a higher increase in the TCA cycle flux F4 in BMW animals between measurement time points T2 and T3.

Interestingly, PBMCs showed comparable behavioral patterns in terms of strain-specific differences as granulocytes (Figure 5D). However, additionally to patterns in oxidative PPP and TCA cycle utilization, we saw that in FBM PBMCs, the pyruvate-derived fraction of acetyl-CoA (F2) decreased upon ASDH and HS while it increased in BMWs; mirroring the pattern of the oxidative PPP. This trend in F2 was exclusive to PBMCs.

3.3 A principal component analysis revealed systematic changes in immunometabolism due to ASDH and HS

Principal component analysis is a powerful tool to detect systematic patterns in larger datasets. It enables to detect links between parameters (in our case flux analysis, mitochondrial respiration and $O_2^{\bullet-}$ production) by describing the variation of the data with fewer dimensions, called principal components. Data from all three measurement time points were included to find sets of fluxes/parameters that behave in systematic manners in response to ASDH and HS. Here, the time frame from T1 to T2 should indicate metabolic adaptations induced by ASDH, HS and the intervention, while T2 to T3 represents effects of ongoing intensive care and, for the HyperOx group, the readaptation to normoxia.

As third components usually covered only a minimal set of fluxes with no recognizable pattern, we focused on the first and second component in our analysis unless mentioned otherwise. They are included in the component overview in Table 1, which describes PCA nomenclature (A-D), all components, their linked parameters, and their covered variance. In all performed PCAs that included all measurement time points, we could not find clustering of HyperOx vs NormOx, or FBM vs BMW groups. We therefore conclude that data variation was mainly caused by cell type and measurement time points and less by intervention or swine strain.

PCA of all PBMC and granulocyte data revealed a cell type-specifc axis (A-PC 1, 37%) that confirmed increased $O_2^{\bullet-}$ production, glycolysis, and PPP metabolism in granulocytes compared to PBMCs, while PBMCs displayed comparatively higher glutamine-fueled TCA cycle utilization. The latter comprised of higher glutamine uptake (F8), the TCA cycle flux F3 and oxaloacetate/aspartate loss (L_{OAA}). A second axis matched negatively with progressing measurement time points (A-PC 2, 22%) and included fluxes of TCA cycle pathways and Routine respiration (Figure 6A).

When performing the PCA with only PBMC data, variation included two axes describing movement along measurement time points: B-PC 1 (34%) was positively linked to increased glycolysis, non-oxidative PPP (dTAL), Routine respiration and $O_2^{\bullet-}$ production with values moving along this axis from T1 to T2. The second component (B-PC 2, 22%) was negatively linked with glutamine-fueled TCA cycle activity, Routine respiration and $O_2^{\bullet-}$ production, implying that these pathways increased from T2 to T3 (Figure 6B). Even though there was no link between oxidative PPP activity and $O_2^{\bullet-}$ production in either PC, Spearman correlations showed linear relations between superoxide production and the

10.3389/fimmu.2023.1319986

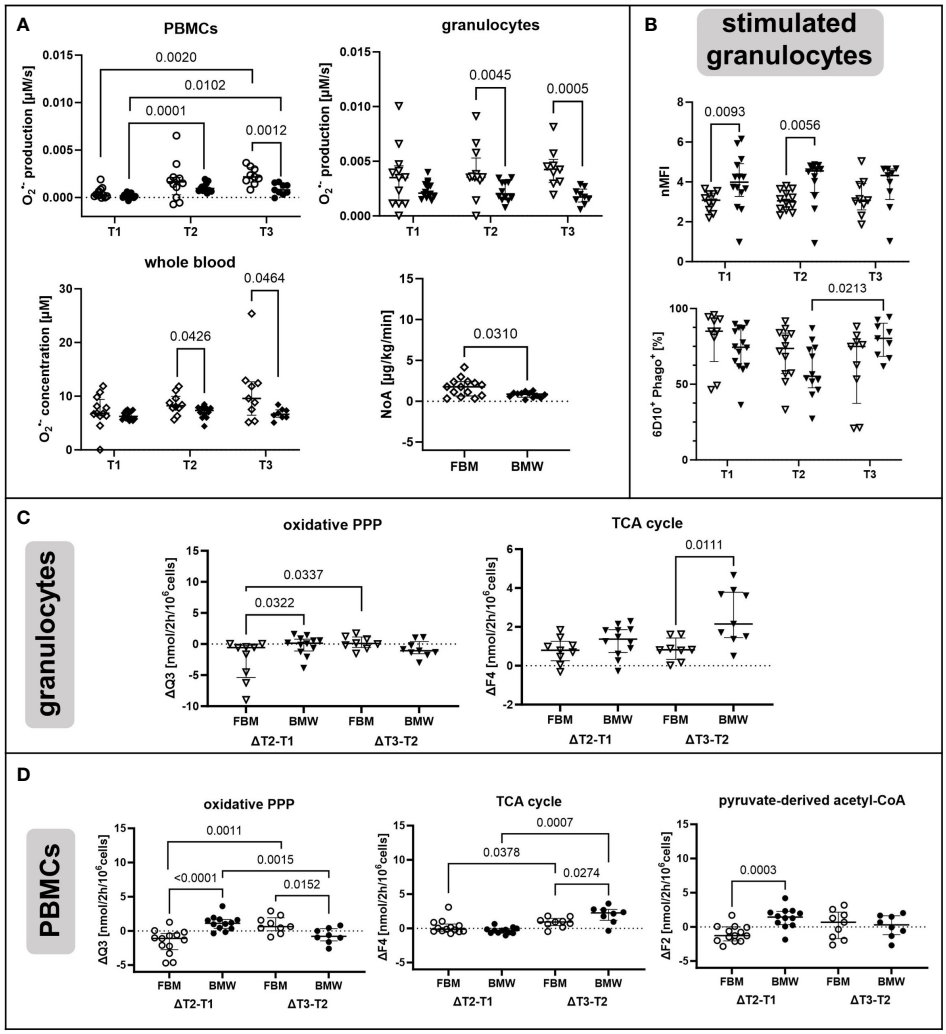

FIGURE 5
Strain-specific effects of ASDH and HS on immunometabolism. Diamonds indicate non-cell type-specific data. PBMCs are depicted as circles and granulocytes as triangles with filled symbols indicating data originating from BMW animals, and empty symbols FBM data. **(A)** $O_2^{\bullet-}$ production by PBMCs and granulocytes and $O_2^{\bullet-}$ concentration in whole blood as determined by ESR at the indicated measurement time points. Averaged noradrenalin (NoA) amount required during the experiment by FBM and BMW animals. PBMCs and granulocyte production: T1 (FBM n = 12, BMW n = 14), T2 (FBM n = 12, BMW n = 12), T3 (FBM n = 9, BMW n = 9). Whole blood concentration: T1 (FBM n = 12, BMW n = 14), T2 (FBM n = 10, BMW n = 12), T3 (FBM n = 9, BMW n = 8). NoA administration: FBM n = 14, BMW n = 12. **(B)** Phagocytic activity of *E.coli* bioparticle-stimulated granulocytes. Data is either presented as normalized mean fluorescence intensity (nMFI) or fraction of phagocytic granulocytes within the granulocyte subset ($6D10^+$ $Phago^+$). T1 (FBM n = 10, BMW n = 14), T2 (FBM n = 12, BMW n = 12), T3 (FBM n = 9, BMW n = 9). **(C)** Fluxes with differences in time-related development in granulocytes between FBM and BMW groups. On the left side of each graph is the change in flux between T1 and T2, on the right side the change between T2 and T3. ΔT2-T1: FBM n = 9, BMW n = 12, and ΔT3-T2: FBM n = 8, BMW n = 9. **(D)** Fluxes with differences in time-related development in PBMCs between FBM and BMW groups. ΔT2-T1: FBM n = 13, BMW n = 12, and ΔT3-T2: FBM n = 9, BMW n = 8. Q3: flux representing oxidative PPP activity. F2: pyruvate-derived fraction of acetyl-CoA. F4: flux from oxaloacetate to α-ketoglutarate. P-values are indicated in the graphs. We performed Mann-Whitney U tests for intergroup differences, and Kruskal-Wallis rank sum tests for time-related effects.

oxidative PPP flux Q3 (r< 0.57), TCA cycle flux F3 (r< 0.40), and Routine respiration (r< 0.52), respectively (data not shown).

In granulocyte data, a first component (C-PC 1, 30%) encompassed fluxes of increased glucose uptake (Q1), glycolysis and PPP. This axis could not be assigned to an identifiable data subset but made up a large proportion in data variance. A second component (C-PC 2) described increased glutamine-fueled TCA cycle fluxes including increased pyruvate carboxylase (F6), Routine respiration, and negatively linked pyruvate-derived acetyl-CoA (F2) and acetyl-CoA loss (L_{ACC}). This component coincided with increasing measurement time points (Figure 6C). In contrast to PBMC data, there was no correlation between $O_2^{\bullet-}$ production, TCA cycle or oxidative PPP activity (Q3). When including flux data from both the granulocyte and stimulated granulocyte dataset, we yielded one larger component linked to glycolytic, non-oxidative PPP (dTAL) and TCA cycle pathways (D-PC 1, 39%) and loosely aligning with increasing measurement time points, and a smaller second component (D-PC 2) explaining about 18% of data variance. The latter component unambiguously separated granulocytes from stimulated granulocytes and entailed variance in PPP fluxes and $O_2^{\bullet-}$ production (Figure 6D).

TABLE 1 Results from principal component analysis.

analyzed dataset	name PCA	#PC	var [%]	dir	metabolic pathways	linked parameters	separated groups
PBMCs & granulocytes all strains T1-T3	A	PC 1	36.8	+	glycolysis PPP	Glyc1, Glyc2, Q1, Q2, Q3, Q4, Q11, dTAL, F2, F5, Inp_{Pyr}, L_{ACC}, $O_2^{\bullet-}$ production	granulo-cytes PBMCs Figure 6A
				–	TCA cycle	F3, F8, L_{OAA}	
		PC 2	21.5	+		Inp_{Pyr}	T1 → T3 Figure 6A
				–	TCA cycle	F3, F4, F6, F8, L_{OAA}, L_{Pyr} Routine respiration	
		PC 3	11.5	+		F5, F9	
				–		F7	
PBMCs all strains T1-T3	B	PC 1	33.8	+	glycolysis non-ox PPP	Glyc1, Glyc2, Q1, Q2, Q11, dTAL, F4, F5, F7, L_{Pyr}, Inp_{Pyr}, L_{ACC}, Routine respiration, $O_2^{\bullet-}$ production	T1 → T2 Figure 6B
				–		L_{OAA}	
		PC 2	21.9	+		Inp_{Pyr}	T2 → T3 Figure 6B
				–	TCA cycle	F3, F4, F6, F7, F8, L_{OAA}, Routine respiration, $O_2^{\bullet-}$ production	
		PC 3	13.2	+		F2, F9, L_{OAA}	
				–		F7	
granulocytes all strains T1-T3	C	PC 1	30.3	+	glycolysis PPP	Glyc1, Glyc2, Q1, Q2, Q3, Q4, Q11, dTAL, Inp_{Pyr}	
				–		F6	
		PC 2	29.3	+		F2, L_{ACC}	T1 → T3 Figure 6C
				–	TCA cycle	F3, F4, F6, F8, L_{OAA}, Routine respiration	
		PC 3	10.0	+		F7	
				–			
granulocytes & stimulated granulocytes BMW T1-T3	D	PC 1	39.3	+	glycolysis non-ox PPP TCA cycle	Glyc1, Glyc2, Q1, Q2, Q11, dTAL, F3, F4, F5, F8, F9, L_{OAA}, L_{Pyr}	T1 → T3 Figure 6D
				–			
		PC 2	18.2	+	PPP	Q3, Q4, Q11, dTAL, L_{ACC}, $O_2^{\bullet-}$ production	stimulation Figure 6D
				–		F5	
		PC 3	17.6	+	non-ox PPP	Q11, dTAL	
				–		F7, L_{ACC}	

We performed PCA with various datasets to identify hidden factors or processes of systematic metabolic change. Complete nomenclature of fluxes is provided in Supplementary Figure 1. var, variance; dir, direction.

The third, comparatively large component entailed further variation in non-oxidative PPP activity (D-PC 3, 18%).

4 Discussion

The present work investigated the effect of targeted hyperoxemia on alterations of immunometabolism in granulocytes and PBMCs in swine with (FBM) and without (BMW) cardiovascular comorbidity. Regarding the clinical parameters, both studies found improved modified Glasgow Coma Scale (MGCS) values in the hyperoxemia groups (7), but only FBM swine had yielded higher brain tissue PO_2 levels during targeted hyperoxemia (8). Neither study reported any other major beneficial or deleterious effects of hyperoxemia during resuscitation and intensive care. As oxygen availability is a major factor in immunometabolism, our study intended to uncover potential undetected effects of targeted hyperoxemia, the swine strain used, and ASDH and HS on circulating immune cells. PBMCs and granulocytes were isolated from whole blood before ASDH and HS (T1), 24 h post ASDH and HS (T2), i.e. at the end of the exposure to targeted hyperoxia, and 48 h post ASDH and HS (T3). Effects of HyperOx or NormOx were expected to manifest at T2 earliest, as treatment was initiated only upon the beginning of resuscitation.

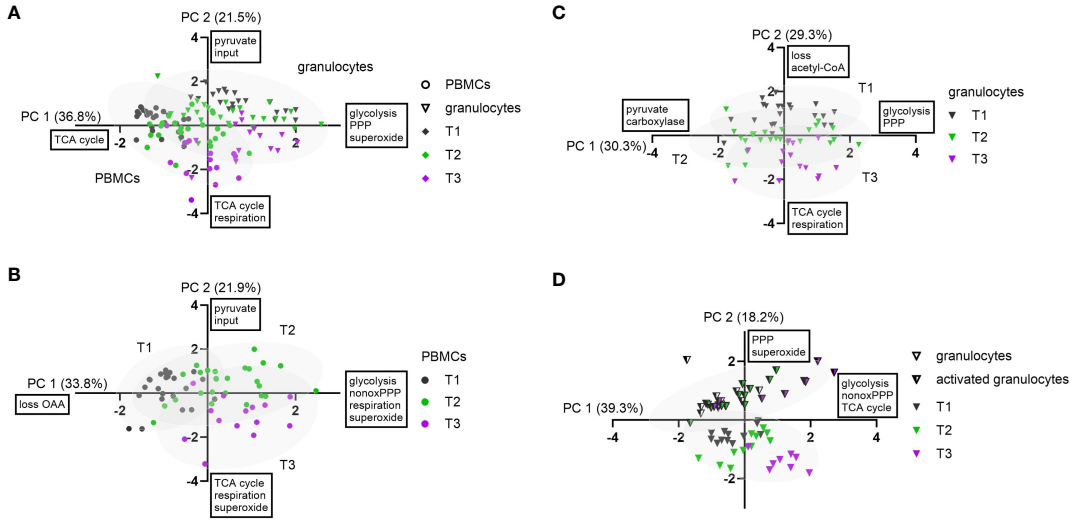

FIGURE 6
Principal component analysis of experimental data. Granulocytes are depicted as triangles and PBMCs as circles. Stimulated granulocytes are indicated as half-filled triangles. For the measurement time points, the following color code was chosen: T1: grey; T2: green; T3: violet. PC 1 and PC 2 scores were plotted in a x-y graph for each dataset. **(A)** Combined data from granulocytes and PBMCs (n = 123, FBM and BMW). Granulocyte and PBMC data are each depicted with their 95% confidence interval (CI) as grey ellipses. **(B)** PCA of combined PBMC data (n = 63, FBM and BMW). Data from each measurement time point are shown with their 95% CI. **(C)** PCA of combined granulocyte data (n = 60, FBM and BMW). Data from each measurement time point are shown with their 95% CI. **(D)** PCA of combined data of BMW granulocytes and *E.coli* bioparticle-stimulated granulocytes (n = 64, BMW). Data from granulocytes and stimulated granulocytes are each presented with their 95% CI.

Neutrophilic granulocytes are severely impacted by substrate and oxygen availability (35). They comprise up to 50 – 70% of the leukocyte population, making them the most abundant circulating immune cells. Neutrophils fight pathogens with a variety of mechanisms including phagocytosis, respiratory burst, and neutrophil extracellular trap (NET) generation. The metabolism of neutrophils is known to be highly glycolytic. Metabolized glucose is broken down into two pyruvate molecules, of which the majority (~ 97%) is converted into lactate while ~ 2% is used to fuel minimal TCA cycle activity. Granulocytes contain less mitochondria than other circulating immune cells, but require intact mitochondrial function for maintaining extended neutrophil activity (36). The PPP, another glucose dependent pathway, is required for ROS production and NETosis (37, 38). This general behavioral pattern is represented in our data showing minimal mitochondrial respiration and otherwise heavy dependence on glycolytic pathways (A-PC 1). After incubation with *E.coli*-derived particles, we saw that both the $O_2^{\bullet-}$ production and the oxidative and non-oxidative PPP activity were markedly increased (D-PC 2). Interestingly, phagocytic stimulation did not impact lactate production. Awasthi et al. have referred lactate production as measured by extracellular acidification to be essential for NETosis (39). Hence, our data suggests a lactate-independent focus on respiratory burst and phagocytosis rather than NETosis by porcine neutrophils that were stimulated *ex vivo*.

With progressing measurement time points, granulocytes increasingly engaged in glutamine-fueled TCA cycle utilization, correlating with increased mitochondrial respiration (C-PC 2). This metabolic adaptation can be explained by greater fractions of immature granulocytes with experiment progression (due to HS and/or blood sampling for immune cell isolation), as *de novo* synthesized granulocytes typically rely on TCA cycle activity and oxidative phosphorylation during differentiation (40–42). The increase in TCA cycle activity was linked with aspartate production (aspartate/oxaloacetate "loss"), which is essential for nucleotide and protein synthesis. The linkage of respiration in this axis can be explained by proliferating cells requiring respiration for aspartate synthesis (43, 44). However, while Sullivan et al. and Birsoy et al. attributed the increase in aspartate synthesis to reductive carboxylation of α-ketoglutarate, our model could not confirm these assumptions, as the utilization of this pathway was not reflected in our labeling patterns (e.g. a higher $^{13}C_5$ glutamine tracer-induced m+3 fraction on aspartate). A second axis detected by PCA encompassed glycolysis and both oxidative and non-oxidative PPP activity including ribose-5-phosphate synthesis, indicating variance in neutrophil activation and proliferation (C-PC 1). Surprisingly, in contrast to activated granulocytes, there was no relation or linkage between $O_2^{\bullet-}$ production and oxidative PPP utilization in unstimulated granulocytes. This suggests that baseline $O_2^{\bullet-}$ production in granulocytes was supported by pathways other than the PPP.

Investigation of PBMCs was more complex than granulocytes due to the very diverse nature of this cell population. Interestingly, by applying PCA we saw that they moved along two distinct metabolic axes over the course of the experiment: During ASDH, HS and subsequent resuscitation, PBMCs firstly increased glycolysis and non-oxidative PPP activity (B-PC 1), and later TCA cycle activity including glutamine uptake and oxaloacetate/aspartate production during long term intensive care (B-PC 2). Both axes were linked with increased mitochondrial respiration and $O_2^{\bullet-}$ production. The linkage of TCA cycle activity, aspartate production, and Routine respiration of the later measurement

time points has been similarly observed in granulocytes, while the correlation of $O_2^{\bullet-}$ production with TCA cycle activity, Routine respiration and non-oxidative PPP activity was exclusive to PBMCs. Even though we saw a correlation between $O_2^{\bullet-}$ production and the oxidative PPP flux Q3 according to the Spearman test, neither component included a linkage of these two parameters. This raises the possibility that changes in $O_2^{\bullet-}$ production might have been mediated by superoxide formation within the respiratory chain (45). Li et al. suggested mitochondrial electron transport chain-derived $O_2^{\bullet-}$ as a source of ROS in monocytes and macrophages, which might contribute to this relation (46). Interestingly, Zink et al. reported no effect of ASDH on PBMC metabolism using the same methods, although with a much more rudimentary metabolic model (47). Moreover, while ASDH was combined with HS in our current study, Zink et al. had investigated ASDH alone in the absence of HS and, hence, without systemic oxygen debt. Therefore, the PCs 1 and 2 aligning with time-dependent effects might be mainly attributed to HS as opposed to ASDH.

The FBM swine strain is characterized by a homozygous R84C mutation in the low-density lipoprotein receptor, leading to a genetic predisposition for atherosclerosis and coronary artery disease whose progression was promoted by a cholesterol-enriched diet. Hypercholesterolemia is known to promote inflammation, e.g., *via* neutrophil activation accompanied by NETosis and elevated ROS production (48). We saw that FBM animals presented with both elevated $O_2^{\bullet-}$ concentration levels in whole blood and $O_2^{\bullet-}$ production rates by granulocytes (T2: $p = 0.0045$; T3: $p = 0.0005$) and PBMCs (T3: $p = 0.0012$). In conclusion, the FBM phenotype increased $O_2^{\bullet-}$ concentration in whole blood and $O_2^{\bullet-}$ production rates by immune cells after induction of ASDH and HS, with a more delayed impact on PBMCs. As mentioned before, $O_2^{\bullet-}$ production as measured with ESR was not linked to fluxes of the oxidative PPP and, in conclusion, acts independently in non-stimulated cells, while phagocytic activation leads to a mutual increase. As a metabolism- and phenotype-independent cause we suspected an impact of noradrenalin infusion, since FBM animals required more NoA support during ASDH and HS than BMW animals. However, the role of catecholamines, in particular NoA, on immune cell function in shock and sepsis is complex and cannot be easily mapped (49). There are a variety of known pro- and anti-inflammatory mechanisms, like pro-inflammatory activity *via* activation of α-receptors (50, 51), high doses of NoA leading to increased ROS and apoptosis in PBMCs (52), prevention of immune cell mobilization in murine trauma (53), or potential deactivation of catecholamines by auto-oxidation (54). Therefore, an atherosclerosis-induced effect on $O_2^{\bullet-}$ production that is not mediated by the metabolic pathways covered in this study has higher plausibility. Another potential factor could be the age of animals, as FBMs were about twice as old as BWM animals due to the required feeding period of the cholesterol-enriched diet (a median of 38 *vs* 16 months, respectively). Overall, FBM and BMW were overlapping in the PCA and could therefore not cleanly be separated based on different flux behavior in ^{13}C-MFA analysis.

While the effect of hypoxia on circulating immune cells is often a topic of investigation, information on hyperoxia-induced changes on metabolism is scarce. Our results suggest that targeted hyperoxemia had attenuated the granulocyte-specific increase in glutamine-fueled TCA cycle activity 24 h post shock. Sagone et al. suggested impaired mitochondrial activity in lymphocytes by hyperoxia, although our results did not replicate the effect of hyperoxia on *i)* glycolysis, *ii)* mitochondrial respiration, and *iii)* other lymphocyte subsets (55). Nevertheless, our study suggests a specific inhibition of TCA cycle acceleration in circulating granulocytes in response to ASDH and HS, without affecting mitochondrial respiration. This could also be caused by a decreased fraction of immature granulocytes. In contrast to granulocytes, there was no consistent effect of hyperoxia across multiple analyzes in PBMCs, except for a slight trend in the utilization of lipid synthesis indicated by the NADPH-providing oxidative PPP and the acetyl-CoA loss. Cells impacted by targeted hyperoxia had a more pronounced decrease in their lipid biosynthesis from the end of differential treatment until the end of the experiment than cells from the control group. However, this effect was only present in animals without cardiovascular co-morbidity.

4.1 Limitations of the study

As mentioned above, the diversity of PBMCs greatly complicated data interpretation. Metabolic plasticity could both be attributed to metabolic switches and changes in population composition. To a lower degree, similar problems arose for granulocytes in terms of mature/immature subsets with different metabolic profiles. Another limitation was sample availability: especially for the NormOx FBM granulocyte T1 data set there were problems with limited cell numbers after purification, as cell requirements were high but the maximally tolerable amount of blood drawn at the individual measurement time points had yielded too few granulocyte numbers. Missing data points of early experiment terminations exacerbated this issue. This was especially relevant for principal component analysis, which greatly benefits from rich data sets, and for statistical analyzes with repeated measures. A third limitation was caused by flux analysis, as not all flux determinations were equally precise. Most reliable were TCA cycle and glycolytic fluxes, while fluxes with greater distance from metabolites captured with GC/MS suffered in precision. This was especially the case for "small" inputs and outputs at pyruvate and acetyl-CoA nodes and for PPP fluxes, as the latter could only be determined through lactate labels. Main PPP metabolites, i.e., sugar phosphates, could not be captured with our derivatization method.

5 Conclusion

In a model of resuscitated porcine ASDH and HS, we saw that ventilation with increased inspiratory O_2 concentrations to achieve target a $P_aO_2 = 200 – 250$ mmHg for 24 h after treatment initiation did not impact mitochondrial respiration of PBMCs or granulocytes. However, Bayesian ^{13}C-MFA results indicated a

reduction in TCA cycle activity in granulocytes compared to cells exposed to normoxemia in the same time period. This change in metabolism did not seem to affect granulocytes' ability to perform phagocytosis or produce superoxide radicals. Animals with a hypercholesterolemic phenotype presented with higher superoxide burden than healthy pigs.

Data availability statement

The raw data supporting the conclusions of this article will be made available by the authors, without undue reservation.

Ethics statement

The animal study was approved by Regierungspräsidium Tübingen, Germany, Reg.-Nr. 1316. The study was conducted in accordance with the local legislation and institutional requirements.

Author contributions

EW: Formal analysis, Investigation, Methodology, Software, Writing – original draft, Writing – review & editing. JV: Conceptualization, Formal analysis, Methodology, Resources, Software, Supervision, Validation, Writing – original draft, Writing – review & editing. MH: Investigation, Methodology, Software, Writing – review & editing. UW: Investigation, Methodology. NS: Investigation. TK: Investigation, Validation. TD: Investigation, Validation. DM: Investigation, Writing – review & editing. AH: Investigation. MG: Investigation. FM: Investigation. RM: Investigation. SM: Investigation. TM: Funding acquisition, Project administration. PA: Investigation, Project administration. EC: Conceptualization, Investigation, Methodology. PR: Writing – review & editing, Conceptualization, Funding acquisition, Project administration, Resources, Supervision, Writing – original draft. FZ: Conceptualization, Formal analysis, Investigation, Methodology, Writing – original draft, Writing – review & editing.

Funding

The author(s) declare financial support was received for the research, authorship, and/or publication of this article. This study was funded by the Deutsche Forschungsgemeinschaft (German Research Foundation, DFG): projects 251293561 (Collaborative Research Center, CRC 1149), 465409392 (Research Unit, FOR 5417), and 278012962 (Ulm University Research Training Group PULMOSENS, GRK 2203).

Acknowledgments

We thank Rosemarie Meyer, Bettina Stahl, Edina Ahmetovic, Carolin Renner, and Vittoria Passarelli for their excellent technical assistance.

Conflict of interest

The authors declare that the research was conducted in the absence of any commercial or financial relationships that could be construed as a potential conflict of interest.

Publisher's note

Supplementary material

The Supplementary Material for this article can be found online at: https://www.frontiersin.org/articles/10.3389/fimmu.2023.1319986/full#supplementary-material

References

1. Barbee RW, Reynolds PS, Ward KR. Assessing shock resuscitation strategies by oxygen debt repayment. *Shock* (2010) 33:113–22. doi: 10.1097/SHK.0b013e3181b8569d

2. Veenith TV, Carter EL, Geeraerts T, Grossac J, Newcombe VF, Outtrim J, et al. Pathophysiologic mechanisms of cerebral ischemia and diffusion hypoxia in traumatic brain injury. *JAMA Neurol* (2016) 73:542–50. doi: 10.1001/jamaneurol.2016.0091

3. Vincent J-L, de Backer D. Circulatory shock. *N Engl J Med* (2013) 369:1726–34. doi: 10.1056/NEJMra1208943

4. Madias JE, Madias NE, Hood WB. Precordial ST-segment mapping. 2. Effects of oxygen inhalation on ischemic injury in patients with acute myocardial infarction. *Circulation* (1976) 53:411–7. doi: 10.1161/01.cir.53.3.411

5. Hartmann C, Loconte M, Antonucci E, Holzhauser M, Hölle T, Katzsch D, et al. Effects of hyperoxia during resuscitation from hemorrhagic shock in swine with preexisting coronary artery disease. *Crit Care Med* (2017) 45:e1270–9. doi: 10.1097/CCM.0000000000002767

6. Singer M, Young PJ, Laffey JG, Asfar P, Taccone FS, Skrifvars MB, et al. Dangers of hyperoxia. *Crit Care* (2021) 25:440. doi: 10.1186/s13054-021-03815-y

7. Datzmann T, Münz F, Hoffmann A, Moehrke E, Binzenhöfer M, Gröger M, et al. An exploratory study investigating the effect of targeted hyperoxemia in a randomized controlled trial in a long-term resuscitated model of combined acute subdural hematoma and hemorrhagic shock in cardiovascular healthy pigs. *Front Immunol* (2023) 14:1123196. doi: 10.3389/fimmu.2023.1123196

8. Datzmann T, Messerer DA, Münz F, Hoffmann A, Gröger M, Mathieu R, et al. The effect of targeted hyperoxemia in a randomized controlled trial employing a long-term resuscitated, model of combined acute subdural hematoma and hemorrhagic shock in swine with coronary artery disease: An exploratory, hypothesis-generating study. *Front Med (Lausanne)* (2022) 9:971882. doi: 10.3389/fmed.2022.971882

9. Demiselle J, Calzia E, Hartmann C, Messerer DA, Asfar P, Radermacher P, et al. Target arterial PO2 according to the underlying pathology: a mini-review of the

available data in mechanically ventilated patients. *Ann Intensive Care* (2021) 11:88. doi: 10.1186/s13613-021-00872-y

10. Huber-Lang M, Lambris JD, Ward PA. Innate immune responses to trauma. *Nat Immunol* (2018) 19:327–41. doi: 10.1038/s41590-018-0064-8

11. Krzywinska E, Stockmann C. Hypoxia, metabolism and immune cell function. *Biomedicines* (2018) 6:1–20. doi: 10.3390/biomedicines6020056

12. Hafner C, Wu J, Tiboldi A, Hess M, Mitulovic G, Kaun C, et al. Hyperoxia induces inflammation and cytotoxicity in human adult cardiac myocytes. *Shock* (2017) 47:436–44. doi: 10.1097/SHK.0000000000000740

13. Hafner C, Wu J, Soto-Gonzalez L, Kaun C, Stojkovic S, Wojta J, et al. Moderate hyperoxia induces inflammation, apoptosis and necrosis in human umbilical vein endothelial cells: An *in-vitro* study. *Eur J Anaesthesiol* (2017) 34:141–9. doi: 10.1097/EJA.0000000000000593

14. Hafner C, Pramhas S, Schaubmayr W, Assinger A, Gleiss A, Tretter EV, et al. Brief high oxygen concentration induces oxidative stress in leukocytes and platelets: A randomized cross-over pilot study in healthy male volunteers. *Shock* (2021) 56:384–95. doi: 10.1097/SHK.0000000000001728

15. O'Reilly PJ, Hickman-Davis JM, Davis IC, Matalon S. Hyperoxia impairs antibacterial function of macrophages through effects on actin. *Am J Respir Cell Mol Biol* (2003) 28:443–50. doi: 10.1165/rcmb.2002-0153OC

16. O'Neill LA, Kishton RJ, Rathmell J. A guide to immunometabolism for immunologists. *Nat Rev Immunol* (2016) 16:553–65. doi: 10.1038/nri.2016.70

17. O'Neill LA, Pearce EJ. Immunometabolism governs dendritic cell and macrophage function. *J Exp Med* (2016) 213:15–23. doi: 10.1084/jem.20151570

18. de Falco B, Giannino F, Carteni F, Mazzoleni S, Kim D-H. Metabolic flux analysis: a comprehensive review on sample preparation, analytical techniques, data analysis, computational modelling, and main application areas. *RSC Adv* (2022) 12:25528–48. doi: 10.1039/d2ra03326g

19. Buescher JM, Antoniewicz MR, Boros LG, Burgess SC, Brunengraber H, Clish CB, et al. A roadmap for interpreting (13)C metabolite labeling patterns from cells. *Curr Opin Biotechnol* (2015) 34:189–201. doi: 10.1016/j.copbio.2015.02.003

20. Wolfschmitt E-M, Hogg M, Vogt JA, Zink F, Wachter U, Hezel F, et al. The effect of sodium thiosulfate on immune cell metabolism during porcine hemorrhage and resuscitation. *Front Immunol* (2023) 14:1125594. doi: 10.3389/fimmu.2023.1125594

21. Olsen AK, Hansen AK, Jespersen J, Marckmann P, Bladbjerg EM. The pig as a model in blood coagulation and fibrinolysis research. *Scand J Lab Anim Sci* (1999) 26 (4). doi: 10.23675/SJLAS.V26I4.850

22. Nichols TC, Bellinger DA, Merricks EP, Raymer RA, Kloos MT, Defriess N, et al. Porcine and canine von Willebrand factor and von Willebrand disease: hemostasis, thrombosis, and atherosclerosis studies. *Thrombosis* (2010) 2010:461238. doi: 10.1155/2010/461238

23. Datzmann T, Hoffmann A, McCook O, Merz T, Wachter U, Preuss J, et al. Effects of sodium thiosulfate (Na2S2O3) during resuscitation from hemorrhagic shock in swine with preexisting atherosclerosis. *Pharmacol Res* (2020) 151:104536. doi: 10.1016/j.phrs.2019.104536

24. Messerer DA, Gaessler H, Hoffmann A, Gröger M, Benz K, Huhn A, et al. The H2S donor sodium thiosulfate (Na2S2O3) does not improve inflammation and organ damage after hemorrhagic shock in cardiovascular healthy swine. *Front Immunol* (2022) 13:901005. doi: 10.3389/fimmu.2022.901005

25. Münz F, Wolfschmitt E-M, Zink F, Abele N, Hogg M, Hoffmann A, et al. Porcine blood cell and brain tissue energy metabolism: Effects of "early life stress". *Front Mol Biosci* (2023) 10:1113570. doi: 10.3389/fmolb.2023.1113570

26. Chance B, Williams GR. Respiratory enzymes in oxidative phosphorylation. III. The steady state. *J Biol Chem* (1955) 217:409–27. doi: 10.1016/S0021-9258(19)57191-5

27. Chan LY, Yim EK, Choo AB. Normalized median fluorescence: an alternative flow cytometry analysis method for tracking human embryonic stem cell states during differentiation. *Tissue Eng Part C Methods* (2013) 19:156–65. doi: 10.1089/ten.TEC.2012.0150

28. Hogg M, Wolfschmitt E-M, Wachter U, Zink F, Radermacher P, Vogt JA. Bayesian 13 C-metabolic flux analysis of parallel tracer experiments in granulocytes: a directional shift within the non-oxidative pentose phosphate pathway supports phagocytosis. *Metabolites* (2024) 14:24. doi: 10.3390/metabo14010024

29. van Winden WA, Wittmann C, Heinzle E, Heijnen JJ. Correcting mass isotopomer distributions for naturally occurring isotopes. *Biotechnol Bioeng* (2002) 80:477–9. doi: 10.1002/bit.10393

30. Stan Development Team. *RStan: the R interface to Stan*. Available at: https://mc-stan.org/.

31. Stifel U, Wolfschmitt E-M, Vogt J, Wachter U, Vettorazzi S, Tews D, et al. Glucocorticoids coordinate macrophage metabolism through the regulation of the tricarboxylic acid cycle. *Mol Metab* (2022) 57:101424. doi: 10.1016/j.molmet.2021.101424

32. Antoniewicz MR, Kelleher JK, Stephanopoulos G. Elementary metabolite units (EMU): a novel framework for modeling isotopic distributions. *Metab Eng* (2007) 9:68–86. doi: 10.1016/j.ymben.2006.09.001

33. Efron B, Tibshirani R. Bootstrap methods for standard errors, confidence intervals, and other measures of statistical accuracy. *Statist Sci* (1986) 1:54–75. doi: 10.1214/ss/1177013815

34. Babamoradi H, van den Berg F, Rinnan Å. Bootstrap based confidence limits in principal component analysis — A case study. *Chemometrics Intelligent Lab Syst* (2013) 120:97–105. doi: 10.1016/j.chemolab.2012.10.007

35. Injarabian L, Devin A, Ransac S, Marteyn BS. Neutrophil Metabolic Shift during their Lifecycle: Impact on their Survival and Activation. *Int J Mol Sci* (2019) 21:1–23. doi: 10.3390/ijms21010287

36. Fossati G, Moulding DA, Spiller DG, Moots RJ, White MR, Edwards SW. The mitochondrial network of human neutrophils: role in chemotaxis, phagocytosis, respiratory burst activation, and commitment to apoptosis. *J Immunol* (2003) 170:1964–72. doi: 10.4049/jimmunol.170.4.1964

37. Baillet A, Hograindleur M-A, El Benna J, Grichine A, Berthier S, Morel F, et al. Unexpected function of the phagocyte NADPH oxidase in supporting hyperglycolysis in stimulated neutrophils: key role of 6-phosphofructo-2-kinase. *FASEB J* (2017) 31:663–73. doi: 10.1096/fj.201600720R

38. Azevedo EP, Rochael NC, Guimarães-Costa AB, de Souza-Vieira TS, Ganilho J, Saraiva EM, et al. A metabolic shift toward pentose phosphate pathway is necessary for amyloid fibril- and phorbol 12-myristate 13-acetate-induced neutrophil extracellular trap (NET) formation. *J Biol Chem* (2015) 290:22174–83. doi: 10.1074/jbc.M115.640094

39. Awasthi D, Nagarkoti S, Sadaf S, Chandra T, Kumar S, Dikshit M. Glycolysis dependent lactate formation in neutrophils: A metabolic link between NOX-dependent and independent NETosis. *Biochim Biophys Acta Mol Basis Dis* (2019) 1865:165542. doi: 10.1016/j.bbadis.2019.165542

40. Jeon J-H, Hong C-W, Kim EY, Lee JM. Current understanding on the metabolism of neutrophils. *Immune Netw* (2020) 20:e46. doi: 10.4110/in.2020.20.e46

41. Riffelmacher T, Clarke A, Richter FC, Stranks A, Pandey S, Danielli S, et al. Autophagy-dependent generation of free fatty acids is critical for normal neutrophil differentiation. *Immunity* (2017) 47:466–480.e5. doi: 10.1016/j.immuni.2017.08.005

42. Simsek T, Kocabas F, Zheng J, Deberardinis RJ, Mahmoud AI, Olson EN, et al. The distinct metabolic profile of hematopoietic stem cells reflects their location in a hypoxic niche. *Cell Stem Cell* (2010) 7:380–90. doi: 10.1016/j.stem.2010.07.011

43. Sullivan LB, Gui DY, Hosios AM, Bush LN, Freinkman E, Vander Heiden MG. Supporting aspartate biosynthesis is an essential function of respiration in proliferating cells. *Cell* (2015) 162:552–63. doi: 10.1016/j.cell.2015.07.017

44. Birsoy K, Wang T, Chen WW, Freinkman E, Abu-Remaileh M, Sabatini DM. An essential role of the mitochondrial electron transport chain in cell proliferation is to enable aspartate synthesis. *Cell* (2015) 162:540–51. doi: 10.1016/j.cell.2015.07.016

45. Quijano C, Trujillo M, Castro L, Trostchansky A. Interplay between oxidant species and energy metabolism. *Redox Biol* (2016) 8:28–42. doi: 10.1016/j.redox.2015.11.010

46. Li Y, Zhu H, Kuppusamy P, Zweier JL, Trush MA. Mitochondrial electron transport chain-derived superoxide exits macrophages: implications for mononuclear cell-mediated pathophysiological processes. *React Oxyg Species (Apex)* (2016) 1:81–98. doi: 10.20455/ros.2016.815

47. Zink F, Vogt J, Wachter U, Hartert J, Horchler M, Zhang X, et al. Effects of acute subdural hematoma-induced brain injury on energy metabolism in peripheral blood mononuclear cells. *Shock* (2021) 55:407–17. doi: 10.1097/SHK.0000000000001642

48. Dhawan UK, Bhattacharya P, Narayanan S, Manickam V, Aggarwal A, Subramanian M. Hypercholesterolemia impairs clearance of neutrophil extracellular traps and promotes inflammation and atherosclerotic plaque progression. *Arterioscler Thromb Vasc Biol* (2021) 41:2598–615. doi: 10.1161/ATVBAHA.120.316389

49. Hartmann C, Radermacher P, Wepler M, Nußbaum B. Non-hemodynamic effects of catecholamines. *Shock* (2017) 48:390–400. doi: 10.1097/SHK.0000000000000879

50. Stolk RF, van der Pasch E, Naumann F, Schouwstra J, Bressers S, van Herwaarden AE, et al. Norepinephrine dysregulates the immune response and compromises host defense during sepsis. *Am J Respir Crit Care Med* (2020) 202:830–42. doi: 10.1164/rccm.202002-0339OC

51. Flierl MA, Rittirsch D, Nadeau BA, Sarma JV, Day DE, Lentsch AB, et al. Upregulation of phagocyte-derived catecholamines augments the acute inflammatory response. *PloS One* (2009) 4:e4414. doi: 10.1371/journal.pone.0004414

52. Cosentino M, Rasini E, Colombo C, Marino F, Blandini F, Ferrari M, et al. Dopaminergic modulation of oxidative stress and apoptosis in human peripheral blood lymphocytes: evidence for a D1-like receptor-dependent protective effect. *Free Radic Biol Med* (2004) 36:1233–40. doi: 10.1016/j.freeradbiomed.2004.02.065

53. Oberbeck R, van Griensven M, Nickel E, Tschernig T, Wittwer T, Pape H-C. Influence of beta-adrenoceptor antagonists on hemorrhage-induced cellular immune suppression. *Shock* (2002) 18:331–5. doi: 10.1097/00024382-200210000-00007

54. Macarthur H, Westfall TC, Riley DP, Misko TP, Salvemini D. Inactivation of catecholamines by superoxide gives new insights on the pathogenesis of septic shock. *Proc Natl Acad Sci U.S.A.* (2000) 97:9753–8. doi: 10.1073/pnas.97.17.9753

55. Sagone AL. Effect of hyperoxia on the carbohydrate metabolism of human lymphocytes. *Am J Hematol* (1985) 18:269–74. doi: 10.1002/ajh.2830180308

frontiers | Frontiers in Immunology

TYPE Original Research
PUBLISHED 11 January 2024
DOI 10.3389/fimmu.2023.1253637

OPEN ACCESS

EDITED BY
Gan Zhao,
University of Pennsylvania, United States

REVIEWED BY
Nadine Ahmed Kerr,
University of Miami, United States
Veronika Grau,
University of Giessen, Germany
Wilhelm Bertrams,
University of Marburg, Germany

*CORRESPONDENCE
Borna Relja
info@bornarelja.com

†These authors have contributed equally to this work

RECEIVED 05 July 2023
ACCEPTED 20 December 2023
PUBLISHED 11 January 2024

CITATION
Zhou Y, Meng F, Köhler K, Bülow JM, Wagner A, Neunaber C, Bundkirchen K and Relja B (2024) Age-related exacerbation of lung damage after trauma is associated with increased expression of inflammasome components. *Front. Immunol.* 14:1253637. doi: 10.3389/fimmu.2023.1253637

Age-related exacerbation of lung damage after trauma is associated with increased expression of inflammasome components

Yuzhuo Zhou[1,2], Fanshuai Meng[1,3], Kernt Köhler[4], Jasmin Maria Bülow[1], Alessa Wagner[1], Claudia Neunaber[2], Katrin Bundkirchen[2†] and Borna Relja[1*†]

[1]University Ulm, Department of Trauma, Hand, Plastic and Reconstructive Surgery, Translational and Experimental Trauma Research, Ulm, Germany, [2]Hannover Medical School, Department of Trauma Surgery, Hannover, Germany, [3]Uniklinik RWTH Aachen, Department of Trauma and Reconstructive Surgery, Aachen, Germany, [4]Justus Liebig University Giessen, Institute of Veterinary Pathology, Giessen, Germany

Background: Trauma, a significant global cause of mortality and disability, often leads to fractures and hemorrhagic shock, initiating an exaggerated inflammatory response, which harms distant organs, particularly the lungs. Elderly individuals are more vulnerable to immune dysregulation post-trauma, leading to heightened organ damage, infections, and poor health outcomes. This study investigates the role of NF-κB and inflammasomes in lung damage among aged mice post-trauma.

Methods: Twelve male C57BL/6J mice underwent hemorrhagic shock and a femoral fracture (osteotomy) with external fixation (Fx) (trauma/hemorrhage, THFx), while another 12 underwent sham procedures. Mice from young (17-26 weeks) and aged (64-72 weeks) groups (n=6) were included. After 24h, lung injury was assessed by hematoxylin-eosin staining, prosurfactant protein C (SPC) levels, HMGB1, and *Muc5ac* qRT-PCR. Gene expression of *Nlrp3* and *Il-1β*, and protein levels of IL-6 and IL-1β in lung tissue and bronchoalveolar lavage fluid were determined. Levels of lung-infiltrating polymorphonuclear leukocytes (PMNL) and activated caspase-3 expression to assess apoptosis, as well as NLRP3, ASC, and Gasdermin D (GSDMD) to assess the expression of inflammasome components were analyzed via immunostaining. To investigate the role of NF-κB signaling, protein expression of phosphorylated and non-phosphorylated p50 were determined by western blot.

Results: *Muc5ac*, and SPC as lung protective proteins, significantly declined in THFx versus sham. THFx-aged exhibited significantly lower SPC and higher HMGB1 levels versus THFx-young. THFx significantly increased activated caspase-3 versus both sham groups, and THFx-aged had significantly more caspase-3 positive cells versus THFx-young. IL-6 significantly increased in both sham and THFx-aged groups versus corresponding young groups. THFx significantly enhanced PMNL in both groups versus corresponding sham groups. This increase was further heightened in THFx-aged versus THFx-young. Expression of p50 and phosphorylated p50 increased in all aged

groups, and THFx-induced p50 phosphorylation significantly increased in THFx-aged versus THFx-young. THFx increased the expression of inflammasome markers IL-1β, NLRP3, ASC and GSDMD versus sham, and aging further amplified these changes significantly.

Conclusion: This study's findings suggest that the aging process exacerbates the excessive inflammatory response and damage to the lung following trauma. The underlying mechanisms are associated with enhanced activation of NF-κB and increased expression of inflammasome components.

KEYWORDS

femur fracture, hemorrhagic shock, aging, pulmonary injury, inflammasome, NF-KappaB

1 Introduction

Trauma is a major leading cause of death among young adults worldwide, whereby femur fracture being a significant type of traumatic musculoskeletal injury that increases mortality and can cause pulmonary complications such as acute respiratory distress syndrome (ARDS) (1, 2). Femoral fractures are often accompanied by hemorrhagic shock (HS) (3), that can reduce oxygen or nutrient supply to vital organs (4), leading to remote lung injury (RLI). Damaged tissues in a state of ischemia and hypoxia following HS can release damage-associated molecular patterns (DAMPs) and other inflammatory mediators like cytokines, including interleukin (IL)-1β or IL-6 (5–7). These biomolecules can activate and attract neutrophils, leading to apoptosis in the lungs (8–11). IL-6, a biomarker and key driver of injury-induced inflammation after trauma and HS (7, 12), can be transiently suppressed in a murine model by administering anti-IL-6 antibody, which resulted in reduced lung injury and suppression in the levels of key inflammatory mediators following trauma and HS (7). Trauma-induced pro-inflammatory changes can be concomitant with enhanced neutrophil infiltration and apoptosis, as well as general lung injury, and increased activation levels of the nuclear factor-kappa (NF-κ)B *in vivo* (12–14). Adjacent to the NF-κB signaling pathway, which comprises the p50/p65 and the inhibitor of κB (IκB) protein, it was shown that femoral fracture and hemorrhagic shock induced presence of pro-inflammatory markers, of which among others the inflammasome-activated IL-1β was associated with enhanced neutrophil infiltration into the lungs, apoptosis and general lung injury in mice (15). Trauma-induced oxidative stress and DAMPs can trigger the formation of the nucleotide-binding domain (NOD)-like receptor protein (NLRP)3 inflammasome (16, 17). Once initiated by stimuli, for instance endotoxin such as lipopolysaccharide, NLRP3 proteins polymerize in the NLRP3 inflammasome multiprotein complex, which in turn promotes the recruitment and activation of Pro-caspase-1, and thus, the maturation of IL-1β leading to inflammatory response (18). Reduced NLRP3 inflammasome-mediated IL-1β release and decreased caspase-3 concentrations, thus lead to inhibited apoptosis and pyroptosis alleviated pulmonary pathological damage and improved the survival rate of the sepsis mice *via* the MAPK/NF-κB/NLRP3 pathway (19).

The epidemiology of trauma-associated complications during the hospital stay continues to evolve. Recently, it was shown that an ageing population with increasing incidence of multiple organ failure, particularly in males, stay longer on intensive care units (ICU) and requires increasingly more hospital resources without improvement in survival (20). Aging is accompanied by an increase in circulating pro-inflammatory cytokines and pro-apoptotic factors, even in the absence of infection, suggesting a low-level chronic inflammatory state, known as "inflammaging" (21, 22). This state is evident in the elevated levels of circulating as well as pro-inflammatory cytokines in the lung, such as of IL-1β, IL-6, IL-8, and TNF-α (23, 24). The aging process leads to changes in primary and secondary lymphoid tissues, which causes the lung tissue to become less flexible, and decreasing the lung's ability to respond to trauma (23). Moreover, there is a higher activity of caspase-3 in aged individuals' heart, which further exacerbates the problem (25). Unbiased genome-wide analyses exposed age/stress-related epigenetic effects with a proinflammatory profile and altered NF-κB-related gene networks (26).

Thus, the pulmonary environment becomes more inflammatory with increasing age (27, 28). Interestingly, there is an increased NLRP3 inflammasome activity in aged and stressed lungs, which increased the expression of mature IL-1β in aged individuals (29, 30). These age-related changes in innate and adaptive immunity suggest that aged individuals may not respond to immunological threats such as trauma as effectively as younger individuals. However, the exact mechanistic drivers of aging-related inflammatory modulations in trauma are not entirely understood. Based on this background, the study aimed to investigate the effect of aging on inflammatory changes and the underlying mechanisms that cause lung injury in mice after femur fracture and hemorrhagic shock, with a distinct focus on the NF-κB signaling pathway as well as on the expression of inflammasome components.

2 Materials and methods

2.1 Animal husbandry

All animal studies were carried out in strict accordance with the German Animal Law and with the permission of the local authorities in Lower Saxony, Germany (approval number: 33.12-42502-04-17/2491). Young (17 - 26 weeks) and aged (64-72 weeks) male C57BL/6J mice (Janvier Labs, Le Genest-Saint-Isle, France) were used for the experiments (31). The animals were kept in individual cages under standardized conditions at the Central Animal Laboratory of the Hannover Medical School, where cages, bedding and drinking bottles were frequently changed and standard softwood granules (Altromin GmbH, Lage, Germany) for experimental animals were used as litter material.

2.2 Group distribution

24 male C57BL/6J mice held in conventional animal room were randomly assigned to one of the four groups. Animals in sham groups (sham young: n = 6; sham aged: n = 6) received the femoral artery catheterization and an external fixator, but no osteotomy or blood loss were induced. In trauma groups (THFx young: n = 6, THFx aged: n = 6) hemorrhagic shock with resuscitation was induced and an external fixator followed by osteotomy (Fx) of the femur was applied (trauma/hemorrhage, THFx). Young mice were 17 - 26 weeks and aged mice were 64 - 72 weeks old. The animals were sacrificed 24 hours after experiment induction.

2.3 Experimental model

All surgical procedures were performed under deep inhalation anesthesia using isoflurane (Baxter Deutschland GmbH, Unterschleißheim, Germany) as described before (3, 31, 32). Surgical procedure was initiated after repeated periodic verification of the negative interphalangeal reflex in mice. Mice were kept warm during the procedure using a heating pad and the eyes were protected from drying out with Bepanthen eye ointment. An intraoperative analgesia with 5 mg/kg body weight carprofen (Zoetis inc.) and 1 mg/kg body weight butorphanol (Zoetis inc., USA) were injected subcutaneously (s.c.). Prilocaine hydrochloride Aspen Germany GmbH, Germany was used for local anesthesia at the surgical site. Metamizole (Ratiopharm GmbH, Germany) at 200 mg/kg bodyweight was mixed into drinking water for postoperative analgesia, and carprofen and butorphanol were injected s.c. according to indication. After surgery, the animals were placed under warmth and red light until full consciousness is regained, then housed in independent cages to avoid them behaving aggressively towards each other, which could affect the healing of the surgical wound. After surgery, animals were regularly controlled and assessed for vital signs and mobility. All surgical procedures were conducted as described before (3, 31, 32). In the sham and trauma groups, a catheter was inserted into the left femoral artery and an external fixator (MouseExFix simple L 100%, RISystem, Davos, Switzerland) was implanted into the right femur. Animals in the trauma groups (THFx young; THFx aged) underwent a pressure-controlled hemorrhagic shock (HS). In brief, after insertion of the catheter into the left femoral artery, blood was collected until the mean arterial blood pressure reached 35 ± 5 mm Hg. The hypovolemic state of shock was maintained for a total of 90 minutes. The animals were then re-infused with four times the amount of blood drawn (up to maximum 2.4 ml) using body warm Ringer's solution within 30 minutes and afterwards the catheter was removed. The external fixator was placed, and diaphysis was osteotomized in THFx groups centrally between the two middle pins using a 0.44 mm diameter wire saw (Gigly wire saw, RISystem). Prolene 6-0 (Ethicon, Cincinnati, USA) was used to suture the wounds and the animals were allowed to move freely immediately after the experiments were completed.

2.4 Harvesting procedures

After 24 hours of surgery, the animals were euthanized with an intraperitoneal injection of 75 mg/kg body weight of ketamine (Zoetis inc.) and 1 mg/kg body weight of medetomidine (Zoetis inc.). The abdominal cavity was opened, and a heparinized sharp 25-gauge syringe was used to puncture the heart for blood collection, followed by cervical dislocation. Afterwards, the incision was widened along the chest wall to the trachea. To flush the lungs, a 25-gauge needle was punctured into the trachea and a 19-gauge syringe containing 1.1 ml of phosphate-buffered saline (PBS) was inserted. The lungs were flushed with 1.1 ml of PBS and 800 µl of bronchoalveolar lavage fluid (BALF) were collected. BALF was centrifuged at 1164 x g for 5 min at 4°C and the supernatant was frozen at -80°C for subsequent analysis. The upper trachea was closed with a blunt clamp followed by perfusion of 20 ml of PBS through the heart using a 21-gauge blunt-tipped syringe to ensure systemic perfusion of the mouse. The left lung was ligated and removed, rapidly frozen in liquid nitrogen, and stored at -80°C. Furthermore, 10 ml of 4% buffered Zn-Formalin was perfused using a 21-gauge syringe for the right lung lobe, which was then removed and fixed overnight for subsequent (immuno)histological analyses.

2.5 Examination of lung damage

The samples were fixed in 4% buffered Zn-Formalin overnight, then, embedded in paraffin and sliced into 3 µm sections, which were stained with hematoxylin-eosin (HE). Specifically, the lung sections were deparaffinized, rehydrated, and stained with hemalum solution according to Mayer's method (Carl Roth, Karlsruhe, Germany) for 10 minutes at room temperature (RT). After decolorization in rinse water for 10 minutes, the sections were counterstained with eosin (Carl Roth, Karlsruhe, Germany) for 3 minutes at RT. Histological damage in the HE-stained sections was assessed for each group in a blinded manner. To quantify the histopathological damage in the lungs, independent examiners assessed the lungs using the method described previously. Briefly, sections of lungs were examined for desquamation, dystelectasis/

atelectasis, emphysema, congestion, interstitial thickness/infiltration with inflammatory cells, and bronchial exudate (33, 34).

2.6 Quantification of protein expression levels in BALF

To assess the severity of lung injury and the status of the lung barrier, levels of pro-inflammatory mediators in the BALF were evaluated. The concentrations of cleaved IL-1β and IL-6 in BALF were determined by performing mouse-specific enzyme-linked immunosorbent assays (ELISAs) using kits from R&D Systems (Minneapolis, USA) following the manufacturer's instructions. The measurements were obtained using an Infinite M200 microplate reader (Tecan, Männedorf, Switzerland).

2.7 Ribonucleic acid isolation, reverse transcription and semi-quantitative polymerase chain reaction

RNA extraction from the lung homogenate that was obtained by mechanical disruption using the Precellys 24 Homogenizer (Bertin Technologies, Montigny-le-Bretonneux, France) and the buffer from the RNeasy assay (Qiagen, Hilden, Germany) was performed following the manufacturer's protocol. To remove any remaining DNA, the sample was treated with the RNase-free DNase kit (Qiagen, Hilden, Germany). Qualitative and quantitative analysis of RNA was conducted with the Tecan's NanoQuant Plate on the Spark M10 Microplate Reader (Tecan, Männedorf, Switzerland). For cDNA synthesis, the iScript™ cDNA Synthesis Kit (BioRad, Hercules, USA) was used according to the manufacturer's instructions. Quantification of gene expression levels for *Muc5ac* (qMnuCED0061472), *Nlrp3* (qMmuCID0010647), and *Il-1β* (qMnuCED0045755) was performed using the PrimePCR SYBR Green Assay (BioRad, Hercules, USA) with specific primer sets for mouse. The housekeeping gene (control), *Gapdh* (qMnuCED0027467), was also quantified. *Gapdh* was chosen as control since no observed differences between aged, traumatized or sham groups were found. For all primers, the amplification specificities were confirmed by melting curve analysis, and no template controls were applied for detecting contamination or non-specific amplification. The PCR reaction was carried out with a total reaction volume of 25 µl and SYBR green qPCR Master Mix (BioRad) according to the manufacturer's instructions. The reaction was performed using the C1000 Touch Thermal Cycler with the CFX96 Touch Real-Time PCR Detection System (BioRad, Hercules, USA). Finally, the relative expression level of each target gene was determined using the comparative threshold-cycle (CT) method (2^{-DDCT} method), which involved normalizing the expression of each target gene to that of *Gapdh*.

2.8 Western blotting

Lung tissue was homogenized in lysis buffer (Invitrogen™, FNN0021) at 4°C and centrifuged at 20.000 x g for 30 min at 4°C. The resulting supernatants were stored at -80°C for later analysis. Electrophoresis was performed on 20 µg protein lysate separated by a 12% polyacrylamide SDS gel and then transferred to a nitrocellulose membrane (Amersham-Buchler, Braunschweig, Germany). A rabbit polyclonal anti-NFkB p105/p50 (phospho S337) antibody (ab28849, 1:1000 dilution) was used to detect phosphorylated p50, and a rabbit monoclonal recombinant anti-NFkB p105/p50 antibody [E381] (ab32360, 1:2000 dilution) (Abcam, Cambridge, UK) was used to detect non-phosphorylated p50. Monoclonal beta-Actin antibody (sc-47778, 1:1000 dilution, Santa Cruz) was used as loading control for measuring beta-actin. Blots were blocked in a blocking buffer (10% non-fat dry milk in 1 mM Tris, 150 mM NaCl, pH 7.4) for one hour at RT, then incubated with primary antibodies in bovine serum albumin (BSA) containing 0.5% Tween 20 and 0.5% BSA at 4°C on a 35 rpm shaker overnight according to the manufacturer's instructions. As secondary antibody a horseradish peroxidase-conjugated anti-rabbit IgG antibody (ab288151, 1:10000 dilution, Abcam) was subsequently applied for one hour at room temperature on the shaker. Proteins were detected using ECL™ Western blot detection reagent (GE Healthcare, Munich, Germany). After measuring the phosphorylated p50, nitrocellulose membrane was washed in TBS, then pp50 antibody was eluted for 2 × 15 minutes in stripping buffer (0.2 M glycine, 0.1% SDS, 1% Tween20, pH 2.2), and washed 3 × 5 minutes in TBST (0.05% Tween20 in TBS) on rocker with 50 rpm. The membrane was blocked for 1.5 hours in blocking buffer, and then incubated with p50 or β-actin antibodies overnight at 4°C. After incubation, the membrane was washed 2 × 15 minutes with TBST and 1 × 15 minutes with TBS (20 mM Tris-Base, 0.15 M NaCl, pH 7.6), and afterwards incubated with the secondary antibody as described above. The signals were digitized, and the ImageJ software was used to determine the integrated density of the individual bands for protein expression normalization to β-actin by densitometry using ImageJ software.

2.9 Immunohistology staining of NLRP3, HMGB1, ASC, Gasdermin D, SPC, active caspase-3 and neutrophil elastase

The lung tissue sections (3 µm) were subjected to dewaxing using Xylene (Merck, Darmstadt, Germany) or Roti Histol (Carl Roth, Karlsruhe, Germany) twice for 5 minutes and then rehydrated using descending alcohol series with 100%, 90%, and 70% concentrations sequentially for 2 x 5 minutes, then rinsed in distilled water for 2 x 5 minutes. Heat-induced epitope retrieval (HIER) was conducted using R-Universal epitope recovery buffer (Aptum, Kassel, Germany) in the 2100-Retriever (Prestige Medical, Blackburn, England) at 121°C for 20 minutes following the manufacturer`s manual. The slides were blocked and permeabilized with 150 µl of blocking solution (5% goat serum (Jackson immunoresearch), 0.05% TritonX, 0.05% Tween 20 in 1 x PBS) for 20 minutes at room temperature in a humidified incubation chamber. Afterwards, slides were washed in distilled water twice for 3 minutes. Lung sections were incubated with primary antibodies against Nucleotide-binding oligomerization

domain (NOD)-like receptor (NLR) protein (NLRP)3 (1:200, rabbit anti-mouse, Cell signaling Technology, USA, #151015), Apoptosis-associated speck-like protein containing a CARD (ASC) (1:200, rabbit anti-mouse, Cell signaling Technology, USA, #67824), Gasdermin D (GSDMD) (1:200, rabbit anti-mouse, Cell signaling Technology, #39754), Prosurfactant protein C (SPC) (1:500, rabbit anti-mouse, Abcam USA, Ab90716), and High-mobility group box 1 protein (HMGB1) (1:200, rabbit anti-mouse, Abcam USA, Ab18256), which were diluted as suggested by the manufacturers in the Antibody Dilution Buffer (Dako Cytomation) and incubated overnight at 4°C in a humidified incubation chamber. Active caspase-3 (1:300, rabbit anti-mouse, anti-cleaved caspase-3 (Asp175), #9661, Cell Signaling Technology, USA), and neutrophil elastase (NE) (1:200, rabbit anti-mouse, Bioss, bs-6982R, USA) antibodies were incubated for one hour at room temperature in a humidified incubation chamber. Incubation of primary antibodies was followed by washing according to the washing steps after blocking. Endogenous peroxidase was blocked by adding 3% hydrogen peroxide and incubation for 15 minutes at room temperature followed. After another washing step, the secondary antibody conjugated with horseradish peroxidase (Histofine Simple Stain Mouse MAX PO (R), Nichirei Biosciences Inc.) was incubated for 60 minutes at room temperature in a humidified incubation chamber according to manufacturers' instructions. This was followed by another washing procedure and 3-amino-9-ethylcarbazol (AEC, DCS Innovative Diagnostik-Systeme, Hamburg) was used to detect specific binding. Hematoxylin (Carl Roth, Karlsruhe, Germany), was used for counterstaining, and stained slides were mounted with mounting medium (Merck, 108562). Unstained sections for tissue background control were used. No primary antibody controls incubated with just the antibody diluent, without the primary antibodies were applied to determine if the secondary antibody is binding non-specifically to cellular components that do not contain the protein of interest, resulting in false positives or non-specific binding. Isotype control antibodies Normal Rabbit IgG (rabbit, Cell signaling Technology, USA, #2729) and Rabbit IgG, polyclonal - Isotype Control (rabbit anti-mouse, Abcam USA, Ab171870) were used in the control samples and incubated with the same concentrations under the same experimental conditions as applied for the corresponding primary antibody. Imaging was conducted using the Zeiss Axio Observer Z1 microscope with a 40 x objective except for ASC, that was captured with a 63 x objective (Zeiss, Göttingen, Germany). ImageJ software was used for evaluation, with counting of positively stained cells in 25 high-power fields (HPF).

2.10 Statistical analysis

The statistical analysis was conducted using GraphPad Prism 6 (GraphPad Software, Inc., San Diego, CA). Data were tested for normal distribution using Shapiro-Wilk normality test. Based on the histogram and Shapiro–Wilk test, the non-parametric Kruskal-Wallis test, which does not assume a normal distribution of the residuals, followed by Dunn's *post hoc* test for the correction of multiple comparisons was applied. The results were presented as mean and standard error of the mean, and statistically significant differences are indicated as p-value less than 0.05.

3 Results

3.1 Impact of aging on lung damage after THFx

In this experiment, animals received an external fixator and underwent osteotomy and hemorrhagic shock with subsequent resuscitation as shown in Figure 1A. The study analyzed the differences in lung histomorphology, gene expression of the lung protective protein Muc5ac in homogenized lung tissue, prosurfactant protein C (SPC) expression as a marker of alveolar damage, and HMGB1 expression in lungs between groups (Figures 1, 2). The results showed that THFx induced a strong histopathological lung injury with alveolar wall thickening and resulting alveolar space loss, with the most prominent damage observed in the THFx aged group compared to all other groups (Figure 1B). The histomorphological differences between the groups show increased lung injury in the THFx young group and further enhanced in the THFx aged group compared to both sham groups (lung injury score: sham young = 2, sham aged = 2, THFx young = 3, and THFx aged = 4). In addition, the gene expression of *Muc5ac* was significantly decreased in the THFx groups compared to the sham groups ($p < 0.05$, Figure 1C). In order to investigate apoptosis in aged lungs after trauma, active caspase-3 staining was used as a direct indicator of apoptosis ($p < 0.05$, Figures 1D, E). The results showed a significantly higher number of active caspase-3 positive cells (red arrows) in the THFx groups compared to the sham groups ($p < 0.05$, Figure 1E). Additionally, the number of caspase-3 positive cells was higher in the THFx aged group compared to the THFx young group ($p < 0.05$, Figure 1E). Prosurfactant protein C was significantly decreased in both aged groups compared to the corresponding young group ($p < 0.05$, Figures 2A, B). In addition, SPC presence was significantly decreased in the THFx groups compared to the sham groups ($p < 0.05$, Figure 2B). HMGB1 staining showed a significantly higher number of HMGB1 positive cells (red arrows) in the THFx groups compared to the sham groups ($p < 0.05$, Figures 2C, D). Additionally, the number of HMGB1 positive cells was higher in aged groups compared to the young groups ($p < 0.05$, Figure 2D).

3.2 Impact of aging on IL-6 and neutrophil infiltration after THFx

The study evaluated the protein levels of IL-6 in homogenized lung tissue and IL-6 protein concentration in the BALF. The results showed that protein expression of IL-6 in lung tissue was significantly increased in both aged groups, sham and THFx, compared to the corresponding young group ($p < 0.05$, Figure 3A). IL-6 protein expression in the BALF was significantly increased in THFx compared to the young sham group ($p < 0.05$, Figure 3B).

10.3389/fimmu.2023.1253637

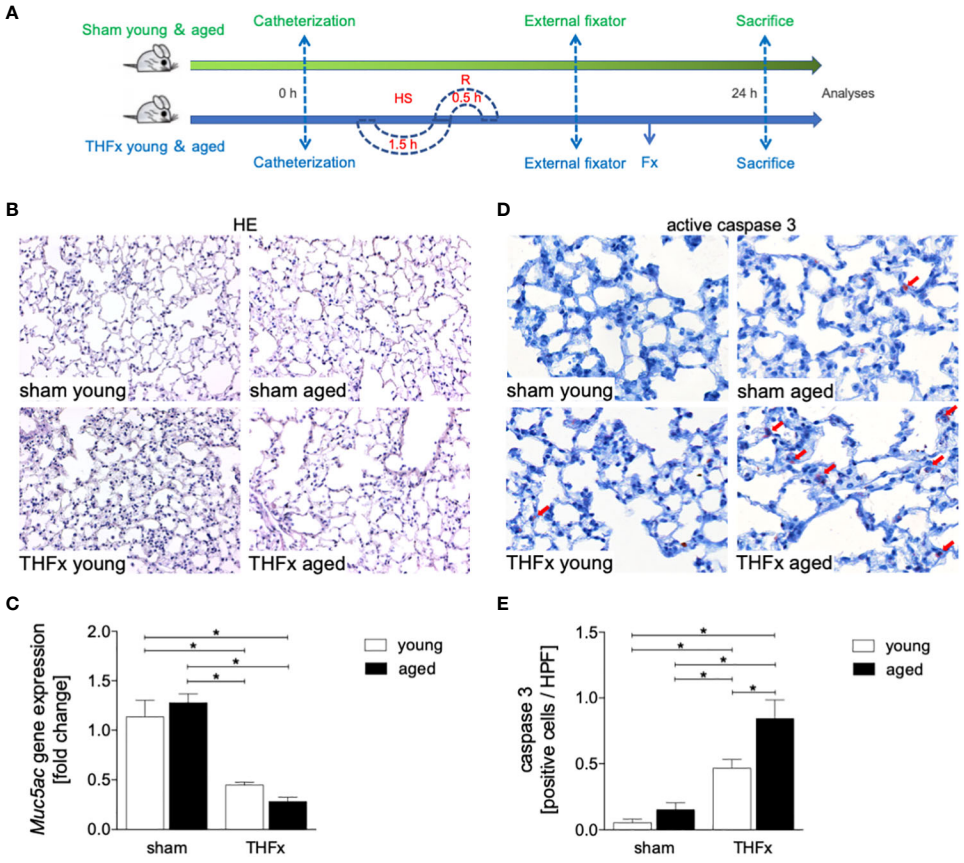

FIGURE 1
The effects of aging on lung damage after hemorrhagic shock (HS) and femoral fracture (Fx) were investigated. **(A)** The experimental design involved young (17 - 26 weeks) and aged (64 - 72 weeks) male C57BL/6J mice, as well as sham (green line) and trauma (blue line) groups. Trauma groups underwent pressure-controlled HS followed by resuscitation (R) with Ringer's solution and Fx (via osteotomy) (THFx), while sham groups received catheterization and an external fixator but no THFx induction. Lung tissue samples were obtained 24 hours after the experiment, and Muc5ac gene expression and positive active caspase-3 cells were assessed. **(B)** Representative lung sections upon hematoxylin/eosin (HE) staining. **(C)** Relative gene expression of Muc5ac. **(D)** Representative lung sections upon the staining of activated caspase-3 with red arrows indicating caspase-3 positively stained cells, and **(E)** quantification of caspase-3 positively stained cells per high power field (HPF). n = 6 per group, * $p < 0.05$ between indicated groups.

Neutrophil infiltration in the lung was quantified by immunohistological staining, showing a significantly increased infiltration of neutrophils in both THFx groups compared to the corresponding sham group ($p < 0.05$, Figures 3C, D). Additionally, the THFx aged group had significantly increased neutrophil infiltration compared to the THFx young group, indicating that aging can worsen the inflammatory response in the lung after trauma ($p < 0.05$, Figures 3C, D).

3.3 Impact of aging on NF-κB activation after THFx

In this study, the impact of aging on the NF-κB signaling was investigated after THFx. Lung tissue homogenates were collected 24 hours after resuscitation, and western blot analysis was performed to measure phosphorylated and non-phosphorylated p50, as indicator for NF-κB activation. The results showed that non-phosphorylated p50 expression levels were significantly higher in both THFx groups compared to the young sham group ($p < 0.05$, Figures 4A, B). Additionally, the THFx young group showed significantly increased levels of non-phosphorylated p50 versus the young sham group, while there was no difference among the aged groups ($p < 0.05$, Figures 4A, B).

Phosphorylated p50 expression levels were significantly higher in both aged groups compared to their corresponding young groups ($p < 0.05$, Figures 4A, C).

3.4 Impact of aging on the expression of inflammasome components after THFx

The gene expression of *Nlrp3* and *Il-1β* was assessed in homogenized lung tissue. Results showed that the expression of *Nlrp3* was significantly higher in THFx groups versus young sham group ($p < 0.05$, Figure 5A).

In addition, the relative gene expression of *Il-1β* in lung tissue was significantly higher in both THFx groups compared to their corresponding sham group ($p < 0.05$, Figures 5B).

10.3389/fimmu.2023.1253637

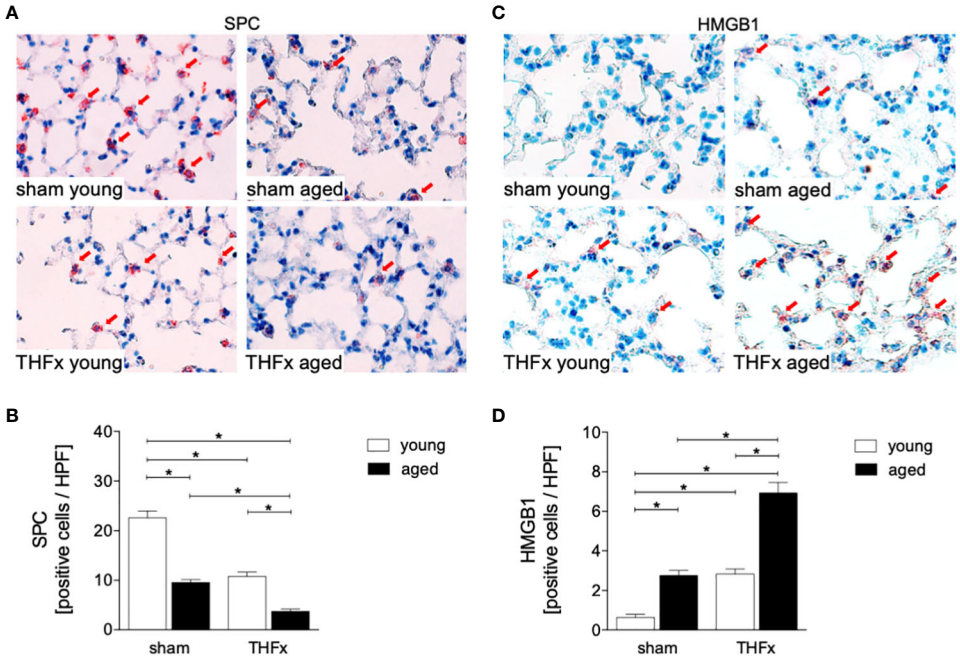

FIGURE 2
The impact of aging on Prosurfactant protein C (SPC) and High-mobility group box 1 protein (HMGB1) expression after hemorrhagic shock (HS) and femoral fracture (Fx). The experimental design included young (17 - 26 weeks) and aged (64 - 72 weeks) male C57BL/6J mice in both sham and trauma groups. The trauma groups underwent pressure-controlled HS followed by resuscitation (R) with Ringer's solution and Fx (via osteotomy) (THFx), while the sham groups received catheterization and an external fixator but no THFx induction. After 24 hours, the mice were euthanized, and **(A)** SPC (red arrows) in lung tissue sections were quantified **(B)**. **(C)** Representative immunohistological HMGB1 staining (red arrows), and **(D)** positively stained cells per high power field (HPF). n = 6 per group, * $p < 0.05$ between indicated groups.

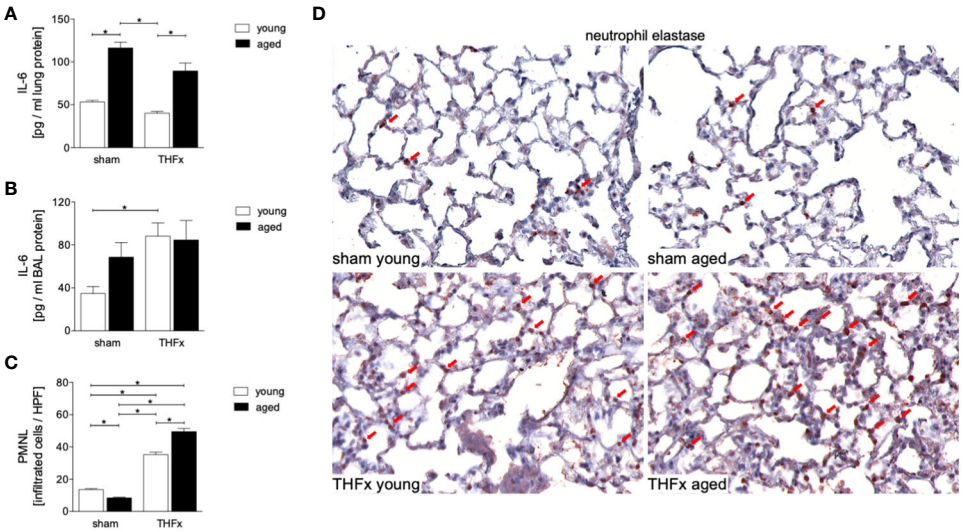

FIGURE 3
The impact of aging on interleukin (IL)-6 protein expression and neutrophil infiltration after hemorrhagic shock (HS) and femoral fracture (Fx) was investigated. The experimental design included young (17 - 26 weeks) and aged (64 - 72 weeks) male C57BL/6J mice in both sham and trauma groups. The trauma groups underwent pressure-controlled HS followed by resuscitation (R) with Ringer's solution and Fx (via osteotomy) (THFx), while the sham groups received catheterization and an external fixator but no THFx induction. After 24 hours, the mice were euthanized, and IL-6 protein expression **(A)** in lung tissue homogenates and **(B)** in bronchoalveolar lavage (BAL) fluid was analyzed. **(C)** Quantification of Neutrophil elastase (NE) positively stained cells per high power field (HPF). **(D)** Representative immunohistological staining of NE as a marker of polymorphonuclear leukocytes (PMNL) in lung sections with red arrows indicating NE-positively stained cells. n = 6 per group, * $p < 0.05$ between indicated groups.

10.3389/fimmu.2023.1253637

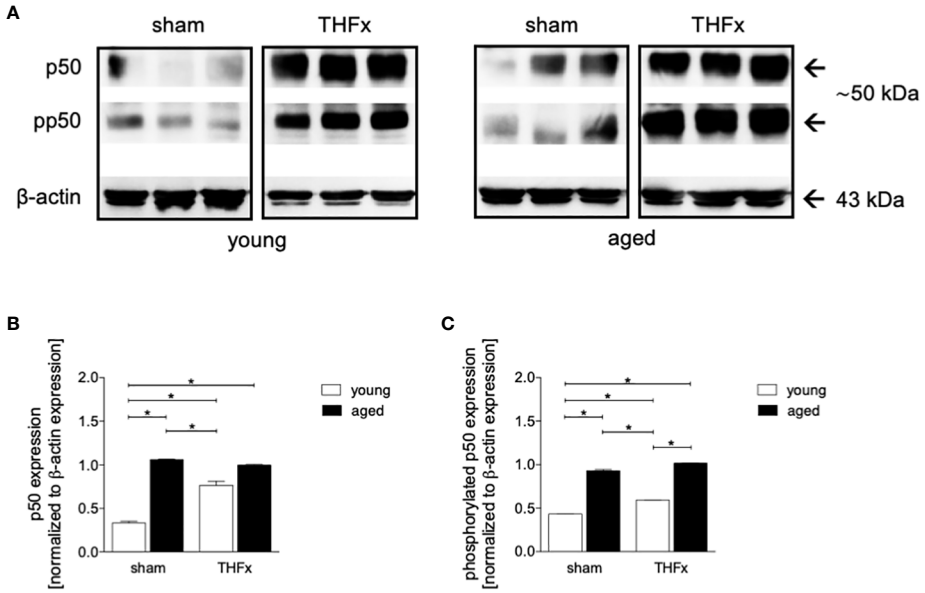

FIGURE 4
The effect of aging on NF-κB following hemorrhagic shock (HS) and femoral fracture (Fx) in young (17 - 26 weeks) and aged (64 - 72 weeks) male C57BL/6J mice is shown. The experimental design included sham and trauma groups, with the trauma groups subjected to pressure-controlled HS followed by resuscitation (R) with Ringer's solution and Fx (via osteotomy) (THFx). The sham groups underwent catheterization and received an external fixator, but no THFx was induced. After 24 hours, the mice were euthanized, and samples were collected. **(A)** Representative western blot analysis of phosphorylated and non-phosphorylated p50 and β-actin, and quantification of **(B)** non-phosphorylated p50 and **(C)** phosphorylated p50 in young and aged sham and THFx mice. n = 4 per group, * $p < 0.05$ between indicated groups.

The concentration of IL-1β in the BALF was significantly higher in THFx groups compared to their corresponding sham group ($p < 0.05$, Figure 5C).

In order to further investigate the expression of inflammasome components in aged lungs after trauma, several markers including NLRP3, ASC and GSDMD were used (Figure 6). The results showed a significantly higher number of NLRP3 positive cells (red arrows) in the THFx groups compared to the corresponding sham group ($p < 0.05$, Figures 6A, B). The number of NLRP3 positive cells was significantly higher in the aged groups compared to the young groups, while the NLRP3 increase was significantly enhanced in the THFx aged group compared to all other groups ($p < 0.05$, Figure 6B).

The number of ASC positive cells (red arrows) was significantly higher in the THFx groups compared to the corresponding sham groups ($p < 0.05$, Figures 6C, D). The number of ASC positive cells was higher in the sham aged group compared to the sham young group ($p < 0.05$, Figure 6D). In the THFx aged group ASC was significantly higher compared to all other groups ($p < 0.05$, Figure 6D).

The number of GSDMD positive cells (red arrows) was significantly higher in the THFx groups compared to the corresponding sham groups ($p < 0.05$, Figures 6E, F). Furthermore, the number of GSDMD positive cells was higher in the sham aged group compared to the sham young group ($p < 0.05$, Figure 6F), and in the THFx aged group GSDMD was significantly higher compared to all other groups ($p < 0.05$, Figure 6F).

4 Discussion

The objective of our study was to explore the mechanisms that cause lung injury in young and aged mice after THFx. Trauma is the leading cause of death and disability worldwide (35). In young mice, femoral fracture following pressure-controlled hemorrhagic shock can cause increased uncontrolled inflammation in the lungs as well as disruption of the pulmonary barrier (33), yet the current research has not fully explained the effects of aging on lung injury and the pulmonary inflammatory response after THFx. Our study aimed to investigate how aging influences the typical NF-κB signaling pathway as well as the expression of inflammasome components that mediate the lung inflammatory response after THFx. Specifically, the study compared the response of young mice aged 17 - 26 weeks and old mice aged 64 - 72 weeks, to gain a better understanding of underlying mechanisms for age-related changes impacting lungs, especially in the context of trauma and hemorrhagic shock. In a recent study applying this model, it was shown that aged mice had significantly lower total bone and callus volume, decreased share of callus per total bone volume, less trabecular structures as well as the reduction of the elastic limit (31), thus, our model of femoral fracture mimics the human situation. Furthermore, it was demonstrated that THFx induced an uncontrolled inflammatory response and lung barrier breakdown in young mice (33), findings that support our hypothesis. This study's results have the potential to guide future research and pre-clinical approaches for addressing these conditions in both younger and older populations.

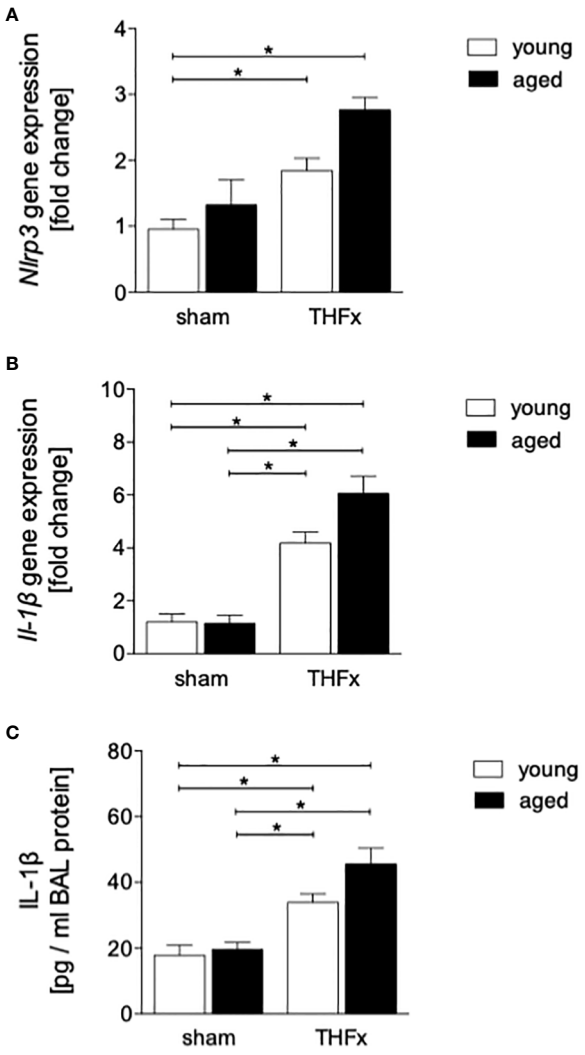

FIGURE 5
The effect of aging on the presence of inflammasome components after hemorrhagic shock (HS) and femoral fracture (Fx) in male mice. The experimental design included young (17 - 26 weeks) and aged (64 - 72 weeks) C57BL/6J mice in both sham and trauma groups. The trauma groups underwent pressure-controlled HS followed by resuscitation (R) with Ringer's solution and Fx (via osteotomy) (THFx), while the sham groups underwent catheterization and received an external fixator, but no THFx was induced. After 24 hours, the mice were euthanized, and sampling was performed. **(A)** The relative gene expression of nucleotide-binding domain (NOD)-like receptor protein (NLRP)3, and **(B)** of interleukin (IL)-1β in lung tissue homogenates. **(C)** Quantification of IL-1β protein concentration in bronchoalveolar lavage (BAL) fluid. n = 6 per group, * $p < 0.05$ between indicated groups.

The results suggest that trauma-induced inflammation and lung damage are exacerbated by the aging process through activation of the NF-κB signaling pathway and eventually inflammasome. The reduction in surfactant protein C in both THFx groups suggests an impaired lung protective response following trauma, which was further exacerbated in the THFx aged group (Figures 1, 2). Reduced *Muc5ac* gene expression in the THFx groups supports increased lung damage following trauma (Figure 1C). Additionally, the increase in activated caspase-3 positive cells in both THFx groups indicates an increased apoptosis after THFx, which was more prominent in the THFx aged group compared to the THFx young group (Figures 1D, E). Similarly, the higher levels of HMGB1 and IL-6 suggest an amplified pro-inflammatory response in aging (Figures 2, 3). The PMNL increase in both young and aged THFx groups compared to sham groups suggests that trauma-induced inflammation attracts more inflammatory cells to the lung, again, with the THFx aged group experiencing a more pronounced effect (Figure 3C). Enhanced expression of p50 and phosphorylated p50 in all aged groups indicates that the NF-κB signaling pathway is activated in aging (Figure 4). Also, the increased expression of inflammasome components as shown by increased IL-1β gene expression and concentration, as well as enhanced NLRP3, ASC and GSDMD expression in lungs following trauma suggests an involvement of the inflammasomes in the exaggerated inflammatory response in the lung following trauma in aged mice (Figures 5, 6). Overall, the study highlights the role of aging in exacerbating the inflammatory response to trauma in lungs.

Trauma-induced cellular destruction with DAMPs release, as also demonstrated in the present study by HMGB1 increase, or translocation of pathogen-associated molecular patterns into the bloodstream is accompanied with the production and release of various inflammatory signals such as IL-1β, TNF-α and IL-6, as well as a significant increase in PMNL activation and infiltration in the lungs (36, 37). In line with these reports, our results demonstrate an increase in the production as well as in the release of pro-inflammatory cytokines, including IL-6 and IL-1β after THFx. Typically, the release of inflammatory mediators after trauma is linked to an enhanced PMNL activity and infiltration in lungs. Störmann et al. found a significant increase in PMNL infiltration in the lungs after polytrauma in pigs (36), which was attributed to the lipid mediator leukotriene (LT)B4 that activates and attracts PMNL to the lungs to participate in post-traumatic lung inflammation (36, 38). Kalsotra et al. have shown that both LTB4 levels and PMNL infiltration were increased in the lungs of mice with brain contusion, and furthermore, were attributed to pulmonary complications following brain injury (39). It was also demonstrated before that IL-6 plays a significant role in inflammatory conditions (7, 12, 40, 41). In our previous *in vivo* study, we found significantly increased IL-6 levels in lung and liver samples after polytrauma compared to sham (42). In line with those and other reports, here, a significant PMNL infiltration into the lungs and an elevated concentration of IL-6 in BAL after THFx was observed (Figure 3). Thus, the development of lung injury and apoptosis in lung cells following THFx is closely associated with the release of inflammatory mediators. Studies using mouse models of indirect acute lung injury (ALI) induced by hemorrhagic shock and sepsis showed that lung inflammation is characterized by the caspase-3-dependent apoptosis of pulmonary epithelial cells (43, 44). The project presented here revealed an increase in caspase-3 levels and SPC indicating lung damage in mice with THFx (Figures 1, 2), which is in consistence with the findings of Zhang et al. (45).

The transcription factor NF-κB complex consists of a group of isoforms that regulate genes involved in the inflammatory response, as well as other biological processes such as cell growth and survival (46). Activation of NF-κB is closely linked to the development of various diseases, including cancer, autoimmune disorders, and

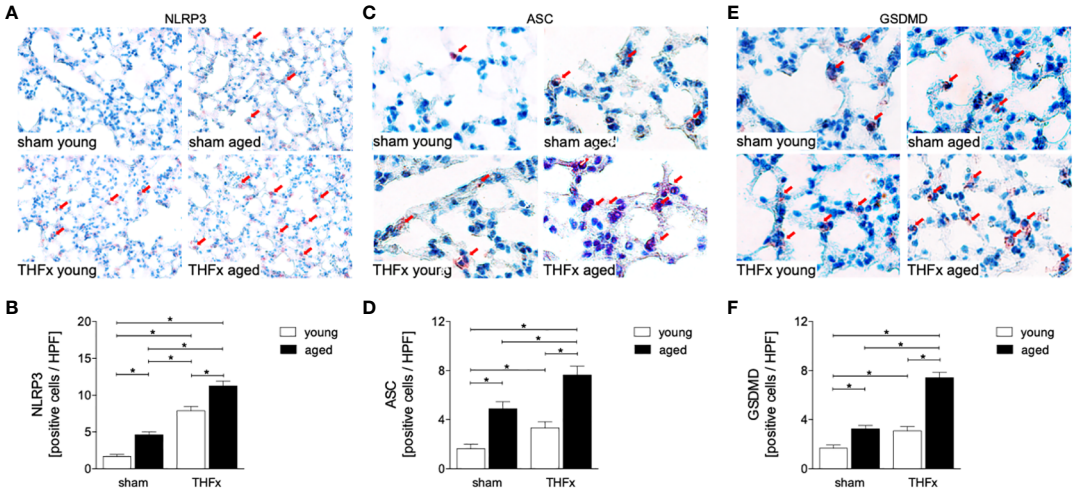

FIGURE 6
The impact of aging on Nucleotide-binding oligomerization domain (NOD)-like receptor (NLR) protein (NLRP)3, Apoptosis-associated speck-like protein containing a CARD (ASC), and Gasdermin D (GSDMD) expression after hemorrhagic shock (HS) and femoral fracture (Fx). The experimental design included young (17 - 26 weeks) and aged (64 - 72 weeks) male C57BL/6J mice in both sham and trauma groups. The trauma groups underwent pressure-controlled HS followed by resuscitation (R) with Ringer's solution and Fx (via osteotomy) (THFx), while the sham groups received catheterization and an external fixator but no THFx induction. After 24 hours, the mice were euthanized, and **(A)** NLRP3 protein expression was assessed and quantified **(B)** in lung tissue sections. **(C)** Representative immunohistological staining of ASC and **(D)** quantification of ASC positively stained cells per high power field (HPF). **(E)** Representative immunohistological staining of GSDMD and **(F)** quantification of GSDMD positively stained cells per HPF. n = 6 per group, * $p < 0.05$ between indicated groups.

chronic inflammation (47). Traumatic injury as also observed in this study, infections, and aging can lead to the activation of the NF-κB pathway and promotion of inflammatory signals (48). Apart from the NF-κB pathway induced by trauma, various DAMPs triggered by trauma, such as mitochondrial DNA, HMGB1, and ATP, can activate Nod-like receptors (NLRs) and promote the formation and activation of NLRP3 (49). The activated NLRP3 inflammasome leads to caspase-1 activation, resulting in the release of mature forms of IL-1β and IL-18 that promote exaggerated inflammatory responses in the circulation and peripheral tissues, leading to cell death, a process known as pyroptosis (50–53). Animal studies have also demonstrated that NLRP3 inflammasomes in lung endothelial cells and alveolar macrophages (AMs) are increasingly activated after hemorrhagic shock, leading to lung inflammation and increased IL-1β expression (54–56). Additionally, the activation of endothelial cell pyroptosis as shown by Yang et al. resulted in increased inflammation and lung damage in mice undergoing HS and LPS challenge (55). Furthermore, Xu et al. reported an increase in NLRP expression in lung endothelial cells after HS, leading to higher IL-1β levels detected in BAL (56). In consistence with these studies, we demonstrated here a significant increase in lung inflammation after THFx, as indicated by a significantly upregulated gene expression of *Nrlp3* in the lung and an increased concentration of IL-1β in BAL (Figure 5). Also, enhanced protein expression of NLRP3, ASC and GSDMD after trauma (Figure 6), and further amplification of these trauma-induced inflammasome-related mediators support the hypothesized of a possible activation of inflammasomes after trauma, and indicate that the heightened expression of inflammasome components may be linked to lung damage after THFx.

As all organisms age, there is a gradual and ongoing increase in chronic inflammation that is not caused by infection or injury (57). Senescent tissues produce various molecules, collectively called senescence-associated secretory phenotype (SASP) such as pro-inflammatory cytokines among others IL-1 (58). These molecules promote the further release of inflammatory cytokines and affect the local environment, leading to systemic and local inflammation through the blood circulation (23). Neutrophil elastase a marker for neutrophils is also associated with aging. In the brain tissue of Alzheimer's disease patients, the activity and concentration of neutrophil elastase gradually increase with age (59). However, the ability of neutrophils to phagocytosis and chemotaxis decreases with aging (60). Aged mice have been shown to have a high frequency of transendothelial migration of neutrophils, which can infiltrate the lungs and cause remote lung injury (RLI) (61). Corberand and colleagues found that there is an increased proportion of neutrophils in bronchoalveolar lavage fluid of healthy older adults (62). Additionally, the pro-inflammatory pulmonary mononuclear macrophage subpopulation increases with age, leading to the secretion of pro-inflammatory cytokines including IL-6, which contribute to inflammation (63, 64). This is in line with our findings showing enhanced pro-inflammatory cytokine levels in lungs from aged mice. According to Balistreri et al., the inflammatory response to trauma in aging mice may be exacerbated due to a stronger activation of NF-κB, indicating that aging may worsen the response through this signaling pathway (65). Similarly, Zhao et al. suggested that NF-κB activity is upregulated in aging mice (66). Also, data from our study indicate that aged mice have stronger NF-κB activation compared to young mice (Figure 4). Notably, the increased levels of apoptotic markers in aging mice are related to the accumulation of mutant mRNA in senescent cells, and

the results of Kujoth et al. suggest that aged mice expressed higher levels of caspase-3 in multiple organs (67). In line with these reports, our results show a significant increase in caspase-3 levels in aged mice after trauma (Figures 1D, E). Also, the NLRP3 inflammasome is involved in the pathogenesis of many age-related diseases. Trauma-induced and aging-related DAMPs are known to induce NLRP3 and IL-1β cleavage (18, 68, 69). It is noteworthy that the discoveries shown in this study disclosed higher levels of gene expression for *Il-1β* and *Nlrp3* as well as enhanced NLRP3, ASC and GSDMD protein expression in traumatized elderly mice, alongside elevated IL-1β protein levels in BAL fluid (Figures 5, 6). Furthermore, this experiment detected a more significant degree of neutrophil infiltration, and lung damage indicated by SPC and HMGB1 in aged lung tissues following THFx compared to younger mice. These findings imply that the aging process intensifies the production of inflammatory agents and neutrophil infiltration in the lung post THFx, resulting in a more severe inflammatory response and damage of the lung tissue.

This study has several limitations that should be acknowledged. Firstly, only male mice and not female mice were used in our experiments. Therefore, the conclusion can only be drawn in the male population, and we need to take factor sex into account in future studies. Secondly, in the clinical setting, geriatric patients may have many relatively complex chronic inflammatory diseases, and we have chosen healthy mice, which may have some impact on the results of studies on inflammation. Moreover, the model we used to induce femur fracture and subsequent immune responses in mice may not fully reflect the clinical situation in humans. The clinical scenario usually involves traumatic injury, hemorrhagic shock caused by uncontrolled bleeding, and femur fixation, whereas our model involves pressure-controlled hemorrhagic shock followed by the insertion of a fixator and femoral osteotomy. Moreover, we did not ventilate with intubation during the anesthesia, and the animals are allowed to perform fully weight-bearing activities directly after they awaken from anesthesia, which is very different from the clinical situation. Another limitation of this study is the lack of protein analyses via western blot. Additionally, we only analyzed lung tissue and BAL fluid from a single time point, which limits the generalizability of our findings to other time points. Future studies examining immune responses at multiple time points and prolonged observation of mice after trauma, are necessary to provide more reliable conclusions.

The study aimed to understand how aging affects lung injury and the pulmonary inflammatory response after THFx in mice. Results showed that aging exacerbates trauma-induced inflammation and lung damage through activation of the NF-κB signaling pathway and increased expression of inflammasome components. Thus, the findings highlight the importance of understanding the mechanisms that contribute to an immunosenescent state in aging and how this may impact the inflammatory response following trauma, and furthermore suggests that the vulnerability to dysregulated post-traumatic immune responses increases with age, which may contribute to a higher risk of trauma-induced organ damage, infectious complications, and increased morbidity and mortality in older patients.

Data availability statement

The raw data supporting the conclusions of this article will be made available by the authors, without undue reservation.

Ethics statement

All animal studies were carried out in strict accordance with the German Animal Law and with the permission of the local authorities in Lower Saxony, Germany (approval number: 33.12-42502-04-17/2491). The study was conducted in accordance with the local legislation and institutional requirements.

Author contributions

YZ: Data curation, Formal analysis, Investigation, Methodology, Validation, Visualization, Writing – original draft. FM: Investigation, Methodology, Writing – review & editing. KK: Methodology, Writing – review & editing. JB: Writing – review & editing. AW: Writing – review & editing. CN: Conceptualization, Funding acquisition, Resources, Supervision, Writing – review & editing. KB: Investigation, Methodology, Supervision, Validation, Writing – original draft. BR: Conceptualization, Data curation, Formal analysis, Funding acquisition, Resources, Supervision, Validation, Visualization, Writing – original draft.

Funding

The author(s) declare financial support was received for the research, authorship, and/or publication of this article. This research was funded by the German Research Foundation DFG with the project number 250170148 and grant numbers DFG RE 3304/9-3, and NE 1932/1-3.

Acknowledgments

We thank Baolin Xu for the support during the *in vivo* experimental phase of this project.

Conflict of interest

The authors declare that the research was conducted in the absence of any commercial or financial relationships that could be construed as a potential conflict of interest.

The reviewer VG declared a shared affiliation with the author KK to the handling editor at the time of the review.

Publisher's note

References

1. Murray CJ, Vos T, Lozano R, Naghavi M, Flaxman AD, Michaud C, et al. Disability-adjusted life years (DALYs) for 291 diseases and injuries in 21 regions, 1990-2010: a systematic analysis for the Global Burden of Disease Study 2010. *Lancet* (2012) 380(9859):2197–223. doi: 10.1016/S0140-6736(12)61689-4

2. Lefaivre KA, Starr AJ, Stahel PF, Elliott AC, Smith WR. Prediction of pulmonary morbidity and mortality in patients with femur fracture. *J Trauma* (2010) 69(6):1527–1535; discussion 1535-1526. doi: 10.1097/TA.0b013e3181f8fa3b

3. Bundkirchen K, Macke C, Reifenrath J, Schack LM, Noack S, Relja B, et al. Severe hemorrhagic shock leads to a delayed fracture healing and decreased bone callus strength in a mouse model. *Clin Orthop Relat Res* (2017) 475(11):2783–94. doi: 10.1007/s11999-017-5473-8

4. Gutierrez G, Reines HD, Wulf-Gutierrez ME. Clinical review: hemorrhagic shock. *Crit Care* (2004) 8(5):373–81. doi: 10.1186/cc2851

5. Jastrow KM 3rd, Gonzalez EA, McGuire MF, Suliburk JW, Kozar RA, Iyengar S, et al. Early cytokine production risk stratifies trauma patients for multiple organ failure. *J Am Coll Surg* (2009) 209(3):320–31. doi: 10.1016/j.jamcollsurg.2009.05.002

6. Ding C, Hong S, Zhang M, Sun Y, Li N, Zhang J, et al. Establishment and evaluation of an in *vitro* blast lung injury model using alveolar epithelial cells. *Front Public Health* (2022) 10:994670. doi: 10.3389/fpubh.2022.994670

7. Zhang Y, Zhang J, Korff S, Ayoob F, Vodovotz Y, Billiar TR. Delayed neutralization of interleukin 6 reduces organ injury, selectively suppresses inflammatory mediator, and partially normalizes immune dysfunction following trauma and hemorrhagic shock. *Shock* (2014) 42(3):218–27. doi: 10.1097/SHK.0000000000000211

8. Huber-Lang M, Lambris JD, Ward PA. Innate immune responses to trauma. *Nat Immunol* (2018) 19(4):327–41. doi: 10.1038/s41590-018-0064-8

9. Wutzler S, Lustenberger T, Relja B, Lehnert M, Marzi I. Pathophysiology of multiple trauma: intensive care medicine and timing of treatment. *Chirurg* (2013) 84 (9):753–8. doi: 10.1007/s00104-013-2477-0

10. Chen L, Zhao H, Alam A, Mi E, Eguchi S, Yao S, et al. Postoperative remote lung injury and its impact on surgical outcome. *BMC Anesthesiol* (2019) 19(1):30. doi: 10.1186/s12871-019-0698-6

11. Papayannopoulos V. Neutrophils stepping through (to the other side). *Immunity* (2018) 49(6):992–4. doi: 10.1016/j.immuni.2018.12.006

12. Millar MW, Fazal F, Rahman A. Therapeutic targeting of NF-kappaB in acute lung injury: A double-edged sword. *Cells* (2022) 11(20): 3317. doi: 10.3390/cells11203317

13. Relja B, Wagner N, Franz N, Dieteren S, Mors K, Schmidt J, et al. Ethyl pyruvate reduces acute lung damage following trauma and hemorrhagic shock via inhibition of NF-kappaB and HMGB1. *Immunobiology* (2018) 223(3):310–8. doi: 10.1016/j.imbio.2017.10.037

14. Dieteren S, Franz N, Kohler K, Nowak A, Ehnert S, Surov A, et al. Ethyl pyruvate reduces systemic leukocyte activation via caspase-1 and NF-kappaB after blunt chest trauma and haemorrhagic shock. *Front Med (Lausanne)* (2020) 7:562904. doi: 10.3389/fmed.2020.562904

15. Tang J, Xu L, Zeng Y, Gong F. Effect of gut microbiota on LPS-induced acute lung injury by regulating the TLR4/NF-kB signaling pathway. *Int Immunopharmacol* (2021) 91:107272. doi: 10.1016/j.intimp.2020.107272

16. Wei J, Wang H, Wang H, Wang B, Meng L, Xin Y, et al. The role of NLRP3 inflammasome activation in radiation damage. *BioMed Pharmacother* (2019) 118:109217. doi: 10.1016/j.biopha.2019.109217

17. Sayan M, Mossman BT. The NLRP3 inflammasome in pathogenic particle and fibre-associated lung inflammation and diseases. *Part Fibre Toxicol* (2016) 13(1):51. doi: 10.1186/s12989-016-0162-4

18. Franchi L, Eigenbrod T, Munoz-Planillo R, Nunez G. The inflammasome: a caspase-1-activation platform that regulates immune responses and disease pathogenesis. *Nat Immunol* (2009) 10(3):241–7. doi: 10.1038/ni.1703

19. Guo Y, Zhang H, Lv Z, Du Y, Li D, Fang H, et al. Up-regulated CD38 by daphnetin alleviates lipopolysaccharide-induced lung injury via inhibiting MAPK/NF-kappaB/NLRP3 pathway. *Cell Commun Signal* (2023) 21(1):66. doi: 10.1186/s12964-023-01041-3

20. King KL, Dewar DC, Briggs GD, Jones M, Balogh ZJ. Postinjury multiple organ failure in polytrauma: more frequent and potentially less deadly with less crystalloid. *Eur J Trauma Emerg Surg* (2023). doi: 10.1007/s00068-022-02202-8

21. Bartlett DB, Firth CM, Phillips AC, Moss P, Baylis D, Syddall H, et al. The age-related increase in low-grade systemic inflammation (Inflammaging) is not driven by cytomegalovirus infection. *Aging Cell* (2012) 11(5):912–5. doi: 10.1111/j.1474-9726.2012.00849.x

22. Franceschi C, Capri M, Monti D, Giunta S, Olivieri F, Sevini F, et al. Inflammaging and anti-inflammaging: a systemic perspective on aging and longevity emerged from studies in humans. *Mech Ageing Dev* (2007) 128(1):92–105. doi: 10.1016/j.mad.2006.11.016

23. Schneider JL, Rowe JH, Garcia-de-Alba C, Kim CF, Sharpe AH, Haigis MC. The aging lung: Physiology, disease, and immunity. *Cell* (2021) 184(8):1990–2019. doi: 10.1016/j.cell.2021.03.005

24. Moliva JI, Rajaram MV, Sidiki S, Sasindran SJ, Guirado E, Pan XJ, et al. Molecular composition of the alveolar lining fluid in the aging lung. *Age (Dordr)* (2014) 36(3):9633. doi: 10.1007/s11357-014-9633-4

25. Kwak HB, Lee Y, Kim JH, Van Remmen H, Richardson AG, Lawler JM. MnSOD overexpression reduces fibrosis and pro-apoptotic signaling in the aging mouse heart. *J Gerontol A Biol Sci Med Sci* (2015) 70(5):533–44. doi: 10.1093/gerona/glu090

26. Zannas AS, Jia M, Hafner K, Baumert J, Wiechmann T, Pape JC, et al. Epigenetic upregulation of FKBP5 by aging and stress contributes to NF-kappaB-driven inflammation and cardiovascular risk. *Proc Natl Acad Sci USA* (2019) 116 (23):11370–9. doi: 10.1073/pnas.1816847116

27. Canan CH, Gokhale NS, Carruthers B, Lafuse WP, Schlesinger LS, Torrelles JB, et al. Characterization of lung inflammation and its impact on macrophage function in aging. *J Leukoc Biol* (2014) 96(3):473–80. doi: 10.1189/jlb.4A0214-093RR

28. Boyd AR, Shivshankar P, Jiang S, Berton MT, Orihuela CJ. Age-related defects in TLR2 signaling diminish the cytokine response by alveolar macrophages during murine pneumococcal pneumonia. *Exp Gerontol* (2012) 47(7):507–18. doi: 10.1016/j.exger.2012.04.004

29. Lara PC, Macias-Verde D, Burgos-Burgos J. Age-induced NLRP3 inflammasome over-activation increases lethality of SARS-coV-2 pneumonia in elderly patients. *Aging Dis* (2020) 11(4):756–62. doi: 10.14336/AD.2020.0601

30. Stout-Delgado HW, Cho SJ, Chu SG, Mitzel DN, Villalba J, El-Chemaly S, et al. Age-dependent susceptibility to pulmonary fibrosis is associated with NLRP3 inflammasome activation. *Am J Respir Cell Mol Biol* (2016) 55(2):252–63. doi: 10.1165/rcmb.2015-0222OC

31. Bundkirchen K, Ye W, Nowak AJ, Lienenklaus S, Welke B, Relja B, et al. Fracture healing in elderly mice and the effect of an additional severe blood loss: A radiographic and biomechanical murine study. *Bioengineering (Basel)* (2023) 10(1): 31. doi: 10.3390/bioengineering10010070

32. Bundkirchen K, Macke C, Angrisani N, Schack LM, Noack S, Fehr M, et al. Hemorrhagic shock alters fracture callus composition and activates the IL6 and RANKL/OPG pathway in mice. *J Trauma Acute Care Surg* (2018) 85(2):359–66. doi: 10.1097/TA.0000000000001952

33. Noack L, Bundkirchen K, Xu B, Gylstorff S, Zhou Y, Kohler K, et al. Acute intoxication with alcohol reduces trauma-induced proinflammatory response and barrier breakdown in the lung via the wnt/beta-catenin signaling pathway. *Front Immunol* (2022) 13:866925. doi: 10.3389/fimmu.2022.866925

34. Matute-Bello G, Downey G, Moore BB, Groshong SD, Matthay MA, Slutsky AS, et al. Acute Lung Injury in Animals Study G: An official American Thoracic Society workshop report: features and measurements of experimental acute lung injury in animals. *Am J Respir Cell Mol Biol* (2011) 44(5):725–38. doi: 10.1165/rcmb.2009-0210ST

35. van Breugel JMM, Niemeyer MJS, Houwert RM, Groenwold RHH, Leenen LPH, van Wessem KJP. Global changes in mortality rates in polytrauma patients admitted to the ICU-a systematic review. *World J Emerg Surg* (2020) 15(1):55. doi: 10.1186/s13017-020-00330-3

36. Stormann P, Auner B, Schimunek L, Serve R, Horst K, Simon TP, et al. Leukotriene B4 indicates lung injury and on-going inflammatory changes after severe trauma in a porcine long-term model. *Prostaglandins Leukot Essent Fatty Acids* (2017) 127:25–31. doi: 10.1016/j.plefa.2017.09.014

37. Zhang Q, Raoof M, Chen Y, Sumi Y, Sursal T, Junger W, et al. Circulating mitochondrial DAMPs cause inflammatory responses to injury. *Nature* (2010) 464 (7285):104–7. doi: 10.1038/nature08780

38. Colom B, Bodkin JV, Beyrau M, Woodfin A, Ody C, Rourke C, et al. Leukotriene B4-neutrophil elastase axis drives neutrophil reverse transendothelial cell migration *in vivo*. *Immunity* (2015) 42(6):1075–86. doi: 10.1016/j.immuni.2015.05.010

39. Kalsotra A, Zhao J, Anakk S, Dash PK, Strobel HW. Brain trauma leads to enhanced lung inflammation and injury: evidence for role of P4504Fs in resolution. *J Cereb Blood Flow Metab* (2007) 27(5):963–74. doi: 10.1038/sj.jcbfm.9600396

40. Conti P, Ronconi G, Caraffa A, Gallenga CE, Ross R, Frydas I, et al. Induction of pro-inflammatory cytokines (IL-1 and IL-6) and lung inflammation by Coronavirus-19 (COVI-19 or SARS-CoV-2): anti-inflammatory strategies. *J Biol Regul Homeost Agents* (2020) 34(2):327–31. doi: 10.23812/CONTI-E

41. Houssiau FA, Devogelaer JP, Van Damme J, de Deuxchaisnes CN, Van Snick J. Interleukin-6 in synovial fluid and serum of patients with rheumatoid arthritis and other inflammatory arthritides. *Arthritis Rheum* (1988) 31(6):784–8. doi: 10.1002/art.1780310614

42. Relja B, Yang B, Bundkirchen K, Xu B, Kohler K, Neunaber C. Different experimental multiple trauma models induce comparable inflammation and organ injury. *Sci Rep* (2020) 10(1):20185. doi: 10.1038/s41598-020-76499-z

43. Perl M, Chung CS, Perl U, Lomas-Neira J, de Paepe M, Cioffi WG, et al. Fas-induced pulmonary apoptosis and inflammation during indirect acute lung injury. *Am J Respir Crit Care Med* (2007) 176(6):591–601. doi: 10.1164/rccm.200611-1743OC

44. Perl M, Chung CS, Perl U, Thakkar R, Lomas-Neira J, Ayala A. Therapeutic accessibility of caspase-mediated cell death as a key pathomechanism in indirect acute lung injury. *Crit Care Med* (2010) 38(4):1179–86. doi: 10.1097/CCM.0b013e3181d4563f

45. Zhang H, Sun T, Liu Z, Zhang J, Wang X, Liu J. Systemic inflammatory responses and lung injury following hip fracture surgery increases susceptibility to infection in aged rats. *Mediators Inflammation* (2013) 2013:536435. doi: 10.1155/2013/536435

46. Nowak AJ, Relja B. The impact of acute or chronic alcohol intake on the NF-kappaB signaling pathway in alcohol-related liver disease. *Int J Mol Sci* (2020) 21 (24):9407. doi: 10.3390/ijms21249407

47. Hoesel B, Schmid JA. The complexity of NF-kappaB signaling in inflammation and cancer. *Mol Cancer* (2013) 12:86. doi: 10.1186/1476-4598-12-86

48. Barnabei L, Laplantine E, Mbongo W, Rieux-Laucat F, Weil R. NF-kappaB: at the borders of autoimmunity and inflammation. *Front Immunol* (2021) 12:716469. doi: 10.3389/fimmu.2021.716469

49. Tschopp J, Schroder K. NLRP3 inflammasome activation: The convergence of multiple signalling pathways on ROS production? *Nat Rev Immunol* (2010) 10(3):210–5. doi: 10.1038/nri2725

50. Said-Sadier N, Ojcius DM. Alarmins, inflammasomes and immunity. *BioMed J* (2012) 35(6):437–49. doi: 10.4103/2319-4170.104408

51. Bortolotti P, Faure E, Kipnis E. Inflammasomes in tissue damages and immune disorders after trauma. *Front Immunol* (2018) 9:1900. doi: 10.3389/fimmu.2018.01900

52. Starzl R, Wolfram D, Zamora R, Jefferson B, Barclay D, Ho C, et al. Cardiac arrest disrupts caspase-1 and patterns of inflammatory mediators differently in skin and muscle following localized tissue injury in rats: insights from data-driven modeling. *Front Immunol* (2015) 6:587. doi: 10.3389/fimmu.2015.00587

53. Maslanik T, Mahaffey L, Tannura K, Beninson L, Greenwood BN, Fleshner M. The inflammasome and danger associated molecular patterns (DAMPs) are implicated in cytokine and chemokine responses following stressor exposure. *Brain Behav Immun* (2013) 28:54–62. doi: 10.1016/j.bbi.2012.10.014

54. Xiang M, Shi X, Li Y, Xu J, Yin L, Xiao G, et al. Hemorrhagic shock activation of NLRP3 inflammasome in lung endothelial cells. *J Immunol* (2011) 187(9):4809–17. doi: 10.4049/jimmunol.1102093

55. Yang J, Zhao Y, Zhang P, Li Y, Yang Y, Yang Y, et al. Hemorrhagic shock primes for lung vascular endothelial cell pyroptosis: role in pulmonary inflammation following LPS. *Cell Death Dis* (2016) 7(9):e2363. doi: 10.1038/cddis.2016.274

56. Xu P, Wen Z, Shi X, Li Y, Fan L, Xiang M, et al. Hemorrhagic shock augments Nlrp3 inflammasome activation in the lung through impaired pyrin induction. *J Immunol* (2013) 190(10):5247–55. doi: 10.4049/jimmunol.1203182

57. Franceschi C, Bonafe M, Valensin S, Olivieri F, De Luca M, Ottaviani E, et al. Inflamm-aging. An evolutionary perspective on immunosenescence. *Ann N Y Acad Sci* (2000) 908:244–54. doi: 10.1111/j.1749-6632.2000.tb06651.x

58. Basisty N, Kale A, Jeon OH, Kuehnemann C, Payne T, Rao C, et al. A proteomic atlas of senescence-associated secretomes for aging biomarker development. *PloS Biol* (2020) 18(1):e3000599. doi: 10.1371/journal.pbio.3000599

59. Stock AJ, Kasus-Jacobi A, Pereira HA. The role of neutrophil granule proteins in neuroinflammation and Alzheimer's disease. *J Neuroinflamm* (2018) 15(1):240. doi: 10.1186/s12974-018-1284-4

60. Chatta GS, Andrews RG, Rodger E, Schrag M, Hammond WP, Dale DC. Hematopoietic progenitors and aging: alterations in granulocytic precursors and responsiveness to recombinant human G-CSF, GM-CSF, and IL-3. *J Gerontol* (1993) 48(5):M207–212. doi: 10.1093/geronj/48.5.M207

61. Barkaway A, Rolas L, Joulia R, Bodkin J, Lenn T, Owen-Woods C, et al. Age-related changes in the local milieu of inflamed tissues cause aberrant neutrophil trafficking and subsequent remote organ damage. *Immunity* (2021) 54(7):1494–1510 e1497. doi: 10.1016/j.immuni.2021.04.025

62. Corberand J, Ngyen F, Laharrague P, Fontanilles AM, Gleyzes B, Gyrard E, et al. Polymorphonuclear functions and aging in humans. *J Am Geriatr Soc* (1981) 29 (9):391–7. doi: 10.1111/j.1532-5415.1981.tb02376.x

63. Albright JM, Dunn RC, Shults JA, Boe DM, Afshar M, Kovacs EJ. Advanced age alters monocyte and macrophage responses. *Antioxid Redox Signal* (2016) 25(15):805–15. doi: 10.1089/ars.2016.6691

64. Hearps AC, Martin GE, Angelovich TA, Cheng WJ, Maisa A, Landay AL, et al. Aging is associated with chronic innate immune activation and dysregulation of monocyte phenotype and function. *Aging Cell* (2012) 11(5):867–75. doi: 10.1111/j.1474-9726.2012.00851.x

65. Balistreri CR, Candore G, Accardi G, Colonna-Romano G, Lio D. NF-kappaB pathway activators as potential ageing biomarkers: targets for new therapeutic strategies. *Immun Ageing* (2013) 10(1):24. doi: 10.1186/1742-4933-10-24

66. Zhao J, Li X, McGowan S, Niedernhofer LJ, Robbins PD. NF-kappaB activation with aging: characterization and therapeutic inhibition. *Methods Mol Biol* (2015) 1280:543–57. doi: 10.1007/978-1-4939-2422-6_32

67. Kujoth GC, Hiona A, Pugh TD, Someya S, Panzer K, Wohlgemuth SE, et al. Mitochondrial DNA mutations, oxidative stress, and apoptosis in mammalian aging. *Science* (2005) 309(5733):481–4. doi: 10.1126/science.1112125

68. Kayagaki N, Stowe IB, Lee BL, O'Rourke K, Anderson K, Warming S, et al. Caspase-11 cleaves gasdermin D for non-canonical inflammasome signalling. *Nature* (2015) 526(7575):666–71. doi: 10.1038/nature15541

69. Shimada K, Crother TR, Karlin J, Dagvadorj J, Chiba N, Chen S, et al. Oxidized mitochondrial DNA activates the NLRP3 inflammasome during apoptosis. *Immunity* (2012) 36(3):401–14. doi: 10.1016/j.immuni.2012.01.009

frontiers | Frontiers in Immunology

TYPE Review
PUBLISHED 25 January 2024
DOI 10.3389/fimmu.2024.1353990

OPEN ACCESS

EDITED BY
Pietro Ghezzi,
University of Urbino Carlo Bo, Italy

REVIEWED BY
Vidya P. Kumar,
Armed Forces Radiobiology Research Institute, United States
Lynnette H. Cary,
Uniformed Services University of the Health Sciences, United States
Christopher D. Porada,
Wake Forest University, United States

*CORRESPONDENCE
Ping Wang
pwang@northwell.edu

RECEIVED 11 December 2023
ACCEPTED 15 January 2024
PUBLISHED 25 January 2024

CITATION
Yamaga S, Aziz M, Murao A, Brenner M and Wang P (2024) DAMPs and radiation injury. *Front. Immunol.* 15:1353990. doi: 10.3389/fimmu.2024.1353990

DAMPs and radiation injury

Satoshi Yamaga[1], Monowar Aziz[1,2], Atsushi Murao[1], Max Brenner[1,2] and Ping Wang[1,2]*

[1]Center for Immunology and Inflammation, The Feinstein Institutes for Medical Research, Manhasset, NY, United States, [2]Departments of Surgery and Molecular Medicine, Zucker School of Medicine at Hofstra/Northwell, Manhasset, NY, United States

The heightened risk of ionizing radiation exposure, stemming from radiation accidents and potential acts of terrorism, has spurred growing interests in devising effective countermeasures against radiation injury. High-dose ionizing radiation exposure triggers acute radiation syndrome (ARS), manifesting as hematopoietic, gastrointestinal, and neurovascular ARS. Hematopoietic ARS typically presents with neutropenia and thrombocytopenia, while gastrointestinal ARS results in intestinal mucosal injury, often culminating in lethal sepsis and gastrointestinal bleeding. This deleterious impact can be attributed to radiation-induced DNA damage and oxidative stress, leading to various forms of cell death, such as apoptosis, necrosis and ferroptosis. Damage-associated molecular patterns (DAMPs) are intrinsic molecules released by cells undergoing injury or in the process of dying, either through passive or active pathways. These molecules then interact with pattern recognition receptors, triggering inflammatory responses. Such a cascade of events ultimately results in further tissue and organ damage, contributing to the elevated mortality rate. Notably, infection and sepsis often develop in ARS cases, further increasing the release of DAMPs. Given that lethal sepsis stands as a major contributor to the mortality in ARS, DAMPs hold the potential to function as mediators, exacerbating radiation-induced organ injury and consequently worsening overall survival. This review describes the intricate mechanisms underlying radiation-induced release of DAMPs. Furthermore, it discusses the detrimental effects of DAMPs on the immune system and explores potential DAMP-targeting therapeutic strategies to alleviate radiation-induced injury.

KEYWORDS

DAMPs, radiation, necrosis, apoptosis, eCIRP, HMGB1

Introduction

The increasing threat of unexpected exposure to ionizing radiation implicates the urgent unmet need for developing medical countermeasures. The global communities must be united to confront a broad range of nuclear threats. These encompass the detonation of sophisticated and improvised nuclear weapons, potential terrorist deployment of radiologic dispersal devices (i.e., dirty bombs), attacks on nuclear power plants, and the occurrence of accidents at these facilities caused by technical failure or natural disasters as happened in

Chernobyl, Ukraine in 1986 and Fukushima, Japan in 2011 (1–4). Exposure to high doses of radiation can cause serious health problems known as acute radiation syndrome (ARS), consisting of three major sub-syndromes, hematopoietic (H), gastrointestinal (GI), and neurovascular (NV) ARS (5, 6). Medical countermeasures for ARS are classified into radioprotectors administered before radiation exposure, radiation mitigators administered shortly after radiation exposure and before symptoms appear, and radiation therapeutics administered after symptoms of radiation exposure appear (7). At the moment, the U.S. Food and Drug Administration (FDA) has approved two radioprotectors to be used in the context of radiotherapy: the free radical scavenger Amifostine and the recombinant human keratinocyte growth factor Palifermin (8). The FDA has also approved six radiomitigating medical countermeasures: the granulocyte colony-stimulating factors (G-CSF) Neupogen (filgrastim), Neulasta (pegfilgrastim), Udenyka (pegfilgrastim-cbqv), and Stimufend (pegfilgrastim-fpgk), the granulocyte-macrophage colony-stimulating factor (GM-CSF) Leukine (sargramostim), and thrombopoietin receptor agonist Nplate (romiplostim) (9). These radiomitigators are not approved as radioprotectors and only mitigate hematopoietic dysfunction to some extent. There are no FDA-approved medical countermeasures available for GI-ARS or NV-ARS. The major mechanisms of medical countermeasures currently under development include free radical scavenging, DNA damage reduction, DNA repair promotion, apoptosis inhibition, and GI recovery, in addition to the promotion of hematopoiesis (10, 11).

Exposure to ionizing radiation induces the release of damage-associated molecular patterns (DAMPs) by DNA damage and several types of cell death (12). A growing body of evidence suggests that DAMPs play pro-inflammatory roles and are associated with disease severity and organ damage in several diseases (13, 14). DAMPs hold the potential to function as mediators that exacerbate radiation-induced organ injuries, ultimately worsening survival outcomes. This review aims to comprehensively outline the mechanisms underlying radiation injury, with a particular focus on the involvement of DAMPs. Furthermore, we delve into potential therapeutic interventions aimed at mitigating radiation-induced DAMPs and their associated consequences.

Abbreviations: ARS, acute radiation syndrome; ASC, apoptosis-associated speck-like protein containing a CARD; cGAS, cyclic GMP-AMP synthase; DAMPs, damage-associated molecular patterns; exRNA, extracellular RNA; GI-ARS, gastrointestinal-ARS; GPX4, glutathione peroxidase 4; GSDMD, Gasdermin D; GSH, glutathione; HSPs, heat shock proteins; H-ARS, hematopoietic-ARS; HMGB1, high mobility group box 1; IFNs, interferons; MOMP, mitochondria outer membrane permeabilization; mtDNA, mitochondrial DNA; MLKL, mixed lineage kinase domain like pseudokinase; MVBs, multivesicular bodies; NLRP3, NLR family pyrin domain containing 3; NLRs, NOD-like receptors; NF-κB, nuclear factor kappa B; NV-ARS, neurovascular-ARS; PAMPs, pathogen-associated molecular patterns; RCI, radiation-combined injury; ROS, reactive oxygen species; RAGE, receptor for advanced glycation end products; RIPK, receptor-interacting serine/threonine-protein kinase; SAA, serum amyloid A; STING, stimulator of interferon genes; TLRs, Toll-like receptors; TBI, total body irradiation; TREM-1, triggering receptor expressed on myeloid cells-1; TNF, tumor necrosis factor.

Acute radiation syndrome (ARS)

The hematopoietic system emerges as the most vulnerable organ to ARS, with discernible symptoms of H-ARS manifesting following exposure to total body irradiation (TBI) exceeding 2 gray (Gy) in humans (15). Depending on the dose of ionizing radiation, death of hematopoietic stem and progenitor cells and apoptosis of lymphocytes occur (16). Notably, lymphopenia becomes apparent within 6-24 hours after radiation exposure (17). Subsequent to this initial event of the loss of lymphocytes, neutropenia, thrombocytopenia, and anemia ensue, depending on the radiation dose, based on the half-life of these cells and cell fragments in the circulation (18). GI-ARS generally occurs in individuals following exposure to TBI exceeding 5 Gy (19). Radiation exposure damages progenitor cells in the crypts and differentiated cells in the villi cannot turn over due to the loss of the progenitor and stem cells (20, 21). Injury to the intestinal mucosal barrier results in the infiltration of antigens and bacteria into the intestinal wall from the lumen. This breach gives rise to various complications, including the onset of secretory diarrhea resulting in severe protein loss and electrolyte dysfunction, bacterial translocation from the intestinal lumen into the circulation, and intestinal hemorrhage (22). These complications collectively contribute to the lethal sepsis and bleeding along with neutropenia and thrombocytopenia due to H-ARS (23). NV-ARS occurs after TBI with over 10 Gy in humans (19). Damage to the central nervous system involves disruptions in capillary circulation, blood-brain barrier integrity, interstitial edema, and the onset of acute inflammation. NV-ARS results in death within a few days of radiation exposure (19). Human data following radiation exposure indicates that the $LD_{50/60}$, estimating the radiation dose causing lethality in 50% of a population within 60 days, ranges from 3.3-4.5 Gy without medical management to 6-7 Gy with medical intervention, including antimicrobial agents and blood transfusions (17, 23). In addition to ionizing radiation, nuclear explosions also release energy in the form of heat and shock waves (3). Thus, in situations involving nuclear explosions, 60-70% of victims may suffer from a radiation-combined injury (RCI) that includes burns and trauma (24). As a result, RCI can be lethal at low radiation doses due to infections (and possibly increased release of DAMPs, as described later in this review) in patients with burns and trauma (22, 25).

Oxidative stress causes DNA damage by reactive oxygen species (ROS) generated after the ionization of water in the cells. Ionizing radiation can also induce direct DNA damage including single- and double-strand breaks (26). The DNA damage response induces a reversible cell cycle arrest to give cells time to repair damage (12). When DNA damage cannot be resolved by the repair process, the DNA damage response converts into a signal pathway of apoptotic cell death or senescence, most often through p53-dependent mechanisms (27). Mitotic catastrophe can occur when cells undergo DNA damage during mitosis or enter mitosis with DNA damage. Mitotic catastrophe causes the formation of cells with

multi-micronuclei or two nuclei (28). These cells are unable to complete the cell cycle, ultimately leading to their entry into senescence or their demise through apoptosis or necrosis (27). Exposure to ionizing radiation can affect not only nuclear DNA, but also other cellular organelles including mitochondria, Golgi apparatus, and lysosomes (29). Mitochondria serve as the primary generators of ROS within the cells. Radiation-induced mitochondrial DNA damage induces ROS generation, leading to a decrease in mitochondrial membrane potential and inducing mitochondria outer membrane permeabilization (MOMP) (29). The subsequent release of cytochrome c and activation of caspase-9 lead to apoptosis (30).

Recent studies have unveiled non-apoptotic signaling pathways of programmed cell death such as necroptosis, pyroptosis, and ferroptosis as additional forms of ionizing radiation-induced cell death. For instance, oxidative stress induced by ionizing radiation activates the inflammasome pathway, causing pyroptosis and contributing to organ damage (31, 32). Necroptosis in the intestine has been shown to contribute to mortality after lethal radiation exposure (33). Furthermore, the accumulation of ROS resulting from radiation exposure has been linked to the induction of ferroptosis, correlating with H-ARS, GI-ARS, and radiation-induced lung injury (34–36).

Damage-associated molecular patterns (DAMPs)

The immune system initiates an immune response against invasive pathogens based on the distinction of 'self' from 'non-self' (37). Innate immune cells express pattern recognition receptors, such as Toll-like receptors (TLRs), recognizing pathogen-associated molecular patterns (PAMPs) (37). Pathogen-independent immune responses are also initiated by recognition of DAMPs released from stressed or damaged cells (38). DAMPs activate innate immune cells such as neutrophils, macrophages, and dendritic cells (39). Consequently, various cytokines and chemokines are released, activating adaptive immune responses (40). DAMPs also activate non-immune cells such as epithelial cells, endothelial cells, and fibroblasts, leading to the release of inflammatory mediators (37). Typical endogenous DAMPs include extracellular cold-inducible RNA-binding protein (eCIRP), high mobility group box 1 (HMGB1), histones, heat shock proteins (HSPs), ATP, and nuclear and mitochondrial DNA (mtDNA), extracellular RNA (exRNA), and uric acid (38). The major DAMP-recognizing pattern recognition receptors include TLRs, NOD-like receptors (NLRs), RIG-I-like receptors, and C-type lectin receptors (41). Following the recognition of DAMPs, TLRs interact with myeloid differentiation factor 88 and TIR-domain-containing adaptor-inducing beta interferon to phosphorylate downstream mitogen-activated protein kinases, leading to activation of the transcription factors, activator protein-1 and nuclear factor kappa B (NF-κB) (37). DAMPs also transduce signals through the receptor for advanced glycation end products (RAGE), triggering receptor expressed on myeloid cells-1 (TREM-1), G-protein-coupled receptors, transient receptor potential, and P2X7 receptor channels (37).

The release of DAMPs has been observed in radiation injury and a number of other diseases including sepsis, trauma, ischemia-reperfusion injury, brain injuries, and radiation exposure (39, 42–45). In sepsis, host recognition of DAMPs is a critical contributor to an excessive immune response. Circulating DAMPs correlate with disease severity, and their inhibition has been shown to improve outcomes in experimental models of sepsis (38, 39). In severe trauma, the escalation of the innate immune response due to exposure to DAMPs leads to coagulopathy and excessive inflammation, resulting in multiple organ dysfunction, such as intestinal barrier dysfunction and acute lung injury (46). In intestinal ischemia-reperfusion injury, circulating mtDNA correlates with inflammatory responses and contributes to intestinal injury (43). Excessive inflammatory signaling induced by DAMPs can exhaust hematopoiesis and induce dysfunction of hematopoietic stem cells (47). Furthermore, the DAMPs-mediated neuroinflammation after traumatic brain injury, subarachnoid hemorrhage, and cerebral ischemia exacerbates secondary damage of the central nerve system by promoting cerebral edema or triggering vascular spasm and microthrombi (48). Given that these clinical complications are frequently observed in ARS, it is evident that the release of DAMPs can exacerbate the outcomes in ARS.

DAMP release after radiation injury

Radiation-induced cell damage can signal the immune system to potential danger through the release of DAMPs, akin to the molecular pattern recognition seen in microorganisms. Inflammation resulting from an excess of DAMP release has the potential to worsen radiation-induced tissue and organ damage, emphasizing the significance of DAMP modulation as potential mitigation for radiation injury (49). Here, we provide a summary of the major DAMPs released during radiation injury, and explore interventions aimed at enhancing outcomes (Table 1).

Extracellular cold-inducible RNA-binding protein (eCIRP)

Intracellular CIRP is an RNA chaperone that functions as a cellular stress response protein (58). Once outside of the cell, eCIRP plays an important role as an endogenous inflammatory mediator acting as a new DAMP in radiation injury, sepsis, hemorrhagic shock, and ischemia-reperfusion injury (58, 59). eCIRP induces the production of proinflammatory cytokines and chemokines in macrophages via the TLR4/MD2 complex and NF-κB signaling axis. Accordingly, it contributes to tissue damage by upregulating ICAM-1 expression and promoting excessive NET formation in neutrophils (58, 60). eCIRP can also bind to TREM-1, worsening organ damage and prognosis by promoting inflammation (61). eCIRP has been shown to suppress the bacterial phagocytosis of macrophages by promoting the formation of STAT3-βPIX complex and suppressing the activation of Rac1 (62). We have recently

TABLE 1 Targeting DAMPs in radiation injury.

DAMPs	Radiation model	Interventions	Outcomes	References
eCIRP	6.5 Gy TBI, X-ray, C57BL/6 mice	CIRP knockout/TREM-1 knockout	Improves overall survival rate	(49)
HMGB1	6.5 Gy PBI, X-ray, C57BL/6 mice	Glycyrrhizin	Decreases pro-inflammatory cytokine production and mitigates intestinal injury	(50)
	20 Gy PBI, X-ray, C57BL/6 mice	Glycyrrhizin	Decreases pro-inflammatory cytokine production and mitigates lung injury	(51)
mtDNA	6 Gy TBI, γ-ray, C57BL/6 mice	VDAC1 inhibitor (mtDNA release inhibition)	Decreases type I-IFN mRNA expression and mitigates hematopoietic injury	(52)
exRNA	10 Gy TBI, γ-ray, BALB/c mice	TLR3/double-stranded RNA complex inhibitor	Mitigates intestinal injury and improves overall survival rate	(53)
	9 Gy TBI, γ-ray, BALB/c mice	Exosome inhibitor	Improves overall survival rate	(54)
SAA	2-8 Gy TBI/PBI, X-ray, C57BL/6 mice	N/A	Useful for radiation biodosimetry at 24 hours after irradiation	(55, 56)
	12, 14 Gy PBI, X-ray, C57BL/6 mice	N/A	Useful for radiation biodosimetry at 3 and 4 days after irradiation	(57)

CIRP, cold-inducible RNA-binding protein; DAMPs, damage-associated molecular patterns; exRNA, extracellular RNA; HMGB1, high mobility group box 1; IFN, interferon; mtDNA, mitochondrial DNA; SAA, serum amyloid A; PBI, partial body irradiation; TBI, total body irradiation; TLR, Toll-like receptor; TREM-1, triggering receptor expressed on myeloid cells-1; VDAC, voltage-dependent anion channel; N/A, not available.

demonstrated that high-dose ionizing radiation induces eCIRP release in the peritoneal cavity of irradiated mice and in the cell culture supernatant of irradiated mouse peritoneal cells (49). Moreover, the radiation-induced eCIRP release upregulated the expression of TREM-1 on macrophages, and mice knocked out for CIRP or TREM-1 had improved 30-day survival rates after 6.5 Gy TBI (49). Therefore, targeting the eCIRP-TREM-1 axis holds promise as a therapeutic strategy for post-radiation injury, potentially attenuating lethal infections and sepsis (49).

High mobility group box 1 (HMGB1)

HMGB1 is a nuclear protein that acts as a DNA chaperone (63). As a DAMP, HMGB1 binds to pattern recognition receptors, including RAGE, TLR2, TLR4, TLR9, and TREM-1, to induce inflammatory responses (64, 65). In a murine model of sepsis, HMGB1, released from macrophages, has been shown to function as a late lethal mediator (66). In acute lung injury and hepatic ischemia-reperfusion injury models, administration of anti-HMGB1 antibody reduces lung neutrophil influx and pulmonary edema and mitigates liver damage (67, 68). Exposure to ionizing radiation increases in both cellular mRNA expression and serum protein levels of HMGB1 in a dose-dependent manner in experimental mice model (69). Glycyrrhizin, one of the inhibitors of HMGB1, reduced the release of serum inflammatory cytokines in abdominal irradiated mice (6.5 Gy) through the downregulation of the HMGB1/TLR4 signaling pathway and significantly attenuated intestinal injury (50). In thoracic irradiated mice, glycyrrhizin also reduced inflammatory cytokines in the bronchoalveolar lavage fluid and mitigated radiation-induced lung injury by inhibiting downstream transcription factors related to the HMGB1/TLR4 axis (51).

Mitochondrial DNA (mtDNA)

mtDNA is susceptible to ionizing radiation compared to nuclear DNA due to the lack of protective histones and limited repair mechanism (29). Mitochondrial dysfunction resulting from failure of DNA repair leads to the release of mitochondrial components including cytochrome c, ATP, mtDNA, and mtRNA (29). The mtDNA in the cytosol is recognized by the cyclic GMP-AMP synthase (cGAS) to activate the stimulator of interferon genes (STING) signaling pathway, resulting in the production of type I interferons (IFNs) (65, 70). Excessive production of type I IFNs can cause exhaustion in hematopoietic stem cells (71, 72). In the 6 Gy TBI model, mtDNA released into the cytosol has been reported to activate the cGAS-STING pathway and induced type I IFN production, and inhibition of the mtDNA release ameliorated hematopoietic tissue injury (52). The mtDNA released into the cytoplasm can also bind to and activate the NLRP3 inflammasome, which leads to the release of inflammatory cytokines such as IL-1β and IL-18 followed by

pyroptosis (31). Previous studies have shown that pyroptosis in intestinal cells occurred through NLRP3 activation, inducing intestinal injury in the abdominal irradiation model (73, 74). These studies suggest that mtDNA exacerbates ARS pathophysiology and could be a potential therapeutic target for GI-ARS by mitigating pyroptosis and inflammation.

Extracellular RNA (exRNA)

exRNA from host cells is carried along microvesicles and exosomes which protect exRNA from enzyme degradation (75). exRNA acts as a pivotal signaling molecule to mediate communication between cells, but can also serve as DAMPs (75, 76). TLR3 has been known to recognize not only double strand RNA released from virus-infected cells but also endogenous exRNA released from necrotic cells, promoting inflammation and organ dysfunction in autoimmune diseases and sepsis (77–79). It has been shown that large exRNA released from the host small intestine after ionizing radiation exposure induced extensive crypt cell death via TLR3 and inhibition of exRNA binding to TLR3 improved survival in 10 Gy TBI by preventing GI-ARS (53). In the mouse model after 9 Gy TBI, the release of microRNAs (miRNAs) via exosomes worsened intestinal injury by promoting apoptosis and DNA damage of intestinal cells (54). These findings implicate a potential detrimental role for exRNA in ARS.

Serum amyloid A (SAA)

In a radiological event, mass screenings are necessary to triage exposed and non-exposed individuals and to determine the severity of the radiation dose to the exposed population (55). Established biomarkers for estimating radiation dose in exposed individuals are quantification of chromosomal aberrations and γ-H2AX, a marker of DNA double-strand breaks, but these tests are only available in laboratories with trained personnel. Serum amyloid A (SAA) is one of the proteins associated with acute phase reactions resulting from inflammation, infection, trauma, or other events (80). SAA has also been reported as a radiation-responsive biomarker in TBI and partial-body irradiation (PBI) models (55–57, 81). In the mice, after 2-8 Gy TBI, SAA is significantly increased at 24 hours after irradiation compared to controls (55, 56). In the mouse PBI model of GI-ARS, SAA levels significantly increase 3 and 4 days after irradiation with 12 Gy and 14 Gy, respectively (57). Although the serum concentration of SAA increases within a few hours after irradiation and returns to the baseline within 7 days after irradiation, combinations of SAA with other biomarkers provide greater accuracy for the assessment of radiation injury especially, at the acute phase (56, 81).

Mechanisms of DAMP release – passive pathways

The pathways of DAMP release can be categorized into two primary pathways: i) passive release and ii) active release (38). Passive release is primarily linked to cell death processes, including apoptosis, necrosis/necroptosis, pyroptosis, and ferroptosis. Concurrently, DAMPs are actively released through secretion mechanisms such as exocytosis in the forms of lysosomes and exosomes (38). Below, we have outlined the universal approaches to DAMP release. Given that radiation injury is directly associated with these cell death events or initiates pathways relevant to the active release of DAMPs, it is reasonable to infer that these processes are linked to the mechanisms governing DAMPs release in ARS (Figure 1).

Apoptosis

Apoptosis is a form of programmed cell death, initiated by two distinct p53-dependent signaling pathways: the extrinsic and intrinsic apoptosis (82). In the extrinsic receptor-mediated pathway, extracellular death receptors are activated by ligand binding and death-inducible signaling complex (DISC) is formed at the intracellular tail of the receptor to activate pro-caspase-8, or pro-caspase-10, with adapter proteins such as Fas-associated via death domain. The extrinsic apoptosis is also induced by dependence receptors, which mediate lethal signals in the absence of their ligand, and pro-caspase-9 is activated (83, 84). Activated caspase-8 (or caspase-10) and caspase-9 eventually activate executioner caspase-3 and caspase-7 to induce apoptosis (83). On the other hand, severe DNA damage induced by radiation mainly activates the intrinsic pathway (82). A transcription factor p53 induces pro-apoptosis Bcl family proteins including BAX, NOXA and PUMA (85, 86). These proteins mediate MOMP, resulting in the release of mitochondrial proteins into the cytosol (82). Cytochrome c binds to apoptotic peptidase-activating factor 1 and pro-caspase-9 to form apoptosomes that ultimately activate caspase-3 and caspase-7 via the activation of caspase-9 (12, 82). During apoptosis, DAMPs such as HMGB1, ATP, histones, and exRNA are released into the extracellular space (87–90).

Necrosis/necroptosis

Necrosis is an accidental cell death caused by external stimuli such as physical and chemical stress and heat (91). In necrotic cell death, the increased cell expansion disrupts the plasma membrane. As a result, cytoplasmic contents and pro-inflammatory molecules are released into the extracellular space (92). DAMPs, including HMGB1, HSP, and ATP, are shown to be released from necrotic cells (91, 93, 94). Necroptosis is a form of programmed cell death dependent on the activation of receptor-interacting serine/threonine-protein kinase 1 (RIPK1). RIPK1 activation can be caused by the stimulation of tumor necrosis factor (TNF) receptor and other death receptors such as Fas. Activated RIPK1 recruits RIPK3 and this complex phosphorylates mixed lineage kinase domain-like pseudokinase (MLKL) (95). Phosphorylated MLKL forms MLKL oligomers and translocates to the plasma membrane, resulting in inducing membrane permeabilization and cell disruption (95). The inhibition of necroptosis has been shown to decrease HMGB1 release in an LPS-induced intestinal injury model, demonstrating the contribution of necroptosis to the release

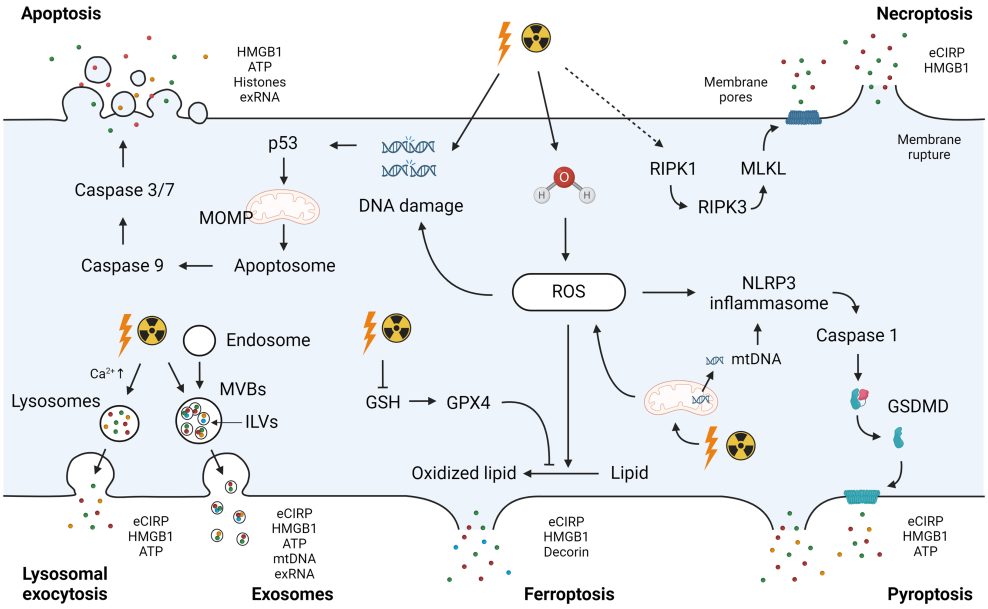

FIGURE 1
Radiation-induced DAMPs release. Exposure to ionizing radiation causes direct DNA damage or ROS-induced DNA damage to activate the intrinsic pathway of apoptosis. Mitochondrial damage by ionizing radiation amplifies ROS production and contributes to DNA damage. ROS accumulation after radiation exposure due to GPX4 impairment and GSH depletion induces the oxidation of polyunsaturated fatty acids in membrane phospholipids, leading to ferroptosis. Radiation-induced ROS leads to activation of the NLRP3 inflammasome. The NLRP3 inflammasome complex activates caspase-1 to cleave GSDMD and form a membrane pore with the GSDMD-N domain, inducing pyroptosis. Ionizing radiation causes the activation of RIPK1, which recruits RIPK3 to phosphorylate MLKL. Phosphorylated MLKL forms MLKL oligomers, leading to necroptosis. DAMPs including eCIRP, HMGB1, ATP, histones, exRNA, and mtDNA can be released as a passive release mechanism after these cell deaths. Mitochondrial dysfunction results in the release of mitochondrial components including mtDNA into the cytosol. Secretion mechanisms such as exocytosis in the forms of lysosomes and exosomes cause active release of DAMPs. DAMPs, damage-associated molecular patterns; ROS, reactive oxygen species; GPX4, glutathione peroxidase 4; GSH, glutathione; NLRP3, NLR family pyrin domain containing 3; GSDMD, Gasdermin D; RIPK, receptor-interacting serine/threonine-protein kinase; MLKL, mixed lineage kinase domain like pseudokinase; eCIRP, extracellular cold-inducible RNA-binding protein; HMGB1, high mobility group box 1; exRNA, extracellular RNA; mtDNA, mitochondrial DNA; MOMP, mitochondria outer membrane permeabilization; MVBs, multivesicular bodies; ILVs, intraluminal vesicles.

of HMGB1 (96). eCIRP has also been demonstrated to be released by necroptosis in a sepsis model (97).

Pyroptosis

Pyroptosis is a lytic cell death process that allows the release of potential immunostimulatory molecules. This programmed cell death can be induced by the canonical and non-canonical pathways (98). In the canonical pathway, pathogen-derived molecules are recognized by inflammasomes. For example, cell stressors including bacteria, viruses, and DAMPs induce potassium efflux, leading to NIMA-related kinase 7 binding to NLR family pyrin domain containing 3 (NLRP3). Subsequently, NLRP3 oligomerization is induced to activate pro-caspase 1 through the adaptor protein ASC (apoptosis-associated speck-like protein containing a CARD) (99). Caspase-1 processes and activates pro-IL-1β and pro-IL-18 and cleaves Gasdermin D (GSDMD) to form a membrane pore with the GSDMD-N domain. In the non-canonical pathway, endotoxin from Gram-negative bacteria directly activates pro-caspase-4 or pro-caspase-5 in humans (or pro-caspase-11 in mice), which also cleave GSDMD. Small DAMPs such as eCIRP (17-19 kDa) are then released through GSDMD's pores along with IL-1β and IL-18 (100, 101). The release of larger DAMPs, such as HMGB1, can ensue when irreversible GSDMD pores cause terminal cell rupture (102, 103).

Ferroptosis

Ferroptosis is a form of programmed cell death characterized by the iron-dependent accumulation of lipid peroxidation (104). At the steady state, intracellular glutathione peroxidase 4 (GPX4) utilizes glutathione (GSH) to reduce lipid peroxidation generated by ROS. However, ROS accumulation due to the impairment of GPX4 and depletion of GSH causes the oxidation of polyunsaturated fatty acids in membrane phospholipids through an intracellular iron-dependent mechanism, leading to ferroptosis (83, 104). DAMPs released by ferroptosis include eCIRP, HMGB1, and decorin, a small leucine-rich proteoglycan of the extracellular matrix (105–107). Decorin, similar to HMGB1, binds to TLR4 and RAGE to induce pro-inflammatory signaling (107, 108).

Mechanisms of DAMP release – active pathways

Exosomes

Exosomes are nano-sized membrane vesicles released upon fusion of multivesicular bodies (MVBs) with the plasma membrane and contain a variety of proteins, lipids, and nucleic

acids (109). The endosomal membranes in early endosomes invaginate to form intraluminal vesicles (ILVs) in the lumen of the vesicular organelles (110). ILVs mature into MVBs by the endosome sorting complex required for transporting (ESCRT)-dependent or ESCRT-independent mechanism. MVBs are then transported to the plasma membrane dependent on their interaction with actin and the microtubule cytoskeleton to be released into the extracellular environment as exosomes (110). Exosomal DAMPs include HMGB1, HSPs, ATP, histones, mtDNA, and eCIRP (111–116). Increased DAMPs in exosomes induce inflammation and exacerbate organ dysfunction in a plethora of disorders including sepsis (117).

Lysosomal exocytosis

Lysosomal exocytosis is another mechanism of active release of DAMPs. After stimulation of a cell receptor, an increase in intracellular Ca^{2+} is detected by synaptotagmin, which is an intracellular calcium sensor on lysosomes. The lysosomes are mobilized to the microtubule organizing center to be associated with the kinesin and transported to the site of secretion (118). The lysosomes dock and fuse with the plasma membrane through soluble *N*-ethylmaleimide-sensitive factor attachment proteins receptor (SNARE) complex Rab proteins, leading to secretion of the soluble components (118, 119). HMGB1, ATP, and eCIRP have been shown to be released by lysosomal exocytosis (58, 120, 121).

DAMPs in sepsis and multiple organ failure after radiation injury

Sepsis from enteric microorganisms in GI-ARS is the major cause of morbidity and mortality in radiation injury (19). The breakdown of the mucosal barrier due to disruption of the intestinal epithelium leads to severe secretory diarrhea and translocation of bacteria into the systemic circulation, resulting in severe sepsis (20). Furthermore, damage to the intestinal mucosa and sepsis of enteric origin occur even after TBI in the H-ARS dose range (122). DAMPs generated by the disruption of the intestinal mucosal barrier in sepsis are transported through the mesenteric lymphatics into the systemic circulation, developing multiple organ failure such as acute lung injury and further deteriorating intestinal barrier injury (123). In RCI with burn and trauma, the pathophysiological role of DAMPs remains unexplored. In severe burns, DAMPs are released from the injured tissue, inducing systemic inflammatory response (124). Immunological exhaustion due to the excessive inflammatory response leads to inhibition of the innate and acquired immune systems, resulting in increased susceptibility to bacterial infections not only from the skin but also from the lung or gut microbiota to cause severe sepsis (124, 125). Furthermore, DAMPs release in trauma is associated with the development of organ injuries such as acute lung injury and acute renal failure (126, 127). DAMPs are also involved in the activation of coagulation pathways, leading to coagulopathy during trauma (124). Additionally, DAMPs have been suggested to induce post-traumatic immunosuppression (42). In the context of RCI, DAMPs may play a critically detrimental role in multiple organ failure and compromised immune systems, thereby exacerbating the prognosis of the patients.

Future perspectives

Medical countermeasures for ARS are currently limited and only available for H-ARS (128). We described DAMPs as exacerbating factors and potential therapeutic targets for ARS. Pharmacological strategies targeting DAMPs to inhibit immune responses include the uses of monoclonal antibodies, peptides, decoy receptors, and small molecules (129). CIRP-derived small peptides that inhibit eCIRP binding to the TLR4-MD2 complex and binding to TREM-1 have been developed and shown to attenuate sepsis, acute kidney injury, and hepatic ischemia-reperfusion injury (61, 130–132). A molecule that directly neutralizes eCIRP has also been identified to improve acute lung injury and survival in sepsis (133). Additionally, we have recently described an engineered oligopeptide that effectively promotes eCIRP clearance from the circulation leading to markedly improved outcomes in sepsis (134). Anti-HMGB1 antibodies have been to be effective in various experimental models such as abdominal sepsis and hemorrhagic shock (63, 135, 136). Small molecules that bind to and block HMGB1, such as glycyrrhizin, and decoy receptors that block HMGB1-RAGE signaling, such as soluble RAGE, also improved several inflammatory disease models (137, 138). exRNAs include non-coding RNA (ncRNA) such as miRNAs, long non-coding RNAs, and circular RNAs as well as messenger RNAs. Recently, miRNAs have been identified as potential biomarkers for various diseases, including radiation injury (139). In experimental radiation models, serum miRNA profiling has been shown to be able to identify exposure to radiation and predict the extent of ARS and the probability of survival, potentially facilitating timely intervention after radiation exposure (140, 141). The high stability and reproducibility of serum miRNAs make them attractive candidates as biomarkers of radiation injury (141). The function of specific ncRNAs as DAMPs in radiation injury remains unclear and may be the subject for future research. In the context of RCI resulting from nuclear explosions, more than half of the patients are accompanied by burns and trauma, resulting in more complicated and severe radiation injury (24). FDA-approved countermeasures for H-ARS alone have failed to improve survival in RCI (24). DAMPs released in burn and trauma injury have potential links with the mechanical injury, ischemia/reperfusion injury, metabolic acidosis, and hypoxia, culminating in multiple organ failure (124). These findings underscore the potential of DAMPs-targeting strategies in addressing the challenges posed by RCI.

Conclusions

In conclusion, exposure to ionizing radiation causes direct DNA damage and oxidative stress, leading to cell death. The subsequent release of DAMPs has the potential to worsen ARS across various body compartments. However, there is a scarcity of studies specifically

addressing DAMPs in the context of radiation injury. A more profound comprehension of the role of DAMPs in radiation injury could pave the way for the development of innovative therapeutic strategies to mitigate the impact of nuclear and radiological threats and accidents.

Author contributions

SY: Data curation, Formal Analysis, Investigation, Methodology, Writing – original draft, Writing – review & editing. MA: Conceptualization, Funding acquisition, Methodology, Resources, Supervision, Validation, Writing – original draft, Writing – review & editing. AM: Investigation, Methodology, Writing – original draft, Writing – review & editing. MB: Formal Analysis, Investigation, Supervision, Visualization, Writing – review & editing, Funding acquisition. PW: Conceptualization, Funding acquisition, Project administration, Resources, Supervision, Writing – review & editing.

Funding

The author(s) declare financial support was received for the research, authorship, and/or publication of this article. This work was partially supported by the National Institutes of Health (NIH) grants U01AI170018, U01AI133655, and R35GM118337.

Acknowledgments

Figure 1 was created using BioRender.com.

Conflict of interest

The authors declare that the research was conducted in the absence of any commercial or financial relationships that could be construed as a potential conflict of interest.

Publisher's note

References

1. Christodouleas JP, Forrest RD, Ainsley CG, Tochner Z, Hahn SM, Glatstein E. Short-term and long-term health risks of nuclear-power-plant accidents. *N Engl J Med* (2011) 364(24):2334–41. doi: 10.1056/NEJMra1103676

2. Hasegawa A, Tanigawa K, Ohtsuru A, Yabe H, Maeda M, Shigemura J, et al. Health effects of radiation and other health problems in the aftermath of nuclear accidents, with an emphasis on Fukushima. *Lancet* (2015) 386(9992):479–88. doi: 10.1016/S0140-6736(15)61106-0

3. Obrador E, Salvador-Palmer R, Villaescusa JI, Gallego E, Pellicer B, Estrela JM, et al. Nuclear and radiological emergencies: biological effects, countermeasures and biodosimetry. *Antioxid (Basel)* (2022) 11(6):1098. doi: 10.3390/antiox11061098

4. Hirohashi N, Shime N, Fujii T. Beyond the unthinkable: are we prepared for rare disasters? *Anaesth Crit Care Pain Med* (2023) 42(4):101266. doi: 10.1016/j.accpm.2023.101266

5. Dainiak N. Medical management of acute radiation syndrome and associated infections in a high-casualty incident. *J Radiat Res* (2018) 59(suppl_2):ii54–64. doi: 10.1093/jrr/rry004

6. Dorr H, Meineke V. Acute radiation syndrome caused by accidental radiation exposure - therapeutic principles. *BMC Med* (2011) 9:126. doi: 10.1186/1741-7015-9-126

7. Singh VK, Newman VL, Romaine PL, Wise SY, Seed TM. Radiation countermeasure agents: an update (2011-2014). *Expert Opin Ther Pat* (2014) 24 (11):1229–55. doi: 10.1517/13543776.2014.964684

8. Aliper AM, Bozdaganyan ME, Sarkisova VA, Veviorsky AP, Ozerov IV, Orekhov PS, et al. Radioprotectors.Org: an open database of known and predicted radioprotectors. *Aging (Albany NY)* (2020) 12(15):15741–55. doi: 10.18632/aging.103815

9. U.S. Food and Drug Administration. *Radiological and Nuclear Emergency Preparedness Information from FDA* (2023). Available at: https://www.fda.gov/emergency-preparedness-and-response/mcm-issues/radiological-and-nuclear-emergency-preparedness-information-fda (Accessed November 22, 2023).

10. Singh VK, Seed TM, Olabisi AO. Drug discovery strategies for acute radiation syndrome. *Expert Opin Drug Discovery* (2019) 14(7):701–15. doi: 10.1080/17460441.2019.1604674

11. Liu L, Liang Z, Ma S, Li L, Liu X. Radioprotective countermeasures for radiation injury (Review). *Mol Med Rep* (2023) 27(3):66. doi: 10.3892/mmr.2023.12953

12. Rodriguez-Ruiz ME, Vitale I, Harrington KJ, Melero I, Galluzzi L. Immunological impact of cell death signaling driven by radiation on the tumor microenvironment. *Nat Immunol* (2020) 21(2):120–34. doi: 10.1038/s41590-019-0561-4

13. Zhou M, Aziz M, Wang P. Damage-associated molecular patterns as double-edged swords in sepsis. *Antioxid Redox Signal* (2021) 35(15):1308–23. doi: 10.1089/ars.2021.0008

14. Hu Q, Ren H, Ren J, Liu Q, Wu J, Wu X, et al. Released mitochondrial DNA following intestinal ischemia reperfusion induces the inflammatory response and gut barrier dysfunction. *Sci Rep* (2018) 8(1):7350. doi: 10.1038/s41598-018-25387-8

15. Shao L, Luo Y, Zhou D. Hematopoietic stem cell injury induced by ionizing radiation. *Antioxid Redox Signal* (2014) 20(9):1447–62. doi: 10.1089/ars.2013.5635

16. Heylmann D, Rodel F, Kindler T, Kaina B. Radiation sensitivity of human and murine peripheral blood lymphocytes, stem and progenitor cells. *Biochim Biophys Acta* (2014) 1846(1):121–9. doi: 10.1016/j.bbcan.2014.04.009

17. Dainiak N, Waselenko JK, Armitage JO, MacVittie TJ, Farese AM. The hematologist and radiation casualties. *Hematol Am Soc Hematol Educ Program* (2003), 473–96. doi: 10.1182/asheducation-2003.1.473

18. Dainiak N. Hematologic consequences of exposure to ionizing radiation. *Exp Hematol* (2002) 30(6):513–28. doi: 10.1016/s0301-472x(02)00802-0

19. Dainiak N, Gent RN, Carr Z, Schneider R, Bader J, Buglova E, et al. Literature review and global consensus on management of acute radiation syndrome affecting nonhematopoietic organ systems. *Disaster Med Public Health Prep* (2011) 5(3):183–201. doi: 10.1001/dmp.2011.73

20. Moussa L, Usunier B, Demarquay C, Benderitter M, Tamarat R, Semont A, et al. Bowel radiation injury: complexity of the pathophysiology and promises of cell and tissue engineering. *Cell Transplant* (2016) 25(10):1723–46. doi: 10.3727/096368916X691664

21. Ayyaz A, Kumar S, Sangiorgi B, Ghoshal B, Gosio J, Ouladan S, et al. Single-cell transcriptomes of the regenerating intestine reveal a revival stem cell. *Nature* (2019) 569(7754):121–5. doi: 10.1038/s41586-019-1154-y

22. Kiang JG, Olabisi AO. Radiation: A poly-traumatic hit leading to multi-organ injury. *Cell Biosci* (2019) 9:25. doi: 10.1186/s13578-019-0286-y

23. Waselenko JK, MacVittie TJ, Blakely WF, Pesik N, Wiley AL, Dickerson WE, et al. Medical management of the acute radiation syndrome: recommendations of the strategic national stockpile radiation working group. *Ann Intern Med* (2004) 140 (12):1037–51. doi: 10.7326/0003-4819-140-12-200406150-00015

24. Kiang JG, Blakely WF. Combined radiation injury and its impacts on radiation countermeasures and biodosimetry. *Int J Radiat Biol* (2023) 99(7):1055–65. doi: 10.1080/09553002.2023.2188933

25. Jacob A, Shah KG, Wu R, Wang P. Ghrelin as a novel therapy for radiation combined injury. *Mol Med* (2010) 16(3-4):137–43. doi: 10.2119/molmed.2009.00154

26. Nikitaki Z, Hellweg CE, Georgakilas AG, Ravanat JL. Stress-induced DNA damage biomarkers: applications and limitations. *Front Chem* (2015) 3:35. doi: 10.3389/fchem.2015.00035

27. Adjemian S, Oltean T, Martens S, Wiernicki B, Goossens V, Vanden Berghe T, et al. Ionizing radiation results in a mixture of cellular outcomes including mitotic catastrophe, senescence, methuosis, and iron-dependent cell death. *Cell Death Dis* (2020) 11(11):1003. doi: 10.1038/s41419-020-03209-y

28. Huang X, Tran T, Zhang L, Hatcher R, Zhang P. DNA damage-induced mitotic catastrophe is mediated by the Chk1-dependent mitotic exit DNA damage checkpoint. *Proc Natl Acad Sci U.S.A.* (2005) 102(4):1065–70. doi: 10.1073/pnas.0409130102

29. Shimura T. Mitochondrial signaling pathways associated with DNA damage responses. *Int J Mol Sci* (2023) 24(7):6128. doi: 10.3390/ijms24076128

30. Averbeck D, Rodriguez-Lafrasse C. Role of mitochondria in radiation responses: epigenetic, metabolic, and signaling impacts. *Int J Mol Sci* (2021) 22(20):11047. doi: 10.3390/ijms222011047

31. Cheng H, Chen L, Huang M, Hou J, Chen Z, Yang X. Hunting down Nlrp3 inflammasome: an executioner of radiation-induced injury. *Front Immunol* (2022) 13:967989. doi: 10.3389/fimmu.2022.967989

32. Liu YG, Chen JK, Zhang ZT, Ma XJ, Chen YC, Du XM, et al. Nlrp3 inflammasome activation mediates radiation-induced pyroptosis in bone marrow-derived macrophages. *Cell Death Dis* (2017) 8(2):e2579. doi: 10.1038/cddis.2016.460

33. Huang Z, Epperly M, Watkins SC, Greenberger JS, Kagan VE, Bayir H. Necrostatin-1 rescues mice from lethal irradiation. *Biochim Biophys Acta* (2016) 1862(4):850–6. doi: 10.1016/j.bbadis.2016.01.014

34. Zhang X, Tian M, Li X, Zheng C, Wang A, Feng J, et al. Hematopoietic protection and mechanisms of ferrostatin-1 on hematopoietic acute radiation syndrome of mice. *Int J Radiat Biol* (2021) 97(4):464–73. doi: 10.1080/09553002.2021.1876956

35. Li X, Zhuang X, Qiao T. Role of ferroptosis in the process of acute radiation-induced lung injury in mice. *Biochem Biophys Res Commun* (2019) 519(2):240–5. doi: 10.1016/j.bbrc.2019.08.165

36. Wang L, Wang A, Fu Q, Shi Z, Chen X, Wang Y, et al. Ferroptosis plays an important role in promoting ionizing radiation-induced intestinal injuries. *Biochem Biophys Res Commun* (2022) 595:7–13. doi: 10.1016/j.bbrc.2022.01.068

37. Gong T, Liu L, Jiang W, Zhou R. Damp-sensing receptors in sterile inflammation and inflammatory diseases. *Nat Rev Immunol* (2020) 20(2):95–112. doi: 10.1038/s41577-019-0215-7

38. Murao A, Aziz M, Wang H, Brenner M, Wang P. Release mechanisms of major damps. *Apoptosis* (2021) 26(3-4):152–62. doi: 10.1007/s10495-021-01663-3

39. Denning NL, Aziz M, Gurien SD, Wang P. Damps and nets in sepsis. *Front Immunol* (2019) 10:2536. doi: 10.3389/fimmu.2019.02536

40. Chen GY, Nunez G. Sterile inflammation: sensing and reacting to damage. *Nat Rev Immunol* (2010) 10(12):826–37. doi: 10.1038/nri2873

41. Cao X. Self-regulation and cross-regulation of pattern-recognition receptor signalling in health and disease. *Nat Rev Immunol* (2016) 16(1):35–50. doi: 10.1038/nri.2015.8

42. Vourc'h M, Roquilly A, Asehnoune K. Trauma-induced damage-associated molecular patterns-mediated remote organ injury and immunosuppression in the acutely ill patient. *Front Immunol* (2018) 9:1330. doi: 10.3389/fimmu.2018.01330

43. Zhang X, Wu J, Liu Q, Li X, Li S, Chen J, et al. Mtdna-sting pathway promotes necroptosis-dependent enterocyte injury in intestinal ischemia reperfusion. *Cell Death Dis* (2020) 11(12):1050. doi: 10.1038/s41419-020-03239-6

44. Paudel YN, Angelopoulou E, Piperi C, Othman I, Shaikh MF. Hmgb1-mediated neuroinflammatory responses in brain injuries: potential mechanisms and therapeutic opportunities. *Int J Mol Sci* (2020) 21(13):4609. doi: 10.3390/ijms21134609

45. Ratikan JA, Micewicz ED, Xie MW, Schaue D. Radiation takes its toll. *Cancer Lett* (2015) 368(2):238–45. doi: 10.1016/j.canlet.2015.03.031

46. Huber-Lang M, Lambris JD, Ward PA. Innate immune responses to trauma. *Nat Immunol* (2018) 19(4):327–41. doi: 10.1038/s41590-018-0064-8

47. Jost PJ, Hockendorf U. Necroinflammation emerges as a key regulator of hematopoiesis in health and disease. *Cell Death Differ* (2019) 26(1):53–67. doi: 10.1038/s41418-018-0194-4

48. Balanca B, Desmurs L, Grelier J, Perret-Liaudet A, Lukaszewicz AC. Damps and rage pathophysiology at the acute phase of brain injury: an overview. *Int J Mol Sci* (2021) 22(5):2439. doi: 10.3390/ijms22052439

49. Yamaga S, Murao A, Ma G, Brenner M, Aziz M, Wang P. Radiation upregulates macrophage trem-1 expression to exacerbate injury in mice. *Front Immunol* (2023) 14:1151250. doi: 10.3389/fimmu.2023.1151250

50. Zhang XM, Hu X, Ou JY, Chen SS, Nie LH, Gao L, et al. Glycyrrhizin ameliorates radiation enteritis in mice accompanied by the regulation of the Hmgb1/Tlr4 pathway. *Evid Based Complement Alternat Med* (2020) 2020:8653783. doi: 10.1155/2020/8653783

51. Zheng L, Zhu Q, Xu C, Li M, Li H, Yi PQ, et al. Glycyrrhizin mitigates radiation-induced acute lung injury by inhibiting the Hmgb1/Tlr4 signalling pathway. *J Cell Mol Med* (2020) 24(1):214–26. doi: 10.1111/jcmm.14703

52. Guan H, Zhang W, Xie D, Nie Y, Chen S, Sun X, et al. Cytosolic release of mitochondrial DNA and associated Cgas signaling mediates radiation-induced hematopoietic injury of mice. *Int J Mol Sci* (2023) 24(4):4020. doi: 10.3390/ijms24044020

53. Takemura N, Kawasaki T, Kunisawa J, Sato S, Lamichhane A, Kobiyama K, et al. Blockade of Tlr3 protects mice from lethal radiation-induced gastrointestinal syndrome. *Nat Commun* (2014) 5:3492. doi: 10.1038/ncomms4492

54. Li H, Jiang M, Zhao SY, Zhang SQ, Lu L, He X, et al. Exosomes are involved in total body irradiation-induced intestinal injury in mice. *Acta Pharmacol Sin* (2021) 42(7):1111–23. doi: 10.1038/s41401-021-00615-6

55. Sproull M, Kramp T, Tandle A, Shankavaram U, Camphausen K. Serum amyloid a as a biomarker for radiation exposure. *Radiat Res* (2015) 184(1):14–23. doi: 10.1667/RR13927.1

56. Sproull M, Kramp T, Tandle A, Shankavaram U, Camphausen K. Multivariate analysis of radiation responsive proteins to predict radiation exposure in total-body irradiation and partial-body irradiation models. *Radiat Res* (2017) 187(2):251–8. doi: 10.1667/RR14558.1

57. Kumar VP, Wuddie K, Tsioplaya A, Weaver A, Holmes-Hampton GP, Ghosh SP. Development of a multi-organ radiation injury model with precise dosimetry with focus on Gi-Ars. *Radiat Res* (2023) 201(1):19–34. doi: 10.1667/RADE-23-00068.1

58. Qiang X, Yang WL, Wu R, Zhou M, Jacob A, Dong W, et al. Cold-inducible Rna-binding protein (Cirp) triggers inflammatory responses in hemorrhagic shock and sepsis. *Nat Med* (2013) 19(11):1489–95. doi: 10.1038/nm.3368

59. Aziz M, Brenner M, Wang P. Extracellular Cirp (Ecirp) and inflammation. *J Leukoc Biol* (2019) 106(1):133–46. doi: 10.1002/JLB.3MIR1118-443R

60. Ode Y, Aziz M, Wang P. Cirp increases Icam-1(+) phenotype of neutrophils exhibiting elevated inos and nets in sepsis. *J Leukoc Biol* (2018) 103(4):693–707. doi: 10.1002/JLB.3A0817-327RR

61. Denning NL, Aziz M, Murao A, Gurien SD, Ochani M, Prince JM, et al. Extracellular Cirp as an endogenous trem-1 ligand to fuel inflammation in sepsis. *JCI Insight* (2020) 5(5):e134172. doi: 10.1172/jci.insight.134172

62. Zhou M, Aziz M, Yen HT, Ma G, Murao A, Wang P. Extracellular Cirp dysregulates macrophage bacterial phagocytosis in sepsis. *Cell Mol Immunol* (2023) 20(1):80–93. doi: 10.1038/s41423-022-00961-3

63. Venereau E, De Leo F, Mezzapelle R, Careccia G, Musco G, Bianchi ME. Hmgb1 as biomarker and drug target. *Pharmacol Res* (2016) 111:534–44. doi: 10.1016/j.phrs.2016.06.031

64. Yang H, Wang H, Andersson U. Targeting inflammation driven by Hmgb1. *Front Immunol* (2020) 11:484. doi: 10.3389/fimmu.2020.00484

65. Nofi CP, Wang P, Aziz M. Chromatin-associated molecular patterns (Camps) in sepsis. *Cell Death Dis* (2022) 13(8):700. doi: 10.1038/s41419-022-05155-3

66. Wang H, Bloom O, Zhang M, Vishnubhakat JM, Ombrellino M, Che J, et al. Hmg-1 as a late mediator of endotoxin lethality in mice. *Science* (1999) 285(5425):248–51. doi: 10.1126/science.285.5425.248

67. Abraham E, Arcaroli J, Carmody A, Wang H, Tracey KJ. Hmg-1 as a mediator of acute lung inflammation. *J Immunol* (2000) 165(6):2950–4. doi: 10.4049/jimmunol.165.6.2950

68. Tsung A, Sahai R, Tanaka H, Nakao A, Fink MP, Lotze MT, et al. The nuclear factor Hmgb1 mediates hepatic injury after murine liver ischemia-reperfusion. *J Exp Med* (2005) 201(7):1135–43. doi: 10.1084/jem.20042614

69. Kim HC, Oh H, You JS, Chung YE. Glycyrrhizin ameliorating sterile inflammation induced by low-dose radiation exposure. *Sci Rep* (2021) 11(1):18356. doi: 10.1038/s41598-021-97800-8

70. Mills EL, Kelly B, O'Neill LAJ. Mitochondria are the powerhouses of immunity. *Nat Immunol* (2017) 18(5):488–98. doi: 10.1038/ni.3704

71. Sato T, Onai N, Yoshihara H, Arai F, Suda T, Ohteki T. Interferon regulatory factor-2 protects quiescent hematopoietic stem cells from type I interferon-dependent exhaustion. *Nat Med* (2009) 15(6):696–700. doi: 10.1038/nm.1973

72. Xia P, Wang S, Ye B, Du Y, Li C, Xiong Z, et al. A circular Rna protects dormant hematopoietic stem cells from DNA sensor Cgas-mediated exhaustion. *Immunity* (2018) 48(4):688–701 e7. doi: 10.1016/j.immuni.2018.03.016

73. Wu D, Han R, Deng S, Liu T, Zhang T, Xie H, et al. Protective effects of flagellin a N/C against radiation-induced Nlr pyrin domain containing 3 inflammasome-dependent pyroptosis in intestinal cells. *Int J Radiat Oncol Biol Phys* (2018) 101(1):107–17. doi: 10.1016/j.ijrobp.2018.01.035

74. Hu L, Chen H, Zhang X, Feng Z, Zhang H, Meng Q. Rosiglitazone ameliorates radiation-induced intestinal inflammation in rats by inhibiting Nlrp3 inflammasome and Tnf-alpha production. *J Radiat Res* (2020) 61(6):842–50. doi: 10.1093/jrr/rraa062

75. Wu D, Tao T, Eshraghian EA, Lin P, Li Z, Zhu X. Extracellular Rna as a kind of communication molecule and emerging cancer biomarker. *Front Oncol* (2022) 12:960072. doi: 10.3389/fonc.2022.960072

76. Preissner KT, Fischer S, Deindl E. Extracellular Rna as a versatile damp and alarm signal that influences leukocyte recruitment in inflammation and infection. *Front Cell Dev Biol* (2020) 8:619221. doi: 10.3389/fcell.2020.619221

77. Chattopadhyay S, Sen GC. Dsrna-activation of Tlr3 and Rlr signaling: gene induction-dependent and independent effects. *J Interferon Cytokine Res* (2014) 34(6):427–36. doi: 10.1089/jir.2014.0034

78. Brentano F, Schorr O, Gay RE, Gay S, Kyburz D. Rna released from necrotic synovial fluid cells activates rheumatoid arthritis synovial fibroblasts via toll-like receptor 3. *Arthritis Rheum* (2005) 52(9):2656–65. doi: 10.1002/art.21273

79. Cavassani KA, Ishii M, Wen H, Schaller MA, Lincoln PM, Lukacs NW, et al. Tlr3 is an endogenous sensor of tissue necrosis during acute inflammatory events. *J Exp Med* (2008) 205(11):2609–21. doi: 10.1084/jem.20081370

80. Sack GH Jr. Serum amyloid a - a review. *Mol Med* (2018) 24(1):46. doi: 10.1186/s10020-018-0047-0

81. Ossetrova NI, Sandgren DJ, Blakely WF. Protein biomarkers for enhancement of radiation dose and injury assessment in nonhuman primate total-body irradiation model. *Radiat Prot Dosimetry* (2014) 159(1-4):61–76. doi: 10.1093/rpd/ncu165

82. Speidel D. Transcription-independent P53 apoptosis: an alternative route to death. *Trends Cell Biol* (2010) 20(1):14–24. doi: 10.1016/j.tcb.2009.10.002

83. Galluzzi L, Vitale I, Aaronson SA, Abrams JM, Adam D, Agostinis P, et al. Molecular mechanisms of cell death: recommendations of the nomenclature committee on cell death 2018. *Cell Death Differ* (2018) 25(3):486–541. doi: 10.1038/s41418-017-0012-4

84. Galluzzi L, Vitale I, Abrams JM, Alnemri ES, Baehrecke EH, Blagosklonny MV, et al. Molecular definitions of cell death subroutines: recommendations of the nomenclature committee on cell death 2012. *Cell Death Differ* (2012) 19(1):107–20. doi: 10.1038/cdd.2011.96

85. Oda E, Ohki R, Murasawa H, Nemoto J, Shibue T, Yamashita T, et al. Noxa, a Bh3-only member of the Bcl-2 family and candidate mediator of P53-induced apoptosis. *Science* (2000) 288(5468):1053–8. doi: 10.1126/science.288.5468.1053

86. Nakano K, Vousden KH. Puma, a novel proapoptotic gene, is induced by P53. *Mol Cell* (2001) 7(3):683–94. doi: 10.1016/s1097-2765(01)00214-3

87. Jiang W, Bell CW, Pisetsky DS. The relationship between apoptosis and high-mobility group protein 1 release from murine macrophages stimulated with lipopolysaccharide or polyinosinic-polycytidylic acid. *J Immunol* (2007) 178 (10):6495–503. doi: 10.4049/jimmunol.178.10.6495

88. Wu D, Ingram A, Lahti JH, Mazza B, Grenet J, Kapoor A, et al. Apoptotic release of histones from nucleosomes. *J Biol Chem* (2002) 277(14):12001–8. doi: 10.1074/jbc.M109219200

89. Elliott MR, Chekeni FB, Trampont PC, Lazarowski ER, Kadl A, Walk SF, et al. Nucleotides released by apoptotic cells act as a find-me signal to promote phagocytic clearance. *Nature* (2009) 461(7261):282–6. doi: 10.1038/nature08296

90. Reich CF 3rd, Pisetsky DS. The content of DNA and Rna in microparticles released by Jurkat and Hl-60 cells undergoing in vitro apoptosis. *Exp Cell Res* (2009) 315(5):760–8. doi: 10.1016/j.yexcr.2008.12.014

91. Nicotera P, Leist M, Ferrando-May E. Intracellular Atp, a switch in the decision between apoptosis and necrosis. *Toxicol Lett* (1998) 102-103:139–42. doi: 10.1016/s0378-4274(98)00298-7

92. Edinger AL, Thompson CB. Death by design: apoptosis, necrosis and autophagy. *Curr Opin Cell Biol* (2004) 16(6):663–9. doi: 10.1016/j.ceb.2004.09.011

93. Scaffidi P, Misteli T, Bianchi ME. Release of chromatin protein Hmgb1 by necrotic cells triggers inflammation. *Nature* (2002) 418(6894):191–5. doi: 10.1038/nature00858

94. Basu S, Binder RJ, Suto R, Anderson KM, Srivastava PK. Necrotic but not apoptotic cell death releases heat shock proteins, which deliver a partial maturation signal to dendritic cells and activate the Nf-Kappa B pathway. *Int Immunol* (2000) 12 (11):1539–46. doi: 10.1093/intimm/12.11.1539

95. Pasparakis M, Vandenabeele P. Necroptosis and its role in inflammation. *Nature* (2015) 517(7534):311–20. doi: 10.1038/nature14191

96. Liu Y, Xu Q, Wang Y, Liang T, Li X, Wang D, et al. Necroptosis is active and contributes to intestinal injury in a piglet model with lipopolysaccharide challenge. *Cell Death Dis* (2021) 12(1):62. doi: 10.1038/s41419-020-03365-1

97. Reilly B, Tan C, Murao A, Nofi C, Jha A, Aziz M, et al. Necroptosis-mediated Ecirp release in sepsis. *J Inflammation Res* (2022) 15:4047–59. doi: 10.2147/JIR.S370615

98. Nagata S, Tanaka M. Programmed cell death and the immune system. *Nat Rev Immunol* (2017) 17(5):333–40. doi: 10.1038/nri.2016.153

99. Frank D, Vince JE. Pyroptosis versus necroptosis: similarities, differences, and crosstalk. *Cell Death Differ* (2019) 26(1):99–114. doi: 10.1038/s41418-018-0212-6

100. Evavold CL, Ruan J, Tan Y, Xia S, Wu H, Kagan JC. The pore-forming protein gasdermin D regulates interleukin-1 secretion from living macrophages. *Immunity* (2018) 48(1):35–44 e6. doi: 10.1016/j.immuni.2017.11.013

101. Tan C, Reilly B, Jha A, Murao A, Lee Y, Brenner M, et al. Active release of Ecirp via gasdermin D channels to induce inflammation in sepsis. *J Immunol* (2022) 208 (9):2184–95. doi: 10.4049/jimmunol.2101004

102. Lamkanfi M, Sarkar A, Vande Walle L, Vitari AC, Amer AO, Wewers MD, et al. Inflammasome-dependent release of the alarmin Hmgb1 in endotoxemia. *J Immunol* (2010) 185(7):4385–92. doi: 10.4049/jimmunol.1000803

103. Vasudevan SO, Behl B, Rathinam VA. Pyroptosis-induced inflammation and tissue damage. *Semin Immunol* (2023) 69:101781. doi: 10.1016/j.smim.2023.101781

104. Stockwell BR, Friedmann Angeli JP, Bayir H, Bush AI, Conrad M, Dixon SJ, et al. Ferroptosis: A regulated cell death nexus linking metabolism, redox biology, and disease. *Cell* (2017) 171(2):273–85. doi: 10.1016/j.cell.2017.09.021

105. Wen Q, Liu J, Kang R, Zhou B, Tang D. The release and activity of Hmgb1 in ferroptosis. *Biochem Biophys Res Commun* (2019) 510(2):278–83. doi: 10.1016/j.bbrc.2019.01.090

106. Shimizu J, Murao A, Nofi C, Wang P, Aziz M. Extracellular Cirp promotes Gpx4-mediated ferroptosis in sepsis. *Front Immunol* (2022) 13:903859. doi: 10.3389/fimmu.2022.903859

107. Liu J, Zhu S, Zeng L, Li J, Klionsky DJ, Kroemer G, et al. Dcn released from ferroptotic cells ignites ager-dependent immune responses. *Autophagy* (2022) 18 (9):2036–49. doi: 10.1080/15548627.2021.2008692

108. Merline R, Moreth K, Beckmann J, Nastase MV, Zeng-Brouwers J, Tralhao JG, et al. Signaling by the matrix proteoglycan decorin controls inflammation and cancer through Pdcd4 and Microrna-21. *Sci Signal* (2011) 4(199):ra75. doi: 10.1126/scisignal.2001868

109. Henne WM, Stenmark H, Emr SD. Molecular mechanisms of the membrane sculpting Escrt pathway. *Cold Spring Harb Perspect Biol* (2013) 5(9):a016766. doi: 10.1101/cshperspect.a016766

110. Hessvik NP, Llorente A. Current knowledge on exosome biogenesis and release. *Cell Mol Life Sci* (2018) 75(2):193–208. doi: 10.1007/s00018-017-2595-9

111. Collett GP, Redman CW, Sargent IL, Vatish M. Endoplasmic reticulum stress stimulates the release of extracellular vesicles carrying danger-associated molecular pattern (Damp) molecules. *Oncotarget* (2018) 9(6):6707–17. doi: 10.18632/oncotarget.24158

112. Gupta S, Knowlton AA. Hsp60 trafficking in adult cardiac myocytes: role of the exosomal pathway. *Am J Physiol Heart Circ Physiol* (2007) 292(6):H3052–6. doi: 10.1152/ajpheart.01355.2006

113. Sakaki H, Tsukimoto M, Harada H, Moriyama Y, Kojima S. Autocrine regulation of macrophage activation via exocytosis of Atp and activation of P2y11 receptor. *PloS One* (2013) 8(4):e59778. doi: 10.1371/journal.pone.0059778

114. Nair RR, Mazza D, Brambilla F, Gorzanelli A, Agresti A, Bianchi ME. Lps-challenged macrophages release microvesicles coated with histones. *Front Immunol* (2018) 9:1463. doi: 10.3389/fimmu.2018.01463

115. Guescini M, Genedani S, Stocchi V, Agnati LF. Astrocytes and glioblastoma cells release exosomes carrying Mtdna. *J Neural Transm (Vienna)* (2010) 117(1):1–4. doi: 10.1007/s00702-009-0288-8

116. Murao A, Tan C, Jha A, Wang P, Aziz M. Exosome-mediated Ecirp release from macrophages to induce inflammation in sepsis. *Front Pharmacol* (2021) 12:791648. doi: 10.3389/fphar.2021.791648

117. Murao A, Brenner M, Aziz M, Wang P. Exosomes in sepsis. *Front Immunol* (2020) 11:2140. doi: 10.3389/fimmu.2020.02140

118. Blott EJ, Griffiths GM. Secretory lysosomes. *Nat Rev Mol Cell Biol* (2002) 3 (2):122–31. doi: 10.1038/nrm732

119. Buratta S, Tancini B, Sagini K, Delo F, Chiaradia E, Urbanelli L, et al. Lysosomal exocytosis, exosome release and secretory autophagy: the autophagic- and endo-lysosomal systems go extracellular. *Int J Mol Sci* (2020) 21(7):2576. doi: 10.3390/ijms21072576

120. Gardella S, Andrei C, Ferrera D, Lotti LV, Torrisi MR, Bianchi ME, et al. The nuclear protein Hmgb1 is secreted by monocytes via a non-classical, vesicle-mediated secretory pathway. *EMBO Rep* (2002) 3(10):995–1001. doi: 10.1093/embo-reports/kvf198

121. Zhang Z, Chen G, Zhou W, Song A, Xu T, Luo Q, et al. Regulated Atp release from astrocytes through lysosome exocytosis. *Nat Cell Biol* (2007) 9(8):945–53. doi: 10.1038/ncb1620

122. Wang J, Shao L, Hendrickson HP, Liu L, Chang J, Luo Y, et al. Total body irradiation in the "Hematopoietic" Dose range induces substantial intestinal injury in non-human primates. *Radiat Res* (2015) 184(5):545–53. doi: 10.1667/RR14191.1

123. Assimakopoulos SF, Triantos C, Thomopoulos K, Fligou F, Maroulis I, Marangos M, et al. Gut-origin sepsis in the critically ill patient: pathophysiology and treatment. *Infection* (2018) 46(6):751–60. doi: 10.1007/s15010-018-1178-5

124. Pantalone D, Bergamini C, Martellucci J, Alemanno G, Bruscino A, Maltinti G, et al. The role of damps in burns and hemorrhagic shock immune response: pathophysiology and clinical issues. *Review Int J Mol Sci* (2021) 22(13):7020. doi: 10.3390/ijms22137020

125. Zhang P, Zou B, Liou YC, Huang C. The pathogenesis and diagnosis of sepsis post burn injury. *Burns Trauma* (2021) 9:tkaa047. doi: 10.1093/burnst/tkaa047

126. Cohen MJ, Brohi K, Calfee CS, Rahn P, Chesebro BB, Christiaans SC, et al. Early release of high mobility group box nuclear protein 1 after severe trauma in humans: role of injury severity and tissue hypoperfusion. *Crit Care* (2009) 13(6):R174. doi: 10.1186/cc8152

127. Zhang BF, Wang PF, Cong YX, Lei JL, Wang H, Huang H, et al. Anti-high mobility group box-1 (Hmgb1) antibody attenuates kidney damage following experimental crush injury and the possible role of the tumor necrosis factor-alpha and C-jun N-terminal kinase pathway. *J Orthop Surg Res* (2017) 12(1):110. doi: 10.1186/s13018-017-0614-z

128. Singh VK, Seed TM. Radiation countermeasures for hematopoietic acute radiation syndrome: growth factors, cytokines and beyond. *Int J Radiat Biol* (2021) 97(11):1526–47. doi: 10.1080/09553002.2021.1969054

129. Land WG. Use of damps and samps as therapeutic targets or therapeutics: A note of caution. *Mol Diagn Ther* (2020) 24(3):251–62. doi: 10.1007/s40291-020-00460-z

130. Zhang F, Brenner M, Yang WL, Wang P. A cold-inducible Rna-binding protein (Cirp)-derived peptide attenuates inflammation and organ injury in septic mice. *Sci Rep* (2018) 8(1):3052. doi: 10.1038/s41598-017-13139-z

131. McGinn J, Zhang F, Aziz M, Yang WL, Nicastro J, Coppa GF, et al. The protective effect of a short peptide derived from cold-inducible Rna-binding protein in renal ischemia-reperfusion injury. *Shock* (2018) 49(3):269–76. doi: 10.1097/SHK.0000000000000988

132. Borjas T, Jacob A, Yen H, Patel V, Coppa GF, Aziz M, et al. Inhibition of the interaction of Trem-1 and Ecirp attenuates inflammation and improves survival in hepatic ischemia/reperfusion. *Shock* (2022) 57(2):246–55. doi: 10.1097/SHK.0000000000001894

133. Murao A, Jha A, Ma G, Chaung W, Aziz M, Wang P. A synthetic Poly(a) tail targeting extracellular cirp inhibits sepsis. *J Immunol* (2023) 211(7):1144–53. doi: 10.4049/jimmunol.2300228

134. Nofi CP, Tan C, Ma G, Kobritz M, Prince J, Wang H, et al. A novel opsonic Ecirp inhibitor for lethal sepsis. *J Leukoc Biol* (2023). doi: 10.1093/jleuko/qiad119

135. Suda K, Kitagawa Y, Ozawa S, Saikawa Y, Ueda M, Ebina M, et al. Anti-high-mobility group box chromosomal protein 1 antibodies improve survival of rats with sepsis. *World J Surg* (2006) 30(9):1755–62. doi: 10.1007/s00268-005-0369-2

136. Yang R, Harada T, Mollen KP, Prince JM, Levy RM, Englert JA, et al. Anti-Hmgb1 neutralizing antibody ameliorates gut barrier dysfunction and improves survival after hemorrhagic shock. *Mol Med* (2006) 12(4-6):105–14. doi: 10.2119/2006-00010.Yang

137. Zhao F, Fang Y, Deng S, Li X, Zhou Y, Gong Y, et al. Glycyrrhizin protects rats from sepsis by blocking Hmgb1 signaling. *BioMed Res Int* (2017) 2017:9719647. doi: 10.1155/2017/9719647

138. Raman KG, Sappington PL, Yang R, Levy RM, Prince JM, Liu S, et al. The role of rage in the pathogenesis of intestinal barrier dysfunction after hemorrhagic shock. *Am J Physiol Gastrointest Liver Physiol* (2006) 291(4):G556–65. doi: 10.1152/ajpgi.00055.2006

139. May JM, Bylicky M, Chopra S, Coleman CN, Aryankalayil MJ. Long and short non-coding Rna and radiation response: A review. *Transl Res* (2021) 233:162–79. doi: 10.1016/j.trsl.2021.02.005

140. Acharya SS, Fendler W, Watson J, Hamilton A, Pan Y, Gaudiano E, et al. Serum micrornas are early indicators of survival after radiation-induced hematopoietic injury. *Sci Transl Med* (2015) 7(287):287ra69. doi: 10.1126/scitranslmed.aaa6593

141. Fendler W, Malachowska B, Meghani K, Konstantinopoulos PA, Guha C, Singh VK, et al. Evolutionarily conserved serum micrornas predict radiation-induced fatality in nonhuman primates. *Sci Transl Med* (2017) 9(379):eaa12408. doi: 10.1126/scitranslmed.aal2408

frontiers | Frontiers in Immunology

TYPE Original Research
PUBLISHED 26 January 2024
DOI 10.3389/fimmu.2024.1347453

OPEN ACCESS

EDITED BY
Christoph Thiemermann,
Queen Mary University of London,
United Kingdom

REVIEWED BY
Sian M Henson,
Queen Mary University of London,
United Kingdom
Basilia Zingarelli,
Cincinnati Children's Hospital Medical Center,
United States

*CORRESPONDENCE
Monowar Aziz
Maziz1@northwell.edu
Atsushi Murao
Amurao@northwell.edu

RECEIVED 30 November 2023
ACCEPTED 09 January 2024
PUBLISHED 26 January 2024

CITATION
Murao A, Jha A, Aziz M and Wang P (2024) Transcriptomic profiling of immune cells in murine polymicrobial sepsis.
Front. Immunol. 15:1347453.
doi: 10.3389/fimmu.2024.1347453

Transcriptomic profiling of immune cells in murine polymicrobial sepsis

Atsushi Murao[1]*, Alok Jha[1], Monowar Aziz[1,2]* and Ping Wang[1,2]

[1]Center for Immunology and Inflammation, The Feinstein Institutes for Medical Research, Manhasset, NY, United States, [2]Departments of Surgery and Molecular Medicine, Zucker School of Medicine at Hofstra/Northwell, Manhasset, NY, United States

Introduction: Various immune cell types play critical roles in sepsis with numerous distinct subsets exhibiting unique phenotypes even within the same cell population. Single-cell RNA sequencing (scRNA-seq) enables comprehensive transcriptome profiling and unbiased cell classification. In this study, we have unveiled the transcriptomic landscape of immune cells in sepsis through scRNA-seq analysis.

Methods: We induced sepsis in mice by cecal ligation and puncture. 20 h after the surgery, the spleen and peritoneal lavage were collected. Single-cell suspensions were processed using a 10× Genomics pipeline and sequenced on an Illumina platform. Count matrices were generated using the Cell Ranger pipeline, which maps reads to the mouse reference transcriptome, GRCm38/mm10. Subsequent scRNA-seq analysis was performed using the R package Seurat.

Results: After quality control, we subjected the entire data set to unsupervised classification. Four major clusters were identified as neutrophils, macrophages, B cells, and T cells according to their putative markers. Based on the differentially expressed genes, we identified activated pathways in sepsis for each cell type. In neutrophils, pathways related to inflammatory signaling, such as NF-κB and responses to pathogen-associated molecular patterns (PAMPs), cytokines, and hypoxia were activated. In macrophages, activated pathways were the ones related to cell aging, inflammatory signaling, and responses to PAMPs. In B cells, pathways related to endoplasmic reticulum stress were activated. In T cells, activated pathways were the ones related to inflammatory signaling, responses to PAMPs, and acute lung injury. Next, we further classified each cell type into subsets. Neutrophils consisted of four clusters. Some subsets were activated in inflammatory signaling or cell metabolism, whereas others possessed immunoregulatory or aging properties. Macrophages consisted of four clusters, namely, the ones with enhanced aging, lymphocyte activation, extracellular matrix organization, or cytokine activity. B cells consisted of four clusters, including the ones possessing the phenotype of cell maturation or aging. T cells consisted of six clusters, whose phenotypes include molecular translocation or cell activation.

10.3389/fimmu.2024.1347453

Conclusions: Transcriptomic analysis by scRNA-seq has unveiled a comprehensive spectrum of immune cell responses and distinct subsets in the context of sepsis. These findings are poised to enhance our understanding of sepsis pathophysiology, offering avenues for targeting novel molecules, cells, and pathways to combat infectious diseases.

KEYWORDS

sepsis, single-cell RNA sequencing, neutrophil, macrophage, lymphocyte

Introduction

Sepsis is a critical infectious disease condition accompanied by organ dysfunction due to dysregulated host immune response to invading pathogens (1). It is estimated that 49 million people suffer from sepsis, resulting in 11 million deaths worldwide every year (2). Pathogen-associated molecular patterns (PAMPs), such as LPS, and damage-associated molecular patterns (DAMPs), including, but not limited to, extracellular cold-inducible RNA-binding protein (eCIRP), high mobility group box 1 (HMGB1), and histone H3, initiate immune responses through the stimulation of pattern recognition receptors (PRRs), leading to the activation of transcription factors, such as NF-κB, to induce inflammation (3–6). Different kinds of immune cells, such as neutrophils, macrophages, B cells, and T cells, coordinately play critical roles during sepsis (7). It is now known that each cell type consists of quite a few subsets (8). Those subsets exhibit a distinct phenotype reflected by genomic differences even within the same cell population (8). For instance, neutrophils, which were traditionally thought as a terminally differentiated single population, are now known to consist of many subsets, such as aged, antigen-presenting, intercellular adhesion molecule-1 (ICAM-1)-expressing, and low-density neutrophils and antigen-presenting aged neutrophils (APANs) in sepsis (9–13). T-cell and macrophage polarization is no longer highlighted as a simple Th1/Th2 and M1/M2 dichotomy as once thought (8). In addition, numerous cellular molecules change their status cell by cell in sepsis, contributing to the disease development (14). It should also be noted that the distribution and phenotype of cells differ between the organs in sepsis. Considering that immune cells mediate crosstalk between the site of infection and systemic inflammation in sepsis (15, 16), assessments of immune cell activities at the focus of infection along with that of remote organs are important to precisely delineate the pathophysiology of this deadly disorder.

Single-cell RNA sequencing (scRNA-seq) enables us to comprehensively screen the genetic status in individual cells and classify the cells into clusters in an unbiased way (17, 18). We are able to not only identify major cell populations, such as neutrophils, macrophages, and lymphocytes, but also further clusterize them into minor subsets unbiasedly (17). Moreover, based on the differentially expressed genes of the cluster, activated pathways can be statistically determined using specific algorithms, such as gene set enrichment analysis (GSEA) (19). A growing number of studies implement scRNA-seq to accelerate the understanding of different disorders (20–22). Furthermore, it also facilitates drug development and transition from the bench to the bedside (20, 21). In this study, we have delved into the transcriptomic landscape of immune cells in sepsis through scRNA-seq analysis. Using intraabdominal septic mice, we have revealed the frequency and status of neutrophils, macrophages, B cells, and T cells in the peritoneal cavity, the focus of infection, and spleen, a remote immune organ, simultaneously. We further classified those major cell populations into subtypes, which showed distinct characteristics in inflammatory response, cellular aging, and metabolism. These discoveries identifying new pathways offer future research areas in sepsis to advance our understanding of its pathophysiology, potentially leading to therapeutics targeting the novel molecules, cells, and pathways to address this deadly disease syndrome.

Abbreviations: scRNA-seq, single-cell RNA sequencing; CLP, cecal ligation and puncture; PAMPs, pathogen-associated molecular patterns; PRRs, pattern-recognition receptors; DAMPs, damage-associated molecular patterns; NF-κB, muclear factor kappa-light-chain-enhancer of activated B cells; RP, ribosomal protein; NES, normalized enrichment score.

Materials and methods

Animals

Male C57BL/6 mice, 8–12 weeks old, were purchased from Charles River Laboratories (Wilmington, MA). The mice were housed in a temperature-controlled room with 12-h intermittent light and dark cycles and fed a standard mouse chow diet with drinking water. All animal experiments were performed following the National Institutes of Health Guide for the Care and Use of Laboratory Animals and were approved by our Institutional Animal Care and Use Committee (IACUC).

Mouse model of sepsis

Polymicrobial sepsis was induced in mice by cecal ligation and puncture (CLP) (9). In brief, mice were anesthetized with 2%

isoflurane inhalation, and a midline abdominal incision was created. The cecum was securely tied off with a 4–0 silk suture at 1 cm proximal from its distal extremity and then punctured twice using a 22-gauge needle to create two small through-and-through pores. Sham animals were subjected to a laparotomy without CLP. Following the surgery, 1 mL of normal saline was subcutaneously (*s.c.*) injected to avoid surgery-induced dehydration and 0.05 mg/kg buprenorphine was *s.c.* injected as an analgesic. 20 h after the surgery, the peritoneal lavage and spleen were harvested. Samples were pooled from three mice per group.

Isolation of peritoneal cells and splenocytes

Peritoneal lavage was collected by washing with cold PBS and centrifuged at 300 × g for 5 min at 4°C. The cell pellets were then resuspended into complete RPMI medium. Spleens were grounded and passed through a 70-µm nylon cell strainer. The splenocyte suspension was centrifuged at 300 × g for 5 min at 4°C. The cell pellet was suspended in 1-mL red blood cell (RBC) lysing buffer (BD Biosciences) to lyse the RBCs in the suspension, followed by washing of the cells with PBS. The cell pellets were then resuspended into complete RPMI medium.

Droplet-based scRNA-seq and genomic mapping

Cells from the peritoneal cavity and spleen of sham and CLP mice were sorted for scRNA-seq using the 10× Genomics Chromium platform. Library preparation was conducted according to the recommended protocol for the Next GEM Single Cell 3' Library Kit v3.1 (no. 1000121; 10× Genomics). Libraries were sequenced on the Illumina NextSeq 2000 sequencing platform to a mean depth of approximately 40,000 reads per cell. The Cell Ranger count pipeline (v6.0.0, 10× Genomics) was used to align FASTQs to the mouse reference genome (gex-mm10-2020-A, 10× Genomics) and produce digital gene-cell count matrices and to perform quality control of the mapping results.

Primary assessment with Cell Ranger for cells from the peritoneal cavity of septic mice reported 6,596 cells with a median of 4,972 unique molecular identifiers per cell and a median of 1,122 genes per cell at 75.3% sequence saturation, with a mean of 46,465 reads per cell. Primary assessment with Cell Ranger for cells from the spleen of septic mice reported 7,423 cells with a median of 3,483 unique molecular identifiers per cell and a median of 1,310 genes per cell at 72.0% sequence saturation, with a mean of 41,567 reads per cell. Primary assessment with Cell Ranger for cells from the peritoneal cavity of sham mice reported 5,462 cells with a median of 12,014 unique molecular identifiers per cell and a median of 2,984 genes per cell at 56.2% sequence saturation, with a mean of 46,645 reads per cell. Primary assessment with Cell Ranger for cells from the spleen of sham mice reported 8,148 cells with a median of 3,741 unique molecular identifiers per cell and a median of 1,362 genes per cell at 64.4% sequence saturation, with a mean of 35,614 reads per cell.

Single-cell sequencing quantification

DoubletFinder was used to identify doublets. After filtering out doublets, Seurat v4.1.3 was used to filter out cells expressing less than 200 genes and all cells with more than 5% mitochondrial genes. Among cells from the peritoneal cavity of septic mice, 6,164 singlets were kept and 432 cells were removed through quality control. Among cells from the spleen of septic mice, 3,137 singlets were kept and 4,286 cells were removed through quality control. Among cells from the peritoneal cavity of sham mice, 4,288 singlets were kept and 1,174 cells were removed through quality control. Among cells from the spleen of sham mice, 5,367 singlets were kept and 2,781 cells were removed through quality control. Gene expression normalization and cell clustering were done using the SCTransform pipeline (23) with percent mitochondrial reads regressed out and batch effects corrected using Harmony (24). To apply the SCTransform process implemented in Seurat (25), we began by using the "SCTransform" function to normalize the data and regress out mitochondrial mapping percentage as a confounding source of variation, as is standard (23). We then used the "RunPCA" function to run a principal component analysis (PCA), using the variable features (genes) to compute the principal components (PCs). Next, we used Harmony to correct for batch effects (based on sequencing run and the origin of the cells from peritoneal cavity vs. spleen), with the SCTransformed data used as the input, for a maximum of 50 rounds of Harmony (each involving at most 100 rounds of clustering and a correction step). Subsequently, we used the "RunUMAP" function to utilize the Uniform Manifold Approximation and Projection (UMAP) approach to dimensionality reduction, using the first 20 dimensions of the harmonized data as the input features to the UMAP. Finally, the "FindNeighbors" function was used to compute the 20 nearest neighbors for a given dataset based on the first 20 dimensions of the harmonized data, and the "FindClusters" function was applied to identify clusters of cells by a shared nearest neighbor (SNN) modularity optimization-based clustering algorithm.

Gene set enrichment analysis

A gene set enrichment analysis (GSEA) was performed using fgsea 1.26.0, an R package. In this case, Molecular Signatures Database (MSigDB) v2022.1 was used as the source of annotated gene sets for GSEA. GSEA was conducted separately for each cell cluster of interest identified using Seurat.

Statistical analysis

For single-cell sequencing analysis using Seurat, differential expression testing was based on the Wilcoxon rank-sum test (also

known as the Mann–Whitney U test), a non-parametric test used to compare two independent samples (26).

For GSEA using fgsea, an enrichment score (ES) was calculated based on a vector of gene-level t-statistics from a differential expression test, with an empirical null distribution calculated by sampling random gene sets for each input pathway of interest. Then, a P-value was estimated by taking the number of random gene sets with the same or more extreme ES value divided by the total number of generated gene sets, and multiple hypothesis correction was applied, yielding adjusted P-values.

Results

Profiles of neutrophils, macrophages, B cells, and T cells in sepsis

We induced sepsis in mice by CLP and isolated cells from the peritoneal cavity and spleen. The cells were then processed *via* the 10× Genomics scRNA-seq pipeline. After quality control (Supplementary Figure 1), we subjected the entire data set to unsupervised classification. This classification resulted in 14 clusters (#0–13), which were lined up in the order of cell numbers (Figure 1A, Supplementary Figures 2, 3). Then, we sought to identify the cell types of the four major clusters using the putative markers *Cd14*, myeloid cells; *Cd19*, *Ms4a1*, B cells; and *Cd2*, *Cd3d/e*, *Cd4*, *Cd8a*, T cells (Figure 1B), along with the markers for other cell types (Supplementary Figure 4). Two major clusters were identified to be myeloid cells (#0, #1) (Supplementary Figure 5), and we further distinguished them by the markers for neutrophils (*Ly6g*) and macrophages (*Adgre1*). As such, each of the four major clusters was identified as follows: #0, neutrophils; #1, macrophages; #2, B cells; #3, T cells (Figure 1A). Next, we assessed the differences in cell distribution among the two compartments in sham and septic conditions. Neutrophils existed predominantly in the peritoneal cavity of septic mice and to a lesser extent in the spleen of sham and septic mice, whereas they were barely detectable in the peritoneal cavity of sham mice (Figure 1C). Macrophages existed predominantly in the peritoneal cavity of sham mice and to a lesser extent in the spleen of sham and septic mice, whereas they were barely detectable in the peritoneal cavity of septic mice (Figure 1C). B cells existed mainly in the peritoneal cavity and spleen of sham mice and to a lesser extent in the spleen of septic mice, whereas they were barely detectable in the peritoneal cavity of septic mice (Figure 1C). T cells were found mainly in the spleen of sham and septic mice and to a lesser extent in the peritoneal cavity of sham and septic mice (Figure 1C). Hence, variations in the presence of innate and adaptive immune cells across different compartments have been noted under both normal and septic conditions.

Transcriptomic heterogeneity in neutrophils, macrophages, B cells, and T cells in sepsis

We then compared transcriptomic differences caused by sepsis in each cell type by identifying differentially expressed genes and

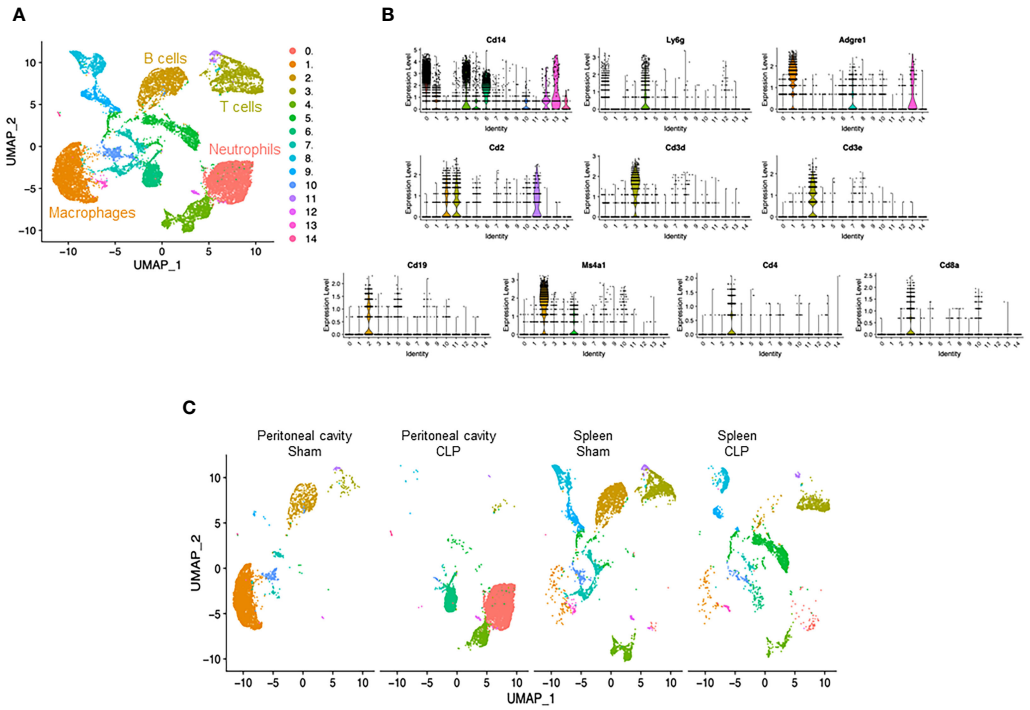

FIGURE 1
Identification of neutrophils, macrophages, B cells, and T cells. **(A)** UMAP plots showing the results of post-filtering unsupervised random forest classification of all groups combined. **(B)** Violin plots of key markers used for identifying cell types. **(C)** UMAP plots showing the post-filtering unsupervised random forest classification of each group (peritoneal cavity of sham and CLP, spleen of sham and CLP).

pathways in CLP mice compared with sham mice. In neutrophils, the most differentially expressed genes in septic mice compared with the control were *Cxcl2*, *Ccl4*, *CCl3*, *Il1rn*, *Fth1*, *Cxcl3*, *Thbs1*, *Acod1*, *Ier3*, and *Sod2* (Figure 2A, Supplementary Table 1). Based on these differentially expressed genes, pathways activated in the neutrophils of CLP mice were determined to be the ones related to inflammatory signaling such as NF-κB and responses to PAMPs, cytokines, and hypoxia (Table 1). In macrophages, the most differentially expressed genes after sepsis include *S100a9*, *S100a8*, *Hbb-bs*, *Fth1*, *AW112010*, *Spic*, *Cxcl2*, *Cd14*, *Hmox1*, and *Vcam1* (Figure 2B, Supplementary Table 2). Activated pathways in macrophages of septic mice were the ones related to cell aging, inflammatory signaling such as NF-κB, and responses to PAMPs (Table 2). In B cells, the most upregulated genes in septic mice were *Ighg2c*, *Jchain*, *Ighm*, *Iglv1*, *Mtq*, *Xbp1*, *Gm49980*, *Herpud1*, *Ly6c2*, and *Sec11c* (Figure 2C, Supplementary Table 3). Activated pathways relevant to B cells according to these genes were mostly the ones related to endoplasmic reticulum stress (Table 3). In T cells, the most differentially expressed genes in septic mice include *Cxcl2*, *Emb*, *Junb*, *Vps37b*, *Ifngr1*, *4932438A13Rik*, *Ptpn22*, *Mt1*, *Zeb1*, and *S100a8* (Figure 2D, Supplementary Table 4). The activated pathways in T cells of septic mice were the ones related to inflammatory signaling such as NF-κB, responses to PAMPs, and acute lung injury (Table 4). Overall, in sepsis different kinds of cells are activated and exhibited enhanced inflammatory signaling pathways in response to inflammatory mediators and circulatory failure.

Neutrophil subset analysis

To explore potential subsets within a cell type, we individually subjected each cell type to further classification. We found that neutrophils consisted of four clusters (Figure 3A). Cluster #0 was the major population and almost exclusively found in the peritoneal cavity of septic mice (Figure 3B), suggesting that this subtype plays a dominant role specifically at the site of infection. On the other hand, cluster #1 was found in both peritoneal cavity and spleen (Figure 3B), suggesting that this subset may migrate and localize in different compartments transiently. cluster #2 was almost exclusively found in the peritoneal cavity of septic mice similar to cluster #0 (Figure 3B). Cluster #3, the smallest population, was mostly found in the peritoneal cavity of septic mice but also to a lesser extent in the spleen of sham and septic mice (Figure 3B). Next, we listed the most differentially expressed genes for each cluster compared with the rest of neutrophils. In cluster #0, *Csf3*, *Chka*, *Hmox1*, *Hcar2*, *Camp*, *Cstb*, *Gde1*, *Gadd45g*, *Cpeb4*, and *Syne1* were the most upregulated genes (Supplementary Table 5). Positively differential pathways in this cluster were the ones related to iron uptake, transport and homeostasis, secondary lysosome and

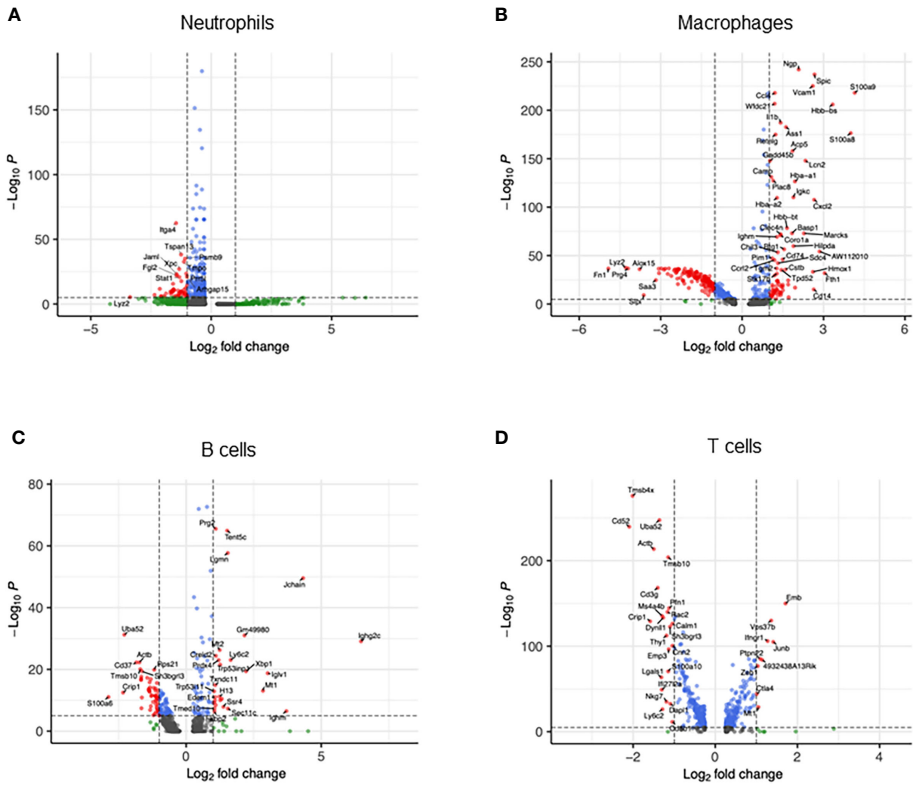

FIGURE 2
Transcriptomic heterogeneity caused by sepsis. Volcano plots showing the differentially expressed genes of CLP vs. sham in **(A)** neutrophils, **(B)** macrophages, **(C)** B cells, and **(D)** T cells.

TABLE 1 Differentially expressed pathways in septic neutrophils.

pathway	NES
HALLMARK_TNFA_SIGNALING_VIA_NFKB	3.26
GALINDO_IMMUNE_RESPONSE_TO_ENTEROTOXIN	3.09
SEKI_INFLAMMATORY_RESPONSE_LPS_UP	2.89
GROSS_HYPOXIA_VIA_ELK3_DN	2.86
NEMETH_INFLAMMATORY_RESPONSE_LPS_UP	2.83
GROSS_HYPOXIA_VIA_ELK3_AND_HIF1A_UP	2.63
GOBP_INFLAMMATORY_RESPONSE	2.57
HALLMARK_INFLAMMATORY_RESPONSE	2.49
GOBP_CELLULAR_RESPONSE_TO_INTERLEUKIN_1	2.49
GOMF_CYTOKINE_ACTIVITY	2.48
FOSTER_TOLERANT_MACROPHAGE_UP	2.45
REL_TARGET_GENES	2.45
GOBP_RESPONSE_TO_INTERLEUKIN_1	2.45
WP_LUNG_FIBROSIS	2.45
GOMF_CYTOKINE_RECEPTOR_BINDING	2.45
PLASARI_TGFB1_TARGETS_1HR_UP	2.43
TABULA_MURIS_SENIS_BLADDER_ENDOTHELIAL_CELL_AGEING	2.41
RASHI_RESPONSE_TO_IONIZING_RADIATION_2	2.4
LIAN_LIPA_TARGETS_6M	2.4
GOMF_SIGNALING_RECEPTOR_REGULATOR_ACTIVITY	2.4
LIAN_LIPA_TARGETS_3M	2.4
GROSS_ELK3_TARGETS_DN	2.39
GROSS_HYPOXIA_VIA_ELK3_ONLY_UP	2.39
ZHENG_IL22_SIGNALING_UP	2.39
SAFFORD_T_LYMPHOCYTE_ANERGY	2.35
GOBP_PATTERN_RECOGNITION_RECEPTOR_SIGNALING_PATHWAY	2.35
GERY_CEBP_TARGETS	2.34
GROSS_HYPOXIA_VIA_HIF1A_DN	2.34
RASHI_RESPONSE_TO_IONIZING_RADIATION_1	2.33
HALLMARK_HYPOXIA	2.33

NES, normalized enrichment score.

amino acid regulation by mammalian target of rapamycin complex 1 (mTORC1), and glycolysis and glucogenesis (Table 5). In cluster #1, the most upregulated genes were *Il1b*, *Pou2f2*, *Emp3*, *Ifitm1*, *Gm19951*, *Nr4a1*, *Pglyrp1*, *Prr13*, *S100a6*, and *Klf2* (Supplementary Table 5). The activated pathways were the ones related to cell aging, negative regulation of protein serine/threonine kinase, e.g., MAPK, and immunoregulatory cell–cell interaction (Table 5). In cluster #2, *Saa3*, *Orm1*, *Il10*, *Plin2*, *Csf3*, *Sod2*, *Lamp1*, *Gde1*, *Fnip2*, and *Cd63* were the most upregulated genes (Supplementary Table 5). The activated pathways in this cluster were the ones related to hematopoietic late progenitor cells, protein–lipid complex, plasminogen activation, inflammatory response, and fever generation (Table 5). In cluster #3, *Edn1*, *Rpsa*, *Rpl13*, *Spp1*, *Rpl32*, *Rps24*, *Rps20*, *Rps19*, *Rps8*, and *Rplp0* were the most upregulated genes (Supplementary Table 5), which reflected the activated pathways related to ribosome (Table 5). Taken together, neutrophils consist of different kinds of subsets, which include enhanced effector functions or immunoregulatory properties as well as altered cell metabolism.

Macrophage subset analysis

Macrophages consisted of four clusters (Figure 4A). Two major clusters, cluster #0 and #1, were mostly found in the peritoneal cavity of sham mice (Figure 4B), suggesting they are bona fide peritoneal resident macrophages. Cluster #2 was the main population in the spleen of sham and CLP mice and also found in the peritoneal cavity of sham mice (Figure 4B), indicating that this population may have motility. Cluster #3, the smallest population, was mostly found in the peritoneal cavity of CLP mice (Figure 4B), suggesting they are specific to the site of infection. In cluster #0, the most upregulated genes were *Slpi*, *Chil3*, *S100a4*, *S100a6*, *Fabp5*, *Prtn3*, *Apoc2*, *Cd52*, *Tmem176b*, and *Fabp4* (Supplementary Table 6). Activated pathways in this cluster were signal-recognition particle (SPR)-dependent cotranslational protein targeting the membrane, ribosome, and cell aging (Table 6). In cluster #1, the most upregulated genes were *Cxcl13, Apoc1, Vsig4, Wnt2, Tgfb2, Timd4, C4b, Cald1, Scn1b*, and *Cdkn2a* (Supplementary Table 6). Activated pathways in this cluster were related to extracellular matrix organization, cytokine activity, coagulation, and cell adhesion mediated by integrin (Table 6). In cluster #2, the most upregulated genes were *S100a9, S100a8, Cd74, AW112010, Hmox1, Vcam1, Hbb-bs, Marcks, Spic*, and *Aif1* (Supplementary Table 6). Pathways activated in this cluster were cell aging and lymphocyte activation, adhesion, and proliferation (Table 6). In cluster #3, the most upregulated genes were *S100a9, S100a8, Cd74, AW112010, Hmox1, Vcam1, Hbb-bs, Marcks, Spic*, and *Aif1* (Supplementary Table 6). Pathways activated in this cluster were E2F and Myc targets (Table 6). Together, macrophage subsets exhibit different properties in cell aging, inflammatory activity, and mobility.

B-cell subset analysis

B cells consisted of four clusters (Figure 5A). Cluster #0 was found mainly in the spleen of sham mice and to a lesser extent in the peritoneal cavity of sham and spleen of septic mice (Figure 5B). Cluster #1 was found mainly in the peritoneal cavity of sham mice and to a lesser extent in the spleen of sham and septic mice (Figure 5B). Clusters #2 and #3 consisted of a low number of cells and were

10.3389/fimmu.2024.1347453

TABLE 2 Differentially expressed pathways in septic macrophages.

pathway	NES
TABULA_MURIS_SENIS_LIVER_MYELOID_LEUKOCYTE_AGEING	2.99
GALINDO_IMMUNE_RESPONSE_TO_ENTEROTOXIN	2.97
SEKI_INFLAMMATORY_RESPONSE_LPS_UP	2.75
TABULA_MURIS_SENIS_HEART_AND_AORTA_CARDIOMYOCYTE_AGEING	2.64
TABULA_MURIS_SENIS_MARROW_PRECURSOR_B_CELL_AGEING	2.56
TABULA_MURIS_SENIS_LIMB_MUSCLE_MACROPHAGE_AGEING	2.55
TABULA_MURIS_SENIS_GONADAL_ADIPOSE_TISSUE_MYELOID_CELL_AGEING	2.54
HALLMARK_TNFA_SIGNALING_VIA_NFKB	2.54
TABULA_MURIS_SENIS_BLADDER_ENDOTHELIAL_CELL_AGEING	2.46
TABULA_MURIS_SENIS_SPLEEN_CD8_POSITIVE_ALPHA_BETA_T_CELL_AGEING	2.45
RASHI_NFKB1_TARGETS	2.42
WP_LUNG_FIBROSIS	2.4
GOBP_PEPTIDYL_CYSTEINE_MODIFICATION	2.36
GOBP_RESPONSE_TO_HYDROGEN_PEROXIDE	2.36
TABULA_MURIS_SENIS_SUBCUTANEOUS_ADIPOSE_TISSUE_MYELOID_CELL_AGEING	2.36
TABULA_MURIS_SENIS_SPLEEN_T_CELL_AGEING	2.35
TABULA_MURIS_SENIS_BLADDER_BLADDER_UROTHELIAL_CELL_AGEING	2.33
HOUSTIS_ROS	2.33
GOBP_TRANSITION_METAL_ION_HOMEOSTASIS	2.33
GOBP_IRON_ION_HOMEOSTASIS	2.33
TABULA_MURIS_SENIS_KIDNEY_KIDNEY_DISTAL_CONVOLUTED_TUBULE_EPITHELIAL_CELL_AGEING	2.31
CHYLA_CBFA2T3_TARGETS_DN	2.31
TABULA_MURIS_SENIS_MARROW_HEMATOPOIETIC_PRECURSOR_CELL_AGEING	2.3
JIANG_AGING_HYPOTHALAMUS_UP	2.3
TABULA_MURIS_SENIS_LUNG_MATURE_NK_T_CELL_AGEING	2.3
GOBP_RESPONSE_TO_REACTIVE_OXYGEN_SPECIES	2.25
VILIMAS_NOTCH1_TARGETS_UP	2.24
TABULA_MURIS_SENIS_MARROW_MACROPHAGE_AGEING	2.24
TABULA_MURIS_SENIS_SPLEEN_CD4_POSITIVE_ALPHA_BETA_T_CELL_AGEING	2.23
GOBP_CELLULAR_TRANSITION_METAL_ION_HOMEOSTASIS	2.22

NES, normalized enrichment score.

found in three different samples (Figure 5B). B cells are known to be classified into B-1 and B-2 cells. Using the genes identified to be specific for either B-1 and B-2 cells in a previous study (27), clusters #0 and #2 aligned well with B-2 cells and cluster #1 aligned well with B-1 cells (Supplementary Figure 6). In cluster #0, the most upregulated genes were *Ighd*, *Ebf1*, *Mef2c*, *Fcer2a, Btg1, BE692007, H2-Aa, Vpreb3, H2-Ab1*, and *Cd69* (Supplementary Table 7). Pathways activated in this cluster were as follows: mature B lymphocyte, MHC protein complex, plasma cell, large pre-B-2 lymphocytes, protein complex binding (Table 7). In cluster #1, the most upregulated genes were *S100a6*, *Crip1*, *Vim*, *Ahnak*, *Plac8*, *S100a4*, *Iglc1, Lgals1, Tagln2*, and *Lyz2* (Supplementary Table 7). Activated pathways according to these genes were related to ribosomes and aging (Table 7). In cluster #2, the most upregulated genes were *Hmgb2, Ncl, Mif, Npm1, Hist1h1b, Eif5a, Ran, Nme1, Stmn1*, and *Pclaf* (Supplementary Table 7). Activated pathways in this cluster were mostly the ones related to cell aging (Table 7). In cluster #3, the most upregulated genes were *Jchain*, *Ighg2c, Jchain, Ighg2b, Igkc, Ighm, Slpi, Iglv1, Hsp90b1, Xbp1*, and *Iglc1* (Supplementary Table 7). Activated pathways in this cluster were related to the endoplasmic reticulum (Table 7). Taken together, B cells encompass both B-1 and B-2 cell types, with

TABLE 3 Differentially expressed pathways in septic B cells.

pathway	NES
PASQUALUCCI_LYMPHOMA_BY_GC_STAGE_UP	3.83
GOCC_ENDOPLASMIC_RETICULUM_PROTEIN_CONTAINING_COMPLEX	2.93
MORI_PLASMA_CELL_UP	2.92
LAZARO_GENETIC_MOUSE_MODEL_HIGH_GRADE_LARGE_CELL_NEUROENDOCRINE_LUNG_CARCINOMA_UP	2.68
REACTOME_BINDING_AND_UPTAKE_OF_LIGANDS_BY_SCAVENGER_RECEPTORS	2.67
GOBP_ENDOPLASMIC_RETICULUM_TO_CYTOSOL_TRANSPORT	2.66
VANASSE_BCL2_TARGETS_UP	2.57
GOBP_PROTEIN_EXIT_FROM_ENDOPLASMIC_RETICULUM	2.55
GOBP_RESPONSE_TO_ENDOPLASMIC_RETICULUM_STRESS	2.53
GOCC_NUCLEAR_OUTER_MEMBRANE_ENDOPLASMIC_RETICULUM_MEMBRANE_NETWORK	2.51
GOCC_ENDOPLASMIC_RETICULUM_CHAPERONE_COMPLEX	2.51
GOMF_IMMUNOGLOBULIN_RECEPTOR_BINDING	2.49
GOCC_IMMUNOGLOBULIN_COMPLEX	2.47
REACTOME_ROLE_OF_PHOSPHOLIPIDS_IN_PHAGOCYTOSIS	2.47
QI_PLASMACYTOMA_DN	2.46
GOBP_PHAGOCYTOSIS_RECOGNITION	2.45
GOCC_INTRINSIC_COMPONENT_OF_ENDOPLASMIC_RETICULUM_MEMBRANE	2.44
GOBP_ANTIGEN_PROCESSING_AND_PRESENTATION_OF_PEPTIDE_ANTIGEN_VIA_MHC_CLASS_IB	2.42
chr16A3	2.4
BURTON_ADIPOGENESIS_3	2.4
BOYLAN_MULTIPLE_MYELOMA_PCA3_DN	2.4
SHIN_B_CELL_LYMPHOMA_CLUSTER_2	2.4
GOCC_MHC_CLASS_I_PROTEIN_COMPLEX	2.39
GOBP_ANTIGEN_PROCESSING_AND_PRESENTATION_VIA_MHC_CLASS_IB	2.39
GOBP_ERAD_PATHWAY	2.37
GOBP_COMPLEMENT_ACTIVATION	2.35
chr8C5	2.34
GOCC_ENDOPLASMIC_RETICULUM_LUMEN	2.34
GOMF_ANTIGEN_BINDING	2.33
GOBP_DEFENSE_RESPONSE_TO_BACTERIUM	2.33

NES, normalized enrichment score.

their respective subsets exhibiting distinct phenotypes indicative of cell maturation or aging. This represents the diverse developmental stages these cells undergo, playing crucial roles in both innate and adaptive immune functions during sepsis.

T-cell subset analysis

T cells consisted of six clusters (Figure 6A). Cluster #0 was found almost exclusively in the spleen of CLP mice and to a lesser extent in the peritoneal cavity of CLP mice (Figure 6B). On the other hand, clusters #2 and #3 were exclusive to the spleen of sham mice (Figure 6B). Cluster #1 was found mainly in the spleen of sham mice and also existed in the peritoneal cavity of sham mice and to a lesser extent in the spleen of CLP mice (Figure 6B). Cluster #4 was found mainly in the spleen of CLP mice and to a lesser extent in the spleen of sham mice and peritoneal cavity of CLP mice (Figure 6B). Cluster #5 formed a small population in the spleen of sham and CLP mice and the peritoneal cavity of sham mice (Figure 6B). Considering the high expressions of *Cd8b1* and *Cd8a* (Supplementary Table 8), cluster #3 seemed to be CD8 T cells. In cluster #0, the most upregulated genes were *Emb*, *Vps37b*, *Ifngr1*,

10.3389/fimmu.2024.1347453

TABLE 4 Differentially expressed pathways in septic T cells.

pathway	NES
HALLMARK_TNFA_SIGNALING_VIA_NFKB	2.7
GROSS_HYPOXIA_VIA_ELK3_DN	2.56
RASHI_RESPONSE_TO_IONIZING_RADIATION_2	2.55
GALINDO_IMMUNE_RESPONSE_TO_ENTEROTOXIN	2.51
SEKI_INFLAMMATORY_RESPONSE_LPS_UP	2.51
MCDOWELL_ACUTE_LUNG_INJURY_UP	2.42
YAO_TEMPORAL_RESPONSE_TO_PROGESTERONE_CLUSTER_1	2.37
CHIARADONNA_NEOPLASTIC_TRANSFORMATION_KRAS_CDC25_DN	2.34
GROSS_ELK3_TARGETS_DN	2.33
RASHI_NFKB1_TARGETS	2.28
MARSON_FOXP3_TARGETS_DN	2.27
VARELA_ZMPSTE24_TARGETS_UP	2.27
GOBP_CELLULAR_TRANSITION_METAL_ION_HOMEOSTASIS	2.26
GOBP_RESPONSE_TO_MOLECULE_OF_BACTERIAL_ORIGIN	2.23
GERY_CEBP_TARGETS	2.2
TABULA_MURIS_SENIS_HEART_AND_AORTA_SMOOTH_MUSCLE_CELL_AGEING	2.19
MA_MYELOID_DIFFERENTIATION_DN	2.19
ABBUD_LIF_SIGNALING_1_UP	2.17
TABULA_MURIS_SENIS_BLADDER_ENDOTHELIAL_CELL_AGEING	2.16
GOBP_TRANSITION_METAL_ION_HOMEOSTASIS	2.15
LIAN_LIPA_TARGETS_6M	2.14
GOBP_INFLAMMATORY_RESPONSE	2.13
GOBP_REGULATION_OF_NUCLEAR_TRANSCRIBED_MRNA_POLY_A_TAIL_SHORTENING	2.13
GOBP_CYTOPLASMIC_PATTERN_RECOGNITION_RECEPTOR_SIGNALING_PATHWAY	2.13
LIAN_LIPA_TARGETS_3M	2.13
GOBP_POSITIVE_REGULATION_OF_ERYTHROCYTE_DIFFERENTIATION	2.13
GOBP_IRON_ION_HOMEOSTASIS	2.12
ZHENG_FOXP3_TARGETS_IN_THYMUS_UP	2.12
CHYLA_CBFA2T3_TARGETS_DN	2.12
MIR_467A_3P	2.11

NES, normalized enrichment score.

Junb, Fam241a, Ptpn22, Gramd3, Klhl6, 4932438A13Rikm, and *Zeb1* (Supplementary Table 8). The pathways revealed that ribosome, cytoplasmic translation, and serum and rapamycin sensitive genes were upregulated (Table 8). In cluster #1, the most upregulated genes were *Igfbp4, Tspan32, Actb, Uba52, Cd52, Ly6c1, Tmsb4x, Ifi27l2a, Trbc2*, and *Limd2* (Supplementary Table 8). Activated pathways in this cluster were related to ribosome- and SRP-dependent co-translational protein targeting to the membrane (Table 8). In cluster #2, the most upregulated genes were *Ccl5, S100a6, Ly6c2, S100a4, Lgals1, Nkg7, AW112010, S100a10, Crip1*, and *Ahnak* (Supplementary Table 8). Activated pathways in this cluster were mostly related to cell aging (Table 8). In cluster #3, the most upregulated genes were *Cd8b1*, Cd8a, *Dapl1*, *Ccr9, Arl4c, Nkg7, Uba52, Tubb5, Cd52*, and *Dnajc15* (Supplementary Table 8). Activated pathways in this cluster were related to ribosome and structural molecule activity (Table 8). In cluster #4, the most upregulated genes were *Cxcl2*, *Lcn2*, *Fth1*, *Ccl4*, *Slpi*, *Ccl3*, *Neat1*, *Fcer1g*, *Ifitm2*, and *Mt1* (Supplementary Table 8). Activated pathways in this cluster were related to hypoxia, cell aging, and TNF-α signaling *via* NF-κB (Table 8). In cluster #5, the most upregulated genes were *Cd74*, *Igkc*, *H2-Aa*, *Cd79a*, *H2-Eb1*, *H2-Ab1*, *Ighm*, *Ly6d*, *Iglc2*, and *Ebf1* (Supplementary Table 8).

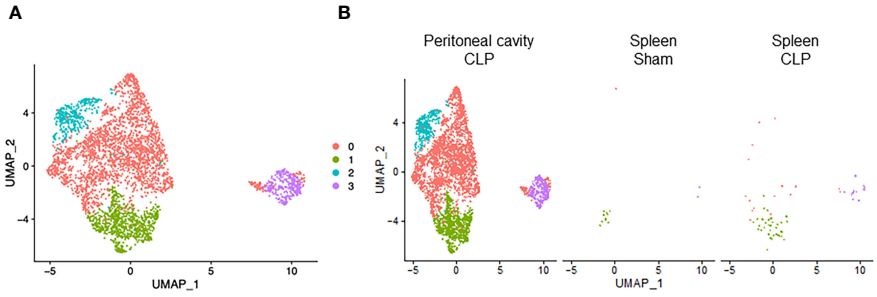

FIGURE 3
Distribution of neutrophil subsets. UMAP plots showing the subsets of neutrophils in **(A)** all groups combined and **(B)** each group.

TABLE 5 Differentially expressed pathways in neutrophil subsets.

CL	pathway	NES
0	REACTOME_IRON_UPTAKE_AND_TRANSPORT	2.29
0	GOCC_SECONDARY_LYSOSOME	2.24
0	GOBP_TRANSITION_METAL_ION_HOMEOSTASIS	2.23
0	REACTOME_AMINO_ACIDS_REGULATE_MTORC1	2.2
0	GOBP_CELLULAR_TRANSITION_METAL_ION_HOMEOSTASIS	2.2
0	GOBP_PEPTIDE_CROSS_LINKING	2.18
0	GOCC_PEPTIDASE_INHIBITOR_COMPLEX	2.18
0	MODY_HIPPOCAMPUS_POSTNATAL	2.13
0	WP_GLYCOLYSIS_AND_GLUCONEOGENESIS	2.12
0	GOCC_AUTOLYSOSOME	2.08
0	GOMF_CYSTEINE_TYPE_ENDOPEPTIDASE_INHIBITOR_ACTIVITY	2.06
0	ZFP617_TARGET_GENES	2.02
0	TABULA_MURIS_SENIS_BLADDER_ENDOTHELIAL_CELL_AGEING	2.01
0	GROSS_HYPOXIA_VIA_ELK3_DN	1.99
0	GOBP_NEGATIVE_REGULATION_OF_OXIDOREDUCTASE_ACTIVITY	1.87
0	REACTOME_TRANSPORT_OF_SMALL_MOLECULES	1.86
0	REACTOME_DOWNREGULATION_OF_SMAD2_3_SMAD4_TRANSCRIPTIONAL_ACTIVITY	1.86
0	REACTOME_PEXOPHAGY	1.85
0	GOBP_COLLATERAL_SPROUTING	1.84
0	GOBP_ETHANOLAMINE_CONTAINING_COMPOUND_METABOLIC_PROCESS	1.63
1	TABULA_MURIS_SENIS_SUBCUTANEOUS_ADIPOSE_TISSUE_MYELOID_CELL_AGEING	2.66
1	TABULA_MURIS_SENIS_MAMMARY_GLAND_STROMAL_CELL_AGEING	2.43
1	TABULA_MURIS_SENIS_MAMMARY_GLAND_MACROPHAGE_AGEING	2.42
1	LAZARO_GENETIC_MOUSE_MODEL_HIGH_GRADE_SMALL_CELL_NEUROENDOCRINE_LUNG_CARCINOMA_DN	2.35
1	TABULA_MURIS_SENIS_LUNG_B_CELL_AGEING	2.33
1	GOBP_NEGATIVE_REGULATION_OF_MAP_KINASE_ACTIVITY	2.32
1	BOYLAN_MULTIPLE_MYELOMA_D_DN	2.31

(Continued)

TABLE 5 Continued

CL	pathway	NES
1	REACTOME_IMMUNOREGULATORY_INTERACTIONS_BETWEEN_A_LYMPHOID_AND_A_NON_LYMPHOID_CELL	2.28
1	GOCC_CYTOPLASMIC_SIDE_OF_MEMBRANE	2.26
1	TABULA_MURIS_SENIS_SPLEEN_CD4_POSITIVE_ALPHA_BETA_T_CELL_AGEING	2.2
1	GOBP_NEGATIVE_REGULATION_OF_PROTEIN_SERINE_THREONINE_KINASE_ACTIVITY	2.19
1	QI_PLASMACYTOMA_UP	2.17
1	GOBP_REGULATION_OF_INSULIN_RECEPTOR_SIGNALING_PATHWAY	2.16
1	GOMF_ACTIN_BINDING	2.16
1	GOCC_EXTRINSIC_COMPONENT_OF_CYTOPLASMIC_SIDE_OF_PLASMA_MEMBRANE	2.15
1	TORCHIA_TARGETS_OF_EWSR1_FLI1_FUSION_UP	2.13
1	GOBP_REGULATION_OF_PLATELET_ACTIVATION	2.13
1	GOCC_SIDE_OF_MEMBRANE	2.13
1	GOBP_REGULATION_OF_CELL_MORPHOGENESIS	2.13
1	GOBP_RESPONSE_TO_ORGANOPHOSPHORUS	2.12
2	IVANOVA_HEMATOPOIESIS_LATE_PROGENITOR	2.46
2	GOCC_PROTEIN_LIPID_COMPLEX	2.29
2	GOBP_PLASMINOGEN_ACTIVATION	2.05
2	REACTOME_SYNTHESIS_OF_15_EICOSATETRAENOIC_ACID_DERIVATIVES	-1.62
2	BIERIE_INFLAMMATORY_RESPONSE_TGFB1	-1.63
2	GOBP_POSITIVE_REGULATION_OF_FEVER_GENERATION	-1.63
2	GOBP_POSITIVE_REGULATION_OF_HEAT_GENERATION	-1.63
2	GOBP_REGULATION_OF_FEVER_GENERATION	-1.63
2	GOBP_REGULATION_OF_HEAT_GENERATION	-1.63
2	SHIN_B_CELL_LYMPHOMA_CLUSTER_6	-1.63
2	GOMF_NITRIC_OXIDE_SYNTHASE_REGULATOR_ACTIVITY	-1.82
2	GOBP_APOPTOTIC_PROCESS	-1.82
2	GOBP_NEGATIVE_REGULATION_OF_MOLECULAR_FUNCTION	-1.9
2	ELL2_TARGET_GENES	-1.91
2	LAZARO_GENETIC_MOUSE_MODEL_HIGH_GRADE_SMALL_CELL_NEUROENDOCRINE_LUNG_CARCINOMA_DN	-1.91
2	NFATC2_TARGET_GENES	-1.92
2	GOBP_RESPONSE_TO_INTERLEUKIN_17	-1.93
2	TABULA_MURIS_SENIS_LIVER_NK_CELL_AGEING	-1.97
2	GOBP_POSITIVE_REGULATION_OF_P38MAPK_CASCADE	-1.99
2	TABULA_MURIS_SENIS_LIMB_MUSCLE_T_CELL_AGEING	-2
3	GOCC_RIBOSOMAL_SUBUNIT	3.76
3	GOCC_RIBOSOME	3.75
3	GOMF_STRUCTURAL_CONSTITUENT_OF_RIBOSOME	3.75
3	GOCC_CYTOSOLIC_RIBOSOME	3.74
3	WP_CYTOPLASMIC_RIBOSOMAL_PROTEINS	3.72
3	GOMF_STRUCTURAL_MOLECULE_ACTIVITY	3.68

(Continued)

TABLE 5 Continued

CL	pathway	NES
3	REACTOME_NONSENSE_MEDIATED_DECAY_NMD_INDEPENDENT_OF_THE_EXON_JUNCTION_COMPLEX_EJC	3.66
3	REACTOME_MAJOR_PATHWAY_OF_RRNA_PROCESSING_IN_THE_NUCLEOLUS_AND_CYTOSOL	3.64
3	GOBP_CYTOPLASMIC_TRANSLATION	3.64
3	REACTOME_SRP_DEPENDENT_COTRANSLATIONAL_PROTEIN_TARGETING_TO_MEMBRANE	3.63
3	REACTOME_NONSENSE_MEDIATED_DECAY_NMD	3.6
3	REACTOME_FORMATION_OF_A_POOL_OF_FREE_40S_SUBUNITS	3.59
3	REACTOME_EUKARYOTIC_TRANSLATION_INITIATION	3.58
3	REACTOME_TRANSLATION	3.54
3	GOCC_CYTOSOLIC_LARGE_RIBOSOMAL_SUBUNIT	3.43
3	GOCC_LARGE_RIBOSOMAL_SUBUNIT	3.41
3	TABULA_MURIS_SENIS_KIDNEY_EPITHELIAL_CELL_OF_PROXIMAL_TUBULE_AGEING	3.39
3	TABULA_MURIS_SENIS_THYMUS_PROFESSIONAL_ANTIGEN_PRESENTING_CELL_AGEING	3.38
3	TABULA_MURIS_SENIS_SPLEEN_NK_CELL_AGEING	3.34
3	BILANGES_SERUM_AND_RAPAMYCIN_SENSITIVE_GENES	3.33

CL, cluster; NES, normalized enrichment score.

Activated pathways in this cluster were mostly irrelevant to T cells (Table 8), suggesting that the population was too small to be

TABLE 6 Differentially expressed pathways in macrophage subsets.

CL	pathway	NES
0	REACTOME_SRP_DEPENDENT_COTRANSLATIONAL_PROTEIN_TARGETING_TO_MEMBRANE	3.48
0	WP_CYTOPLASMIC_RIBOSOMAL_PROTEINS	3.08
0	CHIARADONNA_NEOPLASTIC_TRANSFORMATION_KRAS_CDC25_DN	2.99
0	MCBRYAN_PUBERTAL_TGFB1_TARGETS_DN	2.97
0	TABULA_MURIS_SENIS_MARROW_MEGAKARYOCYTE_ERYTHROID_PROGENITOR_CELL_AGEING	2.96
0	GOCC_CYTOSOLIC_RIBOSOME	2.91
0	REACTOME_NONSENSE_MEDIATED_DECAY_NMD_INDEPENDENT_OF_THE_EXON_JUNCTION_COMPLEX_EJC	2.85
0	TABULA_MURIS_SENIS_MARROW_GRANULOCYTE_AGEING	2.85
0	TABULA_MURIS_SENIS_MARROW_GRANULOCYTOPOIETIC_CELL_AGEING	2.79
0	INGRAM_SHH_TARGETS_DN	2.75
0	GOMF_STRUCTURAL_CONSTITUENT_OF_RIBOSOME	2.73
0	GOCC_CYTOSOLIC_LARGE_RIBOSOMAL_SUBUNIT	2.71
0	HALLMARK_KRAS_SIGNALING_UP	2.69
0	BREDEMEYER_RAG_SIGNALING_NOT_VIA_ATM_DN	2.4
0	TABULA_MURIS_SENIS_MARROW_ERYTHROBLAST_AGEING	2.37
0	REACTOME_FORMATION_OF_FIBRIN_CLOT_CLOTTING_CASCADE	2.37
0	HARRIS_BRAIN_CANCER_PROGENITORS	2.35
0	REACTOME_TRIGLYCERIDE_METABOLISM	2.16
0	GOCC_CHYLOMICRON	2.1

(Continued)

TABLE 6 Continued

CL	pathway	NES
0	BOYLAN_MULTIPLE_MYELOMA_C_D_DN	2.09
1	REACTOME_EXTRACELLULAR_MATRIX_ORGANIZATION	2.5
1	GOMF_CYTOKINE_ACTIVITY	2.5
1	HALLMARK_COAGULATION	2.5
1	MIR_5101	2.47
1	GOMF_HEPARIN_BINDING	2.44
1	GOBP_CELL_ADHESION_MEDIATED_BY_INTEGRIN	2.4
1	GOMF_CARGO_RECEPTOR_ACTIVITY	2.39
1	GOCC_COLLAGEN_CONTAINING_EXTRACELLULAR_MATRIX	2.38
1	GOMF_OPSONIN_BINDING	2.38
1	GOCC_EXTERNAL_ENCAPSULATING_STRUCTURE	2.35
1	GOMF_COMPLEMENT_BINDING	2.35
1	GOBP_REGULATION_OF_CELLULAR_RESPONSE_TO_GROWTH_FACTOR_STIMULUS	2.35
1	GOMF_G_PROTEIN_COUPLED_RECEPTOR_BINDING	2.3
1	REACTOME_ELASTIC_FIBRE_FORMATION	2.3
1	REACTOME_MOLECULES_ASSOCIATED_WITH_ELASTIC_FIBRES	2.3
1	LEE_BMP2_TARGETS_UP	2.29
1	CUI_TCF21_TARGETS_2_DN	2.29
1	AFFAR_YY1_TARGETS_UP	2.27
1	GOBP_INTEGRIN_ACTIVATION	2.26
1	GOBP_TRANSMEMBRANE_RECEPTOR_PROTEIN_SERINE_THREONINE_KINASE_SIGNALING_PATHWAY	2.25
2	TABULA_MURIS_SENIS_LIMB_MUSCLE_MACROPHAGE_AGEING	3.02
2	GOBP_POSITIVE_REGULATION_OF_LYMPHOCYTE_ACTIVATION	2.96
2	ICHIBA_GRAFT_VERSUS_HOST_DISEASE_35D_UP	2.91
2	GOBP_POSITIVE_REGULATION_OF_LEUKOCYTE_CELL_CELL_ADHESION	2.9
2	QI_PLASMACYTOMA_UP	2.88
2	WUNDER_INFLAMMATORY_RESPONSE_AND_CHOLESTEROL_UP	2.88
2	DESCARTES_ORGANOGENESIS_WHITE_BLOOD_CELLS	2.83
2	REACTOME_RHO_GTPASE_EFFECTORS	2.83
2	GOBP_POSITIVE_REGULATION_OF_LEUKOCYTE_PROLIFERATION	2.82
2	TABULA_MURIS_SENIS_SPLEEN_CD8_POSITIVE_ALPHA_BETA_T_CELL_AGEING	2.81
2	TABULA_MURIS_SENIS_SPLEEN_T_CELL_AGEING	2.81
2	LIAN_LIPA_TARGETS_6M	2.79
2	GOBP_LEUKOCYTE_CELL_CELL_ADHESION	2.78
2	LIAN_LIPA_TARGETS_3M	2.78
2	YU_MYC_TARGETS_DN	2.78
2	TABULA_MURIS_SENIS_LIVER_MYELOID_LEUKOCYTE_AGEING	2.77
2	TABULA_MURIS_SENIS_MARROW_HEMATOPOIETIC_PRECURSOR_CELL_AGEING	2.76
2	GOBP_ANTIGEN_PROCESSING_AND_PRESENTATION_OF_EXOGENOUS_PEPTIDE_ANTIGEN	2.76

(Continued)

10.3389/fimmu.2024.1347453

TABLE 6 Continued

CL	pathway	NES
2	GOBP_POSITIVE_REGULATION_OF_CELL_ACTIVATION	2.75
2	TABULA_MURIS_SENIS_MARROW_MONOCYTE_AGEING	2.72
3	HALLMARK_E2F_TARGETS	3.08
3	BURTON_ADIPOGENESIS_3	2.98
3	LAZARO_GENETIC_MOUSE_MODEL_HIGH_GRADE_LARGE_CELL_NEUROENDOCRINE_LUNG_CARCINOMA_UP	2.97
3	HALLMARK_MYC_TARGETS_V1	2.96
3	MARKEY_RB1_ACUTE_LOF_UP	2.93
3	MORI_IMMATURE_B_LYMPHOCYTE_DN	2.9
3	LAZARO_GENETIC_MOUSE_MODEL_HIGH_GRADE_SMALL_CELL_NEUROENDOCRINE_LUNG_CARCINOMA_UP	2.88
3	MORI_LARGE_PRE_BII_LYMPHOCYTE_UP	2.87
3	BERENJENO_TRANSFORMED_BY_RHOA_UP	2.82
3	MORI_PRE_BI_LYMPHOCYTE_UP	2.8
3	GOBERT_OLIGODENDROCYTE_DIFFERENTIATION_UP	2.79
3	HOFFMANN_LARGE_TO_SMALL_PRE_BII_LYMPHOCYTE_UP	2.79
3	HALLMARK_G2M_CHECKPOINT	2.73
3	KAMMINGA_EZH2_TARGETS	2.73
3	KONG_E2F3_TARGETS	2.72
3	ISHIDA_E2F_TARGETS	2.72
3	REACTOME_ACTIVATION_OF_THE_PRE_REPLICATIVE_COMPLEX	2.71
3	GOBP_DNA_REPLICATION	2.71
3	REACTOME_ACTIVATION_OF_ATR_IN_RESPONSE_TO_REPLICATION_STRESS	2.7
3	GOBP_DNA_TEMPLATED_DNA_REPLICATION	2.7

CL, cluster; NES, normalized enrichment score.

classified properly. Together, T cells subsets have distinct characteristics in molecular translocation or cell activation.

Discussion

In this study, we have explored the transcriptomic profiling of immune cells including neutrophils, macrophages, B cells, and T cells in intra-abdominal sepsis using scRNA-seq, recognizing the pivotal roles these cells play in the host's defense against pathogens. We have unveiled the frequency, phenotype, and subsets of those cell populations in the peritoneal cavity and spleen. While millions of cells were conveniently isolated from the peritoneal cavity of each mouse, the processing capacity for scRNA-seq using the 10x Genomics kit was limited to a maximum of 10,000. Consequently, the UMAPs generated reflect the proportion of the processed cells

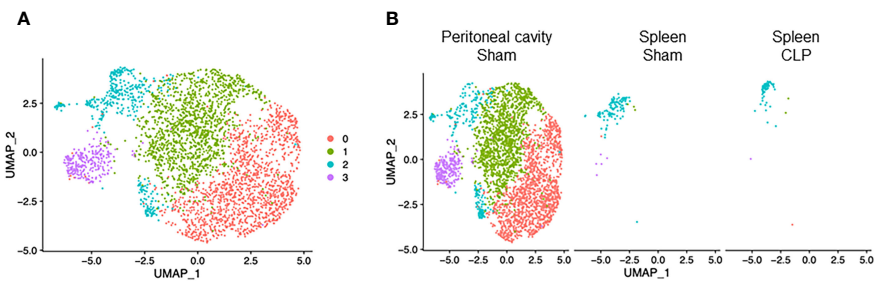

FIGURE 4
Distribution of macrophage subsets. UMAP plots showing the subsets of macrophages in **(A)** all groups combined and **(B)** each group.

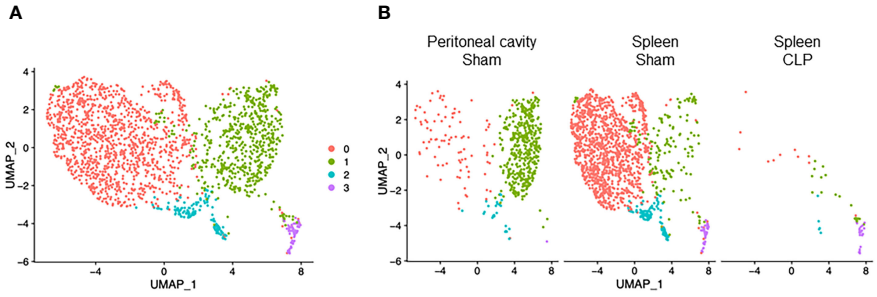

FIGURE 5
Distribution of B cell subsets. UMAP plots showing the subsets of B cells in **(A)** all groups combined and **(B)** each group.

TABLE 7 Differentially expressed pathways in B cell subsets.

CL	pathway	NES
0	MORI_MATURE_B_LYMPHOCYTE_UP	3.41
0	MORI_PLASMA_CELL_DN	3.18
0	YU_MYC_TARGETS_DN	3.17
0	GOCC_MHC_PROTEIN_COMPLEX	3.16
0	GOMF_MHC_PROTEIN_COMPLEX_BINDING	2.86
0	MORI_LARGE_PRE_BII_LYMPHOCYTE_DN	2.86
0	GOCC_MHC_CLASS_II_PROTEIN_COMPLEX	2.8
0	GOMF_MHC_CLASS_II_PROTEIN_COMPLEX_BINDING	2.8
0	GOBP_ANTIGEN_PROCESSING_AND_PRESENTATION_OF_EXOGENOUS_PEPTIDE_ANTIGEN	2.67
0	GOBP_PEPTIDE_ANTIGEN_ASSEMBLY_WITH_MHC_CLASS_II_PROTEIN_COMPLEX	2.64
0	ZHENG_FOXP3_TARGETS_IN_T_LYMPHOCYTE_DN	2.58
0	GOBP_ANTIGEN_PROCESSING_AND_PRESENTATION_OF_EXOGENOUS_PEPTIDE_ANTIGEN_VIA_MHC_CLASS_II	2.57
0	GOBP_ANTIGEN_PROCESSING_AND_PRESENTATION_OF_EXOGENOUS_ANTIGEN	2.57
0	GOMF_PEPTIDE_ANTIGEN_BINDING	2.51
0	GOBP_REGULATION_OF_HUMORAL_IMMUNE_RESPONSE	2.48
0	GOBP_T_CELL_DIFFERENTIATION_IN_THYMUS	2.44
0	MIR_106A_3P_MIR_17_3P	2.42
0	MIR_20B_3P	2.42
0	PASQUALUCCI_LYMPHOMA_BY_GC_STAGE_DN	2.41
0	LAZARO_GENETIC_MOUSE_MODEL_HIGH_GRADE_LARGE_CELL_NEUROENDOCRINE_LUNG_CARCINOMA_DN	2.4
1	TABULA_MURIS_SENIS_SPLEEN_MATURE_NK_T_CELL_AGEING	2.93
1	WP_CYTOPLASMIC_RIBOSOMAL_PROTEINS	2.88
1	GOCC_CYTOSOLIC_RIBOSOME	2.85
1	TABULA_MURIS_SENIS_SUBCUTANEOUS_ADIPOSE_TISSUE_B_CELL_AGEING	2.84
1	TABULA_MURIS_SENIS_HEART_AND_AORTA_FIBROBLAST_OF_CARDIAC_TISSUE_AGEING	2.81
1	REACTOME_NONSENSE_MEDIATED_DECAY_NMD_INDEPENDENT_OF_THE_EXON_JUNCTION_COMPLEX_EJC	2.77
1	REACTOME_SRP_DEPENDENT_COTRANSLATIONAL_PROTEIN_TARGETING_TO_MEMBRANE	2.77

(Continued)

10.3389/fimmu.2024.1347453

TABLE 7 Continued

CL	pathway	NES
1	GOBP_CYTOPLASMIC_TRANSLATION	2.76
1	REACTOME_NONSENSE_MEDIATED_DECAY_NMD	2.74
1	REACTOME_FORMATION_OF_A_POOL_OF_FREE_40S_SUBUNITS	2.73
1	TABULA_MURIS_SENIS_HEART_AND_AORTA_LEUKOCYTE_AGEING	2.71
1	GOMF_STRUCTURAL_MOLECULE_ACTIVITY	2.66
1	TABULA_MURIS_SENIS_MARROW_ERYTHROBLAST_AGEING	2.66
1	BILANGES_SERUM_AND_RAPAMYCIN_SENSITIVE_GENES	2.65
1	REACTOME_EUKARYOTIC_TRANSLATION_INITIATION	2.63
1	GOCC_CYTOSOLIC_LARGE_RIBOSOMAL_SUBUNIT	2.62
1	GOMF_STRUCTURAL_CONSTITUENT_OF_RIBOSOME	2.61
1	TABULA_MURIS_SENIS_KIDNEY_MACROPHAGE_AGEING	2.6
1	TABULA_MURIS_SENIS_MAMMARY_GLAND_MACROPHAGE_AGEING	2.57
1	TABULA_MURIS_SENIS_KIDNEY_FIBROBLAST_AGEING	2.56
2	HALLMARK_MYC_TARGETS_V1	2.7
2	TABULA_MURIS_SENIS_THYMUS_THYMOCYTE_AGEING	2.61
2	TABULA_MURIS_SENIS_SPLEEN_PROERYTHROBLAST_AGEING	2.5
2	TABULA_MURIS_SENIS_TONGUE_BASAL_CELL_OF_EPIDERMIS_AGEING	2.48
2	TABULA_MURIS_SENIS_LUNG_CLASSICAL_MONOCYTE_AGEING	2.44
2	GOCC_MYELIN_SHEATH	2.42
2	KARLSSON_TGFB1_TARGETS_UP	2.41
2	GOBP_TELOMERE_MAINTENANCE_VIA_TELOMERE_LENGTHENING	2.38
2	GOBP_RNA_TEMPLATED_DNA_BIOSYNTHETIC_PROCESS	2.36
2	MORI_PRE_BI_LYMPHOCYTE_UP	2.36
2	MORI_LARGE_PRE_BII_LYMPHOCYTE_UP	2.34
2	MORI_IMMATURE_B_LYMPHOCYTE_DN	2.34
2	GOCC_PROTON_TRANSPORTING_ATP_SYNTHASE_COMPLEX	2.33
2	ISHIDA_E2F_TARGETS	2.3
2	GOMF_UNFOLDED_PROTEIN_BINDING	2.3
2	LE_EGR2_TARGETS_UP	2.3
2	GOCC_TELOMERASE_HOLOENZYME_COMPLEX	2.29
2	GOBP_REGULATION_OF_PROTEIN_LOCALIZATION_TO_CHROMOSOME_TELOMERIC_REGION	2.28
2	HALLMARK_E2F_TARGETS	2.28
2	BERENJENO_TRANSFORMED_BY_RHOA_UP	2.28
3	PASQUALUCCI_LYMPHOMA_BY_GC_STAGE_UP	3.29
3	GOCC_ENDOPLASMIC_RETICULUM_PROTEIN_CONTAINING_COMPLEX	2.91
3	GOCC_NUCLEAR_OUTER_MEMBRANE_ENDOPLASMIC_RETICULUM_MEMBRANE_NETWORK	2.86
3	GOBP_RESPONSE_TO_ENDOPLASMIC_RETICULUM_STRESS	2.8
3	GOCC_ORGANELLE_SUBCOMPARTMENT	2.76
3	MORI_PLASMA_CELL_UP	2.73

(Continued)

10.3389/fimmu.2024.1347453

TABLE 7 Continued

CL	pathway	NES
3	GOCC_ENDOPLASMIC_RETICULUM	2.53
3	GOBP_ERAD_PATHWAY	2.53
3	GOCC_INTRINSIC_COMPONENT_OF_ENDOPLASMIC_RETICULUM_MEMBRANE	2.51
3	GOBP_UBIQUITIN_DEPENDENT_ERAD_PATHWAY	2.47
3	BOYLAN_MULTIPLE_MYELOMA_C_D_DN	2.47
3	GOBP_PROTEIN_LOCALIZATION_TO_ENDOPLASMIC_RETICULUM	2.46
3	BOYLAN_MULTIPLE_MYELOMA_PCA1_UP	2.45
3	GOBP_RESPONSE_TO_TOPOLOGICALLY_INCORRECT_PROTEIN	2.43
3	GOBP_ESTABLISHMENT_OF_PROTEIN_LOCALIZATION_TO_ENDOPLASMIC_RETICULUM	2.43
3	QI_PLASMACYTOMA_DN	2.41
3	GOBP_ENDOPLASMIC_RETICULUM_TO_GOLGI_VESICLE_MEDIATED_TRANSPORT	2.39
3	GOCC_ENDOPLASMIC_RETICULUM_LUMEN	2.39
3	GOBP_GLYCOPROTEIN_METABOLIC_PROCESS	2.39
3	GOBP_RESPONSE_TO_UNFOLDED_PROTEIN	2.37

CL, cluster; NES, normalized enrichment score.

rather than the absolute cell counts. Notably, in CLP-induced sepsis mice, neutrophils emerged as the predominant population within the peritoneal cavity, thereby causing other cell types to appear relatively few in the UMAP (in terms of percentage of whole-cell population). We chose spleen as it is one of the most important lymphoid organs for the immune system. Moreover, circulating cells pass through or are trapped within the spleen; thus, splenocytes reflect the blood cells to a certain extent. Peritoneal cavity was chosen as the site of infection, where robust innate immune activities can be observed in response to the pathogens. We did not include PBMCs as they barely contain neutrophils, which are arguably the most important cell type during sepsis (3). Whole blood leukocytes, which contain neutrophils, would be worth evaluating but could be fragile for lengthy red blood cell lysis.

It has been traditionally thought that sepsis consists of an acute pro-inflammatory (hyperdynamic) phase and a later immunosuppressive (hypodynamic) state. This could still hold true in terms of the overall immune balance, but it is now known that both pro- and anti-inflammatory mediators and cells coexist from the early stage of sepsis (28). Thus, it is important to evaluate the status of cells not in bulk but individually to precisely understand their roles and potential interaction with other cells during sepsis. In fact, our scRNA-seq analysis revealed that the most cell types exhibited pro-inflammatory phenotypes such as increased gene levels of chemokines and DAMPs, including *Cxcl2*, *Ccl4*, *CCl3*, *S100a9*, and *S100a8*, and NF-κB activation in septic mice, whereas many of the subsets within the cell type were not characterized by the typical pro-inflammatory genes or pathways. Considering the fact that previously proposed sepsis drugs, which target the canonical pro-inflammatory mediators or signaling such as PAMPs or PRRs, have failed in the clinical trials (29), a more focused cell-specific approach might be needed to break through the current situation.

In the present study, we have identified multiple subsets within each major cell population in an unbiased way. Differentially expressed genes indicated that subsets were distinct from others in different ways, such as enhanced effector functions, immunoregulatory responses, cellular metabolism, and aging. The further assessments of phenotypical changes in different environments for individual clusters would enable us to define the characteristics of those subsets more clearly. It may also be interesting to investigate whether those

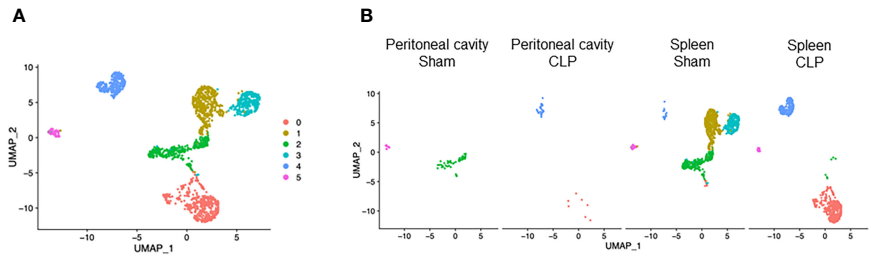

FIGURE 6
Distribution of T-cell subsets. UMAP plots showing the subsets of T cells in **(A)** all groups combined and **(B)** each group.

TABLE 8 Differentially expressed pathways in T cell subsets.

CL	pathway	NES
0	WP_CYTOPLASMIC_RIBOSOMAL_PROTEINS	3.2
0	GOBP_CYTOPLASMIC_TRANSLATION	2.99
0	BILANGES_SERUM_AND_RAPAMYCIN_SENSITIVE_GENES	2.97
0	GOCC_CYTOSOLIC_RIBOSOME	2.9
0	GOMF_RRNA_BINDING	2.86
0	REACTOME_NONSENSE_MEDIATED_DECAY_NMD_INDEPENDENT_OF_THE_EXON_JUNCTION_COMPLEX_EJC	2.81
0	REACTOME_SRP_DEPENDENT_COTRANSLATIONAL_PROTEIN_TARGETING_TO_MEMBRANE	2.8
0	REACTOME_EUKARYOTIC_TRANSLATION_INITIATION	2.75
0	REACTOME_FORMATION_OF_A_POOL_OF_FREE_40S_SUBUNITS	2.75
0	REACTOME_NONSENSE_MEDIATED_DECAY_NMD	2.74
0	REACTOME_MAJOR_PATHWAY_OF_RRNA_PROCESSING_IN_THE_NUCLEOLUS_AND_CYTOSOL	2.66
0	TABULA_MURIS_SENIS_HEART_AND_AORTA_LEUKOCYTE_AGEING	2.63
0	BILANGES_SERUM_RESPONSE_TRANSLATION	2.58
0	GOMF_STRUCTURAL_CONSTITUENT_OF_RIBOSOME	2.53
0	GOBP_RIBOSOME_ASSEMBLY	2.46
0	TABULA_MURIS_SENIS_KIDNEY_FIBROBLAST_AGEING	2.45
0	GOCC_RIBOSOMAL_SUBUNIT	2.45
0	GOCC_RIBOSOME	2.45
0	GOBP_CYTOPLASMIC_PATTERN_RECOGNITION_RECEPTOR_SIGNALING_PATHWAY	2.38
0	TABULA_MURIS_SENIS_BLADDER_BLADDER_CELL_AGEING	2.35
1	GOCC_CYTOSOLIC_RIBOSOME	3.53
1	WP_CYTOPLASMIC_RIBOSOMAL_PROTEINS	3.44
1	GOCC_CYTOSOLIC_LARGE_RIBOSOMAL_SUBUNIT	3.35
1	REACTOME_SRP_DEPENDENT_COTRANSLATIONAL_PROTEIN_TARGETING_TO_MEMBRANE	3.35
1	REACTOME_FORMATION_OF_A_POOL_OF_FREE_40S_SUBUNITS	3.26
1	REACTOME_NONSENSE_MEDIATED_DECAY_NMD_INDEPENDENT_OF_THE_EXON_JUNCTION_COMPLEX_EJC	3.24
1	GOMF_STRUCTURAL_CONSTITUENT_OF_RIBOSOME	3.1
1	REACTOME_EUKARYOTIC_TRANSLATION_INITIATION	3.09
1	GOCC_RIBOSOMAL_SUBUNIT	3.03
1	REACTOME_NONSENSE_MEDIATED_DECAY_NMD	3.02
1	GOMF_STRUCTURAL_MOLECULE_ACTIVITY	3
1	GOCC_CYTOSOLIC_SMALL_RIBOSOMAL_SUBUNIT	2.95
1	REACTOME_MAJOR_PATHWAY_OF_RRNA_PROCESSING_IN_THE_NUCLEOLUS_AND_CYTOSOL	2.84
1	GOBP_CYTOPLASMIC_TRANSLATION	2.81
1	GOCC_RIBOSOME	2.81
1	GOCC_ACTIN_FILAMENT_BUNDLE	2.8
1	GOCC_LARGE_RIBOSOMAL_SUBUNIT	2.75
1	TABULA_MURIS_SENIS_DIAPHRAGM_SKELETAL_MUSCLE_SATELLITE_CELL_AGEING	2.7
1	GOCC_SMALL_RIBOSOMAL_SUBUNIT	2.68

(Continued)

TABLE 8 Continued

CL	pathway	NES
1	HSF2_TARGET_GENES	2.65
2	TABULA_MURIS_SENIS_MAMMARY_GLAND_T_CELL_AGEING	3.05
2	TABULA_MURIS_SENIS_LUNG_CD4_POSITIVE_ALPHA_BETA_T_CELL_AGEING	2.92
2	TABULA_MURIS_SENIS_SPLEEN_CD8_POSITIVE_ALPHA_BETA_T_CELL_AGEING	2.79
2	TABULA_MURIS_SENIS_LUNG_CD8_POSITIVE_ALPHA_BETA_T_CELL_AGEING	2.68
2	TABULA_MURIS_SENIS_MAMMARY_GLAND_B_CELL_AGEING	2.67
2	TABULA_MURIS_SENIS_MAMMARY_GLAND_MACROPHAGE_AGEING	2.65
2	TABULA_MURIS_SENIS_BROWN_ADIPOSE_TISSUE_T_CELL_AGEING	2.65
2	LI_INDUCED_T_TO_NATURAL_KILLER_UP	2.61
2	TABULA_MURIS_SENIS_SPLEEN_T_CELL_AGEING	2.6
2	TABULA_MURIS_SENIS_MARROW_HEMATOPOIETIC_PRECURSOR_CELL_AGEING	2.55
2	TABULA_MURIS_SENIS_LUNG_B_CELL_AGEING	2.51
2	TABULA_MURIS_SENIS_THYMUS_DN4_THYMOCYTE_AGEING	2.49
2	TABULA_MURIS_SENIS_SUBCUTANEOUS_ADIPOSE_TISSUE_B_CELL_AGEING	2.45
2	TABULA_MURIS_SENIS_KIDNEY_MACROPHAGE_AGEING	2.45
2	TABULA_MURIS_SENIS_KIDNEY_T_CELL_AGEING	2.45
2	TABULA_MURIS_SENIS_GONADAL_ADIPOSE_TISSUE_B_CELL_AGEING	2.45
2	GOBP_NATURAL_KILLER_CELL_ACTIVATION	2.44
2	GOLDRATH_ANTIGEN_RESPONSE	2.44
2	GOCC_COLLAGEN_CONTAINING_EXTRACELLULAR_MATRIX	2.41
2	GOCC_EXTERNAL_ENCAPSULATING_STRUCTURE	2.4
3	GOCC_CYTOSOLIC_RIBOSOME	3.62
3	WP_CYTOPLASMIC_RIBOSOMAL_PROTEINS	3.58
3	GOMF_STRUCTURAL_CONSTITUENT_OF_RIBOSOME	3.56
3	GOCC_RIBOSOMAL_SUBUNIT	3.47
3	GOCC_RIBOSOME	3.45
3	GOMF_STRUCTURAL_MOLECULE_ACTIVITY	3.44
3	REACTOME_FORMATION_OF_A_POOL_OF_FREE_40S_SUBUNITS	3.44
3	REACTOME_NONSENSE_MEDIATED_DECAY_NMD_INDEPENDENT_OF_THE_EXON_JUNCTION_COMPLEX_EJC	3.39
3	REACTOME_SRP_DEPENDENT_COTRANSLATIONAL_PROTEIN_TARGETING_TO_MEMBRANE	3.38
3	REACTOME_MAJOR_PATHWAY_OF_RRNA_PROCESSING_IN_THE_NUCLEOLUS_AND_CYTOSOL	3.38
3	REACTOME_EUKARYOTIC_TRANSLATION_INITIATION	3.37
3	GOBP_CYTOPLASMIC_TRANSLATION	3.31
3	REACTOME_TRANSLATION	3.31
3	GOCC_CYTOSOLIC_LARGE_RIBOSOMAL_SUBUNIT	3.3
3	REACTOME_NONSENSE_MEDIATED_DECAY_NMD	3.28
3	GOCC_LARGE_RIBOSOMAL_SUBUNIT	3.26
3	BILANGES_SERUM_AND_RAPAMYCIN_SENSITIVE_GENES	3.01
3	GOCC_CYTOSOLIC_SMALL_RIBOSOMAL_SUBUNIT	2.83

(Continued)

10.3389/fimmu.2024.1347453

TABLE 8 Continued

CL	pathway	NES
3	GOCC_POLYSOMAL_RIBOSOME	2.82
3	GOCC_SMALL_RIBOSOMAL_SUBUNIT	2.81
4	GROSS_HYPOXIA_VIA_ELK3_DN	2.82
4	RASHI_RESPONSE_TO_IONIZING_RADIATION_2	2.66
4	TABULA_MURIS_SENIS_MARROW_GRANULOCYTOPOIETIC_CELL_AGEING	2.64
4	LIAN_LIPA_TARGETS_6M	2.59
4	LIAN_LIPA_TARGETS_3M	2.58
4	TABULA_MURIS_SENIS_PANCREAS_PANCREATIC_BETA_CELL_AGEING	2.57
4	HALLMARK_TNFA_SIGNALING_VIA_NFKB	2.56
4	GERY_CEBP_TARGETS	2.55
4	HESS_TARGETS_OF_HOXA9_AND_MEIS1_DN	2.52
4	TABULA_MURIS_SENIS_SPLEEN_MACROPHAGE_AGEING	2.51
4	GOBP_INFLAMMATORY_RESPONSE	2.5
4	GOBP_RESPONSE_TO_MOLECULE_OF_BACTERIAL_ORIGIN	2.49
4	TABULA_MURIS_SENIS_MAMMARY_GLAND_BASAL_CELL_AGEING	2.49
4	GALINDO_IMMUNE_RESPONSE_TO_ENTEROTOXIN	2.49
4	TABULA_MURIS_SENIS_SUBCUTANEOUS_ADIPOSE_TISSUE_MYELOID_CELL_AGEING	2.48
4	SEKI_INFLAMMATORY_RESPONSE_LPS_UP	2.48
4	CHYLA_CBFA2T3_TARGETS_DN	2.47
4	MIR_467A_3P	2.47
4	MIR_669B_3P	2.45
4	MIR_669F_3P	2.45
5	HOFFMANN_SMALL_PRE_BII_TO_IMMATURE_B_LYMPHOCYTE_UP	3.02
5	GOBP_B_CELL_ACTIVATION	3
5	GOBP_B_CELL_RECEPTOR_SIGNALING_PATHWAY	2.98
5	GOBP_B_CELL_MEDIATED_IMMUNITY	2.96
5	MORI_MATURE_B_LYMPHOCYTE_UP	2.92
5	MORI_LARGE_PRE_BII_LYMPHOCYTE_DN	2.92
5	GOBP_B_CELL_DIFFERENTIATION	2.91
5	YU_MYC_TARGETS_DN	2.89
5	GOBP_REGULATION_OF_B_CELL_ACTIVATION	2.89
5	TABULA_MURIS_SENIS_KIDNEY_FENESTRATED_CELL_AGEING	2.89
5	TABULA_MURIS_SENIS_LUNG_NON_CLASSICAL_MONOCYTE_AGEING	2.87
5	GOBP_REGULATION_OF_B_CELL_PROLIFERATION	2.86
5	GOBP_B_CELL_PROLIFERATION	2.84
5	MORI_IMMATURE_B_LYMPHOCYTE_UP	2.77
5	GOBP_ANTIGEN_PROCESSING_AND_PRESENTATION_OF_EXOGENOUS_ANTIGEN	2.76
5	GOBP_ANTIGEN_PROCESSING_AND_PRESENTATION_OF_PEPTIDE_ANTIGEN	2.76
5	GOBP_ANTIGEN_PROCESSING_AND_PRESENTATION	2.76

(Continued)

TABLE 8 Continued

CL	pathway	NES
5	GOBP_ANTIGEN_PROCESSING_AND_PRESENTATION_OF_EXOGENOUS_PEPTIDE_ANTIGEN	2.75
5	GOBP_ANTIGEN_PROCESSING_AND_PRESENTATION_OF_PEPTIDE_OR_POLYSACCHARIDE_ANTIGEN_VIA_MHC_CLASS_II	2.73
5	TABULA_MURIS_SENIS_THYMUS_PROFESSIONAL_ANTIGEN_PRESENTING_CELL_AGEING	2.72

CL, cluster; NES, normalized enrichment score.

subsets play any roles in other disease conditions. In fact, M1/M2 macrophages, which were initially studied extensively in oncology (30), are now known to contribute to sepsis and other disorders as well (31). The subsets in the present study were statistically defined in an unbiased way based on their gene expressions. Nevertheless, it is important to validate their significance in a focused approach. Isolation of specific subsets by cell sorting and studying them *in vitro* or adoptively transferring them *in vivo* would certify their impacts on the diseases more directly and strongly.

All major cell populations we analyzed here contained at least one subset possessing cellular aging properties. Cellular aging is regulated by metabolic and epigenetic changes and has a close relation with cell death mechanisms, both of which can be reflected by transcriptomics (32). We have previously shown that aged neutrophils significantly contributed to the development of sepsis. eCIRP, the major DAMP in sepsis, inhibited neutrophil apoptosis to induce aged neutrophils (10). Neutrophils possessing both aged and antigen-presenting properties induced Th1 differentiation to aggravate acute lung injury and worsen survival in sepsis (9). Moreover, this novel neutrophil subset was also identified in septic patients (9). In addition to neutrophils, however, cellular aging has not been studied extensively in most of other immune cell types such as macrophages and lymphocytes especially in sepsis. Our study implies the need for investigating cellular aging in different populations to better understand sepsis pathophysiology. Cellular aging can occur in response to cellular stress or damage irrespective of animals' age (9, 10). Mice used in our study were in the same age for each group; thus, the difference in cellular aging status was unlikely to be due to the age of the animals. Nevertheless, it would be worth investigating whether cellular aging can be influenced by the age of the animals during sepsis in the future studies. It is also meaningful to evaluate the molecules and pathways related to cell death simultaneously to grasp the mechanisms of cellular aging from a wider perspective. Our previous studies revealed several novel subtypes of neutrophils, including APANs, nectin-2, and serpin B2 neutrophils, which were found to be upregulated during sepsis (9, 10, 33). However, our latest scRNA-seq data could not distinctly demonstrate these specific neutrophil subtypes. This discrepancy might be attributed to the limited resolution in the clustering process and the relatively low occurrence of these cell types in our current dataset.

Each cell population also contained subpopulations expressing the genes related to ribosomes, the organelles that facilitate protein synthesis from mRNA (34). Ribosomes are composed of ribosomal RNA, such as 18S (35), and ribosomal proteins (RP), such as RPSA, RPL13, and RPS24 (36). The roles of ribosomes are better known in viral rather than bacterial infection since host ribosomes are crucial for the expression of viral proteins (37). Our data suggest that ribosomes could be an interesting focus to be investigated in bacterial sepsis too. Ribosomal activities may be enhanced in sepsis with the demand for producing inflammatory molecules against infection or compensating lost proteins due to cellular damage. This system needs to be tightly regulated to avoid aberrant immune responses, which can cause tissue injury. It would also be of significance to combine the transcriptomics with proteomics to evaluate ribosomal activities since mRNA is translated to proteins by ribosomes (34).

To induce sepsis, we subjected mice to CLP, which is arguably the most-used animal model of sepsis. CLP depicts intraabdominal polymicrobial sepsis, a severe pathological condition with an extremely poor prognosis (38). Nevertheless, it has to be carefully considered when interpreting preclinical findings of sepsis and applying it in patients since sepsis is a heterogenetic disorder that can be caused in different ways. In addition to the polymicrobial model of sepsis, studying *E. coli* or endotoxemia or in some sterile injury model of sepsis can be informative to compare and contrast the gene expression profile among various model systems and conclude which model may mimic more closely with human sepsis in terms of transcriptional landscape (38). In this study, we analyzed samples from two compartments, peritoneal cavity and spleen. Since sepsis is accompanied by injury in multiple organs, including, but not limited to, lungs, liver, kidneys, and central nervous system (1), it would be of interest to further analyze our data along with the transcriptome of those different organs.

We studied the transcriptomic profile of immune cells in sepsis using the samples collected at 20 h after CLP. This specific time point was selected based on our extensive research in this area (5, 9, 13, 39). At that time point of CLP-induced sepsis, we have observed significant immune responses characterized by changes in leukocyte count, increased activation of immune cells, increased release of pro-inflammatory cytokines, and the elevation of organ injury markers in blood (5, 9, 13, 39). Conducting analyses at various time points is crucial; however, it often yields complex datasets that can be challenging to analyze comprehensively and conclusively correlate. Our data offer a valuable foundation for generating hypotheses and further exploration. Further studies on the dynamics of specific genes/pathways of interest as selected from our scRNA-seq data could enhance our understanding of disease severity. This approach would enable the correlation of gene expression profiles with systemic inflammation and organ function, thereby providing a more comprehensive understanding of the intricate dynamics underlying sepsis progression.

We acknowledge the limitations of our study. First, we collected the samples only at one time point as aforementioned; therefore, some of the cell populations were barely found in certain samples. This could also be the reason why some prominent pathways that are well known

to be activated in sepsis, such as NLRP3 inflammasome pathway (40), were not significantly altered in our data. Additional evaluation at earlier and later time points would precisely depict the kinetics of the cell frequency and phenotype. Second, only observational data were included in the present study and the interventional studies were not conducted on the genes or cells we mentioned here. Knockdown or specific depletion of those genes or cells would firmly demonstrate the significance of our findings. Third, our paper does not contain human data. Recently, more and more scRNA-seq data have been available in the public database (41). Nevertheless, in addition to blood samples, it is still challenging to obtain patient samples from closed compartments or organs, such as peritoneal cavity or spleen, especially during sepsis. Incorporating patient data from these regions would contribute valuable insights and enhance the clinical relevance of animal studies.

In summary, we have comprehensively evaluated the distribution, phenotype, and subsets of immune cells under normal and septic conditions by implementing scRNA-seq. The frequency and characteristics of cells altered dramatically after sepsis in different compartments, and each cell population consisted of distinct subtypes. We have identified novel areas within sepsis that remain largely unexplored, notably encompassing cell aging across diverse cell types and ribosomal activities. These less traveled scientific areas present an enticing opportunity for future investigations. To further substantiate our current findings, there is a need for more targeted interventional studies concentrating on specific molecules and cells. The eagerly anticipated results from such studies will add rigor to and validate our present discoveries.

Data availability statement

The datasets presented in this study can be found in online repositories. The names of the repository/repositories and accession number(s) can be found below: GSE249975 (GEO).

Ethics statement

The animal study was approved by Feinstein Institutes for Medical Research. The study was conducted in accordance with the local legislation and institutional requirements.

Author contributions

AM: Conceptualization, Data curation, Formal Analysis, Investigation, Methodology, Software, Validation, Visualization, Writing – original draft, Writing – review & editing. AJ: Conceptualization, Formal Analysis, Investigation, Methodology, Software, Writing – review & editing. MA: Conceptualization, Formal Analysis, Funding acquisition, Investigation, Methodology, Project administration, Resources, Supervision, Validation, Visualization, Writing – original draft, Writing – review & editing. PW: Conceptualization, Formal Analysis, Funding acquisition, Project administration, Resources, Supervision, Writing – review & editing.

Funding

The author(s) declare financial support was received for the research, authorship, and/or publication of this article. MA is supported by the National Institutes of Health (NIH) grants R01GM129633 and PW is supported by NIH grants R35GM118337 and U01AI170018.

Acknowledgments

We acknowledge Robert Adelson for helping with the scRNA-seq data analysis.

Conflict of interest

The authors declare that the research was conducted in the absence of any commercial or financial relationships that could be construed as a potential conflict of interest.

Publisher's note

Supplementary material

The Supplementary Material for this article can be found online at: https://www.frontiersin.org/articles/10.3389/fimmu.2024.1347453/full#supplementary-material

References

1. Singer M, Deutschman CS, Seymour CW, Shankar-Hari M, Annane D, Bauer M, et al. The third international consensus definitions for sepsis and septic shock (Sepsis-3). *JAMA* (2016) 315(8):801–10. doi: 10.1001/jama.2016.0287.

2. Rudd KE, Johnson SC, Agesa KM, Shackelford KA, Tsoi D, Kievlan DR, et al. Global, regional, and national sepsis incidence and mortality, 1990-2017: analysis for the Global Burden of Disease Study. *Lancet* (2020) 395(10219):200–1110.1016/S0140-6736(19)32989-7.

3. Denning NL, Aziz M, Gurien SD, Wang P. DAMPs and NETs in sepsis. *Front Immunol* (2019) 10:2536. doi: 10.3389/fimmu.2019.02536

4. Aziz M, Brenner M, Wang P. (eCIRP) and inflammation. *J Leukoc Biol* (2019) 106 (1):133–46. doi: 10.1002/JLB.3MIR1118-443R

5. Qiang X, Yang WL, Wu R, Zhou M, Jacob A, Dong W, et al. Cold-inducible RNA-binding protein (CIRP) triggers inflammatory responses in hemorrhagic shock and sepsis. *Nat Med* (2013) 19(11):1489–95. doi: 10.1038/nm.3368

6. Nofi CP, Wang P, Aziz M. Chromatin-associated molecular patterns (CAMPs) in sepsis. *Cell Death Dis* (2022) 13(8):700. doi: 10.1038/s41419-022-05155-3

7. van der Poll T, Shankar-Hari M, Wiersinga WJ. . *Immunity* (2021) 54(11):2450–64. doi: 10.1016/j.immuni.2021.10.012

8. Fang P, Li X, Dai J, Cole L, Camacho JA, Zhang Y, et al. Immune cell subset differentiation and tissue inflammation. *J Hematol Oncol* (2018) 11(1):97. doi: 10.1186/s13045-018-0637-x

9. Jin H, Aziz M, Murao A, Kobritz M, Shih AJ, Adelson RP, et al. Antigen-presenting aged neutrophils induce CD4+ T cells to exacerbate inflammation in sepsis. *J Clin Invest* (2023) 133(14):e164585. doi: 10.1172/JCI164585

10. Shimizu J, Murao A, Aziz M, Wang P. Extracellular CIRP inhibits neutrophil apoptosis to promote its aging by upregulating SerpinB2 in sepsis. *Shock* (2023) 60 (3):450–60. doi: 10.1097/SHK.0000000000002187

11. Vono M, Lin A, Norrby-Teglund A, Koup RA, Liang F, Loré K. Neutrophils acquire the capacity for antigen presentation to memory CD4. *Blood* (2017) 129 (14):1991–2001. doi: 10.1182/blood-2016-10-744441

12. Murao A, Arif A, Brenner M, Denning NL, Jin H, Takizawa S, et al. Extracellular CIRP and TREM-1 axis promotes ICAM-1-Rho-mediated NETosis in sepsis. *FASEB J* (2020) 34(7):9771–86. doi: 10.1096/fj.202000482R

13. Takizawa S, Murao A, Ochani M, Aziz M, Wang P. Frontline Science: Extracellular CIRP generates a proinflammatory Ly6G. *J Leukoc Biol* (2021) 109 (6):1019–32. doi: 10.1002/JLB.3HI0620-416R

14. Sun P, Cui M, Jing J, Kong F, Wang S, Tang L, et al. Deciphering the molecular and cellular atlas of immune cells in septic patients with different bacterial infections. *J Transl Med* (2023) 21(1):777. doi: 10.1186/s12967-023-04631-4

15. Giridharan VV, Generoso JS, Lence L, Candiotto G, Streck E, Petronilho F, et al. A crosstalk between gut and brain in sepsis-induced cognitive decline. *J Neuroinflammation.* (2022) 19(1):114. doi: 10.1186/s12974-022-02472-4

16. Sun J, Zhang J, Wang X, Ji F, Ronco C, Tian J, et al. Gut-liver crosstalk in sepsis-induced liver injury. *Crit Care* (2020) 24(1):614. doi: 10.1186/s13054-020-03327-1

17. Papalexi E, Satija R. Single-cell RNA sequencing to explore immune cell heterogeneity. *Nat Rev Immunol* (2018) 18(1):35–45. doi: 10.1038/nri.2017.76

18. Wang F, Chen M, Ma J, Wang C, Wang J, Xia H, et al. Integrating bulk and single-cell sequencing reveals the phenotype-associated cell subpopulations in sepsis-induced acute lung injury. *Front Immunol* (2022) 13:981784. doi: 10.3389/fimmu.2022.981784

19. Viasus D, Nonell L, Restrepo C, Figueroa F, Donado-Mazarrón C, Carratalà J. A systematic review of gene expression studies in critically ill patients with sepsis and community-acquired pneumonia. *Biomedicines* (2023) 11(10):2755. doi: 10.3390/biomedicines11102755

20. Xu X, Hua X, Mo H, Hu S, Song J. Single-cell RNA sequencing to identify cellular heterogeneity and targets in cardiovascular diseases: from bench to bedside. *Basic Res Cardiol* (2023) 118(1):7. doi: 10.1007/s00395-022-00972-1

21. Davis-Marcisak EF, Deshpande A, Stein-O'Brien GL, Ho WJ, Laheru D, Jaffee EM, et al. From bench to bedside: Single-cell analysis for cancer immunotherapy. *Cancer Cell* (2021) 39(8):1062–80. doi: 10.1016/j.ccell.2021.07.004

22. Qi X, Yu Y, Sun R, Huang J, Liu L, Yang Y, et al. Identification and characterization of neutrophil heterogeneity in sepsis. *Crit Care* (2021) 25(1):50. doi: 10.1186/s13054-021-03481-0

23. Hafemeister C, Satija R. Normalization and variance stabilization of single-cell RNA-seq data using regularized negative binomial regression. *Genome Biol* (2019) 20 (1):296. doi: 10.1186/s13059-019-1874-1

24. Korsunsky I, Millard N, Fan J, Slowikowski K, Zhang F, Wei K, et al. Fast, sensitive and accurate integration of single-cell data with Harmony. *Nat Methods* (2019) 16(12):1289–96. doi: 10.1038/s41592-019-0619-0

25. Hao Y, Hao S, Andersen-Nissen E, Mauck WM, Zheng S, Butler A, et al. Integrated analysis of multimodal single-cell data. *Cell* (2021) 184(13):3573–87.e29. doi: 10.1016/j.cell.2021.04.048

26. Soneson C, Robinson MD. Bias, robustness and scalability in single-cell differential expression analysis. *Nat Methods* (2018) 15(4):255–61. doi: 10.1038/nmeth.4612

27. Luo Y, Wang J, Li K, Li M, Xu S, Liu X, et al. Single-cell genomics identifies distinct B1 cell developmental pathways and reveals aging-related changes in the B-cell receptor repertoire. *Cell Biosci* (2022) 12(1):57. doi: 10.1186/s13578-022-00795-6

28. Mira JC, Gentile LF, Mathias BJ, Efron PA, Brakenridge SC, Mohr AM, et al. Sepsis pathophysiology, chronic critical illness, and persistent inflammation-immunosuppression and catabolism syndrome. *Crit Care Med* (2017) 45(2):253–62. doi: 10.1097/CCM.0000000000002074

29. Cavaillon JM, Singer M, Skirecki T. Sepsis therapies: learning from 30 years of failure of translational research to propose new leads. *EMBO Mol Med* (2020) 12(4): e10128. doi: 10.15252/emmm.201810128

30. Pan Y, Yu Y, Wang X, Zhang T. Tumor-associated macrophages in tumor immunity. *Front Immunol* (2020) 11:583084. doi: 10.3389/fimmu.2020.583084

31. Wang Z. The role of macrophages polarization in sepsis-induced acute lung injury. *Front Immunol* (2023) 14:1209438. doi: 10.3389/fimmu.2023.1209438

32. Ren R, Ocampo A, Liu GH, Izpisua Belmonte JC. Regulation of stem cell aging by metabolism and epigenetics. *Cell Metab* (2017) 26(3):460–74. doi: 10.1016/j.cmet.2017.07.019

33. Murata K, Murao A, Aziz M, Wang P. Extracellular CIRP induces novel nectin-2 + (CD112+) neutrophils to promote th1 differentiation in sepsis. *J Immunol* (2023) 210 (3):310–21. doi: 10.4049/jimmunol.2200308

34. Sonneveld S, Verhagen BMP, Tanenbaum ME. Heterogeneity in mRNA translation. *Trends Cell Biol* (2020) 30(8):606–18. doi: 10.1016/j.tcb.2020.04.008

35. Martin F, Ménétret JF, Simonetti A, Myasnikov AG, Vicens Q, Prongidi-Fix L, et al. Ribosomal 18S rRNA base pairs with mRNA during eukaryotic translation initiation. *Nat Commun* (2016) 7:12622. doi: 10.1038/ncomms12622

36. Wei J, Kishton RJ, Angel M, Conn CS, Dalla-Venezia N, Marcel V, et al. Ribosomal proteins regulate MHC class I peptide generation for immunosurveillance. *Mol Cell* (2019) 73(6):1162–73.e5. doi: 10.1016/j.molcel.2018.12.020

37. Miller CM, Selvam S, Fuchs G. Fatal attraction: The roles of ribosomal proteins in the viral life cycle. *Wiley Interdiscip Rev RNA.* (2021) 12(2):e1613. doi: 10.1002/wrna.1613

38. Assinger A, Schrottmaier WC, Salzmann M, Rayes J. Platelets in sepsis: an update on experimental models and clinical data. *Front Immunol* (2019) 10:1687. doi: 10.3389/fimmu.2019.01687

39. Murao A, Jha A, Ma G, Chaung W, Aziz M, Wang P. A synthetic poly(A) tail targeting extracellular CIRP inhibits sepsis. *J Immunol* (2023) 211(7):1144–53. doi: 10.4049/jimmunol.2300228

40. Biasizzo M, Kopitar-Jerala N. Interplay between NLRP3 inflammasome and autophagy. *Front Immunol* (2020) 11:591803. doi: 10.3389/fimmu.2020.591803

41. Van de Sande B, Lee JS, Mutasa-Gottgens E, Naughton B, Bacon W, Manning J, et al. Applications of single-cell RNA sequencing in drug discovery and development. *Nat Rev Drug Discovery* (2023) 22(6):496–520. doi: 10.1038/s41573-023-00688-4

frontiers | Frontiers in Immunology

TYPE Original Research
PUBLISHED 14 March 2024
DOI 10.3389/fimmu.2024.1368448

OPEN ACCESS

EDITED BY
Christoph Thiemermann,
Queen Mary University of London,
United Kingdom

REVIEWED BY
Jianmin Chen,
Queen Mary University of London,
United Kingdom
Marcin Filip Osuchowski,
Ludwig Boltzmann Institute for Experimental and Clinical Traumatology, Austria

*CORRESPONDENCE
Haichao Wang
hwang@northwell.edu

†These authors have contributed equally to this work

RECEIVED 10 January 2024
ACCEPTED 04 March 2024
PUBLISHED 14 March 2024

CITATION
Qiang X, Chen W, Zhu CS, Li J, Qi T, Lou L, Wang P, Tracey KJ and Wang H (2024) Therapeutic potential of procathepsin L-inhibiting and progesterone-entrapping dimethyl-β-cyclodextrin nanoparticles in treating experimental sepsis.
Front. Immunol. 15:1368448.
doi: 10.3389/fimmu.2024.1368448

Therapeutic potential of procathepsin L-inhibiting and progesterone-entrapping dimethyl-β-cyclodextrin nanoparticles in treating experimental sepsis

Xiaoling Qiang[1,2†], Weiqiang Chen[1,2†], Cassie Shu Zhu[1,2†], Jianhua Li[1], Timothy Qi[1], Li Lou[1], Ping Wang[1,2], Kevin J. Tracey[1,2] and Haichao Wang[1,2*]

[1]The Feinstein Institutes for Medical Research, Northwell Health, Manhasset, NY, United States, [2]Donald and Barbara Zucker School of Medicine at Hofstra/Northwell, Hempstead, NY, United States

The pathogenic mechanisms of bacterial infections and resultant sepsis are partly attributed to dysregulated inflammatory responses sustained by some late-acting mediators including the procathepsin-L (pCTS-L). It was entirely unknown whether any compounds of the U.S. Drug Collection could suppress pCTS-L-induced inflammation, and pharmacologically be exploited into possible therapies. Here, we demonstrated that a macrophage cell-based screening of a U.S. Drug Collection of 1360 compounds resulted in the identification of progesterone (PRO) as an inhibitor of pCTS-L-mediated production of several chemokines [e.g., Epithelial Neutrophil-Activating Peptide (ENA-78), Monocyte Chemoattractant Protein-1 (MCP-1) or MCP-3] and cytokines [e.g., Interleukin-10 (IL-10) or Tumor Necrosis Factor (TNF)] in primary human peripheral blood mononuclear cells (PBMCs). *In vivo*, these PRO-entrapping 2,6-dimethal-β-cyclodextrin (DM-β-CD) nanoparticles (containing 1.35 mg/kg PRO and 14.65 mg/kg DM-β-CD) significantly increased animal survival in both male (from 30% to 70%, n = 20, $P = 0.041$) and female (from 50% to 80%, n = 30, $P = 0.026$) mice even when they were initially administered at 24 h post the onset of sepsis. This protective effect was associated with a reduction of sepsis-triggered accumulation of three surrogate biomarkers [e.g., Granulocyte Colony Stimulating Factor (G-CSF) by 40%; Macrophage Inflammatory Protein-2 (MIP-2) by 45%; and Soluble Tumor Necrosis Factor Receptor I (sTNFRI) by 80%]. Surface Plasmon Resonance (SPR) analysis revealed a strong interaction between PRO and pCTS-L ($K_D = 78.2 \pm 33.7$ nM), which was paralleled with a positive correlation between serum PRO concentration and serum pCTS-L level ($\rho = 0.56$, $P = 0.0009$) or disease severity (Sequential Organ Failure Assessment, SOFA; $\rho = 0.64$, $P = 0.0001$) score in septic patients. Our observations support a promising opportunity to explore DM-β-CD nanoparticles entrapping lipophilic drugs as possible therapies for clinical sepsis.

KEYWORDS

innate immune cells, procathepsin-L, progesterone, 2,6-dimethyl-β-cyclodextrin, sepsis

Introduction

Bacterial infections and associated sepsis are probably the most prominent causes of death in hospitals, accounting for almost 20% of total deaths globally (1). Its pathogenic mechanisms partially attribute to dysregulated inflammatory responses to microbial infections that are initiated by early cytokines [e.g., interleukin-1 (IL-1) and tumor necrosis factor (TNF)] but sustained by late-acting mediators including high mobility group box 1 (HMGB1) (2, 3) and procathepsin-L (pCTS-L) (4, 5). For example, upon initial innate recognition of many "pathogen-associated molecular patterns molecules" (PAMPs, e.g., bacterial lipopolysaccharide, LPS) by corresponding pattern recognition receptors (PRRs) such as the toll-like receptor 4 (TLR4) (6), monocytes and macrophages sequentially produce "early" cytokines [e.g., TNF and interleukin-1β (IL-1β)] (7–9), toxic chemicals (e.g., lactate) (10–12), and late-acting mediators such as HMGB1 (2) and pCTS-L (4). In comparison with early cytokines, these late-acting mediators can be therapeutically targeted in delayed regimens (4, 13), thereby offering relatively wider therapeutic windows (5). It is therefore necessary to find small molecule drugs capable of suppressing pCTS-L-mediated dysregulated inflammation to develop potential therapeutic strategies for inflammatory diseases.

The US Drug Collection contains 1360 FDA-approved small molecule drugs that have reached clinical trials as evidenced by their assignment of the United States Adopted Names (USAN) and inclusion in the United States Pharmacopeia (USP) Dictionary, the authorized list of established names for drugs in the United States. These small molecule drugs can interact with specific protein targets in the body to confer a therapeutic effect, but possess distinct advantages such as oral administration convenience, target specificity, cell penetration, and cost-effectiveness. They serve as a basis for high throughput screening of established drugs for potential new activities (14). In this study, we developed a 96-well-based assay to screen for small molecule drugs that could suppress the pCTS-L-mediated dysregulated inflammation and confer protection against experimental sepsis. Here, we presented substantial evidence to suggest: i) a hormone, progesterone (PRO), as an inhibitor of pCTS-L-mediated dysregulated inflammation; and ii) a PRO-entrapping 2,6-dimethyl-β-cyclodextrin (DM-β-CD) nanoparticles as a potential therapy in a preclinical setting.

Materials and methods

Materials

Murine macrophage RAW 264.7 cell line was purchased from the American Type Culture Collection (ATCC). Human blood samples were obtained from the New York Blood Center (Long Island City, NY, USA) to harvest primary human peripheral blood mononuclear cells (PBMCs) by density gradient centrifugation as previously described (4, 15, 16). Both macrophage cultures and PBMCs were routinely incubated in DMEM media containing 1% streptomycin/penicillin and 10% fecal bovine serum or 10% human serum. When cell densities reached 80-90% confluence, adherent macrophages or PBMCs were stimulated with bacterial endotoxins (lipopolysaccharides, LPS, *E. coli* 0111:B4, #L4130, Sigma-Aldrich) or recombinant human or murine pCTS-L protein in the absence or in the presence of each of the 1360 compounds in the U.S. Collection of Drug (10 mM in DMSO), as well as progesterone (Cat. # P0130, Sigma-Aldrich) solubilized in ethanol (5 mg/ml) or entrapped into 2,6-dimethyl-β-cyclodextrin (DM-β-CD, Cat. #H0513, Sigma-Aldrich) nanoparticles. The progesterone-carrying DM-β-CD nanoparticles (containing 84.4 mg progesterone per 1000 mg of the PRO/DM-β-CD complex) were also purchased from Sigma-Aldrich (Cat. # P7556). The extracellular levels of various cytokines and chemokines were respectively measured by using ELISA kits or Cytokine Antibody Arrays as previously described (4, 15, 16).

Generation and purification of recombinant murine and human pCTS-L proteins

Recombinant murine and human pCTS-L proteins containing an N-terminal 6×Histidine tag were respectively expressed in *E. coli* BL21 (DE3) pLysS cells and purified to homogeneity as previously described (4, 16). Briefly, upon sonication to disrupt the bacterial cell wall, the inclusion bodies containing pCTS-L proteins were harvested via differential centrifugation technique following sequential washings in 1% Triton X-100 dissolved in 1 × PBS buffer The purified inclusion bodies were subsequently dissolved in high concentration of urea solution (8.0 M), and then refolded by dialysis in Tris buffer (10 mM, pH 8.0). Afterward, recombinant pCTS-L proteins were purified by histidine-affinity chromatography technique and Triton X-114 extractions. The endotoxin content of recombinant pCTS-L proteins was estimated to be < 0.01 U per μg of pCTS-L protein.

High-throughput screening of U.S. collection of drugs for pCTS-L inhibitors

We obtained the U.S. Collection of 1360 drugs (Supplementary Table 1, 10 mM in DMSO) from the MicroSource Discovery System Inc., and used this chemical library to search for potential pCTS-L inhibitors as previously described (16). Briefly, murine macrophage-like RAW 264.7 cells were challenged with murine pCTS-L protein in the absence or in the presence of each drug at several concentrations for 16 h, and levels of TNF in macrophage-conditioned medium was measured using specific TNF DuoSet ELISA kit (Cat# DY410, R&D Systems).

Murine or Human Cytokine Antibody Arrays

Murine Cytokine Antibody Array Kits (Cat.# AAM-CYT-3-8, RayBiotech Inc., Norcross, GA, USA) were employed to measure the relative levels of 62 cytokines/chemokines in macrophage cell culture-conditioned medium or murine serum as previously

described (4, 15, 16). Similarly, human Cytokine Antibody C3 Array Kits (Cat.# AAH-CYT-3-8) were employed to measure the relative levels of 42 cytokines/chemokines in human PBMC-conditioned culture medium as previously described (4, 15, 16).

Animal model of experimental sepsis

Adult male and female Balb/C mice (7-8 weeks old, 20-25 g body weight) were purchased from Charles River Laboratories (Wilmington, MA), housed in a temperature-controlled room on a 12-h light-dark cycle, and acclimated for at least 5-7 days before usage. Every attempt was made to limit the number of animals used in the present study as per the ARRIVE guidelines for reducing the number of animals in scientific research developed by the British National Centre for the Replacement, Refinement and Reduction of Animals in Research (NC3Rs). Additionally, all experiments were performed in accordance with the International Expert Consensus Initiative for Improvement of Animal Modeling in Sepsis - Minimum Quality Threshold in Pre-Clinical Sepsis Studies (MQTiPSS) (17), which includes practices such as randomization of animals in each experimental group, delayed therapeutic interventions with therapeutic agents (e.g., PRO-entrapping DM-β-CD nanoparticles) (18), establishment of specific criteria for euthanasia of moribund septic animals (e.g., labored breathing, minimized response to human touch, and immobility), as well as the administration of fluid resuscitation and antibiotics (19). This study was administratively approved by the IACUC of the Feinstein Institutes for Medical Research (FIMR, Protocol # 2017-003 Term II; Date of Approval, April 28th, 2020).

Adult male or female Balb/C mice aged 7-8 weeks and weighing 20-25 g underwent a surgical procedure referred to as "cecal ligation and puncture" (CLP) to induce experimental sepsis as previously outlined (4, 15, 16). Briefly, the cecum of Balb/C mice was surgically exposed, ligated approximately 5.0 mm from the cecal tip, and punctured once with a 22-gauge syringe needle. Prior to CLP surgery, all experimental animals received a buprenorphine injection (0.05 mg/kg, s.c.) to alleviate immediate surgical pain, because repetitive use of buprenorphine in the CLP model could paradoxically elevate sepsis surrogate markers and animal lethality (20, 21), leading to unnecessary use of more animals per experimental group. Additionally, a small dose of bupivacaine and lidocaine was locally injected around the incision site immediately after CLP surgery. Approximately 30 min post CLP surgery, all experimental animals were subcutaneously injected with imipenem/cilastatin (0.5 mg/mouse) (Primaxin, Merck & Co., Inc.), followed by resuscitation with sterile saline solution (20 ml/kg). Septic animals were only given a single dose of antibiotics before pharmacological administration of PRO-entrapping DM-β-CD nanoparticles at 24 h post CLP, worrying that subsequent antibiotics treatment may adversely affect the therapeutic efficacy of PRO-entrapping DM-β-CD nanoparticles. Before treatment, animals were randomly assigned to control vehicle and experimental groups, and PRO dissolved in sesame oil (Cat. #S3547, Sigma-Aldrich; 2.0 mg/ml) or water after complexation with DM-β-CD to form nanoparticles (containing 84.4 mg PRO per 1000 mg of PRO/DM-β-CD complex) was intraperitoneally injected to septic mice at various time points post CLP surgery. Animal survival was observed for two weeks to ensure no late death occurred. To elucidate the potential protective mechanisms of PRO-entrapping DM-β-CD nanoparticles, a separate group of Balb/C mice were subjected to CLP, and DM-β-CD vehicle (14.65 mg/kg) or PRO-entrapping DM-β-CD nanoparticles (containing 1.35 mg/kg PRO and 14.65 mg/kg DM-β-CD) were administered at 2 h and 20 h post CLP. At 24 h post CLP, animals were euthanized to collect blood and measure serum levels of various cytokines and chemokines using murine Cytokine Antibody Arrays or markers of tissue injury using specific colorimetric enzymatic assays.

Measurement of tissue injury markers

Blood samples were harvested at 24 h post CLP following intraperitoneal administrations of DM-β-CD vehicle (14.65 mg/kg) or PRO-entrapping DM-β-CD nanoparticles (containing 1.35 mg/kg PRO and 14.65 mg/kg DM-β-CD) at 2 h and 20 h post CLP, and centrifuged at 3000 x g for 10 min to collect serum. Serum levels of liver injury markers such as aspartate aminotransferase (AST, Cat. No. 7561), and lactate dehydrogenase (LDH, Cat. No. 7572) were determined using specific colorimetric enzymatic assays (Pointe Scientific, Canton, MI) according to manufacturer's instructions as previously described (15).

Open Surface Plasmon Resonance (SPR)

We employed the Nicoya Lifesciences' gold-nanoparticle-based Open Surface Plasmon Resonance (OpenSPR) technology (Kitchener, ON, Canada) to characterize protein-drug interaction following the manufacturer's instructions. Briefly, recombinant pCTS-L was immobilized on NTA sensor chip (Cat. # SEN-Au-100-10-NTA) as previously described (4, 22), and DMSO solution of PRO was applied as an analyte at different concentrations. The sensorgrams of the dynamic ligand-analyte interaction were recorded over time to estimate the equilibrium dissociation constant (K_D) (Nicoya Lifesciences).

Systemic accumulation of PRO and pCTS-L in septic patients

This study was administratively approved by the institutional review board (IRB) of the FIMR (IRB protocol #18-0184) and consented by all patients participants who were diagnosed with sepsis or septic shock based on the Sepsis-3 criteria (23). Small volume of blood samples (5.0 ml) was obtained from eleven septic patients recruited to the Long Island Jewish Medical Center or North Shore University Hospital between 2018-2019 at three time points: Time 0 (within 24 h of the initial diagnosis); Time 24 h (24 h post the initial diagnosis); and Time 72 h (72 h post the initial diagnosis). The demographics of these eleven septic patients have been reported previously (4), but briefly described in the

Supplementary Table 2. These clinical samples were assayed for pCTS-L levels using human pCTS-L ELISA kit (Cat.# MBS7254442, MyBioSource.com) with reference to standard cure generated from using recombinant human pCTS-L. In parallel, the serum concentrations of progesterone were measured by using highly sensitive ELISA kit (Cat. # ADI-901-011, ENZO Life Sciences, Inc., Farmingdale, NY, USA).

Statistical analysis

All data were initially evaluated for normality by the Shapiro-Wilk test before conducting appropriate statistical tests. The Student's t test was used to compare two independent experimental groups. For comparison among multiple groups with non-normal (skewed) distribution (as assessed by the Shapiro-Wilk test), the statistical difference was evaluated with the non-parametric Kruskal-Wallis ANOVA test followed by the Dunn's test. The Kaplan-Meier method was employed to compare the differences in mortality rates between two different groups along with the nonparametric log-rank *post hoc* test. Finally, the Spearman rank correlation coefficient test was used to evaluate associations between two quantitative variables that exhibited non-normal distribution. Statistical significance was defined as a P value less than 0.05.

Results

Identification of PRO as an inhibitor of pCTS-L-mediated TNF secretion

To explore novel pCTS-L inhibitors, we adapted a macrophage cell-based bioassay that we recently developed (16) to screen a U.S. Collection of 1360 drugs supplied as 10.0 mM Dimethyl Sulfoxide (DMSO) solutions in seventeen 96-well microplates for possible activities to inhibit pCTS-L-stimulated TNF secretion (Figure 1A). We optimized the experimental conditions by respectively titrating the concentration of pCTS-L protein (to 1.0 μg/ml) and the confluence of macrophage cultures (to 80-90%). A complete screening of 1360 drugs of the U.S. Collection resulted in the identification of progesterone (PRO) and three analogs (i.e., dydrogesterone, exemestane, and medroxyprogesterone acetate; Figure 1B) as inhibitors of pCTS-L-stimulated TNF production. When dissolved in DMSO, PRO dose-dependently attenuated pCTS-L-mediated TNF secretion with an estimated IC around 20.0 μM (Figure 1B) without affecting mitochondrial metabolic activity (MTT assay) or cell viability (Trypan blue uptake, Supplementary Figure 1).

PRO inhibited pCTS-L-mediated secretion of TNF and several chemokines in primary human peripheral blood mononuclear cells (PBMCs)

To confirm PRO's pCTS-L-inhibitory activities, we first dissolved it in ethanol before testing its effects on pCTS-L-stimulated production of 42 cytokines and chemokines in primary human PBMCs. In agreement with our earlier report (4), pCTS-L markedly stimulated the secretion of a few chemokines (e.g., ENA-78, GRO, and MCP-1) and cytokines (e.g., TNF, IL-6 and IL-10) (Figure 2). However, the pCTS-L-mediated TNF production was markedly inhibited by the co-administration of PRO at a relatively high dose (40 μM, Figure 2), an almost most effective dose that suppressed pCTS-L-induced TNF secretion in dose-response studies using murine macrophages (Figure 1B) as well as primary PBMCs from several different donors. Likewise, the pCTS-L-triggered secretion of several other cytokines (e.g., IL-10) and chemokines (e.g., ENA-78 and MCP-1) was similarly suppressed by PRO (Figure 2). Consistent with our earlier reports (16, 24), endotoxins effectively stimulated the secretion of several chemokines (MCP-1, ENA-78 and GRO) and cytokines (e.g., TNF, IL-6 and IL-10) in primary human PBMCs (Figure 2). However, PRO was unable to affect LPS-induced production of any cytokines/chemokines (Figure 2) even at the concentration that markedly inhibited pCTS-L-mediated cytokine/chemokine production, suggesting that PRO selectively inhibited pCTS-L-mediated inflammation.

PRO-carrying 2,6-dimethyl-β-cyclodextrin (DM-β-CD) nanoparticles similarly inhibited pCTS-L-induced inflammation

The β-cyclodextrin (β-CD) is defined as cyclic oligosaccharides of seven glucopyranoses in its β-chair conformation (Figure 3A), thereby displaying the shape of truncated cone with an outer hydrophilic surface that render it water-soluble and an inner hydrophobic core (25) that can entrap hydrophobic molecules (e.g., PRO). To increase the water-solubility of β-CD, the hydroxyl groups of the inner hydrophobic cavity (position 2) and the outer hydrophilic surface (position 6) of β-CD can be substituted with hydrophobic methyl moieties to produce the 2,6-dimethyl-β-cyclodextrin (DM-β-CD, Figure 3A), which still displayed the shape of cone with slightly less symmetry and smaller inner cavity (Figure 3A). As a lipophilic sterol, PRO could be inserted into the hydrophobic inner cavity of two DM-β-CD molecules at 1:2 molar ratio (Figure 3A). These PRO-carrying DM-β-CD nanoparticles dose-dependently suppressed pCTS-L-mediated production of a few cytokines (e.g., TNF, IL-6 and IL-10) and chemokines (GRO, IL-8 and MCP-3) in human PBMCs (Figure 3B), confirming that PRO-carrying DM-β-CD nanoparticles maintained pCTS-L-inhibiting properties of PRO under pharmacological conditions.

PRO-carrying DM-β-CD nanoparticles protected both male and female mice from microbial infections

To assess the PRO's therapeutic efficacy, we first dissolved PRO in Sesame oil containing various unsaturated fatty acids that could emulsify and dissolve lipophilic PRO in the form of micelles (26–30). When dissolved in sesame oil, PRO did not show any

10.3389/fimmu.2024.1368448

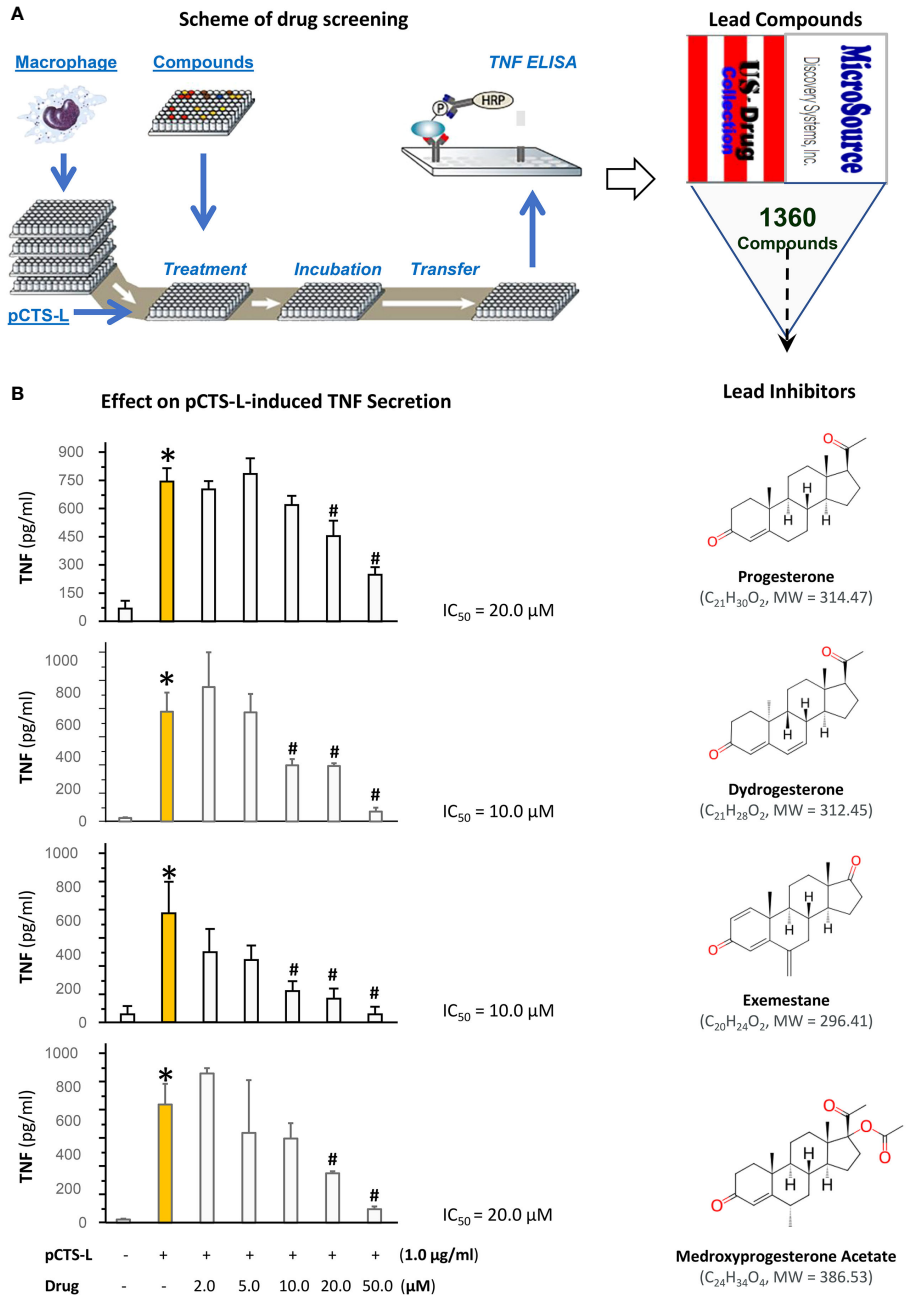

FIGURE 1
High-throughput screening of a U.S. Collection of 1360 Drugs for potential inhibitors of pCTS-L-mediated TNF production. **(A)** The scheme for the 96-well plate-based high-throughput screening of potential pCTS-L inhibitors was adapted from our recent publication (16). Murine macrophage-like RAW 264.7 cells were cultured until 80-90% confluence and challenged with recombinant murine pCTS-L in the absence or in the presence of each of the 1360 compounds at different concentrations for 16 h. The levels of TNF in the macrophage-conditioned medium were measured by using ELISA. **(B)** Effects of progesterone and three analogs on pCTS-L-induced TNF secretion by murine macrophage cultures. Note that all four lead compounds dose-dependently inhibited pCTS-L-induced TNF secretion by murine macrophage cultures. *, $P < 0.05$ versus "- pCTS-L"; #, $P < 0.05$ versus "+ pCTS-L", non-parametric Kruskal-Wallis ANOVA test.

protection against sepsis within a dose range of 1.0 mg/kg to 8.0 mg/kg (Figure 4A, Left Panel). When given intraperitoneally at a relatively high dose (16 mg/kg) at 2 h and 24 h post CLP, PRO promoted a marked protection against sepsis, significantly increasing animal survival rates from 30% to 70% (Figure 4A). In an effort to enhance its pharmacological efficacy, PRO was entrapped into DM-β-CD nanoparticles to enhance its water-solubility and bioavailability, and further tested in an animal model of experimental sepsis induced by cecal ligation and puncture (CLP). The PRO-carrying DM-β-CD nanoparticles was given at 24 h after CLP, which was a time point when circulating pCTS-L plateaued and some animals started to succumb to death (4). As a vehicle control, DM-β-CD (14.65 mg/kg) itself did not affect animal survival rate when it was given at 24 h and 48 h post

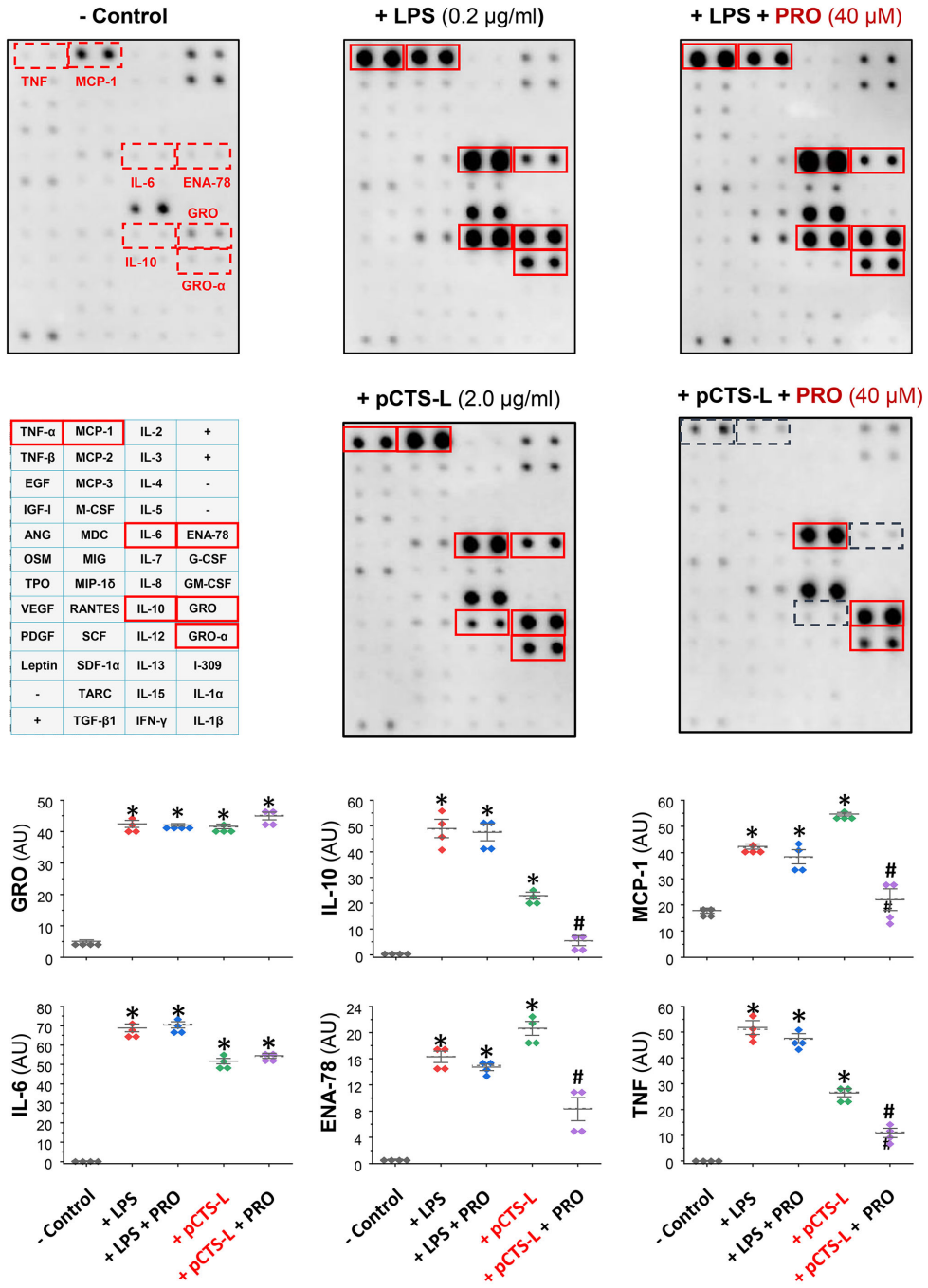

FIGURE 2
Progesterone selectively suppressed the pCTS-L-mediated productions of several cytokines/chemokines in primary human peripheral blood mononuclear cells (PBMCs). Human PBMCs were challenged with human pCTS-L (2.0 μg/ml) or LPS (0.2 μg/ml) in the absence or in the presence of PRO (40 μM in ethanol) for 16 h. The levels of various cytokines and chemokines in human PBMC-conditioned medium were measured by using Cytokine Antibody Array kits (in arbitrary units, AU). *, $P < 0.05$ versus "- pCTS-L"; #, $P < 0.05$ versus "+ pCTS-L", non-parametric Kruskal-Wallis ANOVA test.

CLP surgery (Figure 4A). In contrast, the PRO-carrying DM-β-CD nanoparticles significantly rescued both male and female mice from infections even when the 1st dose was intraperitoneally administered at 24 h post CLP (Figure 4A). This effective protective dose of PRO entrapped in the DM-β-CD nanoparticles (even when initially given at 24 h post CLP) was almost 10-fold lower than the dosage of progesterone dissolved in sesame oil (when first given at 2 h post CLP.) The calculated molar concentration of PRO (MW = 314.47 Daltons; 1.4 mg/kg) intraperitoneally injected into septic animals was estimated to be > 4.5 μM and comparable to the effective concentrations (10 μM) of PRO in inhibiting pCTS-L-induced dysregulated inflammation *in vitro* (Figure 3B).

To elucidate the underlying protective mechanisms of PRO, we assessed its impact on CLP sepsis-triggered inflammation and tissue

10.3389/fimmu.2024.1368448

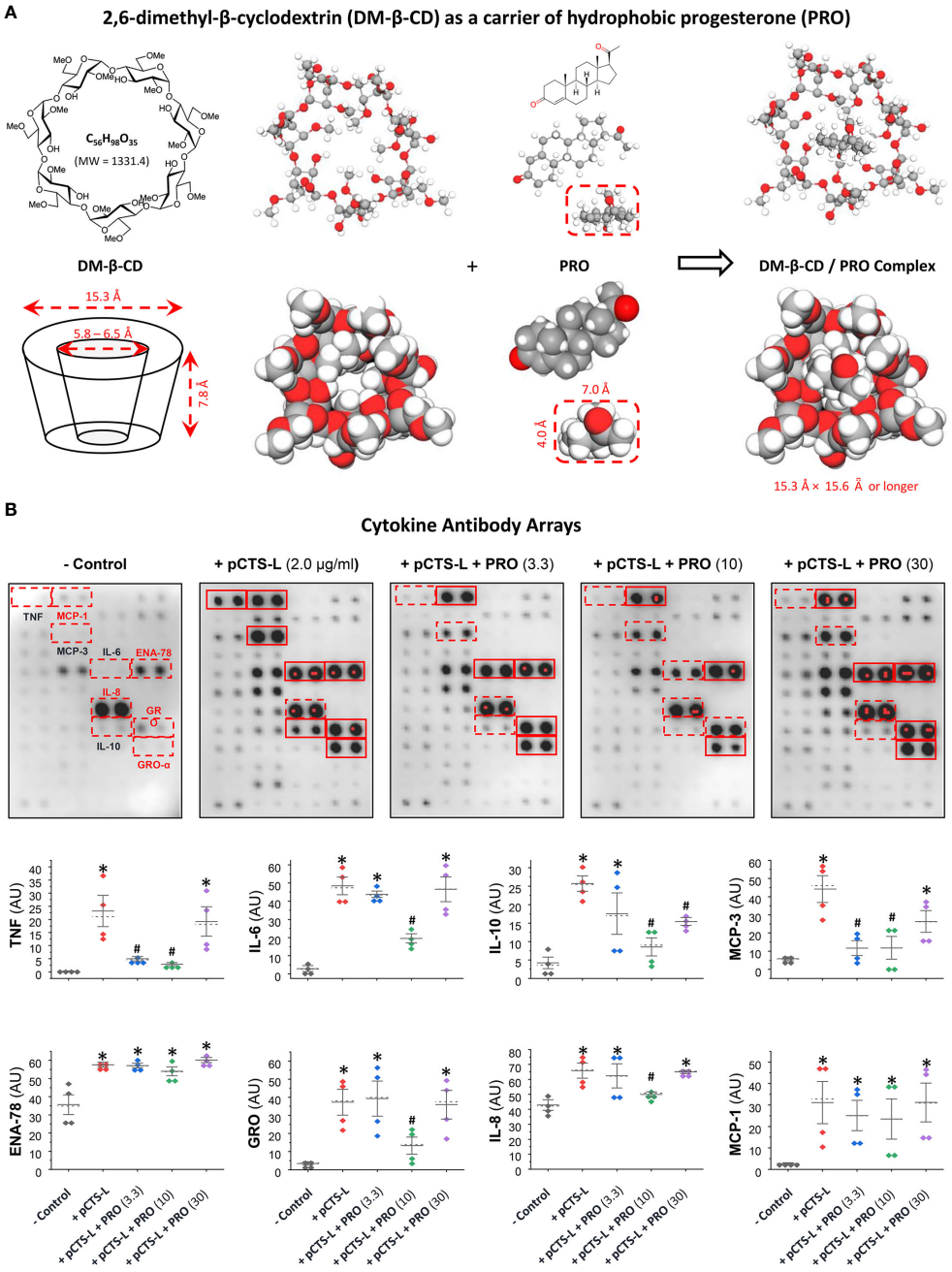

FIGURE 3
PRO-carrying DM-β-CD nanoparticles significantly inhibited pCTS-L-stimulated production of several cytokines and chemokines in human PBMCs. **(A)** Structures of DM-β-CD and PRO as well as the inclusion complex of these two molecules. Given its lipophilic nature, PRO can easily be intercalated and embedded into the hydrophobic inner cavity of the truncated cone structure of two DM-β-CD molecules. **(B)** PRO significantly inhibited pCTS-L-stimulated production of several cytokines and chemokines. Human PBMCs were challenged with recombinant human pCTS-L in the absence or in the presence of DM-β-CD/PRO complexes at different concentrations (μM) for 16 h, and extracellular concentrations of cytokines and chemokines were measured by using Cytokine Antibody Arrays. *, $P < 0.05$ versus "- pCTS-L"; #, $P < 0.05$ versus "+ pCTS-L", non-parametric Kruskal-Wallis ANOVA test.

injury. In agreement with our previous report (4), experimental sepsis markedly elevated blood levels of G-CSF, MIP-2 and sTNFR1 (Figure 4B). In contrast to DM-β-CD vehicle, which did not affect sepsis-triggered systemic accumulation of any cytokines or chemokines, PRO-carrying DM-β-CD nanoparticles significantly reduced sepsis-triggered elevation of MIP-2 and sTNFRI (Figure 4B). Furthermore, in contrast to DM-β-CD vehicle, which did not affect sepsis-triggered release of liver enzymes (such as AST) or other general tissue injury markers such as LDH, PRO-carrying DM-β-CD nanoparticles significantly reduced the levels of AST and LDH in septic animals (Figure 4C), suggesting that PRO-entrapping DM-β-CD nanoparticles protect mice against infections partly by suppressing sepsis-mediated dysregulated inflammation and tissue injury.

10.3389/fimmu.2024.1368448

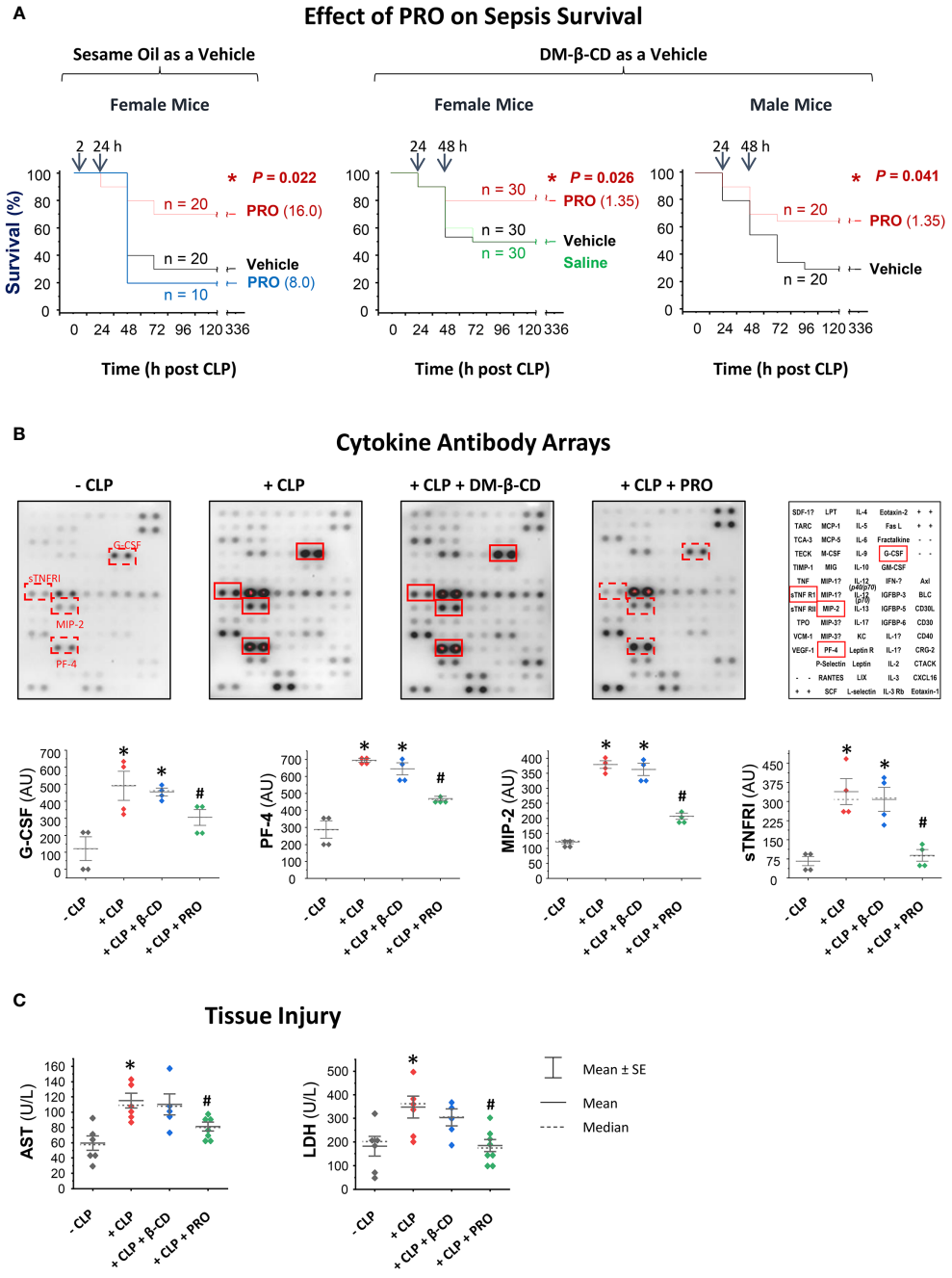

FIGURE 4
PRO-carrying DM-β-CD nanoparticles rescued mice from sepsis partially by attenuating sepsis-triggered inflammation. **(A)** PRO-containing sesame oil or PRO-entrapping DM-β-CD nanoparticles protected or rescued mice from experimental sepsis. Male (M) and/or female (F) Balb/C mice were subjected to CLP, and PRO-containing sesame oil or PRO/DM-β-CD nanoparticles were intraperitoneally administered at indicated doses and time points. *, P < 0.05 versus saline or vehicle (sesame oil or DM-β-CD) controls. **(B, C)** PRO-carrying DM-β-CD nanoparticles attenuated CLP-triggered systemic inflammation and tissue injury. Balb/C mice were subjected to CLP, and PRO/DM-β-CD nanoparticles (containing 1.35 mg/kg PRO and 14.65 mg/kg DM-β-CD) or DM-β-CD vehicle (14.65 mg/kg) were administered at 2 h and 20 h post CLP, and then euthanized at 24 h post CLP to collect blood and measure serum levels of various cytokines and chemokines (in arbitrary units, AU) as well as markers of tissue injury (AST and LDH) using specific colorimetric enzymatic assays. *, P < 0.05 versus " - CLP"; #, P < 0.05 versus "+ CLP", non-parametric Kruskal-Wallis ANOVA test.

PRO interacted and positively correlated with pCTS-L in clinical sepsis

To gain further insight into PRO's protective mechanisms, we examined the possible interaction and relationship between systemic accumulation PRO and pCTS-L in clinical sepsis. SPR analysis revealed a strong interaction between PRO and pCTS-L, as evidenced by the relatively low equilibrium dissociation constant (KD, Figure 5A) for PRO-pCTS-L interaction, suggesting that PRO might bind pCTS-L to inhibit its proinflammatory properties under pharmacological conditions. In agreement with previous findings of a marked (1 - 5 folds) elevation of blood PRO levels in septic

animals (31) or patients with severe sepsis (32) or septic shock (33), we found a significant increase of serum PRO levels in septic mice (Figure 5B), as well as a parallel positive correlation with Sequential Organ Failure Assessment (SOFA, Supplementary Table 1) score and serum pCTS-L concentrations in patients with clinical sepsis (Figure 5C), confirming a possible progesterone upregulation as a potential protective mechanism against infections.

Discussion

Currently, there is no effective therapies for clinical sepsis other than some adjunctive care such as administration of antibiotics and resuscitation of fluid (34–36). Therefore, it might still be important to explore small-molecule inhibitors to attenuate late-acting pathogenic mediators that may have relatively wider therapeutic windows (5). Here, we showed that a lipophilic hormone, PRO, selectively impaired pCTS-L-triggered production of several chemokines (e.g., ENA-78, MCP-1 or MCP-3) and cytokines (e.g., TNF, IL-6 or IL-10) without affecting LPS-induced TNF production. Our findings were in agreement with previous reports that PRO failed to inhibit LPS-stimulated TNF production in human PBMCs (37, 38). Nevertheless, it has been shown that PRO could inhibit LPS-stimulated production and secretion of TNF, IL-6, IL-12 or nitric oxide in other types of immune cells such as macrophages (39–43) and microglial cells (44, 45)

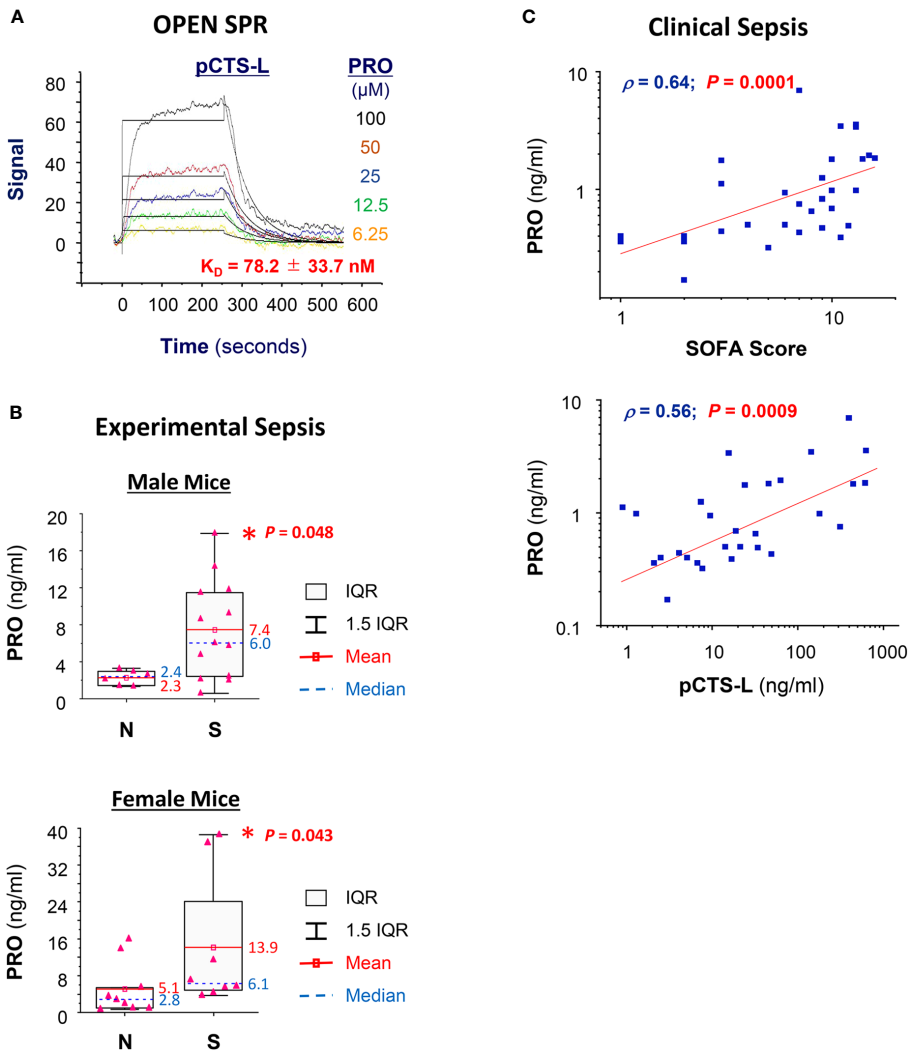

FIGURE 5
PRO interacted and positively correlated with pCTS-L in clinical sepsis. **(A)** SPR analysis of PRO/pCTS-L interaction. Recombinant pCTS-L with an N-terminal 6 × His tag was immobilized onto nitrilotriacetic acid (NTA)-conjugated chip, and an analyte of PRO solution (in DMSO) was injected at several increasing concentrations (6.25, 12.5, 25.0, 50.0 and 100.0 μM) to estimate the KD of PRO-pCTS-L interaction. PRO was injected for a contact time of 250 seconds at increasing concentrations, and dissociation was monitored for 300 seconds. The 1:1 model fit to the raw data is shown as solid black lines. The K_D was shown as the mean ± SEM of three independent experiments. **(B)** Elevation of serum PRO levels in septic mice at 24 h post CLP surgery. Male Balb/C mice were subjected to CLP surgery, and animals were sacrificed at 24 h post CLP to harvest blood and to compare serum PRO levels between normal healthy ("N") and septic ("S") mice. *, $P < 0.05$ versus normal healthy mice (N), non-parametric Kruskal-Wallis ANOVA test. **(C)** Correlation between serum PRO concentrations and sequential organ failure assessment (SOFA) score as well as serum pCTS-L levels in septic patients.

potentially via PRO receptor-independent mechanisms (42). The discrepancies between divergent effects of progesterone on LPS-induced responses in different cell types remain a subject of future investigation. Nevertheless, as a steroid hormone produced primarily by the ovaries in women and, to a lesser extent, by the adrenal glands in both men and women, PRO occupies a crucial role in regulating menstrual cycles of the female reproductive system as well as innate immune responses against microbial infections.

Consequently, PRO-carrying DM-β-CD nanoparticles rescued both male and female mice from microbial infections even when they were initially given at 24 hours post the disease onset. This finding mirrored previous observations that systemic administration of PRO attenuated endotoxin-induced hypotension (46), CLP-induced systemic inflammation (47), as well as dysregulated inflammatory responses elicited by viral infections with SARS-CoV-2 (48, 49) and hepatitis C virus (50). When given locally, however, subcutaneous implanting PRO adversely thinned the cervicovaginal epithelium and adversely enhanced vaginal transmission of Simian immunodeficiency virus (SIV) (51), genital herpes infection (52) or HIV infection (53). It will thus be important to determine whether systemic administration of PRO at pharmacological doses will confer universal protection against all bacterial and viral infections in future preclinical and clinical investigations.

Because the lipophilic PRO is not soluble in water, we employed either sesame oil to emulsify it into micelles or DM-β-CD to complex with it to produce water-soluble PRO-carrying DM-β-CD-based nanoparticles. In the water solution, DM-β-CD displays the shape of truncated cone with a hydrophilic outer surface that renders it water-soluble and a hydrophobic inner cavity that entraps small hydrophobic molecules such as PRO (54, 55). This combined internal hydrophobic cavity along with external hydrophilicity enables DM-β-CD to form "host-guest" complexes with hydrophobic PRO via van der Waals forces and hydrophobic interactions (56). Although both a partial and a complete inclusion may occur, free-energy calculations favored the partial inclusion event for DM-β-CD and PRO (56), in which the complexation was initiated by inclusion of PRO into the first DM-β-CD to produce the 1:1 complex, but continued with the engagement of the second DM-β-CD to generate the more stable 1:2 complex (55, 57). Therefore, the hydrophobic part of PRO can be hidden within the inner hydrophobic cores of two DM-β-CD molecules, thereby potentially improving the solubility, stability, as well as bioavailability of the PRO *in vivo* (58). However, the entrapment of this hydrophobic PRO by DM-β-CD is reversible, enabling rapid dissociation of PRO from the complexes upon their dilution in biological fluids (58, 59). PRO was released from DM-β-CD within hours (59), and the dissociated PRO could potentially bind pCTS-L to interrupt some of its proinflammatory properties. The free DM-β-CDs could be gradually removed from the circulation within 36 h, destining to organs with increased blood flow velocities such as the spleen, liver, and kidney (60), where it can be metabolized (60) or excreted via glomerular filtration (61).

Regardless of whether PRO was solubilized in organic solvents (e.g., DMSO or ethanol) or entrapped in DM-β-CD-based nanoparticles, it similarly suppressed pCTS-L-induced secretion of several chemokines (e.g., ENA-78, MCP-1, GRO, or MCP-3) and cytokines (e.g., TNF or IL-10) in human PBMCs. The intricate mechanisms of PRO-mediated suppression of pCTS-L-stimulated inflammation will be an interesting subject for future investigations. In light of the essential involvement of TLR4 and RAGE in pCTS-L-induced inflammation (4), it will be interesting to determine whether PRO interacts with pCTS-L to interfere with its interaction with TLR4 or RAGE receptors. This is plausible, because pCTS-L-neutralizing antibodies inhibited pCTS-L-stimulated inflammation by disrupting pCTS-L interaction with PRRs such as TLR4 and RAGE (4).

To our best knowledge, the DM-β-CD-based nanoparticle technology has not yet been used to explore the therapeutic potential of PRO in any animal models of microbial infections. Consistent with its inhibitory activity in inhibiting late-acting mediator pCTS-L-induced cytokine/chemokine production in human PBMCs, we found that delayed administration of PRO-carrying DM-β-CD nanoparticles effectively rescued both male and female mice from microbial infections even when they were initially given at 24 h post onset of infections. Currently, the mechanism for PRO-mediated protection remains elusive, but appeared to attribute to its attenuation of sepsis- or pCTS-L-induced dysregulated inflammation and tissue injury. Indeed, PRO-carrying DM-β-CD nanoparticles significantly attenuated sepsis-triggered accumulation of G-CSF, sTNFRI and MIP-2/GRO-β, three pCTS-L-inducible surrogate markers of experimental sepsis (20, 62, 63). Our findings were in agreement with an earlier report (47), and support the possibility that PRO protects mice against sepsis partially by suppressing sepsis-triggered dysregulated inflammation. In light of the pathogenic involvement of pCTS-L in other inflammatory diseases such as pancreatitis (64), atherosclerosis (65), renal disease (66), vascular intimal hyperplasia (67), arthritis (68) and colitis (69), it will be interesting to explore the therapeutic potential of PRO-carrying DM-β-CD nanoparticles in other inflammatory diseases.

There are a few limitations in the current study: (i) We did not assess systemic inflammatory cytokine profiles at later stages of sepsis, because many septic animals in the control group might have succumbed to sepsis between 24 - 48 h post CLP (as depicted in Figure 4A), rendering blood sampling at later time points after the death of some septic animals in the control vehicle group practically infeasible. Even if post-mortem blood collection was still feasible, post-mortem tissue decomposition could lead to the release of cellular contents (including cytokines) into the surrounding environment, resulting in artificially elevated cytokine levels in post-mortem samples. Thus, sampling at later time points particularly after the death of septic animals in the control group might introduce confounding variables that hinder the interpretability of the systemic inflammatory profile, rendering them ineligible for the inclusion of comprehensive assessment of systemic inflammation at later points (e.g., 48 h post CLP). (ii) We do not know if PRO-entrapping DM-β-CD nanoparticles are orally active and protective against sepsis and other bacterial or viral infections. (iii) We do not know why progesterone selectively inhibits pCTS-L-mediated inflammation, although the robust

interaction between progesterone and pCTS-L may contribute to the observed selectivity, allowing progesterone to inhibit pCTS-L-mediated inflammation without impacting LPS-mediated cytokine/chemokine production. (iv) It remains elusive why PRO-entrapping DM-β-CD nanoparticles exhibited a bell-shaped dose-response curve in inhibiting pCTS-L-mediated inflammatory response, although this type of bell-shaped dose-response curve has also been observed in the context of PRO-mediated protection against cerebral ischemic injury (70, 71), wherein a higher dose (32 mg/kg) exhibited reduced efficacy compared to lower doses (e.g., 8 mg/kg or 16 mg/kg). Bell-shaped concentration-response curves typically indicate more complex biological effects, such as receptor saturation or dual mechanisms of action with multiple binding sites or targets of DM-β-CD complexes. For instance, at extremely higher concentrations (5 - 50 mM), β-CD and derivatives (e.g., DM-β-CD) can extract lipophilic molecules such as cholesterol from cytoplasmic membranes (72, 73), thereby disrupting lipid rafts to interfere with innate immune responses to microbial infections (74, 75). Similarly, at extremely high concentrations (in the ranges of mM), another β-CD derivative, 2-Hydroxypropyl-β-cyclodextrin, also exhibited some pro-inflammatory properties as evidenced by the increased expression and release of cytokines (such as TNF and CCL2/MCP-1) by murine macrophages (75). At present, it is not yet known whether DM-β-CD possesses similar weak proinflammatory properties in complexation with PRO that could be attributed to the bell-shaped dose-response cure of PRO/DM-β-CD complexes. Despite these limitations of this study, our findings of PRO as a selective inhibitor of pCTS-L-mediated dysregulated inflammation have supported a promising opportunity of developing novel DM-β-CD-based nanoparticles to treat microbial infections. Therefore, it will be critical to further develop PRO-entrapping DM-β-CD-based nanoparticles and further translate our pre-clinical research into clinical treatment of bacterial infections.

Data availability statement

The original contributions presented in the study are included in the article/Supplementary Materials, further inquiries can be directed to the corresponding author/s.

Ethics statement

This study was administratively approved by the institutional review board (IRB) of the FIMR (IRB protocol #18-0184). The studies were conducted in accordance with the local legislation and institutional requirements. The participants provided their written informed consent to participate in this study. Our animal study was approved by the Institutional Animal Care and Use Committee (IACUC) of the FIMR (Protocol # 2017-003 Term II, approved on April 28th, 2020). The study was conducted in accordance with the local legislation and institutional requirements.

Author contributions

XQ: Writing – review & editing, Methodology, Investigation, Formal analysis, Data curation. WC: Writing – review & editing, Methodology, Investigation, Data curation. CZ: Writing – review & editing, Methodology, Investigation, Data curation. JL: Writing – review & editing, Resources. TQ: Writing – review & editing, Investigation, Data curation. LL: Writing – review & editing, Investigation, Formal analysis. PW: Writing – review & editing, Conceptualization. KT: Writing – review & editing, Resources. HW: Writing – review & editing, Writing – original draft, Supervision, Project administration, Funding acquisition, Formal analysis, Conceptualization.

Funding

The author(s) declare that financial support was received for the research, authorship, and/or publication of this article. Our work was partly supported by the National Institutes of Health (NIH) grants R01AT005076 and R35GM145331.

Conflict of interest

The authors declare that the research was conducted in the absence of any commercial or financial relationships that could be construed as a potential conflict of interest.

Publisher's note

Supplementary material

The Supplementary Material for this article can be found online at: https://www.frontiersin.org/articles/10.3389/fimmu.2024.1368448/full#supplementary-material

References

1. Rudd KE, Johnson SC, Agesa KM, Shackelford KA, Tsoi D, Kievlan DR, et al. Global, regional, and national sepsis incidence and mortality, 1990-2017: analysis for the global burden of disease study. *Lancet*. (2020) 395:200–11. doi: 10.1016/S0140-6736(19)32989-7

2. Wang H, Bloom O, Zhang M, Vishnubhakat JM, Ombrellino M, Che J, et al. Hmg-1 as a late mediator of endotoxin lethality in mice. *Science*. (1999) 285:248–51. doi: 10.1126/science.285.5425.248

3. Tang D, Kang R, Zeh HJ, Lotze MT. The multifunctional protein hmgb1: 50 years of discovery. *Nat Rev Immunol*. (2023) 23:824–41. doi: 10.1038/s41577-023-00894-6

4. Zhu CS, Qiang X, Chen W, Li J, Lan X, Yang H, et al. Identification of procathepsin L (Pcts-L)-neutralizing monoclonal antibodies to treat potentially lethal sepsis. *Sci Adv*. (2023) 9:eadf4313. doi: 10.1126/sciadv.adf4313

5. Li J, Zhu CS, He L, Qiang X, Chen W, Wang H. A two-decade journey in identifying high mobility group box 1 (Hmgb1) and procathepsin L (Pcts-L) as potential therapeutic targets for sepsis. *Expert Opin Ther Targets*. (2023) 27:575–91. doi: 10.1080/14728222.2023.2239495

6. Poltorak A, He X, Smirnova I, Liu MY, Huffel CV, Du X, et al. Defective lps signaling in C3h/hej and C57bl/10sccr mice: mutations in tlr4 gene. *Science*. (1998) 282:2085–8. doi: 10.1126/science.282.5396.2085

7. Tracey KJ, Fong Y, Hesse DG, Manogue KR, Lee AT, Kuo GC, et al. Anti-cachectin/tnf monoclonal antibodies prevent septic shock during lethal bacteraemia. *Nature*. (1987) 330:662–4. doi: 10.1038/330662a0

8. Dinarello CA. Biologic basis for interleukin-1 in disease. *Blood*. (1996) 87:2095–147. doi: 10.1182/blood.V87.6.2095.bloodjournal8762095

9. Song Y, Shi Y, Ao LH, Harken AH, Meng XZ. Tlr4 mediates lps-induced ho-1 expression in mouse liver: role of tnf-alpha and il-1beta. *World J Gastroenterol*. (2003) 9:1799–803. doi: 10.3748/wjg.v9.i8.1799

10. Fan M, Yang K, Wang X, Chen L, Gill PS, Ha T, et al. Lactate promotes endothelial-to-mesenchymal transition via snail1 lactylation after myocardial infarction. *Sci Adv*. (2023) 9:eadc9465. doi: 10.1126/sciadv.adc9465

11. Yang K, Fan M, Wang X, Xu J, Wang Y, Tu F, et al. Lactate promotes macrophage hmgb1 lactylation, acetylation, and exosomal release in polymicrobial sepsis. *Cell Death Differ*. (2022) 29:133–46. doi: 10.1038/s41418-021-00841-9

12. Yang L, Xie M, Yang M, Yu Y, Zhu S, Hou W, et al. Pkm2 regulates the warburg effect and promotes hmgb1 release in sepsis. *Nat Commun*. (2014) 5:4436. doi: 10.1038/ncomms5436.:4436

13. Yang H, Ochani M, Li J, Qiang X, Tanovic M, Harris HE, et al. Reversing established sepsis with antagonists of endogenous high-mobility group box 1. *Proc Natl Acad Sci U.S.A*. (2004) 101:296–301. doi: 10.1073/pnas.2434651100

14. Zhang MM, Qiao Y, Ang EL, Zhao H. Using natural products for drug discovery: the impact of the genomics era. *Expert Opin Drug Discovery*. (2017) 12:475–87. doi: 10.1080/17460441.2017.1303478

15. Chen W, Qiang X, Wang Y, Zhu S, Li J, Babaev A, et al. Identification of tetranectin-targeting monoclonal antibodies to treat potentially lethal sepsis. *Sci Transl Med*. (2020) 12:12/539. doi: 10.1126/scitranslmed.aaz3833

16. Chen W, Zhu CS, Qiang X, Chen S, Li J, Wang P, et al. Development of procathepsin L (Pcts-L)-inhibiting lanosterol-carrying liposome nanoparticles to treat lethal sepsis. *Int J Mol Sci*. (2023) 24. doi: 10.3390/ijms24108649

17. Osuchowski MF, Ayala A, Bahrami S, Bauer M, Boros M, Cavaillon JM, et al. Minimum quality threshold in pre-clinical sepsis studies (Mqtipss): an international expert consensus initiative for improvement of animal modeling in sepsis. *Shock*. (2018) 50:377–80. doi: 10.1097/shk.0000000000001212

18. Zingarelli B, Coopersmith CM, Drechsler S, Efron P, Marshall JC, Moldawer L, et al. Part I: minimum quality threshold in preclinical sepsis studies (Mqtipss) for study design and humane modeling endpoints. *Shock*. (2019) 51:10–22. doi: 10.1097/shk.0000000000001243

19. Hellman J, Bahrami S, Boros M, Chaudry IH, Fritsch G, Gozdzik W, et al. Part iii: minimum quality threshold in preclinical sepsis studies (Mqtipss) for fluid resuscitation and antimicrobial therapy endpoints. *Shock*. (2019) 51:33–43. doi: 10.1097/shk.0000000000001209

20. Chen W, Brenner M, Aziz M, Chavan SS, Deutschman CS, Diamond B, et al. Buprenorphine markedly elevates a panel of surrogate markers in a murine model of sepsis. *Shock*. (2019) 52:550–3. doi: 10.1097/SHK.0000000000001361

21. Cotroneo TM, Hugunin KM, Shuster KA, Hwang HJ, Kakaraparthi BN, Nemzek-Hamlin JA. Effects of buprenorphine on a cecal ligation and puncture model in C57bl/6 mice. *J Am Assoc Lab Anim Sci*. (2012) 51:357–65.

22. Zhu SC, Li J, Wang. H. Use of open surface plasma resonance (Openspr) to characterize teh binding affinity of protein-protein interactions. *Bio-Protocol*. (2023) 13. doi: 10.21769/BioProtoc.4795

23. Shankar-Hari M, Phillips GS, Levy ML, Seymour CW, Liu VX, Deutschman CS, et al. Developing a new definition and assessing new clinical criteria for septic shock: for the third international consensus definitions for sepsis and septic shock (Sepsis-3). *JAMA*. (2016) 315:775–87. doi: 10.1001/jama.2016.0289

24. Zhang M, Caragine T, Wang H, Cohen PS, Botchkina G, Soda K, et al. Spermine inhibits proinflammatory cytokine synthesis in human mononuclear cells: A counterregulatory mechanism that restrains the immune response. *J Exp Med*. (1997) 185:1759–68. doi: 10.1084/jem.185.10.1759

25. Duchêne D, Bochot A. Thirty years with cyclodextrins. *Int J Pharm*. (2016) 514:58–72. doi: 10.1016/j.ijpharm.2016.07.030

26. Auger CJ, Jessen HM, Auger AP. Microarray profiling of gene expression patterns in adult male rat brain following acute progesterone treatment. *Brain Res*. (2006) 1067:58–66. doi: 10.1016/j.brainres.2005.10.033

27. Russo SJ, Sun WL, Minerly AC, Weierstall K, Nazarian A, Festa ED, et al. Progesterone attenuates cocaine-induced conditioned place preference in female rats. *Brain Res*. (2008) 1189:229–35. doi: 10.1016/j.brainres.2007.10.057

28. Sun WL, Luine VN, Zhou L, Wu HB, Weierstall KM, Jenab S, et al. Acute progesterone treatment impairs spatial working memory in intact male and female rats. *Ethn Dis*. (2010) 20:S1–83-7.

29. O'Connor CA, Cernak I, Johnson F, Vink R. Effects of progesterone on neurologic and morphologic outcome following diffuse traumatic brain injury in rats. *Exp Neurol*. (2007) 205:145–53. doi: 10.1016/j.expneurol.2007.01.034

30. Uphouse L, Guptarak J, Hiegel C. Progesterone reduces the inhibitory effect of a serotonin 1b receptor agonist on lordosis behavior. *Pharmacol Biochem Behav*. (2010) 97:317–24. doi: 10.1016/j.pbb.2010.08.017

31. Dembek K, Timko K, Moore C, Johnson L, Frazer M, Barr B, et al. Longitudinal assessment of adrenocortical steroid and steroid precursor response to illness in hospitalized foals. *Domest Anim Endocrinol*. (2023) 82:106764. doi: 10.1016/j.domaniend.2022.106764

32. Angstwurm MW, Gaertner R, Schopohl J. Outcome in elderly patients with severe infection is influenced by sex hormones but not gender. *Crit Care Med*. (2005) 33:2786–93. doi: 10.1097/01.ccm.0000190242.24410.17

33. Feng JY, Liu KT, Abraham E, Chen CY, Tsai PY, Chen YC, et al. Serum estradiol levels predict survival and acute kidney injury in patients with septic shock–a prospective study. *PloS One*. (2014) 9:e97967. doi: 10.1371/journal.pone.0097967

34. Buchman TG, Simpson SQ, Sciarretta KL, Finne KP, Sowers N, Collier M, et al. Sepsis among medicare beneficiaries: 1. The burdens of sepsis, 2012-2018. *Crit Care Med*. (2020) 48:276–88. doi: 10.1097/CCM.0000000000004224

35. Tindal EW, Armstead BE, Monaghan SF, Heffernan DS, Ayala A. Emerging therapeutic targets for sepsis. *Expert Opin Ther Targets*. (2021) 25:175–89. doi: 10.1080/14728222.2021.1897107

36. Reinhart K, Daniels R, Kissoon N, MaChado FR, Schachter RD, Finfer S. Recognizing sepsis as a global health priority - a who resolution. *N Engl J Med*. (2017) 377:414–7. doi: 10.1056/NEJMp1707170

37. Bouman A, Schipper M, Heineman MJ, Faas M. 17beta-estradiol and progesterone do not influence the production of cytokines from lipopolysaccharide-stimulated monocytes in humans. *Fertil Steril*. (2004) 82 Suppl 3:1212–9. doi: 10.1016/j.fertnstert.2004.05.072

38. Amory J, Lawler R, Shields L. Hydroxyprogesterone caproate and progesterone increase tumor necrosis factor-alpha production in lipopolysaccharide stimulated whole blood from non-pregnant women. *J Perinat Med*. (2005) 33:506–9. doi: 10.1515/jpm.2005.089

39. Miller L, Hunt JS. Regulation of tnf-alpha production in activated mouse macrophages by progesterone. *J Immunol*. (1998) 160:5098–104. doi: 10.4049/jimmunol.160.10.5098

40. Jones LA, Anthony JP, Henriquez FL, Lyons RE, Nickdel MB, Carter KC, et al. Toll-like receptor-4-mediated macrophage activation is differentially regulated by progesterone via the glucocorticoid and progesterone receptors. *Immunology*. (2008) 125:59–69. doi: 10.1111/j.1365-2567.2008.02820.x

41. Su L, Sun Y, Ma F, Lü P, Huang H, Zhou J. Progesterone inhibits toll-like receptor 4-mediated innate immune response in macrophages by suppressing nf-kappab activation and enhancing socs1 expression. *Immunol Lett*. (2009) 125:151–5. doi: 10.1016/j.imlet.2009.07.003

42. Wolfson ML, Schander JA, Bariani MV, Correa F, Franchi AM. Progesterone modulates the lps-induced nitric oxide production by a progesterone-receptor independent mechanism. *Eur J Pharmacol*. (2015) 769:110–6. doi: 10.1016/j.ejphar.2015.11.005

43. Miller L, Alley EW, Murphy WJ, Russell SW, Hunt JS. Progesterone inhibits inducible nitric oxide synthase gene expression and nitric oxide production in murine macrophages. *J Leukoc Biol*. (1996) 59:442–50. doi: 10.1002/jlb.59.3.442

44. Müller E, Kerschbaum HH. Progesterone and its metabolites 5-dihydroprogesterone and 5-3-tetrahydroprogesterone decrease lps-induced no release in the murine microglial cell line, bv-2. *Neuro Endocrinol Lett*. (2006) 27:675–8.

45. Lei B, Mace B, Dawson HN, Warner DS, Laskowitz DT, James ML. Anti-inflammatory effects of progesterone in lipopolysaccharide-stimulated bv-2 microglia. *PloS One*. (2014) 9:e103969. doi: 10.1371/journal.pone.0103969

46. Zöllner J, Howe LG, Edey LF, O'Dea KP, Takata M, Leiper J, et al. Lps-induced hypotension in pregnancy: the effect of progesterone supplementation. *Shock*. (2020) 53:199–207. doi: 10.1097/shk.0000000000001343

47. Aksoy AN, Toker A, Celık M, Aksoy M, Halıcı Z, Aksoy H. The effect of progesterone on systemic inflammation and oxidative stress in the rat model of sepsis. *Indian J Pharmacol*. (2014) 46:622–6. doi: 10.4103/0253-7613.144922

48. Yuan L, Zhu H, Wu K, Zhou M, Ma J, Chen R, et al. Female sex hormone, progesterone, ameliorates the severity of sars-cov-2-caused pneumonia in the Syrian hamster model. *Signal Transduct Target Ther*. (2022) 7:47. doi: 10.1038/s41392-021-00860-5

49. Ghandehari S, Matusov Y, Pepkowitz S, Stein D, Kaderi T, Narayanan D, et al. Progesterone in addition to standard of care vs standard of care alone in the treatment of men hospitalized with moderate to severe covid-19: A randomized, controlled pilot trial. *Chest*. (2021) 160:74–84. doi: 10.1016/j.chest.2021.02.024

50. Tayel SS, Helmy AA, Ahmed R, Esmat G, Hamdi N, Abdelaziz AI. Progesterone suppresses interferon signaling by repressing tlr-7 and mxa expression in peripheral blood mononuclear cells of patients infected with hepatitis C virus. *Arch Virol*. (2013) 158:1755–64. doi: 10.1007/s00705-013-1673-z

51. Cohen J. Siv transmission. Monkey study prompts high-level public health response. *Science*. (1996) 272:805. doi: 10.1126/science.272.5263.805

52. Kaushic C, Ashkar AA, Reid LA, Rosenthal KL. Progesterone increases susceptibility and decreases immune responses to genital herpes infection. *J Virol*. (2003) 77:4558–65. doi: 10.1128/jvi.77.8.4558-4565.2003

53. Mingjia L, Short R. How oestrogen or progesterone might change a woman's susceptibility to hiv-1 infection. *Aust N Z J Obstet Gynaecol*. (2002) 42:472–5. doi: 10.1111/j.0004-8666.2002.00472.x

54. Kurkov SV, Loftsson T. Cyclodextrins. *Int J Pharm*. (2013) 453:167–80. doi: 10.1016/j.ijpharm.2012.06.055

55. Liu FY, Kildsig DO, Mitra AK. Beta-cyclodextrin/steroid complexation: effect of steroid structure on association equilibria. *Pharm Res*. (1990) 7:869–73. doi: 10.1023/a:1015973218303

56. Cai W, Sun T, Liu P, Chipot C, Shao X. Inclusion mechanism of steroid drugs into beta-cyclodextrins. Insights from free energy calculations. *J Phys Chem B*. (2009) 113:7836–43. doi: 10.1021/jp901825w

57. Zoppetti G, Puppini N, Ospitali F, Fini A. Solid state characterization of progesterone in a freeze dried 1:2 progesterone/hpbcd mixture. *J Pharm Sci*. (2007) 96:1729–36. doi: 10.1002/jps.20671

58. Scavone C, Bonagura AC, Fiorentino S, Cimmaruta D, Cenami R, Torella M, et al. Efficacy and safety profile of diclofenac/cyclodextrin and progesterone/cyclodextrin formulations: A review of the literature data. *Drugs R D*. (2016) 16:129–40. doi: 10.1007/s40268-016-0123-2

59. Memişoğlu E, Bochot A, Sen M, Duchêne D, Hincal AA. Non-surfactant nanospheres of progesterone inclusion complexes with amphiphilic beta-cyclodextrins. *Int J Pharm*. (2003) 251:143–53. doi: 10.1016/s0378-5173(02)00593-8

60. Mu K, Jiang K, Wang Y, Zhao Z, Cang S, Bi K, et al. The biological fate of pharmaceutical excipient B-cyclodextrin: pharmacokinetics, tissue distribution, excretion, and metabolism of B-cyclodextrin in rats. *Molecules*. (2022) 27. doi: 10.3390/molecules27031138

61. Loftsson T, Moya-Ortega MD, Alvarez-Lorenzo C, Concheiro A. Pharmacokinetics of cyclodextrins and drugs after oral and parenteral administration of drug/cyclodextrin complexes. *J Pharm Pharmacol*. (2016) 68:544–55. doi: 10.1111/jphp.12427

62. Osuchowski MF, Welch K, Siddiqui J, Remick DG. Circulating cytokine/inhibitor profiles reshape the understanding of the sirs/cars continuum in sepsis and predict mortality. *J Immunol*. (2006) 177:1967–74. doi: 10.4049/jimmunol.177.3.1967

63. Bozza FA, Salluh JI, Japiassu AM, Soares M, Assis EF, Gomes RN, et al. Cytokine profiles as markers of disease severity in sepsis: A multiplex analysis. *Crit Care*. (2007) 11:R49. doi: 10.1186/cc5783

64. Wartmann T, Mayerle J, Kahne T, Sahin-Toth M, Ruthenburger M, Matthias R, et al. Cathepsin L inactivates human trypsinogen, whereas cathepsin L-deletion reduces the severity of pancreatitis in mice. *Gastroenterology*. (2010) 138:726–37. doi: 10.1053/j.gastro.2009.10.048

65. Kitamoto S, Sukhova GK, Sun J, Yang M, Libby P, Love V, et al. Cathepsin L deficiency reduces diet-induced atherosclerosis in low-density lipoprotein receptor-knockout mice. *Circulation*. (2007) 115:2065–75. doi: 10.1161/CIRCULATIONAHA.107.688523

66. Cao Y, Liu X, Li Y, Lu Y, Zhong H, Jiang W, et al. Cathepsin L activity correlates with proteinuria in chronic kidney disease in humans. *Int Urol Nephrol*. (2017) 49:1409–17. doi: 10.1007/s11255-017-1626-7

67. Cai J, Zhong H, Wu J, Chen RF, Yang H, Al-Abed Y, et al. Cathepsin L promotes vascular intimal hyperplasia after arterial injury. *Mol Med*. (2017) 23:92–100. doi: 10.2119/molmed.2016.00222

68. Schurigt U, Eilenstein R, Gajda M, Leipner C, Sevenich L, Reinheckel T, et al. Decreased arthritis severity in cathepsin L-deficient mice is attributed to an impaired T helper cell compartment. *Inflammation Res*. (2012) 61:1021–9. doi: 10.1007/s00011-012-0495-x

69. Bauer C, Duewell P, Mayer C, Lehr HA, Fitzgerald KA, Dauer M, et al. Colitis induced in mice with dextran sulfate sodium (Dss) is mediated by the nlrp3 inflammasome. *Gut*. (2010) 59:1192–9. doi: 10.1136/gut.2009.197822

70. Wali B, Ishrat T, Won S, Stein DG, Sayeed I. Progesterone in experimental permanent stroke: A dose-response and therapeutic time-window study. *Brain*. (2014) 137:486–502. doi: 10.1093/brain/awt319

71. Yousuf S, Atif F, Sayeed I, Tang H, Stein DG. Progesterone in transient ischemic stroke: A dose-response study. *Psychopharmacol (Berl)*. (2014) 231:3313–23. doi: 10.1007/s00213-014-3556-8

72. Stelzl D, Nielsen TT, Hansen T, di Cagno M. B-cd-dextran polymer for efficient sequestration of cholesterol from phospholipid bilayers: mechanistic and safe-toxicity investigations. *Int J Pharm*. (2015) 496:896–902. doi: 10.1016/j.ijpharm.2015.10.041

73. Kiss T, Fenyvesi F, Bácskay I, Váradi J, Fenyvesi E, Iványi R, et al. Evaluation of the cytotoxicity of beta-cyclodextrin derivatives: evidence for the role of cholesterol extraction. *Eur J Pharm Sci*. (2010) 40:376–80. doi: 10.1016/j.ejps.2010.04.014

74. Horlock AD, Ormsby TJR, Clift MJD, Santos JEP, Bromfield JJ, Sheldon IM. Cholesterol supports bovine granulosa cell inflammatory responses to lipopolysaccharide. *Reproduction*. (2022) 164:109–23. doi: 10.1530/rep-22-0032

75. Houben T, Yadati T, de Kruijf R, Gijbels MJJ, Luiken J, van Zandvoort M, et al. Pro-inflammatory implications of 2-hydroxypropyl-B-cyclodextrin treatment. *Front Immunol*. (2021) 12:716357. doi: 10.3389/fimmu.2021.716357

frontiers | Frontiers in Immunology

TYPE Original Research
PUBLISHED 15 March 2024
DOI 10.3389/fimmu.2024.1365206

OPEN ACCESS

EDITED BY
Madhav Bhatia,
University of Otago, New Zealand

REVIEWED BY
Hua Ren,
East China Normal University, China
Veeresh Kumar Sali,
The University of Iowa, United States

*CORRESPONDENCE
Gang Li
gang.lihndx@163.com
Pengxiang Guo
gpxtcm@163.com

†These authors have contributed equally to this work and share first authorship

RECEIVED 03 January 2024
ACCEPTED 29 February 2024
PUBLISHED 15 March 2024

CITATION
Li G, Yan K, Zhang W, Pan H and Guo P (2024) ARDS and aging: TYMS emerges as a promising biomarker and therapeutic target. *Front. Immunol.* 15:1365206. doi: 10.3389/fimmu.2024.1365206

ARDS and aging: TYMS emerges as a promising biomarker and therapeutic target

Gang Li[1*†], Ke Yan[2†], Wanyi Zhang[1], Haiyan Pan[1] and Pengxiang Guo[3*]

[1]Department of Emergency Medicine, The Third Affiliated Hospital of Zhejiang Chinese Medical University, Hangzhou, Zhejiang, China, [2]School of Life Sciences, Beijing University of Chinese Medicine, Beijing, China, [3]Department of Pharmacology of Chinese Materia Medica, School of Traditional Chinese Pharmacy, China Pharmaceutical University, Nanjing, China

Background: Acute Respiratory Distress Syndrome (ARDS) is a common condition in the intensive care unit (ICU) with a high mortality rate, yet the diagnosis rate remains low. Recent studies have increasingly highlighted the role of aging in the occurrence and progression of ARDS. This study is committed to investigating the pathogenic mechanisms of cellular and genetic changes in elderly ARDS patients, providing theoretical support for the precise treatment of ARDS.

Methods: Gene expression profiles for control and ARDS samples were obtained from the Gene Expression Omnibus (GEO) database, while aging-related genes (ARGs) were sourced from the Human Aging Genomic Resources (HAGR) database. Differentially expressed genes (DEGs) were subjected to functional enrichment analysis to understand their roles in ARDS and aging. The Weighted Gene Co-expression Network Analysis (WGCNA) and machine learning pinpointed key modules and marker genes, with ROC curves illustrating their significance. The expression of four ARDS-ARDEGs was validated in lung samples from aged mice with ARDS using qRT-PCR. Gene set enrichment analysis (GSEA) investigated the signaling pathways and immune cell infiltration associated with TYMS expression. Single-nucleus RNA sequencing (snRNA-Seq) explored gene-level differences among cells to investigate intercellular communication during ARDS onset and progression.

Results: ARDEGs are involved in cellular responses to DNA damage stimuli, inflammatory reactions, and cellular senescence pathways. The MEmagenta module exhibited a significant correlation with elderly ARDS patients. The LASSO, RRF, and XGBoost algorithms were employed to screen for signature genes, including CKAP2, P2RY14, RBP2, and TYMS. Further validation emphasized the potential role of TYMS in the onset and progression of ARDS. Immune cell infiltration indicated differential proportion and correlations with TYMS expression. SnRNA-Seq and cell-cell communication analysis revealed that TYMS is highly expressed in endothelial cells, and the SEMA3 signaling pathway primarily mediates cell communication between endothelial cells and other cells.

Conclusion: Endothelial cell damage associated with aging could contribute to ARDS progression by triggering inflammation. TYMS emerges as a promising diagnostic biomarker and potential therapeutic target for ARDS.

KEYWORDS

ARDS, aging, TYMS, WGCNA, machine learning, immune infiltration, snRNA-seq

1 Introduction

Acute Respiratory Distress Syndrome (ARDS) represents a life-threatening manifestation of severe respiratory failure that can occur in any condition or disease that causes lung injury (1). The pathological changes in ARDS are characterized by diffuse alveolar damage, including damage to alveolar epithelial and pulmonary capillary endothelial cells, inflammation and infiltration of immune cells, widening of interstitial edema, protein-rich edema fluid in the alveoli, fibrous protein deposition, formation of transparent membranes, and microthrombosis (2). These changes lead to dysregulation of the ventilation/perfusion (V/Q) ratio, impaired gas exchange, a significant increase in intrapulmonary shunting, decreased lung compliance, reduced lung volume (baby lung), and ultimately acute hypoxemic respiratory failure (3). The mortality rate of ARDS is as high as 40% (4), making it one of the main reasons for patients to be transferred to the ICU (5). Based on statistics, the incidence rate of ARDS is several tens of cases per 100,000 person-years (6). Numerous studies have shown that elderly patients account for a high proportion of ARDS patients, and age is a significant risk factor affecting the development and prognosis of ARDS (7). Currently, the diagnosis of ARDS mainly relies on clinical manifestations, but the problem of missed diagnosis and delayed diagnosis remains unresolved. Therefore, studying the molecular biological mechanisms of ARDS and identifying potential biomarkers is of great significance for early recognition, diagnosis, and assessment of the severity and prognosis of ARDS.

Increasing evidence suggests that the pathogenesis of ARDS involves multiple biological functions, including inflammatory response (8), oxidative stress (9), apoptosis (10, 11), and endoplasmic reticulum autophagy (12). Amidst these factors, aging is pivotal in the genesis and advancement of ARDS. Aging is a complex and multidimensional process that leads to widespread organ dysfunction (13) and various age-related diseases (14), such as neurodegenerative disorders, diabetes, idiopathic pulmonary fibrosis, etc. (15). DNA damage serves as a primary catalyst for aging, whereas DNA repair acts as a pivotal determinant of aging. Additionally, deficiencies in DNA repair can accelerate the progression of various age-related diseases (16). Lung aging is associated with molecular and physiological changes that result in altered lung function, impaired lung remodeling and regeneration, and increased susceptibility to acute and chronic lung diseases (17). Older patients with sepsis have worse outcomes, which may be related to the decline in immune system function and changes in the pulmonary vascular system in the elderly (18, 19). Immune cell activation is a major mediator of ARDS inflammation, and immunosenescence may affect the pathogenesis and prognosis of elderly ARDS subgroups (20). A cross-age study of ARDS patients showed a correlation between age and neutrophil biomarker myeloperoxidase (MPO) in bronchoalveolar lavage fluid (BALF) (21). Compared with younger groups, Tregs and inflammatory markers increased in older groups (22). Aging is implicated in various pathways of ARDS pathogenesis, yet the precise mechanisms remain elusive. Therefore, further research is needed to understand the relationship between cellular aging, immune infiltration landscape, and their interplay in the context of ARDS disease.

Over the past decade, high-throughput sequencing has experienced rapid development and has permeated various fields of life sciences, significantly advancing the progress of basic medical research (23). GSE163426 is a dataset related to ARDS, containing a large number of samples (47 ARDS patients and five control individuals). In this study, we used various bioinformatics methods to obtain age-related characteristic genes for ARDS. Four hub ARDS-ARDEG genes demonstrated significant diagnostic performance and were validated in external datasets. Additionally, we corroborated the expression levels of the selected genes through animal experiments. Thymidylate Synthetase (TYMS) was identified as a promising diagnostic biomarker for ARDS in aging individuals. We assessed the enriched signaling pathways associated with TYMS expression and involvement in immune cell infiltration. Single-nucleus RNA sequencing highlighted elevated TYMS expression in endothelial cells, indicating its potential role in endothelial dysfunction seen in ARDS. These findings highlight TYMS's multifaceted involvement, particularly its modulation of immune responses and contribution to endothelial proliferation and vascular injury repair, presenting TYMS as a potential therapeutic target for precise intervention in ARDS among the elderly ICU population.

2 Materials and methods

2.1 Data sources

In our study, we acquired two bulk RNA sequencing (bulk-RNAseq) datasets, specifically GSE163426 and GSE84439, from the GEO database. The GSE163426 dataset was utilized as the training

set, encompassing 47 ARDS patients and five control individuals. The validation group, comprising seven sepsis patients and 8 ARDS patients, was derived from the GSE84439 dataset. Additionally, we utilized publicly available single-nucleus RNA sequencing (snRNA-Seq) data obtained from autopsy lung tissues of 19 COVID-19 patients and seven healthy donors. These data, including the corresponding clinical information, can be accessed at the GEO database using the accession number GSE171524.

2.2 Downloading and organizing aging-related genes

In order to identify ARGs for our study, we downloaded data from the HAGR database (https://genomics.senescence.info/) (24). This database comprises the GenAge dataset (307 genes) and the CellAge dataset (949 genes). After combining these datasets and eliminating duplicate genes, we obtained 1256 ARGs for subsequent analysis.

2.3 Identification of aging-related DEGs

To identify ARDEGs, we utilized the R package limma for differential analysis (25). The filtering criteria were set as $|logFC|>1$ and $P<0.05$. This analysis was performed on the ARDS and control samples. The intersection of the DEGs with the ARGs resulted in the identification of ARDEGs.

2.4 Construction of PPI network

Using the Search Tool for the Retrieval of Interacting Genes (STRING) database, we constructed a protein-protein interaction (PPI) network for evaluating the gene interactions among ARDEGs (26).

2.5 Functional and pathway enrichment analysis

The Kyoto Encyclopedia of Genes and Genomes (KEGG) and Gene Ontology (GO) were used in the functional enrichment analysis of ARDEGs (27). The GO analysis involved exploring the biological processes (BP), cellular components (CC), and molecular functions (MF) associated with these ARDEGs.

2.6 Weighted gene co-expression network analysis

The WGCNA analysis was conducted to construct a co-expression network in the GSE163426 dataset, utilizing the scale-free topology criterion (28). The dynamic tree-cutting method with a minimum module size of 30 was used to identify co-expressed gene modules. Gene significance (GS) values and module membership (MM) values were employed to assess the association between gene modules and both ARDS and aging, ultimately determining the key modules.

2.7 Identification of hub ARDS-ARDEGs

The least absolute shrinkage and selection operator (LASSO), Random Forest (RF), and Extreme Gradient Boosting (XGBoost) algorithms were employed as the methods for screening and identifying key ARDS-ARDEGs. LASSO analysis was performed with the glmnet program, and 10-fold cross-validation was used to assess the penalty parameter (29). This approach outperforms traditional regression analysis methods in the assessment of high-dimensional data. XGBoost, a machine learning algorithm based on gradient boosting trees, was employed to assess the importance of ARDEGs in both ARDS and aging (30). The R package XGBoost aided in determining the significance of models constructed with various sets of ARDEGs. The random forest algorithm with recursive feature elimination (RFE) is a supervised machine learning method (31). The RFE approach was conducted by setting the number of decision trees to 500 and identifying aging-associated signature genes with relative importance greater than one. The intersection of aging-associated signature genes obtained through three machine learning filters using the R package Venn was defined as hub ARDS-ARDEGs. To assess the diagnostic utility of hub ARDS-ARDEGs in aging ARDS patients, the receiver operating characteristic curve (ROC) analysis was performed on the GSE1919 and GSE89408 datasets.

2.8 Experimental animals

This study was conducted in accordance with ethical guidelines and received ethical approval from the Ethics Committee of Hangzhou Hibio Technology Co., Ltd. (HB2311003). C57BL/6 mice, including males and females, were procured from Jiangsu Jiangsu Huachuang sino Pharma Tech Co., Ltd. The study utilized young mice (3 months old) and aged mice (18 months old). The ARDS mouse model was induced by intraperitoneal injection of lipopolysaccharide (LPS) (Sigma-Aldrich) at 5mg/kg for young mice and 2.5mg/kg for aged mice. Following 72 hours of LPS administration, the mice were euthanized, and lung tissues were collected for subsequent analysis.

2.9 Histopathological observation of lung tissue

Lung tissue was collected from the middle lobe of the right lung in mice. Following alcohol dehydration, paraffin embedding, and sectioning, the samples were stained with H&E and subsequently examined under an optical microscope to evaluate the extent of lung tissue damage. The freshly removed lung tissue from the left lobe was weighed using an analytical scale to obtain the wet weight (W). The tissue was then dried in an oven until a consistent weight was

reached to calculate the dry weight (D). To determine the degree of pulmonary edema, the formula W/D × 100% was applied to obtain the wet-to-dry weight ratio.

2.10 Quantitative real-time PCR

Reverse transcription of total RNA into complementary DNA (cDNA) was performed using the TOROBlue® qPCR RT Kit after RNA extraction from the upper lobe of the right lung was performed using Trizol (Vazyme). TOROGreen®qPCR Master Mix was used for qRT-PCR. The primer sequences for hub ARDS-ARDEGs are presented in Table S9 of the Supplementary Materials. Internal reference gene GAPDH was employed. Each group included six biological samples.

2.11 Analysis of SnRNA-seq data

The raw matrix in each dataset was normalized using the "LogNormalize" function in Seurat (version 4.3.1) (32). The "RunHarmony" function in the "harmony" package was utilized to reduce the batch effect (33). The "FindVariableFeatures" function was employed to select the top 2000 most variable genes as input data. Principal component analysis was used to determine the 19 best principal components for data integration. Following the acquisition of principal components, several cell types were distinguished using established cell-specific markers, and uniform manifold approximation and projection were utilized to view the cells.

2.12 Cell–cell communication analysis

Based on ligand-receptor interactions, cell-cell communication between several cell clusters was inferred and visualized using the R software's "CellChat" package (34). The "CellChat" tool was used to import the snRNA-seq data that had been normalized using the "Seurat" package. We focused on the secreted signaling pathways and analyzed the communication between all cell types. Moreover, endothelial cells acted as signal senders and receivers in our particular analysis and visualization of the communication between these cells and other cell types.

2.13 Statistical analysis

R software (version 4.3.1) was used to conduct statistical analysis. Two groups were compared using Wilcoxon tests. The association between immune cell infiltration and hub ARDS-ARDEGs expression levels was examined using Spearman correlation analysis. A statistical significance threshold of $P < 0.05$ was applied. The mean ± standard deviation of a minimum of six independent experiments was used to present the statistical analysis of the qRT-PCR data, and unpaired two-tailed Student's t-tests were employed to evaluate differences ($^{*}P < 0.05$; $^{**}P < 0.01$; $^{***}P < 0.001$). For statistical significance, a *P*-value of less than 0.05 was used.

3 Results

3.1 Identification of ARGEGs

The study's procedural diagram is depicted in Figure 1. A total of 2448 DEGs between control and ARDS tracheal aspirates were identified, with 1312 genes up-regulated and 1136 genes down-regulated (Figure 2A). 134 ARDEGs were obtained by the intersection of ARGs and DEGs (Figure 2B; Supplementary Table S1). Using the R program limma, expression matrices of ARGs were taken out of the training set, and their differences were examined. A gene expression heat map was created to see the top 50 genes with the most significant differences (Figure 2C). A close association between ARDEGs at the protein level was found by the PPI protein network analysis (Figure 2D; Supplementary Table S2).

3.2 Functional enrichment analysis of ARDEGs

To understand the potential mechanisms of ARDEGs in ARDS and aging, we employed the R package clusterProfiler to perform GO and KEGG enrichment studies on ARDEGs (Supplementary Tables S3, 4). The GO enrichment analysis in BP showed that the first five ARDEG enrichments were primarily associated with protein phosphorylation, cellular response to DNA damage stimulus, negative regulation of apoptotic process, peptidyl-threonine phosphorylation, and positive regulation of transcription from RNA polymerase II promoter (Figure 3A). The top 20 enriched elements in MF and CC are shown in Figures 3B, C. Furthermore, these ARDEGs were considerably enriched in Cellular senescence, Cell cycle, FoxO signaling pathway, Longevity regulating pathway, and Autophagy (Figure 3D).

3.3 Construction of the weighted gene co-expression network

The R package WGCNA was employed for co-expression network construction, utilizing the variance in gene expression of the initial 75% of genes as a screening criterion. A total of 13,906 genes were encompassed in this network assembly. The determination of the soft threshold power at 12 yielded a scale-free index of 0.85, along with notably favorable mean connectivity, enabling the establishment of a scale-free network (Figures 4A, B). Following this, cluster analysis was conducted to identify highly analogous modules, resulting in the display of the cluster dendrogram (Figure 4C). The correlation among these modules was calculated (Figure 4D). The findings revealed a notable correlation between the MEmagenta module and ARDS (cor=0.34; p=0.01), as well as aging (co=-0.34; p=0.01) (Figure 4E; Supplementary Table S5). Moreover, a significant correlation

10.3389/fimmu.2024.1365206

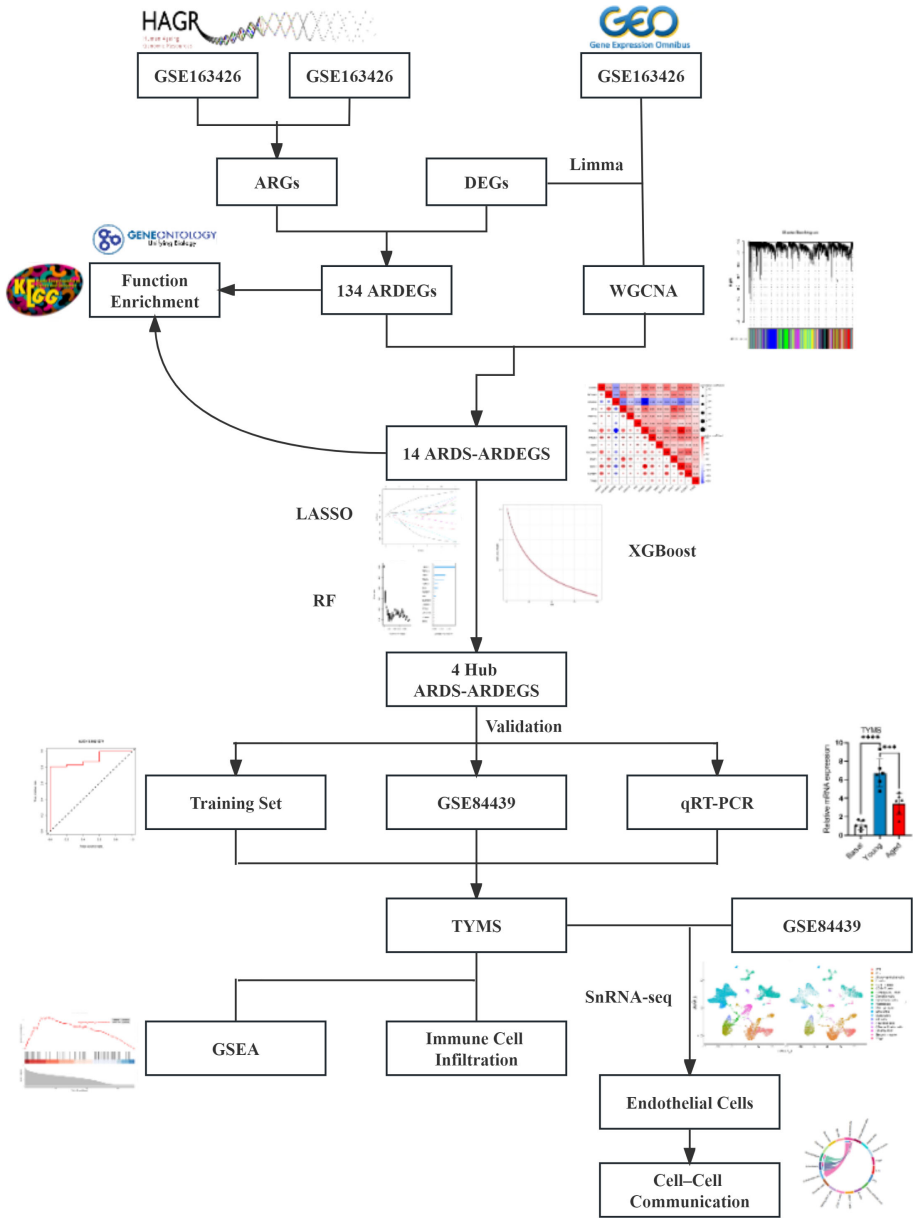

FIGURE 1
The flowchart outlining the methodology of this investigation.

between MM and GS for ARDS within the magenta module (cor=0.3; p=3.8e-14) was observed, as well as aging (co=0.39; p=1.4e-23) (Figures 4F, G). The genes in the magenta module were selected as the candidate genes and compared with ARDEGs, resulting in the identification of 14 genes that were both in the magenta module and associated with ARDS and aging (Figure 4H).

3.4 Correlation and enrichment analysis of ARDS-ARDEGs

We used the Pearson correlation coefficient to assess the relationship between the ARDS-ARDEGs. PSMA2 exhibited a high correlation with TTBPL1 (cor=0.84) (Figure 5A). The KEGG pathway enrichment analysis demonstrated that the top ten enriched pathways associated with ARDS-ARDEGs were primarily involved in Spinocerebellar ataxia, Proteasome, Measles, Hepatitis C, Necroptosis, Influenza A, and the NOD-like receptor signaling pathway (Figure 5B; Supplementary Table S6). According to the GO enrichment analysis, ARDS-ARDEGs are enriched in BP, including the regulation of hematopoietic stem cell differentiation, deoxyribose phosphate biosynthetic process, negative regulation of G2/M transition of the mitotic cell cycle, regulation of the innate immune response, and deoxyribonucleotide biosynthetic process (Figures 5C, D; Supplementary Table S7). The map illustrating the interactions among BP was subsequently constructed (Figure 5E).

10.3389/fimmu.2024.1365206

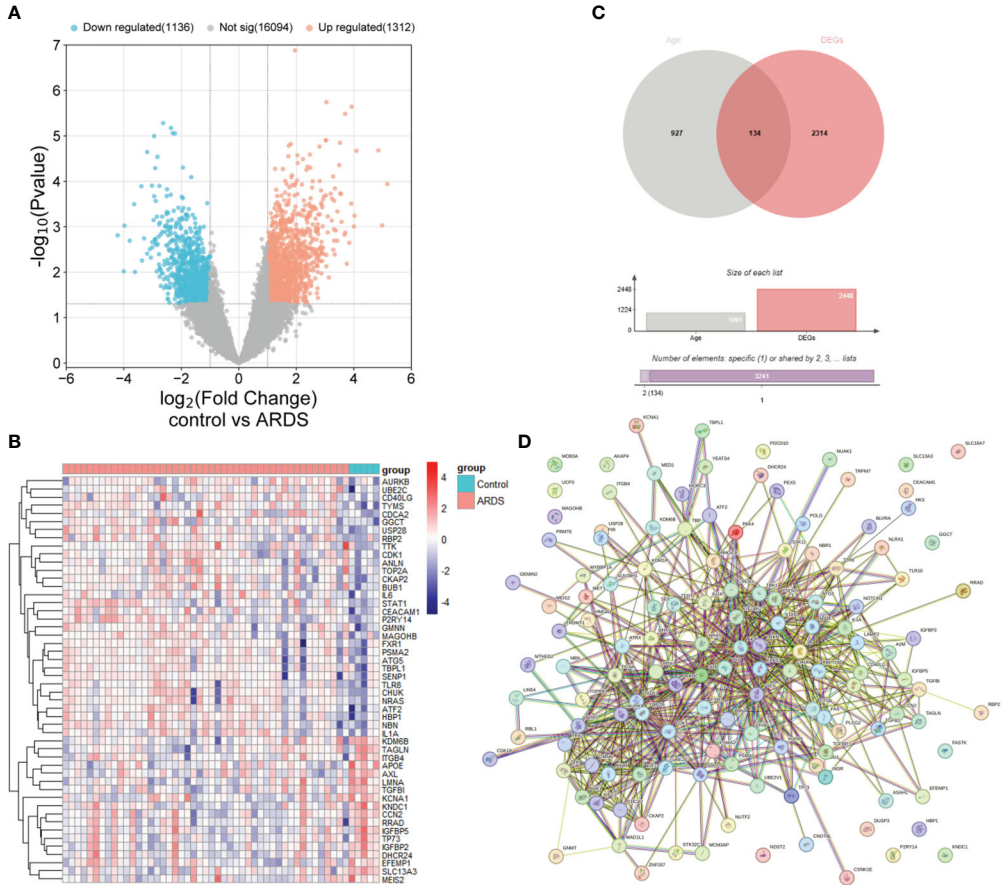

FIGURE 2
Identification of ARDEGs between control and ARDS. **(A)** The differential gene expression between the control and ARDS groups is displayed using a volcano plot. **(B)** A Venn diagram illustrates the overlap between ARGs and DEGs in the ARDS and control groups. **(C)** A heatmap is presented illustrating the expression patterns of the 50 most significant ARDEGs, based on the smallest *p*-values, in both the control and ARDS groups. **(D)** An interaction network map shows protein interactions among the 134 ARDEGs.

3.5 Identification of hub ARDS-ARDEGs via machine learning

Three machine learning algorithms were used to screen hub ARDS-ARDEGs in order to identify signature genes in the elderly population with ARDS: LASSO (Figures 6A, B), RF (Figures 6C, D), and XGBoost (Figure 6E). Following the integration of the outcomes from the three algorithms, we ultimately identified four hub genes: CKAP2, P2RY14, RBP2, and TYMS (Figure 6F; Supplementary Table S8).

3.6 Diagnostic efficacy of hub ARDS-ARDEGs

The ROC analysis revealed that the four hubs ARDS-ARDEG had high diagnostic values in the training set. The area under the curve (AUC) of ROC for these signature genes was observed as follows: 0.902 for CKAP2, 0.843 for P2RY14, 0.770 for RBP2, and 0.834 for TYMS (Figures 7A–D). Furthermore, the screened signature genes demonstrated higher expression levels in individuals with ARDS than those in the healthy control group, indicating a potential role of these genes in the pathogenesis of ARDS (Figures 7E–H). Subsequently, a correlation analysis was conducted between patient age and the expression of hub ARDS-ARDEGs (Figures 7I–L). As patient age increased, the expression of these genes decreased, with TYMS demonstrating the strongest correlation with the aging process.

In addition, the diagnostic efficacy of each signature gene in predicting ARDS was evaluated in an external validation cohort. By GSE84439, the AUC values of ROC for CKAP2, P2RY14, RBP2, and TYMS were 0.411, 0.321, 0.607, and 0.821, respectively (Figures 8A–D). In comparison to sepsis patients, only TYMS demonstrated significant changes in expression among these characteristic genes in ARDS patients, indicating a remarkable upregulation (Figures 8E–H). These observations indicate that TYMS exhibits superior diagnostic efficiency for ARDS, irrespective of whether it is used to distinguish elderly ARDS patients or differentiate sepsis patients.

3.7 Aging inhibited TYMS induction in mice after ARDS modeling

The murine model of ARDS was established by administering LPS to both aged (18 months) and young (3 months) mice. Despite

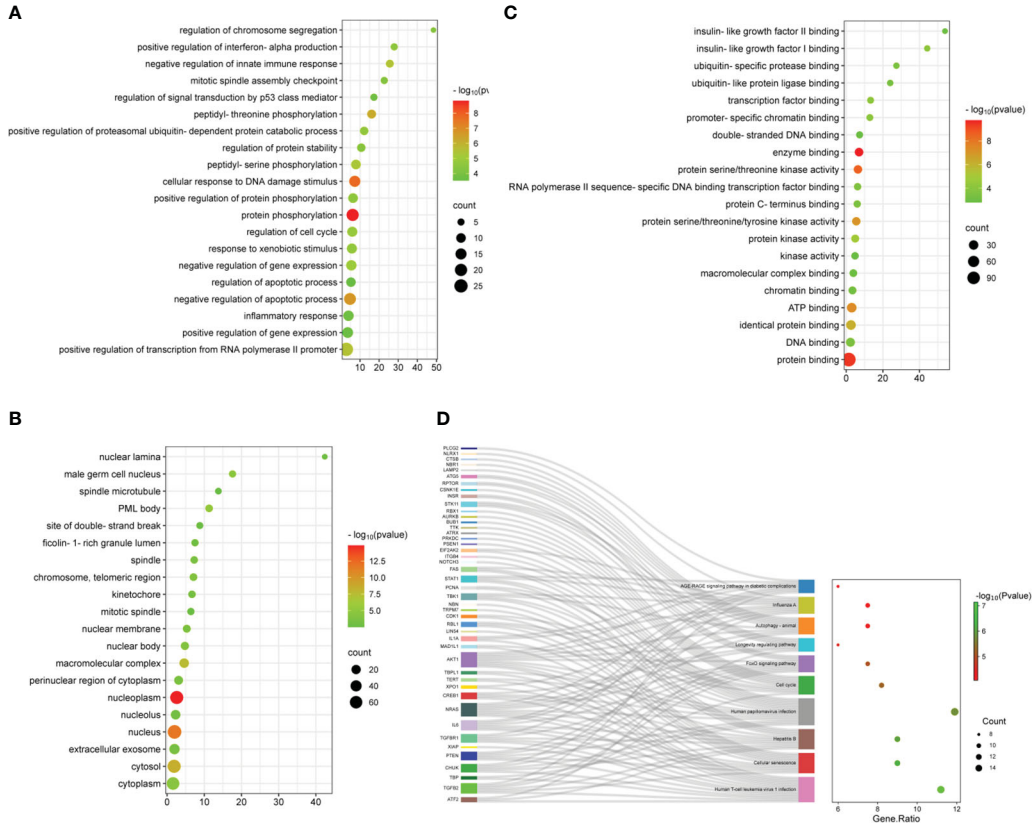

FIGURE 3
Functional enrichment analysis of ARDEGs. **(A)** Depicted are the outcomes of GO enrichment analysis for BP, **(B)** CC, and **(C)** MF. The bubble plot illustrates the top 20 significantly enriched functions, with bubble size representing the number of DEGs (larger circles indicate more DEGs) and color representing the adjusted *p*-value (redder colors indicate smaller *p*-values). **(D)** KEGG enrichment analysis results are visualized in a Sankey dot pathway enrichment plot, displaying the top 10 significantly enriched pathways.

being challenged with a lower dose of LPS (2.5 mg/kg) compared to young adult mice (5 mg/kg), aged mice exhibited more severe lung injury (Figures 9A, B). At 72 hours after LPS administration, aged mice exhibited lung edema, a condition not observed in young adult mice (Figure 9C). To confirm the mRNA expression levels of hub ARDS-ARDEGs, qRT-PCR was performed on total mRNA extracted from lung tissues (Figures 9D–G). After ARDS modeling, the expression of characteristic genes CKAP2, P2RY14, RBP2, and TYMS was significantly altered. Notably, there was a significant disparity in TYMS expression between the young and aged mice after modeling. The findings demonstrated that the four characteristic genes were strongly activated following the onset of ARDS, whereas aging inhibited the proper induction of TYMS expression in the progression of ARDS.

3.8 Difference analysis and GSEA analysis of TYMS grouping

Based on the median TYMS value and a significant threshold of "$P<0.05$" and "$|\log2FC|>1$," tracheal aspirate samples from ARDS patients in the GSE163426 dataset were classified into two groups: a high-expression group and a low-expression group. As a result, 582 genes exhibited up-regulation, and 544 genes displayed down-regulation (Figure 10A). The heat map depicted the top 30 DEGs (Figure 10B). To evaluate the signaling pathways linked to TYMS, GSEA analysis was conducted (Figures 10C–H). The findings demonstrated a significant correlation between TYMS and the regulation of immune system processes, defense response, negative regulation of alpha-beta T cell activation, blood vessel morphogenesis, regulation of cell population proliferation, and negative regulation of inflammatory response.

3.9 Evaluation and analysis of immune cell infiltration

The single-sample gene set enrichment analysis (ssGSEA) algorithm was employed to analyze immune cell infiltration, aiming to discern immunological features (Supplementary Table S10). In ARDS samples, the infiltration levels of Activated CD4 T cells, Activated CD8 T cells, and Effector memory CD4 T cells were significantly increased compared to the healthy control. Conversely, the infiltration of $CD56^{dim}$ natural killer cells and Natural killer cells in ARDS samples was significantly reduced (Figure 11A). Following this, a correlation analysis was conducted, linking the expression of hub genes with immune cell infiltration in ARDS patients (Figure 11B). Notably, a strong correlation exists between TYMS expression and the infiltration of various immune cells. Subsequent

10.3389/fimmu.2024.1365206

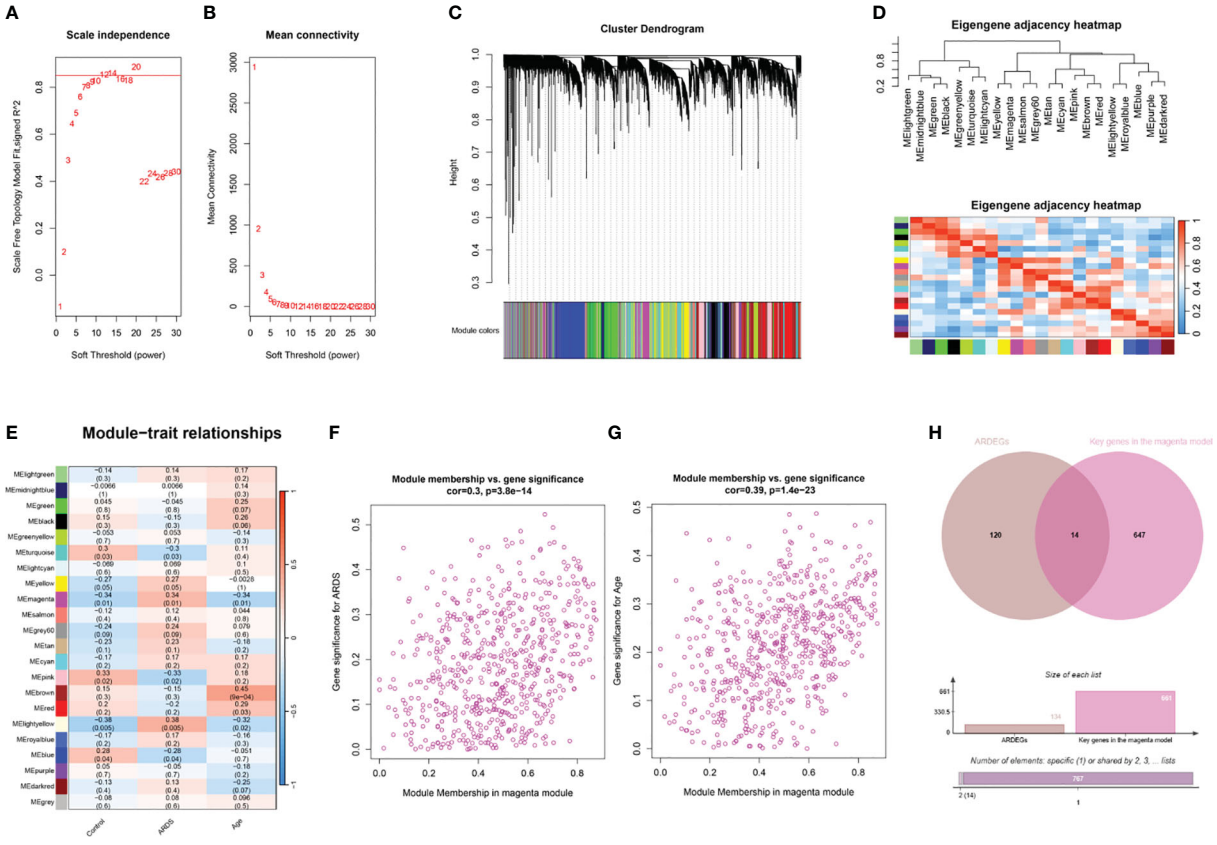

FIGURE 4
WGCNA analysis and identification of ARDS-ARDEGs in GSE163426. **(A)** The soft thresholding power of WGCNA is shown. **(B)** The average connectivity of WGCNA is displayed. **(C)** The top 75% of the gene clustering tree's variance is displayed, with each gene represented by a branch and a co-expression module by a color underneath. **(D)** The association of feature genes between modules is displayed on a heatmap. **(E)** A heatmap illustrating the correlations between the modules and traits is displayed; each color corresponds to a co-expression module, and the numbers indicate the *p*-values and module-trait correlation coefficients. **(F)** The relationship between the ARDS GS and the magenta module's MM is displayed as a scatter plot. **(G)** A scatter plot illustrates the relationship between the magenta module's MM and aging GS. **(H)** The intersection of ARDEGs along with significant genes in the magenta module is shown in a Venn diagram.

analysis involved grouping individuals based on TYMS expression levels to explore the relationship between TYMS and immune cell proportion (Figure 11C). The analysis revealed a significant upregulation in the proportion of activated B cells, Memory B cells, and Type 2 T helper cells in the group exhibiting high TYMS expression.

Conversely, there was a distinct decrease in the proportion of $CD56^{dim}$ natural killer cells, Central memory CD4 T cells, and Immature dendritic cells. Figures 11D–I demonstrate the six correlations between TYMS and the immune cells. These findings indicate an association between TYMS and the regulation of immune responses, thereby enhancing the ability to resist pathogenic microorganisms and inhibiting excessive inflammatory responses.

3.10 Discrimination of cell source of TYMS at single-cell resolution

To investigate the cellular origin of TYMS, we acquired snRNA-Seq data, including data from autopsy lung tissues of approximately 116,000 nuclei taken from the lungs of nineteen individuals who died from COVID-19 and seven control individuals from GSE171524. Based on the clinical information of these 19 patients, it is evident that they were over 55 and presented with concomitant respiratory symptoms. Unsupervised analysis identified 19 distinct cell clusters (Figure 12A). These clusters were recognized as distinct cell types based on the expression levels of established markers: alveolar type I (AT1) cells, alveolar type II (AT2) cells, airway epithelial cells, B cells, $CD4^+$ T cells, $CD8^+$ T cells, cycling NK/T cells, dendritic cells, endothelial cells, fibroblasts, macrophages, mast cells, monocytes, NK cells, neuronal cells, other epithelial cells, plasma cells, smooth muscle cells, and Tregs. The disruption of alveolar epithelial and endothelial barriers was attributed to the loss of AT1 cells, AT2 cells, and endothelial cells and the proliferation of mononuclear/macrophage cells, fibroblast cells, and neuronal cells (Figure 12B). It was discovered that endothelial cells exhibited high TYMS expression (Figure 12C). Compared to the control group, patients with respiratory symptoms manifested a discernible upregulation in TYMS expression within endothelial cells (Figure 12D). The findings above indicate that TYMS is primarily expressed in endothelial cells, and moderate induction may contribute to endothelial regeneration and the

10.3389/fimmu.2024.1365206

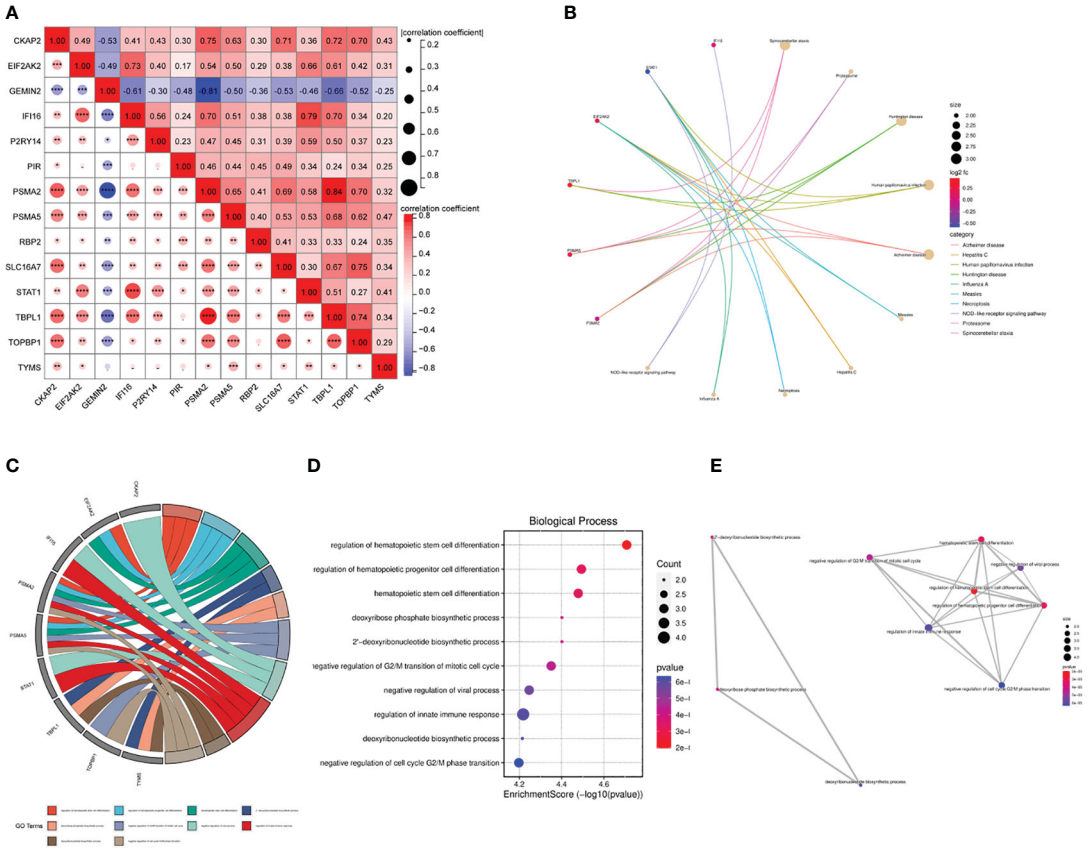

FIGURE 5
The correlation and enrichment analysis of ARDS-ARDEGs. **(A)** The ARDS-ARDEG correlation analysis is shown, with statistical significance denoted by *P<0.05, **P<0.01, and ***P<0.001. **(B)** A circular plot illustrates the top 10 entries for KEGG enrichment analysis of ARDS-ARDEGs. **(C)** A chord plot shows the top 10 BP entries for GO enrichment. **(D)** A bubble plot is presented, displaying the BP entries for GO enrichment. **(E)** A network plot indicates the BP entries associated with the ARDS-ARDEG analysis.

maintenance of endothelial barrier integrity, thereby reducing the infiltration of inflammatory cells and inhibiting the progression of ARDS.

3.11 Investigation of communication between endothelial cells and other cell types

In order to evaluate intercellular communication, expression levels of ligands and their matching receptors are examined. The results above indicate that TYMS is primarily expressed in endothelial cells and is associated with immune cell infiltration. To investigate intercellular communication further, we employed the "CellChat" software package for a comprehensive analysis. Circular plots were generated to visualize the secretion signals involved in intercellular communication across all cell types (Figures 13A, B). The analysis demonstrated that endothelial cells communicate with airway epithelial cells through the VISFATIN signaling pathways (Figure 13C). Moreover, endothelial cells primarily receive signals from AT1 cells, fibroblasts, smooth muscle cells, neuronal cells, fibroblasts, and macrophages (Figure 13D).

Furthermore, we conducted a ligand-receptor pair analysis that identified specific signaling interactions. Endothelial cells were found to preferentially send signals via the NAMPT - INSR pathway while receiving signals through the VEGFA - VEGFR1, IGF1 - IGF1R, ANGPT1 - TEK, SEMA3A - (NRP1+PLXNA2), SEMA3C - (NRP1+PLXNA2), and SEMA3D - (NRP1+PLXNA2) pathways (Figures 13E, F). Intercellular communication between endothelial cells and other cells is predominantly mediated by the SEMA3 signaling pathway, with endothelial cells serving as the primary receiver cells in this pathway (Figure 13G). The SEMA3 signaling pathway exerts a significant influence on the vascular system, contributing to the development and regeneration of blood vessels. Conclusively, these discoveries provide invaluable perspectives on the intercellular dialogue between endothelial cells and various cell types, shedding light on the distinct signaling pathways and molecules implicated in this intricate process.

4 Discussion

ARDS is a common and severe respiratory condition, particularly in the elderly (35). Extensive research has established a close association between ARDS and the patient's systemic or

10.3389/fimmu.2024.1365206

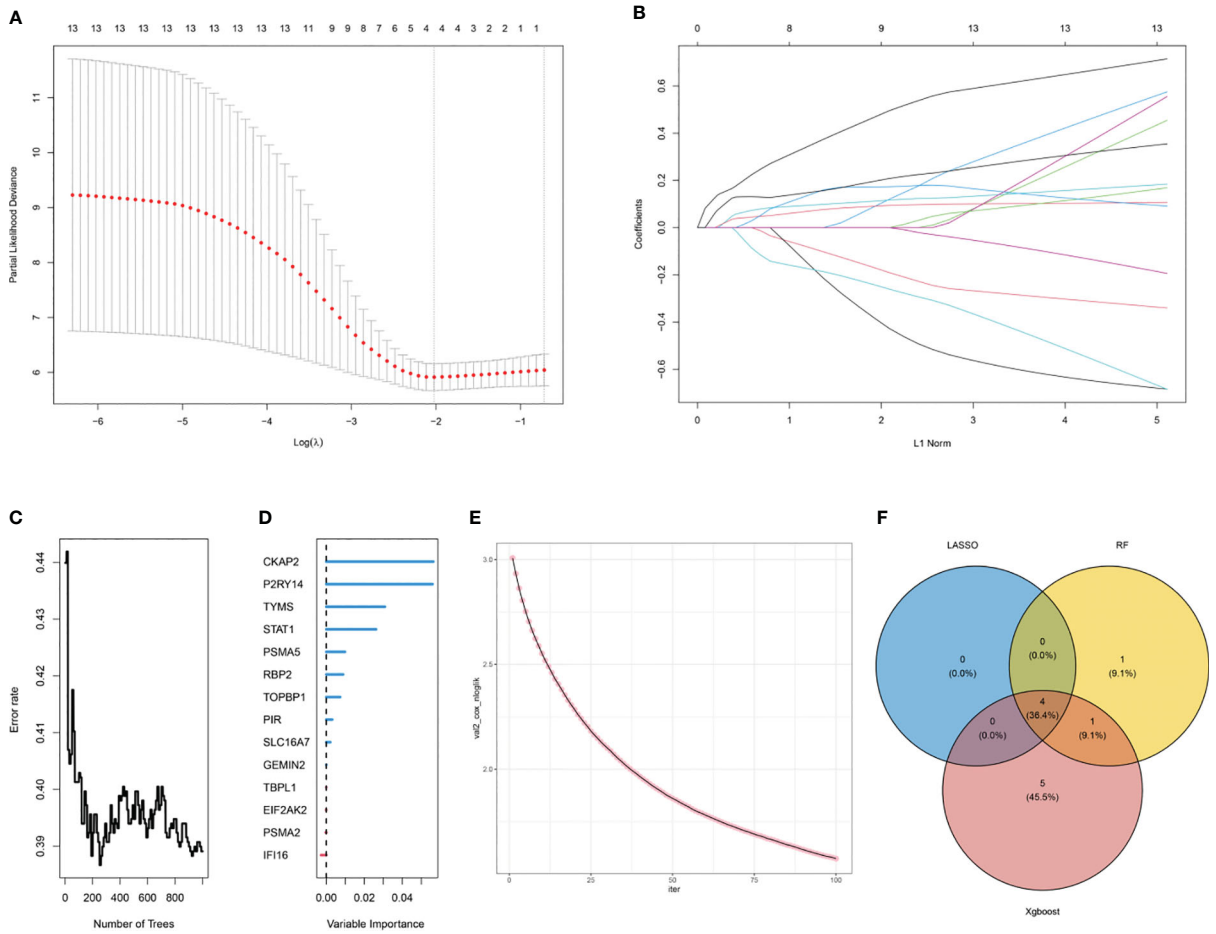

FIGURE 6
Selection of hub ARDS-ARDEGs using machine learning. **(A)** LASSO coefficient computation. The vertical dashed line shows the ideal lambda value. **(B)** Ten-fold cross-validation for LASSO model parameter adjustment. Every curve represents a gene. **(C)** The correlation between the mistake rate and the number of trees in the random forest. **(D)** Relative relevance ranking for ARDS-ARDEGs. **(E)** XGBoost modeling in the ARDS training set. **(F)** Venn diagram illustrating the intersection of genes selected as aging markers using LASSO, random forest, and XGBoost algorithms.

localized inflammatory response, with impairment of the pulmonary endothelial barrier function significantly contributing to lung injury and poor prognosis in sepsis and ARDS (36). Accumulating evidence also emphasizes the role of aging in this context, as ARDS incidence and mortality rates are increased in the elderly population (≥65 years old) (37). Research conducted by Soo Jung Cho et al. suggests that the susceptibility of the elderly to pulmonary diseases may be related to age-related changes in the composition and functionality of endothelial cells (11). Relevant studies have found elevated levels of ATP2B1 expression in ARDS patients, which is associated with endothelial barrier disruption (38). Aging impairs lung resident endothelial cell-mediated endothelial regeneration, leading to persistent inflammatory lung injury and high mortality rates (39). Aging exposes the immune system to sustained immune stressors and inflammatory assaults, contributing to immune senescence (40). These findings provide a solid basis to support the potential link between aging and immune regulation in ARDS.

With the current application of bioinformatics in the field of medicine, new avenues have opened up for scientific research on ARDS, allowing for the discovery of potential essential target genes. This study combines bioinformatics analysis with machine learning strategies to investigate the pathogenesis of ARDS from an aging perspective.

Through our analysis of normal and ARDS patient samples, we have identified 134 ARDEGs. Based on the results of GO and KEGG enrichment analyses, these ARDEGs are primarily involved in cellular responses to DNA damage stimuli, inflammatory reactions, negative regulation of innate immunity, and the FoxO signaling pathway and cellular senescence pathway. Our research highlights the involvement of these genes in inflammation response and aging. Increasing evidence supports the influence of aging on the occurrence of ARDS. For instance, elevated levels of reactive oxygen species production enzyme NADPH oxidase 4 in aging mice enhance endothelial cell permeability, impairing endothelial barrier function (41).

Additionally, KEGG pathway enrichment analysis indicates that these ARGs predominantly participate in the FoxO signaling pathway and lifespan regulation. FOXO transcription factors are crucial determinants of aging and longevity (42). Further research is needed to explore the hub ARDS-ARDEGs.

10.3389/fimmu.2024.1365206

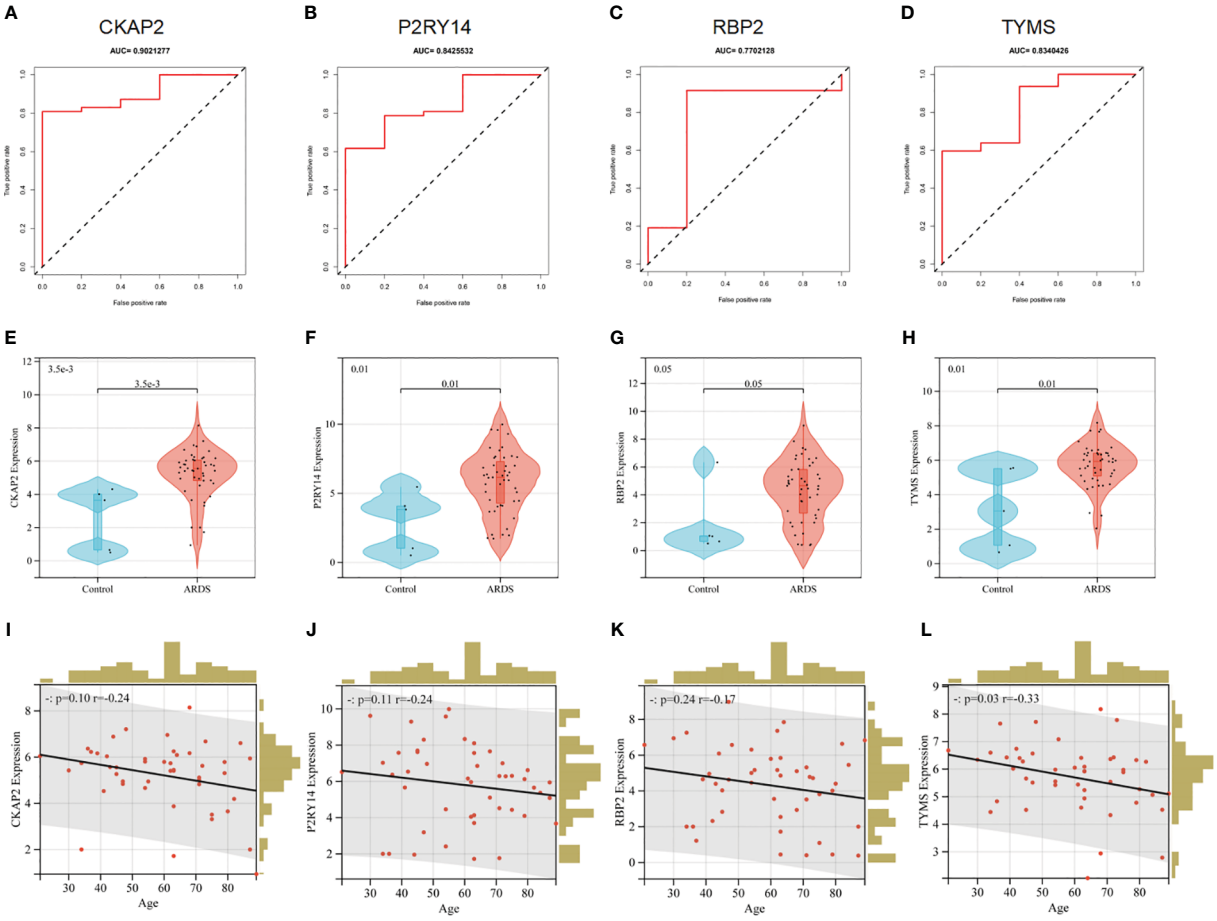

FIGURE 7
Performance of hub ARDS-ARDEGs in the GSE163426 dataset. **(A-D)** ROC curves demonstrate the chosen genes' diagnostic efficacy. The AUC is computed to assess the gene's diagnostic accuracy. **(E–H)** Violin plots show the differences in the expression levels of particular genes between the ARDS patient group and the control group. The control and ARDS patient groups are shown on the x-axis, while the gene expression values are represented on the y-axis. The width of the violin plot represents the density of gene expression values, with a broader plot indicating a higher expression density. **(I-L)** Relationship between the age of ARDS patients and the expression levels of the chosen genes. The x-axis represents the age of ARDS patients, and the y-axis represents the gene expression levels. Each point on the scatter plot represents an individual ARDS patient.

We identified four hub ARDS-ARDEGs (CKNP2, P2RY14, RBP2, and TYMS) using WGCNA analysis and three machine learning screenings (LASSO, RF, XGBoost). Our results indicated that four hub ARDS-ARDEGs were considerably elevated in samples from ARDS patients and had a robust diagnostic ability to predict ARDS.

CKAP2 (Cytoskeleton-associated protein 2, a crucial protein that controls cell proliferation), particularly during mitosis and cytokinesis (43). CKAP2 is up-regulated in a variety of malignant tumors and has diagnostic value in osteosarcoma (44), triple-negative breast cancer (45), gastric cancer, and other tumors (46). It has been reported that the CKAP2 gene plays a role in cell senescence (47), but its pathway needs to be confirmed by further studies. TYMS (Thymidylate synthase) is a gene that plays a crucial role in DNA replication and repair (48). Chen Y reported that the knockdown of TYMS resulted in reactive oxygen species generation, DNA damage, and cellular senescence (49). Restoring the expression and activity of FoxM1 may potentially enhance the functionality of endothelial cells and promote vascular neogenesis and repair (50). Additionally, as a downstream target of FoxM1, TYMS could be involved in the endothelial cell repair process (51). RBP2 (Retinoblastoma binding protein 2) facilitates the uptake, absorption, and metabolism of retinol (52). Moreover, it is implicated in the development of obesity and associated metabolic disorders (53). Several studies indicate that RBP2 plays a central role in maintaining innate immunity in the intestinal tract (54). Nevertheless, extensive research is still required to attain a comprehensive understanding of RBP2's role in ARDS pathology. P2RY14, a G-protein coupled purinergic receptor, manifests its expression within the placenta, adipose tissue, intestine, stomach, and lung (55). Under conditions of tissue stress, alterations in the expression levels of P2Y14 occur, thereby influencing the processes of cellular aging and apoptosis (56). The expression of P2Y14R in human alveolar epithelial type 2 cells and its impact on IL-8 secretion and neutrophil recruitment suggest its pivotal role in the activation of airway epithelial cells and modulation of immune response (57).

To further validate the results of the bioinformatics analysis, we conducted qRT-PCR to identify and screen the four hub genes using

10.3389/fimmu.2024.1365206

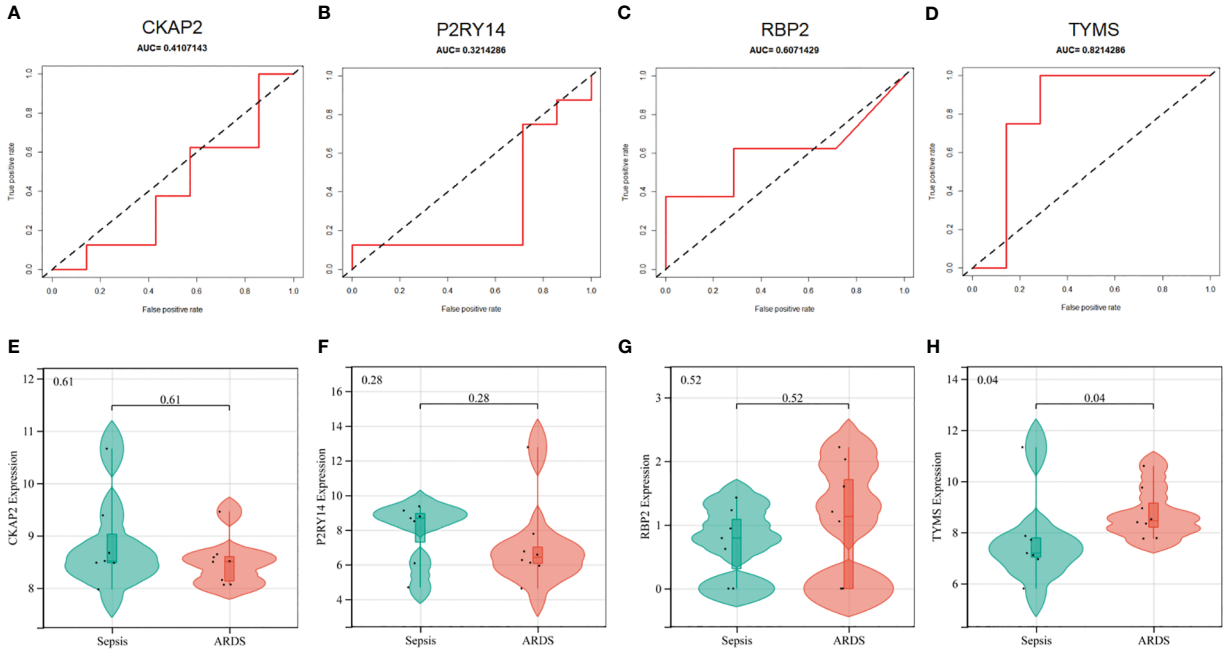

FIGURE 8
Performance of hub ARDS-ARDEGs in the GSE84439 dataset. **(A-D)** Violin plots compare the expression levels of particular genes in patients with ARDS and those with septic shock. **(E-H)** ROC curves indicate the diagnostic performance of the identified genes about ARDS.

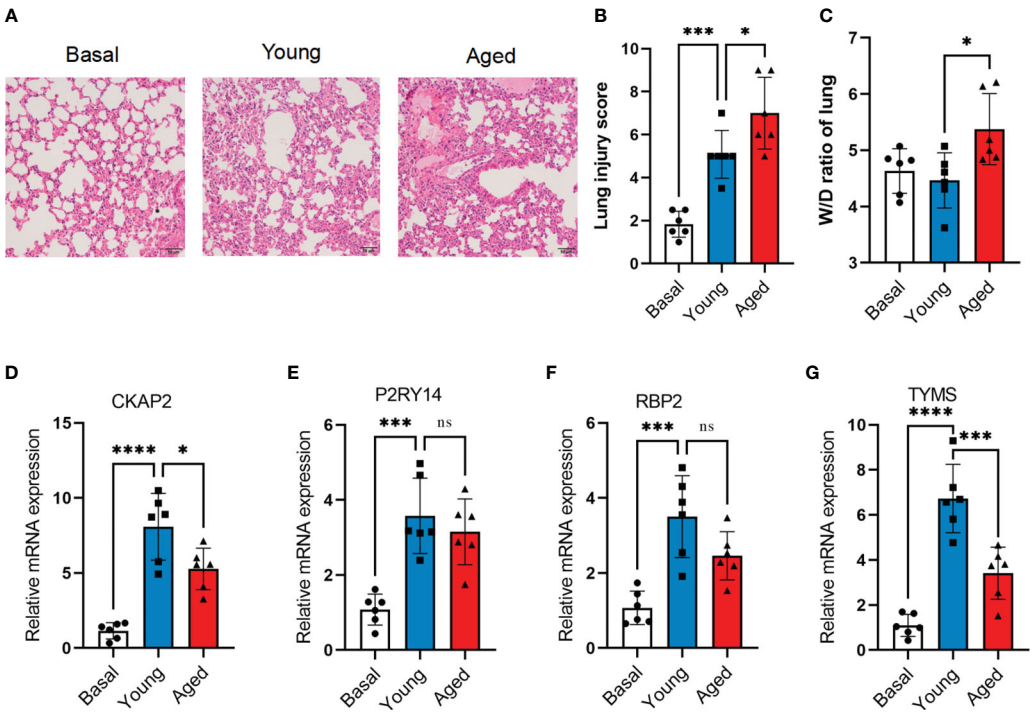

FIGURE 9
Validation of hub ARDS-ARDEGs through total RNA sequencing. **(A)** Histopathological images of lung tissues in LPS-induced ARDS young and aged mice. Scale bar, 50 μm. **(B)** Lung injury scoring analysis based on alveolar wall congestion and inflammatory cell infiltration, bronchovascular peribronchial hemorrhage and inflammatory cell infiltration, bronchial lumen exudate, and endothelial cell swelling, with assignment of each slide area to a severity score ranging from 1 (average) to 4 (severe injury). **(C)** Lung wet-to-dry ratio in young adult and aged mice 72 hours post LPS exposure. **(D-G)** CKAP2, P2RY14, RBP2, and TYMS expression levels in young and aged ARDS mouse models,n = 6 in each group.The data are shown as mean ± standard deviation, and asterisks (*p<0.05, **p<0.01, ***p<0.001, ****p<0.0001) denote statistical significance; "ns" indicates no significance.

10.3389/fimmu.2024.1365206

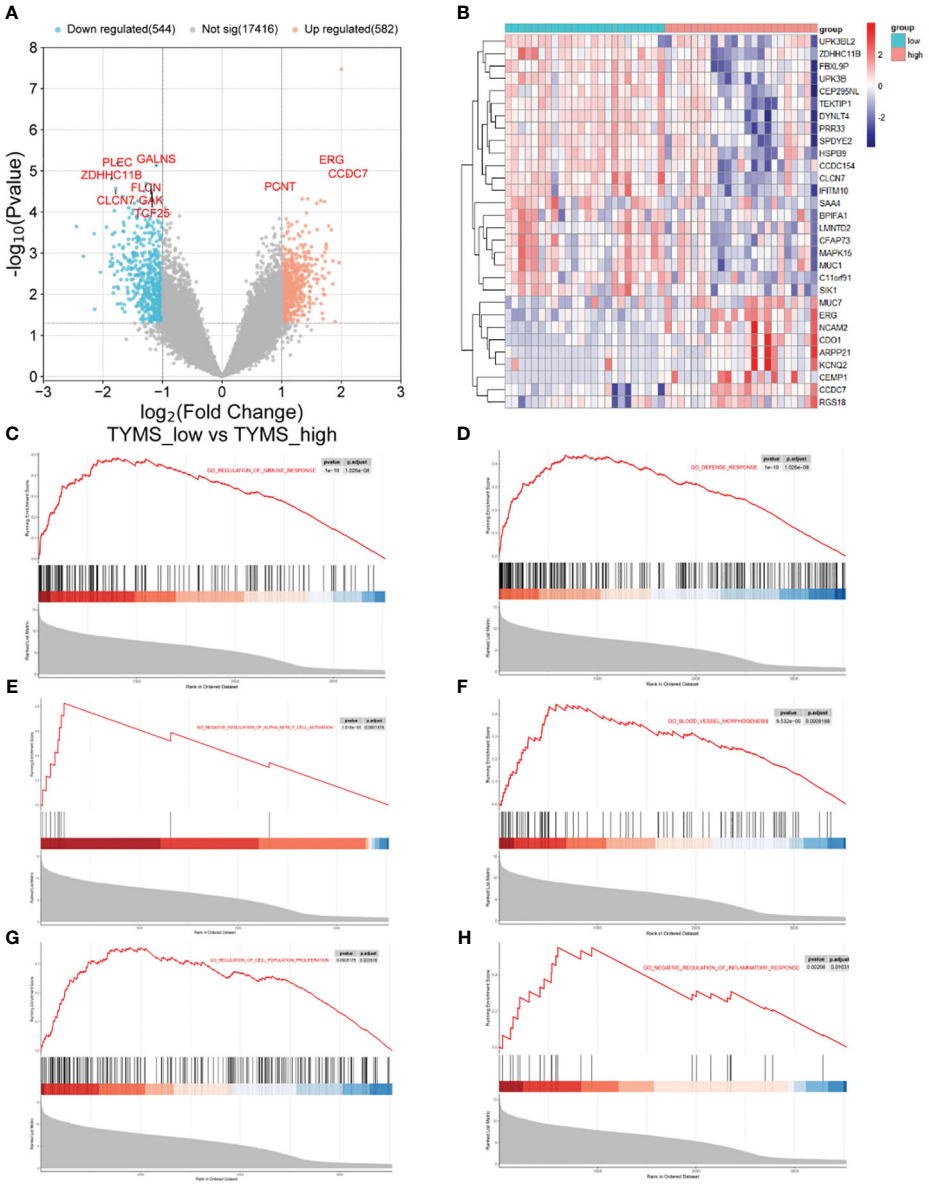

FIGURE 10
The GSEA of different TYMS expression groups in ARDS patients. **(A)** A volcano plot shows the differential gene analysis results between the ARDS patient groups with high and low TYMS expression. **(B)** A cluster heat map, ordered by *p*-value, displaying the top 30 genes linked to TYMS that are differentially expressed. **(C–H)** In the TYMS high expression group of ARDS patients, enrichment analysis reveals the upregulation of signaling pathways involved in the regulation of immune system processes, defense response, negative regulation of alpha-beta T cell activation, blood vessel morphogenesis, regulation of cell population proliferation, and negative regulation of inflammatory response in the TYMS high expression group of ARDS patients.

lung tissue samples from both the control and ARDS model groups of mice. Remarkably, we observed significantly higher expression levels of all four genes in the lung tissues of ARDS mice, aligning with the findings of the bioinformatics analysis. Notably, there was a significant difference in TYMS expression between elderly and young mice after modeling, suggesting its potential as a diagnostic biomarker for elderly ARDS patients. Therefore, our subsequent research will focus on TYMS as the target gene for further exploration.

To investigate the possible biological functions and pathways TYMS may be involved in ARDS, we divided the ARDS dataset GSE163426 into groups based on the expression levels of TYMS and performed GSEA. The results revealed that TYMS plays a critical role in ARDS development by influencing immune inflammation and vascular morphogenesis. These findings are consistent with previous research on ARDS. We then conducted further research to evaluate the immunological infiltration in ARDS utilizing ssGSEA. In ARDS samples, we discovered a substantial increase in the infiltration levels of effector memory CD4 T cells, activated CD8 T cells and activated CD4 T cells. Additionally, TYMS demonstrated a negative correlation with $CD56^{dim}$ natural killer cells, Central memory CD4 T cells, and immature dendritic cells,

10.3389/fimmu.2024.1365206

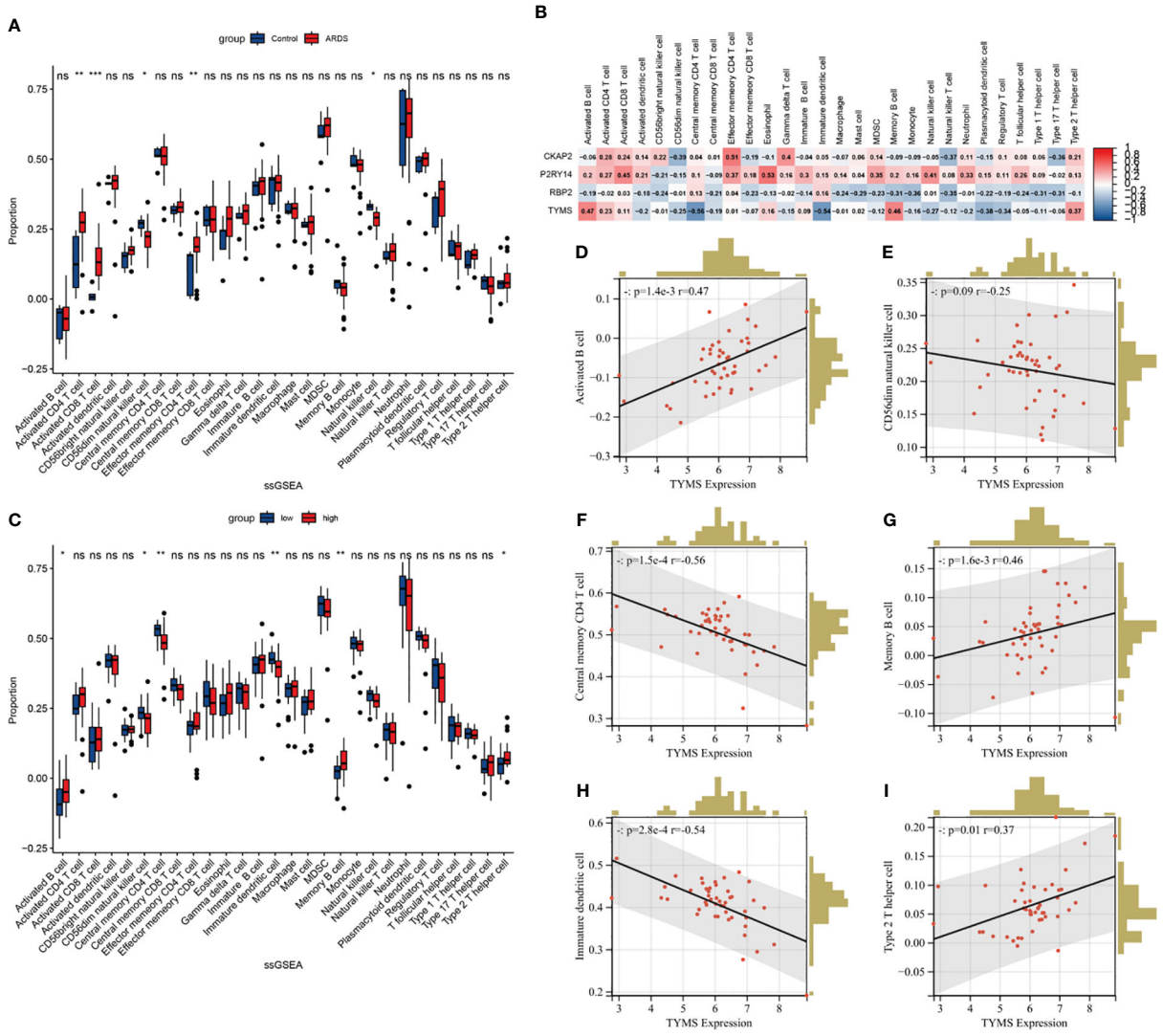

FIGURE 11
The ssGSEA immune infiltration analysis in ARDS patients. **(A)** Boxplot showing the difference in immune cell infiltration between controls and ARDS patients (controls vs. ARDS patients). **(B)** Heatmap depicting the correlation between hub ARDS-ARDEGs expression and different immune cell infiltrations. **(C)** Boxplot showing the differences in immune cell infiltration between high and low expression groups of ARDS patients according to TYMS expression. (high versus low). **(D–I)** The proportion of activated B cells, memory B cells, type 2 T helper cells, $CD56^{dim}$ natural killer cells, central memory CD4 T cells, and immature dendritic cells in ARDS patients correlated with TYMS's expression levels. The significance levels are: $^{*}P < 0.05$, $^{**}P < 0.01$, $^{***}P < 0.001$, $^{****}P < 0.0001$.

and a positive correlation with activated B cells, memory B cells, and Type 2 T helper cells by correlation analysis with immune cells. It has been established that inflammatory and immune-infiltrating cells, such as Type 2 T helper cells, which are mainly responsible for producing IL-4, IL-5, and IL-13 involved in humoral immunity, serve a purpose in the development of ARDS (58).

However, the intricate interaction among these immune cells, their distinct roles in ARDS, and the intricate molecular mechanisms involved still require further investigation for a comprehensive understanding.

Furthermore, we investigated the cellular localization of TYMS based on snRNA-Seq data. The results revealed different proportions of AT1 cells, AT2 cells, endothelial cells, mononuclear/macrophage cells, fibroblast cells, and neuronal cells between the control group and COVID-19-ARDS patients. Remarkably, the proportion of endothelial cells in ARDS patients was significantly lower compared to the healthy control group, indicating impaired endothelial cell function in ARDS patients. The increased proliferation of B cells is associated with improved survival rates in ARDS (59). Additionally, there was a decrease in alveolar epithelial cells in ARDS patients, consistent with the findings of a study by Feng et al. (60). TYMS showed high expression in the endothelial cells of ARDS patients, and moderate induction may contribute to endothelial regeneration and the maintenance of endothelial barrier integrity, thereby reducing the infiltration of inflammatory cells and inhibiting the progression of ARDS.

10.3389/fimmu.2024.1365206

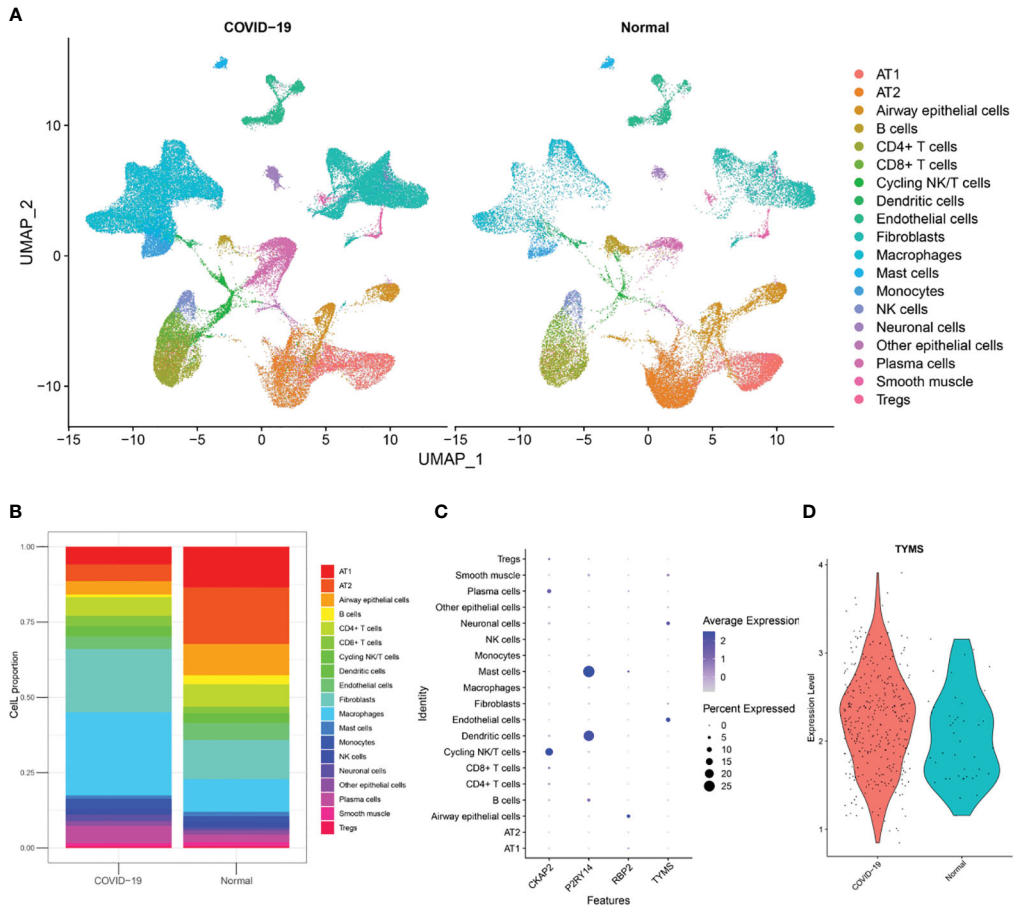

FIGURE 12
Analysis of single-nuclei RNA-Seq data. **(A)** A uniform manifold approximation and projection map showing the 19 cell types found using unsupervised analysis. The data is sourced from post-mortem lung tissue samples of COVID-19 fatal cases and seven healthy donors. **(B)** The 19 cell type proportions. **(C)** Dot plot illustrating the hub ARDS-ARDEGs expression levels in several cell types. **(D)** A violin plot showing how COVID-19 patients and healthy donors differ in the expression of TYMS in endothelial cells.

Within the microenvironment of the tissue, intercellular communication among diverse cell types assumes a consequential role. The results of this study demonstrate that endothelial cells communicate with airway epithelial cells through the VISFATIN signaling pathway. Additionally, endothelial cells receive ligand signals from other cell types, including AT1 cells, fibroblast cells, smooth muscle cells, neurons, fibroblast cells, and macrophages. The SEMA3 signaling pathway mainly mediates cell-to-cell communication between endothelial cells and other cells. The SEMA3 signaling pathway significantly impacts the vascular system, promoting vascular development and regeneration (61). In conclusion, these findings provide valuable insights into the intercellular communication between endothelial cells and other cell types, elucidating the specific signaling pathways and molecules involved.

Our research has limitations. Firstly, information from open databases served as the foundation for all analysis. The species representation, sequencing platforms, molecular types, sample grouping, and sample quality of the GEO collection are all limited. Nevertheless, the datasets utilized in this investigation were the only ones readily available for our analysis. Even though our cohorts have been constructed and confirmed, prospective research with additional validation would be ideal. Extensive research is also required to investigate the possible roles of hub genes in the pathophysiology of ARDS.

Conclusion

Our study utilized bioinformatics analyses and machine learning methods to identify four potential aging-related genes associated with ARDS. The essential genes CKAP2, P2RY14, RBP2, and TYMS were validated using animal samples to determine their expression levels in an animal model through the protective role of TYMS in maintaining the integrity of the pulmonary microvascular endothelial barrier, promoting endothelial cell regeneration, and restoring its function. It could be a novel approach to the management and prevention of ARDS. These discoveries have immediate therapeutic implications, opening the door to more accurate diagnoses and individualized treatment plans. In the end, our study provides important insights for further investigation into ARDS and its treatment modalities

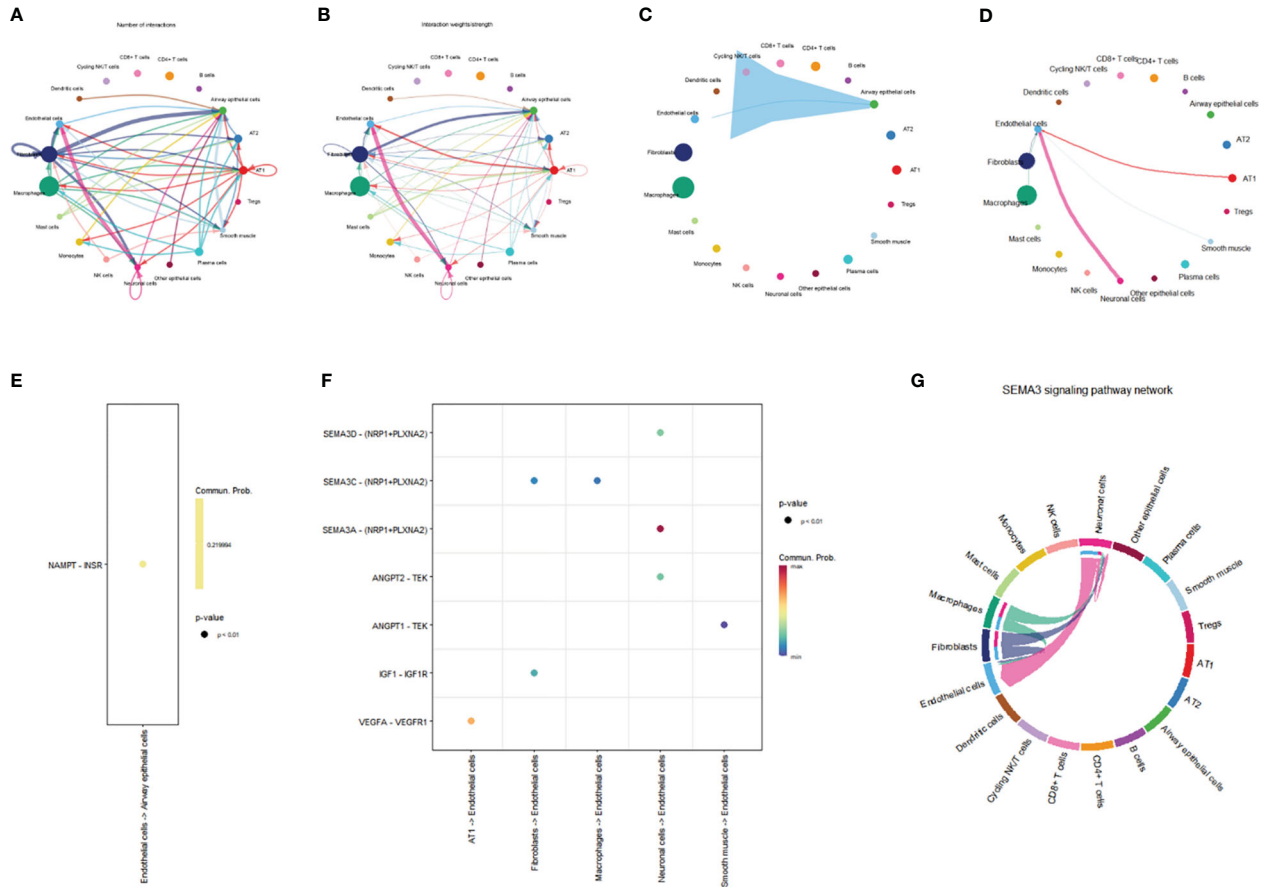

FIGURE 13
Network representation of cell-cell communication. **(A)** Frequency-based network diagram demonstrating the varying degrees of interactions among different cell types. **(B)** Intensity-based network diagram showcasing the strength of interactions among diverse cell populations. **(C)** Communication pathways and their associated intensities originating from endothelial cells are illustrated in a network diagram. **(D)** Communication pathways and their respective strengths through which endothelial cells receive signals are visualized in a network diagram. **(E)** Scatter plot detailing the ligand-receptor signaling patterns emitted by endothelial cells. **(F)** Scatter plot depicting the ligand-receptor signaling received by endothelial cells. **(G)** Chord diagram illustrating the intricate SEMA3 signaling pathway.

while laying the groundwork for experimental and clinical research in the future.

Data availability statement

The original contributions presented in the study are included in the article/supplementary material. Further inquiries can be directed to the corresponding author.

Ethics statement

The animal experimental processes were approved by the Ethics Committee of Hangzhou Hibio Technology Co., Ltd. (HB2311003). The study was conducted in accordance with the local legislation and institutional requirements.

Author contributions

GL: Funding acquisition, Writing – original draft, Writing – review & editing. PG: Data curation, Formal analysis, Visualization, Writing – original draft, Writing – review & editing. KY: Conceptualization, Data curation, Formal analysis, Writing – original draft. WZ: Validation, Writing – original draft. HP: Validation, Writing – original draft.

Funding

The author(s) declare that financial support was received for the research, authorship, and/or publication of this article. This study received support from the Zhejiang Provincial Traditional Chinese Medicine Science and Technology Plan Project (Grant No. 2024ZL528), under the supervision of GL.

Conflict of interest

The authors declare that the research was conducted in the absence of any commercial or financial relationships that could be construed as a potential conflict of interest.

Publisher's note

All claims expressed in this article are solely those of the authors and do not necessarily represent those of their affiliated organizations, or those of the publisher, the editors and the reviewers. Any product that may be evaluated in this article, or claim that may be made by its manufacturer, is not guaranteed or endorsed by the publisher.

Supplementary material

The Supplementary Material for this article can be found online at: https://www.frontiersin.org/articles/10.3389/fimmu.2024.1365206/full#supplementary-material

References

1. Matthay MA, Ware LB, Zimmerman GA. The acute respiratory distress syndrome. *J Clin Invest*. (2012) 1228:2731–40. doi: 10.1172/jci60331

2. Bos LDJ, Ware LB. Acute respiratory distress syndrome: causes, pathophysiology, and phenotypes. *Lancet*. (2022) 40010358:1145–56. doi: 10.1016/s0140-6736(22)01485-4

3. Gorman EA, O'Kane CM, McAuley DF. Acute respiratory distress syndrome in adults: diagnosis, outcomes, long-term sequelae, and management. *Lancet*. (2022) 40010358:1157–70. doi: 10.1016/s0140-6736(22)01439-8

4. Matthay MA, Zemans RL. The acute respiratory distress syndrome: pathogenesis and treatment. *Annu Rev Pathol*. (2011) 6:147–63. doi: 10.1146/annurev-pathol-011110-130158

5. De Freitas Caires N, Gaudet A, Portier L, Tsicopoulos A, Mathieu D and Lassalle P. Endocan, sepsis, pneumonia, and acute respiratory distress syndrome. *Crit Care*. (2018) 221:280. doi: 10.1186/s13054-018-2222-7

6. Pham T, Rubenfeld GD. Fifty years of research in ARDS. The epidemiology of acute respiratory distress syndrome. A 50th birthday review. *Am J Respir Crit Care Med*. (2017) 1957:860–70. doi: 10.1164/rccm.201609-1773CP

7. Laffey JG, Bellani G, Pham T, Fan E, Madotto F, Bajwa EK, et al. Potentially modifiable factors contributing to outcome from acute respiratory distress syndrome: the LUNG SAFE study. *Intensive Care Med*. (2016) 4212:1865–76. doi: 10.1007/s00134-016-4571-5

8. Dang W, Tao Y, Xu X, Zhao H, Zou L, Li Y. The role of lung macrophages in acute respiratory distress syndrome. *Inflammation Res*. (2022) 7112:1417–32. doi: 10.1007/s00011-022-01645-4

9. Cannavò L, Perrone S, Viola V, Marseglia L, Di Rosa G, Gitto E. Oxidative stress and respiratory diseases in preterm newborns. *Int J Mol Sci*. (2021) 22(22):12504. doi: 10.3390/ijms222212504

10. Sauler M, Bazan IS, Lee PJ. Cell death in the lung: the apoptosis-necroptosis axis. *Annu Rev Physiol*. (2019) 81:375–402. doi: 10.1146/annurev-physiol-020518-114320

11. Cho SJ, Stout-Delgado HW. Aging and lung disease. *Annu Rev Physiol*. (2020) 82:433–59. doi: 10.1146/annurev-physiol-021119-034610

12. Liu S, Fang X, Zhu R, Zhang J, Wang H, Lei J, et al. Role of endoplasmic reticulum autophagy in acute lung injury. *Front Immunol*. (2023) 14:1152336. doi: 10.3389/fimmu.2023.1152336

13. Cai Y, Song W, Li J, Jing Y, Liang C, Zhang L, et al. The landscape of aging. *Sci China Life Sci*. (2022) 6512:2354–454. doi: 10.1007/s11427-022-2161-3

14. Childs BG, Durik M, Baker DJ, van Deursen JM. Cellular senescence in aging and age-related disease: from mechanisms to therapy. *Nat Med*. (2015) 2112:1424–35. doi: 10.1038/nm.4000

15. Rossiello F, Jurk D, Passos JF, d'Adda di Fagagna F. Telomere dysfunction in ageing and age-related diseases. *Nat Cell Biol*. (2022) 242:135–47. doi: 10.1038/s41556-022-00842-x

16. Schumacher B, Pothof J, Vijg J, Hoeijmakers JHJ. The central role of DNA damage in the ageing process. *Nature*. (2021) 5927856:695–703. doi: 10.1038/s41586-021-03307-7

17. Verbeken EK, Cauberghs M, Mertens I, Clement J, Lauweryns JM, Van de Woestijne KP. The senile lung. Comparison with normal and emphysematous lungs. 1. Structural aspects. *Chest*. (1992) 1013:793–9. doi: 10.1378/chest.101.3.793

18. Al-Shaer MH, Choueiri NE, Correia ML, Sinkey CA, Barenz TA, Haynes WG. Effects of aging and atherosclerosis on endothelial and vascular smooth muscle function in humans. *Int J Cardiol*. (2006) 1092:201–6. doi: 10.1016/j.ijcard.2005.06.002

19. Ely EW, Wheeler AP, Thompson BT, Ancukiewicz M, Steinberg KP, Bernard GR. Recovery rate and prognosis in older persons who develop acute lung injury and the acute respiratory distress syndrome. *Ann Intern Med*. (2002) 1361:25–36. doi: 10.7326/0003-4819-136-1-200201010-00007

20. Clementi N, Ghosh S, De Santis M, Castelli M, Criscuolo E, Zanoni I, et al. Viral respiratory pathogens and lung injury. *Clin Microbiol Rev*. (2021) 34(3)::e00103–20. doi: 10.1128/cmr.00103-20

21. Schouten LR, van Kaam AH, Kohse F, Veltkamp F, Bos LD, de Beer FM, et al. Age-dependent differences in pulmonary host responses in ARDS: a prospective observational cohort study. *Ann Intensive Care*. (2019) 91:55. doi: 10.1186/s13613-019-0529-4

22. Brandenberger C, Kling KM, Vital M, Christian M. The role of pulmonary and systemic immunosenescence in acute lung injury. *Aging Dis*. (2018) 94:553–65. doi: 10.14336/ad.2017.0902

23. Voelkerding KV, Dames SA, Durtschi JD. Next-generation sequencing: from basic research to diagnostics. *Clin Chem*. (2009) 554:641–58. doi: 10.1373/clinchem.2008.112789

24. Tacutu R, Thornton D, Johnson E, Budovsky A, Barardo D, Craig T, et al. Human Ageing Genomic Resources: new and updated databases. *Nucleic Acids Res*. (2018) 46D1:D1083–d1090. doi: 10.1093/nar/gkx1042

25. Ritchie ME, Phipson B, Wu D, Hu Y, Law CW, Shi W, et al. limma powers differential expression analyses for RNA-sequencing and microarray studies. *Nucleic Acids Res*. (2015) 437:e47. doi: 10.1093/nar/gkv007

26. Szklarczyk D, Gable AL, Lyon D, Junge A, Wyder S, Huerta-Cepas J, et al. STRING v11: protein-protein association networks with increased coverage, supporting functional discovery in genome-wide experimental datasets. *Nucleic Acids Res*. (2019) 47D1:D607–d613. doi: 10.1093/nar/gky1131

27. Yu G, Wang LG, Han Y, He QY. clusterProfiler: an R package for comparing biological themes among gene clusters. *Omics*. (2012) 165:284–7. doi: 10.1089/omi.2011.0118

28. Langfelder P, Horvath S. WGCNA: an R package for weighted correlation network analysis. *BMC Bioinf*. (2008) 9:559. doi: 10.1186/1471-2105-9-559

29. Frost HR, Amos CI. Gene set selection via LASSO penalized regression (SLPR). *Nucleic Acids Res*. (2017) 4512:e114. doi: 10.1093/nar/gkx291

30. Li W, Yin Y, Quan X, Zhang H. Gene expression value prediction based on XGBoost algorithm. *Front Genet*. (2019) 10:1077. doi: 10.3389/fgene.2019.01077

31. Yuan Y, Fu M, Li N, Ye M. Identification of immune infiltration and cuproptosis-related subgroups in Crohn's disease. *Front Immunol*. (2022) 13:1074271. doi: 10.3389/fimmu.2022.1074271

32. Butler A, Hoffman P, Smibert P, Papalexi E, Satija R. Integrating single-cell transcriptomic data across different conditions, technologies, and species. *Nat Biotechnol*. (2018) 365:411–20. doi: 10.1038/nbt.4096

33. Korsunsky I, Millard N, Fan J, Slowikowski K, Zhang F, Wei K, et al. Fast, sensitive and accurate integration of single-cell data with Harmony. *Nat Methods*. (2019) 1612:1289–96. doi: 10.1038/s41592-019-0619-0

34. Jin S, Guerrero-Juarez CF, Zhang L, Chang I, Ramos R, Kuan CH, et al. Inference and analysis of cell-cell communication using CellChat. *Nat Commun*. (2021) 121:1088. doi: 10.1038/s41467-021-21246-9

35. Johnston CJ, Rubenfeld GD, Hudson LD. Effect of age on the development of ARDS in trauma patients. *Chest*. (2003) 1242:653–9. doi: 10.1378/chest.124.2.653

36. Meduri GU, Kohler G, Headley S, Tolley E, Stentz F, Postlethwaite A. Inflammatory cytokines in the BAL of patients with ARDS. Persistent elevation over time predicts poor outcome. *Chest*. (1995) 1085:1303–14. doi: 10.1378/chest.108.5.1303

37. Parcha V, Kalra R, Bhatt SP, Berra L, Arora G, Arora P. Trends and geographic variation in acute respiratory failure and ARDS mortality in the United States. *Chest*. (2021) 1594:1460–72. doi: 10.1016/j.chest.2020.10.042

38. Jiang Y, Rosborough BR, Chen J, Das S, Kitsios GD, McVerry BJ, et al. Single cell RNA sequencing identifies an early monocyte gene signature in acute respiratory distress syndrome. *JCI Insight*. (2020) 5(13):e135678. doi: 10.1172/jci.insight.135678

39. Xiong S, Hong Z, Huang LS, Tsukasaki Y, Nepal S, Di A, et al. IL-1β suppression of VE-cadherin transcription underlies sepsis-induced inflammatory lung injury. *J Clin Invest*. (2020) 1307:3684–98. doi: 10.1172/jci136908

40. Shive C, Pandiyan P. Inflammation, immune senescence, and dysregulated immune regulation in the elderly. *Front Aging*. (2022) 3:840827. doi: 10.3389/fragi.2022.840827

41. Palumbo S, Shin YJ, Ahmad K, Desai AA, Quijada H, Mohamed M, et al. Dysregulated Nox4 ubiquitination contributes to redox imbalance and age-related severity of acute lung injury. *Am J Physiol Lung Cell Mol Physiol*. (2017) 3123:L297–l308. doi: 10.1152/ajplung.00305.2016

42. Martins R, Lithgow GJ, Link W. Long live FOXO: unraveling the role of FOXO proteins in aging and longevity. *Aging Cell*. (2016) 152:196–207. doi: 10.1111/acel.12427

43. Hong KU, Park YS, Seong YS, Kang D, Bae CD, Park J. Functional importance of the anaphase-promoting complex-Cdh1-mediated degradation of TMAP/CKAP2 in regulation of spindle function and cytokinesis. *Mol Cell Biol*. (2007) 2710:3667–81. doi: 10.1128/mcb.01386-06

44. Zhang S, Wang Y, Chen S, Li J. Silencing of cytoskeleton-associated protein 2 represses cell proliferation and induces cell cycle arrest and cell apoptosis in osteosarcoma cells. *BioMed Pharmacother*. (2018) 106:1396–403. doi: 10.1016/j.biopha.2018.07.104

45. Jin XX, Mei YN, Shen Z, Zhu JF, Xing SH, Yang HM, et al. A chalcone-syringaldehyde hybrid inhibits triple-negative breast cancer cell proliferation and migration by inhibiting CKAP2-mediated FAK and STAT3 phosphorylation. *Phytomedicine*. (2022) 101:154087. doi: 10.1016/j.phymed.2022.154087

46. Kim YW, Eom BW, Kook MC, Kim HS, Kim MK, Hwang HL, et al. Clinical implications of proliferation activity in T1 or T2 male gastric cancer patients. *Exp Mol Med*. (2015) 4711:e193. doi: 10.1038/emm.2015.79

47. Avelar RA, Ortega JG, Tacutu R, Tyler EJ, Bennett D, Binetti P, et al. A multidimensional systems biology analysis of cellular senescence in aging and disease. *Genome Biol*. (2020) 211:91. doi: 10.1186/s13059-020-01990-9

48. Wu HL, Gong Y, Ji P, Xie YF, Jiang YZ, Liu GY. Targeting nucleotide metabolism: a promising approach to enhance cancer immunotherapy. *J Hematol Oncol*. (2022) 151:45. doi: 10.1186/s13045-022-01263-x

49. Chen Y, Zhang C, Jin S, Li J, Dai J, Zhang Z, et al. Pemetrexed induces ROS generation and cellular senescence by attenuating TS-mediated thymidylate metabolism to reverse gefitinib resistance in NSCLC. *J Cell Mol Med*. (2023) 2714:2032–44. doi: 10.1111/jcmm.17799

50. Huang X, Zhang X, Machireddy N, Evans CE, Trewartha SD, Hu G, et al. Endothelial FoxM1 reactivates aging-impaired endothelial regeneration for vascular repair and resolution of inflammatory lung injury. *Sci Transl Med*. (2023) 15709: eabm5755. doi: 10.1126/scitranslmed.abm5755

51. Varghese V, Magnani L, Harada-Shoji N, Mauri F, Szydlo RM, Yao S, et al. FOXM1 modulates 5-FU resistance in colorectal cancer through regulating TYMS expression. *Sci Rep*. (2019) 91:1505. doi: 10.1038/s41598-018-38017-0

52. Napoli JL. Cellular retinoid binding-proteins, CRBP, CRABP, FABP5: Effects on retinoid metabolism, function and related diseases. *Pharmacol Ther*. (2017) 173:19–33. doi: 10.1016/j.pharmthera.2017.01.004

53. Lee SA, Yang KJZ, Brun PJ, Silvaroli JA, Yuen JJ, Shmarakov I, et al. Retinol-binding protein 2 (RBP2) binds monoacylglycerols and modulates gut endocrine signaling and body weight. *Sci Adv*. (2020) 611:eaay8937. doi: 10.1126/sciadv.aay8937

54. McDonald KG, Leach MR, Brooke KWM, Wang C, Wheeler LW, Hanly EK, et al. Epithelial expression of the cytosolic retinoid chaperone cellular retinol binding protein II is essential for in *vivo* imprinting of local gut dendritic cells by lumenal retinoids. *Am J Pathol*. (2012) 1803:984–97. doi: 10.1016/j.ajpath.2011.11.009

55. Jokela TA, Kärnä R, Makkonen KM, Laitinen JT, Tammi RH and Tammi MI. Extracellular UDP-glucose activates P2Y14 Receptor and Induces Signal Transducer and Activator of Transcription 3 (STAT3) Tyr705 phosphorylation and binding to hyaluronan synthase 2 (HAS2) promoter, stimulating hyaluronan synthesis of keratinocytes. *J Biol Chem*. (2014) 28926:18569–81. doi: 10.1074/jbc.M114.551804

56. Cho J, Yusuf R, Kook S, Attar E, Lee D, Park B, et al. Purinergic $P2Y_{14}$ receptor modulates stress-induced hematopoietic stem/progenitor cell senescence. *J Clin Invest*. (2014) 1247:3159–71. doi: 10.1172/jci61636

57. Müller T, Bayer H, Myrtek D, Ferrari D, Sorichter S, Ziegenhagen MW, et al. The P2Y14 receptor of airway epithelial cells: coupling to intracellular Ca2+ and IL-8 secretion. *Am J Respir Cell Mol Biol*. (2005) 336:601–9. doi: 10.1165/rcmb.2005-0181OC

58. Weiskopf D, Schmitz KS, Raadsen MP, Grifoni A, Okba NMA, Endeman H, et al. Phenotype and kinetics of SARS-CoV-2-specific T cells in COVID-19 patients with acute respiratory distress syndrome. *Sci Immunol*. (2020) 5(48):eabd2071. doi: 10.1126/sciimmunol.abd2071

59. Zhu G, Liu Y, Zhang W, Huang Y, Li K. CD27(+)TIM-1(+) memory B cells promoted the development of Foxp3(+) Tregs and were associated with better survival in acute respiratory distress syndrome. *Immunol Res*. (2018) 662:281–7. doi: 10.1007/s12026-017-8983-2

60. Feng Z, Jing Z, Li Q, Chu L, Jiang Y, Zhang X, et al. Exosomal STIMATE derived from type II alveolar epithelial cells controls metabolic reprogramming of tissue-resident alveolar macrophages. *Theranostics*. (2023) 133:991–1009. doi: 10.7150/thno.82552

61. Oh WJ, Gu C. The role and mechanism-of-action of Sema3E and Plexin-D1 in vascular and neural development. *Semin Cell Dev Biol*. (2013) 243:156–62. doi: 10.1016/j.semcdb.2012.12.001

frontiers | Frontiers in Immunology

TYPE Original Research
PUBLISHED 19 March 2024
DOI 10.3389/fimmu.2024.1369617

OPEN ACCESS

EDITED BY
Pietro Ghezzi,
University of Urbino Carlo Bo, Italy

REVIEWED BY
Ivana Kawikova,
University of Hartford, United States
Wolfgang Weihs,
Medical University of Vienna, Austria
Christoph Thiemermann,
Queen Mary University of London,
United Kingdom

*CORRESPONDENCE
Stefan Hof
Stefan.hof@med.uni-duesseldorf.de

†These authors have contributed equally to this work and share last authorship

‡In partial fulfillment of the requirements of the MD thesis of LL and MM

RECEIVED 12 January 2024
ACCEPTED 04 March 2024
PUBLISHED 19 March 2024

CITATION
Hof S, Lingens L, Michels M, Marcus C, Kuebart A, Herminghaus A, Bauer I, Picker O, Truse R and Vollmer C (2024) Local carbachol application induces oral microvascular recruitment and improves gastric tissue oxygenation during hemorrhagic shock in dogs.
Front. Immunol. 15:1369617.
doi: 10.3389/fimmu.2024.1369617

Local carbachol application induces oral microvascular recruitment and improves gastric tissue oxygenation during hemorrhagic shock in dogs

Stefan Hof*, Lara Lingens‡, Marius Michels‡, Carsten Marcus, Anne Kuebart, Anna Herminghaus, Inge Bauer, Olaf Picker, Richard Truse† and Christian Vollmer†

Department of Anesthesiology, Duesseldorf University Hospital, Duesseldorf, Germany

Introduction: Hemorrhagic shock is characterized by derangements of the gastrointestinal microcirculation. Topical therapy with nitroglycerine or iloprost improves gastric tissue oxygenation but not regional perfusion, probably due to precapillary adrenergic innervation. Therefore, this study was designed to investigate the local effect of the parasympathomimetic carbachol alone and in combination with either nitroglycerine or iloprost on gastric and oral microcirculation during hemorrhagic shock.

Methods: In a cross-over design five female foxhounds were repeatedly randomized into six experimental groups. Carbachol, or carbachol in combination with either nitroglycerine or iloprost were applied topically to the oral and gastric mucosa. Saline, nitroglycerine, or iloprost application alone served as control groups. Then, a fixed-volume hemorrhage was induced by arterial blood withdrawal followed by blood retransfusion after 1h of shock. Gastric and oral microcirculation was determined using reflectance spectrophotometry and laser Doppler flowmetry. Oral microcirculation was visualized with videomicroscopy. Statistics: 2-way-ANOVA for repeated measurements and Bonferroni post-hoc analysis (mean ± SEM; $p < 0.05$).

Results: The induction of hemorrhage led to a decrease of gastric and oral tissue oxygenation, that was ameliorated by local carbachol and nitroglycerine application at the gastric mucosa. The sole use of local iloprost did not improve gastric tissue oxygenation but could be supplemented by local carbachol treatment. Adding carbachol to nitroglycerine did not further increase gastric tissue oxygenation. Gastric microvascular blood flow remained unchanged in all experimental groups. Oral microvascular blood flow, microvascular flow index and total vessel density decreased during shock. Local carbachol supply improved oral vessel density during shock and oral microvascular flow index in the late course of hemorrhage.

Conclusion: The specific effect of shifting the autonomous balance by local carbachol treatment on microcirculatory variables varies between parts of the gastrointestinal tract. Contrary to our expectations, the improvement of gastric tissue oxygenation by local carbachol or nitroglycerine application was not

related to increased microvascular perfusion. When carbachol is used in combination with local vasodilators, the additional effect on gastric tissue oxygenation depends on the specific drug combination. Therefore, modulation of tissue oxygen consumption, mitochondrial function or alterations in regional blood flow distribution should be investigated.

KEYWORDS

tissue oxygenation, microcirculation, microvascular recruitment, hemorrhagic shock, carbachol, nitroglycerine, iloprost, local drug application

1 Introduction

Despite intensive research, acute traumatic hemorrhage remains a global burden, with a high mortality rate particularly within the first month after injury (1). During this period, the maintenance of intestinal tissue integrity seems to be crucial to reestablish global homeostasis and avoid secondary diseases (2). Unfortunately, hemorrhagic shock is characterized by microcirculatory failure, that is particularly pronounced within the gastrointestinal tract (3) leading to regional hypoxia and tissue injury. Therefore, there is need to detect therapeutic interventions that improve intestinal microcirculation during hemorrhagic shock. As there is a mismatch of macro- and microcirculatory variables in critically ill patients, the sole use of macrocirculatory measurements seems to be insufficient to guide the restoration of regional microcirculation during severe shock states (4). Meanwhile microcirculatory variables revealed to predict multi organ failure more sensitively than macrocirculatory variables in critically ill patients, highlighting the role of microvascular derangements in critically ill patients (5, 6).

There are two mechanisms mainly discussed leading to microvascular impairment during hemorrhagic shock within the gastrointestinal tract. First, excessive blood loss results in intravascular hypovolemia with reduced microvascular perfusion. Here the transfusion of blood products represents a therapeutic concept for hemorrhagic shock treatment (7, 8). Secondly, adrenergic vascular innervation and circulating catecholamines, aiming to ensure the maintenance of an adequate mean arterial perfusion pressure (9, 10), lead to regional vasoconstriction and thus to intestinal hypoperfusion and ischemia (11). The therapeutic approach to reopen collapsed vessels, increase total vessel density and enhance microvascular tissue oxygenation by pharmacological interventions is called microvascular recruitment (12, 13). From an integrated point of view, vascular tone is not only regulated by neurogenic innervation and circulating catecholamines, but is also influenced by regional metabolites like nitric oxide, adenosine and prostaglandins (14). Focusing on the metabolic part of microvascular blood flow regulation, Hilty et al. reported, that challenging the microcirculation by local nitroglycerine exposition is able to quantify the microvascular reserve in healthy volunteers (15), giving the perspective to deal with unphysiological conditions of restricted oxygen availability (16). This concept was successfully transferred into perioperative patients (17). Especially during acute heart failure the titration of low-dose nitroglycerine increases perfused capillary density (18), improves myocardial microcirculation and reduces cardiac filling pressure (19). Further, nitroglycerine reverts clinical manifestations of poor peripheral perfusion in patients undergoing circulatory shock (20). Likewise, iloprost, a prostacyclin analogue with vasodilative properties, demonstrated beneficial effects on microvascular variables and ameliorated endotoxemia-related acute kidney injury as a consequence of an improved tissue oxygenation in rats (21). Beside its potent effect on the microvasculature, iloprost also exerts beneficial effects on intestinal ischemia-reperfusion injury (22, 23) and reduces oxidative stress in a model of colitis in rodents (24).

In accordance with these findings, we successfully used local nitroglycerine and iloprost to increase gastric mucosal oxygenation during hemorrhagic shock in dogs in a previous study. In addition, nitroglycerine attenuated shock-induced impairment of the mucosal barrier integrity (25). Despite the well described vasodilative effect of both agents, regional perfusion markers remained unchanged after topical drug application (25). We supposed that precapillary adrenergic innervation during acute hemorrhage might counteract metabolic vasodilatation by nitric oxide and prostacyclin. Therefore, reducing adrenergic vasoconstriction could reveal as a possible target to maintain residual tissue perfusion. In previous studies, complete regional blockade of the sympathetic nervous system by epidural anesthesia revealed to maintain gastric tissue oxygenation under physiological conditions despite slightly compromised macrocirculatory variables. Unfortunately, peridural anesthesia exerted unfavorable effects on gastric tissue oxygenation during hemorrhagic shock (26, 27). This emphasizes the importance of at least partially preserved functionality of the sympathetic nervous system during hemorrhagic shock. Because the parasympathetic nervous system is the functional antagonist of adrenergic stimulation (28), the application of parasympathomimetic agents could restore the autonomic balance and maintain gastrointestinal perfusion without provoking disadvantageous effects of sympathetic blockade during

acute hemorrhage. Therefore, this study was designed to investigate, if carbachol, a parasympathomimetic agent that acts as an agonist of muscarinic and nicotinic receptors, induces microvascular recruitment, improves oral and gastric microvascular perfusion and enhances tissue oxygenation in hemorrhagic dogs. Beside those microcirculatory considerations, carbachol is reported to improve intestinal barrier function by strengthening apical tight junctions and associated proteins during acute pancreatitis (29), lipopolysaccharide-induced intestinal damage (30) and ethanol-induced epithelial injury (31). Finally, carbachol induces intestinal mucus formation as a part of the physical barrier (32). In summary, these mechanisms including vascular and non-vascular effects could lead to reduced cell and tissue damage as reported during hypoxic challenges (33).

Whether the application of a parasympathomimetic is able to reestablish autonomous balance and leads to an increase of microvascular perfusion and tissue oxygenation during shock is unclear. Additionally, a parasympathomimetic agent in combination with nitroglycerine or iloprost might counteract precapillary adrenergic vasoconstriction and thus additionally improve microvascular flow. The systemic application of nitroglycerine, iloprost and carbachol could further diminish hemodynamic stability. In this context, our group reported the gastrointestinal microcirculation to be susceptible for topical therapies without systemic side effects during hemorrhagic shock (34–36). Thus, we studied the impact of local application of all substances.

The following study was designed to address the following questions:

(i) Does local application of the parasympathomimetic carbachol induce microvascular recruitment of oral microcirculation and increases gastric and oral tissue oxygenation during hemorrhagic shock?

(ii) Does additional local carbachol application further improve microcirculation, when applicated additionally to local nitroglycerine or iloprost treatment during acute hemorrhage?

(iii) Does local carbachol or the combination with either nitroglycerine or iloprost exert systemic side effects on circulatory variables?

2 Materials and methods

2.1 Animals and standard instrumentation

The data set was derived from five healthy female dogs (foxhounds, age: 3 – 10 years, weighing: 28 – 36 kg), that were treated repetitively in accordance with the NIH guidelines for animal care. All experiments were approved by the Local Animal Care and Use Committee (North Rhine- Westphalia State Agency for Nature, Environment, and Consumer Protection, Recklinghausen, Germany; ref. AZ 84-02.04.2012.A152). Animals were bred for experimental purposes and obtained from the animal research facility (ZETT, Zentrale Einrichtung für Tierforschung und wissenschaftliche Tierschutzaufgaben) of the Heinrich-Heine-University Duesseldorf. Food was withheld for 12 h prior to the experiments with free water access to ensure gastric depletion, since digestive activity might change gastrointestinal perfusion. Each dog underwent every experimental protocol in a randomized order and served as its own control (crossover design). Repeated experiments at the same individual reduce the total number of experiments needed to gain statistically significant results according to the 3R principle. Drug application was blinded to the investigators. After the experiments animals did not participate in any other experiment for at least three weeks to avoid carryover effects especially referring to the autonomous vegetative system. No animal was sacrificed during or after the experiments.

All experiments were performed under general anesthesia [induction of anesthesia: 4 $mg \cdot kg^{-1}$ propofol; maintenance of anesthesia: end-tidal sevoflurane 3.0 Vol % (37)] and mechanical ventilation [FiO_2: 0.3, VT: 12.5 $ml \cdot kg^{-1}$ (38)]. No opioids were used due to the atraumatic instrumentation and lack of surgical stimulus and to avoid tissue protection via opioid receptors as side effect. In previous experiments we could show that systemic and regional hypercapnia improve microvascular oxygen saturation (3). Therefore, capnography was used to adjust respiratory rate to achieve normocapnia ($etCO_2$: 35 mmHg). The left carotid artery was catheterized for invasive blood pressure measurement (Gould-Statham pressure transducers P23ID, Elk Grove, IL) and intermittent blood gas analysis (Rapidlab 860, Bayer AG, Germany). Both carotids were externalized before animals participated in the experiments to enable landmark guided arterial catheterization with low complication rates and a sufficient compression after the experiment for adequate hemostasis (39). All animals took part in previous experiments, so we did not perform surgical carotid externalization in direct relation to the described experiments. Transpulmonary thermodilution was used to determine cardiac output (CO [$ml \cdot kg^{-1} \cdot min^{-1}$]). In detail, the arterial catheter inserted to the carotid included a component to register the local temperature of arterial blood. (PiCCO 4.2 non US, PULSION Medical Systems, Munich, Germany). Every 30 minutes 10 ml of cold saline were injected intravenously via a peripheral vein at the forelimb. Alongside the bolus application, definitive temperature of the fluid bolus was registered by a thermistor that was connected to the intravenous catheter. After transpulmonary passage of the cold saline, the decrease of arterial blood temperature was measured in the arterial catheter and enables the calculation of CO. Systemic oxygen delivery (DO_2 [$ml \cdot kg^{-1} \cdot min^{-1}$]) was calculated as total oxygen content of the blood multiplied by cardiac output. The heart rate (HR [$1 \cdot min^{-1}$]) was measured by a spike-triggered electrocardiography (Powerlab, ADInstruments, Castle Hill, Austria). An orogastric tube was inserted to enable microvascular measurement at the gastric mucosa and local drug infusion. After the experiments animals were extubated and kept under direct supervision until they had completely recovered from anesthesia, including achieving an unassisted sufficient intake of wet food and water. Puncture sites were compressed to stop bleeding and

examined to ensure adequate hemostasis. Then, the dogs were given back to their keepers in the animal research facility.

2.2 Experimental protocol

After the induction of general anesthesia, intubation and standardized instrumentation, baseline values were recorded under steady state conditions and animals were randomized to one of six experimental protocols (Figure 1). Steady state conditions were defined as stability of hemodynamic variables (HR [1·min^{-1}] and MAP [mmHg]), microcirculatory measurements (reflectance spectrophotometry) and ventilation variables (etCO_2 [mmHg], etSevo [Vol%]). First, an initial drug bolus was applicated simultaneously to the oral region and the gastric cave as described below. Then, continuous drug infusion was started. After thirty minutes of observation, a fixed-volume hemorrhage was inducted by removing 20% of the estimated total blood volume within 5 min duration via an intravenous peripheral cannula and the arterial catheter (40). According to Advanced Trauma Life Support (ATLS) shock classification, this represents a class II shock (41). Shock was held for one hour without further correction, then the heparinized shed blood was retransfused using a conventional transfusion set with a 200 µm filter. Afterwards, animals were observed for one hour, then experiments were stopped, and animals were led back to spontaneous breathing and consciousness.

2.2.1 Interventional groups

Experimental groups differed according to the combination of nitroglycerine (Nitrolingual infusion, G. Pohl-Boskamp & co KG, Hohenlockstedt, Germany), iloprost (5-cis Iloprost, Cayman Chemicals, Ann Arbor, MI, USA), carbachol (Carbamylcholine chloride, Sigma-Aldrich Corporation, St. Louis, USA) and saline application. All investigators were blinded to the pharmacological treatment. The experimental protocol of acute hemorrhage and retransfusion did not differ between the groups. All experimental groups - including those with a sole nitroglycerine or iloprost treatment - have been performed exclusively for the here addressed research questions and have not been published before.

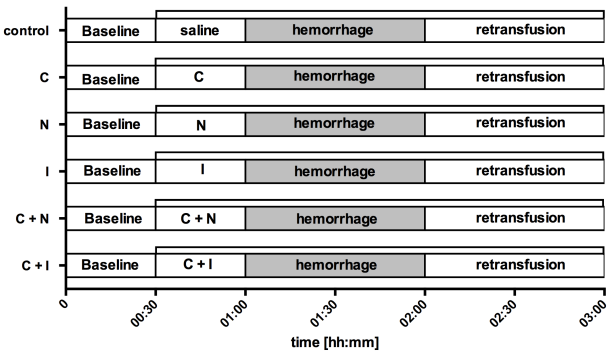

FIGURE 1
Experimental protocol. After the registration of baseline values (00:30) saline (control), carbachol (C), nitroglycerine (N), iloprost (I) or a combination of carbachol with either nitroglycerine (C + N) or iloprost (C + I) was applicated locally to the gastric and oral mucosa (01:00). The initial drug bolus was followed by a continuous rate for the rest of the experiments (∏). Then, hemorrhagic shock was induced by arterial blood withdrawal and measurements were performed after 30 min and 60 min to assess early (01:30) and late (02:00) shock effects. The period of acute hemorrhage is marked grey in this figure. Finally, the removed blood volume was retransfused and measurements were obtained during early (02:30) and late (03:00) course of retransfusion. Time is indicated as [hh:mm].

2.2.2 Saline (control)

Control animals did not receive drug application prior to acute hemorrhage. Instead, a local application of saline was used to exclude volume effects. After an initial gastric bolus of 0.25 ml·kg^{-1} saline, a continuous fluid supplementation was generated by the application of 2 ml·kg^{-1}·h^{-1} at the gastric mucosa and 0.66 ml·kg^{-1}·h^{-1} at the oral mucosa. Total fluid substitution by gastric and oral drug application was equally in all experimental groups.

2.2.3 Nitroglycerine (N)

Animals received an initial gastric nitroglycerine bolus of 25 µg·kg^{-1} followed by 500 µg·kg^{-1}·h^{-1} continuous nitroglycerine application at the gastric mucosa and 165 µg·kg^{-1}·h^{-1} continuous nitroglycerine application at the oral mucosa. The nitroglycerine dose used in this study was reported to improve gastric µHbO_2 in a previous study (25).

2.2.4 Iloprost (I)

Animals received an initial gastric iloprost bolus of 100 ng·kg^{-1} body weight followed by 2 µg·kg^{-1}·h^{-1} continuous iloprost application at the gastric mucosa and 0.66 µg·kg^{-1}·h^{-1} continuous iloprost application at the oral mucosa. The iloprost dose used in this study was reported to improve gastric µHbO_2 in a previous study (25).

2.2.5 Carbachol (C)

Animals received an initial gastric carbachol bolus of 20 µg·kg^{-1} body weight followed by 10 µg·kg^{-1}·h^{-1} continuous carbachol application at the gastric mucosa and 3.33 µg·kg^{-1}·h^{-1} continuous carbachol application at the oral mucosa. The carbachol dose used in this study is adapted to recommendations for the therapeutic approach of cats and dogs (42).

2.2.6 Nitroglycerine + Carbachol (N + C)

To investigate the additional effect of topical carbachol application on nitroglycerine treatment, animals received a gastric bolus of 25 µg·kg^{-1} nitroglycerine and 20 µg·kg^{-1} carbachol. Gastric (nitroglycerine: 500 µg·kg^{-1}·h^{-1}; carbachol: 10 µg·kg^{-1}·h^{-1}) and oral (nitroglycerine 165 µg·kg^{-1}·h^{-1}; carbachol: 3.33 µg·kg^{-1}·h^{-1}) infusion were performed according to the protocol in groups with single drug treatment.

2.2.7 Iloprost + Carbachol (I + C)

To investigate the additional effect of topical carbachol application on iloprost treatment, animals received a gastric bolus of 100 ng·kg^{-1} iloprost and 20 µg·kg^{-1} carbachol. Gastric (iloprost: 2

$\mu g \cdot kg^{-1} \cdot h^{-1}$; carbachol: 10 $\mu g \cdot kg^{-1} \cdot h^{-1}$) and oral (iloprost 0.66 $\mu g \cdot kg^{-1} \cdot h^{-1}$; carbachol: 3.33 $\mu g \cdot kg^{-1} \cdot h^{-1}$) infusion were performed according to the protocol in groups with single drug treatment.

2.3 Measurements

2.3.1 Reflectance spectrophotometry and laser Doppler flowmetry

Gastric and oral microcirculation were evaluated using a combined measurement of two analytic principles: reflectance spectrophotometry and laser Doppler flowmetry (O2C, LEA Medizintechnik, Gießen, Germany). As described previously, white light with a spectrum between 450 nm und 1000 nm wavelength and a diode generated pulse laser (CW-mode, 820 nm) was emitted into the subepithelial tissue of gastric and oral mucosa. Dependent on its oxygen saturation grade, hemoglobin absorbs different wavelengths of white light. Therefore, the averaged hemoglobin saturation can be calculated from the scattered and reflected, complementary light spectrum. Since blood is not distributed equally within the microcirculatory compartment with a predominantly venous proportion and tissue reflectance spectrophotometry is not able to distinguish between arterial and venous vessels, measurements report mainly postcapillary oxygen saturation (μHbO_2). According to the principle of last meadow, μHbO_2 is a marker to determine tissue oxygen reserve under conditions of generally maintained microvascular vessel architecture. Not focusing on the spectral components, but on the total amount of reflected light, relative hemoglobin content (rHb) can be calculated. Thereby, relative hemoglobin content refers to a predetermined volume of the targeted tissue and correlates antiproportionally to the intensity of reflected light. Vessels that are not part of the microcirculatory compartment lead to total light absorption in consequence of the extensive hemoglobin load in larger vessels.

Laser-Doppler flowmetry is based on the frequency shift, that is generated at the surface of moving particles. Since microcirculatory vessels form a tridimensional network, complex algorithms are used to transform the reflected laser signal and results are reported in arbitrary units [aU] (43). All values reported are the average of measurements within 5 min.

2.3.2 Oral incident dark-field imaging

IDF-imaging is based on initial considerations of Sherman et al. and uses epi-illumination to visualize the microcirculation (44). Further improvement of the technical devices and slight changes in the principle of measurement led to a high-resolution handheld camera called Cytocam (Braedius Medical, Huizen, The Netherlands), which is declared to be the third generation videomicroscope for noninvasive microcirculatory assessment. This device is recommended by an international expert group of the European Society of Intensive Care Medicine (ESICM) to evaluate the microcirculation (11). Conceptionally, pulsed green light is emitted to the targeted tissue and reflected by interstitial cells and matrix components. A complex lens system at the tip of the Cytocam device then creates short video sequences of the reflected light. Since light with a wavelength of 530 nm meets the isosbestic point of oxygenated and deoxygenated hemoglobin, illumination of erythrocytes as the main hemoglobin carriers leads to total absorption. Erythrocytes during the tissue passage then occur as dark light recesses and form the contour of microvascular vessels. The videos were recorded according to the quality requirements of an international expert round and saved anonymized for blinded analysis. Total vessel density (TVD) as a marker of microvascular recruitment and perfused vessel density (PVD) as well as the proportion of perfused vessels (PPV) as indices of microvascular perfusion were determined using an automatic analyzing software. Further, the microvascular flow index was calculated to access the predominant microvascular blood flow characteristics. In detail, the screen is divided into four squares and flow is characterized as not existent (scoring = 0), intermittent (scoring = 1), sluggish (scoring = 2) or regular (scoring = 3). To avoid sampling errors, five videos were recorded, and averaged values are reported.

2.4 Statistics

Macro- and microcirculatory data were obtained during the last 5 min of each intervention period under steady-state conditions and are presented as absolute values of mean ± standard error (mean ± SEM) for five dogs. Normal data distribution was assessed in Q-Q-plots (IBM SPSS Statistics, International Business Machine Corp., United States). A two-way analysis of variance for repeated measurements (ANOVA) and a Bonferroni test as *post-hoc* test for statistical analysis (GraphPad Prism version 6.05 for Windows, GraphPad Software, La Jolla California United States) were used to determine differences within and between the experimental groups. $p < 0.05$ is considered as statistically significant. Multiple measurements enable metric statistical testing of microvascular flow index and heterogeneity index as semiquantitative scores that generally require non-parametric analysis (3).

3 Results

3.1 Effect of local drug application on gastric microcirculation

Gastric μHbO_2 did not differ between experimental groups under baseline conditions and remained unchanged after local drug application. The induction of hemorrhagic shock led to a pronounced decrease of μHbO_2 that was diminished by local nitroglycerine and carbachol application (Figure 2) but not with iloprost. Combining carbachol and nitroglycerine did not further increase μHbO_2, whereas adding carbachol to iloprost significantly raised μHbO_2 during acute hemorrhagic shock. Whereas μHbO_2 after 1 h of hemorrhagic shock increased in animals that received nitroglycerine, the beneficial effect of local carbachol application was limited to the initial shock (Table 1). Across all groups, μHbO_2 returned to baseline values after retransfusion of the shed blood.

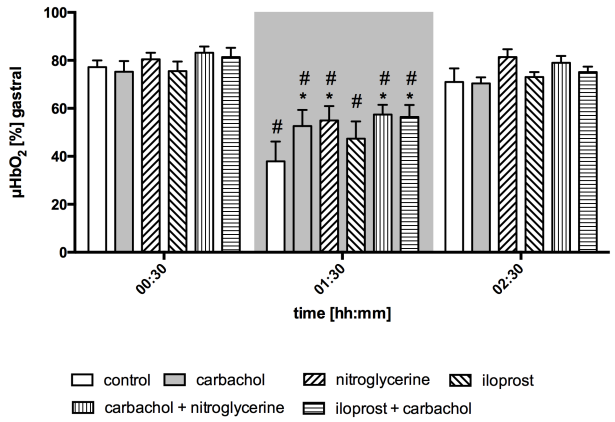

FIGURE 2
Postcapillary oxygen saturation of gastric mucosa. Postcapillary oxygen saturation (μHBO_2) of the gastric mucosa in percentage points (%) under baseline conditions (00:30), during early hemorrhagic shock (01:30) and after retransfusion (02:30) of the shed blood. The period of hemorrhagic shock is visualized by a grey box. Local application with either a sole carbachol, nitroglycerine or iloprost or a combined treatment with nitroglycerine or iloprost and carbachol are marked according to the symbols shown in the legend. The time is indicated as [hh:mm]. Data are presented as mean ± SEM for n = 5 female dogs; * $p < 0.05$ between the indicated experimental group and the control group at one time point. # $p < 0.05$ vs. baseline value. 2-way ANOVA for repeated measurements followed by the Bonferroni *post-hoc* test.

Gastric μflow and rHb remained stable over the time in all experimental groups. There were no differences in gastric μflow and rHb values referring to the experimental groups (Table 1).

3.2 Effect of local drug application on oral microcirculation

Baseline values of oral μHbO_2, μflow and rHb did not differ between experimental groups. Similar to gastric measurements, the induction of hemorrhagic shock led to a significantly decrease of μHbO_2 at the oral mucosa. Neither the local application of carbachol nor the local application of nitroglycerine or iloprost influenced oral μHbO_2 during acute hemorrhage. Furthermore, the combination of local carbachol and nitroglycerine application as well as the combination of local carbachol and iloprost application failed to improve mucosal μHbO_2 during acute hemorrhage (Figure 3). Retransfusion of the taken blood reestablished initial μHbO_2-values at the end of experiments (Table 2). Oral μflow and rHb decreased after shock induction in control animals. None of the treatments improved μflow or rHb during hemorrhagic shock (Table 2). TVD at baseline measurement was similar in all experimental groups. The induction of hemorrhagic shock led to a significant decrease of TVD in all experimental groups. Only the local application of carbachol improved TVD during acute hemorrhage (Figure 4). Initial values of PVD and MFI did not vary between experimental groups. PVD decreased during hemorrhagic shock and was not affected by local drug application. Similarly, MFI decreased in control animals after the induction of acute hemorrhagic shock. After 1 h of the ongoing hemorrhage, MFI was higher in animals that received carbachol compared to controls (Figure 5) and to animals with nitroglycerine or iloprost treatment. PVD and MFI values reached baseline level after retransfusion of the taken blood in all experimental groups (Table 2).

3.3 Effect of local drug application on systemic circulatory variables

Baseline values of CO and DO_2 did not differ between experimental groups. The induction of acute hemorrhagic shock led to a pronounced decrease of CO and DO_2. Retransfusion reestablished adequate CO and DO_2. Local drug application had no effect on systemic circulatory variables (Table 3). Compared to baseline values plasmatic lactate levels increased in all groups with local carbachol application during hemorrhagic shock and remained elevated after blood retransfusion for the rest of the experiments. The cotreatment with nitroglycerine or iloprost mitigated this effect of local carbachol supply on lactate levels during the retransfusion period. At the end of the experiments only the carbachol group had increased lactate levels compared to the control group. Animals that received a sole nitroglycerine or iloprost treatment revealed a slight increase of plasmatic lactate levels, that did not exceed the physiological range. Slight changes of arterial blood gases, pH-value and bicarbonate concentration remained within the physiological range in all experimental groups (Table 4).

4 Discussion

This study investigated the effects of local carbachol alone and in combination with nitroglycerine or iloprost application on gastric and oral microcirculation and tissue oxygenation during hemorrhagic shock. According to literature, all substances might have a potential to induce microvascular recruitment. However, beneficial effects of local nitroglycerine and iloprost application might be partially counteracted by adrenergic vasoconstriction. Therefore, we investigated, if the simultaneous use of the parasympathomimetic carbachol leads to further microvascular recruitment and an improved tissue oxygenation in the gastrointestinal tract by reducing regional sympathetic effects. Since patients with hemorrhagic shock are highly vulnerable to additional adverse events due to the barely compensated hemodynamic situation, we chose local drug application to mitigate systemic side effects of the pharmacological treatment.

The main findings are:

(i) Local carbachol recruits the structural microcirculation of the oral mucosa, that leads to an increase of microvascular flow index in the late course of hemorrhage. Gastric but not oral tissue oxygenation improved during hemorrhagic shock.

10.3389/fimmu.2024.1369617

TABLE 1 Gastric microcirculation.

Variable	group	00:30				01:00				01:30				02:00				02:30				03:00			
μHbO_2 gastral [%]	control	77	±	3		74	±	6		38	±	8	#	45	±	9	#	71	±	6		75	±	5	
	C	75	±	4		76	±	2		53	±	7	#*	58	±	5	#	70	±	3		78	±	2	
	N	81	±	3		83	±	2		55	±	6	#*	61	±	8	#*	81	±	3		80	±	2	
	I	76	±	4		81	±	3		47	±	7	#	53	±	7	#	73	±	2		75	±	4	
	C + N	83	±	3		84	±	2		57	±	4	#*	56	±	7	#	79	±	3		81	±	4	
	C + I	81	±	4		83	±	4		56	±	5	#*	58	±	3	#	75	±	2		80	±	1	
µflow gastral [aU]	control	154	±	29		170	±	9		128	±	10		175	±	21		191	±	18		214	±	26	
	C	177	±	11		195	±	42		121	±	19		117	±	17		156	±	31		141	±	32	
	N	187	±	26		201	±	26		145	±	21		190	±	32		213	±	31		186	±	23	
	I	127	±	24		194	±	21		169	±	31		171	±	31		167	±	34		153	±	18	
	C + N	110	±	14	§	170	±	24		101	±	13		115	±	11		165	±	22		134	±	31	
	C + I	129	±	11		170	±	21		133	±	14		147	±	24		186	±	23		175	±	30	
µvelo gastral [aU]	control	19	±	1		18	±	1		16	±	1		19	±	1		20	±	1		22	±	2	
	C	19	±	1		22	±	3		16	±	2		16	±	1		19	±	2		20	±	2	
	N	21	±	2		21	±	2		17	±	1		20	±	2		22	±	3		21	±	3	
	I	16	±	2		19	±	2		16	±	1		18	±	3		17	±	2		18	±	2	
	C + N	15	±	1	§	19	±	2		14	±	1		14	±	1	§	18	±	1		17	±	2	
	C + I	18	±	1		20	±	2		18	±	1		18	±	2		21	±	2		21	±	3	
rHb gastral [aU]	control	56	±	6		54	±	6		47	±	8		45	±	6		54	±	5		55	±	6	
	C	49	±	5		54	±	7		52	±	5		50	±	4		43	±	5		44	±	7	
	N	60	±	5		64	±	4		55	±	4		54	±	3		64	±	6		59	±	6	
	I	49	±	6		54	±	7		42	±	2		44	±	5		43	±	5		47	±	7	
	C + N	55	±	7		61	±	6		47	±	7		52	±	6		53	±	9		51	±	8	
	C + I	52	±	6		61	±	5		50	±	5		51	±	6		54	±	6		56	±	6	

Postcapillary oxygen saturation (µHbO2; [%]), Microvascular blood flow (µflow; [aU]), microvascular blood flow velocity (µvelo; [aU]) and relative hemoglobin content (rHb; [aU]) of gastric mucosa after a sole or combined local treatment with carbachol (C), nitroglycerine (N) or iloprost (I). The time is indicated as [hh:mm]. Values are reported under baseline conditions (00:30), after drug application (01:00), during early (01:30) and late (02:00) hemorrhage and during early (02:30) and late blood retransfusion (03:00). Data are presented as mean ± SEM for n = 5 female dogs. # $p < 0.05$ vs. baseline values; * $p < 0.05$ vs. control group; § $p < 0.05$ vs. a sole nitroglycerine or iloprost treatment, if carbachol was applicated simultaneously. 2-way ANOVA for repeated measurements followed by Bonferroni post-hoc test.

(ii) Nitroglycerine application results in a potent increase of postcapillary oxygen saturation at the gastric mucosa, that cannot be enhanced further by an additional carbachol treatment. Local iloprost application slightly enhances gastric tissue oxygenation, that can be supplemented sufficiently by local carbachol treatment. Local drug application had no effect on oral microcirculation.

(iii) There are no systemic side effects on circulatory variables after local carbachol, nitroglycerine and iloprost or the combined application.

The main results of pharmacological treatment on gastric and oral mucosa are summarized in Table 5 and are discussed in the following section. Local carbachol application improves gastric μHbO_2 during hemorrhagic shock. Since μHbO_2 mainly represents postcapillary oxygen saturation and the postcapillary region of the microcirculation had shown to be the area of risk under conditions of restricted oxygen delivery, an amelioration of gastric μHbO_2 could indicate an increase of microvascular oxygen reserve after muscarinic stimulation (45). In general, there are three possible reasons for an increase of μHbO_2 values. First, local drug application can induce a redistribution of circulating blood towards the investigated tissue with an increase of microvascular oxygen supply. µflow and rHb of the gastric mucosa remained unchanged over the time and pulmonary oxygen uptake was not restricted by an additional lung injury in this model of hemorrhagic shock. In consequence, microvascular oxygen supply did not increase after local carbachol substitution. Second, alterations of cell metabolism could lead to a reduced oxygen extraction fraction. Carbachol is reported to exert various effects on the physiological cell function of enterocytes. In

10.3389/fimmu.2024.1369617

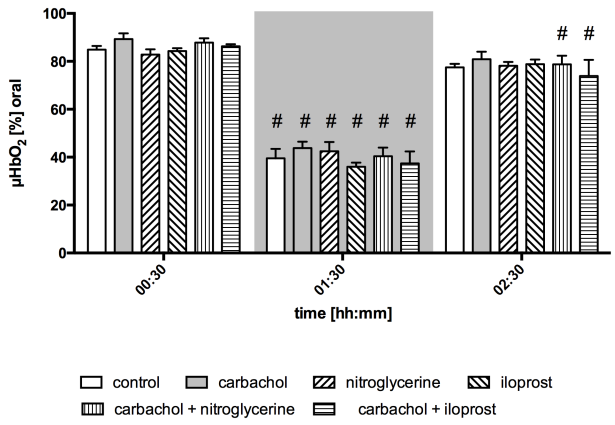

FIGURE 3
Postcapillary oxygen saturation of oral mucosa. Postcapillary oxygen saturation (μHBO_2) of oral mucosa in percentage points (%) under baseline conditions (00:30), during early hemorrhagic shock (01:30) and after retransfusion (02:30) of the shed blood. The period of hemorrhagic shock is visualized by a grey box. Local application with either a sole carbachol, nitroglycerine or iloprost or a combined treatment with nitroglycerine or iloprost and carbachol are marked according to the symbols shown in the legend. The time is indicated as [hh:mm]. Data are presented as mean ± SEM for n = 5 female dogs; # $p < 0.05$ vs. the individual baseline value. There were no differences between the experimental groups at one time point. 2-way ANOVA for repeated measurements followed by the Bonferroni *post-hoc* test.

detail, muscarinic stimulation leads to the phosphorylation of a Na^+/K^+-ATPase α-subunit (46) and liberates intracellular calcium (47). Both, α-subunit phosphorylation and an increased calcium concentration inhibit intestinal Na^+/K^+-ATPase-activity (47). Since maintenance of the electrical membrane potential is an extensively energy consuming process, inhibition of Na^+/K^+-ATPase-activity by carbachol could reduce cellular ATP demand and protect intestinal cells. Further, a slightly shifted electrical membrane potential and changes of the transmembrane ion gradients could influence basic cell metabolism as well. Since plasmatic lactate levels increased in all experimental groups that received carbachol treatment a reduced oxygen extraction fraction cannot only be explained by reduced cellular ATP demand, but also by cellular oxygen utilization disturbance. However, due to the minimal invasive access of the measurements and to avoid microcirculatory alterations after minor trauma related to tissue harvesting *in vivo*, we could not monitor mitochondrial function in this model of acute hemorrhage. Therefore, the reason and clinical relevance of the observed minimal increase of arterial lactate levels remains speculative. As the third possibility, changes of the structural microcirculation could increase gastric μHbO_2 by two mechanisms, microvascular shunting and microvascular recruitment. Microvascular shunting separates tissue from a sufficient gas and nutrient exchange (48) and increases μHbO_2 because of arterio-venous bypassing whereas inhomogeneous tissue perfusion and tissue hypoxia establish consequently over time. In critically ill patients and especially in patients with septic shock this phenomenon is observed frequently and seems to be one of the main microvascular derangements leading to organ failure and an increase of mortality (49). The significance of microvascular shunting and the formation of so called "weak units" (50, 51) in patients with hemorrhagic shock is still unclear. Contrary to microvascular shunting, pharmacological reopening of microvessels could reduce the oxygen diffusion distance from erythrocytes to stroma cells, reduce the total diffusion gradient and improve all over tissue oxygenation. Whereas microvascular shunting is associated with a decreased TVD and PVD, microvascular recruitment leads to an increase of both perfusion markers. In this study, oral TVD increased during hemorrhagic shock after local carbachol application indicating microvascular recruitment. This is additionally supported by our previous observation that improved oxygenation via nitroglycerine improved barrier function (25). In case of microvascular shunting the overall oxygen supply would be reduced and barrier function impaired. However, local carbachol treatment did not improve oral μHbO_2 despite microvascular recruitment. Since oral μflow and PVD did not increase after topical carbachol treatment, we suggest that recruitment of oral vessels by carbachol application is accompanied by insufficient regional oxygen carrier supply during to hemorrhagic shock. Only MFI improved in the late course of hemorrhagic shock indicating favorable properties of carbachol on oral microcirculation. However, results from oral microcirculatory measurements cannot be transferred doubtless to other parts of the gastrointestinal tract, since our group could identify a different response of the oral and gastric microcirculation to topical melatonin treatment (36) and hypothermia (34) in a similar canine model of hemorrhagic shock. The observation that carbachol improves gastric but not oral oxygenation might indicate that during hemorrhage there is a more pronounced sympathetic activation in the oral region whereas the gastric region can still be modulated. As local modulation of the sympathetic and the parasympathetic nervous system is possible without systemic side effects, this seems a promising therapeutic option.

Summing up, muscarinic stimulation by local carbachol application leads to microvascular recruitment at the oral mucosa and improves perfusion quality. In this barely compensated vascular bed, microvascular recruitment by local carbachol application failed to improve regional tissue oxygenation possibly due to a remaining regional lack of microvascular tissue perfusion. At the gastric mucosa, local carbachol application enhances μHbO_2 during hemorrhagic shock. From a mechanistic point of view, a change of the basic energy metabolism and microcirculatory recruitment could explain this effect of local carbachol application, but both mechanisms were not addressed in the experiments to avoid a more invasive instrumentation and microcirculatory alterations after minor trauma.

In a previous study, we could show that local nitroglycerine alone and iloprost alone improve gastric μHbO_2 (25). Novel in this study is the effect of carbachol and the effect of the combination carbachol + nitroglycerine and carbachol + iloprost. The experiments with nitroglycerine alone and iloprost alone were conducted again as control group to generate an independent data set for this publication. Our recent findings are mainly in accordance with this previous data. Nitroglycerine enhanced gastric tissue oxygenation during hemorrhagic shock like described before, whereas local iloprost treatment led to slightly increased μHbO_2 values compared to control animals in this study. However, the

TABLE 2 Oral microcirculation.

Variable	group	00:30				01:00				01:30				02:00				02:30				03:00			
μHbO_2 oral [%]	control	85	±	2		77	±	2		40	±	4	#	44	±	4	#	77	±	1		88	±	2	
	C	89	±	2		86	±	2		44	±	3	#	50	±	3	#	81	±	3		90	±	3	
	N	83	±	2		82	±	4		43	±	4	#	51	±	3	#	78	±	2		88	±	2	
	I	84	±	1		83	±	1		36	±	2	#	48	±	3	#	79	±	2		90	±	4	
	C + N	88	±	2		78	±	2		40	±	4	#	45	±	2	#	79	±	4	#	87	±	2	
	C + I	86	±	1		82	±	4		37	±	5	#	41	±	5	#	74	±	7	#	88	±	3	
µflow oral [aU]	control	121	±	18		72	±	5		39	±	14	#	31	±	7	#	83	±	7		154	±	25	
	C	174	±	19		145	±	26	*	34	±	10	#	40	±	4	#	160	±	35	*	179	±	49	
	N	161	±	30		179	±	36	*	42	±	7	#	36	±	11	#	122	±	36		150	±	25	
	I	172	±	19		148	±	20	*	34	±	8	#	34	±	7	#	121	±	21		193	±	25	
	C + N	158	±	21		176	±	43	*	37	±	6	#	42	±	9	#	119	±	19		176	±	47	
	C + I	148	±	28		129	±	27		57	±	13	#	69	±	20	#	147	±	24		196	±	21	
µvelo oral [aU]	control	24	±	3		19	±	1		15	±	3	#	13	±	1	#	20	±	1		29	±	3	
	C	27	±	2		25	±	3		14	±	2	#	16	±	2	#	29	±	3	*	29	±	5	
	N	27	±	3		31	±	3	*	18	±	3	#	13	±	2	#	24	±	4		26	±	2	
	I	28	±	2		27	±	2		13	±	2	#	13	±	1	#	23	±	2		31	±	4	
	C + N	25	±	2		29	±	5	*	14	±	1	#	16	±	2	#	24	±	3		29	±	5	
	C + I	26	±	4		25	±	5		20	±	4		25	±	5	*§	30	±	4	*	31	±	2	
rHb oral [aU]	control	96	±	3		90	±	2		60	±	5	#	62	±	3	#	84	±	4	#	89	±	2	
	C	101	±	2		98	±	2		68	±	2	#	73	±	6	#*	85	±	4	#	93	±	4	
	N	98	±	3		96	±	2		70	±	3	#	76	±	4	#*	86	±	3	#	93	±	2	
	I	98	±	2		93	±	4		58	±	4	#	68	±	5	#	89	±	4	#	90	±	7	
	C + N	99	±	3		100	±	2		69	±	4	#	70	±	6	#	87	±	6	#	93	±	4	
	C + I	97	±	3		94	±	2		60	±	5	#	64	±	4	#	82	±	5	#	94	±	3	
TVD oral [$mm \cdot mm^{-2}$]	control	19	±	0		19	±	1		13	±	1	#	13	±	1	#	18	±	1		19	±	1	
	C	19	±	1		19	±	1		16	±	1	#*	17	±	1	#*	20	±	1		21	±	1	
	N	19	±	1		19	±	1		14	±	2	#	14	±	1	#	19	±	0		19	±	1	
	I	20	±	1		19	±	1		13	±	2	#	14	±	2	#	18	±	1		20	±	1	
	C + N	19	±	1		19	±	1		15	±	1	#	14	±	1	#	19	±	1		20	±	1	
	C + I	18	±	1		18	±	2		13	±	1	#	14	±	2	#	19	±	2		19	±	1	
PVD oral [$mm \cdot mm^{-2}$]	control	12	±	1		11	±	1		5	±	1	#	5	±	1	#	9	±	2	#	11	±	1	
	C	12	±	1		13	±	1		8	±	1	#	9	±	1	*	14	±	1	*	14	±	1	
	N	12	±	1		12	±	1		6	±	1	#	6	±	1	#	11	±	1		12	±	1	
	I	13	±	2		11	±	1		6	±	1	#	7	±	1	#	11	±	1		12	±	1	
	C + N	11	±	1		12	±	1		6	±	1	#	5	±	1	#	10	±	1		12	±	2	
	C + I	10	±	3		11	±	3		6	±	2	#	7	±	3		10	±	3		12	±	2	
PPV oral [%]	control	62	±	2		59	±	3		40	±	7	#	38	±	7	#	47	±	10		58	±	5	
	C	60	±	5		67	±	4		46	±	6		48	±	4		66	±	4	*	67	±	3	
	N	64	±	2		65	±	3		42	±	6	#	45	±	4	#	59	±	5		59	±	5	
	I	64	±	6		55	±	5		43	±	5	#	45	±	4	#	58	±	4		61	±	4	

(Continued)

10.3389/fimmu.2024.1369617

TABLE 2 Continued

Variable	group	00:30				01:00				01:30				02:00				02:30				03:00			
	C + N	54	±	4		57	±	2		40	±	5		36	±	5	#	52	±	7		55	±	11	
	C + I	54	±	13		56	±	13		41	±	10		47	±	11		52	±	10		57	±	9	
MFI oral	control	2,9	±	0,1		2,8	±	0,1		1,7	±	0,1	#	1,8	±	0,2	#	2,9	±	0,0		2,9	±	0,0	
	C	2,9	±	0,1		2,9	±	0,1		1,7	±	0,3	#	2,3	±	0,2	#*	2,9	±	0,1		2,9	±	0,1	
	N	2,8	±	0,1		2,9	±	0,1		1,5	±	0,3	#	1,7	±	0,2	#	2,8	±	0,1		2,8	±	0,1	
	I	2,8	±	0,1		2,8	±	0,1		1,6	±	0,2	#	1,6	±	0,2	#	2,7	±	0,1		2,9	±	0,1	
	C + N	2,9	±	0,1		3,0	±	0,0		1,6	±	0,3	#	1,8	±	0,2	#	2,8	±	0,1		2,9	±	0,1	
	C + I	2,8	±	0,1		2,8	±	0,2		1,5	±	0,2	#	2,0	±	0,2	#§	2,8	±	0,1		2,9	±	0,1	

Postcapillary oxygen saturation (μHbO2; [%]), Microvascular blood flow (μflow; [aU]), microvascular blood flow velocity (μvelo; [aU]), relative hemoglobin content (rHb; [aU]), total vessel density (TVD; [mm/mm2]), perfused vessel density (PVD; [mm/mm2]), proportion of perfused vessels (PPV; [mm/mm2]) and microvascular flow index (MFI) of gastric mucosa after a sole or combined local treatment with carbachol (C), nitroglycerine (N) or iloprost (I). Values are reported under baseline conditions (00:30), after drug application (01:00), during early (01:30) and late (02:00) hemorrhage and during early (02:30) and late blood retransfusion (03:00). The time is indicated as [hh:mm]. Data are presented as mean ± SEM for n = 5 female dogs. # $p < 0.05$ vs. baseline values; * $p < 0.05$ vs. control group; § $p < 0.05$ vs. a sole nitroglycerine or iloprost treatment, if carbachol was applicated simultaneously. 2-way ANOVA for repeated measurements followed by Bonferroni post-hoc test.

regime of local nitroglycerine and iloprost treatment was in accordance with our previous work. When local iloprost application was supplemented with carbachol, gastric μHbO_2 further increased during hemorrhagic shock. A combined carbachol and nitroglycerine treatment did not reveal an additional effect on gastric tissue oxygenation. On the one hand, those findings could be related to direct effects of nitroglycerine, iloprost and carbachol on gastric microcirculation for example by a different potency to recruit gastric microcirculation. On the other hand, this could be the result of a subcellular crosstalk between two different signaling pathways. Muscarinic stimulation by carbachol application was reported to act via a nitric oxide dependent pathway (52). The combination of endogenous nitric oxide generation during hemorrhagic shock and an exogenous substitution of nitroglycerine could exceed the physiological range of available nitric oxide and lead to a maximal activation of nitric oxide related effects. If muscarinic effects exclusively depend on the nitric oxide pathway, this might explain why carbachol cannot further enhance gastric μHbO_2 when applicated additionally to local nitroglycerine. Nevertheless, positive effects of nitroglycerine do not seem to be partially counteracted by autonomous neurogenic influence.

Prostacyclin effects within the microcirculatory compartment might be related at least in part to a different pathway that includes ATP release from erythrocytes (53, 54). The simultaneous activation of carbachol dependent nitric oxide generation and iloprost related ATP release, could lead to further improvement of gastric tissue oxygenation in incompletely recruited vessels. Additionally, iloprost activates an inosine triphosphate dependent pathway too, formatting a complex network of second messenger activation with various effects on regional homeostasis and cell metabolism. Furthermore, Herminghaus et al. already reported nitroglycerine and iloprost to improve the efficiency of oxidative

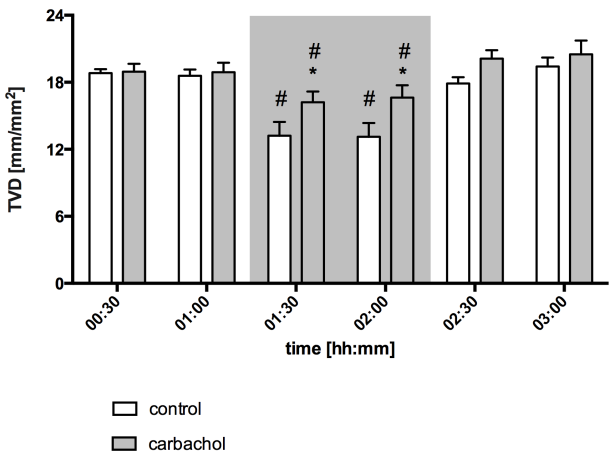

FIGURE 4
Total vessel density of oral mucosa after local carbachol treatment. Total vessel density (TVD) of oral mucosa in mm/mm^2. The period of hemorrhagic shock is visualized by a grey box. Local application with either saline or carbachol is marked according to the symbols shown in the legend. Other experimental groups are not shown for reasons of clarity. The time is indicated as [hh:mm]. Data are presented as mean ± SEM for n = 5 female dogs; * $p < 0.05$ between animals, that received saline or carbachol at one time point. 2-way ANOVA for repeated measurements followed by the Bonferroni *post-hoc* test.

10.3389/fimmu.2024.1369617

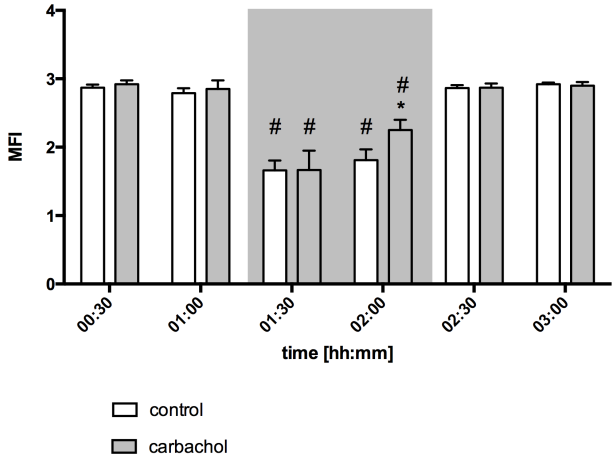

FIGURE 5
Microvascular flow index of oral mucosa after local carbachol treatment: Microvascular flow index (MFI) of oral mucosa. The period of hemorrhagic shock is visualized by a grey box. Local application with either saline or carbachol is marked according to the symbols shown in the legend. Other experimental groups are not shown for reasons of clarity. The time is indicated as [hh:mm]. Data are presented as mean ± SEM for n = 5 female dogs; * $p < 0.05$ between animals, that received saline or carbachol at one time point. 2-way ANOVA for repeated measurements followed by the Bonferroni *post-hoc* test.

TABLE 3 Macrocirculatory variables.

Variable	group	00:30				01:00				01:30				02:00				02:30				03:00			
DO_2 [ml·kg^{-1}·min^{-1}]	control	14	±	1		13	±	1		8	±	0	#	8	±	0	#	14	±	1		14	±	1	
	C	15	±	1		14	±	1		8	±	1	#	9	±	1	#	14	±	1		15	±	1	
	N	14	±	1		13	±	1		7	±	1	#	9	±	0	#	14	±	1		13	±	1	
	I	14	±	1		14	±	0		7	±	0	#	9	±	1	#	14	±	1		14	±	1	
	C + N	14	±	0		13	±	1		8	±	0	#	8	±	0	#	14	±	1		14	±	1	
	C + I	15	±	1		14	±	1		8	±	1	#	9	±	1	#	15	±	1		15	±	1	
SVR [mmHg·l^{-1}·min]	control	22	±	1		24	±	1		31	±	2	#	31	±	2	#	29	±	2	#	24	±	2	
	C	21	±	1		22	±	1		33	±	4	#	32	±	3	#	28	±	1	#	23	±	1	
	N	23	±	2		22	±	2		30	±	2	#	28	±	1	#	24	±	1		22	±	1	
	I	21	±	1		22	±	1		33	±	3	#	31	±	2	#	29	±	2	#	24	±	3	
	C + N	21	±	2		21	±	2		25	±	3	#*§	29	±	3	#*	22	±	1		20	±	1	
	C + I	22	±	1		23	±	2		30	±	2	#	31	±	1	#	28	±	1	#	22	±	1	
CO [ml·kg^{-1}·min^{-1}]	control	81	±	4		81	±	2		48	±	1	#	52	±	2	#	84	±	4		88	±	5	
	C	90	±	6	*	87	±	5		47	±	4	#	56	±	3	#	89	±	5		95	±	6	
	N	83	±	5		78	±	5		42	±	2	#	51	±	2	#	84	±	4		81	±	4	
	I	85	±	3		83	±	1		44	±	2	#	52	±	3	#	84	±	4		89	±	5	
	C + N	88	±	2		81	±	2		47	±	2	#	48	±	2	#	89	±	3		89	±	3	
	C + I	88	±	6		86	±	6		50	±	2	#	56	±	4	#	91	±	6		95	±	6	
SV [ml]	control	24	±	1		24	±	1		15	±	1	#	16	±	1	#	27	±	1	#	27	±	1	#
	C	26	±	1		25	±	1		14	±	1	#	16	±	1	#	28	±	1		30	±	1	#*
	N	25	±	1		23	±	1		13	±	0	#	15	±	1	#	26	±	1		25	±	1	*

(Continued)

TABLE 3 Continued

Variable	group	00:30				01:00				01:30				02:00				02:30				03:00			
	I	25	±	2		24	±	1		13	±	1	#	15	±	1	#	27	±	1	#	29	±	2	#
	C + N	25	±	2		23	±	1		14	±	1	#	14	±	1	#	27	±	1		27	±	1	
	C + I	24	±	1		23	±	1		15	±	1	#	16	±	1	#	27	±	1	#	28	±	1	#
dPmax [$mmHg^{-1}$·s]	control	432	±	24		400	±	22		332	±	22	#	324	±	12	#	392	±	11		428	±	24	
	C	486	±	17		452	±	19		334	±	21	#	362	±	25	#	418	±	30	#	454	±	34	
	N	474	±	21		416	±	39		322	±	25	#	330	±	27	#	404	±	41	#	434	±	49	
	I	486	±	29		464	±	29		326	±	28	#	340	±	25	#	418	±	37	#	428	±	35	
	C + N	476	±	14		428	±	20		300	±	10	#	342	±	17	#	414	±	20	#	436	±	25	
	C + I	482	±	23		450	±	21		358	±	19	#	376	±	22	#	476	±	64	*	514	±	59	*§
MAP [mmHg]	control	60	±	2		64	±	3		48	±	3	#	54	±	2	#	79	±	3	#	69	±	4	#
	C	62	±	2		64	±	2		50	±	2	#	58	±	2	#	82	±	3	#	74	±	3	#
	N	61	±	4		56	±	2		42	±	2	#	48	±	2	#	68	±	2	#	59	±	2	*
	I	59	±	2		60	±	2		47	±	2	#	54	±	1	#	79	±	3	#	67	±	5	#
	C + N	60	±	3		55	±	3		38	±	3	#	46	±	3	#	65	±	3		60	±	3	*
	C + I	60	±	1		62	±	3		46	±	1	#	55	±	2		80	±	1	#	67	±	3	#
HR [min^{-1}]	control	114	±	2		115	±	2		109	±	3		112	±	2		103	±	3	#	108	±	3	#
	C	116	±	4		116	±	3		111	±	2		114	±	3		105	±	4	#	107	±	3	#
	N	112	±	4		114	±	3		110	±	2		114	±	2		107	±	3		109	±	4	
	I	116	±	4		116	±	3		111	±	2	#	117	±	4		104	±	4	#	102	±	4	#*
	C + N	116	±	4		118	±	3		110	±	2		114	±	2		110	±	3	#	111	±	3	#
	C + I	116	±	4	§	116	±	4		110	±	3	#	114	±	2	*	107	±	5	#	108	±	4	#§

Systemic oxygen delivery (DO2; [ml·kg-1·min-1]), systemic vascular resistance (SVR; [mmHg·l-1·min-1]), cardiac output (CO; [ml·kg-1·min-1]), stroke volume (SV; [ml]), index for cardiac inotropy (dPmax; [mmHg-1·sec]), mean arterial pressure (MAP; [mmHg]) and heart rate (HR; [min-1]) after a sole or combined local treatment with carbachol (C), nitroglycerine (N) or iloprost (I). Values are reported under baseline conditions (00:30), after drug application (01:00), during early (01:30) and late (02:00) hemorrhage and during early (02:30) and late blood retransfusion (03:00). The time is indicated as [hh:mm]. Data are presented as mean ± SEM for n = 5 female dogs. # $p < 0.05$ vs. baseline values; * $p < 0.05$ vs. control group; § $p < 0.05$ vs. a sole nitroglycerine or iloprost treatment, if carbachol was applicated simultaneously. 2-way ANOVA for repeated measurements followed by Bonferroni post-hoc test.

phosphorylation in colon homogenates from healthy animals measured by respirometry (55). Therefore, downstream effects of local carbachol, nitric oxide and iloprost application could not only exert effects on microcirculation but influence mitochondrial respiration leading to an increase of gastric μHbO_2. Since subcellular pathways of nitroglycerine, iloprost and carbachol have not been addressed in this study, further research should elucidate subcellular effects of the here used agents under conditions of restricted oxygen delivery.

Finally, drugs were applicated locally to avoid systemic side effects. In the past, our group used various local treatment regimens to improve gastric tissue oxygenation (34–36). None of those trials revealed systemic complications. In accordance, local carbachol application did not reveal systemic side effects on hemodynamic variables and macrohemodynamics were similar between all experimental groups, although we did not measure the intravenous concentration of carbachol in our experiments. During the experiments, we could not observe malignant arrhythmias like ventricular tachycardia or severe bradycardia. Even if local carbachol treatment was combined with either local nitroglycerine or local iloprost application there were no adverse effects on hemodynamic variables. Systemic lactate concentration increased in animals that received local carbachol treatment. However, as the measured values were only slightly higher than in the other experimental groups and plasmatic lactate concentration has many confounding factors, the physiological relevance of this finding remains questionable. Due to the reusable animal model the dogs were continuously under observation by the animal care staff that included veterinarians. Therefore, we state that local application of carbachol is safe and does not influence systemic homeostasis.

This gives the perspective to translate our approach into clinical studies. Local drug application to improve gastric microcirculation should be tested in patients with elective gastroscopy first. If local drug application emphasizes to be safe in healthy patients, the administration during interventional procedures and abdominal surgery should be tested in a second step. Patients with upper gastrointestinal bleeding appear to be the ideal patient population for transferring our results to humans, since these patients must be subjected to endoscopic hemostasis anyway. Local drug application could then follow acute bleeding control in the same session.

TABLE 4 Arterial blood gas analysis.

Variable	group	00:30				01:00				01:30				02:00				02:30				03:00			
S_aO_2 [%]	control	99	±	0		99	±	0		98	±	0	#	98	±	0	#	99	±	0		99	±	0	
	C	99	±	0		99	±	0		98	±	0	#	98	±	0	#	99	±	0		99	±	0	
	N	99	±	0		99	±	0		98	±	0	#*	98	±	0	#*	99	±	0		99	±	0	
	I	99	±	0		99	±	0		98	±	0	#	98	±	0	#	99	±	0		99	±	0	
	C + N	98	±	0		98	±	0		97	±	0	#*	98	±	0	#*	99	±	0		99	±	0	
	C + I	99	±	0		99	±	0		98	±	0	#	98	±	0	#	99	±	0		99	±	0	
p_aO_2 [mmHg]	control	151	±	3		150	±	3		146	±	3		146	±	4		156	±	4		154	±	4	
	C	147	±	2		149	±	4		144	±	4		145	±	3		158	±	2	#	158	±	3	#
	N	150	±	3		150	±	3		140	±	5	#	142	±	4	#	159	±	3	#	157	±	3	#
	I	152	±	2		156	±	2		145	±	4	#	147	±	3		160	±	2	#	160	±	2	#
	C + N	147	±	5		146	±	4		134	±	4	#*	144	±	5		162	±	4	#	161	±	5	#*
	C + N	148	±	3		152	±	4		143	±	3		144	±	2		157	±	4	#	157	±	3	#
p_aCO_2 [mmHg]	control	35	±	0		36	±	0		40	±	1	#	39	±	1	#	36	±	1		37	±	0	#
	C	35	±	1		35	±	1		41	±	1	#	39	±	1	#	36	±	1		36	±	1	
	N	36	±	1		36	±	1		42	±	1	#*	41	±	1	#*	37	±	0		37	±	1	
	I	35	±	1		36	±	1		41	±	1	#	40	±	1	#	36	±	1		36	±	1	
	C + N	36	±	0		37	±	0		43	±	1	#*	41	±	1	#*	37	±	0		37	±	1	
	C + I	35	±	1		36	±	1		41	±	2	#	40	±	2	#	36	±	1		35	±	1	*
pH	control	7.4	±	0.01		7.39	±	0.01		7.32	±	0.02	#	7.33	±	0.02	#	7.37	±	0.01	#	7.37	±	0.01	#
	C	7.4	±	0.01		7.39	±	0.01		7.31	±	0.02	#	7.31	±	0.02	#*	7.36	±	0.02	#	7.36	±	0.02	#
	N	7.39	±	0.01		7.38	±	0.01		7.3	±	0.01	#*	7.31	±	0.01	#*	7.35	±	0.01	#*	7.36	±	0.01	#
	I	7.4	±	0.01		7.39	±	0.01		7.32	±	0.02	#	7.33	±	0.01	#	7.38	±	0.01	#	7.38	±	0.01	#
	C + N	7.39	±	0.01		7.37	±	0.01	*§	7.29	±	0.01	#*	7.29	±	0.01	#*§	7.34	±	0.01	#*	7.35	±	0.01	#
	C + I	7.4	±	0.01		7.39	±	0.01		7.31	±	0.02	#	7.31	±	0.02	#§	7.37	±	0.01	#	7.39	±	0.01	*
HCO_3^- [mmol·l^{-1}]	control	21	±	0		21	±	1		20	±	1	#	20	±	1	#	20	±	0		20	±	0	
	C	21	±	0		21	±	0		20	±	0	#	19	±	1	#*	20	±	1	#*	20	±	0	#
	N	21	±	0		21	±	0		20	±	0	#	20	±	0	#	20	±	0	#	20	±	0	#

(Continued)

10.3389/fimmu.2024.1369617

TABLE 4 Continued

Variable	group	00:30				01:00				01:30				02:00				02:30				03:00			
	I	21	±	0		21	±	0		20	±	0	#	20	±	0	#	20	±	0	#	21	±	0	
	C + N	21	±	0		21	±	0		20	±	0	#	19	±	0	#*§	19	±	0	#*	20	±	0	#
	C + I	21	±	0		21	±	0		20	±	0	#	20	±	1	#	20	±	0	#	20	±	0	#
Lac [mmol·l^{-1}]	control	1.1	±	0.1		1.3	±	0.1		1.6	±	0.2		1.6	±	0.2		1.7	±	0.2		1.6	±	0.2	
	C	0.6	±	0.1		0.8	±	0.1		2.2	±	0.6	#	2.6	±	0.8	#*	2.4	±	0.7	#*	2.4	±	0.7	#*
	N	0.9	±	0.2		1.1	±	0.2		1.5	±	0.1	#	1.6	±	0.1	#	1.4	±	0.1		1.3	±	0.1	
	I	0.9	±	0.1		1.1	±	0.1		1.5	±	0.3	#	1.4	±	0.3		1.2	±	0.3		1.2	±	0.3	
	C + N	0.7	±	0.0		1.0	±	0.1		1.6	±	0.2	#	2.0	±	0.3	#	2.0	±	0.4	#	1.9	±	0.4	#
	C + I	0.9	±	0.0		1.2	±	0.1		2.2	±	0.6	#	2.4	±	0.6	#*	2.1	±	0.6	#	1.9	±	0.5	#
Hb [g·100ml^{-1}]	control	12	±	0		12	±	0		12	±	0		12	±	0		12	±	0		12	±	0	#
	C	12	±	0		12	±	0		12	±	0	#	12	±	0		12	±	0	#	12	±	0	#
	N	12	±	0		12	±	0		13	±	0		12	±	0	*	12	±	0		12	±	0	#
	I	12	±	0		12	±	0		12	±	0		12	±	0		12	±	0		12	±	0	
	C + N	12	±	0		12	±	0	*§	12	±	0		12	±	0	§	12	±	0	§	12	±	0	#§
	C + I	12	±	0		12	±	0		12	±	0		12	±	0		12	±	0		12	±	0	#
Hct [%]	control	37	±	1		37	±	1		38	±	1		37	±	1		37	±	1		36	±	1	#
	C	37	±	1		37	±	1		38	±	1		37	±	1		36	±	1	#	36	±	1	#
	N	38	±	1		38	±	1		38	±	1		38	±	1	*	37	±	1		37	±	1	#
	I	37	±	1		37	±	1		38	±	1		37	±	1		37	±	1		37	±	1	
	C + N	37	±	1		36	±	1		38	±	1		37	±	1	§	36	±	1	§	36	±	1	#§
	C + I	37	±	1		37	±	1		38	±	1		37	±	1		37	±	1		36	±	1	#

Arterial hemoglobin oxygen saturation (SaO2; [%]), oxygen partial pressure (paO2; [mmHg]), carbon dioxide artial pressure (paCO2; [mmHg]), pH-values, bicarbonate concentration (HCO3-; [mmol · l-1]), lactate concentration (Lac; [mmol · l-1]), hemoglobin content (Hb; [g · 100ml-1]) and hematocrit (Hct; [%]) after a sole or combined local treatment with carbachol (C), nitroglycerine (N) or iloprost (I). Values are reported under baseline conditions (00:30), after drug application (01:00), during early (01:30) and late (02:00) hemorrhage and during early (02:30) and late blood retransfusion (03:00). The time is indicated as [hh:mm]. Data are presented as mean ± SEM for n = 5 female dogs. # $p < 0.05$ vs. baseline values; * $p < 0.05$ vs. control group; § $p < 0.05$ vs. a sole nitroglycerine or iloprost treatment, if carbachol was applicated simultaneously. 2-way ANOVA for repeated measurements followed by Bonferroni post-hoc test.

10.3389/fimmu.2024.1369617

10.3389/fimmu.2024.1369617

TABLE 5 Summary of microvascular effects of pharmacological treatment.

	Variable	μHbO_2	μflow	μvelo	rHb	TVD	PVD	PPV	MFI
gastric mucosa	C	↑ [a]	↔	↔	↔				
	N	↑↑	↔	↔	↔				
	I	↔	↔	↔	↔				
	C + N	↑ [a]	↔	↔	↔				
	C + I	↑ [a]	↔	↔	↔				
oral mucosa	C	↔	↔	↔	↑ [b]	↑↑	↑ [b]	↔	↑ [b]
	N	↔	↔	↔	↑ [b]	↔	↔	↔	↔
	I	↔	↔	↔	↔	↔	↔	↔	↔
	C + N	↔	↔	↔	↔	↔	↔	↔	↔
	C + I	↔	↔	↑ [b]	↔	↔	↔	↔	↔

Effects of local pharmacological treatment on gastric and oral microcirculatory variables during hemorrhagic shock are indicated using arrows. If only early (a) or late (b) shock was affected by sole or combined carbachol (C), nitroglycerin (N) or iloprost (I) treatment simple arrows (↑) were used. Beneficial effects during the whole course of shock were indicated by doubled arrows (↑↑). Incident dark-field imaging was performed only at the oral mucosa due to the minimal invasive instrumentation of the animals.

5 Conclusion

Local carbachol application induces favorable effects on oral microcirculation and gastric tissue oxygenation during hemorrhagic shock. Since microvascular perfusion remained unchanged after local carbachol supply, the down-stream effects of carbachol on cell metabolism and mitochondrial function could be interesting targets for tissue protection by local carbachol treatment during hemorrhagic shock and should be investigated in further studies. The effect of additional application of local carbachol to regional vasodilators depends on the combination used to improve microcirculation. Since different parts of the gastrointestinal tract seem to respond differently to local drug application, further studies should clarify, if the findings derived from this study can be translated to other parts of the gastrointestinal tract. However, local carbachol application and the combination with local vasodilators have no effect on the hemodynamic stability during hemorrhagic shock and therefore represent an interesting approach for tissue protection.

Data availability statement

The original contributions presented in the study are included in the article/supplementary material. Further inquiries can be directed to the corresponding author.

Ethics statement

The animal study was approved by Landesamt für Natur, Umwelt und Verbraucherschutz Nordrhein-Westfalen. The study was conducted in accordance with the local legislation and institutional requirements.

Author contributions

SH: Data curation, Formal analysis, Visualization, Writing – original draft. LL: Data curation, Investigation, Writing – review & editing. MM: Data curation, Investigation, Writing – review & editing. CM: Writing – review & editing. AK: Writing – review & editing. AH: Conceptualization, Writing – review & editing. IB: Conceptualization, Project administration, Supervision, Writing – review & editing. OP: Conceptualization, Project administration, Supervision, Writing – review & editing. RT: Conceptualization, Project administration, Supervision, Writing – review & editing. CV: Conceptualization, Project administration, Supervision, Writing – review & editing.

Funding

The author(s) declare that no financial support was received for the research, authorship, and/or publication of this article.

Conflict of interest

The authors declare that the research was conducted in the absence of any commercial or financial relationships that could be construed as a potential conflict of interest.

Publisher's note

References

1. Cannon JW. Hemorrhagic shock. *N Engl J Med*. (2018) 378:370–9. doi: 10.1056/NEJMra1705649

2. Mitra B, Gabbe BJ, Kaukonen KM, Olaussen A, Cooper DJ, Cameron PA. Long-term outcomes of patients receiving a massive transfusion after trauma. *Shock Augusta Ga*. (2014) 42:307–12. doi: 10.1097/SHK.0000000000000219

3. Hof S, Truse R, Weber L, Herminghaus A, Schulz J, Weber APM, et al. Local mucosal CO2 but not O2 insufflation improves gastric and oral microcirculatory oxygenation in a canine model of mild hemorrhagic shock. *Front Med*. (2022) 9:867298. doi: 10.3389/fmed.2022.867298

4. Ince C. Hemodynamic coherence and the rationale for monitoring the microcirculation. *Crit Care Lond Engl*. (2015) 19 Suppl 3:S8. doi: 10.1186/cc14726

5. Sakr Y, Dubois MJ, De Backer D, Creteur J, Vincent JL. Persistent microcirculatory alterations are associated with organ failure and death in patients with septic shock. *Crit Care Med*. (2004) 32:1825–31. doi: 10.1097/01.CCM.0000138558.16257.3F

6. Trzeciak S, McCoy JV, Phillip Dellinger R, Arnold RC, Rizzuto M, Abate NL, et al. Early increases in microcirculatory perfusion during protocol-directed resuscitation are associated with reduced multi-organ failure at 24 h in patients with sepsis. *Intensive Care Med*. (2008) 34:2210–7. doi: 10.1007/s00134-008-1193-6

7. Ferrara G, Edul VSK, Canales HS, Martins E, Canullán C, Murias G, et al. Systemic and microcirculatory effects of blood transfusion in experimental hemorrhagic shock. *Intensive Care Med Exp*. (2017) 5:24. doi: 10.1186/s40635-017-0136-3

8. Schucht JE, Harbrecht BG, Bond LM, Risinger WB, Matheson PJ, Smith JW. Plasma resuscitation improves and restores intestinal microcirculatory physiology following haemorrhagic shock. *Vox Sang*. (2023) 118:863–72. doi: 10.1111/vox.13504

9. Tárnoky K, Nagy S. Relationship to survival of catecholamine levels and dopamine-beta-hydroxylase activity in experimental haemorrhagic shock. *Acta Physiol Hung*. (1983) 61:59–68.

10. Tung CS, Chu KM, Tseng CJ, Yin TH. Adenosine in hemorrhagic shock: possible role in attenuating sympathetic activation. *Life Sci*. (1987) 41:1375–82. doi: 10.1016/0024-3205(87)90612-6

11. Ince C, Boerma EC, Cecconi M, De Backer D, Shapiro NI, Duranteau J, et al. Second consensus on the assessment of sublingual microcirculation in critically ill patients: results from a task force of the European Society of Intensive Care Medicine. *Intensive Care Med*. (2018) 44:281–99. doi: 10.1007/s00134-018-5070-7

12. Spronk PE, Ince C, Gardien MJ, Mathura KR, Oudemans-van Straaten HM, Zandstra DF. Nitroglycerin in septic shock after intravascular volume resuscitation. *Lancet Lond Engl*. (2002) 360:1395–6. doi: 10.1016/S0140-6736(02)11393-6

13. van der Voort PHJ, van Zanten M, Bosman RJ, van Stijn I, Wester JPJ, van Raalte R, et al. Testing a conceptual model on early opening of the microcirculation in severe sepsis and septic shock: a randomised controlled pilot study. *Eur J Anaesthesiol*. (2015) 32:189–98. doi: 10.1097/EJA.0000000000000126

14. Reglin B, Pries AR. Metabolic control of microvascular networks: oxygen sensing and beyond. *J Vasc Res*. (2015) 51:376–92. doi: 10.1159/000369460

15. Hilty MP, Pichler J, Ergin B, Hefti U, Merz TM, Ince C, et al. Assessment of endothelial cell function and physiological microcirculatory reserve by video microscopy using a topical acetylcholine and nitroglycerin challenge. *Intensive Care Med Exp*. (2017) 5:26. doi: 10.1186/s40635-017-0139-0

16. Hilty MP, Merz TM, Hefti U, Ince C, Maggiorini M, Pichler Hefti J. Recruitment of non-perfused sublingual capillaries increases microcirculatory oxygen extraction capacity throughout ascent to 7126 m. *J Physiol*. (2019) 597:2623–38. doi: 10.1113/JP277590

17. Greenwood JC, Talebi FM, Jang DH, Spelde AE, Tonna JE, Gutsche JT, et al. Topical nitroglycerin to detect reversible microcirculatory dysfunction in patients with circulatory shock after cardiovascular surgery: an observational study. *Sci Rep*. (2022) 12:15257. doi: 10.1038/s41598-022-19741-0

18. den Uil CA, Caliskan K, Lagrand WK, van der Ent M, Jewbali LSD, van Kuijk JP, et al. Dose-dependent benefit of nitroglycerin on microcirculation of patients with severe heart failure. *Intensive Care Med*. (2009) 35:1893–9. doi: 10.1007/s00134-009-1591-4

19. den Uil CA, Lagrand WK, Spronk PE, van der Ent M, Jewbali LSD, Brugts JJ, et al. Low-dose nitroglycerin improves microcirculation in hospitalized patients with acute heart failure. *Eur J Heart Fail*. (2009) 11:386–90. doi: 10.1093/eurjhf/hfp021

20. Lima A, van Genderen ME, van Bommel J, Klijn E, Jansem T, Bakker J. Nitroglycerin reverts clinical manifestations of poor peripheral perfusion in patients with circulatory shock. *Crit Care Lond Engl*. (2014) 18:R126. doi: 10.1186/cc13932

21. Johannes T, Ince C, Klingel K, Unertl KE, Mik EG. Iloprost preserves renal oxygenation and restores kidney function in endotoxemia-related acute renal failure in the rat. *Crit Care Med*. (2009) 37:1423–32. doi: 10.1097/CCM.0b013e31819b5f4e

22. Abakay U, Soylu S, Göksel S, Saraç B, Şahin İnan ZD, Çakmak E, et al. Role of pentoxifylline and iloprost in the prevention of ischemia-reperfusion injury in an experimental model of intestine ischemia-reperfusion in rats. *Ulus Travma Ve Acil Cerrahi Derg Turk J Trauma Emerg Surg TJTES*. (2018) 24:398–404. doi: 10.5505/tjtes.2018.22227

23. Tuncer FB, Durmus Kocaaslan FN, Yildirim A, Sacak B, Arabaci Tamer S, Sahin H, et al. Ischemic preconditioning and iloprost reduces ischemia-reperfusion injury in jejunal flaps: an animal model. *Plast Reconstr Surg*. (2019) 144:124–33. doi: 10.1097/PRS.0000000000005708

24. Aytaç E, Teksöz S, Saygılı S, Tortum OB, Yavuz N, Sözer V, et al. Iloprost reduces colitis induced oxidative stress: An experimental study in rats. *Turk J Gastroenterol Off J Turk Soc Gastroenterol*. (2013) 24:224–9.

25. Truse R, Hinterberg J, Schulz J, Herminghaus A, Weber A, Mettler-Altmann T, et al. Effect of topical iloprost and nitroglycerin on gastric microcirculation and barrier function during hemorrhagic shock in dogs. *J Vasc Res*. (2017) 54:109–21. doi: 10.1159/000464262

26. Schwarte LA, Picker O, Höhne C, Fournell A, Scheeren TWL. Effects of thoracic epidural anaesthesia on microvascular gastric mucosal oxygenation in physiological and compromised circulatory conditions in dogs†. *BJA Br J Anaesth*. (2004) 93:552–9. doi: 10.1093/bja/aeh235

27. Vollmer C, Nommensen J, Watolla M, Bauer I, Picker O. Influence of thoracic epidural anesthesia on gastric oxygenation during hypothermia and hemorrhage. *Auton Neurosci Basic Clin*. (2016) 195:1–7. doi: 10.1016/j.autneu.2016.01.004

28. Benarroch EE. Physiology and pathophysiology of the autonomic nervous system. *Contin Minneap Minn*. (2020) 26:12–24. doi: 10.1212/CON.0000000000000817

29. Wang H, Jiang Y, Li H, Wang J, Li C, Zhang D. Carbachol protects the intestinal barrier in severe acute pancreatitis by regulating Cdc42/F-actin cytoskeleton. *Exp Ther Med*. (2020) 20:2828–37. doi: 10.3892/etm.2020.8985

30. Zhang Y, Li J. Carbachol ameliorates lipopolysaccharide-induced intestinal epithelial tight junction damage by down-regulating NF-κβ and myosin light-chain kinase pathways. *Biochem Biophys Res Commun*. (2012) 428:321–6. doi: 10.1016/j.bbrc.2012.10.056

31. Khan RI, Yazawa T, Anisuzzaman ASM, Semba S, Ma Y, Uwada J, et al. Activation of focal adhesion kinase via M1 muscarinic acetylcholine receptor is required in restitution of intestinal barrier function after epithelial injury. *Biochim Biophys Acta*. (2014) 1842:635–45. doi: 10.1016/j.bbadis.2013.12.007

32. Gustafsson JK, Lindén SK, Alwan AH, Scholte BJ, Hansson GC, Sjövall H. Carbachol-induced colonic mucus formation requires transport via NKCC1, K^+ channels and CFTR. *Pflugers Arch*. (2015) 467:1403–15. doi: 10.1007/s00424-014-1595-y

33. Han H, Yang J, Fei S, Liu Z, Zhu S, Dong Q, et al. Protective effect of carbachol postconditioning on hypoxia/reoxygenation-induced injury in human gastric epithelial cells. *Life Sci*. (2016) 144:234–42. doi: 10.1016/j.lfs.2015.11.029

34. Truse R, Smyk M, Schulz J, Herminghaus A, Weber APM, Mettler-Altmann T, et al. Regional hypothermia improves gastric microcirculatory oxygenation during hemorrhage in dogs. *PloS One*. (2019) 14:e0226146. doi: 10.1371/journal.pone.0226146

35. Truse R, Voß F, Herminghaus A, Schulz J, Weber APM, Mettler-Altmann T, et al. Local gastric RAAS inhibition improves gastric microvascular perfusion in dogs. *J Endocrinol*. (2019) 241:235–47. doi: 10.1530/JOE-19-0030

36. Truse R, Nolten I, Schulz J, Herminghaus A, Holtmanns T, Gördes L, et al. Topical melatonin improves gastric microcirculatory oxygenation during hemorrhagic shock in dogs but does not alter barrier integrity of caco-2 monolayers. *Front Med*. (2020) 7:510. doi: 10.3389/fmed.2020.00510

37. Kazama T, Ikeda K. Comparison of MAC and the rate of rise of alveolar concentration of sevoflurane with halothane and isoflurane in the dog. *Anesthesiol*. (1988) 68:435–7. doi: 10.1097/00000542-198803000-00020

38. Dyson DH. Positive pressure ventilation during anesthesia in dogs: Assessment of surface area derived tidal volume. *Can Vet J*. (2012) 53:63–6.

39. van Leersum EC. Eine Methode zur Erleichterung der Blutdruckmessung bei Tieren. *Pflüg Arch Für Gesamte Physiol Menschen Tiere*. (1911) 142:377–95. doi: 10.1007/BF01849124

40. Hof S, Marcus C, Kuebart A, Schulz J, Truse R, Raupach A, et al. A toolbox to investigate the impact of impaired oxygen delivery in experimental disease models. *Front Med*. (2022) 9:869372. doi: 10.3389/fmed.2022.869372

41. ATLS Subcommittee, American College of Surgeons' Committee on Trauma and International ATLS working group. Advanced trauma life support (ATLS®): the ninth edition. *J Trauma Acute Care Surg*. (2013) 74:1363–6.

42. Kraft W, Emmerich IU, Dörfelt R, Abbrederis N, Hirschberger J. *Dosierungsvorschläge für Arzneimittel bei Hund und Katze: MemoVet. 6., überarb. u. aktualisierte Edition*. Stuttgart: Schattauer GmbH. (2014).

43. Möller KO, Nilsson G, Fagrell B. Laser-Doppler Flowmetry for microcirculation monitoring. Introduction. *Technol Health Care Off J Eur Soc Eng Med*. (1999) 7:i–ii.

44. Sherman H, Klausner S, Cook WA. Incident dark-field illumination: a new method for microcirculatory study. *Angiol*. (1971) 22:295–303. doi: 10.1177/000331977102200507

45. Krug A. Mikrozirkulation und Sauerstoffversorgung des Gewebes: Methode des so genannten O2C (oxygen to see). *Phlebologie*. (2006) 35:300–12. doi: 10.1055/s-0037-1622158

46. Collins SA, Pon DJ, Sen AK. Phosphorylation of the alpha-subunit of (Na+ + K+)-ATPase by carbachol in tissue slices and the role of phosphoproteins in stimulus-secretion coupling. *Biochim Biophys Acta*. (1987) 927:392–401. doi: 10.1016/0167-4889(87)90104-2

47. Muscella A, Greco S, Elia MG, Jiménez E, Storelli C, Marsigliante S. Muscarinic acetylcholine receptor activation induces Ca2+ mobilization and Na+/K+-ATPase activity inhibition in eel enterocytes. *J Endocrinol*. (2002) 173:325–34. doi: 10.1677/joe.0.1730325

48. Haase N, Perner A. Central venous oxygen saturation in septic shock–a marker of cardiac output, microvascular shunting and/or dysoxia? *Crit Care Lond Engl*. (2011) 15:184. doi: 10.1186/cc10314

49. Textoris J, Fouché L, Wiramus S, Antonini F, Tho S, Martin C, et al. High central venous oxygen saturation in the latter stages of septic shock is associated with increased mortality. *Crit Care Lond Engl*. (2011) 15:R176. doi: 10.1186/cc10325

50. Hernandez G, Bruhn A, Ince C. Microcirculation in sepsis: new perspectives. *Curr Vasc Pharmacol*. (2013) 11:161–9.

51. Miranda M, Balarini M, Caixeta D, Bouskela E. Microcirculatory dysfunction in sepsis: pathophysiology, clinical monitoring, and potential therapies. *Am J Physiol Heart Circ Physiol*. (2016) 311:H24–35. doi: 10.1152/ajpheart.00034.2016

52. Furchgott RF, Zawadzki JV. The obligatory role of endothelial cells in the relaxation of arterial smooth muscle by acetylcholine. *Nature*. (1980) 288:373–6. doi: 10.1038/288373a0

53. Sprague RS, Goldman D, Bowles EA, Achilleus D, Stephenson AH, Ellis CG, et al. Divergent effects of low-O(2) tension and iloprost on ATP release from erythrocytes of humans with type 2 diabetes: implications for O(2) supply to skeletal muscle. *Am J Physiol Heart Circ Physiol*. (2010) 299:H566–573. doi: 10.1152/ajpheart.00430.2010

54. González-Alonso J. ATP as a mediator of erythrocyte-dependent regulation of skeletal muscle blood flow and oxygen delivery in humans. *J Physiol*. (2012) 590:5001–13. doi: 10.1113/jphysiol.2012.235002

55. Herminghaus A, Eberhardt R, Truse R, Schulz J, Bauer I, Picker O, et al. Nitroglycerin and iloprost improve mitochondrial function in colon homogenate without altering the barrier integrity of caco-2 monolayers. *Front Med*. (2018) 5:291. doi: 10.3389/fmed.2018.00291

frontiers | Frontiers in Immunology

TYPE Original Research
PUBLISHED 18 April 2024
DOI 10.3389/fimmu.2024.1359097

OPEN ACCESS

EDITED BY
Pietro Ghezzi,
University of Urbino Carlo Bo, Italy

REVIEWED BY
Toshiyuki Murai,
Osaka University, Japan
Antonio Junior Lepedda,
University of Sassari, Italy

*CORRESPONDENCE
E. Marion Schneider
marion.schneider@uniklinik-ulm.de

RECEIVED 20 December 2023
ACCEPTED 08 April 2024
PUBLISHED 18 April 2024

CITATION
Kasper R, Rodriguez-Alfonso A, Ständker L, Wiese S and Schneider EM (2024) Major endothelial damage markers identified from hemadsorption filters derived from treated patients with septic shock – endoplasmic reticulum stress and bikunin may play a role. *Front. Immunol.* 15:1359097. doi: 10.3389/fimmu.2024.1359097

Major endothelial damage markers identified from hemadsorption filters derived from treated patients with septic shock – endoplasmic reticulum stress and bikunin may play a role

Robin Kasper[1], Armando Rodriguez-Alfonso[2,3], Ludger Ständker[2], Sebastian Wiese[3] and E. Marion Schneider[1*]

[1]Clinic of Anesthesiology and Intensive Care Medicine, University Hospital Ulm, Ulm, Germany, [2]Core Facility Functional Peptidomics, Ulm University Medical Center, Ulm, Germany, [3]Core Unit Mass Spectrometry and Proteomics (CUMP), Ulm University, Ulm, Germany

Introduction: In septic patients the damage of the endothelial barrier is decisive leading to circulatory septic shock with disseminated vascular coagulation, edema and multiorgan failure. Hemadsorption therapy leads to rapid resolution of clinical symptoms. We propose that the isolation of proteins adsorbed to hemadsorption devices contributes to the identification of mediators responsible for endothelial barrier dysfunction.

Material and methods: Plasma materials enriched to hemadsorption filters (CytoSorb®) after therapy of patients in septic shock were fractionated and functionally characterized for their effect on cell integrity, viability, proliferation and ROS formation by human endothelial cells. Fractions were further studied for their contents of oxidized nucleic acids as well as peptides and proteins by mass spectrometry.

Results: Individual fractions exhibited a strong effect on endothelial cell viability, the endothelial layer morphology, and ROS formation. Fractions with high amounts of DNA and oxidized DNA correlated with ROS formation in the target endothelium. In addition, defined proteins such as defensins (HNP-1), SAA1, CXCL7, and the peptide bikunin were linked to the strongest additive effects in endothelial damage.

Conclusion: Our results indicate that hemadsorption is efficient to transiently remove strong endothelial damage mediators from the blood of patients with septic shock, which explains a rapid clinical improvement of inflammation and endothelial function. The current work indicates that a combination of stressors leads to the most detrimental effects. Oxidized ssDNA, likely derived from mitochondria, SAA1, the chemokine CXCL7 and the human neutrophil peptide alpha-defensin 1 (HNP-1) were unique for their significant negative effect on

endothelial cell viability. However, the strongest damage effect occurred, when, bikunin – cleaved off from alpha-1-microglobulin was present in high relative amounts (>65%) of protein contents in the most active fraction. Thus, a relevant combination of stressors appears to be removed by hemadsorption therapy which results in fulminant and rapid, though only transient, clinical restitution.

KEYWORDS

septic shock, endothelial damage, hemadsorption, oxidized DNA, bikunin/AMBP, SAA1, CXCL7, HNP-1

1 Introduction

Sepsis is responsible for nearly 20% of all global deaths (1). Thus, it remains one of the most challenging diseases in modern medicine and therefore a major focus of scientific research. The disease is characterized by a complex immune dysfunction, which ultimately leads to endothelial damage accompanied by disseminated intravascular coagulation (DIC), multi organ dysfunction and failure. On the cellular level, the interaction of activated leukocytes and platelets with endothelial cells of the vessel wall is particularly crucial (2–6). During infection, so-called PAMPs (pathogen-associated molecular patterns) such as lipopolysaccharides (LPS), flagellins and others lead to the activation of NF-κB and interferon pathways. Moreover, tissue damage by direct and indirect effects would activate pattern recognition receptors (PRR) with the subsequent release of so-called DAMPs (damage-associated molecular patterns), including non-methylated bacterial and mitochondrial DNA, as well as oxidized lipids, adenosine triphosphate (ATP) and proteins from erythrocyte lysates. Cellular proteins such as high mobility group box 1 (HMBG1), heat shock protein (HSP), ATP, eukaryotic cell-free DNA, apoptotic bodies and metabolites such as uric acid upregulate proinflammatory cytokines. Cytokine release also involves the receptor for advanced glycation end products (RAGE) and toll-like receptor (TLR). As a consequence, more leukocytes are attracted to the inflammatory site of tissue damage resulting in systemic inflammation (4, 7–10). Neutrophils are equipped with various effectors for direct and immediate pathogen defense, such as the release of proteases, particle uptake by phagocytosis and the formation of reactive oxygen species (ROS) such as superoxides and hydrogen peroxides as part of the so-called respiratory burst through NADPH oxidases and superoxide dismutases. Furthermore, the formation of so-called NETs (neutrophil extracellular traps) is a key for pathogen control and inflammation. NETs are conglomerates mostly generated by neutrophils through a process called NETosis. They consist of DNA and antimicrobial proteins such as elastase, myeloperoxidase or cathepsin G (8, 10, 11).

Besides tissue damage by NET formation, major activators of the innate immune system are ROS and reactive nitrogen species (RNS) such as peroxinitrite. Besides NADPH oxidases and superoxide dismutases, as mentioned earlier, ROS are also formed by uncoupling the respiratory chain in mitochondria. They have a procoagulant effect by releasing tissue factor and lead to barrier damage via nitration of cytoskeletal proteins and lipid peroxidation (9).

Many studies have focused on these complicated molecular processes and have shown that hardly a single specific signaling pathway or mediator is responsible for the cellular damage, hyperinflammation and subsequent immune insufficiency and sepsis. Attempts to identify a specific biochemical target and use it for targeted therapy have shown little promise (2, 12). In the last decade, hemadsorption therapy such as CytoSorb® (Cytosorbents, USA) has increasingly come into focus. This procedure aims to remove various cytokines, inflammatory mediators, DAMPs and pathogens from a patient's blood by binding hydrophobic substances with a molecular weight of up to approximately 60 kDa. Although questioned in a number of recent publications (13, 14), hypercytokinemia appears to respond to hemeadsorption (15). Elimination of the DAMPs intends to help reconstitute the endothelial wall by interfering with signaling pathways that lead to disseminated intravascular coagulation and vessel leakage. The most sensitive components of endothelial cells are the glycocalyx and junctions likely affected by transmigrating leukocytes as well (5).

The aim of the study was to find a common denominator for endothelial stress and endothelial cell viability. Based on the work of Denzinger et al., the focus was set on the main hypothesis that proteins and DNA - are oxidized by ROS during inflammation. These modified proteins may contribute to a scenario of DAMPs leading to cell injury by targeting different pathways of cell death (7).

2 Material and methods

2.1 Patient collective

Patients were included in the study if they were admitted to the ICU (G1, Intensive Care Unit) of the University Hospital Ulm

within 48 hours due to sepsis and had interleukin-6 (IL-6) levels of more than 500 pg/mL and/or renal failure. Additional inclusion criteria were: Age ≥18 years, need for intensive care, postoperative or posttraumatic condition, SIRS and antibiotic therapy. Patients in neutropenia (<1000/µL), with HIV infection, and pregnancy were excluded. All patients reached septic shock with catecholamine requirement and lactic acidosis (>2 mmol/L serum lactate). Patients were treated following the process guidelines for hemadsorption therapy of the ICU of the University Hospital Ulm. All data collection and specimen collection were performed according to the Declaration of Helsinki and the vote of the Ethics Committee of the University of Ulm (150/16) and with the patient's informed written consent. According to this study protocol, all hemadsorber devices subjected to biochemical analysis were derived from patients with a positive clinical response.

2.2 Isolation of adsorbed proteins

Immediately after the end of hemofiltration treatment, the columns were washed free from blood cells using PBS + 0.005% ethylenediaminetetraacetic acid (ETDA) until the effluent was clear. The contents of 10 hemadsorption devices derived from different septic shock patients were mixed and subjected to detachment of the adsorbed proteins with 50% acetonitrile in water for 1 h. The resin was then centrifuged (4.200 rpm) and the supernatant was filtered (5-13 µm, followed by a 0.45 µm filter). The filtrate was then subjected to ultracentrifugation (1 h and 100,000 xg). The clear supernatant (0.5 L) was diluted 1/10 with water and applied to an ultrafiltration step (cut-off: 30 kDa) to remove albumin. After pooling the samples, the proteins were separated by reversed-phase high performance liquid chromatography (RP-HPLC) at a flow rate of 1.3 mL/min for 40 min. The separated proteins were lyophilized, resuspended in 2 mL of resuspension solution (1% trifluoroacetic acid in water and 5% of buffer containing 80% acetonitrile and 0.1% trifluoroacetic acid in water) and centrifuged at 4,200 rpm for 10 minutes. The supernatant was sterilized by filtration (0.22 µm pore size) and dissolved in cell culture medium. A total of 40 protein fractions was obtained. Protein contents of individual fractions were determined by spectrophotometric methods and adsorption 280 nm; Extinction coefficient of $\epsilon 1\% = 6.58$ was used (16, 17). Ten percent of the reconstituted filtrate were use in our bioassay. Individual fractions were then characterized on the protein/peptide levels using mass spectroscopy, see chapter 6 below for more details.

2.3 Cell culture and endothelial bioassay (confluence, viability and morphology)

Ea.hy926 cells were cultured in Iscove´s modified Dulbecco´s medium (IMDM, Lonza, Switzerland) including 10% fetal calf serum (FCS superior, very low endotoxin, Biochrom, Germany), 3 mM sodium hydrogen carbonate, 25 mM HEPES and 60 µg/mL gentamycin at 37°C and 5% CO_2. For the bioassay cells were seeded in 96-well microplates at a density of $0.5x10^4$ cells/well. After reaching a confluence of 30%, 10% by volume of the respective protein fractions were added in triplicates along with 2.5 µg/mL propidium iodide (PI, Sigma-Aldrich, USA) to determine cell viability. Long-term live cell imaging (IncuCyte® ZOOM, Essen BioScience, USA) was used to observe the cells for 60 hours and subsequently determine confluence and cell viability. A 20x phase contrast and fluorescence microscope with 565-605 nm excitation and 625-705 nm emission was used for image acquisition. 100 nM staurosporine (STS) was used as a positive control.

Confluence was determined by cell densities and viability was quantified as the red object count per well. To assess morphology, cells were imaged after 50 hours of incubation using the Nikon Eclipse Ts2 phase contrast microscope (Nikon, Japan) using a 40x objective.

2.4 ROS formation (MitoSOX ™ Red)

To quantify ROS production in Ea.hy926, cells were seeded at a density of $0.5x10^4$ cells/well in 96-well microplates and cultured until approximately 70% confluence was reached. In triplicates 10% by volume of each protein fraction and 5 µM MitoSOX™ Red reagent (Invitrogen, USA) were added and observed over 6 hours using IncuCyte® ZOOM (20x objective, phase contrast and fluorescence detection with 565-605 nm excitation, 625-705 nm emission). ROS production was quantified by red object count per well. As a positive control, 20 µM vacquinol (Vac) was used (18).

2.5 Quantification of oxDNA and DNA

The DNA/RNA Oxidation Damage ELISA kit from Cayman Chemical (USA) was used to quantify oxidized DNA in the collected fractions. This acetylcholinesterase competitive ELISA allows the detection of previously described proteins released by the body through repair processes after oxidation of certain bases (mainly guanine) in the blood and ultimately excreted in the urine, including 8-OHG, 8-OHdG and 8-hydroxyguanine.

Additionally, the DNA content of adsorbed proteins was quantified fluorescently using Quantus™ Fluorometer (Promega, USA). Transparent 500 µL tubes were filled with 20 µL 1x trypsin/EDTA buffer, 80 µL of the respective fraction, and 100 µL of the fluorescent dye diluted 1:200 in trypsin/EDTA buffer. After incubation for 5 min, the samples were measured in the Quantus™ fluorometer.

2.6 Peptide/protein analysis

For endogenous peptide analysis, the samples were reduced with 5 mM DTT for 20 min at room temperature and carbamidomethylated with 50 mM iodoacetamide for 20 min at 37°C. The samples were previously run under denaturing conditions on 4% to 20% gradient polyacrylamide gels for protein analysis. A polyacrylamide gel lane section (>10 kDa) was separated, and in-gel digested with Trypsin (ThermoFisher

Scientific, USA), at a 1:50 ratio (enzyme:protein) for 16 h at 37°C. The proteolytic fragments were extracted with a mixture of water/acetonitrile (1:1), dried up and then reduced and carbamidomethylated as previously explained.

A 15 µL-aliquot was used for mass spectrometry analysis in an Orbitrap Elite Hybrid mass spectrometry system (Thermo Fisher Scientific, Bremen, Germany) online coupled to an U3000 RSLCnano (Thermo Fisher Scientific, Idstein, Germany) employing an Acclaim PepMap analytical column (75 µm × 500 mm, 2 µm, 100 Å, Thermo Fisher Scientific, Bremen, Germany) at a flow rate of 250 nL/min, as previously described (19). Database searches (PEAKs' standard workflow: *de novo* + PEAKs DB + PEAKs PTM + Spider) were performed using PEAKs X + studio (20–23). For peptide identification, MS/MS spectra were correlated with the UniProt human reference proteome set (UniProt release 2020_08; 20374 reviewed entries). Parent mass error tolerance and fragment mass error tolerance were at 15 ppm and 0.5 Da, respectively. Maximal number of missed cleavages was set at 3. Carbamidomethylated cysteine was considered as a fixed modification; methionine oxidation, carbamylation and N-terminus acetylation were considered as variable modifications. False discovery rates were set on the peptide level to 1%.

2.7 Statistical analysis

SPSS version 26 (IBM, USA) was used for statistical analysis. IncuCyte® ZOOM data were analyzed by one-way analysis of variance (ANOVA) followed by a Bonferroni post-hoc test. The significance level was set at α=0.05.

3 Results

3.1 Endothelial bioassay – confluence, viability, morphology (IncuCyte® ZOOM)

Figure 1 shows the mean confluence after 0, 48 and 96 hours (h) of incubation. After 96 h of incubation, fractions 5, 17, 18, 21, 22 and 23 show a significantly reduced confluence, like the positive control STS 100 nM ($p \leq 0.05$). Fraction 18 only reached 48.95% of confluence, while the negative control with IMDM attained 100%.

Figure 2 shows the cell death as the mean red object count per well after 0, 24 and 48 hours as a result of staining dead cells with propidium iodide. After 48 hours, significantly increased numbers of dead cells are shown by fractions 17, 18, and 21 together with the positive control staurosporine ($p \leq 0.05$). Interestingly, fractions 5, 22 and 23 also showed no significant effect on the viability despite severely reducing the confluence (cf. Figure 1).

After confluence and viability were assessed, selected fractions were photographed by phase contrast microscopy at 40x magnification to evaluate their morphology. For comparison, fraction 19 is shown here as an example of a regular morphology (Figure 3). Fraction 18, which caused a significant decrease in both confluence and viability, appears to induce an apoptotic cell pattern. Notable is the fragmentation of the cells with formation of so-called apoptotic bodies similar to the positive control with staurosporine. Cells under the influence of fraction 22 show a similar appearance, although, despite reduced confluency, viability was not affected.

3.2 ROS formation (MitoSOX ™ Red)

For the detection of ROS in the form of superoxide anions in the next step Ea.hy926 cells were stained with MitoSOX™ Red. Results are shown in Figure 4. After 3 hours, fractions 16, 17, 18, 19, 20 and 24 showed a significant production of ROS compared to the negative control, with fractions 18 and 19 showing more than twice as much red object counts per well than the other fractions. The positive control Vacquinol 20 µM also caused a significant increase in ROS production.

3.3 oxDNA quantification (ELISA)

The fluorescence-based quantification of dsDNA and ssDNA revealed the highest amounts in fraction 7. Further peaks were found in fraction 18 and for ssDNA also in fraction 24. The results are shown in the Supplementary Material (Supplementary Figure 1). The amounts of oxidized DNA were then quantified by an acetylcholinesterase competitive ELISA. Accordingly, fractions 5, 7, 17 and 18 contained high amounts of oxidized DNA (Figure 5).

Fractions 17, 18, 19, 21 and 22 have shown to be most effective on the endothelial cell layer. To identify protein effectors in the active fractions, we continued with protein and peptide identification experiments.

3.4 Peptide analysis of selected fractions 18, 19, 21 and 25

Fractions 18, 19, 21 and 25 were analyzed in greater detail. Using mass spectrometry, the entire peptide and protein profile of these fractions was identified. Fraction 18 was found to be one of the most noticeable fractions across all experiments. As a strong endothelial stressor, it contains high amounts of DNA and oxidized DNA. Fraction 19 also resulted in a very high ROS production but did not show high amounts of DNA nor did it damage endothelial cells compared to fraction 18. Fraction 21 resulted in extensive endothelial damage, although the inducible radical formation was not detected, and its DNA content was low. These observations raised the question of another mediator other than those envisioned from our basic hypothesis. Finally, fraction 25 was selected as a quasi-negative control because it was widely inactive in the bioassay.

The entire peptide and protein profile of these fractions was identified by mass spectrometry. A rank order comparison of the peptides was made for each fraction. Figure 6 shows the cake charts of the respective fractions, including the found peptides, identified as their percentage share of the measured intensities. Here, only the most prevalent peptides are shown. The full peptide content of the fractions 18, 19, 21 and 25 as well as post-translationally modified

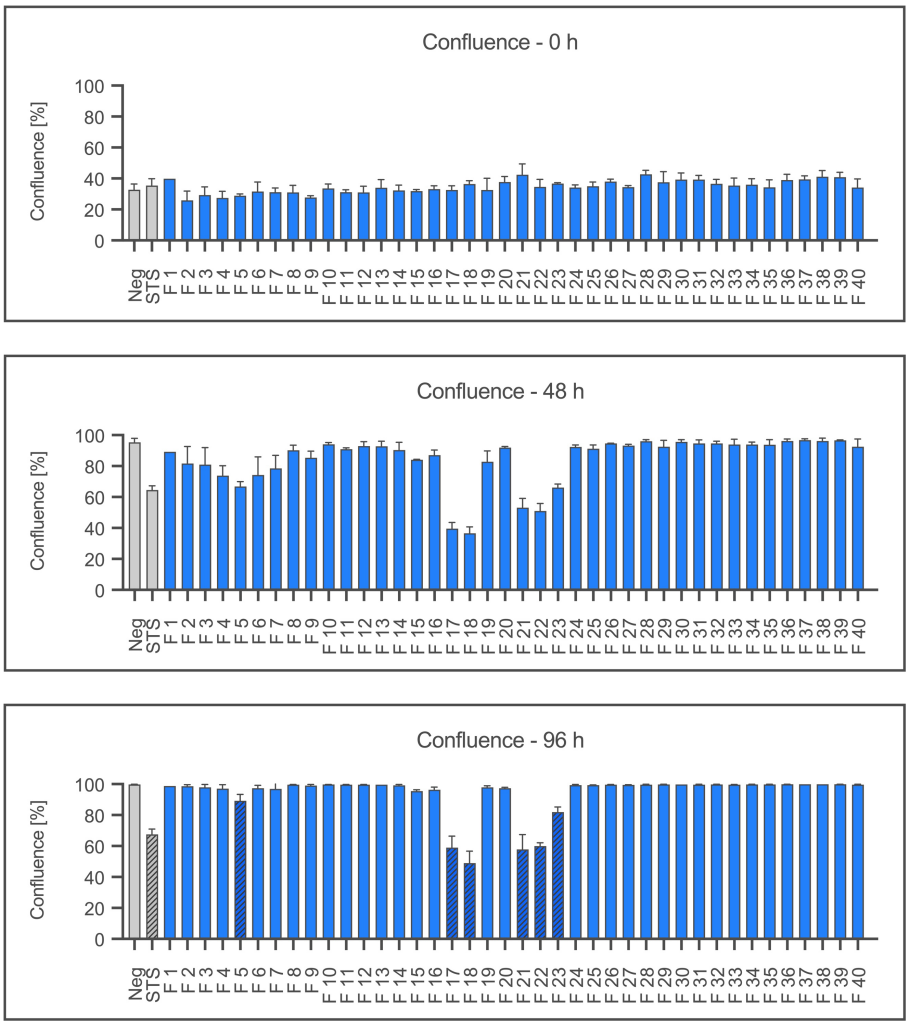

FIGURE 1
Proliferation of Ea.hy926 cells under the influence of CytoSorb fractions. Shown is the mean confluence and standard deviation of the endothelial cells measured using IncuCyte® ZOOM after 0, 48, and 96 hours in percent. Fractions (F) 1-40, the negative control with IMDM (Negative) and the positive control staurosporine (STS) 100 nM are displayed. Statistical analysis was performed after 96 hours. Significant differences to the negative control are marked as hatched columns.

peptides in the form of oxidation are illustrated in the Supplementary Figures 2–5.

High peptide levels of apolipoproteins and fibrinogen were consistently found in all fractions. The critical fraction 18 additionally contained relevant amounts of hemoglobin alpha, hemopexin, and haptoglobin. This was also found in fractions 19 and 21, respectively. Importantly, fractions 18, 19, and 21 were positive for acute-phase protein SAA1, and in fractions 18, 21 and 25, the platelet activation chemokine CXCL7 was present. Fraction 25 was unique in its vitronectin content.

In summary, this type of analysis detected proteins involved in coagulation, matrix proteins, endothelial receptors, and more constituents of degenerative elements such as Myosin Regulatory Light Chain 2, and proteins bound to chylomicrons and triglyceride-rich low and high-density lipoproteins as well as cholesterol. Fetuin A, detected in fraction 19, indicates the presence of liver-derived factors involved in cardiovascular risk and ectopic calcium homeostasis by its binding capacity of LDL and VLDL receptors. LYVE-1 is a CD44 homologue released from lymphatic vessels after injury. PGS-2, syn. decorin, is another matrix member protein involved in collagen fibril assembly.

3.5 Protein analysis of selected fractions 18, 19, 21 and 25

In addition to the peptide profile, the protein profile of fractions 18, 19, 21 and 25 was characterized by mass spectrometry following SDS-PAGE. Due to the large number of proteins found in each fraction, only the most common ones are shown in Figure 7. Supplementary Figures 6–9 show the extended results of these protein analyses. The critical fraction 18 predominantly contains the proteins AMBP (alpha-1-microglobulin/bikunin precursor) and HNP-1 (human neutrophil peptide-1, also: alpha-defensin-1). In general, high intensities of vimentin, SHPS-1 (tyrosine-protein phosphatase non-receptor type substrate 1) and the acute-phase

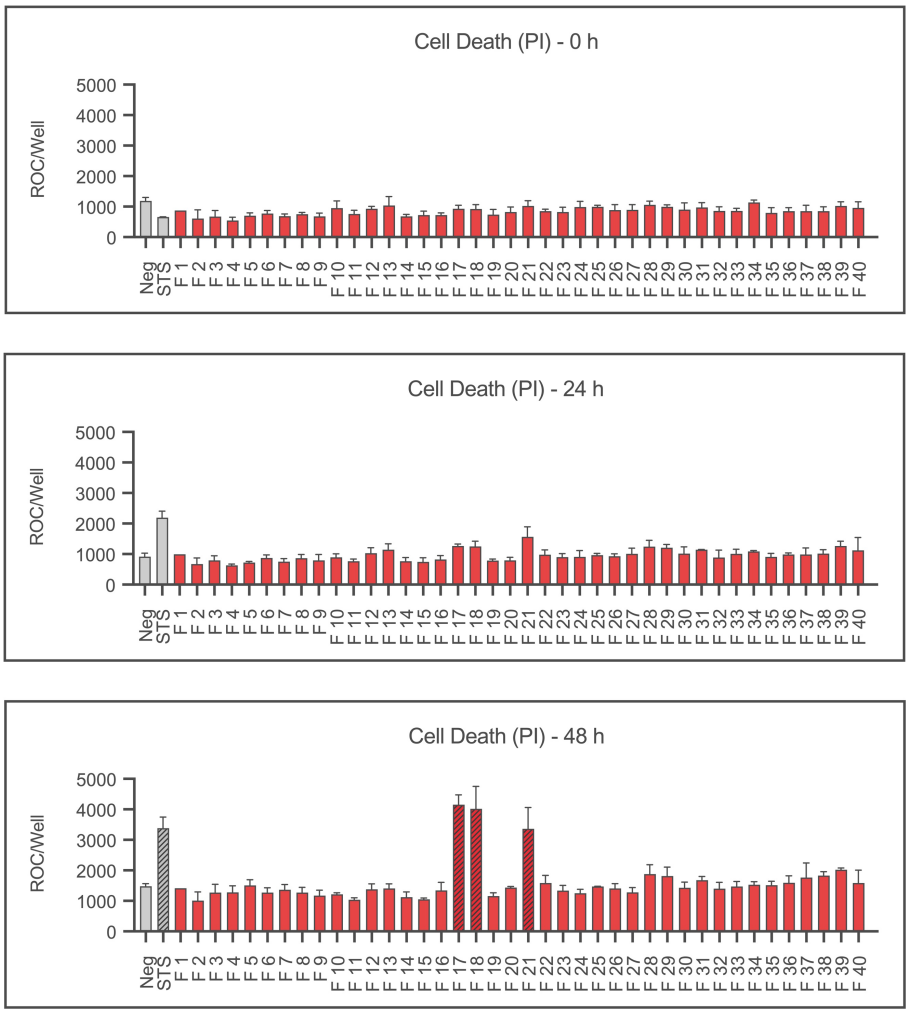

FIGURE 2
Cell death of Ea.hy926 cells under the influence of CytoSorb fractions. Displayed is the cell death of endothelial cells measured using IncuCyte® ZOOM after 0, 24 and 48 hours as mean red object count per well along with the standard deviation. Fractions (F) 1-40, the negative control with IMDM (Negative) and the positive control staurosporine (STS) 100 nM are shown. Statistical analysis was performed after 48 hours. Significant differences to the negative control are marked as hatched columns.

protein SAA1 were detected. Unlike the peptide profiles, hemoglobin-alpha accounted for the highest content in fraction 21. A comparable intensity was found in fraction 19, and a higher intensity occurred in fraction 25.

4 Discussion

The current report focused on the immediate effects by hemadsorption therapy to relieve septic shock in patients treated by intensive care. An endothelial bioassay and protein chemistry of hemadsorbed materials were applied to identify the most detrimental compounds disrupting endothelial cells. The stepwise approach to first fractionate the hemadsorbed material from a panel of devices from 10 patients, as opposed to a single hemadsorber (7) and test the protein fractions on human endothelial cells rather than rat brain-derived microvascular endothelium as in Denzinger et al. (7), confirmed our previous notion, that a definable composition of molecular entities has the most detrimental effect on endothelial cell layers *in vitro*.

4.1 Results from protein analysis of most active fractions 18, 19, 21 and 25

A major component of the most active protein fraction 18 is AMBP (alpha-1-microglobulin/bikunin precursor). Protein analyses identified the AMBP signal as the 16 kDa cleavage product bikunin (also known as inter-alpha-trypsin inhibitor light chain, or ITI-LC for short). The liver is the most important organ to synthesize bikunin from its AMBP precursor protein. AMBP also encodes alpha-1-microglobulin (https://www.ncbi.nlm.nih.gov/gene/259). Maturation of bikunin is associated with proteolytic cleavage of alpha-1-microglobulin and bikunin. The latter is then modified by glycosylation in the Golgi apparatus and further linked to heavy chains through an ester bond with a non-sulfated N-

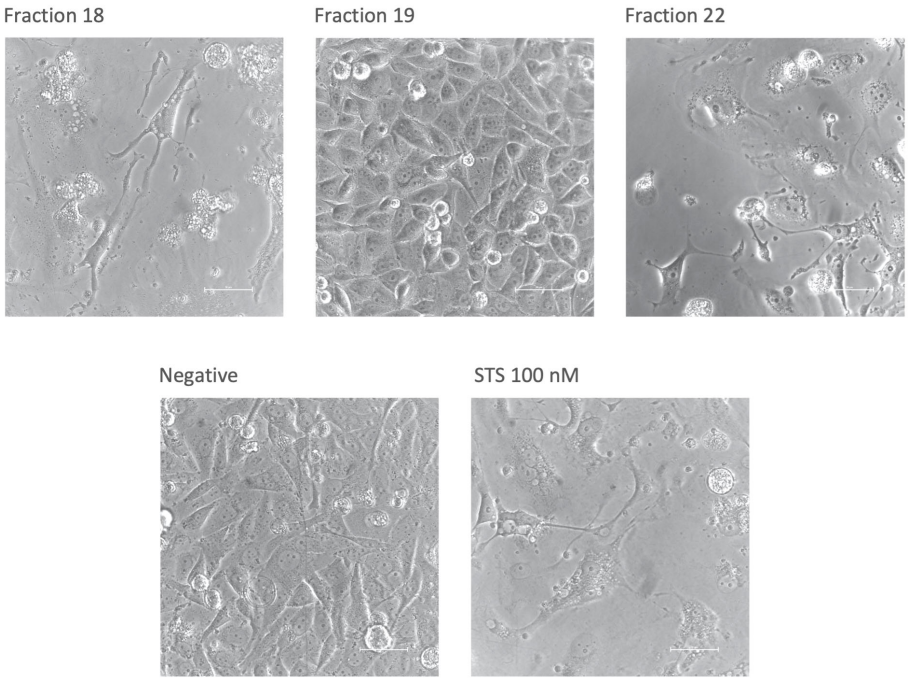

FIGURE 3
Morphology of Ea.hy926 cells after 50 hours under the influence of CytoSorb fractions. Images were taken with phase contrast microscopy (Nikon Eclipse Ts2, Nikon, Japan) at 40x zoom. Shown are the fractions 18, 19 and 22, the negative control with IMDM (Negative) and the positive control with staurosporine (STS) 100 nM. The scale bar equals 50 µm.

acetylgalactosamine (GalNAc) residue of the chondroitin sulfate (CS) chain. This molecule is released into the plasma (24). A schematic describing the synthesis of AMBP encoded peptides is given in Supplementary Figure 12.

Under physiological conditions, the proteoglycan bikunin circulates as an inactive form bound to inter-α-trypsin inhibitor (IαI). IαI family members interact with hyaluronan (HA), inhibit complement, and provide cell regulatory functions (25). IαI molecules from circulation bound to heavy chains (Supplementary Figure 12) are transferred to the extracellular matrix HA, thus forming the serum-derived HA-associated protein-HA complex (SHAP-HA), which supports the formation of new ECM and its stabilization (26). In the context of inflammation in sepsis, bikunin may inhibit a number of tissue damaging serine

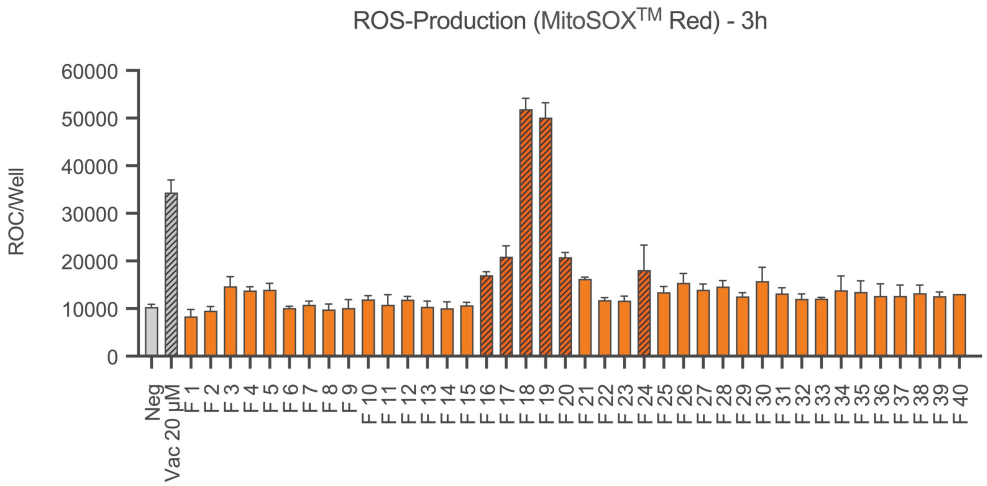

FIGURE 4
ROS production of Ea.hy926 cells under the influence of CytoSorb fractions. Shown is the production of reactive oxygen species (superoxide anions) as the mean red object count per well along with the standard deviation using MitoSOX™ Red. Quantification was performed with IncuCyte® ZOOM after 3 hours. Results for fractions (F) 1-40, the negative control with IMDM (Negative) and the positive control vacquinol (Vac) 20 µM are displayed. Statistical analysis was performed. Significant differences to the negative control are marked as hatched columns.

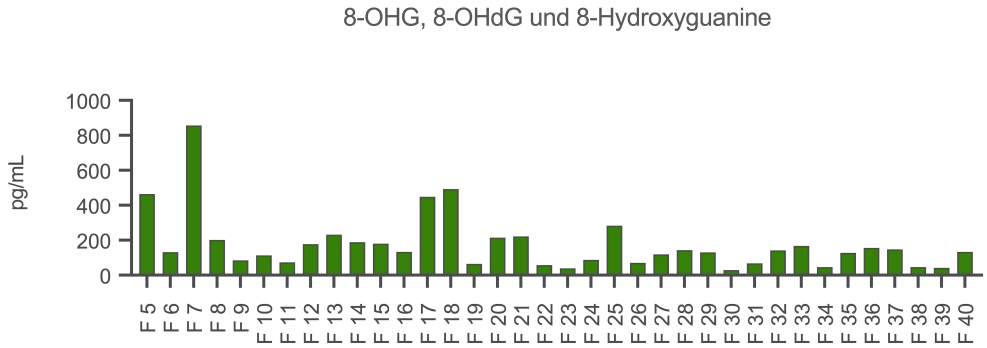

FIGURE 5
Quantification of oxidized DNA in the CytoSorb fractions. Demonstrated is the content of 8-hydroxyguanosine (8-OHG), 8-hydroxy-2'-deoxyguanosine (8-OHdG) and 8-hydroxyguanine in the fractions (F) 5-40 (x-axis) in pg/mL (y-axis). Measurements were carried out by an acetylcholinesterase competitive ELISA (Cayman Chemical, USA).

proteases which are released from neutrophils such as elastase or cathepsin G (27). Moreover, bikunin may inhibit plasmin as well as hyaluronidase and may thus attenuate neutrophil activation (25). Generally, the effects by bikunin are difficult to separate from the alpha-1-microglobulin and the IαI-bound complex, unless an alpha-1-microglobulin knock-out model is applied. This has been carried out by Bergwik and colleagues (28). Here a profound pro-inflammatory effect with endothelial damage has been described as well as fatty acid induced liver damage likely mediated by ER-stress (28). These effects are aggravated by the fact that alpha-1-microglobulin has an antioxidant effect on the organism due to its reductase activity (29). The protective effect by enhanced expression of alpha-1-microglobulin during oxidative stress further leads to better cell uptake and binding to complex I of the respiratory chain to maintain ATP production and prevent cell swelling (30, 31).

Chondoitinase-treated bikunin results in a reduced molecular weight compound with around 25-26 kDa when compared to chrondroitin-bound bikunin with 38 kDa (32). The authors further argued that „Possibly, free bikunin has an inflammation-related function and its normal plasma concentration should therefore be low, as reflected by its rapid turnover." (32). The anti-oxidant and tissue protective functions are clearly linked to the inter-alpha-inhibitor protein (IαIP) not bikunin as shown by Htwe and colleagues (33) (cf. Figure 4 as an example). The authors here determined neutrophils shape changes and summarized: "IAIP, but not bikunin, maintains spherical shape, small size, and smooth surface of human neutrophils and supports capillary passage; IAIP reduced ROS production from neutrophils in a concentration dependent manner, probably through p47phox phosphorylation" (33). According to Kaczmarczyk et al., bikunin is quickly removed from circulation (approximately 7 minutes) not to interfere with tissue reconstitution, which is why excretion via urine as urinary trypsine inhibitor (UTI) or ulinastatin is highly relevant and plasma concentrations do not exceed 5 µg/mL (22). Inflammatory conditions described significant modifications of the bikunin side chains regarding both sulfation and chain length composition of the CS moiety (34). Accordingly, free bikunin has been termed a novel acute phase protein (24). The inhibitory action of bikunin on endothelial cell layers is likely due to the interference with the calcium-dependent transforming growth factor-beta 1 signaling cascade (35). Acquired as well as inherited proteoglycan biosynthesis defects may account for loss of tissue protective effects by bikunin, as described in various forms of the Ehlers Danlos Syndrome linked to deficient synthesis of glycosaminoglycan (36). Thus bikunin identified by altered chondroitin side chains has been identified as a biomarker and acute phase protein (37), see schematic in Supplementary Figure 12.

To test our hypothesis of cytotoxic effects by free bikunin, we performed another series of bioassays with Ea.hy926 endothelium. For this purpose, the cells were incubated for a total of 72 hours with bikunin isolated from human urine at concentrations of 7 and 70 µg/mL. Dead cells were detected by propidium iodide staining, all nuclei were stained with Hoechst33342 and the Live Cell Imaging' system JuLI™ Stage (NanoEnTek.com) was applied for monitoring. Despite the lack of significance, a dose-dependent cytotoxic effect of bikunin on endothelial cells was observed (Supplementary Figures 10, 11).

Another protein of interest in fraction 18 is HNP-1 (Human Neutrophil Peptide-1, syn. Neutrophil defensin 1) which was high in fraction 18 and only found in small amounts in fraction 25. HNP-1, along with HNP-2, HNP-3 and HNP-4, is a member of the α-defensin group which is mainly expressed by neutrophil granulocytes and stored in intracellular vesicles. HNP-1, HNP-2 and HNP-3 have a strong antimicrobial effect by binding as cationic molecules to the enhanced negatively charged phospholipid membranes of bacteria after fusion with the phagosome, causing pore formation (38–42). In sepsis, increased gene copy numbers for HNP1-3 were associated with higher susceptibility to a severe outcome (43). Further studies demonstrated that this increased gene copy number in the mouse model relates to endothelial barrier damage with subsequent organ dysfunction. Chen and colleagues demonstrated the induction of pyroptosis by HNP-1 in murine lung microvascular endothelial cells. Binding of HNP-1 to the so-called P2X7 receptor (purinergic receptor P2X ligand-gated ion channel 7), a PRR, activates the canonical caspase-1 via the NLRP3 inflammasome (44). Caspase-1 further cleaves gasdermin D, giving it the ability to destroy the cell by pore formation and thus plunging it into pyroptosis (45).

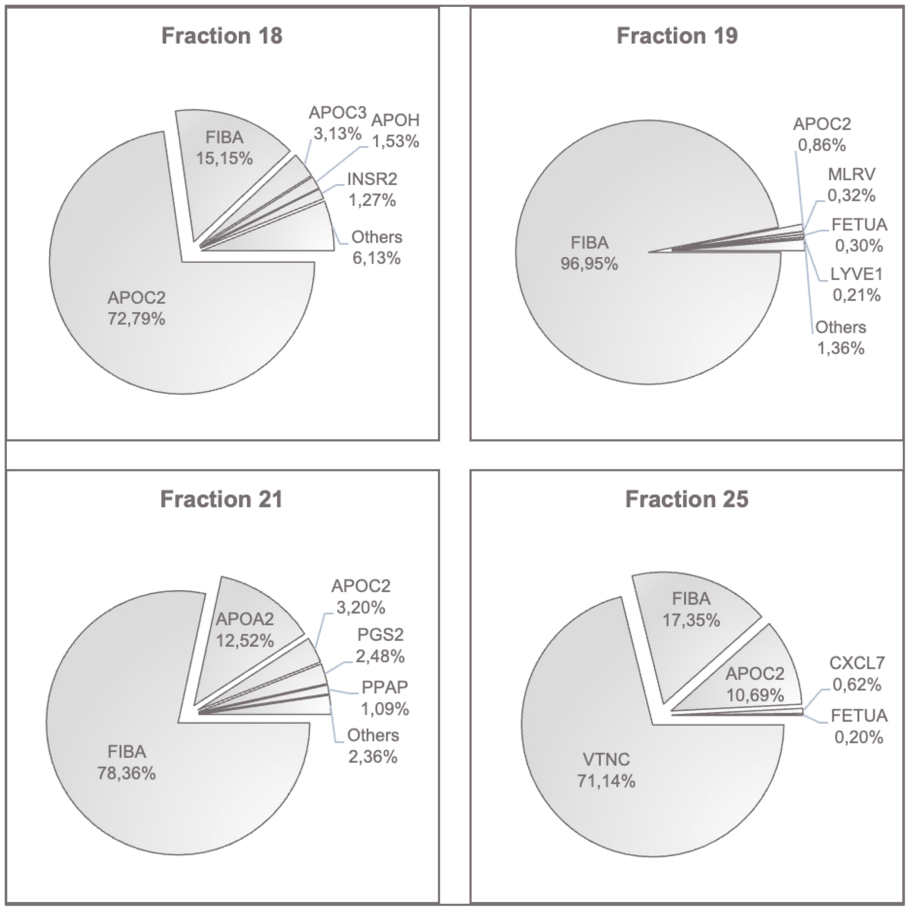

FIGURE 6
Peptides with the highest contents in fractions 18, 19, 21 and 25. The most prevalent peptides in each fraction are shown in percent of the determined intensities. APOC2, Apolipoprotein C-II; FIBA, Fibrinogen Alpha Chain; APOC3, Apolipoprotein C-III; APOH, Beta-2-Glycoprotein 1; INSR2, Insulin Isoform 2; MLRV, Myosin Regulatory Light Chain 2; FETUA, Fetuin A, Alpha-2-HS-Glycoprotein; LYVE1, Lymphatic Vessel Endothelial Hyaluronic Acid Receptor 1; APOA2, Apolipoprotein A-II; PGS2, Decorin; PPAP, Prostatic Acid Phosphatase; VTNC, Vitronectin; CXCL7, Platelet Basic Protein.

The overall protein concentration as well as the abundance of defined proteins in Cytosorb fractions 17, 18, 19, 21 and 25 are shown in the Supplementary Tables 1–6. Based on the spectrophotometric measurements at 280nm, the protein concentrations of Cytosorb fractions were calculated (Supplementary Figure 13).

Fraction 17 was included in these analyses because its cytotoxicity against endothelial cells was similar to fraction 18. The protein profile of fraction 17 revealed relevant amounts of bikunin confirming our assumption of a direct or significantly cooperative cytotoxic effect (Supplementary Figure 13).

4.2 The role of ROS and DNA

As discussed further, the endothelial damage effect by components of fraction 18 are related to the action of bikunin and HNP-1 but also oxidative stressors play an important role by DAMP-PRR-interactions. In the context of septic shock, most important stressors arise from oxidized DNA, related to NETosis and ROS generated in neutrophils. However, the present investigation shows that i) ROS formation alone does not cause damage to the cells. This notion is based on results obtained from fraction 19 with the highest mitochondrial ROS formation but no significant effects on the endothelial cell layer; ii) ssDNA, likely arising from mitochondria, and dsDNA do not constitute major damage effectors due to negative effects by fractions 6 and 25.

However, the combined action of mitochondrial ROS formation in addition to high DNA contents appears to manifest a significant endothelial damage effect, as exemplified by fractions 18 and 19. When incubating endothelial cells with fractions 18 and 19, ROS formation is strong after only 3 h of co-incubation. Fraction 18 is unique by performing consecutive cell damage with final endothelial cell death from 24 h co-incubation onwards. In addition, fraction 18 contains almost twice as much dsDNA and ssDNA when compared with fraction 19. In summary, endothelial damage is likely to occur by oxDNA however only in combination with other mediators. Levels of oxidized DNA are extremely high in fraction #7 but this fraction lacks a significant damage response. However, our previous analysis also stressed the role of oxDNA as a relevant DAMP (7). The likely oxidation of mitochondrial DNA enriched in the ssDNA fraction

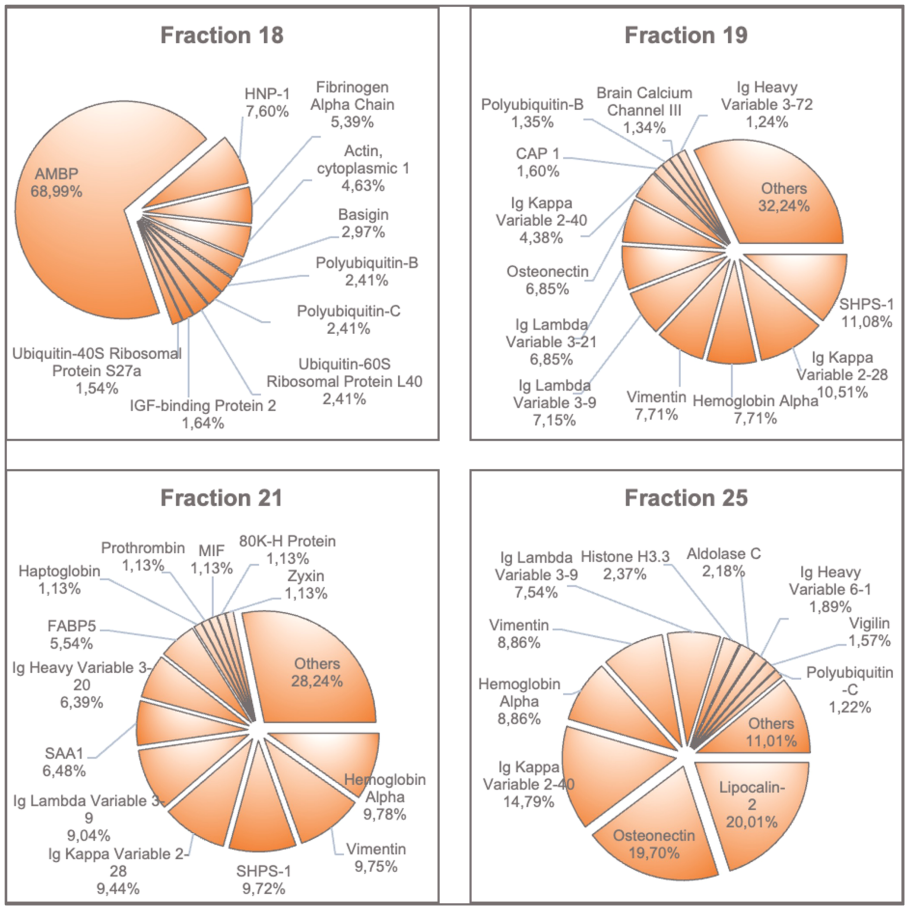

FIGURE 7
Proteins with the highest amounts found in fractions 18, 19, 21 and 25. The most prevalent proteins in each fraction are shown in percent of intensities. AMBP, Alpha-1-Microglobulin/Bikunin Precursor; HNP-1, Neutrophil Defensin 1; SHPS1, Tyrosine-Protein Phosphatase; CAP1, Adenylyl Cyclase-Associated Protein 1; SAA1, Serum Amyloid A-1 Protein; FABP5, Fatty Acid-Binding Protein 5; MIF, Macrophage Migration Inhibitory Factor; 80K-H Protein, Glucosidase 2 Subunit Beta.

occurs by superoxide formation within the mitochondria itself (9). In case of high relevance of ROS and DNA as endothelial stressors, antioxidant interventions as well as blockade of signaling by oxDNA should have a significant effect on outcome, lactate and stay on ICU in patients with septic shock (46, 47).

Importantly, hemadsorption was able to remove the oxidative stressor. Superoxides, such as O_2^-, are formed by an uncoupling of the respiratory chain in the mitochondria. Physiologically, superoxides are neutralized by antioxidant enzymes requiring NADPH (48). However, NADPH is depleted in the septic organism due to the increased formation of superoxide radicals, the so-called "respiratory burst", caused by upregulation of membrane-bound NADPH oxidases (9). Thus, in addition to inhibiting radical detoxification, these events would result in an escalation of radical formation and consequently increase oxidation of cell-free DNA. Increased concentrations of 8-OhdG, which have been previously described in septic patients, affect endothelial cell viability (7, 49). Due to its naked nature, mitochondrial DNA is much more likely to be oxidized as compared to eukaryotic DNA and is highly enriched in 8-OhdG, which then activates STING (stimulator of interferon genes) by acting as a DAMP for cGAS (cyclic GMP-AMP synthase) (50). Activation of the cGAS pathway increases interferons as well as proinflammatory chemokines and cytokines as members of the innate immune defense (50). In addition, inflammasome activation by binding of oxidized DNA to RAGE (receptor of advanced glycation end products) must be considered (51, 52). This context has been discussed previously due to a significant correlation between amounts of oxDNA and RAGE from fractions isolated from a Cytosorb hemofiltrate (7). Results for the central role of oxDNA are supported by the observation that oxDNA may lead to an upregulation of NADPH oxidase 4 with increased ROS-production in HUVECs (53). Another pathway induced by mtDNA and its oxidized metabolites may lead to activation of the toll-like receptor 9 (TLR9) with subsequent release of inflammatory mediators. This receptor of the innate immune system recognizes pathogens by binding unmethylated CpG dinucleotides present in the DNA of the pathogen (54–57). According to the endosymbiotic theory of mitochondrial origin, this mechanism would also explain mtDNA effects, especially since TLR9 cooperates with the pathogen receptor TLR4 upon internalization (58). In critically ill patients, levels of mtDNA correlate significantly with mortality in patients having high

expression of TLR9 (59, 60). Elevated blood mtDNA levels in patients with sepsis or septic shock have been proposed to serve as a biomarker for sepsis (61–63).

4.3 Results from peptide analysis of fractions 18, 19, 21 and 25

In general, the highest signal intensities were generated from fragments of APOC2 (apolipoprotein C-II) and FIBA (fibrinogen alpha chain). During sepsis, lipid metabolism undergoes significant changes. However, APOC2 usually is diminished in this condition (64). Therefore, its involvement as a direct mediator of endothelial cell damage seems unlikely. The reason for the high levels measured could be due to parenteral high caloric nutrition of the patients. FIBA is one of three components of fibrinogen. Besides forming the nd of the physiological coagulation cascade by cross-linking aggregated platelets to form a white thrombus and contributing to the development of a disseminated intravascular coagulation (DIC) in the context of the sepsis, high fibrinogen levels are also considered to be a risk factor for cardiovascular diseases and a biomarker for inflammation (65–67). Tyagi and colleagues demonstrated that fibrinogen in pathologically elevated amounts leads to a disruption of an endothelial cell monolayer with an increase in permeability via ERK (extracellular signal regulated kinase) and F-actin formation (68). Yu and colleagues, on the other hand, demonstrated that fibrinogen, in the form of Fresh Frozen Plasma, has an anti-apoptotic effect on endothelial cells *in vitro* (69). Ultimately, the effect appears to be highly dependent on the clinical condition of an individual patient and to proceed via several potential mechanisms and targets, as summarized by Luyendyk et al. in their review (70).

Fraction 18 was the only one to contain free Hb or its alpha subunit respectively. Furthermore, relevant amounts of Hpx (also present in fraction 19) and Hpt (also present in fraction 21) were found. This observation supports our previous hypothesis, that free Hb is involved in the demise of endothelial cells by acting as another DAMP (7). In contrast, fraction 21, which was also damaging, did not contain Hb, supporting the suggestion that a combination of DAMPs affects vascular integrity. Free heme induces the expression of adhesion molecules via TLR4 in endothelial cells (71, 72). Further, it has been shown that heme, but also Hb, leads to dissolution of the endothelial monolayer and thus contributes to cell extravasation (73–77). Involved in this process are the p38/hsp27 pathway and TLR4-dependent ROS production involving the p38 pathway (74, 76). Heme also led to an activation of the inflammasome via NLRP3 with subsequent IL-1β production in endothelial cells similar to macrophages (78, 79). It was shown that elevated Hb levels were associated with increased mortality as well as increased risk of organ dysfunction (80–85). Red blood cell lysis is triggered by a wide variety of pathways: Disseminated intravascular coagulation, reduced capillary flow, restriction of glucose transport into erythrocytes, alterations of cell membrane properties, hemolytic pathogens, and red blood cell apoptosis (eryptosis) (86). In conclusion, increased release of Hb may contribute to endothelial cell damage and the pathogenesis of sepsis.

Similar to our previous investigation (7), we here confirm the detection of the acute phase protein SAA1 in fractions 18, 19, and 21. This protein is released during inflammatory processes by activation of the NF-kB pathway via TLR4 and RAGE, resulting in the release of the proinflammatory alarmin HMGB1 (87, 88). SAA1 also drives ROS production in endothelial cells and leads to endothelial dysfunction via inhibition of eNOS (89).

Another interesting peptide is CXCL7 found in fractions 18, 21, and 25. This chemokine, which is also known as PBP (Platelet Basic Protein), NAP-2 (Neutrophil Activating Peptide 2) or Beta-TG (Beta-Thromboglobulin), is released in large amounts following platelet activation (90, 91). A trigger for this may be, for example, damage to the vascular endothelium. Via its receptor CXCR2 (CXC chemokine receptor 2), CXCL7 leads to neutrophil recruitment to the site of injury, which in turn promotes the inflammatory reaction (92). An important question in the context of our study is whether this platelet activation was brought about by the sepsis associated pathology, or whether platelet activation occurred from collateral damage by CytoSorb treatment. However, in another study, reduced amounts of CXCL7 (PBP) have been detected after Cytosorb treatment in a lung transplantation model, supporting effective clearance of CXCL7 by this hemadsorption procedure, which favors the sepsis-associated pathology by CXCL7 (93).

Most importantly, some fractions identified here mediated endothelial damage independently from an effect on mitochondrial ROS and with negligible amounts of DNA or oxDNA. These fractions 21 and 22, show a strong influence on the endothelium. Both fractions affect endothelial confluence, but only fraction 21 mediates endothelial cell death. This finding further strengthens the assumption, already explained at the beginning, that possibly not one but an ensemble of multiple mediators ultimately causes cell damage with subsequent organ failure.

In conclusion, the endothelial damage effect by components of fraction 18 are related to the action of bikunin, HNP-1 and oxidative stressors (oxidized and mitochondrial DNA) through DAMP-PRR-interactions. This investigation identified hemadsorbed DNA and protein effector molecules inducing endothelial stress in patients with septic shock. A major limitation of this study is related to the lack of signaling analysis by individual compounds as well as their combinations in the endothelial bioassay. Such studies would provide a more solid knowledge as to whether hemadsorption needs to be either intensified or attenuated. In the case of CXCL7, a higher adsorption capacity might be recommended due to the observations in an ex-vivo lung transplantation model (93). In the case of the current study, blood samples taken from individual patients before and after hemadsorption should be subjected to a similar mass spectrometric analysis. For future experiments, the hemadsorbed protein fraction could be tested in a mouse model or in organoids, which would be superior to unravel organ specific endothelial damage. Before approaching this experimental opportunity, artificial intelligence approaches including cluster analysis of the peptide contents of each fraction isolated, will be realistic to preselect compositions of proteins with and w/o oxDNA for a major effect on endothelial function.

4.4 Limitations of the current study

A limitation to the presented approach are possible matrix effects in samples with a huge disparity in protein abundances, such as plasma. The presence of high amounts of Fibrinogen may limit the ability of the mass spectrometer to effectively sample low abundant peptides. In addition, the type of approach undertaken in the present manuscript is further complicated, as highly abundant peptides with a medium activity might actually hide much stronger molar activities of less abundant peptides. Nevertheless, this study succeeded to identify protein entities adsorbed by hemadsorption from patients in septic shock which correlate with a detrimental effect in our endothelial bioassay. However, so far, only protein fractions with different constituents mediated a defined effect on endothelial bilayer's disruption and cell death. In addition, the proteins non-specifically eliminated by hemadsorption have not been studied. Therefore, future work needs to focus on the mass spectroscopically based analysis of plasma proteins before and after hemadsorption. Preliminary analysis indicates that this approach is relevant to distinguish patients with vs. without clinical improvement after hemadsorption (data not shown). Since recently, delineation of the intracellular pathways regulating endothelial permeability emphasized the unfolded protein response pathways with various protein mediators involved, showed that a positive outcome of ER activation involved global ATF6-mediated protection against disease (94). The morphological observations in our endothelial bioassay showed that ER-stress, vacuolization, and cell blebbing is a likely pathway active in endothelial dysfunction. This ER stress can be targeted and counter regulated by plasma proteins, which might lead the way to substantial post hemadsorption treatment protocols.

5 Conclusion

Defined proteins extracted from CytoSorb hemadsorption devices used in septic patients were tested for their effects on endothelial cell death, the formation of ROS, as well as proliferation and morphology of the endothelial cell layer. The most dramatic effect on endothelial cell layer disruption was mediated by a unique protein fraction containing high amounts of bikunin. The mechanism of action needs further investigation to decide whether sepsis modifies bikunin's sulfation and chain length composition of the CS moiety and whether loss of hyaluronic acid mediated glycocalyx stabilization interferes with calcium signaling and TGF-β signaling. Other fractions with endothelial damage activity emphasize oxidative stress from oxidized nucleic acids, including histones, likely functioning as major DAMPs for the endothelial bilayer. In addition, identification of the protein and peptide profiles of the critical endothelial damage fractions were: Pore forming peptides such as HNP-1, acute phase proteins, such as SAA1, the chemokine CXCL7, and free hemoglobin derivatives.

Importantly, the results confirm the complexity of effector peptides for the pathogenesis of endothelial cell damage in septic shock. The here described endothelial bioassay proved to be sufficient to generate reliable data sets to quantify cell damage in a defined time window and is further suitable to test therapeutically valuable approaches aiming at the reconstitution of the endothelial glycocalyx and microvascular integrity.

Data availability statement

The original contributions presented in the study are included in the article/Supplementary Materials, further inquiries can be directed to the corresponding author/s.

Ethics statement

The studies involving humans were approved by Ethics committee Ulm University. The studies were conducted in accordance with the local legislation and institutional requirements. The participants provided their written informed consent to participate in this study.

Author contributions

RK: Investigation, Writing – original draft, Data curation. AR-A: Data curation, Formal analysis, Investigation, Methodology, Software, Writing – review & editing. LS: Investigation, Methodology, Resources, Writing – review & editing. SW: Data curation, Formal analysis, Methodology, Software, Writing – review & editing. ES: Conceptualization, Investigation, Methodology, Project administration, Resources, Supervision, Writing – original draft.

Funding

The author(s) declare financial support was received for the research, authorship, and/or publication of this article. This work was supported by the DFG (CRC1279) project "Exploiting the Human Peptidome for Novel Antimicrobial and Anticancer Agents", and the VirA Horizon 22 Twinning Grant #952376.

Acknowledgments

We acknowledge the motivating support by our colleagues taking care of our patients with septic shock on ICU (Hendrick Bracht, Eberhard Barth, Manfred Weiss), the team from Cytosorbents for providing technical details of hemadsorption material and also Paul Walther and Julian M. Schneider for processing and visualization of endothelial specimen by scanning electron microscopy. We gratefully acknowledge Carolin Weiss for her support in sample processing for MS analysis. We also want to thank Jan Lawrenz from Molecular Virology, Ulm University, for his discussion and data input regarding bikunin from urine

Conflict of interest

The authors declare that the research was conducted in the absence of any commercial or financial relationships that could be construed as a potential conflict of interest.

Publisher's note

All claims expressed in this article are solely those of the authors and do not necessarily represent those of their affiliated organizations, or those of the publisher, the editors and the reviewers. Any product that may be evaluated in this article, or claim that may be made by its manufacturer, is not guaranteed or endorsed by the publisher.

Supplementary material

The Supplementary Material for this article can be found online at: https://www.frontiersin.org/articles/10.3389/fimmu.2024.1359097/full#supplementary-material

References

1. Rudd KE, Johnson SC, Agesa KM, Shackelford KA, Tsoi D, Kievlan DR, et al. Global, regional, and national sepsis incidence and mortality, 1990–2017: analysis for the Global Burden of Disease Study. *Lancet*. (2020) 395:200–11. doi: 10.1016/S0140-6736(19)32989-7

2. Opal SM, van der Poll T. Endothelial barrier dysfunction in septic shock. *J Internal Med*. (2015) 277:277–93. doi: 10.1111/joim.12331

3. Ley K, Reutershan J. Leucocyte-endothelial interactions in health and disease. In: Moncada S, Higgs A, editors. *The Vascular Endothelium II [Internet]*, vol. 176/II . Handbook of Experimental Pharmacology, Springer Berlin Heidelberg (2006). p. 97–133. Available at: http://link.springer.com/10.1007/3-540-36028-X_4.

4. Aird WC. The role of the endothelium in severe sepsis and multiple organ dysfunction syndrome. *Blood*. (2003) 101:3765–77. doi: 10.1182/blood-2002-06-1887

5. Ince C, Mayeux PR, Nguyen T, Gomez H, Kellum JA, Ospina-Tascón GA, et al. The endothelium in sepsis. *Shock*. (2016) 45:259–70. doi: 10.1097/SHK.0000000000000473

6. Dolmatova EV, Wang K, Mandavilli R, Griendling KK. The effects of sepsis on endothelium and clinical implications. *Cardiovasc Res*. (2021) 117:60–73. doi: 10.1093/cvr/cvaa070

7. Denzinger M, Staendker L, Ehlers K, Schneider JM, Schulz T, Hein T, et al. Bioassay for endothelial damage mediators retrieved by hemoadsorption. *Sci Rep*. (2019) 9:1–13. doi: 10.1038/s41598-019-50517-1

8. Kang JW, Kim SJ, Cho HI, Lee SM. DAMPs activating innate immune responses in sepsis. *Ageing Res Rev*. (2015) 24:54–65. doi: 10.1016/j.arr.2015.03.003

9. Cepinskas G, Wilson JX. Inflammatory response in microvascular endothelium in sepsis: Role of oxidants. *J Clin Biochem Nutr*. (2008) 42:175–84. doi: 10.3164/jcbn.2008026

10. Denning NL, Aziz M, Gurien SD, Wang P. Damps and nets in sepsis. *Front Immunol*. (2019) 10:1–15. doi: 10.3389/fimmu.2019.02536

11. Yu S, Liu J, Yan N. Endothelial dysfunction induced by extracellular neutrophil traps plays important role in the occurrence and treatment of extracellular neutrophil traps-related disease. *IJMS*. (2022) 23:5626. doi: 10.3390/ijms23105626

12. Iskander KN, Osuchowski MF, Stearns-Kurosawa DJ, Kurosawa S, Stepien D, Valentine C, et al. Sepsis: Multiple abnormalities, heterogeneous responses, and evolving understanding. *Physiol Rev*. (2013) 93:1247–88. doi: 10.1152/physrev.00037.2012

13. Becker S, Lang H, Vollmer Barbosa C, Tian Z, Melk A, Schmidt BMW. Efficacy of CytoSorb®: a systematic review and meta-analysis. *Crit Care*. (2023) 27:215. doi: 10.1186/s13054-023-04492-9

14. Pappalardo F, Cardinale A, D'Ettore N, Maj G. Blood purification in critically ill patients: not enough, but still helpful. *Crit Care*. (2023) 27:357. doi: 10.1186/s13054-023-04638-9

15. Jansen A, Waalders NJB, Van Lier DPT, Kox M, Pickkers P. CytoSorb hemoperfusion markedly attenuates circulating cytokine concentrations during systemic inflammation in humans in *vivo*. *Crit Care*. (2023) 27:117. doi: 10.1186/s13054-023-04391-z

16. Noelken ME, Timasheff SN. Preferential solvation of bovine serum albumin in aqueous guanidine hydrochloride. *J Biol Chem*. (1967) 242:5080–5. doi: 10.1016/S0021-9258(18)99478-0

17. Gill SC, Von Hippel PH. Calculation of protein extinction coefficients from amino acid sequence data. *Analytical Biochem*. (1989) 182:319–26. doi: 10.1016/0003-2697(89)90602-7

18. Sander P, Walther P, Moepps B, Hinz M, Mostafa H, Schaefer P, et al. Mitophagy-related cell death mediated by vacquinol-1 and TRPM7 blockade in glioblastoma IV. In: Omerhodžić I, Arnautović K, editors. *Glioma - Contemporary Diagnostic and Therapeutic Approaches [Internet]*. IntechOpen (2019). Available at: https://www.intechopen.com/books/glioma-contemporary-diagnostic-and-therapeutic-approaches/mitophagy-related-cell-death-mediated-by-vacquinol-1-and-trpm7-blockade-in-glioblastoma-iv.

19. Rodríguez-Alfonso A, Heck A, Ruiz-Blanco YB, Gilg A, Ständker L, Kuan SL, et al. Advanced EPI-X4 derivatives covalently bind human serum albumin resulting in prolonged plasma stability. *IJMS*. (2022) 23:15029. doi: 10.3390/ijms232315029

20. Zhang J, Xin L, Shan B, Chen W, Xie M, Yuen D, et al. PEAKS DB: de novo sequencing assisted database search for sensitive and accurate peptide identification. *Mol Cell Proteomics*. (2012) 11:M111.010587. doi: 10.1074/mcp.M111.010587

21. Han X, He L, Xin L, Shan B, Ma B. PeaksPTM: Mass Spectrometry-Based Identification of Peptides with Unspecified Modifications. *J Proteome Res*. (2011) 10:2930–6. doi: 10.1021/pr200153k

22. Han Y, Ma B, Zhang K. SPIDER: SOFTWARE FOR PROTEIN IDENTIFICATION FROM SEQUENCE TAGS WITH DE NOVO SEQUENCING ERROR. *J Bioinform Comput Biol*. (2005) 03:697–716. doi: 10.1142/S0219720005001247

23. Ma B, Johnson R. *De Novo* Sequencing and Homology Searching. *Mol Cell Proteomics*. (2012) 11:O111.014902. doi: 10.1074/mcp.O111.014902

24. Lepedda AJ, Nieddu G, Cannas C, Formato M. Molecular and pathobiological insights of bikunin/UTI in cancer. *Mol Biol Rep*. (2023) 50:1701–11. doi: 10.1007/s11033-022-08117-2

25. Lord MS, Melrose J, Day AJ, Whitelock JM. The inter-α-trypsin inhibitor family: Versatile molecules in biology and pathology. *J Histochem Cytochem*. (2020) 68:907–27. doi: 10.1369/0022155420940067

26. Zhuo L, Hascall VC, Kimata K. Inter-α-trypsin inhibitor, a covalent protein-glycosaminoglycan-protein complex. *J Biol Chem*. (2004) 279:38079–82. doi: 10.1074/jbc.R300039200

27. Gao S, Zhu H, Zuo X, Luo H. Cathepsin G and its role in inflammation and autoimmune diseases. *Arch Rheumatol*. (2018) 33:498–504. doi: 10.5606/ArchRheumatol.2018.6595

28. Bergwik J, Kristiansson A, Welinder C, Göransson O, Hansson SR, Gram M, et al. Knockout of the radical scavenger α1-microglobulin in mice results in defective bikunin synthesis, endoplasmic reticulum stress and increased body weight. *Free Radic Biol Med*. (2021) 162:160–70. doi: 10.1016/j.freeradbiomed.2020.02.019

29. Allhorn M, Klapyta A, Åkerström B. Redox properties of the lipocalin α1-microglobulin: Reduction of cytochrome c, hemoglobin, and free iron. *Free Radic Biol Med*. (2005) 38:557–67. doi: 10.1016/j.freeradbiomed.2004.12.013

30. Olsson MG, Allhorn M, Olofsson T, Åkerström B. Up-regulation of α1-microglobulin by hemoglobin and reactive oxygen species in hepatoma and blood cell lines. *Free Radic Biol Med*. (2007) 42:842–51. doi: 10.1016/j.freeradbiomed.2006.12.017

31. Olsson MG, Rosenlöf LW, Kotarsky H, Olofsson T, Leanderson T, Mörgelin M, et al. The radical-binding lipocalin A1M binds to a complex I subunit and protects mitochondrial structure and function. *Antioxid Redox Signal*. (2013) 18:2017–28. doi: 10.1089/ars.2012.4658

32. Kaczmarczyk A, Blom AM, Alston-Smith J, Sjöquist M, Fries E. Plasma bikunin: Half-life and tissue uptake. *Mol Cell Biochem*. (2005) 271:61–7. doi: 10.1007/s11010-005-5282-3

33. Htwe SS, Wake H, Liu K, Teshigawara K, Stonestreet BS, Lim YP, et al. Inter-α inhibitor proteins maintain neutrophils in a resting state by regulating shape and reducing ROS production. *Blood Advances*. (2018) 2:1923–34. doi: 10.1182/bloodadvances.2018018986

34. Lepedda AJ, Nieddu G, Rocchiccioli S, Ucciferri N, Idini M, De Muro P, et al. Levels of urinary trypsin inhibitor and structure of its chondroitin sulphate moiety in type 1 and type 2 diabetes. *J Diabetes Res*. (2018) 2018:1–9. doi: 10.1155/2018/9378515

35. Kobayashi H, Suzuki M, Tanaka Y, Kanayama N, Terao T. A kunitz-type protease inhibitor, bikunin, inhibits ovarian cancer cell invasion by blocking the calcium-dependent transforming growth factor-β1 signaling cascade. *J Biol Chem*. (2003) 278:7790–9. doi: 10.1074/jbc.M210407200

36. Syx D, Delbaere S, Bui C, De Clercq A, Larson G, Mizumoto S, et al. Alterations in glycosaminoglycan biosynthesis associated with the Ehlers-Danlos syndromes. *Am J Physiology-Cell Physiol*. (2022) 323:C1843–59. doi: 10.1152/ajpcell.00127.2022

37. Haouari W, Dubail J, Lounis-Ouaras S, Prada P, Bennani R, Roseau C, et al. Serum bikunin isoforms in congenital disorders of glycosylation and linkeropathies. *J Inher Metab Disea*. (2020) 43:1349–59. doi: 10.1002/jimd.12291

38. Ganz T. Defensins: antimicrobial peptides of innate immunity. *Nat Rev Immunol*. (2003) 3:710–20. doi: 10.1038/nri1180

39. Lehrer RI, Barton A, Daher KA, Harwig SS, Ganz T, Selsted ME. Interaction of human defensins with Escherichia coli. *Mech bactericidal activity. J Clin Invest*. (1989) 84:553–61. doi: 10.1172/JCI114198

40. Lehrer RI, Lu W. α-Defensins in human innate immunity: α-Defensins. *Immunol Rev*. (2012) 245:84–112. doi: 10.1111/j.1600-065X.2011.01082.x

41. Pazgier M, Hoover DM, Yang D, Lu W, Lubkowski J. Human β-defensins. *Cell Mol Life Sci*. (2006) 63:1294–313. doi: 10.1007/s00018-005-5540-2

42. Lichtenstein A. Mechanism of mammalian cell lysis mediated by peptide defensins. *Evidence an initial alteration plasma membrane. J Clin Invest*. (1991) 88:93–100. doi: 10.1172/JCI115310

43. Chen Q, Hakimi M, Wu S, Jin Y, Cheng B, Wang H, et al. Increased genomic copy number of DEFA1/DEFA3 is associated with susceptibility to severe sepsis in chinese han population. *Anesthesiology*. (2010) 112:1428–34. doi: 10.1097/ALN.0b013e3181d968eb

44. Chen Q, Yang Y, Hou J, Shu Q, Yin Y, Fu W, et al. Increased gene copy number of DEFA1/DEFA3 worsens sepsis by inducing endothelial pyroptosis. *Proc Natl Acad Sci USA*. (2019) 116:3161–70. doi: 10.1073/pnas.1812947116

45. Kelley N, Jeltema D, Duan Y, He Y. The NLRP3 inflammasome: an overview of mechanisms of activation and regulation. *Int J Mol Sci*. (2019) 20:3328. doi: 10.3390/ijms20133328

46. Tyml K. Vitamin C. and microvascular dysfunction in systemic inflammation. *Antioxidants*. (2017) 6:49. doi: 10.3390/antiox6030049

47. Fisher BJ, Kraskauskas D, Martin EJ, Farkas D, Wegelin JA, Brophy D, et al. Mechanisms of attenuation of abdominal sepsis induced acute lung injury by ascorbic acid. *Am J Physiology-Lung Cell Mol Physiol*. (2012) 303:L20–32. doi: 10.1152/ajplung.00300.2011

48. Ighodaro OM, Akinloye OA. First line defence antioxidants-superoxide dismutase (SOD), catalase (CAT) and glutathione peroxidase (GPX): Their fundamental role in the entire antioxidant defence grid. *Alexandria Med J*. (2018) 54:287–93. doi: 10.1016/j.ajme.2017.09.001

49. Bahar I, Elay G, Başkol G, Sungur M, Donmez-Altuntas H. Increased DNA damage and increased apoptosis and necrosis in patients with severe sepsis and septic shock. *J Crit Care*. (2018) 43:271–5. doi: 10.1016/j.jcrc.2017.09.035

50. Xian H, Watari K, Sanchez-Lopez E, Offenberger J, Onyuru J, Sampath H, et al. Oxidized DNA fragments exit mitochondria *via* mPTP- and VDAC-dependent channels to activate NLRP3 inflammasome and interferon signaling. *Immunity*. (2022) 55:1370–1385.e8. doi: 10.1016/j.immuni.2022.06.007

51. Riehl A, Németh J, Angel P, Hess J. The receptor RAGE: Bridging inflammation and cancer. *Cell Commun Signal*. (2009) 7:12. doi: 10.1186/1478-811X-7-12

52. Schmidt AM, Yan SD, Yan SF, Stern DM. The multiligand receptor RAGE as a progression factor amplifying immune and inflammatory responses. *J Clin Invest*. (2001) 108:949–55. doi: 10.1172/JCI200114002

53. Kostyuk SV, Ermakov AV, Alekseeva A, Smirnova TD, Glebova KV, Efremova LV, et al. Role of extracellular DNA oxidative modification in radiation induced bystander effects in human endotheliocytes. *Mutat Res*. (2012) 729:52–60. doi: 10.1016/j.mrfmmm.2011.09.005

54. Hemmi H, Takeuchi O, Kawai T, Kaisho T, Sato S, Sanjo H, et al. A Toll-like receptor recognizes bacterial DNA. *Nature*. (2000) 408:740–5. doi: 10.1038/35047123

55. Kawasaki T, Kawai T. Toll-like receptor signaling pathways. *Front Immunol*. (2014) 5:1–8. doi: 10.3389/fimmu.2014.00461

56. Tsuji N, Tsuji T, Ohashi N, Kato A, Fujigaki Y, Yasuda H. Role of mitochondrial DNA in septic AKI *via* toll-like receptor 9. *J Am Soc Nephrology*. (2016) 27:2009–20. doi: 10.1681/ASN.2015040376

57. Ermakov AV, Konkova MS, Kostyuk SV, Izevskaya VL, Baranova A, Veiko NN. Oxidized extracellular DNA as a stress signal in human cells. *Oxid Med Cell Longev*. (2013) 2013:1–12. doi: 10.1155/2013/649747

58. Marongiu L, Gornati L, Artuso I, Zanoni I, Granucci F. Below the surface: The inner lives of TLR4 and TLR9. *J Leukocyte Biol*. (2019) 106:147–60. doi: 10.1002/JLB.3MIR1218-483RR

59. Nakahira K, Kyung SY, Rogers AJ, Gazourian L, Youn S, Massaro AF, et al. Circulating mitochondrial DNA in patients in the ICU as a marker of mortality: Derivation and validation. *PLoS Med*. (2013) 10:1–12. doi: 10.1371/journal.pmed.1001577

60. Krychtiuk KA, Ruhittel S, Hohensinner PJ, Koller L, Kaun C, Lenz M, et al. Mitochondrial DNA and toll-like receptor-9 are associated with mortality in critically ill patients. *Crit Care Med*. (2015) 43:2633–41. doi: 10.1097/CCM.0000000000001311

61. Bhagirath VC, Dwivedi DJ, Liaw PC. Comparison of the proinflammatory and procoagulant properties of nuclear, mitochondrial, and bacterial DNA. *Shock*. (2015) 44:265–71. doi: 10.1097/SHK.0000000000000397

62. Timmermans K, Kox M, Scheffer GJ, Pickkers P. Plasma nuclear and mitochondrial DNA levels, and markers of inflammation, shock, and organ damage in patients with septic shock. *Shock*. (2016) 45:607–12. doi: 10.1097/SHK.0000000000000549

63. Schäfer ST, Franken L, Adamzik M, Schumak B, Scherag A, Engler A, et al. Mitochondrial DNA: an endogenous trigger for immune paralysis. *Anesthesiology*. (2016) 124:923–33. doi: 10.1097/ALN.0000000000001008

64. Ng PC, Ang IL, Chiu RWK, Li K, Lam HS, Wong RPO, et al. Host-response biomarkers for diagnosis of late-onset septicemia and necrotizing enterocolitis in preterm infants. *J Clin Invest*. (2010) 120:2989–3000. doi: 10.1172/JCI40196

65. Herrick S, Blanc-Brude O, Gray A, Laurent G. Fibrinogen. *Int J Biochem Cell Biol*. (1999) 31:741–6. doi: 10.1016/S1357-2725(99)00032-1

66. Danesh J, Lewington S, Thompson SG, Lowe GDO, Collins R. Plasma fibrinogen level and the risk of major cardiovascular diseases and nonvascular mortality: an individual participant meta-analysis. *JAMA*. (2005) 294(14):1799–1809. doi: 10.1001/jama.294.14.1799

67. Ross R. Atherosclerosis — An inflammatory disease. *Epstein FH editor. N Engl J Med*. (1999) 340:115–26. doi: 10.1056/NEJM199901143400207

68. Tyagi N, Roberts AM, Dean WL, Tyagi SC, Lominadze D. Fibrinogen induces endothelial cell permeability. *Mol Cell Biochem*. (2007) 307:13–22. doi: 10.1007/s11010-007-9579-2

69. Yu Q, Yang B, Davis JM, Ghosn J, Deng X, Doursout MF, et al. Identification of fibrinogen as a key anti-apoptotic factor in human fresh frozen plasma for protecting endothelial cells *in vitro*. *SHOCK*. (2020) 53:646–52. doi: 10.1097/SHK.0000000000001399

70. Luyendyk JP, Schoenecker JG, Flick MJ. The multifaceted role of fibrinogen in tissue injury and inflammation. *Blood*. (2019) 133:511–20. doi: 10.1182/blood-2018-07-818211

71. Merle NS, Paule R, Leon J, Daugan M, Robe-Rybkine T, Poillerat V, et al. P-selectin drives complement attack on endothelium during intravascular hemolysis in TLR-4/heme-dependent manner. *Proc Natl Acad Sci USA*. (2019) 116:6280–5. doi: 10.1073/pnas.1814797116

72. Belcher JD, Chen C, Nguyen J, Milbauer L, Abdulla F, Alayash AI, et al. Heme triggers TLR4 signaling leading to endothelial cell activation and vaso-occlusion in murine sickle cell disease. *Blood*. (2014) 123:377–90. doi: 10.1182/blood-2013-04-495887

73. Ferreira A, Balla J, Jeney V, Balla G, Soares MP. A central role for free heme in the pathogenesis of severe malaria: the missing link? *J Mol Med*. (2008) 86:1097–111. doi: 10.1007/s00109-008-0368-5

74. Singla S, Sysol JR, Dille B, Jones N, Chen J, MaChado RF. Hemin causes lung microvascular endothelial barrier dysfunction by necroptotic cell death. *Am J Respir Cell Mol Biol*. (2017) 57:307–14. doi: 10.1165/rcmb.2016-0287OC

75. Kuck JL, Bastarache JA, Shaver CM, Fessel JP, Dikalov SI, May JM, et al. Ascorbic acid attenuates endothelial permeability triggered by cell-free hemoglobin. *Biochem Biophys Res Commun*. (2018) 495:433–7. doi: 10.1016/j.bbrc.2017.11.058

76. Rafikova O, Williams ER, McBride ML, Zemskova M, Srivastava A, Nair V, et al. Hemolysis-induced lung vascular leakage contributes to the development of pulmonary hypertension. *Am J Respir Cell Mol Biol*. (2018) 59:334–45. doi: 10.1165/rcmb.2017-0308OC

77. Wagener BM, Hu PJ, Oh JY, Evans CA, Richter JR, Honavar J, et al. Role of heme in lung bacterial infection after trauma hemorrhage and stored red blood cell transfusion: A preclinical experimental study. *Brohi K editor. PLoS Med*. (2018) 15:e1002522. doi: 10.1371/journal.pmed.1002522

78. Dutra FF, Alves LS, Rodrigues D, Fernandez PL, de Oliveira RB, Golenbock DT, et al. Hemolysis-induced lethality involves inflammasome activation by heme. *Proc Natl Acad Sci USA*. (2014) 111:E4110–8. doi: 10.1073/pnas.1405023111

79. Erdei J, Tóth A, Balogh E, Nyakundi BB, Bányai E, Ryffel B, et al. Induction of NLRP3 inflammasome activation by heme in human endothelial cells. *Oxid Med Cell Longev*. (2018) 2018:1–14. doi: 10.1155/2018/4310816

80. Adamzik M, Hamburger T, Petrat F, Peters J, de Groot H, Hartmann M. Free hemoglobin concentration in severe sepsis: methods of measurement and prediction of outcome. *Crit Care*. (2012) 16:R125. doi: 10.1186/cc11425

81. Janz DR, Bastarache JA, Peterson JF, Sills G, Wickersham N, May AK, et al. Association between cell-free hemoglobin, acetaminophen, and mortality in patients with sepsis: An observational study*. *Crit Care Med*. (2013) 41:784–90. doi: 10.1097/CCM.0b013e3182741a54

82. Hartmann M, de Groot H. Cell-free hemoglobin: A new player in sepsis pathophysiology. *Crit Care Med*. (2013) 41:e186–9. doi: 10.1097/CCM.0b013e31828e92ac

83. Su D, Roth RI, Yoshida M, Levin J. Hemoglobin increases mortality from bacterial endotoxin. *Infection immunity*. (1997) 65:1258–66. doi: 10.1128/iai.65.4.1258-1266.1997

84. Janz DR, Ware LB. The role of red blood cells and cell-free hemoglobin in the pathogenesis of ARDS. *J Intensive Care*. (2015) 3:20. doi: 10.1186/s40560-015-0086-3

85. Rother RP, Bell L, Hillmen P, Gladwin MT. The clinical sequelae of intravascular hemolysis and extracellular plasma hemoglobin: A novel mechanism of human disease. *JAMA*. (2005) 293:1653. doi: 10.1001/jama.293.13.1653

86. Effenberger-Neidnicht K, Hartmann M. Mechanisms of hemolysis during sepsis. *Inflammation*. (2018) 41:1569–81. doi: 10.1007/s10753-018-0810-y

87. De Buck M, Gouwy M, Wang JM, Van Snick J, Proost P, Struyf S, et al. The cytokine-serum amyloid A-chemokine network. *Cytokine Growth Factor Rev*. (2016) 30:55–69. doi: 10.1016/j.cytogfr.2015.12.010

88. Li W, Zhu S, Li J, D'Amore J, D'Angelo J, Yang H, et al. Serum amyloid A stimulates PKR expression and HMGB1 release possibly through TLR4/RAGE receptors. *Mol Med*. (2015) 21:515–25. doi: 10.2119/molmed.2015.00109

89. Wang X, Chai H, Wang Z, Lin PH, Yao Q, Chen C. Serum amyloid A induces endothelial dysfunction in porcine coronary arteries and human coronary artery endothelial cells. *Am J Physiol Heart Circ Physiol*. (2008) 295:H2399–408. doi: 10.1152/ajpheart.00238.2008

90. Gleissner CA, von Hundelshausen P, Ley K. Platelet chemokines in vascular disease. *Arterioscler Thromb Vasc Biol*. (2008) 28:1920–7. doi: 10.1161/ATVBAHA.108.169417

91. Majumdar S, Gonder D, Koutsis B, Poncz M. Characterization of the human beta-thromboglobulin gene. Comparison with the gene for platelet factor 4. *J Biol Chem*. (1991) 266:5785–9. doi: 10.1016/S0021-9258(19)67665-9

92. Ghasemzadeh M, Kaplan ZS, Alwis I, Schoenwaelder SM, Ashworth KJ, Westein E, et al. The CXCR1/2 ligand NAP-2 promotes directed intravascular leukocyte migration through platelet thrombi. *Blood*. (2013) 121:4555–66. doi: 10.1182/blood-2012-09-459636

93. Niroomand A, Hirdman G, Pierre L, Ghaidan H, Kjellström S, Stenlo M, et al. Proteomic changes to immune and inflammatory processes underlie lung preservation using ex vivo cytokine adsorption. *Front Cardiovasc Med*. (2023) 10:1274444. doi: 10.3389/fcvm.2023.1274444

94. Blackwood EA, Azizi K, Thuerauf DJ, Paxman RJ, Plate L, Kelly JW, et al. Pharmacologic ATF6 activation confers global protection in widespread disease models by reprograming cellular proteostasis. *Nat Commun*. (2019) 10:187. doi: 10.1038/s41467-018-08129-2

frontiers | Frontiers in Immunology

TYPE Original Research
PUBLISHED 07 May 2024
DOI 10.3389/fimmu.2024.1365174

OPEN ACCESS

EDITED BY
Christoph Thiemermann,
Queen Mary University of London,
United Kingdom

REVIEWED BY
Marcin Filip Osuchowski,
Ludwig Boltzmann Institute for Experimental and Clinical Traumatology, Austria
Edward Sherwood,
Vanderbilt University Medical Center,
United States

*CORRESPONDENCE
Alfred Ayala
aayala@lifespan.org

RECEIVED 03 January 2024
ACCEPTED 15 April 2024
PUBLISHED 07 May 2024

CITATION
Wakeley ME, Denning N-L, Jiang J, De Paepe ME, Chung C-S, Wang P and Ayala A (2024) Herpes virus entry mediator signaling blockade produces mortality in neonatal sepsis through induced cardiac dysfunction. *Front. Immunol.* 15:1365174.
doi: 10.3389/fimmu.2024.1365174

Herpes virus entry mediator signaling blockade produces mortality in neonatal sepsis through induced cardiac dysfunction

Michelle E. Wakeley[1], Naomi-Liza Denning[2,3], Jihong Jiang[1,4], Monique E. De Paepe[5], Chun-Shiang Chung[1], Ping Wang[2,3] and Alfred Ayala[1]*

[1]Division of Surgical Research, Department of Surgery, Brown University, Rhode Island Hospital, Providence, RI, United States, [2]Center for Immunology and Inflammation, The Feinstein Institutes for Medical Research, Manhasset, NY, United States, [3]Department of Surgery, Donald and Barbara Zucker School of Medicine at Hofstra/Northwell, Hempstead, NY, United States, [4]Department of Anesthesiology, Shanghai General Hospital, Shanghai Jiao Tong University School of Medicine, Shanghai, China, [5]Department of Pathology, Women and Infants Hospital, Providence, RI, United States

Introduction: Sepsis remains a major source of morbidity and mortality in neonates, and characterization of immune regulation in the neonatal septic response remains limited. HVEM is a checkpoint regulator which can both stimulate or inhibit immune responses and demonstrates altered expression after sepsis. We hypothesized that signaling via HVEM would be essential for the neonatal response to sepsis, and that therefore blockade of this pathway would improve survival to septic challenge.

Methods: To explore this, neonatal mice were treated with cecal slurry (CS), CS with Anti-HVEM antibody (CS-Ab) or CS with isotype (CS-IT) and followed for 7-day survival. Mice from all treatment groups had thymus, lung, kidney and peritoneal fluid harvested, weighed, and stained for histologic evaluation, and changes in cardiac function were assessed with echocardiography.

Results: Mortality was significantly higher for CS-Ab mice (72.2%) than for CS-IT mice (22.2%). CS resulted in dysregulated alveolar remodeling, but CS-Ab lungs demonstrated significantly less dysfunctional alveolar remodeling than CS alone (MCL 121.0 CS vs. 87.6 CS-Ab), as well as increased renal tubular vacuolization. No morphologic differences in alveolar septation or thymic karyorrhexis were found between CS-Ab and CS-IT. CS-Ab pups exhibited a marked decrease in heart rate (390.3 Sh vs. 342.1 CS-Ab), stroke volume (13.08 CS-IT vs. 8.83 CS-Ab) and ultimately cardiac output (4.90 Sh vs. 3.02 CS-Ab) as well as a significant increase in ejection fraction (73.74 Sh vs. 83.75 CS-Ab) and cardiac strain (40.74 Sh vs. 51.16 CS-Ab) as compared to CS-IT or Sham animals.

Discussion: While receptor ligation of aspects of HVEM signaling, via antibody blockade, appears to mitigate aspects of lung injury and thymic involution, stimulatory signaling via HVEM still seems to be necessary for vascular and hemodynamic resilience and overall neonatal mouse survival in response to this experimental polymicrobial septic insult. This dissonance in the activity of anti-

HVEM neutralizing antibody in neonatal animals speaks to the differences in how septic cardiac dysfunction should be considered and approached in the neonatal population.

KEYWORDS

HVEM, neonatal sepsis, immune dysfunction, septic cardiomyopathy, mouse

1 Introduction

Sepsis, a life-threatening organ dysfunction caused by a dysregulated host response to infection, remains an immense clinical challenge responsible for greater than 200,000 patient deaths annually in the United States at an estimated cost of $20 billion (1, 2). The dysregulated host response to infection seen in sepsis is characterized by circulating immune cell influx into distal organs leading to organ failure (3). While work to understand the role of this dysregulated immune response in adult septic outcomes has generated several promising therapeutic targets, little has been done to translate this understanding to the neonatal population (4). This is important as not only is this a vulnerable population for which clinical access as well as animal modeling is more limited than the adult, but the immune system of the neonate is not yet fully developed, and differences would be anticipated in its response to pathogenic challenges (5). Thus, characterization of immune regulation in the neonatal response to septic insult remains an important goal.

Sepsis in adult patients has consistently been demonstrated to produce immune deficiency, which is linked to secondary infections, organ dysfunction and, ultimately, an increased risk of death (6, 7). Early mortality in adult sepsis is most frequently secondary to cardiac dysfunction, while late mortality is most frequently attributed to secondary infection (8–10). Individuals with cardiac dysfunction have a two-fold increase in mortality after sepsis, while those developing secondary infections have worse outcomes than counterparts when matched for injury severity and age (8–10). Mortality after sepsis in neonates is also attributed to organ failure, but more specifically to respiratory distress and cardiac dysfunction. Research exploring the developing immune systems role in this response describe the neonatal reliance on an immature innate immune response, characterized by an overly robust pro-inflammatory response with rapid production of IL-6, IL-8 and TNF-α in higher concentrations than seen in adults, followed by an immature anti-inflammatory response with low IL-10 production (5). Cardiac dysfunction in adults is characterized by a hyperdynamic phase with, decreased ejection fraction and increased cardiac index, resulting from a decreased systemic vascular resistance (11). Advanced studies of coronary artery oxygenation have demonstrated these effects to not be directly related to ischemia (9). Pediatric cardiac dysfunction is instead characterized by a non-hyperdynamic phase with a decreased cardiac output and an increased systemic vascular resistance, and some of this is due to their alteration in cardiac structure where an increase in the type I to type III collagen ratio results in increased cardiac rigidity (5, 9).

The immune response to any stimulus is informed and directed by checkpoint regulators. Checkpoint regulators are a group of transmembrane protein receptors which produce a second 'licensing' signal following T-cell receptor stimulation by an MHC class I or II protein bound with antigen in order to instruct the cell on how to respond to the antigenic stimulus (12). When an antigen is bound by a T-cell receptor (TCR), simultaneous engagement of a checkpoint regulator results in a signal to the immune cell, which may be stimulatory or inhibitory. Stimulation results in immune activation, ultimately resulting in a humoral or cell-mediated immune response (13). Inhibitory signals can result in anergic immune cells not able to respond to further stimulation (14). Multiple checkpoint regulators exist, including the well characterized Programmed cell death receptor 1 (PD-1), Cytotoxic T-lymphocyte Associated protein 4 (CTLA-4), and V-domain Ig suppressor of T-cell activation (VISTA) (15, 16). Herpes Virus Entry Mediator, or HVEM, is another such regulator possessing several unique characteristics that make it an interesting potential therapeutic target (17).

HVEM is a tumor necrosis factor receptor superfamily (TNFRSF) member type 1 transmembrane checkpoint regulator. Discovered through its interaction with Herpes Simplex Virus, HVEM acts to stimulate or inhibit T-cell activation dependent on multiple environmental cues (17, 18). HVEM is expressed on a variety of immune cell subsets and tissues including T-cells, B-cells, and Natural Killer (NK) cells, as well as spleen, lung, liver and kidney (17, 19). HVEM has 5 described ligands, both within and outside of the TNF family including B and T Lymphocyte Attenuator protein (BTLA), CD160, LIGHT, lymphotoxin alpha (LTα), and Herpes Simplex Virus 1. HVEM possesses four cystine rich binding domains, allowing it to interact with multiple ligands simultaneously (20). HVEM can behave as a bidirectional switch, generating a stimulatory immune response when binding LIGHT or LTα, but an inhibitory signal when interacting with BTLA or CD160 (21, 22). Further, HVEM can exist in an inert form when co-expressed in its cis confirmation with BTLA, protecting naïve T-cells from responding to environmental signals (23). Altered expression of HVEM and its

ligands has been demonstrated in critically ill septic adult patients, and in murine sepsis models (24–26).

Many checkpoint regulators play key roles in mediating responses to septic challenge. Deletion of both PD-1, and its primary ligand PDL-1, have both been independently demonstrated to convey survival benefit in adult mice subjected to the cecal ligation and puncture (CLP) model (27, 28). Specifically within neonates, it has been demonstrated that PD-1 deletion similarly conveys a survival benefit without effect on the intraperitoneal bacterial burden using a murine cecal slurry (CS) model (29). HVEM has been demonstrated to play an important role in the immune response to septic challenges in adult models, with Shui et al. demonstrating the HVEM : CD160 interaction to be integral to maintaining host defenses at mucosal barriers in murine models of intestinal and respiratory infections (26). Further, in an adult mouse model of indirect acute lung injury intratracheal HVEM siRNA administration was shown to have a protective effect on lung histology and convey and early survival deficit comparted with controls (30). Northern blot murine tissue surveys demonstrate the highest level of expression in adult spleen and peripheral leukocytes; however, in neonates, HVEM was most heavily expressed in lung and kidney (19). With this in mind, we hypothesized that signaling via HVEM is essential for the neonatal response to intraabdominal sepsis, and sought to characterize its role via intraperitoneal blockade of the stimulatory domains of HVEM in the setting of a septic insult.

2 Materials and methods

2.1 Mice

Wild type (WT) C57BL/6 neonatal (5-7 days old) mice were bred in the Rhode Island Hospital-Central Research Facilities. Pups were housed with parents throughout the duration of the studies and weaned on a standard schedule. All protocols were conducted according to the National Institutes of Health guide for animal care and use and were approved by the Lifespan-Rhode Island Hospital Institutional animal care and use committee (approval number: 0054-18 and 5054-21). Animals were fed standard mouse chow ad libitum, housed in ventilated racks, and kept under standard environmental conditions (12-h:12-h light/dark cycle, 68–72°F, 30%–70% humidity).

2.2 Cecal slurry model

Intraabdominal sepsis was created using the previously described cecal slurry (CS) model (29, 31). Briefly, cecal contents were harvested from an C57BL/6 adult male mouse, purchased through Jackson Laboratories, after CO_2 asphyxiation, then dissolved in dextrose solution to create a slurry of 80 mg/mL concentration. For all studies administering CS, pups were weighed and treated with LD_{70} dose (1.3mg/g BW) of the dextrose cecal slurry intraperitoneally via single injection. After treatment, animals were monitored every 6 hours for 48 hours, then every 12 hours thereafter for survival studies. Sepsis modeling was designed to embody the MQTiPPS principles whenever possible (32). For studies with predetermined end points, animals were euthanized via CO_2 asphyxiation followed by decapitation. All animal work was conducted in accordance with the Animal Welfare Act and National Institute of Health (NIH) guidelines for animal care and use, and protocols were approved by the Institutional Animal Care and Use Committee of Rhode Island Hospital (AWC# 5064-18 and 5054-21).

2.3 Survival studies

WT neonatal littermates were randomized into a total of 8 treatment groups, summarized in Table 1, including Naïve (N, N=4) pups, and pups receiving an intraperitoneal weight based dose of 0.9% saline, or Sham (Sh, N=4), cecal slurry alone (CS, N=28), CS with 20µL Anti-HVEM antibody (~4 mg protein/kg body weight) to the LIGHT stimulatory binding domain (CS-Ab, N=18) (ThermoFisher Scientific, CD270 functional grade monoclonal antibody, LH-1 clone, #16-5962-85), CS with 20µL Armenian hamster IgG isotype (~4 mg protein/kg body weight) (CS-IT, N=18) (eBiosciences, #14-4888-85), CS with 20µL 0.9% normal saline (CS-NS, N=19), 20µL Anti-HVEM antibody to the LIGHT stimulatory binding domain alone (Ab,N=4), or 20µL Anti-HVEM antibody diluted in a weight based volume of normal saline (dAb, N=4). Antibody dosing was selected based on previously published work in adult models (33). Antibody dosing was exclusively administered at the time of CS treatment; no additional dosing was provided. Given all litters did not include 8 pups, every experimental litter was ensured to include control animals (N, Sh, CS, Ab, or dAb treated mice). Pups from each treatment group underwent a 7-day survival study. Following intraabdominal

TABLE 1 Experimental treatment groups.

Treatment	Label	Technique	N
Naïve	N	No treatment	5
Sham	Sh	Intraperitoneal weight-based dose 0.9% saline	4
Cecal Slurry	CS	Cecal slurry alone	28
Cecal Slurry with Isotype	CS-IT	CS with 20µL Armenian hamster IgG isotype	18
Cecal Slurry with Anti-HVEM Antibody	CS-Ab	CS with 20µL Anti-HVEM antibody to the LIGHT stimulatory binding domain	18
Cecal Slurry with Normal Saline	CS-NS	CS with 20µL 0.9% normal saline	19
Anti-HVEM Antibody	Ab	20µL Anti-HVEM antibody to the LIGHT stimulatory binding domain	4
Diluted Anti-HVEM Antibody	dAb	20µL Anti-HVEM antibody diluted in a weight-based volume of normal saline	4

Summary of all treatment groups included in study design, including details of treatment technique and number of pups included in survival studies for each treatment.

injection pups were evaluated every 6hrs for the first 48hrs, then every 12hrs for the remainder of the study. No antibiotics, pain medications, or additional resuscitative fluids were administered. Results were analyzed using a log-rank Kaplan Meier analysis.

2.4 Organ weights

Twelve hrs after treatment, thymus, lung, liver, spleen and kidney samples from naïve mice (N), Sham (Sh), CS, CS-Ab or CS-IT treated mice were collected following euthanasia via decapitation. Pups were weighed at the time of euthanasia and organs were weighed immediately after collection (wet weight). All weights are reported as a ratio of the organ weight in milligrams to the weight of the pup in grams (Table 2). Samples were then formalin fixed for histologic evaluation.

2.5 Histology

Thymus, lung, liver, spleen and kidney formalin fixed samples collected from Sh, CS, CS-Ab or CS-IT treated pups 12 hrs after treatment as well as from Naïve mice were paraffin embedded for sectioning. Sections were either stained with hematoxylin and eosin (H&E), underwent immunohistochemical analysis for HVEM expression (ThermoFisher Scientific, TNFRSF14 Polyclonal antibody, #PA5-20237), or were assessed for apoptotic changes with active Caspase 3 (Clone CM1, BD Biosciences).

H&E-stained lung samples were evaluated by computer assisted morphometric analysis for evidence of age-appropriate alveolar remodeling via mean chord length (MCL). MCL was calculated by superimposing randomly oriented parallel line arrays over a high-powered field (40x magnification) of air exchanging lung parenchyma, then determining the distance between airspace walls, as previously described (34). This process was repeated across 10 random fields per lung then averaged to generate the MCL score, in µm. MCL data is reported as mean distance in µm for an N=4 in each treatment group ± SEM.

Based on prior reports of lymphoid apoptosis as a characteristic result of histologic murine septic tissue injury, H&E stained thymus samples were evaluated for lymphoid apoptosis, or karyorrhexis, utilizing a karyorrhectic index (KI) (35). A karyorrhectic foci was defined as an area containing 3 or more nuclear fragments, and the karyorrhectic index was calculated based on the number of foci identified in 10 random high-powered fields (40x magnification) per tissue sample. KI data is reported as mean for an N=4 in each treatment group ± SEM.

H&E stained kidney samples (N=4 per treatment group) were evaluated for evidence of vacuolar degeneration, tubular epithelial swelling, and desquamation, based on prior descriptions of these characteristic murine indicators of kidney injury (35–37). Images were first acquired at 20x magnification capturing the cortex, then images were magnified to 40x and evaluated for general morphology and presence and extent of vacuolar degeneration and tubular epithelial swelling. This was repeated across 2-3 areas of each tissue sample.

Thymic samples (N=5 per treatment group) were evaluated for HVEM expression utilizing a commercially available polyclonal antibody using the manufacturers protocol. Images were acquired at 40x magnification within the cortical zones for each tissue sample and compared grossly for stain intensity. Thymus samples (N=5 per treatment group) were evaluated for active Caspase 3 according to manufacturer instructions, and additionally underwent immunohistochemical analysis for HVEM expression. Images of 6 random low-powered fields per sample were acquired at 4x magnification and analyzed for stain intensity using ImageJ. Of note, all histologic samples mentioned above were reviewed by a single neonatal pathologist member of the research team (MED) in a blinded fashion utilizing ImageJ software. All results were compared using a Mann-Whittney U test.

2.6 Peritoneal culture analysis

Normal saline was lavaged in the peritoneal cavity of pups 12hrs after treatment with CS, CS-Ab, CS-IT, CS-NS, AB or dAb as well as in Naïve mice (N). Samples were collected at the time of tissue harvest using sterile technique, aliquoted, and cultured for 24 hrs on blood agar plates at 37°C then counted for colony forming units (CFUs). Results are reported as Log_{10} CFU/100µL peritoneal fluid.

2.7 Echocardiography

Twenty-four hrs after treatment, either Sh treatment with normal saline, or sepsis induction with CS-Ab or CS-IT, transthoracic echocardiography was used to assess cardiac function in neonatal mice as described by Denning et al. (38)

TABLE 2 Wet tissue weights as a ratio with pup weight.

Treatment	Pup Weight	Thymus	Lung	Liver	Spleen	Kidney*
Naïve (N=8)	3.51 +/- 0.65	6.41 +/- 1.2	16.33 +/- 1.61	29.27 +/- 5.09	6.25 +/- 1.42	11.25 +/- 2.47
Cecal Slurry (N=5)	3.83 +/- 0.08	2.81 +/- 1.11	12.78 +/- 2.55	17.08 +/- 3.03	8.17 +/- 1.75	7.67 +/- 1.67
CS-IT(N=5)	3.23 +/- 0.38	4.42 +/- 1.53	14.23 +/- 1.73	23.42 +/- 4.13	9.58 +/- 2.62	8.75 +/- 0.67
CS-Ab (N=5)	3.56 +/- 0.26	5.4 +/- 1.53	11.4 +/- 1.5	23.18 +/- 4.67	8.32 +/- 1.59	5.14 +/- 0.52

Treatment groups contained between 5 and 8 pups, pup weight is provided as a group average in grams with the SEM, tissue weights are reported as a ratio of tissue weight in milligrams per pup weight in grams along with SEM. * denotes significant difference between CS-IT and CS-Ab groups, $p<0.05$.

Echocardiography was completed using a 40 MHz center frequency transducer and a Vevo®3100 Imaging System (Fujifilm VisualSonics, Toronto, ON, Canada). Sedation was induced with 2.5% isoflurane, and subsequently was maintained with 0.5–1% isoflurane throughout the echocardiogram. Mice were maintained on a heated table throughout the echocardiogram. Parasternal long axis views were taken in B and M modes, with B mode imaging providing two-dimensional views of the heart and M mode imaging depicting one ultrasound line, chosen from the two-dimensional image, over time (39). VevoLab (Fujifilm VisualSonics) software was used to determine cardiac parameters. VevoStrain (Fujifilm VisualSonics) software was used to measure myocardial strain and strain rate using speckle-tracking echocardiography (40).

2.8 Cytokine arrays

Twenty-four hrs after treatment plasma, thymus, lung, and kidney samples from naïve mice (N), and Sham (Sh), CS, CS-Ab, CS-IT, CS-NS, Ab, or dAb treated mice were collected following euthanasia and stored at -80°C until analysis. Blood samples were collected with sterile technique at the time of decapitation, plasma was subsequently isolated via centrifugation of whole blood at 10,000 rpm, and supernatant (plasma) was collected and stored at -80°C. Plasma samples were analyzed for circulating cytokine profiles according to manufacturer instructions using a commercially available cytokine bead array: LEGENDplex Mouse Inflammation Panel (13-plex) with a V-bottom plate (BioLegend, cat#552364). Serum samples from murine subjects were prepared for analysis per manufacturer's protocol and as previously described by our lab (41). Lung, thymus, and kidney samples were dissociated into cell lysates and prepared for cytokine bead array according to manufacturer protocols. MACSQuant Analyzer 10 (Miltenyi Biotec) was utilized for analysis of all multiplex experiments. Results were analyzed with LEGENDplex software suite (BioLegend). Differences among multiple groups were established with non-parametric Kruskal-Wallis test followed by post-hoc Dunns test using a Bonnferroni correction.

2.9 Statistical analysis

Data are expressed as mean ± SEM. Survival study data was analyzed using a log-rank Kaplan Meier analysis. Multi-group comparisons were performed using Kruskal-Wallis test followed by post-hoc Dunns test using a Bonnferroni correction or a Mann-Whittney U test for simple 2-way comparison. Statistical analysis was undertaken using GraphPad Prism version 8.4.3 for Windows (GraphPad Software, San Diego, California USA, www.graphpad.com). Alpha was set to 0.05.

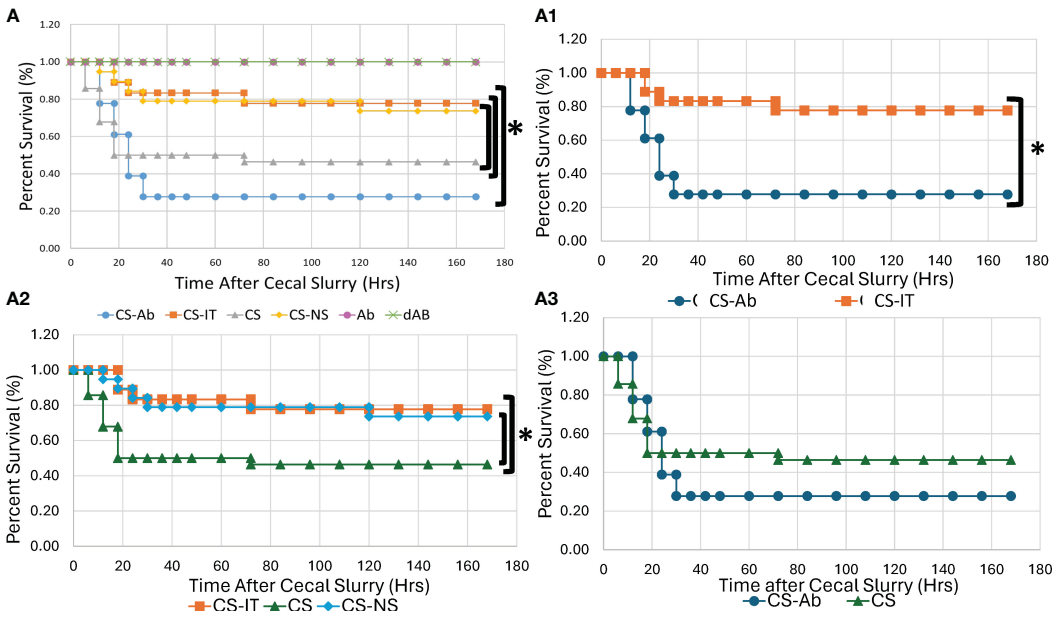

FIGURE 1
Neonatal murine survival after sepsis with intraperitoneal HVEM blockade depicted in Kaplan-Meier curves. **(A)** All Treatment groups. **(A1)** Intraperitoneal HVEM blockade with CS produces a significant survival deficit compared to isotype control, with 5/18 for CS-Ab vs. 14/18 CS-IT groups (p=0.003) **(A2)** CS-IT treated pups survival demonstrated no significant difference from survival of pups treated with CS-NS (14/18 CS-IT vs. 14/19 CS-NS, p=0.949), yet survived significantly better than pups treated with CS alone (14/18 CS-IT vs. 13/28 CS, p=0.035) **(A3)** CS-Ab treatment produced slightly worse survival than CS alone (5/18 CS-Ab vs. 13/28 CS, p=0.327) and the text box labels under Figure 1A1 has been shifted revealing something that was covered with a white box on the version I sent in, the text boxes should be moved to the left 2-3 tabs.

3 Results

3.1 Neonatal mortality is increased after septic insult in the setting of HVEM signaling blockade, occurring despite the resuscitative benefit of additional volume administration

Mortality was significantly higher for CS-Ab mice than for CS-IT mice, with 5 of 18 CS-Ab treated mice survived versus 14 of 18 CS-IT treated mice over a 7-days (p=0.003), depicted in Figure 1A, A1. Within the CS-Ab group, mortality was noted to be rapid, with 84% of deaths occurring by the 24 hr time point. When evaluating CS-IT mice compared to CS treatment alone or CS-NS treatment (Figure 1A2) CS-IT mice survived significantly better than CS alone with 14/18 CS-IT pups surviving to 7 days compared to 13/28 CS pups (p=0.035). However, CS-IT treated pups survival demonstrated no significant difference from survival of pups treated with CS-NS (14/18 CS-IT vs. 14/19 CS-NS, p=0.949). CS-Ab mice demonstrate slightly worse survival than pups treated with CS alone, as shown in Figure 1A3 (p=0.327). Anti-HVEM antibody administration independently, both alone (Ab) in diluted in normal saline (dAb), generated no effect on lethality (Supplementary Figure 1). Finally, consistent with results of prior work within the CS model by our lab, there was no mortality demonstrated for naïve or Sham treatments (Supplementary Figure 1) (29, 42).

3.2 Dysregulated alveolar remodeling associated with CS model and attenuated by HVEM blockade

Histologic responses to HVEM signaling blockade in the lung were evaluated by measuring median cord length, a measure of the normal neonatal process of alveolar remodeling. Naïve lung samples demonstrated appropriate remodeling, while induction of sepsis via CS resulted in significantly dysregulated alveolar remodeling, reflected by an increase in MCL from 86.88 ± 3.43 in naïve mice to 120.95 ± 13.94 in CS treated pups (p <0.05) (Figure 2). Lungs from CS-Ab mice demonstrated a significant reduction in dysfunctional alveolar remodeling compared to CS alone with an MCL of 87.55 ± 3.13 in CS-Ab versus 120.95 ± 13.94 in CS treated samples (p<0.05). CS-Ab lung histology and MCL was found to be most similar to naïve lung samples with their MCL of 86.88 ± 3.43, and CS-Ab MCL was additionally found to be significantly lower than CS-IT treated samples (MCL: 87.55 ± 3.13 CS-Ab vs 110.53 ± 0.96 CS-IT, p= 0.029).

3.3 Sepsis induced thymic karyorrhexis, and this was not altered by CS-Ab or CS-IT treatment, while renal histology demonstrated vacuolar degeneration and mild tubular epithelial swelling

Thymic samples demonstrated increased karyorrhexis induced by CS administration, when compared to Sham samples, 2.75 ± 1.44 Sh vs. 244.25 ± 93.94 CS (Figures 3A, B). CS and CS-Ab had similar increase in thymic karyorrhexis (244.25 ± 93.94 CS vs 393.25 ± 106.16 CS-Ab, p>0.05). CS-Ab samples demonstrated no significant difference when compared to CS-IT samples in terms of thymic lymphoid karyorrhexis (491 ± 65.82 CS-IT vs. 393.25 ± 106.16 CS-Ab., p>0.05). Caspase 3 staining of thymic tissue samples revealed that induction of sepsis via CS resulted in an increased amount of apoptosis within the thymus as compared with naive samples (Figure 4A). This response was similar in the anti-HVEM treated samples but was somewhat ameliorated in CS-IT treated pups. By densitometry, induction of sepsis via CS resulted in significantly higher levels of activated caspase 3 staining in all 3 septic

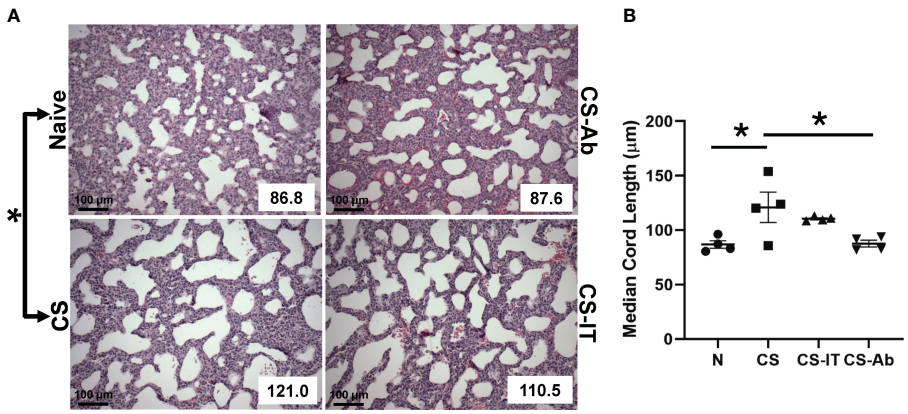

FIGURE 2
Dysregulated alveolar remodeling associated with CS model and attenuated by HVEM blockade: **(A)** H&E stained samples of lungs harvested from Naïve, CS, CS-IT and CS-Ab treated pups 12hrs after IP injection depicted at 40x magnification with mean chord length (MCL) reflected in the lower right corner, provided in µm. **(B)** Histogram depicting the average MCL ± SEM per group: 86.88 µm ± 3.43 N, 97.85 µm ± 9.88 Sh, 120.95 µm ± 13.94 CS, 110.53 µm ± 0.96 CS-IT, and 87.55 µm ± 3.13 CS-Ab. MCL was significantly increased in CS compared with Naïve (p<0.05), and significantly lower in CS-Ab pups than in CS alone (p<0.05). Finally, CS-Ab treated lung samples were found to have significantly shorter MCL than CS-IT treated pups (p=0.029); data is shown as dot plot with mean +/- SEM; * delineates significant differences between specific groups (bar) at p<0.05.

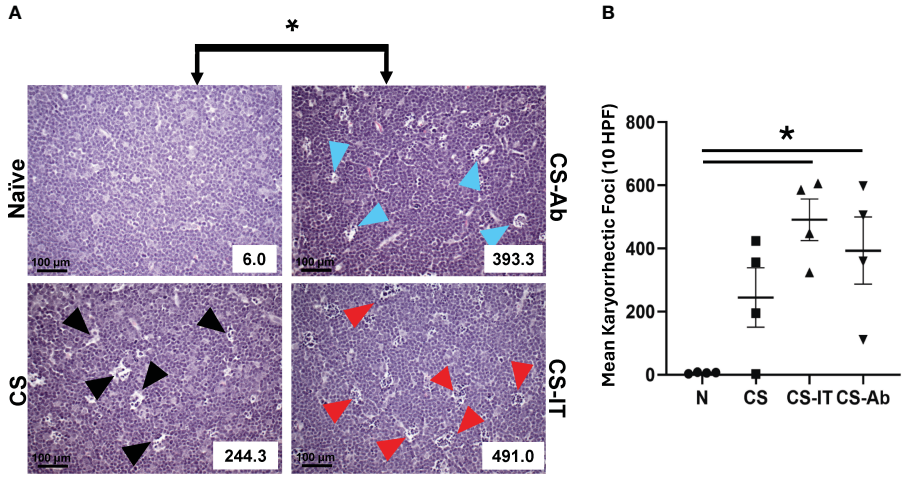

FIGURE 3
(A) Histologic evidence of increased thymic karyorrhexis after CS, not affected by Ab or IT treatment. H&E-stained thymic samples harvested from Naïve, CS, CS-IT and CS-Ab treated pups 12hrs after IP injection depicted at 40x magnification with karyorrhectic index (KI) reflected in the lower right corner. **(B)** Histogram of karyorrhexis indices for each treatment group. Average KI ± SEM: 6 ± 1.08 N, 244.25 ± 93.94 CS, 491 ± 65.82 CS-IT, and 393.25 ± 106.16 CS-Ab. CS-Ab and CS-IT treated pups had significantly higher KI than naïve pups ($p<0.01$) yet were not significantly different than KI observed in mice treated with CS alone ($p>0.05$); data is shown as dot plot with mean +/- SEM; * delineates significant differences between specific groups (bar) at $p<0.05$.

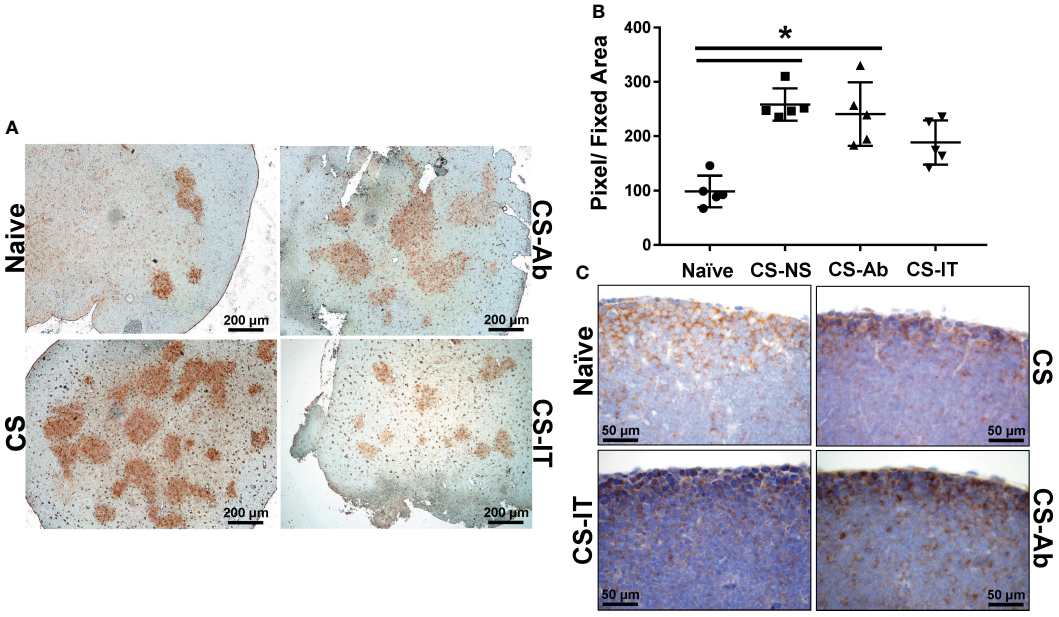

FIGURE 4
Thymic apoptosis is induced by CS administration, attenuated by IT administration. **(A)** Thymus samples harvested from Naïve, CS, CS-IT and CS-Ab treated pups 12hrs after IP injection depicted at 4x magnification following staining for caspase 3 activity. Naïve samples demonstrate mild staining, while staining is increased by CS treatment, CS-Ab samples demonstrated very similar levels of staining to CS samples, while CS-IT demonstrated mild staining. **(B)** Image densitometry plots generated by random sampling of thymic samples stained for active caspase 3 demonstrating no significant difference between CS, CS-Ab, and CS-IT treatment groups caspase 3 staining. All 3 groups treated with CS demonstrate significantly higher active caspase 3 staining than the naïve control. **(C)** Thymus samples harvested from Naïve, CS, CS-IT and CS-Ab treated pups 12hrs after IP injection depicted at 40x magnification following staining for HVEM expression with a polyclonal anti-HVEM antibody. Induction of sepsis results in grossly decreased cortical HVEM staining, which was increased back to naïve levels by CS-Ab administration; data is shown as dot plot with mean +/- SEM; significance * $p<0.05$.

groups compared to naïve, with no significant differences between CS, CS-Ab and CS-IT samples (Figure 4B). CS treated samples showed altered density of HVEM-immunoreactive thymocytes, especially in the subcortical zone compared to naïve (Figure 4C). Grossly, cortical HVEM expression decreased in CS compared to Naïve samples, yet HVEM expression was increased after CS-Ab and CS-IT treatments, more closely resembling Naïve samples.

H&E-stained renal samples (Supplementary Figures 2A, B) demonstrated expected apical vacuolization in Naïve samples, while CS samples demonstrated mildly increased tubular epithelial swelling with minor vacuolar degeneration, CS-IT samples with more variable findings, and, finally, CS-Ab samples demonstrated partial tubular vacuolar degeneration throughout the samples reviewed and showed mild tubular epithelial swelling. Kidney weight was significantly lower in CS-Ab than CS-IT (5.14mg/g ± 0.523 vs 8.75mg/g ± 0.665, p<0.05) (Table 2).

3.4 HVEM signaling blockade results in significant cardiac dysfunction when compared to both Sham and CS-IT treatment

Echocardiography 24 hrs after treatment with Sh, CS-IT and CS-Ab demonstrated that CS-Ab treatment significantly reduced heart rate in neonatal mice when compared to Sh controls (390.3 Sh vs. 342.1 CS-Ab, p=0.020), as depicted in Figure 5A. Similarly, CS-Ab treatment resulted in a decreased stroke volume, or volume of blood pumped out of the left ventricle in each cardiac cycle, when compared to IT controls (13.08 CS-IT vs. 8.83 CS-Ab; p=0.048), though significant variability in the stroke volume of the Sh treated mice meant no difference was appreciated between Sh and CS-IT or CS-Ab (Figure 5B). When looking at ejection fraction, or the percentage of blood the left ventricle pumps with each heartbeat, there was no significant difference between Sh and CS-IT

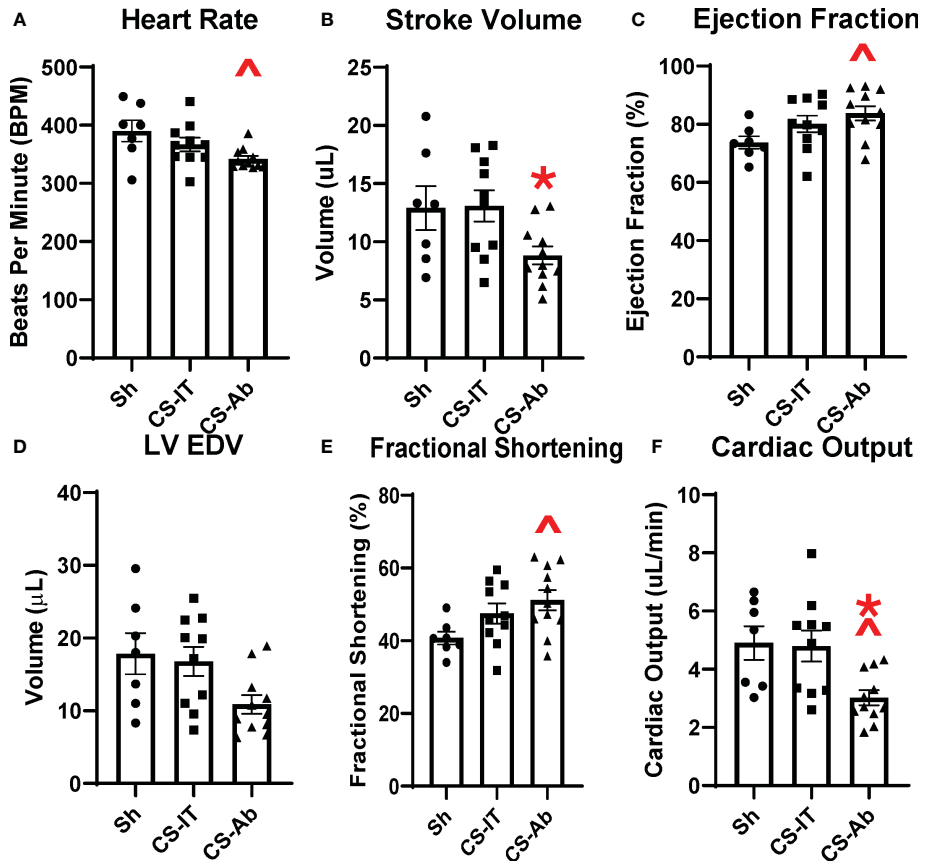

FIGURE 5
Murine echocardiography completed 24 hrs after treatment with Sh (N=7), CS-IT (N=10) or CS-Ab (N=11) **(A)** Heart rate was significantly reduced by CS-Ab treatment compared to sham control (390.3 Sh vs. 342.1 CS-Ab, p=0.020) **(B)** Stroke volume was significantly reduced 24 hrs after CS-Ab treatment compared to CS-IT (13.08 CS-IT vs. 8.83 CS-Ab; p=0.048) **(C)** CS-Ab treatment significantly increased ejection fraction compared to sham pups at 24 hrs post treatment (73.74 Sh vs. 83.75 CS-Ab; p=0.041) **(D)** Left Ventricular End Diastolic Volume was not significantly altered by treatments. **(E)** Fractional shortening was significantly increased by CS-Ab treatment compared to Sham (40.74 Sh vs. 51.16 CS-Ab; p=0.035). **(F)** Cardiac output was significantly reduced after CS-Ab treatment compared to both Sh and CS-IT treated animals. (4.90 Sh vs. 4.80 CS-IT vs. 3.02 CS-Ab; p=0.022 vs. Sh; p = 0.017 vs. CS-IT); data is shown as dot plot with mean +/- SEM; significance: ^= p<0.05 vs. Sh; *=p<0.05 vs. CS-IT.

treated pups (73.74 Sh vs. 80.13 CS-IT; p=0.255), however, CS-Ab treatment resulted in a significant increase in the ejection fraction compared to Sh (73.74 Sh vs. 83.75 CS-Ab; p=0.041; Figure 5C). CS-IT treatment closely resembled Sh treatment when left ventricular end diastolic volume was investigated, though CS-Ab treatment resulted in a trend towards reduced left ventricular end diastolic volume (LVEDV) when compared to Sh or CS-IT treatment, while Sh and CS-IT treatments resulted in nearly identical LVEDV (Sh vs. CS-IT p=0.931; Sh vs. CS-Ab p=0.057, CS-IT vs. CS-Ab p=0.077; Figure 5D). Antibody treatment was further associated with increased fractional shortening, a surrogate for strain, when compared to Sh pups (40.74 Sh vs. 51.16 CS-Ab; p=0.035; Figure 5E). Finally, it was found that CS-Ab treated pups had a reduced cardiac output compared to both sham and IT controls (4.90 Sh vs. 4.80 CS-IT vs. 3.02 CS-Ab; p=0.022 vs. Sh; p = 0.017 vs. CS-IT; Figure 5F).

3.6 Sepsis via CS induced significant differences in multiple circulating cytokine levels, including IFN-γ, TNF-α, MCP-1, IL-10 and IL-6 when compared to naïve and sham controls, however no significant differences between CS-IT or CS-Ab treatment were detected

The plasma cytokine array, depicted in Figure 6, and expanded on in Supplementary Figures 3 and 4, demonstrated multiple differences induced by cecal slurry treatment. IFN-γ levels varied significantly between the 8 tested treatment groups (N, Sh, CS, CS-IT, CS-Ab, CS-NS, Ab, and dAb; p=0.001; Figure 6C; Supplementary Figure 3), while it was specifically detected that sepsis without any resuscitation or antibody treatment (CS) induced significant difference compared to both naïve and sham groups (N vs. CS p=0.0046; Sh vs. CS p=0.041). TNF-α levels also varied significantly between groups (p<0.0001; Figure 6D). Similar to IFN-γ, CS treatment induced significant differences in TNF-α levels compared to both naïve and sham groups (N vs. CS, p=0.0426; Sh vs. CS p=0.0035). However, CS-Ab treatment also significantly increased TNF-α levels compared to Sham controls (Sh vs. CS-Ab, p = 0.014), while CS-IT treatment did not (Sh vs. CS-IT, p=0.052). MCP-1 additionally demonstrated a significant difference between the 8 treatment groups (p<0.0001), with a significant increase in levels after CS, CS-IT, and CS-Ab levels when compared to both naïve and sham pups (N vs. CS, p=0.0038; N vs. CS-IT, p=0.0352; N vs. CS-Ab, p=0.0036; Sh vs. CS, p=0.0005; Sh vs. CS-IT, p=0.0056; and Sh vs. CS-Ab, p = 0.0004) (Figure 6E). CS-NS treatment did not induce a significant increase in MCP-1 compared to naïve mice (N vs. CS-NS, p=0.1268), though it did compared to sham treatment (Sh vs. CS-NS, p=0.0315). No difference was detected between MCP-1 levels at 24 hrs after treatment with CS-IT and CS-Ab (CS-IT vs. CS-Ab, p>0.999). Circulating IL-10 levels were also found to be significantly different between the 8 treatment groups (p<0.0001), and similar to MCP-1 this was found to be due to significant increases after any treatment including CS (CS, CS-IT, and CS-Ab [Supplementary Figure 4]) excepted CS-NS, the resuscitative group, when compared to both naïve and sham pups (N vs. CS, p=0.0106; N vs. CS-IT, p=0.0139; N vs. CS-Ab, p=0.0007; Sh vs. CS, p=0.0178; Sh vs. CS-

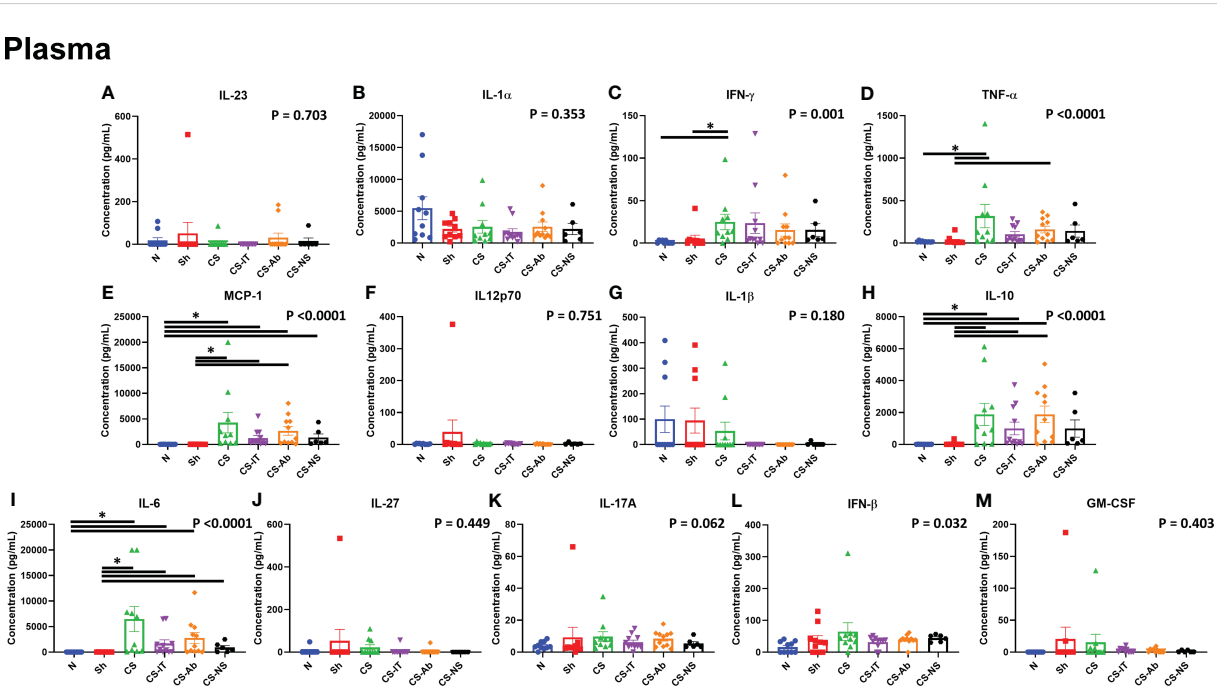

FIGURE 6
Circulating cytokine levels in neonatal mice 24 hours after treatment, mice demonstrate increases in multiple pro-inflammatory cytokines at the 24hr mark after CS treatment, though no specific differences between CS alone, CS-IT or CS-Ab treatments existed. Reported p value reflects non-parametric one-way ANOVA, remainder of indications reflect multiple comparisons test results. **(A)** IL-23 **(B)** IL-1α **(C)** IFN-γ **(D)** TNF-α **(E)** MCP-1 **(F)** IL12p70 **(G)** IL-1β **(H)** IL-10 **(I)** IL-6 **(J)** IL-27 **(K)** IL-17A **(L)** IFN-β **(M)** GM-CSF **(A–M)** Summary graphs show data dot plot and mean +/- SEM all after N, Sh, CS, CS-IT, CS-Ab, and CS-NS treatments, [N *n=10*, Sh *n=10*, CS *n=10*, CS-IT *n=11*, CS-Ab *n=11*, CS-NS *n=6*, Ab *n=6*, dAb *n=6*]; * significant differences between specific groups (bar) delineated relative to Bonferroni corrected "P" value.

IT, p=0.0233; Sh vs. CS-Ab, p = 0.0012; N vs. CS-NS, p=0.0749; Sh vs. CS-NS, p=0.1103). Finally, circulating IL-6 levels followed a very similar pattern, with significant variability between the treatment groups (p<0.0001); related to significant increases after CS treatment groups CS, CS-IT, and CS-Ab compared to naïve and sham groups (N vs. CS p=0.0006; N vs. CS-IT, p=0.0228; N vs. CS-Ab, p=0.005; Sh vs. CS, p<0.0001; Sh vs. CS-IT, p=0.0044; Sh vs. CS-Ab, p = 0.0008). Like MCP-1, CS-NS resuscitation resulted in no significant difference compared to naïve pups (N vs. CS-NS, p=0.1107), but did induce a difference compared to sham controls (Sh vs. CS-NS, p=0.0325), and again, no difference between CS-IT and CS-Ab mice was detected (CS-IT vs. CS-Ab, p>0.999).

3.7 Sepsis induced renal NGal expression and tissue specific increases in inflammatory cytokines TNF-α, MCP-1, IL-10 and IL-6, however HVEM:LIGHT blockade did not alter this expression profile

Western blotting using renal protein samples, depicted in Supplementary Figure 2C, demonstrate that NGal expression is induced by the administration of CS and maintained in both the CS-Ab and CS-IT groups. Kidney cytokine levels demonstrated the most significant changes as a result of CS treatment compared to sham and naïve control pups. First, TNF-α levels were significantly altered amongst treatment groups (p=0.0002; Figure 7A), with CS and CS-Ab leading to increased levels (N vs. CS, p=0.0256; N vs. CS-Ab, p=0.0062). TNF-α levels were also increased after CS-Ab treatment when compared to dAb (CS-Ab vs. dAb, p=0.0280). Kidney MCP-1 levels varied significantly between treatment groups (p<0.0001, Figure 7B), with specific increases in CS and CS-Ab when compared to independent antibody administration (CS vs. Ab, p=0.0291; CS-Ab vs. Ab, p=0.0196). IL-10 levels in kidney samples varied significantly between the 8 treatment groups (p=0.0006, Figure 7C), with CS resulting in increased IL-10 when compared to naïve, except in the setting of resuscitation with normal saline (N vs. CS, p=0.0173; N vs. CS-IT, p=0.0401; N vs. CS-Ab, p=0.0028; N vs. CS-NS, p>0.999), but only CS-Ab treatment increased IL-10 compared to sham (Sh vs. CS-Ab, p=0.0330; Sh vs. CS-NS, p>0.999). However, no difference in renal IL-10 levels between CS-IT and CS-Ab treated pups was found (CS-IT vs. CS-Ab, p>0.999). Finally, kidney IL-6 levels were significantly altered by treatment (p=0.0001, Figure 7D). Treatment with CS and CS-Ab

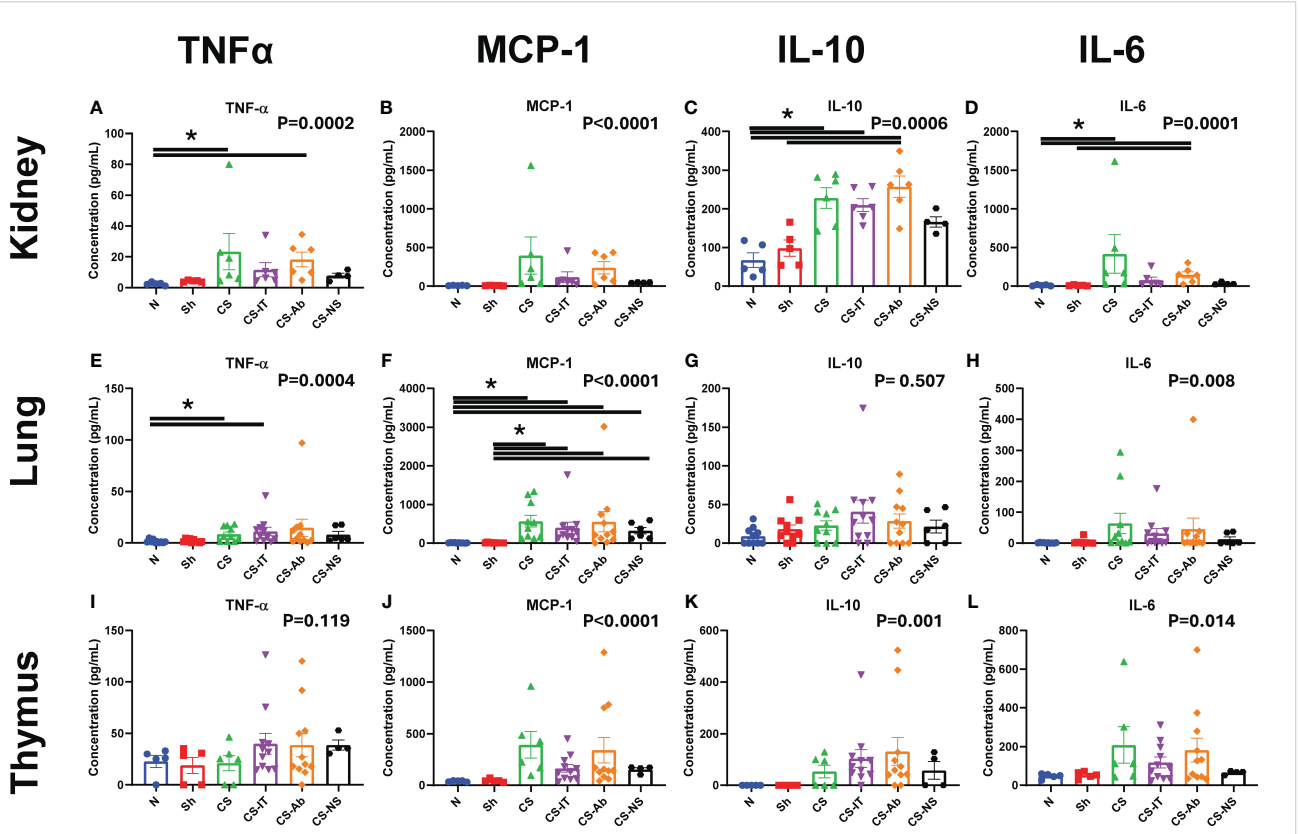

FIGURE 7
Tissue specific cytokine levels 24 hours after treatment in neonatal mice. Mice demonstrate increases in MCP-1 levels in tissue consistently after treatment, while TNFα, IL-10 and IL-6 levels are less diffusely altered. Reported p value reflects non-parametric one-way ANOVA, remainder of indications reflect multiple comparisons test results. **(A)** Kidney TNFα **(B)** Kidney MCP-1 **(C)** Kidney IL-10 **(D)** TNF-α **(E)** Lung TNFα **(F)** Lung MCP-1 **(G)** Lung IL-10 **(H)** Lung IL-6 **(I)** Thymus TNFα **(J)** Thymus MCP-1 **(K)** Thymus IL-10 **(L)** Thymus IL-6 **(A–L)** Summary graphs show data dot plot and mean +/- SEM all after N, Sh, CS, CS-IT, CS-Ab, and CS-NS treatments, [Kidney N *n=5*, Sh *n=5*, CS *n=6* CS-IT *n=6*, CS-Ab *n=6*, CS-NS *n=4;* Lung N *n=10*, Sh *n=10*, CS *n=10*, CS-IT *n=11*, CS-Ab *n=11*, CS-NS *n=6;* Thymus N *n=5*, Sh *n=5*, CS *n=6*, CS-IT *n=11*, CS-Ab *n=11*, CS-NS *n=4*]; significant differences between specific groups (bar) delineated relative to Bonferroni corrected "P" value. * p<0.05.

10.3389/fimmu.2024.1365174

resulted in significantly higher levels of IL-6 than naïve and sham, while treatment with CS-IT and CS-NS did not (N vs. CS, p=0.0126; N vs. CS-IT, p=0.1423; N vs. CS-Ab, p=0.0151; N vs. CS-NS, p=0.7793; Sh vs. CS-Ab, p = 0.0186). No difference in renal IL-6 levels between CS-IT and CS-Ab was detected (CS-IT vs. CS-Ab, p>0.999). No differences were detected between groups in the other 9 tested cytokines, as depicted in Supplementary Figure 5.

Lung samples also demonstrate cytokine level fluctuation. TNF-α levels varied significantly between the tested groups (p=0.0004; Figure 7E), with differences after CS induction by CS or CS-IT, though not by CS-Ab (N vs. CS, p=0.0408; N vs. CS-IT, p=0.0171; N vs. CS-Ab, p=0.1063). MCP-1 levels varied significantly between the 8 treatment groups (p<0.0001; Figure 7F), with sepsis inciting increases in CS, CS-IT, CS-Ab and CS-NS treated pups compared to naïve or sham animals (N vs. CS, p=0.0011; N vs. CS-IT, p=0.0048; N vs. CS-Ab, p=0.0216; N vs. CS-NS, p=0.0399; Sh vs. CS, p=0.0009; Sh vs. CS-IT, p=0.0039; Sh vs. CS-Ab, p = 0.0176; Sh vs. CS-NS, p=0.0338). Unlike other tissues, no significant difference in IL-10 levels were noted between the treatment groups (p=0.507; Figure 7G), though IL-6 levels did vary between the 8 treatment groups (p=0.008; Figure 7H), though no specific difference between individual groups means was detected when multiple comparisons testing was completed. No differences were detected between groups in the other 9 tested cytokines, as depicted in Supplementary Figure 6.

When looking at cytokine levels in the thymus, there was no significant difference in TNF-α levels between any groups (p= 0.119; Figure 7I). Thymus samples did however demonstrate significant variation in MCP-1 levels between the 8 tested groups (p<0.0001; Figure 7J). This MCP-1 variability was driven by differences between CS and CS-Ab treated groups when compared to Ab or dAb treated mice (CS vs. Ab, p=0.0182; CS vs. dAb, p=0.0049; CS-Ab vs. dAb, p=0.0241). IL-10 levels in the thymus also significantly varied amongst the 8 tested groups (p=0.001, Figure 7K), however no marked difference between any two individual groups was detected via multiple comparisons testing. The same was true of thymic IL-6 levels, where significant variability between the 8 tested groups (p=0.014, Figure 7L), but no significant difference between any two specific groups was observed. No differences were detected between groups in the other 9 tested cytokines, as depicted in Supplementary Figure 7.

3.8 Cecal Slurry treatment produced a significant increase in intraperitoneal bacterial burden; however, this was not altered by CS-Ab, CS-IT or CS-NS treatments

CS-Ab treated mice were found to have no significant difference from CS-IT controls in colony forming units in the peritoneal fluid 12hrs after septic insult (p = 0.903, Figure 8). Peritoneal lavage samples from naïve pups demonstrated no bacterial burden, while all the CS groups exhibited a marked increase in CFUs (0.00 N vs. CS 39783.8, p= 0.032, vs. 72753.8 CS-Ab, p=0.049, vs. 67258.8 CS-IT, p=0.044, and vs. 72534.5 CS-NS, p=0.020). No significant difference in number of CFUs identified existed between the CS, CS-Ab, and CS-IT treated animals (p=0.66, Figure 8). Finally, Ab and dAb treated mice both had low levels of intraperitoneal bacteria, significantly less than any CS treated group (440.6 Ab vs. dAb 659.8 vs. 39784 CS; p=0.013).

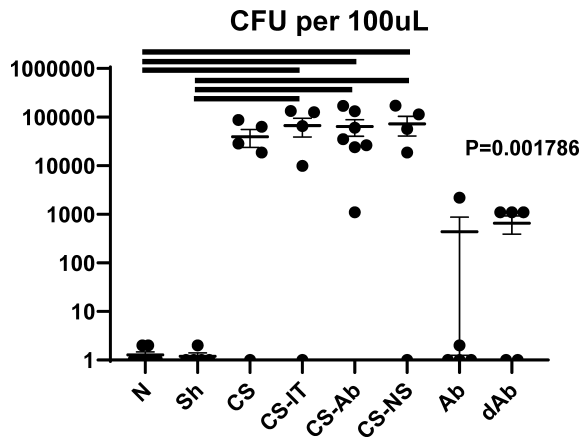

FIGURE 8
Intraperitoneal bacterial burden. Colony forming units per 100μL of peritoneal fluid presented in log scale, naïve mice demonstrated no bacterial burden whereas all CS treated groups demonstrated significantly more CFUs than naïve samples (0.00 N vs. CS 39783.8, p= 0.032, vs. 72753.8 CS-Ab, p=0.049, vs. 67258.8 CS-IT, p=0.044, and vs. 72534.5 CS-NS, p=0.020). No significant difference between number of CFUs identified existed between the 4 CS treated groups (p=0.66).

4 Discussion

This investigation demonstrated intraperitoneal blockade of the HVEM:LIGHT signaling axis resulted in a rapid survival deficit for neonatal mice facing intraabdominal septic challenge. Histologically, this survival deficit was associated with preserved lung histology, thymic karyorrhexis similar to mice who underwent isolated CS treatment, increased thymic cortical HVEM expression, and moderate renal tubular vacuolar degeneration indicative of renal injury. Bacterial burden was not significantly affected by antibody treatment. HVEM:LIGHT signaling blockade produced reduced heart rate and stroke volume, with increases in ejection fraction and fractional shortening, ultimately producing significantly reduced cardiac output compared to sham and CS-IT pups. In total, these results demonstrate checkpoint regulator HVEM is integral to the neonatal response to septic challenge. The rapid lethality and mixed picture of histologic evidence of tissue injury implicate systemic cardiovascular collapse as the cause of death. However, the mechanistic link between HVEM blockade and this cardiac dysfunction was less clear in our investigation. The possibility remains that the observed cardiac dysfunction was due to a robust early cytokine release in the first 18 hours after treatment, given

the subtle signals present at 24 hours post treatment, but firm establishment of this causal link will require more investigation.

4.1 Survival to septic insult was significantly reduced by HVEM:LIGHT blockade, suggesting an important role for HVEM in septic responses, while resuscitation demonstrated meaningful impact in post-septic survival

It is logical that blockade of the HVEM:LIGHT binding domain results in significantly worse survival to sepsis as the HVEM:LIGHT interaction produces a powerful immune stimulatory response (17). Upon ligation with LIGHT, a robust stimulatory signal results as HVEM recruits TRAF2 to its intracellular domain, activating NFκB, and promoting cell survival (43). Without the ability to stimulate, HVEM is still able to bind and interact with inhibitory ligands BTLA and CD160, generating an uninterrupted inhibitory signal and preventing appropriate immune mobilization (20). Death from isolated blockade of the LIGHT binding domain of HVEM suggests that HVEM triggered immune stimulation is a key component of the immediate neonatal response to sepsis. In this study, death after anti-HVEM antibody administration in sepsis was rapid, implicating more acute phenomena such as cardiovascular collapse or hyperinflammatory cytokine storm. Early mortality in sepsis is almost universally attributed to cardiac dysfunction, in both adults and neonates (9, 44).

Independent delivery of anti-HVEM in the absence of a septic stimuli did not produce lethality, indicating signaling via HVEM:LIGHT is not essential for survival, growth and development in the absence of immune stimulation. CS-IT samples survived significantly better than pups treated with CS alone, and postulate this may be a resuscitative effect of the 20μL of IP fluid mice received with isotype or antibody administration. While this volume is small enough to be negligible in many cases, neonatal study subjects weighed an average of 3.5 grams, making this volume a substantial percentage of their body weight. This was tested by administering CS with an equal volume of 0.9% saline (20μL), and this resuscitation did improve neonatal survival compared to CS alone (14/19 CS-NS vs. 13/28 CS, p=0.037), and more closely recapitulated the isotype groups survival. Knowing this, the survival deficit generated by HVEM:LIGHT blockade, despite the inevitable delivery of this same resuscitation volume, is even more impressive.

4.2 HVEM:LIGHT blockade protected normal lung development during septic insult, suggesting a unique and specific role for HVEM signaling in indirect acute lung injury of sepsis

Histologically, HVEM blockade was protective of normal lung development during sepsis, producing morphology most similar to naïve controls despite associated lethality. In contrast, CS-IT lung samples demonstrated histology most similar to the CS alone group despite their robust survival. The low MCL observed in CS-Ab reflects appropriate alveolar remodeling known to occur during the neonatal period in lung development (34). This lung protective effect mirrors results published by Cheng et al. using an adult model of indirect acute lung injury in which intratracheal HVEM siRNA administration was protective of normal lung histology (30). However, in that case, with a more localized delivery of HVEM blockade, a transient survival benefit was derived in the 48hrs following the single intratracheal administration. Septic patients are known to suffer lung injury even in sepsis driven by a compartment outside of the thorax, though this is particularly true in neonates (35). This demonstration, coupled with the feasibility of local intratracheal instillation provides a potentially viable therapeutic strategy to protect neonates from lung injury associated with sepsis, warranting more extensive, focused investigation in the future (30). Additionally, lung protection in the setting of increased mortality suggests the cause of death in these neonates is from an alternate source of septic lethality, such as cardiac dysfunction. One limitation of this study is that neonatal mouse size prohibited use of physiologic measures of impact of this lung injury such as measuring oxygen or CO_2 exchange, which would characterize the impact of these histologic changes more clearly.

4.3 Septic challenge induced signs of AKI and steroid stress within the thymus is not altered by HVEM:LIGHT blockade, despite apparent changes in HVEM expression in the thymic cortex after sepsis

Prior studies of tissue injury in murine sepsis have illustrated lymphoid tissues are particularly susceptible to steroid stress after septic challenge with profound lymphoid organ apoptosis (35, 45). Analysis of H&E-stained thymic samples demonstrated karyorrhexis induced by the CS model, similar in all groups receiving CS, regardless of Ab or IT treatment. These results were confirmed by active caspase 3 staining which suggested increased apoptosis in CS samples with no change in apoptotic extent with antibody administration. This indicates that HVEM:LIGHT blockade does not affect steroid induced injury to lymphoid organs after sepsis, nor does fluid resuscitation. The increased thymic cortical HVEM staining seen in CS-Ab samples suggests HVEM blockade and sepsis do affect the HVEM expression, though the exact extent is not clear.

Acute kidney injury (AKI) is the second most common organ injured as a result of sepsis, behind lung, in adult patients (35). While aging is a major risk factor for severity of kidney injury or failure after sepsis, septic patients of all ages are at risk of AKI, and AKI has an additive negative effect portending a 70% risk of mortality (35, 37). Renal histology showed increased vacuolar degeneration in the tubular cells after sepsis (CS), which was more pronounced in CS-Ab treated mice along with tubular epithelial swelling, both common histologic markers of AKI. Further indications of AKI in septic pups was demonstrated by

western blotting, where NGal expression, a biomarker of acute kidney injury, was increased after CS but not significantly altered by resuscitation or CS-Ab.

4.4 Significant cardiac dysfunction including significant reduction in cardiac output after CS-Ab treatment accounts for survival deficit

Septic cardiac dysfunction is a well-documented cause of acute mortality after sepsis. Typically occurring with more rapidity than multi-system organ failure, a great deal of research into the central mechanism of this sepsis-associated cardiac dysfunction has failed to identify a specific cause (9). Previously, the role for circulating DAMPs, cytokines, oxidative stress, calcium homeostasis and alterations in nitric oxide production have all been described to contribute to septic cardiac dysfunction (44, 46, 47). Alterations in surface innate immune receptors on cardiomyocytes, including Toll-like receptors, have also been associated with septic cardiac dysfunction, however, the roll of checkpoint regulators such as HVEM in this process have been less clearly defined (46). This study demonstrates that HVEM:LIGHT blockade results in significant cardiac dysfunction in neonates after sepsis, with alterations in nearly every measured parameter of cardiac activity. Blockade resulted in reduced heart rate and stroke volume, suggesting reduction in the necessary compensatory cardiac response to septic hypovolemia. HVEM:LIGHT blockade also increased ejection fraction and fractional shortening, indicating higher strain after sepsis. Finally, blockade produced a significant reduction in cardiac output compared to both Sham and CS-IT treated pups, providing an explanation for the disparate mortality between treatment groups. Interestingly, LVEDV was nearly identical for sham animals and those treated with CS-IT, where sepsis would be expected to result in a hypovolemic shock and reduced LVEDV, arguing that CS-IT survival differed from CS-Ab treatment from a resuscitative benefit.

HVEM is expressed on cardiomyocytes, though no specific role for its presence has been previously defined (19). Looking at mechanistic causes of septic cardiac dysfunction, many of the same cytokines noted to be alternatively produced in neonates after sepsis produce changes in cardiomyocytes that precipitate the cardiac dysfunction. Increases in TNF-α lead to myocyte apoptosis, while increased IL-1, IL-8 and TNF-α increase nitric oxide production which causes DNA damage and ATP depletion which occurs through a decrease in fatty acid and glucose oxidation in the cardiomyocytes. Finally, the increase in NFκB, the direct downstream result of HVEM signaling, impairs beta adrenergic signaling which also leads to apoptosis (9, 11, 44). Given the rapid nature of the mortality noted in the HVEM:LIGHT blockade, peaking between 18 and 24 hrs post insult, cardiac dysfunction is a fitting explanation of mortality as it is classically acute in nature and poorly tolerated, however, this study is limited in its single timepoint examination and expansion to additional timepoint would better illuminate this (9).

4.5 Inflammatory cytokine expression was altered by induction of sepsis, and often improved with resuscitation, however HVEM:LIGHT blockade did not alter this at the 24 hr time point

Exploration of inflammatory cytokines at 24 hrs post treatment in the plasma, lung, kidney and thymus, common sites of immune injury, demonstrated several interesting signals. Not surprisingly, in response to CS there was a consistent and marked rise in a number of the pro-inflammatory cytokines in the blood of the neonatal pups, with some echo at the organ level within the kidney and lungs. These tissue specific inflammatory cytokine changes mirror those typically encountered following experimental infectious challenge in many other neonatal and adult sepsis models, and in septic patients (25, 26). Throughout all explored tissues, sepsis increased pro-inflammatory cytokines like TNFα, MCP-1, IL-10 and IL-6 compared to sham animals, regardless of HVEM:LIGHT blockade. However, this effect was often lost with the addition of the equal volume normal saline resuscitation (CS-NS), a clear depiction of the benefit of fluid resuscitation in septic shock. Interestingly, in multiple areas CS-IT treatment similarly resulted in a loss of this significant pro-inflammatory cytokine increase, speaking to the resuscitative benefit of the volume administered with antibody blockade. Further, in the kidney, TNFα increased compared to sham animals only in CS and CS-Ab pups, the highest mortality groups, and those with the most significant evidence of histologic kidney injury.

While HVEM:LIGHT blockade had both negative effects on the CS neonates cardiac function and overall mortality, and improvement in lung injury at 24 hours, this would appear to be generally independent of alteration in the systemic or local organ pro-inflammatory cytokine milieu. On its face, this does not support a role for HVEM:LIGHT induced cytokine signaling as a basis for these morbid changes, and likely speaks to another aspect of HVEM:LIGHT signaling. As previous works have described, HVEM signaling is complex with multiple possible outcomes of ligation depending on the available domains ligated, so it is possible the mortality from HVEM:LIGHT blockade is driven by the preponderance of HVEM:BTLA signaling, however this too ultimately functions via changes in inflammatory cytokines (17, 48). That said, the key limitation to this cytokine exploration is the assessment at a singular acute time point. Given the mortality occurs beginning around 18 hrs after treatment, it is possible that cytokine fluctuations do occur but are transient, and resolving by the 24 hr mark explored here. Also, that anti-body blockade could not alter the CS induced increase in neonatal thymic apoptosis or cause thymic tissue cytokine changes is not totally surprising as this has been documented to be the result of altered steroid levels and largely independent of changes in TNF family members like, TNF and FasL (45). Irrespective, while we cannot completely rule out the role of HVEM:LIGHT driven pro-inflammatory mediator production, locally or systemically, to account for the changes in morbidity and mortality reported here, it is likely that another more tissue specific aspect of HVEM:LIGHT signaling is needed to explain it and will be the basis for future studies.

4.6 Future directions

Together, our findings of increased lethality, lung protection, stable thymic apoptosis, acute kidney injury, cytokine alterations, and cardiac dysfunction provide compelling evidence for HVEM's role in neonatal immune responses to septic challenge. The complexity of HVEM, with its multitude of ligands, and its ability to interact with multiple stimuli simultaneously, serves as both a limitation and a tool. It enables tissue and environmentally targeted outcomes but demands meticulous and extensive interrogation to clarify its multitude of signaling outcomes. The developing neonatal immune system is transitioning from the in-utero environments necessitation of tolerance to a world of aggressive and virulent pathogens, and this ontogeny adds an additional layer of complexity to understanding HVEM's importance fully (49). While checkpoint regulators such as HVEM are often characterized to act in influencing adaptive responses, the clear effect of HVEM:LIGHT blockade in the neonatal acute death from sepsis hints at a role for regulators such as HVEM in guiding innate responses as well. Ultimately this exploration demonstrates that cardiovascular collapse produces this acute mortality with HVEM:LIGHT blockade, and while other organ systems demonstrated impacts from sepsis consistent with prior research, little else demonstrated the impact of the cardiac dysfunction.

Future experiments are needed to further clarify the specific mechanisms underlying the role HVEM signaling plays in the septic immune response of neonates. The lung protective effect of HVEM:LIGHT blockade, specifically the option of localized administration of anti-HVEM as a potential therapeutic avenue for indirect septic lung injury, requires investigation. While thymic steroid stress was noted at the 24 hr time point, future investigation should explore these impacts at additional time intervals to better identify the impact of the differential cortical HVEM expression noted after sepsis. Characterization of the impact of AKI should involve correlation of blockade with biomarkers such as Creatinine and Blood Urea Nitrogen (BUN). Finally, further work is necessary to better characterize the tissue specific expression of HVEM and all of its ligands, especially in cardiomyocytes. It will be imperative to continue to work to align the understanding of HVEM signaling with the known neonatal immune activity and development. Correlation of these findings with appropriate biomarkers to target potential future therapeutics holds promise of harnessing HVEM to minimize the mortal risks of cardiac dysfunction, lung and/or kidney injury in response to septic challenges.

Data availability statement

The original contributions presented in the study are included in the article/Supplementary Material. Further inquiries can be directed to the corresponding author.

Ethics statement

All protocols were conducted according to the National Institutes of Health guide for animal care and use and were approved by the Lifespan-Rhode Island Hospital Institutional animal care and use committee (approval number: 0054-18 and 5054-21). The study was conducted in accordance with the local legislation and institutional requirements.

Author contributions

MW: Writing – review & editing, Writing – original draft, Visualization, Validation, Software, Project administration, Methodology, Investigation, Formal analysis, Data curation, Conceptualization. N-LD: Writing – review & editing, Writing – original draft, Software, Methodology, Investigation, Formal analysis, Data curation. JJ: Writing – review & editing, Methodology, Investigation, Formal analysis. MP: Writing – review & editing, Writing – original draft, Methodology, Investigation, Formal analysis. C-SC: Methodology, Investigation, Writing – review & editing, Supervision. PW: Writing – review & editing, Supervision, Project administration, Methodology, Investigation, Formal analysis. AA: Writing – review & editing, Writing – original draft, Supervision, Resources, Project administration, Funding acquisition, Conceptualization.

Funding

The author(s) declare financial support was received for the research, authorship, and/or publication of this article. This work was supported by the National Institutes of Health through awards R01ES016669 (EMA Study), P50HD103526, and P50MH106438. This work was supported by the National Institutes of Health [grant numbers R35 GM118097 (AA, C-SC), and R35 GM118337 (PW, N-LD)], the Armand D. Versaci Research Scholar in Surgical Sciences Fellowship (MW), fellowship support from Shanghai General hospital (JJ) as well as a post-doctoral fellowship award from the National Institutes of Health [grant number T32 GM065085 (MW)].

Acknowledgments

Histological processing for H&E staining reported in this publication was supported by the Molecular Pathology Core of the COBRE Center for Cancer Research Development funded by the National Institute of General Medical Sciences of the National Institute of Health under Award Number P30 GM110759/P20 GM103421/P20 RR017695.

Conflict of interest

The authors declare that the research was conducted in the absence of any commercial or financial relationships that could be construed as a potential conflict of interest.

Publisher's note

All claims expressed in this article are solely those of the authors and do not necessarily represent those of their affiliated organizations, or those of the publisher, the editors and the reviewers. Any product that may be evaluated in this article, or claim that may be made by its manufacturer, is not guaranteed or endorsed by the publisher.

Supplementary material

The Supplementary Material for this article can be found online at: https://www.frontiersin.org/articles/10.3389/fimmu.2024.1365174/full#supplementary-material

References

1. Murphy SL, Xu J, Kochaneck KD. Deaths: Preliminary Data for 2010. In: *National Vital Statistics Report*, vol. 60. National Center for Health Statistic, Hyattsville, MD (2012).

2. Singer M, Deutschman CS, Seymour CW, Shankar-Hari M, Annane D, Bauer M, et al. The third international consensus definitions for sepsis and septic shock (Sepsis-3). *Jama*. (2016) 315:801–10. doi: 10.1001/jama.2016.0287

3. Rittirsch D, Flierl MA, Ward PA. Harmful molecular mechanisms in sepsis. *Nat Rev Immunol*. (2008) 8:776–87. doi: 10.1038/nri2402

4. Hotchkiss RS, Colston E, Yende S, Angus DC, Moldawer LL, Crouser ED, et al. Immune checkpoint inhibition in sepsis: A phase 1b randomized, placebo-controlled, single ascending dose study of antiprogrammed cell death-ligand 1 (BMS-936559). *Crit Care Med*. (2019) 47(5):632–42. doi: 10.1097/CCM.0000000000003685

5. Raymond SL, Stortz JA, Mira JC, Larson SD, Wynn JL, Moldawer LL. Immunological defects in neonatal sepsis and potential therapeutic approaches. *Front Pediatrics*. (2017) 5. doi: 10.3389/fped.2017.00014

6. Gunst M, Ghaemmaghami V, Gruszecki A, Urban J, Frankel H, Shafi S. Changing epidemiology of trauma deaths leads to a bimodal distribution. *Proc (Bayl Univ Med Cent)*. (2010) 23:349–54. doi: 10.1080/08998280.2010.11928649

7. Ma XY, Tian LX, Liang HP. Early prevention of trauma-related infection/sepsis. *Mil Med Res*. (2016) 3:33. doi: 10.1186/s40779-016-0104-3

8. Kimura F, Shimizu H, Yoshidome H, Ohtsuka M, Miyazaki M. Immunosuppression following surgical and traumatic injury. *Surg Today*. (2010) 40:793–808. doi: 10.1007/s00595-010-4323-z

9. Luce WA, Hoffman TM, Bauer JA. Bench-to-bedside review: Developmental influences on the mechanisms, treatment and outcomes of cardiovascular dysfunction in neonatal versus adult sepsis. *Crit Care*. (2007) 11:228. doi: 10.1186/cc6091

10. Spruijt NE, Visser T, Leenen LP. A systematic review of randomized controlled trials exploring the effect of immunomodulative interventions on infection, organ failure, and mortality in trauma patients. *Crit Care*. (2010) 14:R150. doi: 10.1186/cc9218

11. Liu X, Hall SRR, Wang Z, Huang H, Ghanta S, Di Sante M, et al. Rescue of neonatal cardiac dysfunction in mice by administration of cardiac progenitor cells. *utero Nat Commun*. (2015) 6:8825. doi: 10.1038/ncomms9825

12. Bretscher P, Cohn M. A theory of self-nonself discrimination. *Science*. (1970) 169:1042–9. doi: 10.1126/science.169.3950.1042

13. Lafferty KJ, Cunningham AJ. A new analysis of allogeneic interactions. *Aust J Exp Biol Med Sci*. (1975) 53:27–42. doi: 10.1038/icb.1975.3

14. Wherry EJ, Blattman JN, Murali-Krishna K, van der Most R, Ahmed R. Viral persistence alters CD8 T-cell immunodominance and tissue distribution and results in distinct stages of functional impairment. *J Virol*. (2003) 77:4911–27. doi: 10.1128/JVI.77.8.4911-4927.2003

15. Fallon EA, Biron-Girard BM, Chung CS, Lomas-Neira J, Heffernan DS, Monaghan SF, et al. A novel role for coinhibitory receptors/checkpoint proteins in the immunopathology of sepsis. *J Leukoc Biol*. (2018) 2:1–31. doi: 10.1002/JLB.2MIR0917-377R

16. Wang J, Wu G, Manick B, Hernandez V, Renelt M, Erickson C, et al. VSIG-3 as a ligand of VISTA inhibits human T-cell function. *Immunology*. (2019) 156:74–85. doi: 10.1111/imm.13001

17. Cai G, Freeman GJ. The CD160, BTLA, LIGHT/HVEM pathway: a bidirectional switch regulating T-cell activation. *Immunol Rev*. (2009) 229:244–58. doi: 10.1111/j.1600-065X.2009.00783.x

18. Montgomery RI, Warner MS, Lum BJ, Spear PG. Herpes simplex virus-1 entry into cells mediated by a novel member of the TNF/NGF receptor family. *Cell*. (1996) 87:427–36. doi: 10.1016/S0092-8674(00)81363-X

19. Marsters SA, Ayres TM, Skubatch M, Gray CL, Rothe M, Ashkenazi A. Herpesvirus entry mediator, a member of the tumor necrosis factor receptor (TNFR) family, interacts with members of the TNFR-associated factor family and activates the transcription factors NF-kappaB and AP-1. *J Biol Chem*. (1997) 272:14029–32. doi: 10.1074/jbc.272.22.14029

20. Murphy KM, Nelson CA, Sedý JR. Balancing co-stimulation and inhibition with BTLA and HVEM. *Nat Rev Immunol*. (2006) 6:671–81. doi: 10.1038/nri1917

21. Ware CF, Sedy JR. TNF Superfamily Networks: bidirectional and interference pathways of the herpesvirus entry mediator (TNFSF14). *Curr Opin Immunol*. (2011) 23:627–31. doi: 10.1016/j.coi.2011.08.008

22. Wang Y, Subudhi SK, Anders RA, Lo J, Sun Y, Blink S, et al. The role of herpesvirus entry mediator as a negative regulator of T cell-mediated responses. *J Clin Invest*. (2005) 115:711–7. doi: 10.1172/JCI22982

23. Cheung TC, Oborne LM, Steinberg MW, Macauley MG, Fukuyama S, Sanjo H, et al. T cell intrinsic heterodimeric complexes between HVEM and BTLA determine receptivity to the surrounding microenvironment. *J Immunol*. (2009) 183:7286–96. doi: 10.4049/jimmunol.0902490

24. Shubin NJ, Chung CS, Heffernan DS, Irwin LR, Monaghan SF, Ayala A. BTLA expression contributes to septic morbidity and mortality by inducing innate inflammatory cell dysfunction. *J Leukoc Biol*. (2012) 92:593–603. doi: 10.1189/jlb.1211641

25. Shubin NJ, Monaghan SF, Heffernan DS, Chung CS, Ayala A. B and T lymphocyte attenuator expression on CD4+ T-cells associates with sepsis and subsequent infections in ICU patients. *Crit Care*. (2013) 17:R276. doi: 10.1186/cc13131

26. Shui JW, Larange A, Kim G, Vela JL, Zahner S, Cheroutre H, et al. HVEM signalling at mucosal barriers provides host defence against pathogenic bacteria. *Nature*. (2012) 488:222–5. doi: 10.1038/nature11242

27. Huang X, Chen Y, Chung CS, Yuan Z, Monaghan SF, Wang F, et al. Identification of B7-H1 as a novel mediator of the innate immune/proinflammatory response as well as a possible myeloid cell prognostic biomarker in sepsis. *J Immunol*. (2014) 192:1091–9. doi: 10.4049/jimmunol.1302252

28. Huang X, Venet F, Wang YL, Lepape A, Yuan Z, Chen Y, et al. PD-1 expression by macrophages plays a pathologic role in altering microbial clearance and the innate inflammatory response to sepsis. *Proc Natl Acad Sci U S A*. (2009) 106:6303–8. doi: 10.1073/pnas.0809422106

29. Young WA, Fallon EA, Heffernan DS, Efron PA, Cioffi WG, Ayala A. Improved survival after induction of sepsis by cecal slurry in PD-1 knockout murine neonates. *Surgery*. (2017) 161:1387–93. doi: 10.1016/j.surg.2016.11.008

30. Cheng T, Bai J, Chung CS, Chen Y, Fallon EA, Ayala A. Herpes virus entry mediator (HVEM) expression promotes inflammation/ organ injury in response to experimental indirect-acute lung injury. *Shock*. (2019) 51:487–94. doi: 10.1097/SHK.0000000000001174

31. Wynn JL, Scumpia PO, Delano MJ, O'Malley KA, Ungaro R, Abouhamze A, et al. Increased mortality and altered immunity in neonatal sepsis produced by generalized peritonitis. *Shock*. (2007) 28:675–83. doi: 10.1097/shk.0b013e3180556d09

32. Osuchowski MF, Ayala A, Bahrami S, Bauer M, Boros M, Cavaillon JM, et al. Minimum quality threshold in pre-clinical sepsis studies (MQTiPSS): an international expert consensus initiative for improvement of animal modeling in sepsis. *Shock*. (2018) 50:377–80. doi: 10.1097/SHK.0000000000001212

33. Xu Y, Flies AS, Flies DB, Zhu G, Anand S, Flies SJ, et al. Selective targeting of the LIGHT-HVEM costimulatory system for the treatment of graft-versus-host disease. *Blood*. (2007) 109:4097–104. doi: 10.1182/blood-2006-09-047332

34. De Paepe ME, Rubin LP, Jude C, Lesieur-Brooks AM, Mills DR, Luks FI. Fas ligand expression coincides with alveolar cell apoptosis in late-gestation fetal lung

development. *Am J Physiol Lung Cell Mol Physiol.* (2000) 279:L967–976. doi: 10.1152/ajplung.2000.279.5.L967

35. Craciun FL, Iskander KN, Chiswick EL, Stepien DM, Henderson JM, Remick DG. Early murine polymicrobial sepsis predominantly causes renal injury. *Shock.* (2014) 41:97–103. doi: 10.1097/SHK.0000000000000073

36. Doi K, Leelahavanichkul A, Hu X, Sidransky KL, Zhou H, Qin Y, et al. Pre-existing renal disease promotes sepsis-induced acute kidney injury and worsens outcome. *Kidney Int.* (2008) 74:1017–25. doi: 10.1038/ki.2008.346

37. Liu C, Hu J, Mao Z, Kang H, Liu H, Fu W, et al. Acute kidney injury and inflammatory response of sepsis following cecal ligation and puncture in d-galactose-induced aging rats. *Clin Interv Aging.* (2017) 12:593–602. doi: 10.2147/CIA

38. Denning NL, Aziz M, Diao L, Prince JM, Wang P. Targeting the eCIRP/TREM-1 interaction with a small molecule inhibitor improves cardiac dysfunction in neonatal sepsis. *Mol Med.* (2020) 26:121. doi: 10.1186/s10020-020-00243-6

39. Lindsey ML, Kassiri Z, Virag JAI, de Castro Brás LE, Scherrer-Crosbie M. Guidelines for measuring cardiac physiology in mice. *Am J Physiol Heart Circ Physiol.* (2018) 314:H733–h752. doi: 10.1152/ajpheart.00339.2017

40. Hoffman M, Kyriazis ID, Lucchese AM, de Lucia C, Piedepalumbo M, Bauer M, et al. Myocardial strain and cardiac output are preferable measurements for cardiac dysfunction and can predict mortality in septic mice. *J Am Heart Assoc.* (2019) 8: e012260. doi: 10.1161/JAHA.119.012260

41. Wakeley ME, Armstead BE, Gray CC, Tindal EW, Heffernan DS, Chung CS, et al. Lymphocyte HVEM/BTLA co-expression after critical illness demonstrates severity indiscriminate upregulation, impacting critical illness-induced immunosuppression. *Front Med (Lausanne).* (2023) 10:1176602. doi: 10.3389/fmed.2023.1176602

42. Fallon EA, Chun TT, Young WA, Gray C, Ayala A, Heffernan DS. Program cell death receptor-1-mediated invariant natural killer T-cell control of peritoneal macrophage modulates survival in neonatal sepsis. *Front Immunol.* (2017) 8:1469. doi: 10.3389/fimmu.2017.01469

43. Bechill J, Muller WJ. Herpesvirus entry mediator (HVEM) attenuates signals mediated by the lymphotoxin beta receptor (LTbetaR) in human cells stimulated by the shared ligand LIGHT. *Mol Immunol.* (2014) 62:96–103. doi: 10.1016/j.molimm.2014.06.013

44. Drosatos K, Lymperopoulos A, Kennel PJ, Pollak N, Schulze PC, Goldberg IJ. Pathophysiology of sepsis-related cardiac dysfunction: driven by inflammation, energy mismanagement, or both? *Curr Heart Fail Rep.* (2015) 12:130–40. doi: 10.1007/s11897-014-0247-z

45. Ayala A, Herdon CD, Lehman DL, DeMaso CM, Ayala CA, Chaudry IH. The induction of accelerated thymic programmed cell death during polymicrobial sepsis: control by corticosteroids but not tumor necrosis factor. *Shock.* (1995) 3:259–67. doi: 10.1097/00024382-199504000-00003

46. Lv X, Wang H. Pathophysiology of sepsis-induced myocardial dysfunction. *Mil Med Res.* (2016) 3:30. doi: 10.1186/s40779-016-0099-9

47. Martin L, Horst K, Chiazza F, Oggero S, Collino M, Brandenburg K, et al. The synthetic antimicrobial peptide 19-2.5 attenuates septic cardiomyopathy and prevents down-regulation of SERCA2 in polymicrobial sepsis. *Sci Rep.* (2016) 6:37277. doi: 10.1038/srep37277

48. Wakeley ME, Gray CC, Monaghan SF, Heffernan DS, Ayala A. Check point inhibitors and their role in immunosuppression in sepsis. *Crit Care Clin.* (2020) 36:69–88. doi: 10.1016/j.ccc.2019.08.006

49. Goenka A, Kollmann TR. Development of immunity in early life. *J Infect.* (2015) 71 Suppl 1:S112–120. doi: 10.1016/j.jinf.2015.04.027

frontiers | Frontiers in Immunology

TYPE Original Research
PUBLISHED 13 May 2024
DOI 10.3389/fimmu.2024.1382003

OPEN ACCESS

EDITED BY
Guido Moll,
Charité University Medicine Berlin, Germany

REVIEWED BY
Hjalmar Bouma,
University Medical Center Groningen, Netherlands
Kaice LaFavers,
Indiana University Bloomington, United States

*CORRESPONDENCE
Sina M. Coldewey
sina.coldewey@med.uni-jena.de

†These authors have contributed equally to this work

RECEIVED 04 February 2024
ACCEPTED 09 April 2024
PUBLISHED 13 May 2024

CITATION
Dennhardt S, Ceanga I-A, Baumbach P, Amiratashani M, Kröller S and Coldewey SM (2024) Cell-free DNA in patients with sepsis: long term trajectory and association with 28-day mortality and sepsis-associated acute kidney injury. *Front. Immunol.* 15:1382003. doi: 10.3389/fimmu.2024.1382003

Cell-free DNA in patients with sepsis: long term trajectory and association with 28-day mortality and sepsis-associated acute kidney injury

Sophie Dennhardt[1,2†], Iuliana-Andreea Ceanga[1,2†], Philipp Baumbach[1,2†], Mona Amiratashani[1,2], Sarah Kröller[1,2] and Sina M. Coldewey[1,2,3*]

[1]Department of Anesthesiology and Intensive Care Medicine, Jena University Hospital, Friedrich Schiller University Jena, Jena, Germany, [2]Septomics Research Centre, Jena University Hospital, Friedrich Schiller University Jena, Jena, Germany, [3]Center for Sepsis Control and Care, Jena University Hospital, Jena, Germany

Introduction: Outcome-prediction in patients with sepsis is challenging and currently relies on the serial measurement of many parameters. Standard diagnostic tools, such as serum creatinine (SCr), lack sensitivity and specificity for acute kidney injury (AKI). Circulating cell-free DNA (cfDNA), which can be obtained from liquid biopsies, can potentially contribute to the quantification of tissue damage and the prediction of sepsis mortality and sepsis-associated AKI (SA-AKI).

Methods: We investigated the clinical significance of cfDNA levels as a predictor of 28-day mortality, the occurrence of SA-AKI and the initiation of renal replacement therapy (RRT) in patients with sepsis. Furthermore, we investigated the long-term course of cfDNA levels in sepsis survivors at 6 and 12 months after sepsis onset. Specifically, we measured mitochondrial DNA (mitochondrially encoded NADH-ubiquinone oxidoreductase chain 1, *mt-ND1*, and mitochondrially encoded cytochrome C oxidase subunit III, *mt-CO3*) and nuclear DNA (nuclear ribosomal protein S18, *n-Rps18*) in 81 healthy controls and all available samples of 150 intensive care unit patients with sepsis obtained at 3 ± 1 days, 7 ± 1 days, 6 ± 2 months and 12 ± 2 months after sepsis onset.

Results: Our analysis revealed that, at day 3, patients with sepsis had elevated levels of cfDNA (*mt-ND1*, and *n-Rps18*, all $p<0.001$) which decreased after the acute phase of sepsis. 28-day non-survivors of sepsis (16%) had higher levels of cfDNA (all $p<0.05$) compared with 28-day survivors (84%). Patients with SA-AKI had higher levels of cfDNA compared to patients without AKI (all $p<0.05$). Cell-free DNA was also significantly increased in patients requiring RRT (all $p<0.05$). All parameters improved the AUC for SCr in predicting RRT (AUC=0.88) as well as APACHE II in predicting mortality (AUC=0.86).

Conclusion: In summary, cfDNA could potentially improve risk prediction models for mortality, SA-AKI and RRT in patients with sepsis. The predictive value of cfDNA, even with a single measurement at the onset of sepsis, could offer a significant advantage over conventional diagnostic methods that require

repeated measurements or a baseline value for risk assessment. Considering that our data show that cfDNA levels decrease after the first insult, future studies could investigate cfDNA as a "memoryless" marker and thus bring further innovation to the complex field of SA-AKI diagnostics.

KEYWORDS

acute kidney injury, cell-free DNA, intensive care unit, mitochondrial DNA, mortality, nuclear DNA, renal replacement therapy, sepsis

1 Introduction

Patients with sepsis have a high mortality risk. By definition, they develop infection-related organ dysfunction, with sepsis-related acute kidney injury (SA-AKI) occurring particularly frequently. With an overall mortality estimated at around 27% which increases to 42% for patients with sepsis admitted to the intensive care unit (ICU) (1), sepsis remains a diagnostic and therapeutic challenge across the medical field. The care of sepsis patients is complex and requires intensive clinical and laboratory monitoring for early diagnosis of complications and organ damage. In clinical practice, this often translates into high frequency blood sample tests acquisition, as well as intensive monitoring of clinical parameters and calculation of clinical risk scores (such as APACHE II). These procedures, while currently the standard of care for patients with sepsis, have several drawbacks such as increased costs, time-consuming management, and proneness to errors (e. g. in automated APACHE II protocols). Furthermore, diagnosing sepsis-associated organ damage may be delayed due to a lack of baseline values for specific patients, as it may be, for example, the case in patients who develop SA-AKI. The presence of AKI has a severe impact on patient outcome and is associated with prolonged hospitalization and ICU stay, disability, poor quality of life and higher mortality (2, 3). Both conditions – sepsis and AKI – are mutually reinforcing and worsen each other's prognosis (2, 4, 5). Despite its impact on patient outcomes, predicting the development of SA-AKI remains elusive, especially at onset and early stages. The diagnostic challenge arises from the lack of injury markers that directly relate to the degree of kidney damage, which can currently only be determined by tissue biopsy (6). The diagnostic markers serum creatinine (SCr) and urine output have both low sensitivity and specificity for AKI (7, 8), especially in the presence of sepsis. Therefore, the development and refinement of clinical methods to quantify organ dysfunction and disease severity in patients with sepsis is necessary and remains the subject of current research.

Liquid biopsies can be employed to quantify endogenous cell-free DNA (cfDNA), which is either released from dying cells during necrosis, apoptosis or actively secreted during netosis, as a special form of pathogen-induced cell death, which releases neutrophil extracellular traps (NETs) (9). While resembling an anti-viral host response strategy, NETs also contribute to a thrombo-inflammatory state (10). Via TLR9-receptor signaling, cfDNA can act as danger-associated molecular patterns (DAMPs) further exacerbating the inflammatory response (11). These innate immune response mechanisms are described as being triggers for AKI (12), but it remains debatable whether cfDNA is merely a marker of tissue-injury during sepsis and SA-AKI or has its own role in the pathophysiology of the condition (13). Cell-free DNA can be detected in different samples, such as blood, urine, saliva, as well as other body fluids (14–16). Cell-free DNA shows good potential for predicting outcomes and correlates, among others, with prognosis in patients with inflammation (17), myocardial infarction (18, 19), and stroke (20, 21). More recently, liquid biopsies have been correlated with the degree of tissue damage, hence being proposed as markers of inflammation, kidney dysfunction, morbidity and mortality in patients with sepsis. While some studies suggest that both nuclear DNA (nDNA) and mitochondrial DNA (mtDNA) have limited roles in sepsis (22), others reported that mtDNA might serve as a predictor for 28-day mortality in patients with sepsis originating from mixed infection sites (22–24). Cell-free DNA may also have the potential to predict kidney damage in SA-AKI, complications of SA-AKI, or mortality in patients with sepsis. However, its clinical role in patients with sepsis is currently unclear due to conflicting reports. The aims of our study were to investigate both the potential of cfDNA as a prognostic marker for 28-day mortality in patients with sepsis and its significance in predicting the need for renal replacement therapy (RRT) in patients with AKI as well as to present the dynamic of cfDNA from the acute phase of sepsis up to 12 months after sepsis onset.

2 Material and methods

2.1 Study design and study population

In the present study, cfDNA was analyzed in blood samples from patients with sepsis and healthy controls who participated in the prospective longitudinal ICROS study ("Identification of cardiovascular and molecular prognostic factors for the medium-

term and long-term outcomes of sepsis") (25). For a detailed description of this study, we refer to the published protocol (25). Briefly, patients with surgical and non-surgical sepsis admitted to the ICU of Jena University Hospital were enrolled between 24/05/2018 and 24/03/2021. Sepsis was diagnosed according to the Sepsis-3 criteria (26). Main exclusion criteria included significant heart, end-stage renal or hepatic disease, pregnancy or breastfeeding as well as therapeutic limitation or a do-not-resuscitate order. We excluded patients with COVID-19-associated sepsis from the analysis as they were not part of the original study protocol and COVID-19 patients were not within the scope of this analysis.

In the acute phase of sepsis, study visits took place 3 ± 1 days (T1) and 7 ± 1 days (T2) after sepsis onset. In addition, study visits took place in the early recovery phase (T3, ICU-discharge, ± 3 days) and late recovery phase 6 ± 2 months (T4) and12 ± 2 months (T5) after sepsis onset.

In addition, 81 healthy volunteers were recruited between 09/05/2018 and 16/06/2022. The study was conducted in accordance with the Declaration of Helsinki and approved by the Ethics Committee of the Friedrich-Schiller-University Jena (ClinicalTrials registration: NCT03620409). Every participant, legal representative or proxy gave their signed written informed consent or, if none of the situations applied, an independent medical doctor was consulted for preliminary consent (25).

2.2 Clinical data collection

Clinical data was gathered from the electronic patient data management system COPRA 6©, at the screening visit and the in-hospital visits (T1, T2). We also recorded data regarding the patients' kidney function before and after admission to the ICU, the need for RRT during the first 28 days of ICU stay, 28-day mortality, as well as the Acute Physiology and Chronic Health Evaluation (APACHE) II score at T1. APACHE II was chosen because it is usually measured at ICU admission and does not need sequential measurement to predict negative outcomes. It is a complex assessment tool including 12 physiological parameters and the patient's medical history and age.

2.3 Diagnosis of AKI and sepsis-associated AKI

AKI was diagnosed according to the current KDIGO criteria (27) based on one of the following: increase in SCr ≥ 0.3 mg/dL within 48 hours, or an increase in SCr ≥ 1.5 times from baseline (that is known or presumed to have occurred within the past 7 days), or urine volume < 0.5mL/kg/h for 6 hours. In order to diagnose AKI, baseline SCr was needed, a laboratory value which was not available for all patients. After careful consideration of the literature (28–31) and analyzing the particularities of our cohort, we decided to infer the missing information regarding baseline SCr by reviewing the patients' electronic data over the last 365 days before ICU admission. In cases where patients had no history of kidney disease and a retrospective determination of the SCr was not possible (n=23 patients) the mean value of the laboratory reference interval for SCr was used as the baseline values. Since normal SCr levels vary by age and sex, reference ranges are adjusted (32) by the test manufacturer (Roche diagnostics) to take into account these two variables. Additionally, we have gathered daily information regarding the urinary output during the ICU stay up to 28 days. This allowed us to check the validity of our diagnosis and to potentially detect cases where an AKI diagnosis would be unlikely based on the SCr alone (e. g. patients with low nutritional scores, low muscle mass, malnourished patients). SA-AKI was defined based on the recommendation of the 28th Acute Disease Quality Initiative workgroup, as AKI diagnosed in the presence of sepsis (2).

2.4 Blood sampling

Blood samples used for the present study were obtained on T1, T2, T4, and T5. At each time point, plasma was snap-frozen in liquid nitrogen and stored at −80°C for later DNA isolation and quantification. Cell-free DNA was not measured at ICU-discharge (T3) due to the high variability of this time point (ICU discharge ranging between 1 day and 108 days).

2.5 Isolation and quantification of cfDNA

Plasma obtained from EDTA-anticoagulated whole blood was centrifuged again at 3 000 g and 4°C to obtain platelet-poor plasma. To isolate cell- and microvesicle-free DNA only, the platelet-poor plasma was then filtered through a 0.2 µm PVDF membrane filter tube (Whatman). 200 µl of the filtered plasma were used for DNA isolation with the QiaAmp DNA kit (Qiagen). According to the producer's manual, carrier DNA (poly dA:dT, Invivogen) was added to the isolation buffer to increase the isolation yield. Isolated DNA was quantified spectrophotometrically and diluted to 0.325 ng/µl for direct use in qPCR. Mitochondrial DNA quantification was performed by quantitative real-time PCR on a CFX96™ Touch Real-Time PCR Detection System (Bio-Rad Laboratories, Inc.) using SsoAdvanced™ Universal SYBR® Green Supermix (Bio-Rad) and PrimePCR™ assays *mt-ND1* (NADH-ubiquinone oxidoreductase chain 1, qHsaCED0021828) and *mt-CO3* (cytochrome C oxidase subunit III, qHsaCED0048405; Bio-Rad Laboratories, Inc.). Nuclear DNA quantification was performed by quantitative real-time PCR on a CFX96™ Touch Real-Time PCR Detection System (Bio-Rad Laboratories, Inc.) using SsoAdvanced™ Universal Probes Supermix (Bio-Rad) and PrimePCR™ probe assay *n-Rps18* (ribosomal protein S18, qHsaCEP0040177; Bio-Rad Laboratories, Inc.). Copy numbers of *mt-ND1*, *mt-CO3* and *n-Rps18* were extrapolated from standard curves of serially diluted template DNA (2 million copies/µl stock concentration).

2.6 Primary and secondary aims and outcome measures

The primary aim was the evaluation of the prognostic relevance of cfDNA (values of *mt-ND1*, *mt-CO3*, *n-Rps18* at T1) for 28-day

10.3389/fimmu.2024.1382003

mortality. Secondary aims comprised the evaluation of the prognostic relevance of cfDNA (values of *mt-ND1*, *mt-CO3*, *n-Rps18* at T1) for RRT up to day 28 after sepsis onset. Further aims comprised the characterization of cfDNA in the acute phase of sepsis (T1, T2) and long-term recovery after sepsis (T4, T5). This included the group comparisons between patients with sepsis and healthy controls.

2.7 Statistical analysis

2.7.1 Descriptive analysis

We report median and interquartile range (IQR; first to third quartile; Q_1–Q_3) for continuous variables. For categorical variables, we report absolute and relative frequencies (%). Due to the high range in variables of cfDNA, we performed log10-transformation. To account for zero values, 1 was added to each value.

2.7.2 Statistical tests

For unpaired comparisons of metric variables, we applied Mann-Whitney *U* tests (two groups) or Kruskal-Wallis-test with Dunn's *post hoc* tests (more than two groups). For paired metric data (long-term courses), Friedman tests with Dunn's *post hoc* tests were applied. For unpaired categorical variables, we applied Fisher's exact tests.

2.7.3 Binary logistic regression models

Twenty-eight-day mortality. We tested 2 series of logistic regression models with 28-day mortality as dependent variable. In the first series, we evaluated the prognostic value of SCr and cfDNA variables. The models were built with three different biomarker combinations as independent variables: model A contained only SCr, model B contained *mt-ND1*, *mt-CO3* and *n-Rps18* and model C contained SCr, *mt-ND1*, *mt-CO3* and *n-Rps18*. In the second series, we followed the same approach, but instead of SCr, we modeled APACHE-II scores at T1 as an established score for mortality prediction.

RRT (up to day 28). For RRT as dependent variable, three different biomarker combinations as covariates were tested: model A contained only SCr, model B contained *mt-ND1*, *mt-CO3* and *n-Rps18* and model C contained SCr *mt-ND1*, *mt-CO3* and *n-Rps18*.

For all models, we report the odds ratio (OR) including 95% confidence interval (95% CI) and the p value. With a variance inflation factor (VIF) of less than 10, we have assumed an acceptable level of multicollinearity (Supplementary Table 1). Model based predicted probabilities were calculated for each patient and model and then analyzed using in receiver operating characteristic (ROC) curve analysis. We report values of sensitivity and specificity for the optimal cut-off based on Youden's index. Finally, we tested the superiority of all models B and C compared to all models A using DeLong's tests (one sided testing).

Data were analyzed with the CFX Manager™ 3.1 software (Bio-Rad Laboratories, Inc.), GraphPad Prism 7.05 for Windows (GraphPad Software, Inc., San Diego, CA, USA), IBM SPSS Statistics for Windows, Version 27.0 (Armonk, NY: IBM Corp) and R (Version 4.1.0) under R Studio (Version 1.4.1717). We considered p values <0.05 as statistically significant.

3 Results

The patient inclusion and number of patients with blood samples are summarized in Figure 1.

3.1 Demographic and clinical characteristics

Of the 150 patients with sepsis included in this analysis, 56 (37.3%) patients were female. The median age was 66 years (IQR: 56–75). We found no significant differences in age and sex between patients and healthy controls (median [IQR], age: 65 [53–73], p=0.404; sex: n=30/81, 37% females). Patients had a significantly

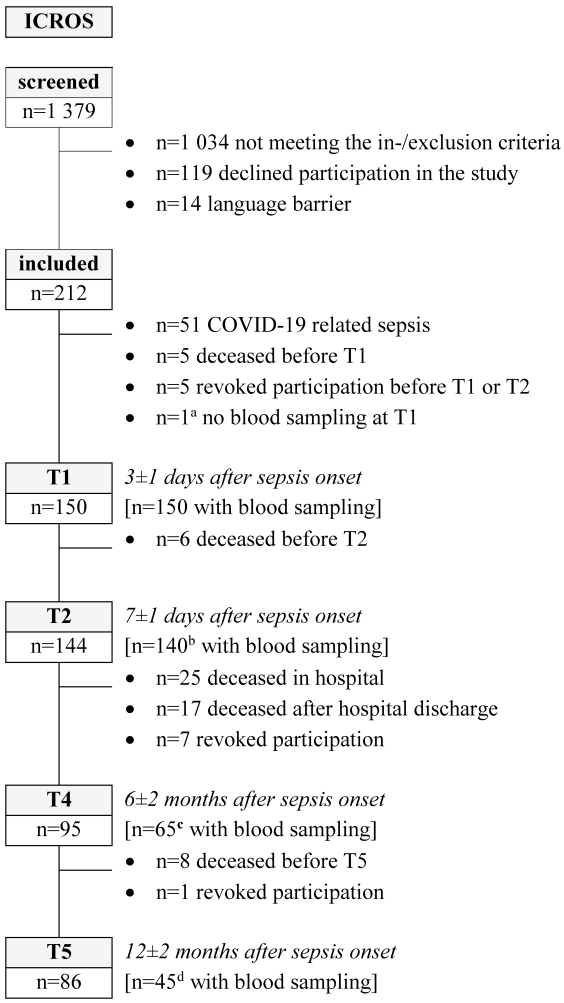

FIGURE 1
Patient flow chart. The study visit T3 (discharge from intensive care unit, ± 3 days) was not part of this analysis [[a] excluded from analyses because not available for the primary endpoint; [b] refusal (n=2), no blood sampling (n=1) or already discharged from hospital (n=1); [c] refusal (n=6) or phone interview (n=24); [d] refusal (n=9), phone interview (n=26) or not sufficient plasma available to measure cell-free DNA (n=6)]. Further, 81 healthy controls were included in the ICROS-study and current analysis (ICROS, Identification of cardiovascular and molecular prognostic factors for the medium-term and long-term outcomes of sepsis).

10.3389/fimmu.2024.1382003

higher body mass index (BMI, 27.8 [23.7–32.4], p<0.001) and Charlson comorbidity index (CCI, 2 [1–4], p<0.001) compared to healthy controls (BMI: 25.3 [23.0–27.2], CCI: 0 [0–0]). Further clinical characteristics of the patients are shown in Table 1.

Forty-one percent of patients had preexisting chronic kidney disease (CKD), 54.7% were diagnosed with SA-AKI (either on admission or during the ICU stay) and 28.7% with AKI on CKD. Renal replacement therapy was needed in 29.3% of the patients. Twenty-four patients (16.0%) died within 28 days.

3.2 Levels of circulating mtDNA and nDNA are elevated in patients with sepsis

We first tested the hypothesis that cfDNA is increased in the acute phase of sepsis (T1), reflecting tissue injury. For this, we assessed the copy numbers of *mt-ND1, mt-CO3* and *n-Rps18* as surrogate parameters for cfDNA in plasma.

At T1, copy numbers of *mt-ND1* (median [IQR]; sepsis 963 [444–2 890] *vs* controls 678 [242–1 313], p=0.0006) and *n-Rps18* (sepsis 1 477 [528–4 721] *vs* controls 48 [0–220], p < 0.0001), but not *mt-CO3* (sepsis 447 [167–1 450] *vs* controls 324 [170–739], p=0.1145), were elevated in patients with acute sepsis compared to controls (Figures 2A–C).

3.3 Levels of circulating mtDNA and nDNA decrease after the acute phase of sepsis

We hypothesized that cfDNA is increased only in the acute phase of sepsis, and normalizes in the long course, as organ damage subsides. To test this hypothesis, we studied the longitudinal course of cfDNA over T2, T4 and T5.

First, we compared the long-term course in all patients with available data (varying patient numbers per study visit; Figure 1) to healthy controls. While copy numbers of *mt-ND1* and *n-Rps18* were significantly elevated at T1 and T2 compared to healthy controls, the copy numbers at T4 and T5 returned to control level (Figures 3A, C, Supplementary Table 2). In contrast, copy numbers of *mt-CO3* were comparable to control levels at T1 and T2 and significantly decreased at T4 and T5 compared to healthy controls (Figure 3B, Supplementary Table 2).

Second, we analyzed only survivors with the complete long-term course up to 12 months after sepsis onset (n=41 patients with blood sampling for all study visits). We observed no differences between T1 and T2 (Figures 3D–F, Supplementary Table 2). However, all three variables were significantly lower at T4 compared with T1 and T2 (Figures 3D–F, Supplementary Table 2). The copy number of *n-Rps18* was also significantly lower at T5 compared with T1 and T2 (Figure 3F, Supplementary Table 2). In conclusion, with the exception of *mt-CO3*, cfDNA is increased in the early stages of sepsis but decreases in the long-term after recovery from sepsis.

TABLE 1 Patient characteristics.

Variable	Patients with sepsis (n=150)
Age (years)	66 (56–76)
Sex (female)	56 (37.3%)
Body Mass Index (kg/m²)	27.8 (23.7–32.4)
Charlson Comorbidity Index (points)	2 (1–4)
APACHE II at ICU admission (points)	23 (17–28)
SOFA at sepsis onset (points)	9 (7–11)
Sepsis focus	
Respiratory	72 (48%)
Wound/bone/soft tissue	19 (12.7%)
Intra-Abdominal	55 (36.7%)
Urogenital	19 (12.7%)
Primary bacteraemia	6 (4%)
Other	17 (11.4%)
Multiple foci	35 (23.3%)
Type of referral	
Surgical: emergency	55 (36.7%)
Surgical: elective	46 (30.7%)
Non-surgical emergency	49 (32.7%)
CKD stage	
None	89 (59.3%)
1	1 (0.7%)
2	28 (18.7%)
3	25 (16.6%)
4	6 (4%)
5	1 (0.7%)
AKI stage	
None	68 (45.3%)
1	12 (8%)
2	15 (10%)
3	55 (36.7%)
AKI on CKD (yes)	43 (28.7%)
RRT (yes)	44 (29.3%)
Discharge within 28 days (yes)	108 (72.0%)
28-day mortality (non-survivors)	24 (16.0%)
Length of stay: ICU (days)	10 (4–23)
Length of stay: hospital (days)	30 (20–47)

AKI, acute kidney injury: defined according to the KDIGO criteria: either an increase in serum creatinine (SCr) ≥ 0.3 mg/dL within 48 hours, or an increase in SCr ≥ 1.5 times from baseline, or urine volume < 0.5mL/kg/h for 6 hours; APACHE II, Acute Physiology and Chronic Health Evaluation II; CKD, chronic kidney disease; ICU, intensive care unit; RRT, renal replacement therapy; SOFA, Sequential Organ Failure Assessment.
Data are presented as median (interquartile range) or count (percentage).

10.3389/fimmu.2024.1382003

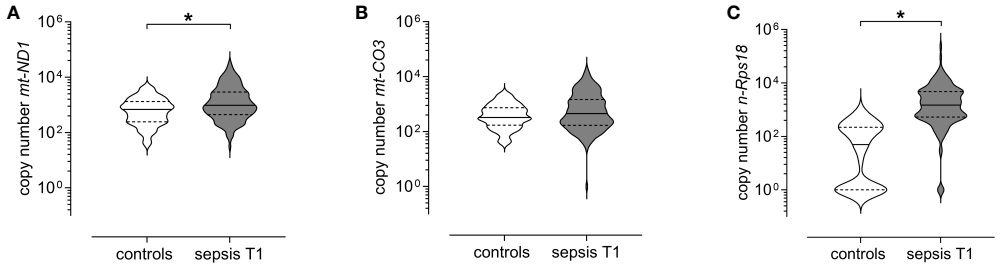

FIGURE 2
Levels of circulating mitochondrial DNA and nuclear DNA at T1 (3 ± 1 days after sepsis onset) are elevated in patients with sepsis. Copy numbers of **(A)** mitochondrially encoded NADH-ubiquinone oxidoreductase chain 1 (*mt-ND1*), **(B)** mitochondrially encoded cytochrome C oxidase subunit III (*mt-CO3*) and **(C)** nuclear ribosomal protein S18 (*n-Rps18*) were determined by quantitative real-time PCR in plasma from healthy controls (n=81) and patients with sepsis (n=150) at T1. The y-axis is log10-transformed. The data is displayed as violin plots (solid lines: median, dashed lines: first and third quartiles; *p < 0.05 Mann-Whitney *U* test).

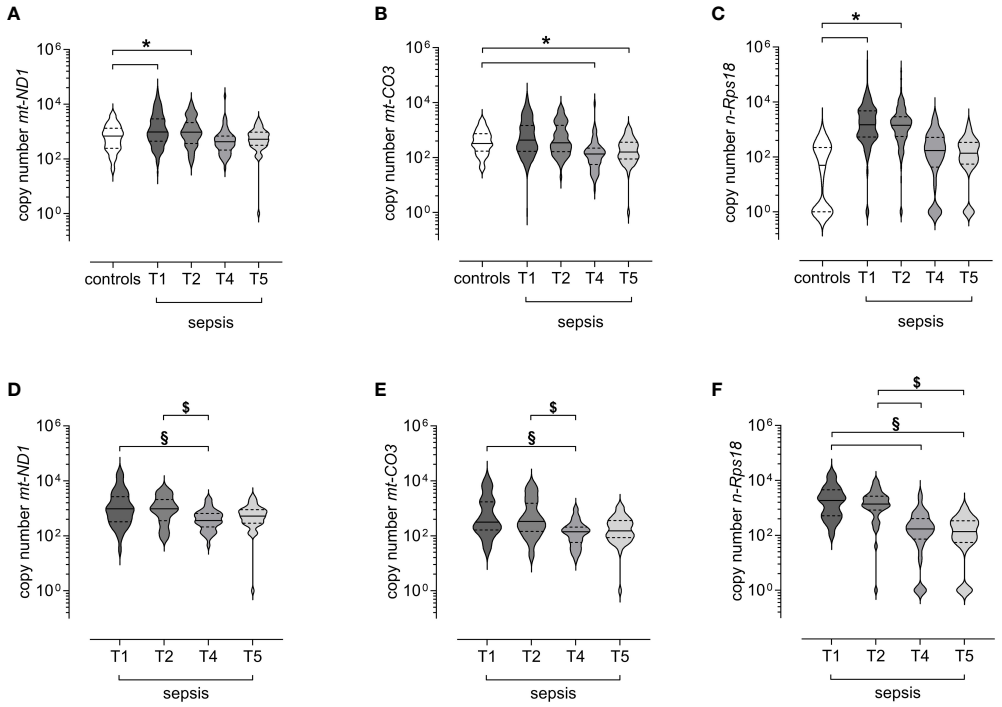

FIGURE 3
Levels of circulating mitochondrial DNA and nuclear DNA decrease after the acute phase of sepsis. Copy numbers of **(A)** mitochondrially encoded NADH-ubiquinone oxidoreductase chain 1 (*mt-ND1*), **(B)** mitochondrially encoded cytochrome C oxidase subunit III (*mt-CO3*), and **(C)** nuclear ribosomal protein S18 (*n-Rps18*) were determined by quantitative real-time PCR in plasma from healthy controls (n=81) and all available samples of patients with sepsis obtained at 3 ± 1 days (T1, n=150), 7 ± 1 days (T2, n=140), 6 ± 2 months (T4, n=65) and 12 ± 2 months (T5, n=45) after sepsis onset. Copy numbers of **(D)** *mt-ND1*, **(E)** *mt-CO3*, and **(F)** *n-Rps18* from survivors of sepsis with the complete long-term course up to 12 months after sepsis onset (n=41 patients with blood sampling for all study visits). The y-axis is log10-transformed. The data is displayed as violin plots (solid lines: median, dashed lines: first and third quartiles; *p < 0.05 versus controls in Dunn's *post hoc* test for the Kruskal-Wallis-tests; §p < 0.05 *vs* T1, $p < 0.05 *vs* T2 in Dunn's *post hoc* test for the Friedman tests).

3.4 Levels of circulating mtDNA and nDNA predict 28-day mortality in sepsis

We hypothesize that circulating cfDNA levels reflect the degree of tissue damage and sepsis severity and may therefore be higher in non-survivors than in survivors of sepsis.

When stratified for 28-day mortality, we observed significantly higher copy numbers of *mt-ND1* (median [IQR]; non-survivors 2 342 [931–5 937] *vs* survivors 837 [361–2 506], p=0.002, Figure 4A), *mt-CO3* (non-survivors 959 [335–2 470] *vs* survivors 373 [156–1 336], p=0.028, Figure 4B) and *n-Rps18* (non-survivors 4 123 [919–12 437] *vs* survivors 1 294 [500–4 433], p=0.006, Figure 4C) in 28-day non-survivors (16%, n=24/150) compared with 28-day survivors. AKI is a known risk factor for mortality in patients with sepsis. In our study, 13 out of 44 patients requiring RRT died within 28 days. Of the 24 non-survivors, 21 either presented with or developed AKI during their ICU stay. Therefore, we performed binary logistic regression and ROC curve analysis to assess the

predictive potential of SCr and the three cfDNA parameters for 28-day mortality.

Serum creatinine alone was a poor predictor of 28-day mortality (AUC=0.67, Figure 5A and Table 2). However, the three cfDNA parameters non-significantly improved the prediction (AUC=0.72, Figure 5A and Table 2, DeLong Test: one-sided test of superiority p=0.245), while the combination of all four parameters yielded the highest predictive value for 28-day mortality (AUC=0.78, Figure 5A and Table 2, DeLong Test *vs* SCr alone: one-sided test of superiority p<0.01).

Next, we analyzed the predictive value of cfDNA when compared to APACHE II, an established and routinely used clinical score. Analogous to our one-point analysis of cfDNA at T1, APACHE II does not need sequential measurements during ICU stay, but can reflect severity of disease and predict mortality in critically ill patients (33, 34). In our cohort, APACHE II scores at T1 were not available for 22 patients due to multiple missing values. We therefore excluded these patients from the analysis. Interestingly, APACHE II scores only correlated poorly with cfDNA (Spearman's ρ=0.251, p=0.004 for *mt-ND1*, ρ=0.268, p=0.002 for *mt-CO3* and ρ=0.272, p=0.002 for *n-Rps18*) at T1. As expected, we found that APACHE II predicts 28-day mortality (AUC=0.84, Figure 5B and Table 2). The model with cfDNA performed poorer (AUC=0.74, DeLong Test: one-sided test of superiority p=0.948). Nonetheless, the combined model performed best (AUC=0.88, Figure 5B and Table 2, DeLong Test *vs* APACHE II alone: one-sided test of superiority p=0.026). In the combined model, *mt-ND1* and *mt-CO3* significantly contributed to the prediction of 28-day mortality (Table 2).

3.5 Levels of circulating mtDNA and nDNA are elevated in patients with sepsis-associated AKI

We next evaluated whether cfDNA can be used as a marker for SA-AKI. Even though attention has been lately shifted to the role of mtDNA in AKI, studies analyzing the relationship between AKI and nDNA are scarce.

In our cohort, SA-AKI was diagnosed in 54.7% of patients. At T1, patients with SA-AKI showed significantly elevated levels of *mt-ND1* (median [IQR]; with SA-AKI 1393 [483–4 004] *vs* without SA-AKI 637 [313–1 523], p<0.001), *mt-CO3* (with SA-AKI 686 [255–2 507] *vs* without SA-AKI 249 [133–1 158], p<0.001) and *n-Rps18* (with SA-AKI 2 235 [602–5 773] *vs* without SA-AKI 890 [449–3 222], p=0.006) (Figures 6A–C).

3.6 Levels of circulating mtDNA and nDNA are elevated in patients with sepsis requiring RRT

Having found that cfDNA is increased in SA-AKI, we next investigated whether levels of cfDNA scale with the severity of SA-AKI. As a clinically relevant stage, we chose the need of RRT (equivalent to AKI stage 3) up to day 28 as a comparator.

Forty-four of the patients with sepsis required RRT during their ICU stay. We observed elevated levels of *mt-ND1* (median [IQR]; with RRT 2 273 [973–6 661] *vs* without RRT 775 [328–2 125], p<0.001), *mt-CO3* (with RRT 1 211 [376–4 064] *vs* without RRT 267 [128–977], p<0.001), and *n-Rps18* (with RRT 3 939 [1 003–9 494] *vs* without RRT 1 028 [489–3 474], p<0.001) in patients with RRT compared to patients without RRT (Figures 7A–C).

All patients requiring RRT suffered from AKI, however, not all patients with AKI required RRT. Therefore, we analyzed patients with sepsis and AKI with and without RRT. When looking only at patients with SA-AKI, those receiving RRT also had higher levels of cfDNA compared to patients with SA-AKI without RRT, as follows (Figures 7D–F): *mt-ND1* (median [IQR]; with RRT 2 273 [973–6 661] *vs* without RRT 882 [415–2 280], p=0.003), *mt-CO3* (with RRT 1 211 [376–4 064] *vs* without RRT 401 [101–845], p<0.001), *n-Rps18* (with RRT 3 939 [1 003–9 494] *vs* without RRT 1 672 [533–4 646], p=0.036).

3.7 Levels of circulating *mt-CO3* improve the predictive value of serum creatinine for RRT

The increase of cfDNA in sepsis may not specifically reflect SA-AKI, but rather other confounders, such as the severity of sepsis. To better quantify this relationship, we performed binary logistic regression and ROC curve analysis to compare the potential of mt- and nDNA as a biomarker for RRT and compared these to the currently universally used SCr.

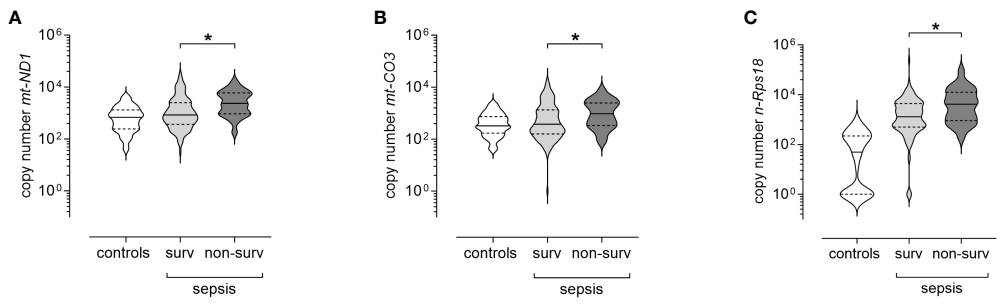

FIGURE 4
Levels of circulating mitochondrial DNA and nuclear DNA at T1 (3 ± 1 days after sepsis onset) are elevated in 28-day non-survivors of sepsis. Copy numbers of **(A)** mitochondrially encoded NADH-ubiquinone oxidoreductase chain 1 (*mt-ND1*), **(B)** mitochondrially encoded cytochrome C oxidase subunit III (*mt-CO3*) and **(C)** nuclear ribosomal protein S18 (*n-Rps18*) were determined by quantitative real-time PCR in plasma at T1 in 28-day survivors (surv, n=126) and non-survivors (non-surv, n=24). Healthy controls are shown for reference purposes (n=81). The y-axis is log10-transformed. The data is displayed as violin plots (solid lines: median, dashed lines: first and third quartiles; *p < 0.05, Mann-Whitney *U* test).

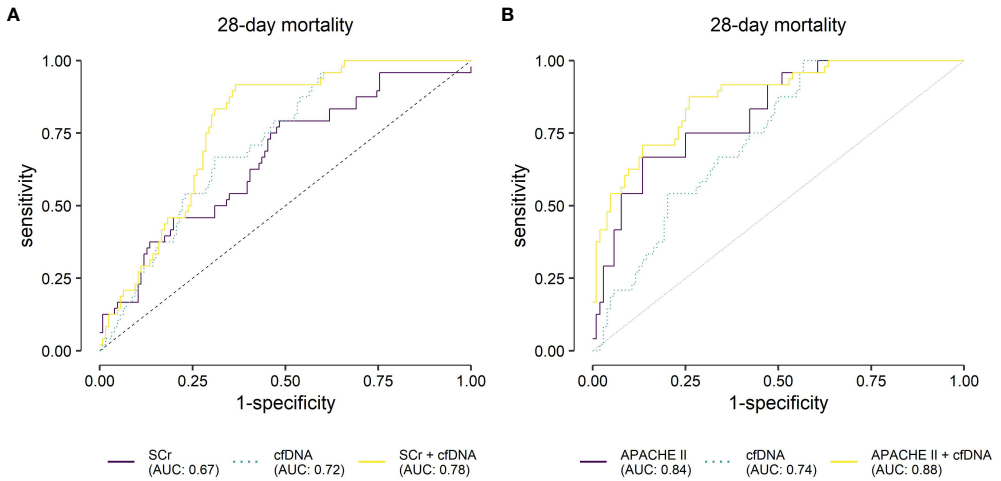

FIGURE 5
Receiver operating characteristic analysis for the predicted probabilities of the binary logistic regression models for 28-day mortality. **(A)** Evaluation of serum creatinine (SCr), mitochondrially encoded NADH-ubiquinone oxidoreductase chain 1 (*mt-ND1*), mitochondrially encoded cytochrome C oxidase subunit III (*mt-CO3*) and nuclear ribosomal protein S18 (*n-Rps18*) at T1 (3 ± 1 days after sepsis onset) and their combination as predictive biomarkers for 28-day mortality in patients with sepsis (n=24/150 non-survivors). Cell-free (cfDNA) comprises nuclear and mitochondrial DNA. **(B)** Evaluation of APACHE II, *mt-ND1*, *mt-CO3*, *n-Rps18* at T1 and their combination as predictive biomarkers for 28-day mortality in patients with sepsis (n=24/128 non-survivors) in patients with available Acute Physiology and Chronic Health Evaluation II scores (APACHE II). AUC, area under the curve.

The combination of *mt-ND1*, *mt-CO3* and *n-Rps18* yielded a lower diagnostic performance (AUC=0.77, DeLong Test *vs* SCr alone: one-sided test of superiority p=0.845) than SCr (AUC=0.83, Figure 8 and Table 3). However, combining SCr with the three cfDNA variables resulted in a significantly improved diagnostic performance (AUC=0.88, Table 3, DeLong Test *vs* SCr alone: one-sided test of superiority p=0.047). The composite model C including SCr and the DNA parameters shows slight improvements in specificity (Table 3). Interestingly, next to SCr, only *mt-CO3* contributed significantly to the prediction of RRT (Table 3).

4 Discussion

In this study, the applicability of liquid biopsies in the form of circulating cfDNA was investigated in a mixed population of 150 surgical and non-surgical patients with sepsis. We measured two genes of mitochondrial cfDNA, *mt-ND1* (within the mitochondrial complex I) and *mt-CO3* (within the mitochondrial complex IV), as well as a nuclear gene of cfDNA, *n-Rps18*. Mitochondrial DNA has been previously investigated in patients with kidney damage (35–37), while nuclear cfDNA has been studied for possible associations with tissue and organ damage in sepsis and septic shock (22, 38). Our analysis investigated the trajectory of cfDNA, as well as the predictive and prognostic value of cfDNA for 28-day mortality in patients with sepsis, its association with AKI and its role in predicting the need for RRT in patients with AKI.

4.1 *mt-ND1* and nDNA are increased in patients with sepsis and return to control values during long-term recovery

Similar to previous data (22, 39, 40), we found that, compared to healthy controls, patients with sepsis have significantly higher levels of cfDNA in the acute phase of sepsis. Nuclear DNA in particular, and to a lesser extent mtDNA, showed significantly increased levels in the acute phase of sepsis (in our study defined as T1, 3 ± 1 days after onset of sepsis and as T2, 7 ± 1 days) as a possible reflection of acute tissue damage. Other studies performed serial measurements of cfDNA and found increased levels of nDNA up to 28 days after the onset of sepsis or septic shock (22). To the authors' knowledge, ours is the first study to look at the long-term dynamics of cfDNA up to 6 and 12 months after sepsis. We found in our cohort that the initially high levels of cfDNA decrease over time. The greatest change was seen with nDNA, raising the question whether nDNA is more relevant in the acute phase of sepsis compared with mtDNA. Hawkins et al. found that nDNA, but not mtDNA, was associated with adverse outcomes, and nDNA at 12 hours (but not at 1, 4, or 7 days) after sepsis onset was a predictor of 28-day mortality (along APACHE II and SOFA scores) (40). Such a narrow time window casts doubt over the reliability and clinical utility of nDNA as a predictor of adverse events in patients with sepsis. Timmermans et al. also found elevated nDNA levels in patients with septic shock that correlated weakly with the inflammatory response and markers of organ damage, but reported no clinical outcomes (22).

10.3389/fimmu.2024.1382003

TABLE 2 Logistic regression and Receiver Operating Characteristic (ROC) analysis for 28-day mortality.

		Logistic regression		ROC analysis			
Model	Variable	OR (95% CI)	p	AUC (95% CI)	Cut-off	sensitivity	specificity
SCr							
A	SCr[a]	1.73 (1.16–2.58)	**0.007**	0.67 (0.55–0.79)	0.12	79.2	52.4
B	*mt-ND1*	5.36 (0.61–47.14)	0.130	0.72 (0.63–0.82)	0.10	95.8	41.3
	mt-CO3	0.42 (0.08–2.22)	0.306				
	n-Rps18	1.77 (0.79–3.97)	0.168				
C	SCr[a]	1.69 (1.09–2.60)	**0.018**	0.78 (0.70–0.86)	0.14	91.7	64.3
	mt-ND1	6.79 (0.74–62.37)	0.091				
	mt-CO3	0.35 (0.06–1.95)	0.231				
	n-Rps18	1.50 (0.68–3.30)	0.313				
APACHE II							
A	APACHE II[a]	4.67 (2.40–9.08)	**<0.001**	0.84 (0.75–0.92)	0.35	66.7	86.5
B	*mt-ND1*	6.47 (0.81–51.80)	0.079	0.74 (0.65–0.83)	0.11	100.0	44.2
	mt-CO3	0.34 (0.07–1.66)	0.181				
	n-Rps18	1.82 (0.82–4.03)	0.143				
C	APACHE II[a]	5.77 (2.60–12.77)	**<0.001**	0.88 (0.80–0.95)	0.16	87.5	75.0
	mt-ND1	26.81 (2.22–323.77)	**0.010**				
	mt-CO3	0.09 (0.01–0.61)	**0.013**				
	n-Rps18	1.26 (0.52–3.03)	0.608				

APACHE II, Acute Physiology and Chronic Health Evaluation II; mt-ND1, mitochondrially encoded NADH-ubiquinone oxidoreductase chain 1; mt-CO3, mitochondrially encoded cytochrome C oxidase subunit III; n-Rps18, nuclear ribosomal protein S18; AUC, area under the curve; OR, odds ratio; 95% CI, 95% confidence interval; [a] values of SCr and APACHE II were z-standardized before modeling (mean=0, standard deviation=1); p, p value of the OR (p<0.05 are printed in bold).
Results are reported for the models with serum creatinine (SCr, n=150; n=24/150 non-survivors) and APACHE II scores at T1 (n=128 patients; n=24/128 non-survivors) as main covariable.

4.2 Cell-free DNA is increased in non-survivors of sepsis and can improve the predictive value of APACHE II for mortality

We found that cfDNA can contribute to the prediction of 28-day mortality, both alone and by increasing the AUC of APACHE II. Our results confirm the already existing body of work that showed that cfDNA has the power to improve risk prediction models (41–43) which could lend it an important role in therapy decisions in the ICU. An important observation is that only one determination of cfDNA (at T1) was sufficient for this improvement, hence such determinations may be economically viable. As discussed above, despite a stronger increase in nDNA during early sepsis, mtDNA had a stronger predictive value both for RRT (*mt-CO3*), as well as for mortality (*mt-ND1* and *mt-CO3*). This

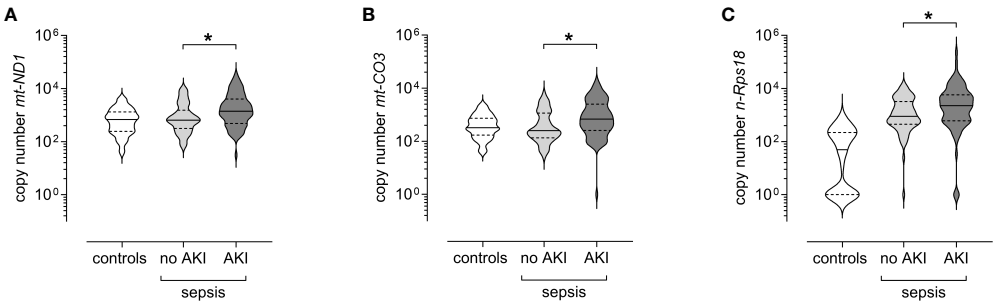

FIGURE 6
Levels of circulating mitochondrial DNA and nuclear DNA at T1 (3 ± 1 days after sepsis onset) are elevated in patients with sepsis-associated AKI. Copy numbers of **(A)** mitochondrially encoded NADH-ubiquinone oxidoreductase chain 1 (*mt-ND1*), **(B)** mitochondrially encoded cytochrome C oxidase subunit III (*mt-CO3*), and **(C)** nuclear ribosomal protein S18 (*n-Rps18*) were determined by quantitative real-time PCR in plasma from patients with sepsis and AKI (AKI, n=82) or without AKI (no AKI, n=68) obtained at T1. Healthy controls are shown for reference purposes (n=81). The y-axis is log10-transformed. The data is displayed as violin plots (solid lines: median, dashed lines: first and third quartiles; *p < 0.05 Mann-Whitney *U* test).

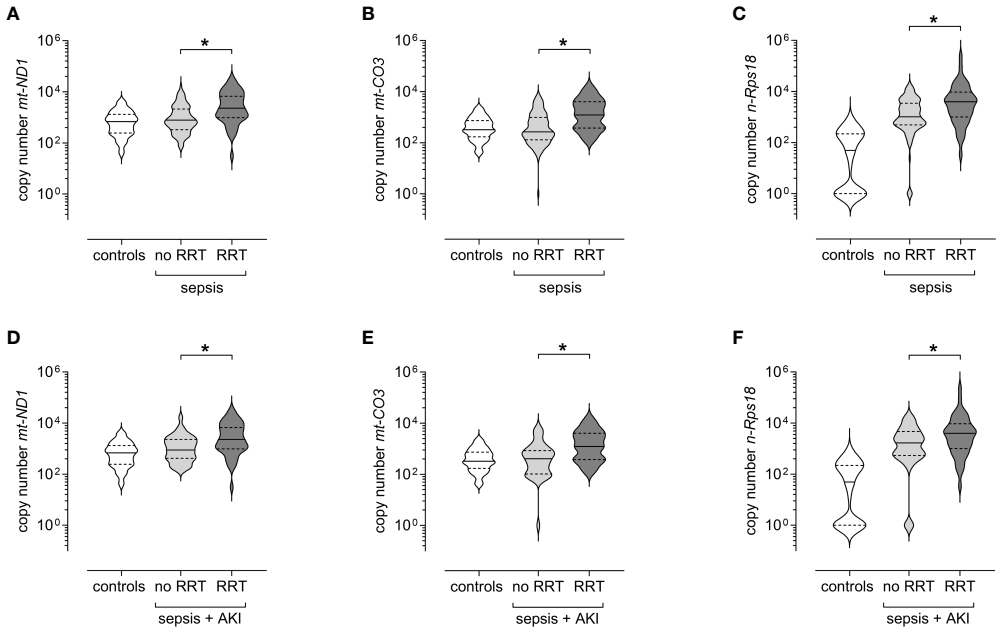

FIGURE 7
Circulating levels of mitochondrial DNA and nuclear DNA at T1 (3 ± 1 days after sepsis onset) are elevated in patients with sepsis requiring renal replacement therapy (RRT) up to day 28. Copy numbers of **(A)** mitochondrially encoded NADH-ubiquinone oxidoreductase chain 1 (*mt-ND1*), **(B)** mitochondrially encoded cytochrome C oxidase subunit III (*mt-CO3*) and **(C)** nuclear ribosomal protein S18 (*n-Rps18*) were determined by quantitative real-time PCR in plasma obtained at T1 from patients with sepsis who required RRT up to day 28 (n=44) and patients with sepsis who did not (n=106). Healthy controls are shown for reference purposes (n=81). Copy numbers of **(D)** *mt-ND1*, **(E)** *mt-CO3* and **(F)** *n-Rps18* were determined by quantitative real-time PCR in plasma obtained at T1 from patients with sepsis and AKI who required RRT up to day 28 (n=44) and patients with sepsis and AKI who did not (n=38). Healthy controls are shown for reference purposes (n=81). The y-axis is log10-transformed. The data is displayed as violin plots (solid lines: median, dashed lines: first and third quartiles; *p < 0.05 Mann-Whitney *U* test).

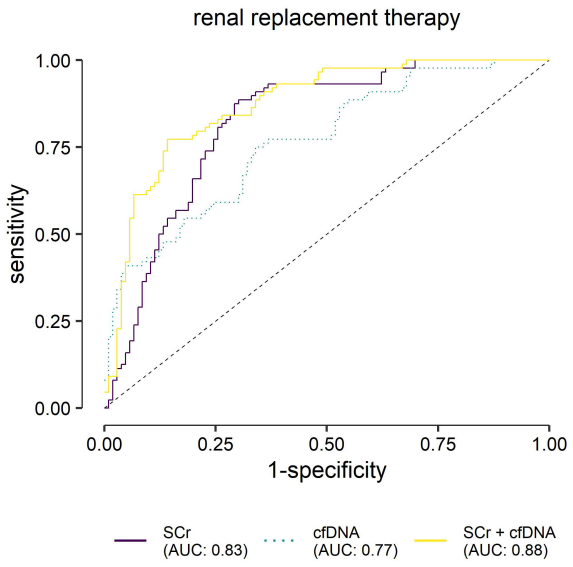

FIGURE 8
Receiver operating characteristic analysis for the predicted probabilities of the binary logistic regression models for renal replacement therapy (RRT). Evaluation of serum creatinine (SCr), mitochondrially encoded NADH-ubiquinone oxidoreductase chain 1 (*mt-ND1*), mitochondrially encoded cytochrome C oxidase subunit III (*mt-CO3*) and nuclear ribosomal protein S18 (*n-Rps18*) at T1 (3 ± 1 days after sepsis onset), and their combination as biomarkers for RRT (n=44/150) in patients with sepsis. Cell-free (cfDNA) comprises nuclear and mitochondrial DNA.

raises the question whether mtDNA may act as both markers and mediators of secondary tissue damage. Indeed, mtDNA has been proposed to mediate inflammatory pathways by acting as a potent damage-associated molecular patterns (DAMPs) (43, 44). Future studies will need to look at the individual trajectories of mitochondrial cfDNA and nuclear cfDNA to examine specific correlations with individual outcomes such as AKI or all-cause sepsis mortality.

4.3 Cell-free DNA is increased in SA-AKI, and can improve the predictive value of serum creatinine for RRT

Diagnosing AKI in the context of sepsis remains a difficult task. The KDIGO definition is based on SCr and urine output (2, 45). However, these parameters reflect kidney function and have limited value in detecting kidney injury (8, 46), which is the paramount characteristic of AKI, as recognized in its name. One of the biggest conundrums concerns the baseline creatinine value, which should be considered when calibrating the acute decrease in kidney function. In many patients such values are missing, which leads to delays in diagnosis. The interest is shifting toward finding biomarkers which could describe renal injury. In the investigated cohort, SA-AKI could be diagnosed in around 55% of patients, an incidence comparable with that presented in other studies (47–49). In our study, cfDNA was not only increased in SA-AKI, but it also scaled with the intensity of renal damage, which was mirrored by the need for RRT. Due to the clinical

TABLE 3 Logistic regression and Receiver Operating Characteristic (ROC) analysis for renal replacement therapy up to day 28 (n=150 patients).

		Logistic regression		ROC analysis			
Model	Variable	OR (95% CI)	p	AUC (95% CI)	Cut-off	sensitivity	specificity
A	SCr	2.97 (1.95–4.52)	**<0.001**	0.83 (0.76–0.89)	0.21	88.6	70.8
B	*mt-ND1*	0.29 (0.06–1.41)	0.125	0.77 (0.69–0.85)	0.27	75.0	67.0
	mt-CO3	9.87 (2.34–41.58)	**0.002**				
	n-Rps18	2.21 (1.04–4.73)	**0.040**				
C	SCr	3.41 (2.08–5.57)	**<0.001**	0.88 (0.82–0.93)	0.39	77.3	86.8
	mt-ND1	0.35 (0.06–2.22)	0.266				
	mt-CO3	13.3 (2.46–71.97)	**0.003**				
	n-Rps18	1.58 (0.75–3.32)	0.226				

SCr, serum creatinine (z-standardized before modeling; mean=0, standard deviation=1); mt-ND1, mitochondrially encoded NADH-ubiquinone oxidoreductase chain 1; mt-CO3, mitochondrially encoded cytochrome C oxidase subunit III; n-Rps18, nuclear ribosomal protein S18; AUC, area under the curve; OR, odds ratio; 95% CI, 95% confidence interval; p, p value of the OR (p<0.05 are printed in bold).

impact of RRT and to the fact that it can directly affect the outcome in patients with sepsis, we focused our attention further on the relationship between cfDNA and the need for RRT. According to KDIGO, the need for RRT translates to a stage 3 AKI. Interestingly, despite the fast turnover of cfDNA, the values determined at T1 (3 days after sepsis onset) still carried prognostic value regarding SA-AKI stage 3 (equivalent to RRT) during the first 28 days of ICU treatment. While some animal studies found a relationship between cfDNA and AKI (37), data from human studies are still heterogeneous and, at times, contradictory. Similar to our data, but in a smaller patient population, Clementi et al. could also correlate levels of cfDNA to development of AKI and the need for RRT in patients with sepsis (50). Intriguingly, other studies could correlate cfDNA levels in urine with AKI, but not plasmatic cfDNA (51). In our study, cfDNA showed a promising predictive capability for RRT (AUC 0.77) and could significantly improve the prediction capacity of SCr for the same event, with *mt-CO3* showing the most substantial contribution. With the addition of mtDNA to the model, AUC reached 0.88. From a clinical standpoint, this finding may be of value since it only requires measurement of *mt-CO3* at one time point and does not require a baseline value before the onset of sepsis, as is the case with creatinine.

5 Limitations and strengths

One of the major strengths of the present study is that we were able to describe the long-term trajectory of cfDNA in sepsis survivors. This study followed patients up to 12 months after the onset of sepsis and provides valuable data on the dynamics of the mitochondrial and nuclear DNA over time.

Our study also has some limitations. An important limitation, given the rapid elimination rate of cfDNA, is the lack of serial measurements during the acute phase of sepsis. Determining the temporal relationship between cfDNA levels and the development of SA-AKI would likely have improved the prognostic value of our markers.

Another limitation, similar to many other studies investigating SA-AKI, resides in the difficulty of diagnosing AKI based on the current KDIGO criteria in patients where SCr over the last 7 days is missing. We conscientiously reviewed the patients' electronic medical records and were thus able to complete any missing information. Even though this method is in line with the current literature (52), we cannot exclude with certainty that we did not under- or overestimated the incidence of AKI or the staging of the injury, a pitfall common with other similar investigations (53).

In future studies, it would be interesting to address whether nDNA and mtDNA levels differ depending on the clinical phenotype of SA-AKI. This should take into account the variety of pathophysiological mechanisms that seem to play a role in triggering damage in SA-AKI. In addition, it would be interesting to gain insights into the relationship between circulating cfDNA and urinary DNA in order to investigate which markers and measurements provide more reliable data. In addition, it would be interesting to gain insights into the relationship between circulating cfDNA and urinary DNA to investigate which markers and measurements provide more reliable data, as recent studies have shown that urinary mtDNA levels predict the severity of AKI (54) and sepsis-associated AKI (55).

The lack of diversity as well as the relatively modest size of our patient cohort must also be addressed, as this may limit the generalizability of the results. Future analysis could attempt to investigate more diverse and larger populations. In particular, the predictive models should be validated in independent cohorts in order to clarify the prognostic relevance cfDNA in the clinical setting.

6 Conclusion

In conclusion, our study provides important data on the clinical value of Cell-free DNA, represented here by *mt-ND1*, *mt-CO3* and *n-Rps18* in patients with sepsis. Cell-free DNA parameters alone may play a role in predicting mortality and morbidity in patients with sepsis. However, they could be much more valuable as part of composite scores. Of considerable advantage is the predictive value of such markers even with a single measurement at the onset of sepsis, and the fact that no baseline measurement is required. Especially the latter

could help to accelerate the diagnosis of sepsis complications such as SA-AKI in patients with previous renal damage. Considering that our data show that cfDNA levels decrease after the initial insult, future studies could investigate cfDNA as a "memoryless" marker.

Data availability statement

The original contributions presented in the study are included in the article/Supplementary Material, further inquiries can be directed to the corresponding author/s.

Ethics statement

The study was approved by the Ethics Committee of the Friedrich Schiller University Jena. The study was conducted in accordance with the local legislation and institutional requirements. Every participant, legal representative or proxy gave their signed written informed consent or, if none of the situations applied, an independent medical doctor was consulted for preliminary consent.

Author contributions

SD: Conceptualization, Data curation, Formal analysis, Investigation, Methodology, Visualization, Writing – original draft, Writing – review & editing. I-AC: Data curation, Formal analysis, Methodology, Writing – original draft, Writing – review & editing. PB: Formal analysis, Methodology, Visualization, Writing – review & editing. MA: Data curation, Investigation, Writing – review & editing. SK: Formal analysis, Visualization, Writing – review & editing. SMC: Conceptualization, Funding acquisition, Methodology, Project administration, Resources, Visualization, Writing – original draft, Writing – review & editing.

Funding

The author(s) declare financial support was received for the research, authorship, and/or publication of this article. The research leading to these results has received funding from the Federal Ministry of Education and Research (BMBF; ZIK Septomics Research Center, Translational Septomics, grant no. 03Z22JN12 to SMC and ICROVID, grant no. 03COV07 to SMC).

Acknowledgments

We thank the entire team of the Research Group Translational Septomics (head SMC) in the Department of Anaesthesiology and Intensive Care Medicine, Jena University Hospital (JUH) for conducting the clinical study, data collection and sample collection and processing. We thank the study nurse team of the Department of Anaesthesiology and Intensive Care Medicine, JUH, for their assistance. We thank the doctors and nurses of the intensive care units of JUH, where the patients were enrolled, for their support.

Conflict of interest

The authors declare that the research was conducted in the absence of any commercial or financial relationships that could be construed as a potential conflict of interest.

Publisher's note

Supplementary material

The Supplementary Material for this article can be found online at: https://www.frontiersin.org/articles/10.3389/fimmu.2024.1382003/full#supplementary-material

References

1. Fleischmann-Struzek C, Mellhammar L, Rose N, Cassini A, Rudd KE, Schlattmann P, et al. Incidence and mortality of hospital- and ICU-treated sepsis: results from an updated and expanded systematic review and meta-analysis. *Intensive Care Med.* (2020) 46:1552–62. doi: 10.1007/s00134-020-06151-x

2. Zarbock A, Nadim MK, Pickkers P, Gomez H, Bell S, Joannidis M, et al. Sepsis-associated acute kidney injury: consensus report of the 28th Acute Disease Quality Initiative workgroup. *Nat Rev Nephrol.* (2023) 19:401–17. doi: 10.1038/s41581-023-00683-3

3. Bagshaw SM, Uchino S, Bellomo R, Morimatsu H, Morgera S, Schetz M, et al. Septic acute kidney injury in critically ill patients: clinical characteristics and outcomes. *Clin J Am Soc Nephrol.* (2007) 2:431–9. doi: 10.2215/CJN.03681106

4. Hoste EAJ, Kellum JA, Selby NM, Zarbock A, Palevsky PM, Bagshaw SM, et al. Global epidemiology and outcomes of acute kidney injury. *Nat Rev Nephrol.* (2018) 14:607–25. doi: 10.1038/s41581-018-0052-0

5. Zarbock A, Gomez H, Kellum JA. Sepsis-induced acute kidney injury revisited: pathophysiology, prevention and future therapies. *Curr Opin Crit Care.* (2014) 20:588–95. doi: 10.1097/MCC.0000000000000153

6. Kellum JA, Romagnani P, Ashuntantang G, Ronco C, Zarbock A, Anders H-J. Acute kidney injury. *Nat Rev Dis Primers.* (2021) 7:52. doi: 10.1038/s41572-021-00284-z

7. Peerapornratana S, Manrique-Caballero CL, Gómez H, Kellum JA. Acute kidney injury from sepsis: current concepts, epidemiology, pathophysiology, prevention and treatment. *Kidney Int.* (2019) 96:1083–99. doi: 10.1016/j.kint.2019.05.026

8. Waikar SS, Betensky RA, Bonventre JV. Creatinine as the gold standard for kidney injury biomarker studies? *Nephrol Dial Transplant.* (2009) 24:3263–5. doi: 10.1093/ndt/gfp428

9. Amiel C, Blanchet F, Friedlander G, Nitenberg A. Renal functional reserve. *Nephrol Dial Transplant.* (1990) 5:763–70. doi: 10.1093/ndt/5.9.763

10. Shi C, Yang L, Braun A, Anders H-J. Extracellular DNA-A danger signal triggering immunothrombosis. *Front Immunol*. (2020) 11:568513. doi: 10.3389/fimmu.2020.568513

11. Zhang Q, Raoof M, Chen Y, Sumi Y, Sursal T, Junger W, et al. Circulating mitochondrial DAMPs cause inflammatory responses to injury. *Nature*. (2010) 464:104–7. doi: 10.1038/nature08780

12. Liu J, Jia Z, Gong W. Circulating mitochondrial DNA stimulates innate immune signaling pathways to mediate acute kidney injury. *Front Immunol*. (2021) 12:680648. doi: 10.3389/fimmu.2021.680648

13. Martin L, Thiemermann C. Mitochondrial DNA in acute kidney injury: chicken or egg? *Shock*. (2018) 49:352–3. doi: 10.1097/SHK.0000000000000966

14. Celec P, Vlková B, Lauková L, Bábíčková J, Boor P. Cell-free DNA: the role in pathophysiology and as a biomarker in kidney diseases. *Expert Rev Mol Med*. (2018) 20: e1. doi: 10.1017/erm.2017.12

15. Hummel EM, Hessas E, Müller S, Beiter T, Fisch M, Eibl A, et al. Cell-free DNA release under psychosocial and physical stress conditions. *Transl Psychiatry*. (2018) 8:236. doi: 10.1038/s41398-018-0264-x

16. de MFS, VG B, Dos Santos L, Costa G, PF V, Campos LCG. Properties and application of cell-free DNA as a clinical biomarker. *Int J Mol Sci*. (2021) 22. doi: 10.3390/ijms22179110

17. Zhong X-Y, von MühlenenI, Li Y, Kang A, AK G, Tyndall A, et al. Increased concentrations of antibody-bound circulatory cell-free DNA in rheumatoid arthritis. *Clin Chem*. (2007) 53:1609–14. doi: 10.1373/clinchem.2006.084509

18. Chang CP-Y, Chia R-H, Wu T-L, Tsao K-C, Sun C-F, Wu JT. Elevated cell-free serum DNA detected in patients with myocardial infarction. *Clin Chim Acta*. (2003) 327:95–101. doi: 10.1016/S0009-8981(02)00337-6

19. Destouni A, Vrettou C, Antonatos D, Chouliaras G, Traeger-Synodinos J, Patsilinakos S, et al. Cell-free DNA levels in acute myocardial infarction patients during hospitalization. *Acta Cardiol*. (2009) 64:51–7. doi: 10.2143/AC.64.1.2034362

20. O'Connell GC, Petrone AB, Tennant CS, Lucke-Wold N, Kabbani Y, Tarabishy AR, et al. Circulating extracellular DNA levels are acutely elevated in ischaemic stroke and associated with innate immune system activation. *Brain Inj*. (2017) 31:1369–75. doi: 10.1080/02699052.2017.1312018

21. Rainer TH, Wong LKS, Lam W, Yuen E, Lam NYL, Metreweli C, et al. Prognostic use of circulating plasma nucleic acid concentrations in patients with acute stroke. *Clin Chem*. (2003) 49:562–9. doi: 10.1373/49.4.562

22. Timmermans K, Kox M, Scheffer GJ, Pickkers P. Plasma nuclear and mitochondrial DNA levels, and markers of inflammation, shock, and organ damage in patients with septic shock. *Shock*. (2016) 45:607–12. doi: 10.1097/SHK.0000000000000549

23. Mao J-Y, Li D-K, Zhang H-M, Wang X-T, Liu D-W. Plasma mitochondrial DNA levels are associated with acute lung injury and mortality in septic patients. *BMC Pulm Med*. (2021) 21:66. doi: 10.1186/s12890-021-01437-2

24. Wang L, Zhou W, Wang K, He S, Chen Y. Predictive value of circulating plasma mitochondrial DNA for Sepsis in the emergency department: observational study based on the Sepsis-3 definition. *BMC Emerg Med*. (2020) 20:25. doi: 10.1186/s12873-020-00320-3

25. Coldewey SM, Neu C, Baumbach P, Scherag A, Goebel B, Ludewig K, et al. Identification of cardiovascular and molecular prognostic factors for the medium-term and long-term outcomes of sepsis (ICROS): protocol for a prospective monocentric cohort study. *BMJ Open*. (2020) 10:e036527. doi: 10.1136/bmjopen-2019-036527

26. Singer M, Deutschman CS, Seymour CW, Shankar-Hari M, Annane D, Bauer M, et al. The third international consensus definitions for sepsis and septic shock (Sepsis-3). *JAMA*. (2016) 315:801–10. doi: 10.1001/jama.2016.0287

27. Kellum JA, Lameire N. Diagnosis, evaluation, and management of acute kidney injury: a KDIGO summary (Part 1). *Crit Care*. (2013) 17:204. doi: 10.1186/cc11454

28. Siew ED, Ikizler TA, Matheny ME, Shi Y, Schildcrout JS, Danciu I, et al. Estimating baseline kidney function in hospitalized patients with impaired kidney function. *Clin J Am Soc Nephrol*. (2012) 7:712–9. doi: 10.2215/CJN.10821011

29. Siew ED, Matheny ME. Choice of reference serum creatinine in defining acute kidney injury. *Nephron*. (2015) 131:107–12. doi: 10.1159/000439144

30. Bouchard J. Estimating baseline serum creatinine for assessing acute kidney injury: not a one size fits all approach. *Kidney Int Rep*. (2021) 6:562–4. doi: 10.1016/j.ekir.2021.01.030

31. Gaião S, Cruz DN. Baseline creatinine to define acute kidney injury: is there any consensus? *Nephrol Dial Transplant*. (2010) 25:3812–4. doi: 10.1093/ndt/gfq454

32. Pottel H, Vrydags N, Mahieu B, Vandewynckele E, Croes K, Martens F. Establishing age/sex related serum creatinine reference intervals from hospital laboratory data based on different statistical methods. *Clin Chim Acta*. (2008) 396:49–55. doi: 10.1016/j.cca.2008.06.017

33. Knaus WA, Draper EA, Wagner DP, Zimmerman JE. APACHE II: a severity of disease classification system. *Crit Care Med*. (1985) 13:818–29. doi: 10.1097/00003246-198510000-00009

34. Sadaka F, EthmaneAbouElMaali C, Cytron MA, Fowler K, Javaux VM, O'Brien J. Predicting mortality of patients with sepsis: A comparison of APACHE II and APACHE III scoring systems. *J Clin Med Res*. (2017) 9:907–10. doi: 10.14740/jocmr3083w

35. Duann P, Lin P-H. Mitochondria damage and kidney disease. *Adv Exp Med Biol*. (2017) 982:529–51. doi: 10.1007/978-3-319-55330-6_27

36. Timmermans K, Kox M, Vaneker M, van den Berg M, John A, van Laarhoven A, et al. Plasma levels of danger-associated molecular patterns are associated with immune suppression in trauma patients. *Intensive Care Med*. (2016) 42:551–61. doi: 10.1007/s00134-015-4205-3

37. Tsuji N, Tsuji T, Ohashi N, Kato A, Fujigaki Y, Yasuda H. Role of mitochondrial DNA in septic AKI via toll-like receptor 9. *J Am Soc Nephrol*. (2016) 27:2009–20. doi: 10.1681/ASN.2015040376

38. Faust HE, Oniyide O, Wang Y, Forker CM, Dunn T, Yang W, et al. Early plasma nuclear DNA, mitochondrial DNA, and nucleosome concentrations are associated with acute kidney injury in critically ill trauma patients. *Crit Care Explor*. (2022) 4:e0663. doi: 10.1097/CCE.0000000000000663

39. Jing Q, Leung CHC, Wu AR. Cell-free DNA as biomarker for sepsis by integration of microbial and host information. *Clin Chem*. (2022) 68:1184–95. doi: 10.1093/clinchem/hvac097

40. Hawkins RB, Stortz JA, Holden DC, Wang Z, Raymond SL, Cox MC, et al. Persistently increased cell-free DNA concentrations only modestly contribute to outcome and host response in sepsis survivors with chronic critical illness. *Surgery*. (2020) 167:646–52. doi: 10.1016/j.surg.2019.11.018

41. Avriel A, Paryente Wiessman M, Almog Y, Perl Y, Novack V, Galante O, et al. Admission cell free DNA levels predict 28-day mortality in patients with severe sepsis in intensive care. *PloS One*. (2014) 9:e100514. doi: 10.1371/journal.pone.0100514

42. Merkle J, Daka A, Deppe AC, Wahlers T, Paunel-Görgülü A. High levels of cell-free DNA accurately predict late acute kidney injury in patients after cardiac surgery. *PloS One*. (2019) 14:e0218548. doi: 10.1371/journal.pone.0218548

43. Nakahira K, Kyung S-Y, Rogers AJ, Gazourian L, Youn S, Massaro AF, et al. Circulating mitochondrial DNA in patients in the ICU as a marker of mortality: derivation and validation. *PloS Med*. (2013) 10:e1001577. doi: 10.1371/journal.pmed.1001577

44. Harrington JS, Choi AMK, Nakahira K. Mitochondrial DNA in sepsis. *Curr Opin Crit Care*. (2017) 23:284–90. doi: 10.1097/MCC.0000000000000427

45. Khwaja A. KDIGO clinical practice guidelines for acute kidney injury. *Nephron Clin Pract*. (2012) 120:c179–84. doi: 10.1159/000339789

46. Waikar SS, Betensky RA, Emerson SC, Bonventre JV. Imperfect gold standards for kidney injury biomarker evaluation. *J Am Soc Nephrol*. (2012) 23:13–21. doi: 10.1681/ASN.2010111124

47. Vincent J-L, Sakr Y, Sprung CL, Ranieri VM, Reinhart K, Gerlach H, et al. Sepsis in European intensive care units: results of the SOAP study. *Crit Care Med*. (2006) 34:344–53. doi: 10.1097/01.CCM.0000194725.48928.3A

48. Bagshaw SM, George C, Bellomo R. Early acute kidney injury and sepsis: a multicentre evaluation. *Crit Care*. (2008) 12:R47. doi: 10.1186/cc6863

49. Peters E, Antonelli M, Wittebole X, Nanchal R, François B, Sakr Y, et al. A worldwide multicentre evaluation of the influence of deterioration or improvement of acute kidney injury on clinical outcome in critically ill patients with and without sepsis at ICU admission: results from The Intensive Care Over Nations audit. *Crit Care*. (2018) 22:188. doi: 10.1186/s13054-018-2112-z

50. Clementi A, Virzì GM, Brocca A, Pastori S, de CM, Marcante S, et al. The role of cell-free plasma DNA in critically ill patients with sepsis. *Blood Purif*. (2016) 41:34–40. doi: 10.1159/000440975

51. Jansen MPB, Pulskens WP, Butter LM, Florquin S, Juffermans NP, Roelofs JJTH, et al. Mitochondrial DNA is released in urine of SIRS patients with acute kidney injury and correlates with severity of renal dysfunction. *Shock*. (2018) 49:301–10. doi: 10.1097/SHK.0000000000000967

52. Graversen HV, Jensen SK, Vestergaard SV, Heide-Jørgensen U, Christiansen CF. Defining baseline creatinine for identification of AKI in population-based laboratory databases: A danish nationwide cohort study. *Kidney360*. (2022) 3:232–41. doi: 10.34067/KID.0006082021

53. Siew ED, Matheny ME, Ikizler TA, Lewis JB, Miller RA, Waitman LR, et al. Commonly used surrogates for baseline renal function affect the classification and prognosis of acute kidney injury. *Kidney Int*. (2010) 77:536–42. doi: 10.1038/ki.2009.479

54. Ho PW-L, Pang W-F, Luk CC-W, Ng JK-C, Chow K-M, Kwan BC-H, et al. Urinary mitochondrial DNA level as a biomarker of acute kidney injury severity. *Kidney Dis (Basel)*. (2017) 3:78–83. doi: 10.1159/000475883

55. Hu Q, Ren J, Ren H, Wu J, Wu X, Liu S, et al. Urinary mitochondrial DNA identifies renal dysfunction and mitochondrial damage in sepsis-induced acute kidney injury. *Oxid Med Cell Longev*. (2018) 2018:8074936. doi: 10.1155/2018/8074936

frontiers | Frontiers in Immunology

TYPE Original Research
PUBLISHED 20 June 2024
DOI 10.3389/fimmu.2024.1352789

OPEN ACCESS

EDITED BY
Christoph Thiemermann,
Queen Mary University of London,
United Kingdom

REVIEWED BY
Ivana Kawikova,
University of Hartford, United States
Craig Coopersmith,
Emory University, United States

*CORRESPONDENCE
E. Marion Schneider
marion.Schneider@uniklinik-ulm.de

RECEIVED 08 December 2023
ACCEPTED 07 February 2024
PUBLISHED 20 June 2024

CITATION
Guggemos J, Fuller SJ, Skarratt KK, Mayer B and Schneider EM (2024) Loss-of-function/gain-of-function polymorphisms of the ATP sensitive P2X7R influence sepsis, septic shock, pneumonia, and survival outcomes. *Front. Immunol.* 15:1352789. doi: 10.3389/fimmu.2024.1352789

Loss-of-function/gain-of-function polymorphisms of the ATP sensitive P2X7R influence sepsis, septic shock, pneumonia, and survival outcomes

Johanna Guggemos[1], Stephen J. Fuller[2,3], Kristen K. Skarratt[2,3], Benjamin Mayer[4] and E. Marion Schneider[1*]

[1]Clinic for Anesthesiology and Intensive Care Medicine, Ulm University Hospital, Ulm, Germany, [2]Nepean Clinical School, Faculty of Medicine and Health, The University of Sydney, Kingswood, NSW, Australia, [3]Department of Haematology, Nepean Hospital, Penrith, NSW, Australia, [4]Institute for Epidemiology and Medical Biometry, Ulm University, Ulm, Germany

Introduction: Extracellular ATP (eATP) released from damaged cells activates the P2X7 receptor (P2X7R) ion channel on the surface of surrounding cells, resulting in calcium influx, potassium efflux and inflammasome activation. Inherited changes in the P2X7R gene (*P2RX7*) influence eATP induced responses. Single nucleotide polymorphisms (SNPs) of *P2RX7* influence both function and signaling of the receptor, that in addition to ion flux includes pathogen control and immunity.

Methods: Subjects (n = 105) were admitted to the ICU at the University Hospital Ulm, Germany between June 2018 and August 2019. Of these, subjects with a diagnosis of sepsis (n = 75), were also diagnosed with septic shock (n = 24), and/or pneumonia (n = 42). Subjects with pneumonia (n = 43) included those without sepsis (n = 1), sepsis without shock (n = 29) and pneumonia with septic shock (n = 13). Out of the 75 sepsis/septic shock patients, 33 patients were not diagnosed with pneumonia. Controls (n = 30) were recruited to the study from trauma patients and surgical patients without sepsis, septic shock, or pneumonia. SNP frequencies were determined for 16 *P2RX7* SNPs known to affect P2X7R function, and association studies were performed between frequencies of these SNPs in sepsis, septic shock, and pneumonia compared to controls.

Results: The loss-of-function (LOF) SNP rs17525809 (T253C) was found more frequently in patients with septic shock, and non-septic trauma patients when compared to sepsis. The LOF SNP rs2230911 (C1096G) was found to be more frequent in patients with sepsis and septic shock than in non-septic trauma patients. The frequencies of these SNPs were even higher in sepsis and septic patients with pneumonia. The current study also confirmed a previous study by our group that showed a five SNP combination that included the GOF SNPs rs208294 (C489T) and rs2230912 (Q460R) that was designated #21211 was associated with increased odds of survival in severe sepsis.

Discussion: The results found an association between expression of LOF *P2RX7* SNPs and presentation to the ICU with sepsis, and septic shock compared to control

ICU patients. Furthermore, frequencies of LOF SNPs were found to be higher in sepsis patients with pneumonia compared to those without pneumonia. In addition, a five SNP GOF combination was associated with increased odds of survival in severe sepsis. These results suggest that *P2RX7* is required to control infection in pneumonia and that inheritance of LOF variants increases the risk of sepsis when associated with pneumonia. This study confirms that *P2RX7* genotyping in pneumonia may identify patients at risk of developing sepsis. The study also identifies P2X7R as a target in sepsis associated with an excessive immune response in subjects with GOF SNP combinations.

KEYWORDS

P2RX7, loss-of-function (LOF), gain-of-function (GOF) single nucleotide polymorphisms (SNP), linkage disequilibrium, pneumonia, sepsis, septic shock, ATP

1 Introduction

The clinical course of critically ill patients requiring intensive care involves systemic inflammation to clear pathogens followed by profound immunosuppression to allow healing and recovery. Tissue damage and bacterial or viral infections trigger upregulation and activation of the pattern-recognition receptor (PRR)/danger-associated molecular pattern (DAMP) receptor, P2X7 receptor (P2X7R) which activates the inflammasome and subsequent cytokine release. This characterizes sepsis as a disease with multifactorial debilitating conditions and loss of immune control to nosocomial and community-acquired infections with a high risk of death. The imbalance of the immune response appears to be responsible for the high risk of mortality in patients with sepsis, making it a major problem for intensive care units worldwide.

In 1972, Burnstock introduced the concept of purinergic signaling, describing adenosine triphosphate (ATP) as a major stressor for cells and tissues. In contrast, its metabolite adenosine, generated by cell surface expressed nucleotidases, was found to be a major immunosuppressor (1). ATP release occurs due to tissue damage, hypoxia, mechanical stimulation, changes in osmotic pressure (2), surgery (3), and hemorrhage (4). The most severe form of sepsis, septic shock, is associated with failure of the vascular system and metabolic insufficiency, resulting in hypotension and elevated serum lactate (5). In addition to its role in inflammation and immune dysfunction, P2X7R has been shown to be an essential receptor for macrophage-mediated bacterial killing (6). Furthermore, recent evidence suggests that P2X7R stimulation may modulate the host response by dampening inflammation by stimulating CD14 release from macrophages (7).

The controversial molecular evidence for P2X7R influencing tissue damage, inflammation, and immune dysfunction may be related in part to its high numbers of genetic polymorphisms including both loss-of-function (LOF) and gain-of-function (GOF) single nucleotide polymorphisms (SNPs) (8). Several studies have investigated the effect of SNP characteristics and their effect on P2X7R ion channel function and pro-inflammatory cytokine release (9–11). In addition to SNPs, the receptor can be modified by alternative splicing events (12–14).

P2X7R consists of three P2X7 protein subunits and is found on the membranes of cell surfaces and intracellular organelles (15). Inflammatory conditions can differentially modulate the membrane expression of P2X7 and affect eATP signaling in defined phases of sepsis (16).

In one of our previous studies, combinations of LOF and GOF SNPs were identified in patients with sepsis and in patients with virus-induced hemophagocytic syndromes which appear to be related to better survival and higher frequencies in patients with hemophagocytic lymphohistiocytosis (HLH) (17).

The current genetic association study measured the allele frequencies of LOF and GOF SNPs of the P2X7 gene (*P2RX7*) in intensive care unit (ICU) patients who were either non-septic or suffered from sepsis, septic shock, with and without pneumonia. It was hypothesized that LOF *P2RX7* SNPs might protect against excessive systemic inflammation and sepsis, but at the expense of pathogen clearance, whereas GOF *P2RX7* SNPs might be linked to better pathogen control, but increased risk of sepsis.

2 Materials and methods

2.1 Study population

This study was approved by the Ethics Committee of Ulm University (application no. 284/18). Subjects (n = 105) for the study were recruited from the anesthesiologic ICU at the University Hospital Ulm, Germany between June 2018 and August 2019 (see Figure 1). Subjects were aged between 18 and 84 years and there were 77 males and 28 females. The mean age of the patients was 61.06 years (SD 15.82 years). Clinical information for each patient included is given in Supplementary Table 1, including information on co-morbidities, sterile trauma/hemorrhage, obesity, diabetes

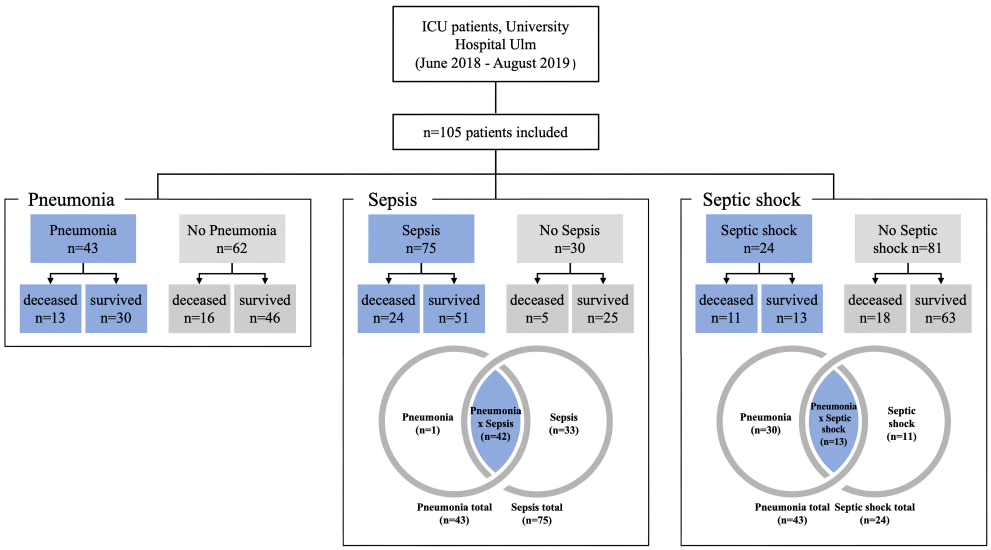

FIGURE 1
Subject and control groupings for analysis. Patients with pneumonia, sepsis or septic shock are shown as blue fields and the corresponding controls are shown in grey.

type 2, malignancies, chronic obstructive pulmonary disease (COPD), asthma, alcohol or nicotine abuse, organ dysfunction syndromes, as well as infections before manifesting critical illness. Thirty patients were non-septic, 75 patients were diagnosed with sepsis, of which 24 patients were in septic shock (Figure 1). Forty-two patients had pneumonia and sepsis including 13 patients with septic shock. Out of the 75 sepsis/septic shock patients, 33 patients did not suffer from pneumonia (Figure 1).

Non-septic patients comprised two major groups: i) patients with polytrauma (n=9) and ii) patients with major surgical interventions (n=25) including tumor resection (n=2), surgery related to a vascular disease (n=9) or neurosurgery (n=6). A total of n=6 patients from the polytrauma group underwent surgery during their stay in the ICU. The remaining three patients underwent surgery for hemorrhagic shock, compartment syndrome, and atypical gastric resection due to obesity. There were only two patients who did not belong to one of the two main groups: One patient was monitored in the ICU for Stanford type B aortic dissection, and the other patient had a bowel obstruction that did not require surgery (see Supplementary Table 1 for more details).

2.2 Study design, DNA isolation, and genotyping

Following the patients' characteristics given in Figure 1, a total of 105 patients were studied. The first step was to determine how many patients had sepsis (n=75) and how many did not have sepsis (n=30). Using these two groups, we investigated whether there were statistical differences with regard to the genetics of *P2RX7*. Subsequently, we studied for differences in *P2RX7* SNP frequencies in patients with septic shock (n=24) and patients without septic shock (n=81). Finally, this study calculated *P2RX7* SNP frequencies for all patients with pneumonia (n=43) versus patients without pneumonia (n=62) Figure 1.

Semi-automated DNA purification was done by using a Maxwell 16® LEV Blood DNA Kit and a Maxwell 16® (#AS1290, Promega®) (https://www.promega.com) instrument. A total of 300 µl of fresh EDTA blood from each patient (pseudonymized by a KeyPat-Id number), was mixed with 300 µl of Promega lysis buffer plus 30 µl Proteinase K (supplied in the kit). The samples were then vortexed for 10 seconds and incubated at 56°C for 20 min using a water bath. The high temperature and the detergents guanidinium thiocyanate (50-75%) and polyethylene glycol tert-octyl-phenyl ether (Triton-X, < 2%), which are components of the lysis buffer, lead to lysis of cell and nuclear membranes. The proteinase K degrades various proteins. Histones are also degraded, enabling the release of genomic DNA (gDNA). After the incubation time, the lysed blood sample was pipetted into well No.1 of the Maxwell 16® cartridge. The cartridges were placed into the cartridge holder with a plunger and an additional tube, containing 60 µl elution buffer. The cartridge holder was then placed inside the Maxwell 16® Instrument and the machine was started. The Maxwell 16® instrument uses paramagnetic particles, the MagnaCel™ particle, which takes advantage of the cellulose binding capacity of nucleic acids. During the automated purification process, gDNA is bound to the paramagnetic particle, washed with ethanol and eventually released into the elution buffer. Absorbance measurements determined the grade of genomic deoxyribonucleic acid (gDNA) using the NanoDrop® 1000 version 3.8.1 (https://www.thermofisher.com). After DNA isolation, 16 *P2RX7* SNPs (Table 1, Figures 2, 3A) were genotyped using MassARRAY® technology following the manufacturers advice from Agena Bioscience (https://www.agenabio.com).

TABLE 1 Visualization of the investigated SNPs with location in the gene/protein, the change in the amino acid chain and the impact on receptor function.

dbSNP ID	amino acid change	position	function
rs2393799 (C-762T)	–	promotor	Decreased receptor expression (18)
rs35933842 (G151 + 1T)	-	intron 1	Splice site mutation, P2X7 null allele (14)
rs17525809 (T253C)	Val-76>Ala	exon 2	Partial LOF (11, 19)
rs28360447 (G474A)	Gly-150>Arg	exon 5	LOF (11)
rs208294 (C489T)	His-155>Tyr	exon 5	GOF (20)
rs208307 (C641-5G)	-	intron 6	Promotes exon 7, 8 skipping, null function (13)
rs7958311 (G835A)	His-270>Arg	exon 8	Remains unclear [LOF (21), GOF (11)]
rs7958316 (G853A)	Arg-276>His	exon 8	LOF (11)
rs28360457 (G946A)	Arg-307>Gln	exon 9	LOF (22)
rs1718119 (G1068A)	Ala-348>Thr	exon 11	GOF (11)
rs2230911 (C1096G)	Thr-357>Ser	exon 11	LOF (21)
rs2230912 (A1405G)	Gln-460>Arg	exon 13	Remains unclear [LOF (11), GOF (23)]
rs3751143 (A1513C)	Glu-496>Ala	exon 13	LOF (9, 19)
rs3751142 (G1628T)	Leu534Leu	exon 13	Synonymous variant (24)
rs1653624 (T1729A)	Ile-568>Asn	exon 13	LOF (19, 25)
rs1621388 (G1772A)	Pro582Pro	exon 13	Synonymous variant (24, 26)

2.3 Statistical analysis

IBM SPSS® version 26 was used for statistical data analysis with an $\alpha<0.05$ level of significance used for all calculations. Patient characteristics such as age, sex, or length of stay were first tested for normal distribution using the Kolmogorov-Smirnov and Shapiro-Wilk tests. Because the data were not normally distributed, differences between mean tendencies were calculated using the Mann-Whitney U test. Odds ratios (OR) and 95% confidence intervals (CI) were reported for significant results.

All *P2RX7* SNPs (n=16) were first tested for deviations from Hardy Weinberg Equilibrium (HWE). Next, linkage disequilibrium (LD) was determined for all SNPs using Haploview version 4.2 and analyzed according to the Broad Institute's standard coloring scheme (27). A logarithm of the odds (LOD) score ≥2 between two SNPs indicates genetic linkage, as opposed to a random result. In accordance with literature recommendations, SNPs with minor allele frequency (MAF) <1% were excluded from further calculations (28). To test for sample-to-population consistency, MAFs in the present patient population were compared with published frequencies from the Allele Frequency Aggregator (ALFA) project of the National Center for Biotechnology Information (NCBI) Database of Genotypes and Phenotypes (dbGaP) (Table 2) (29). Each SNP was then tested for association with the clinical endpoints of pneumonia, sepsis, and septic shock using either the chi-squared test or, if $n \leq 5$, Fisher's exact test. Two models were performed for the analysis: Model 1 analyzed differences in the absolute numbers of genetic variants [wildtype (WT), heterozygous mutation (HET), and homozygous mutation (HOM)], whereas Model 2 selected differences based on allele frequencies. The OR was calculated to determine the strength of the associations identified as statistically significant. A *post hoc* analysis with Bonferroni correction was required before calculating the OR in Model 1 for cases with homozygous SNPs.

In addition to the analysis of individual SNPs, a combination of five SNPs (*rs208294 (C489T), rs28360457 (G946A), rs2230912 (A1405G), rs3751143 (A1513C)*, and *rs1653624* (T1729A)) (17) was studied. The SNP genotype was coded as 1, 2 or 3 according to how many copies of the minor allele they carried (1 = WT, 2 = HET, 3 = HOM). Depending on the number of individuals with each haplotype, a chi-squared or Fisher's exact test was used to identify associations.

3 Results

3.1 Analysis of the study population

Patients with pneumonia and sepsis had significantly prolonged hospital and ICU stays compared to all patients. On average, patients spent 46.6 days in the hospital and 20.3 days in the ICU. Patients with pneumonia spent on average 55.1 days in the hospital (p=0.006) and 25.9 days in the ICU (p=0.001). Patients with sepsis spent on average 53.2 days in hospital (p=0.005) and 24.3 days in ICU (p<0.001). In contrast, septic shock patients had shorter hospital and ICU stays than the overall study population (38.5 vs. 18.7 days, respectively). Septic shock patients were older than other patients (mean age 65.92 vs. 61.06 years, respectively) and were more likely to die [45.8% vs. 27.6%, respectively, p=0.023; OR: 2.96 (1.14-7.73)]. In the entire cohort, 29 patients (27.6%) died, of which 18 patients were male (62.1%) and 11 patients were female (37.9%).

3.2 Calculation of the Hardy-Weinberg equilibrium and linkage disequilibrium

All 16 SNPs were first tested for deviation from HWE, with only two SNPs [*rs2230911 (C1096G)* and *rs3751142 (G1628T)*] deviating from HWE (Table 3). The SNPs *rs35933842 (G151 + 1T)* and *rs28360457 (G946A)* were excluded from further analysis because of

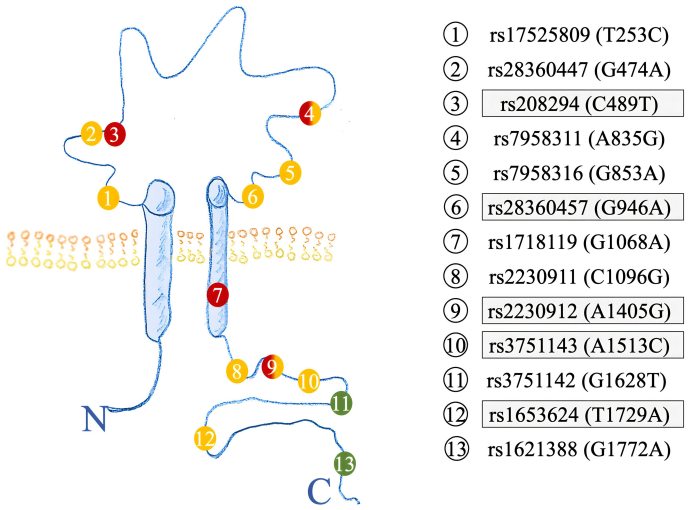

FIGURE 2
Structure of the P2X7R highlighting the amino acid location of SNPs investigated. Previous SNPs analyzed in (17) are highlighted in grey. GOF SNPs are red, LOF SNPs yellow, and synonymous SNPs colored in green.

a MAF <1% (Table 3). Most of the calculated allele frequencies were consistent with the globally published frequencies from the ALFA project (29). Using the European cohort as a reference, only minor deviations >5% were found at *rs2393799 (C- 762T)*. LD analysis showed a block with high LD between *rs7958311 (G835A), rs1718119 (G1068A), rs2230911 (C1096G), rs2230912 (A1405G), rs3751143 (A1513C), rs3751142 (G1628T)* and *rs1621388 (G1772A)*. In addition, further pairwise LD existed in the investigated cohort (Figure 3D).

3.3 Association of SNPs with clinical endpoints

Four SNPs showed statistically significant associations with the clinical outcomes of pneumonia and/or sepsis, but no association with septic shock or death (Table 4). Two of them were characterized as LOF [*rs17525809 (T253C)*, and *rs2230911 (C1096G)*], and *rs3751142 (G1628T)* and *rs1621388 (G1772A)* are synonymous SNPs with as yet unknown effect on P2X7R function. These results suggest that genetics related to impaired P2X7R function and signaling may play a role in pneumonia and sepsis.

The minor variant of *rs17525809 (T253C)* was linked to reduced risk of developing pneumonia [Model 1: p=0.021, OR HET/WT: 0.24 (0.06 – 0.87), Model 2: MAF cohort with pneumonia 0.035 vs. MAF cohort without pneumonia 0.121, p=0.028, OR minor/major 0.26 (0.07 – 0.94)] and sepsis [Model 1: p=0.001, OR HET/WT: 0.18 (0.06 – 0.52), Model 2: MAF cohort with sepsis 0.047 vs. MAF cohort without sepsis 0.183, p=0.001, OR minor/major: 0.22 (0.08 – 0.59)]. However, as shown in Supplementary Figure 1, a closer look at the data reveals that the heterozygous genotype of the LOF SNP *rs17525809 (T253C)* is more frequent in sepsis patients with pneumonia than in sepsis patients without pneumonia (6/29 vs 3/22, respectively). An imbalance in *rs17525809* (T253C) genotype frequency was also observed when comparing septic and non septic patients.

The minor variant of the LOF SNP *rs2230911 (C1096G)* was associated with a higher risk of developing pneumonia [Model 1: p=0.012, OR HET/WT: 7.15 (1.43 - 35.67), Model 2: MAF cohort with pneumonia 0.140 vs. MAF cohort without pneumonia 0.032, p=0.004, OR minor/major 4.85 (1.51 - 15.63)] and sepsis [Model 1: p=0.045, OR HET/WT: -, Model 2: MAF cohort with sepsis 0.107 vs. MAF cohort without sepsis 0.000, p=0.007, OR minor/major: -]. Furthermore, the cohort of patients with sepsis or septic shock plus pneumonia had the highest proportion of heterozygous and homozygous mutant genotypes of this SNP (see Supplementary Figure 2).

Subsequent LD calculation with D'=1 showed that the LOF SNP *rs2230911 (C1096G)* and the synonymous SNP *rs3751142 (G1628T)* were in strong linkage Figure 3D. In the current cohort of patients analyzed, every patient with a mutation in the LOF SNP *rs2230911 (C1096G)* was also mutated for *rs3751142 (G1628T)*. As our study is still ongoing, n=250 patients have now been sequenced, of which only two patients were found to differ in the aforementioned combination of SNPs (data not shown).

The present study also found an association between the major variant G of *rs1621388 (G1772A)* and a higher prevalence of sepsis cases in Model 2 [Model 1: p=0.078, Model 2: MAF cohort with sepsis 0.313 vs. MAF cohort without sepsis 0.483, p=0.021, OR minor/major 0.49 (0.26-0.90)]. The association with *rs1621388 (G1772A)* was not statistically significant after Bonferroni correction in Model 1. As shown in Supplementary Figure 3, the distribution of wild-type, heterozygous and homozygous mutant variants in our group of non-septic patients is almost equal between wild-type, heterozygous and homozygous mutant genotypes. Sepsis and septic shock patients had lower frequencies of the minor variant. There is no systematic change in these SNP variations when including cases with and without pneumonia. Interestingly, this SNP was in complete LD with the GOF SNP *rs1718119 (G1068A)* (Figure 3A).

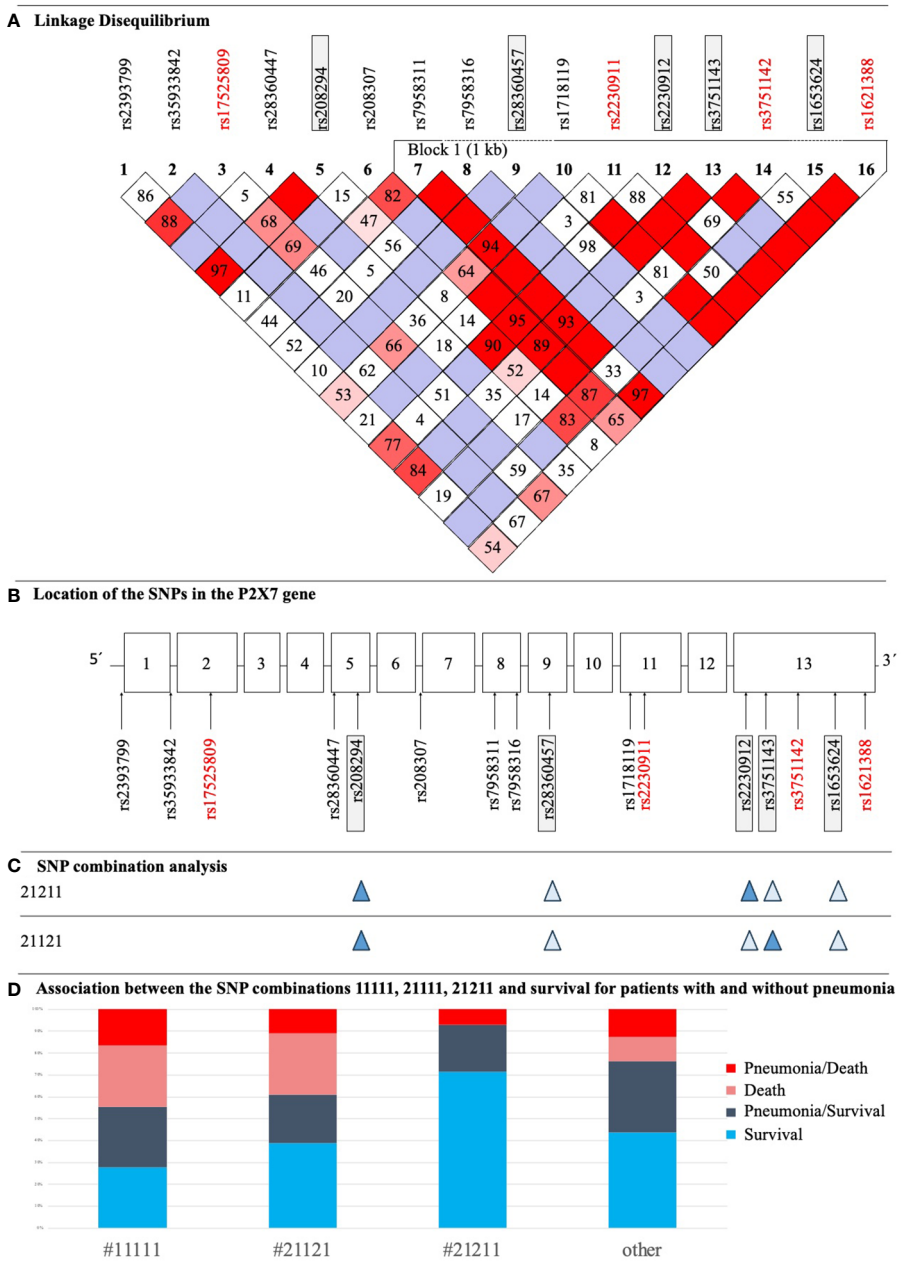

FIGURE 3
(A) LD Plot of *P2RX7*. The display was performed according to the Broad Institute's Standard Color Scheme. The number in the boxes refers to the coefficient D'. SNPs that showed associations with pneumonia and/or sepsis are in red. **(B)** Structure of the *P2RX7* gene with the location of studied SNPs. SNPs with statistically significant results in the current study are highlighted red, SNPs being part of the SNP combination model are highlighted in grey boxes. **(C)** Illustration of two important SNP combinations related to survival, filled symbols indicate heterozygosity and open symbols indicate wildtype genotypes of the respective SNP. **(D)** Distribution of patients with sepsis with and without pneumonia, who survived/died and their corresponding P2RX7 SNP combinations as defined in a previous study (17).

3.4 SNP combinations

In addition to analyzing individual SNPs, this study also investigated associations with previously identified genotype combinations consisting of five *P2RX7* SNPs (Figure 3B). Analysis revealed trends between three combinations and clinical outcomes that were just above the threshold for statistical significance. #11111 and #21111 showed adverse effects for ICU patients: #11111 (n=18) was associated with higher mortality [p=0.085, OR 2.60 (0.90 - 7.48)] and #21111 (n=14) with more frequent development of pneumonia [p=0.054, OR 3.06 (0.94 - 9.89)]. In contrast, #21211 (heterozygous at rs208294 His-155>Tyr, rs22309122 Gln-460>Arg, and WT at three other SNPs) (n=14) increased the likelihood of patient survival [p=0.105, OR 0.18 (0.02 - 1.42)]. For clarity, the distribution of #11111, #21121, (heterozygous at rs208294 His-155>Tyr, and rs3751146 Glu-496>Ala, and WT at three other SNPs), #21211 and others among patient groups is shown in Figure 3C. 5/10 patients with *#11111* without pneumonia survived, and 5/8 with pneumonia

10.3389/fimmu.2024.1352789

TABLE 2 Comparison of MAFs of SNPs in our cohort with published MAFs from the ALFA project (MAF dbSNP accessed 4/1/2024 https://www.ncbi.nlm.nih.gov/snp/ALFAAlleleFrequency).

	GLOBAL	EUROPE	COHORT n=105
rs2393799 (C-762T)	C=0.75697 T=0.24303	C=0.82278 T=0.17722	C=0.75238 T=0.24761
rs35933842 (G151 + 1T)	G=0.99243 T=0.00757	G=0.99177 T=0.00823	G=0.99523 T=0.00476
rs17525809 (T253C)	T=0.93101 C=0.06899	T=0.92747 C=0.07253	T=0.91428 C=0.08571
rs28360447 (G474A)	G=0.98412 A=0.01588	G=0.98279 A=0.01721	G=0.98571 A=0.01428
rs208294 (C489T)	C=0.54850 T=0.45150	C=0.55220 T=0.44780	C=0.52884 T=0.47115
rs208307 (C641-5G)	C=0.70101 G=0.29899	C=0.69956 G=0.30044	C=0.68571 G=0.31428
rs7958311 (G835A)	G=0.74385 A=0.25615	G=0.74711 A=0.25289	G=0.75714 A=0.24285
rs7958316 (G853A)	G=0.98106 A=0.01894	G=0.97922 A=0.02078	G=0.98571 A=0.01428
rs28360457 (G946A)	G=0.98759 A=0.01241	G=0.98652 A=0.01348	G=0.99047 A=0.00952
rs1718119 (G1068A)	G=0.61770 A=0.38230	G=0.60919 A=0.39081	G=0.65048 A=0.34951
rs2230911 (C1096G)	C=0.91342 G=0.08659	C=0.9236 G=0.0764	C=0.92380 G=0.07619
rs2230912 (A1405G)	A=0.84448 G=0.15553	A=0.83368 G=0.16632	A=0.84761 G=0.15238
rs3751143 (A1513C)	A=0.81091 C=0.18909	A=0.81076 C=0.18924	A=0.77142 C=0.22857
rs3751142 (G1628T)	G=0.90755 T=0.09245	G=0.92216 T=0.07784	G=0.92380 T=0.07619
rs1653624 (T1729A)	T=0.98173 A=0.01827	T=0.97967 A=0.02033	T=0.98058 A=0.01941
rs1621388 (G1772A)	G=0.62878 A=0.37122	G=0.61737 A=0.38263	G=0.63809 A=0.36190

survived. In patients with *#21121* and low ion channel function (17), 4/6 patients had pneumonia and survived and 7/12 patients had no pneumonia and survived. In patients with *#21211* and high ion channel activity (17), 4/14 patients had pneumonia of which 1 died (Figure 3D). In the remaining haplotypes, 24/30 patients survived without pneumonia, n=25 had pneumonia of which n=7 patients died.

4 Discussion

4.1 Clinical aspects of the sample

Several aspects of the collected clinical data and sample distribution suggest that this cohort is a representative study population. The analysis confirmed longer hospitalization and ICU stays for pneumonia and sepsis, but not for septic shock (5).

TABLE 3 Hardy-Weinberg-equilibrium (HWE) and Minor Allele Frequencies (MAFs) of the investigated SNPs.

dbSNP ID	HWE		MAF
	Chi^2-test	p-value	
rs2393799 (C-762T)	1.801	0.180	0.248
rs35933842 (G151 + 1T)	0.002	0.961	**0.005***
rs17525809 (T253C)	0.923	0.337	0.086
rs28360447 (G474A)	0.022	0.882	0.014
rs208294 (C489T)	0.183	0.669	0.471
rs208307 (C641-5G)	0.544	0.461	0.314
rs7958311 (G835A)	0.010	0.918	0.243
rs7958316 (G853A)	0.022	0.882	0.014
rs28360457 (G946A)	0.010	0.922	**0.010***
rs1718119 (G1068A)	0.377	0.539	0.350
rs2230911 (C1096G)	**10.985***	**0.001***	0.076
rs2230912 (A1405G)	0.180	0.671	0.152
rs3751143 (A1513C)	1.936	0.164	0.229
rs3751142 (G1628T)	**10.985***	**0.001***	0.076
rs1653624 (T1729A)	0.040	0.841	0.019
rs1621388 (G1772A)	0.902	0.342	0.362

SNPs deviating from HWE or with an MAF <1% are highlighted in bold letter with *.

Shorter ICU stays for septic shock patients are similar to published data sets with higher mortality among septic shock patients. Similar to large multicenter studies, the gender distribution in the ICU is strongly skewed towards males (73%) (30). Many patients studied here, were obese and suffered from diabetes (Supplementary Table 1). We found that type II diabetes ICU patients present with significantly higher numbers of inflammatory monocytes (31). Since P2X7R expression is a hallmark of inflammation, future studies should address sepsis in obesity and type II diabetes as a separate study population (31).

4.2 LD block

This present study revealed an LD block between seven SNPs comprising a base length of one kb. The full length of *P2RX7* is 53 kb (32). In addition, pairwise LD was observed for several SNPs. A previous study in an Australian population identified an LD block in exons 11 to 13. The Australian haplotype overlapped with the haplotype of this study for five SNPs: *rs1718119 (G1068A)*, *rs2230911 (C1096G)*, *rs2230912 (A1405G)*, and *rs3751143 (A1513C)*. The LD block for the sample of this study also included *rs7958311 (G835A)*, *rs3751142 (G1628T)*, and *rs1621388 (G1772A)*. The variants *rs3751142 (G1628T)* and *rs1621388 (G1772A)* were not examined in the comparative study, while the LD block did not include *rs7958311 (G835A)* despite high LD levels (8, 11).

TABLE 4 Presentation of the significant associations between SNPs and clinical endpoints.

(A) Demonstration of associations between genetic variants with pneumonia											
SNP	Total	Genotype frequency			Model 1			Model 2			
		WT	HET	HOM	p-value	OR	95% CI	MAF	p-value	OR	95% CI
rs17525809 (T253C)											
Pneumonia	43	40	3	-	0.021	0.24	(0.06 - 0.87)	0.035	0.028	0.26	(0.07 - 0.94)
Non-pneumonia	62	47	15	-				0.121			
rs2230911 (C1096G)											
Pneumonia	43	33	8	2	0.012	7.15	(1.43 - 35.67)	0.140	0.004	4.85	(1.51 - 15.63)
Non-pneumonia	62	59	2	1				0.032			
rs3751142 (G1628T)											
Pneumonia	43	33	8	2	0.012	7.15	(1.43 - 35.67)	0.140	0.004	4.85	(1.51 - 15.63)
Non-pneumonia	62	59	2	1				0.032			
rs1621388 (G1772A)											
Pneumonia	43	21	18	4	0.318			0.302	0.135	0.64	(0.36 - 1.15)
Non-pneumonia	62	24	26	12				0.403			
(B) Demonstration of associations between genetic variants with sepsis											
SNP	Total	Genotype frequency			Model 1			Model 2			
		WT	HET	HOM	p-value	OR	95% CI	MAF	p-value	OR	95% CI
rs17525809 (T253C)											
Sepsis	75	68	7		0.001	0.18	(0.06 - 0.52)	0.047	0.001	0.22	(0.08 - 0.59)
Non-sepsis	30	19	11					0.183			
rs2230911 (C1096G)											
Sepsis	75	62	10	3	0.045			0.107	0.007		
Non-sepsis	30	30						0.000			
rs3751142 (G1628T)											
Sepsis	75	62	10	3	0.045			0.107	0.007		
Non-sepsis	30	30						0.000			
rs1621388 (G1772A)											
Sepsis	75	36	31	8	0.078			0.313	0.021	0.49	(0.26 - 0.90)
Non-sepsis	30	9	13	8				0.483			

Remarkably, mutations in the GOF SNP *rs1718119 (G1068A)* and the synonymous SNP *rs1621388 (G1772A)* were identical in all patients presenting with a heterozygous or homozygous mutated genotype but differed in other SNPs. The same was observed for the LOF SNP, *rs2230911 (C1096G)* and synonymous SNP, *rs3751142 (G1628T)*, but no homozygous mutant genotypes were identified in these two SNPs.

This strong LD between the aforementioned GOF and LOF SNPs on the one hand as well as the combined presence of minor variants of GOF and LOF SNPs in a defined individual is likely linked to the biological function of this receptor since other SNPs in this LD block are not identically mutated in a number of other patients.

4.3 rs17525809 (T253C)

The SNP *rs17525809 (T253C)* is located in exon 2, which encodes a part of the extracellular loop of P2X7R. The minor variant causes an exchange of valine to alanine at position 76 of the protein (11). The amino acid change of this SNP affects both ion flux and fluorescent dye uptake of the P2X7R pore. Studies in

multiple sclerosis (MS) have shown that the T allele, which is more common in MS patients, results in a 1.71-fold higher calcium influx into the cytosol of transfected cells compared to P2X7R with the C allele. Thus, the SNP corresponds to a LOF variant (11, 19). Previous studies have only performed functional assays for homozygous mutations of *rs17525809 (T253C)*. Therefore, the effect of heterozygous mutations on the functionality of the receptor remains unclear.

In the current cohort, the minor variant of this SNP was identified as a heterozygous and not as a homozygous mutation. Similarly, previous publications have reported that a homozygous *rs17525809 (T253C)* variant is rare (33, 34). In our study, the minor allele of *rs17525809 (T253C)* was associated with a lower OR for pneumonia and sepsis in ICU patients. The minor allele C was linked to a 4.17-fold lower risk of developing pneumonia in model 1 and a 5.56-fold lower risk of developing sepsis. The heterozygous genotype of the LOF SNP *rs17525809 (T253C)* was also more frequent in sepsis patients with pneumonia. Furthermore, not only the pneumonia/sepsis cohorts, but also the non-sepsis group showed an imbalance of *rs17525809 (T253C)* with a higher frequency of the minor allele than in reported healthy controls. A possible explanation for this imbalance may be related to the high relative numbers of individuals with obesity. In the non-septic patients, 10/30 patients had a BMI of >30 kg/m², compared to 13/24 septic shock patients with a BMI >30 kg/m² (Supplementary Table 1). There is evidence for the function of P2X7R signaling in energy metabolism, fat mass and weight gain (35), and it is likely that this impacts the association between *P2RX7* SNPs and sepsis.

In previously published studies, the effect of *rs17525809 (T253C)* varies depending on the investigated pathology. In chronic inflammatory diseases such as gout or MS, the LOF variant was protective (33, 36). In the context of cervical cancer, a functional P2X7R may be beneficial for targeting tumor cells (34). Synthesizing previously study results with the findings of this study, *rs17525809 (T253C)* may be protective in severe infections such as pneumonia and early sepsis inflammasome associated illness by attenuating cytokine levels such as IL-1β and IL-18.

4.4 rs2230911 (C1096G)

The second SNP with a significant association was *rs2230911 (C1096G)*, which causes an amino acid exchange from threonine to serine at position 357 (11). Considering the structure of P2X7R, this amino acid exchange is located in the cytoplasmic juxtamembrane domain. This part of the receptor mediates most of the P2X7R-induced effects, including macropore formation (26, 37). Within the juxtamembrane region, *rs2230911 (C1096G)* lies in a cholesterol recognition amino acid consensus (CRAC) motif (26). Such a region has the potential for interaction with cholesterol (38). For P2X7R, cholesterol decreases ion channel and macropore opening and limits excessive receptor activation (39). Subsequently, *rs2230911 (C1096G)* leads to a reduced functionality of P2X7R in both ion channel and macropore formation (21). Several LOF SNPs individually affect the properties and signaling events of P2X7R depending on their location in the gene. For example, rs2230911 (C1096G) impacts the pore formation of the receptor, which is probably due to its location in the C-terminus (21).

In addition to the above-described location in the CRAC motif, *rs2230911 (C1096G)* is part of a threonine-serine cluster (357 TYSS 360) which has been postulated to be a potential binding motif for β-arrestin-2. This binding would lead to the internalization of the receptor which is equivalent to its degradation and inactivation (40). In the SNP association analysis, heterozygous mutation carriers for *rs2230911 (C1096G)* had a higher occurrence of pneumonia and sepsis.

Previously published reports showed a detrimental effect of the SNP in the context of various pathologies and patients carrying rs2230911 (C1096G) may be prone to develop severe infections due to predisposing comorbidities. The minor allele of *rs2230911 (C1096G)* was linked to several comorbidities including gout, hyperglycemia with an additional risk of progression to diabetes mellitus or metabolic syndrome (41), and obesity (42). Similarly, in acute mycobacterial infection, effective killing of pathogens was only possible in the presence of a well-functioning P2X7R in the absence of the *rs2230911 (C1096G)* mutation (21). These findings suggest that carrying the LOF variant *rs2230911 (C1096G)* increases the risk of developing mycobacterial infections and may be also associated with decreased clearance of lung pathogens.

4.5 *rs3751142 (G1628T)*

In this study, two synonymous SNPs showed statistically significant results for the clinical endpoints pneumonia and/or sepsis. Although the MAF of the whole cohort was consistent with published allele frequencies (Table 2), patients who were septic or had pneumonia had significantly higher MAF than the respective control cohorts (Table 4). This could be a consequence of LD with functionally relevant non-synonymous SNPs. In this cohort *rs3751142 (G1628T)* is in complete LD with the non-synonymous LOF SNP *rs2230911 (C1096G)*. Although synonymous SNPs do not lead to amino acid substitutions, changes in the nucleotide sequence of messenger ribonucleic acid (mRNA) can alter protein expression levels, protein isoform expression or protein folding (43).

The *rs3751142 (G1628T)* SNP is in exon 13 at an exonic splice enhancer site and may cause exon skipping or decrease mRNA stability leading to nonsense-mediated mRNA decay (24, 26, 44). The results presented here indicate that the sepsis cohort carried more heterozygous genotypes, and the cohort of patients suffering from sepsis plus pneumonia had the highest proportion of heterozygous and homozygously mutated genotypes at this RNA stability related SNP position. According to dbSNP *rs3751142 (G1628T)* (http://www.ncbi.nlm.nih.gov/SNP/snp_ref. cgi?locusId05027), has a MAF of 0.089, which is slightly higher in a Korean healthy donor cohort (45). Accordingly, SNP variation is low in non-septic patients, increased in patients with sepsis and

septic shock, but further increased in patients with pneumonia (both sepsis and septic shock pneumonia patients).

As a relevant observation of P2X7R in sepsis, a recent study addressed the function of P2X7R in patients with early versus late sepsis, and convincingly demonstrated that P2X7R expression is upregulated in the early phase of sepsis. In contrast, in the later phases of sepsis, the P2X7R is released from the membrane and potent immunosuppressive signaling driven by the ATP degradation product adenosine is more prevalent (16). Then, non-functional P2X7R associated with *rs2230911 (C1096G)* and *rs3751142 (G1628T)* might predispose to an increased risk of pneumonia. One reason could be that P2X7R plays an important role in the lung microenvironment, such as in the paracrine regulation of surfactant exocytosis by P2X7R-positive type I alveolar epithelial cells. This is critical for the protection of alveolar barrier and fluid homeostasis (46). Thus, a functioning P2X7R may be protective in the lung, allowing ATP-inducible cytokine release, clearance of non-opsonized particles and pathogens, and promotion of immunity. Therefore, in cases at risk of pneumonia, the organ specific function of P2X7R requires higher functionality, increased and stable expression densities, that is in part provided by GOF SNPs. This would not interfere with a second signal from lung infecting pathogens and allow ATP-induced calcium influx to stimulate inflammasome activation in alveolar epithelial cells and antigen presenting cells to promote immunity. Thus, tissue localization and regulation of expression by polymorphisms in miRNA-based regulatory events (47) play an important role in coordinating inflammation and immunity.

4.6 *rs1621388 (G1772A)*

The major variant G of rs1621388 (G1772A) had a higher prevalence in sepsis cases in Model 2. The SNP r*s1621388 (G1772A)* is a synonymous SNP, that is in LD with the GOF SNP *rs1718119 (G1068A)*. The *rs1621388 (G1772A)* SNP is located at an exonic splice enhancer site but is also part of the codon for proline 582 located in an LPS binding domain in the C-terminus of P2X7R (44). Binding of LPS has been shown to lower the pore opening threshold of P2X7R (48). It is conceivable that changes in codon usage could change protein folding, altering the LPS binding site. Further investigation of the role of synonymous SNPs in P2X7R function is required to prove their functional and disease-associated properties. But it can be hypothesized that this SNP results in a GOF phenotype by lowering the threshold of P2X7R activation through the binding of endotoxin and its interaction with lipopolysaccharide binding protein (LBP) and bacterial permeability increasing protein (BPI) in the C-terminal region (44).

Future studies should address the selective contribution of gram-negative versus gram-positive bacteria for the development of sepsis in SNP *rs1621388 (G1772A)* genotypes, especially since this SNP is in LD with the GOF SNP *rs1718119 (G1068A)*.

rs1718119 (G1068A) has previously been shown to increase inflammasome activation through P2X7R activation (11). The trend observation of likely inferior P2X7R activation and signaling in patients with sepsis, septic shock with and without pneumonia should be noted.

4.7 Previously identified *P2RX7* genotypes

Combination SNP analysis in the current study did not reveal a statistically significant result. However, several trends emerged: Firstly, patients with *#11111* were 2.6 times more likely to die [p=0.085, OR 2.60 (0.90 - 7.48)]. This SNP combination consists of five wild-type SNPs indicating a highly functional P2X7R. This is linked to high sensitivity to its ligand ATP, pore formation, induction of apoptosis and regulation of phagocytosis (49, 50). Secondly, the combination *#21111* contains a heterozygous mutation of *rs208294 (C489T)* with simultaneous presence of four wild-type SNPs at *rs28360457 (G946A), rs2230912 (A1405G), rs3751143 (A1513C)*, and *rs1653624 (T1729A)*. *#21111* was associated with a 3.1-fold higher incidence of pneumonia [(p=0.054, OR 3.06 (0.94 - 9.89)]. The previously cited study in a large MS patients cohort showed that the calcium influx in variants encoded by the minor allele A of *rs208294 (C489T)*, is 3.82 higher than those encoded by the G allele of this SNP (36).

These results correspond to the highest ion flux linked to genotype #21211, which includes a heterozygous mutation of the GOF SNP *rs208294 (C489T)*, and the partial LOF SNP *rs2230912 (A1405G)* (17). These results are consistent with other studies documenting enhanced receptor function by the *rs208294 (C489T)* polymorphism even in heterozygous individuals (51, 52). This combination showed a tendency to an increased likelihood of patients' survival [p=0.105, OR 0.18 (0.02 - 1.42)].

In addition to trauma and sepsis, chemotherapy of tumors is linked to massive ATP release and P2X7R activation. A recent validation study on functional SNPs and outcome after chemotherapy in colorectal carcinoma showed that the *P2RX7* GOF SNP *rs208294 (C489T)* was associated with worse overall survival (OS) and progression free survival, however the *P2RX7* LOF SNP *rs2230911 (C1096G)* was prognostic and predictive, showing improved OS in patients who received oxaliplatin (53). The heterozygous genotype of the LOF *rs17525809 (T253C)* -TC was shown to be associated with higher expression of the gene than wildtype TT genotype (54).

4.8 Conclusion

In conclusion, this study provides evidence for the functional relevance of P2X7R to combat sepsis and pneumonia, a severe combination of acquired immune deficiency and life threatening infection. A functionally reduced *P2RX7* variant has been identified by the presence of LOF SNPs. Whereas LOF SNPs may be protective against the detrimental effects of hypercytokinemia and excessive systemic inflammation, including neuroinflammation (55, 56), a SNP-defined and well-functioning P2X7R may be necessary and protective for lung infections and pneumonia by supporting ATP-inducible cytokine release, clearance of pathogens, and

promotion of immunity. The LOF SNP *rs17525809 (T253C)*, and synonymous SNP, *rs1621388 (G1772A)*, appear to be linked to a lower OR for both sepsis and pneumonia for the former and sepsis alone for the latter SNP, whereas the LOF SNP *rs2230911 (C1096G)* and synonymous SNP, *rs3751142 (G1628T)*, that is related to exon skipping and splice variant expression are linked to higher OR especially in pneumonia. Further evidence for the relevance of SNP combinations is provided by the identification of a previously reported SNP genotype #21211 [17] which is more frequent in sepsis survivors. To better understand the genetic implications of the P2X7R and identify conditions which improve by blocking or activating P2X7R, functional assays with patient-derived macrophages may be helpful (57). in addition, the time course of sepsis as a clinical condition is of relevance to appropriately address P2X7R as a therapeutic target (16). Further studies might concentrate on longitudinal observational studies including the documentation of comorbidities as well as early and late states of sepsis, septic shock, the manifestation of acute respiratory distress syndrome, and pneumonia. These clinical states should be characterized by inflammatory biomarkers as well as levels of plasma ATP, soluble P2X7R and sCD14 including functional immune capacity tests.

4.9 Limitations of the study

The study results are to be interpreted in the context of several limitations, which were mostly of a structural type. Above all, the sample size of n = 105 patients limited the creation of subgroups described by more detailed clinical information. Additionally, the clinical data did not sufficiently include the pre-existing diseases and conditions of the patients despite the critical roles such pre-morbidities play in clinical outcomes (58). In the context of likely different *P2RX7* genotypes linked to functional phenotypes that manifest in sepsis versus successful control of respiratory diseases, a future clinical study should be initiated to selectively compare cases with pneumonia independently from sepsis. A focus of this study should be to document *P2RX7* genotypes, inflammasome activation, and pathogen control. Moreover, future studies need to account for LD between different SNPs and thus differentiate between association and causality of findings.

Despite the above-described limitations, this study provides some evidence on the extent to which genetic variants have a protective or detrimental effect in critically ill patients.

Author's note

According to recent findings: Zorina-Lichtenwalter, K., A. R. Ase, V. Verma, A. I. M. Parra, S. Komarova, A. Khadra, P. Séguéla and L. Diatchenko (2024). "Characterization of Common Genetic Variants in P2RX7 and Their Contribution to Chronic Pain Conditions." The Journal of Pain 25(2): 545-556. P2RX7 GOF and LOF functions and genotypes should be distinguished by their effects on channel opening and pore formation which may require functional assays of SNP-genotyped patients' derived cells and tissues.

Data availability statement

The original contributions presented in the study are publicly available. This data can be found here: https://oparu.uni-ulm.de/items/12deb668-2371-41f6-b77a-115d8af31887.

Ethics statement

The studies involving humans were approved by Ulm University, Ethics committee. The studies were conducted in accordance with the local legislation and institutional requirements. Written informed consent for participation in this study was provided by the participants' legal guardians/next of kin.

Author contributions

JG: Investigation, Writing – original draft. SF: Conceptualization, Funding acquisition, Investigation, Writing – original draft. KS: Methodology, Investigation, Writing – review & editing. BM: Methodology, Writing – review & editing, Project administration. ES: Conceptualization, Methodology, Project administration, Supervision, Writing – original draft.

Funding

The author(s) declare financial support was received for the research, authorship, and/or publication of this article. Genotyping of the current cohort was supported by Nepean Medical Research Foundation Project Grant (2018), entitled: P2X7 genotype and haplotype association study in sepsis and severe influenza. This research was also funded by European Union's Horizon 2020 research VirA (under grant agreement no. 952376, www.vira-twinning.eu).

Acknowledgments

We thank colleagues from the Clinic of Anesthesiology and Intensive Care at Ulm University Hospital for their contribution in study patients' recruitment. Preliminary results are available in a thesis entitled "Polymorphismen des purinergen Rezeptors P2X7 bei Patienten mit Pneumonie, Sepsis und septischem Schock" and available at *https://oparu.uni-ulm.de/xmlui/bitstream/handle/123456789/51076/Diss_Guggemos.pdf?sequence=3&isAllowed=y*.

Conflict of interest

The authors declare that the research was conducted in the absence of any commercial or financial relationships that could be construed as a potential conflict of interest.

Publisher's note

All claims expressed in this article are solely those of the authors and do not necessarily represent those of their affiliated organizations, or those of the publisher, the editors and the reviewers. Any product that may be evaluated in this article, or claim that may be made by its manufacturer, is not guaranteed or endorsed by the publisher.

Supplementary material

The Supplementary Material for this article can be found online at: https://www.frontiersin.org/articles/10.3389/fimmu.2024.1352789/full#supplementary-material

References

1. Burnstock G. P2X ion channel receptors and inflammation. *Purinergic Signal*. (2016) 12:59–67. doi: 10.1007/s11302-015-9493-0

2. Gallucci S, Matzinger P. Danger signals: SOS to the immune system. *Curr Opin Immunol*. (2001) 13:114–9. doi: 10.1016/S0952-7915(00)00191-6.

3. Komalavilas P, Luo W, Guth CM, Jolayemi O, Bartelson RI, Cheung-Flynn J, et al. Vascular surgical stretch injury leads to activation of P2X7 receptors and impaired endothelial function. *PloS One*. (2017) 12:e0188069. doi: 10.1371/journal.pone.0188069.

4. Zhao H, Chen Y, Feng H. P2X7 receptor-associated programmed cell death in the pathophysiology of hemorrhagic stroke. *Curr Neuropharmacology*. (2018) 16:1282–95. doi: 10.2174/1570159X16666180516094500.

5. Singer M, Deutschman CS, Seymour CW, Shankar-Hari M, Annane D, Bauer M, et al. The third international consensus definitions for sepsis and septic shock (Sepsis-3). *JAMA*. (2016) 315:801–10. doi: 10.1001/jama.2016.0287

6. Csóka B, Németh ZH, Törő G, Idzko M, Zech A, Koscsó B, et al. Extracellular ATP protects against sepsis through macrophage P2X7 purinergic receptors by enhancing intracellular bacterial killing. *FASEB J*. (2015) 29:3626–37. doi: 10.1096/fj.15-272450

7. Alarcón-Vila C, Baroja-Mazo A, de Torre-Minguela C, Martínez CM, Martínez-García JJ, Martínez-Banaclocha H, et al. CD14 release induced by P2X7 receptor restricts inflammation and increases survival during sepsis. *Elife*. (2020) 9:e60849. doi: 10.7554/eLife.60849.

8. Fuller SJ, Stokes L, Skarratt KK, Gu BJ, Wiley JS. Genetics of the P2X7 receptor and human disease. *Purinergic Signal*. (2009) 5:257–62. doi: 10.1007/s11302-009-9136-4

9. Gu BJ, Zhang W, Worthington RA, Sluyter R, Dao-Ung P, Petrou S, et al. A Glu-496 to Ala polymorphism leads to loss of function of the human P2X7 receptor. *J Biol Chem*. (2001) 276:11135–42. doi: 10.1074/jbc.M010353200.

10. Smart ML, Gu B, Panchal RG, Wiley J, Cromer B, Williams DA, et al. P2X7 receptor cell surface expression and cytolytic pore formation are regulated by a distal C-terminal region. *J Biol Chem*. (2003) 278:8853–60. doi: 10.1074/jbc.M211094200

11. Stokes L, Fuller SJ, Sluyter R, Skarratt KK, Gu BJ, Wiley JS. Two haplotypes of the P2X7 receptor containing the Ala-348 to Thr polymorphism exhibit a gain-of-function effect and enhanced interleukin-1β secretion. *FASEB J*. (2010) 24:2916–27. doi: 10.1096/fj.09-150862

12. Di Virgilio F, Dal Ben D, Sarti AC, Giuliani AL, Falzoni S. The P2X7 receptor in infection and inflammation. *Immunity*. (2017) 47:15–31. doi: 10.1016/j.immuni.2017.06.020

13. Skarratt KK, Gu BJ, Lovelace MD, Milligan CJ, Stokes L, Glover R, et al. A P2RX7 single nucleotide polymorphism haplotype promotes exon 7 and 8 skipping and disrupts receptor function. *FASEB J*. (2020) 34:3884–901. doi: 10.1096/fj.201901198RR

14. Skarratt KK, Fuller SJ, Sluyter R, Dao-Ung L, Gu BJ, Wiley JS. A 5′ intronic splice site polymorphism leads to a null allele of the P2X7 gene in 1–2% of the Caucasian population. *FEBS Lett*. (2005) 579:2675–8. doi: 10.1016/j.febslet.2005.03.091

15. North RA. Molecular physiology of P2X receptors. *Physiol Rev*. (2002) 82:1013–67. doi: 10.1152/physrev.00015.2002.

16. Martínez-Banaclocha H, García-Palenciano C, Martínez-Alarcón L, Amores-Iniesta J, Martín-Sánchez F, Ercole GA, et al. Purinergic P2X7 receptor expression increases in leukocytes from intra-abdominal septic patients. *Front Immunol*. (2023) 14. doi: 10.3389/fimmu.2023.1297249.

17. Geistlinger J, Du W, Groll J, Liu F, Hoegel J, Foehr KJ, et al. P2RX7 genotype association in severe sepsis identified by a novel Multi-Individual Array for rapid screening and replication of risk SNPs. *Clin Chim Acta*. (2012) 413:39–47. doi: 10.1016/j.cca.2011.05.023

18. Taheri M, Sarani H, Moazeni-Roodi A, Naderi M, Hashemi M. Association between P2X7 polymorphisms and susceptibility to tuberculosis: an updated meta-analysis of case-control studies. *Medicina*. (2019) 55:298. doi: 10.3390/medicina55060298.

19. Roger S, Mei Z-Z, Baldwin JM, Dong L, Bradley H, Baldwin SA, et al. Single nucleotide polymorphisms that were identified in affective mood disorders affect ATP-activated P2X7 receptor functions. *J Psychiatr Res*. (2010) 44:347–55. doi: 10.1016/j.jpsychires.2009.10.005

20. Cabrini G, Falzoni S, Forchap SL, Pellegatti P, Balboni A, Agostini P, et al. A His-155 to Tyr polymorphism confers gain-of-function to the human P2X7 receptor of human leukemic lymphocytes. *J Immunol*. (2005) 175:82–9. doi: 10.4049/jimmunol.175.1.82.

21. Shemon AN, Sluyter R, Fernando SL, Clarke AL, Dao-Ung L-P, Skarratt KK, et al. A thr357 to ser polymorphism in homozygous and compound heterozygous subjects causes absent or reduced P2X7 function and impairs ATP-induced mycobacterial killing by macrophages. *J Biol Chem*. (2006) 281:2079–86. doi: 10.1074/jbc.M507816200

22. Gu BJ, Sluyter R, Skarratt KK, Shemon AN, Dao-Ung L, Fuller SJ, et al. An Arg307 to Gln polymorphism within the ATP-binding site causes loss of function of the human P2X7 receptor. *J Biol Chem*. (2004) 279:31287–95. doi: 10.1074/jbc.M313902200.

23. Denlinger LC, Coursin DB, Schell K, Angelini G, Green DN, Guadarrama AG, et al. Human P2X7 pore function predicts allele linkage disequilibrium. *Clin Chem*. (2006) 52:995–1004. doi: 10.1373/clinchem.2005.065425

24. Gadeock S, Pupovac A, Sluyter V, Spildrejorde M, Sluyter R. P2X7 receptor activation mediates organic cation uptake into human myeloid leukaemic KG-1 cells. *Purinergic Signal*. (2012) 8:669–76. doi: 10.1007/s11302-012-9320-9.

25. Wiley JS, Dao-Ung L, Li C, Shemon AN, Gu BJ, Smart ML, et al. An Ile-568 to Asn polymorphism prevents normal trafficking and function of the human P2X7 receptor. *J Biol Chem*. (2003) 278:17108–13. doi: 10.1074/jbc.M212759200.

26. Kopp R, Krautloher A, Ramírez-Fernández A, Nicke A. P2X7 interactions and signaling - making head or tail of it. *Front Mol Neurosci*. (2019) 12:183. doi: 10.3389/fnmol.2019.00183

27. Broad institute. LD Display. (2022) 2022):.

28. Laurie CC, Doheny KF, Mirel DB, Pugh EW, Bierut LJ, Bhangale T, et al. Quality control and quality assurance in genotypic data for genome-wide association studies. *Genet Epidemiol*. (2010) 34:591–602. doi: 10.1002/gepi.20516

29. Phan L, Jin Y, Zhang H, Quiana W, Shektman E, Shaw D, et al. ALFA: allele frequency aggregator. *National center for biotechnology information, U.S. Natl Library Med*. (2020) 2022.

30. Vincent J-L, Rello J, Marshall J, Silva E, Anzueto A, Martin CD, et al. International study of the prevalence and outcomes of infection in intensive care units. *JAMA*. (2009) 302:2323–9. doi: 10.1001/jama.2009.1754

31. Ning D, Garg K, Mayer B, Schick B, Bracht H, Barth E, et al. Monocyte subtype expression patterns in septic patients with diabetes are distinct from patterns observed in obese patients. *Front Med*. (2023) 9:1026298. doi: 10.3389/fmed.2022.1026298.

32. Buell GN, Talabot F, Gos A, Lorenz J, Lai E, Morris MA, et al. Gene structure and chromosomal localization of the human P2X7 receptor. *Receptors channels*. (1998) 5:347–54.

33. Tao J-H, Cheng M, Tang J-P, Dai X-J, Zhang Y, Li X-P, et al. Single nucleotide polymorphisms associated with P2X7R function regulate the onset of gouty arthritis. *PloS One*. (2017) 12:e0181685. doi: 10.1371/journal.pone.0181685

34. Yang Y-C, Chang T-Y, Chen T-C, Lin W-S, Chang S-C, Lee Y-J. Functional variant of the P2X7 receptor gene is associated with human papillomavirus-16 positive cervical squamous cell carcinoma. *Oncotarget*. (2016) 7:82798–803. doi: 10.18632/oncotarget.v7i50.

35. Coccurello R, Volonté C. P2X7 Receptor in the management of energy homeostasis: implications for obesity, dyslipidemia, and insulin resistance. *Front Endocrinol*. (2020) 11:199. doi: 10.3389/fendo.2020.00199.

36. Oyanguren-Desez O, Rodriguez-Antiguedad A, Villoslada P, Domercq M, Alberdi E, Matute C. Gain-of-function of P2X7 receptor gene variants in multiple sclerosis. *Cell Calcium*. (2011) 50:468–72. doi: 10.1016/j.ceca.2011.08.002

37. Adinolfi E, Cirillo M, Woltersdorf R, Falzoni S, Chiozzi P, Pellegatti P, et al. Trophic activity of a naturally occurring truncated isoform of the P2X7 receptor. *FASEB J*. (2010) 24:3393–404. doi: 10.1096/fj.09-153601.

38. Epand RM. Proteins and cholesterol-rich domains. *Biochim Biophys Acta Biomembr*. (2008) 1778:1576–82. doi: 10.1016/j.bbamem.2008.03.016.

39. Robinson LE, Shridar M, Smith P, Murrell-Lagnado RD. Plasma membrane cholesterol as a regulator of human and rodent P2X7 receptor activation and sensitization. *J Biol Chem*. (2014) 289:31983–94. doi: 10.1074/jbc.M114.574699

40. Feng Y-H, Wang L, Wang Q, Li X, Zeng R, Gorodeski GI. ATP stimulates GRK-3 phosphorylation and β-arrestin-2-dependent internalization of P2X7 receptor. *Am J Physiol Cell Physiol*. (2005) 288:C1342–56. doi: 10.1152/ajpcell.00315.2004.

41. Ying Y, Chen Y, Li Z, Huang H, Gong Q. Investigation into the association between P2RX7 gene polymorphisms and susceptibility to primary gout and hyperuricemia in a Chinese Han male population. *Rheumatol Int*. (2017) 37:571–8. doi: 10.1007/s00296-017-3669-6.

42. Liu X, Rao S, Gong C, Li T, Ding L, Wang S, et al. Purinergic P2X7 receptor functional genetic polymorphisms are associated with the susceptibility to obesity in Chinese postmenopausal women. *Menopause*. (2018) 25:329–35. doi: 10.1097/GME.0000000000000991

43. Hunt R, Sauna ZE, Ambudkar SV, Gottesman MM, Kimchi-Sarfaty C. Silent (Synonymous) SNPs: should we care about them? In: Komar A, editor. *Single Nucleotide Polymorphisms. Methods in Molecular Biology*. Humana Press, Totowa, NJ (2009). p. 23–39.

44. Denlinger LC, Fisette PL, Sommer JA, Watters JJ, Prabhu U, Dubyak GR, et al. Cutting edge: the nucleotide receptor P2X7 contains multiple protein- and lipid-interaction motifs including a potential binding site for bacterial lipopolysaccharide. *J Immunol*. (2001) 167:1871–6. doi: 10.4049/jimmunol.167.4.1871

45. Lee SW, Lee S, Oh DH, Park D, Kim H, Choi JR, et al. Genetic association for P2X7R rs3751142 and CARD8 rs2043211 polymorphisms for susceptibility of gout in Korean men: multi-center study. *J Korean Med Sci*. (2016) 31:1566–70. doi: 10.3346/jkms.2016.31.10.1566.

46. Mishra A, Chintagari NR, Guo Y, Weng T, Su L, Liu L. Purinergic P2X7 receptor regulates lung surfactant secretion in a paracrine manner. *J Cell Sci*. (2011) 124:657–68. doi: 10.1242/jcs.066977.

47. Vereczkei A, Abdul-Rahman O, Halmai Z, Nagy G, Szekely A, Somogyi A, et al. Association of purinergic receptor P2RX7 gene polymorphisms with depression symptoms. *Prog Neuro-Psychopharmacol Biol Psychiatry*. (2019) 92:207–16. doi: 10.1016/j.pnpbp.2019.01.006.

48. Yang D, He Y, Muñoz-Planillo R, Liu Q, Núñez G. Caspase-11 requires the pannexin-1 channel and the purinergic P2X7 pore to mediate pyroptosis and endotoxic shock. *Immunity*. (2015) 43:923–32. doi: 10.1016/j.immuni.2015.10.009

49. Xu S, Lin Y, Liu W, Zhu X, Liu D, Tong M, et al. The P2X7 receptor mediates NLRP3-dependent IL-1β secretion and promotes phagocytosis in the macrophage response to Treponema pallidum. *Int Immunopharmacol*. (2020) 82:106344. doi: 10.1016/j.intimp.2020.106344.

50. Gu BJ, Saunders BM, Jursik C, Wiley JS. The P2X7-nonmuscle myosin membrane complex regulates phagocytosis of nonopsonized particles and bacteria by a pathway attenuated by extracellular ATP. *Blood J Am Soc Hematol*. (2010) 115:1621–31. doi: 10.1182/blood-2009-11-251744.

51. Wilhelm K, Ganesan J, Müller T, Dürr C, Grimm M, Beilhack A, et al. Graft-versus-host disease is enhanced by extracellular ATP activating P2X7R. *Nat Med*. (2010) 16:1434–8. doi: 10.1038/nm.2242

52. Pellegatti P, Raffaghello L, Bianchi G, Piccardi F, Pistoia V, Di Virgilio F. Increased level of extracellular ATP at tumor sites: *in vivo* imaging with plasma membrane luciferase. *PloS One*. (2008) 3:e2599. doi: 10.1371/journal.pone.0002599

53. Park HA, Seibold P, Edelmann D, Benner A, Canzian F, Alwers E, et al. Validation of genetic markers associated with survival in colorectal cancer patients treated with oxaliplatin-based chemotherapy. *Cancer epidemiology Biomarkers Prev*. (2022) 31:352–61. doi: 10.1158/1055-9965.EPI-21-0814.

54. GTEx Consortium, Ardlie KG, Deluca DS, Segrè AV, Sullivan TJ, Young TR, et al. The Genotype-Tissue Expression (GTEx) pilot analysis: multitissue gene regulation in humans. *Science*. (2015) 348:648–60. doi: 10.1126/science.1262110

55. Martínez-García JJ, Martínez-Banaclocha H, Angosto-Bazarra D, de Torre-Minguela C, Baroja-Mazo A, Alarcón-Vila C, et al. P2X7 receptor induces mitochondrial failure in monocytes and compromises NLRP3 inflammasome activation during sepsis. *Nat Commun*. (2019) 10:2711. doi: 10.1038/s41467-019-10626-x

56. Alves VS, da Silva JP, Rodrigues FC, Araújo SMB, Gouvêa AL, Leite-Aguiar R, et al. P2X7 receptor contributes to long-term neuroinflammation and cognitive impairment in sepsis-surviving mice. *Front Pharmacol*. (2023) 14. doi: 10.3389/fphar.2023.1179723.

57. Schneider ME, Vorlaender K, Ma X, Du W, Weiss M. Role of ATP in trauma-associated cytokine release and apoptosis by P2X7 ion channel stimulation. *Ann New York Acad Sci*. (2006) 1090:245–52. doi: 10.1196/annals.1378.027

58. Iskander KN, Osuchowski MF, Stearns-Kurosawa DJ, Kurosawa S, Stepien D, Valentine C, et al. Sepsis: multiple abnormalities, heterogeneous responses, and evolving understanding. *Physiol Rev*. (2013) 93:1247–88. doi: 10.1152/physrev.00037.2012.

Frontiers in Immunology

Explores novel approaches and diagnoses to treat immune disorders.

The official journal of the International Union of Immunological Societies (IUIS) and the most cited in its field, leading the way for research across basic, translational and clinical immunology.

Discover the latest Research Topics

See more →

Frontiers

Avenue du Tribunal-Fédéral 34
1005 Lausanne, Switzerland
frontiersin.org

Contact us

+41 (0)21 510 17 00
frontiersin.org/about/contact